University of Wollongong
Research Online

University of Wollongong Thesis Collection 2017+ University of Wollongong Thesis Collections

2018

Geoarchaeology of the Soa Basin, Flores, Indonesia: New considerations on stratigraphy, chronology and palaeoenvironment

Ruly Setiawan
University of Wollongong

UNIVERSITY OF WOLLONGONG

COPYRIGHT WARNING

You may print or download ONE copy of this document for the purpose of your own research or study. The University does not authorise you to copy, communicate or otherwise make available electronically to any other person any copyright material contained on this site. You are reminded of the following:

This work is copyright. Apart from any use permitted under the Copyright Act 1968, no part of this work may be reproduced by any process, nor may any other exclusive right be exercised, without the permission of the author.

Copyright owners are entitled to take legal action against persons who infringe their copyright. A reproduction of material that is protected by copyright may be a copyright infringement. A court may impose penalties and award damages in relation to offences and infringements relating to copyright material. Higher penalties may apply, and higher damages may be awarded, for offences and infringements involving the conversion of material into digital or electronic form.

Unless otherwise indicated, the views expressed in this thesis are those of the author and do not necessarily represent the views of the University of Wollongong.

Recommended Citation

Setiawan, Ruly, Geoarchaeology of the Soa Basin, Flores, Indonesia: New considerations on stratigraphy, chronology and palaeoenvironment, Doctor of Philosophy thesis, School of Earth, Atmospheric and Life Sciences, University of Wollongong, 2018. https://ro.uow.edu.au/theses1/506

Research Online is the open access institutional repository for the University of Wollongong. For further information contact the UOW Library: research-pubs@uow.edu.au

Geoarchaeology of the Soa Basin, Flores, Indonesia: New considerations on stratigraphy, chronology and palaeoenvironment

A thesis submitted in fulfilment of the requirements for the award of the degree

Doctor of Philosophy

from

University of Wollongong

by

Ruly Setiawan

B.Sc (Hons Geological Engineering) Gadjah Mada University

Centre for Archaeological Science
School of Earth, Atmospheric and Life Sciences
Faculty of Science, Medicine and Health

2018

Certification

I, Ruly Setiawan, declare that this thesis, submitted in fulfilment of the requirements for the award of Doctor of Philosophy, in the School of Earth, Atmospheric and Life Sciences, University of Wollongong, is wholly my own work unless otherwise referenced or acknowledged. The document has not been submitted for qualifications at any other academic institution.

Ruly Setiawan

June 2018

ABSTRACT

The Soa Basin, Flores contains abundant assemblages of stone tools and fossil remains, which occurred between Early Pleistocene and Middle Pleistocene. This study has used an interdisciplinary approach, integrating field and laboratory analyses, to examine geoarchaeological archives of the Soa Basin. Since the stratigraphic framework was still problematic, this study performed detailed investigations on temporal and spatial distributions of the lithological units by using lithofacies analysis and tephrostratigraphy that are combined with the $^{40}Ar/^{39}Ar$ dating technique to obtain reliable ages and establishing a new chrono-stratigraphical framework.

The tephra records and additional chronological data demonstrate new considerations with regard to stratigraphic positions and the time of accumulation of artifacts and fossils and also permit a correlation of several important archaeological and/or palaeontological sites. The oldest Ola Kile Formation contains two pyroclastic density current (PDC) deposits, the Aesessa Ignimbrite (AEI) and Lowo Mali Ignimbrite (LMI), representing two major events of caldera-forming processes, derived from the Welas Caldera Complex (WCC) and the Keli Lambo Volcanic Complex (KLVC), respectively.

The lower part of the Tuff Member comprises four distal tephra-fall units, which belong to the Tangi Talo Tephra (TTl-T1, TTL-T2, TTL-T4 and TTL-T5), while the upper part of the Tuff Member constitutes three PDC deposits, including the Wolo Sege Ignimbrite (WSI), Turekeo Ignimbrite (TRI) and Pumaso Tephra (PMS), and a chemically unique tephra-fall deposit named Kopowatu Tephra (KPW).

The single grain $^{40}Ar/^{39}Ar$ dating method has been applied to plagioclase crystal from TTL-T5 and on hornblende crystals from PMS, which yielded ages of 1.27±0.03 Ma and 0.81±0.04 Ma, respectively. In addition, fission track methods dated the KPW at 0.90±0.07 Ma. These dated pyroclastic deposits can be placed in the global climate perspective, which TTL-T5, WSI and PMS are good

isochronous layers underpin volcanic eruptions that were occurred during MIS 39-38, MIS 29-28 and MIS 21-20, respectively. The youngest tephra succession of the Ola Bula Formation is well- preserved in the lacustrine succession of the Limestone Member, named as the Piga Tephra (PGT). The PGT from the lowermost part of the Limestone Member sequence has been dated at 0.65±0.02 Ma ago, which is ascribed to MIS 17-16.

The geochemical data indicate that pyroclastic deposits of the Tuff Member were derived from at least four volcanoes. The Keli Lambo Volcanic Complex (KLVC) is the major volcano depositing five pyroclastic units, TTL-T2, TTL-T5, WSI, TRI and PMS. Another distal ash, the KPW, is characterised by a very high potassium content, and has a geochemical similarity with the oldest Toba Tuff (OTT). This KPW possibly originated from the Toba volcano, ~3000 km to the west of the Soa Basin. However, the possibility of another, unknown high-K source cannot be excluded. According to the discrimination diagrams of CaO, ΣFeO and K_2O contents of glass shards, the sources of TTL-T1 and WLW are informally given as Volcano "Z", while the TTL-T4 is designated as Volcano "X". With respect to TTL-T2, this tephra can be derived from either the KLVC or Volcano "Z".

By using detailed lithofacies analysis in several stratigraphic columns, this study has added new information about lithological variation of the Ola Bula Formation and improved the general stratigraphy of the Soa Basin. The oldest formation of the basin, the Ola Kile Formation, consists of primary volcaniclastic deposits (FA–I), lahar deposits (FA–IV), channel deposits (FA–V), palaeosols (FA–IX) and localised effusive volcanic bodies (FA–III). The Ola Kile Formation has a total thickness of 100–200 m and was deposited until 1.86 Ma in a terrestrial (fluvial) environment.

The Ola Kile Formation is overlain by the Ola Bula Formation and the contact between these two formations indicates an angular unconformity. The overall Ola Bula sequence is relatively horizontal and the total thickness is *ca*. 100–120 m. The lowermost Member of the Ola Bula Formation, The Tuff Member, consists of (in descending abundance order) palaeosols (FA IX), primary

volcaniclastics (FA–I), resedimented volcaniclastics (FA–II), laharic deposits (FA–IV), channel deposits (FA–V), and locally floodplain deposits (FA–VII). The Tuff Member was deposited between 1.86 Ma and 0.81 Ma in a fluvial setting and has ~50–60 m of maximum thickness.

The Sandstone Member of the Ola Bula Formation conformably overlies the Tuff Member but there is no sharp transition between these two members. This member predominantly consists of channel deposits (FA–V) and palaeosols (FA–IX), with minor pyroclastic deposits (FA–I), lahars (FA–IV), sheet flood (FA–VI) and floodplain facies (FA–VII). The majority of sediments, with a total thickness of ~20–30 m, were deposited in a fluvial environment during a period between 0.81 Ma and 0.65 Ma.

The youngest member of the Ola Bula Formation, the Limestone Member, has a thickness of up to 10 m and comprises an interbedding of micritic limestones, claystones and basaltic–rhyolitic pyroclastic tephra-fall deposits. This Limestone Member lies conformably above the Sandstone Member. Sediments of the Limestone Member were deposited in a lacustrine environment, which developed since ~0.65 Ma ago.

Fossil assemblages occur in the lower part of the Tuff Member and throughout the Sandstone Member of the Ola Bula Formation, and are absent from the Ola Kile Formation and the Limestone Member of the Ola Bula Formation. On the other hand, stone artifacts occur in the upper part of the Tuff Member throughout the Sandstone Member.

In the Tuff Member, two main fossil layers have been documented. The oldest fossil beds that contain pygmy stegodon, giant turtle, crocodile, and Komodo dragon are only found at Tangi Talo and no artifacts have been recovered from this site. All fossils accumulated in clay-rich laharic deposits, dated at ~1.42 Ma and situated ~2 m below TTL-T5, which has an age of ~1.27 Ma. This study has securely defined the timing of the faunal turnover, which occurred c. 400,000 years earlier than previously envisaged. Other artifact-bearing layers of the Tuff Member are well-preserved at Wolosege and Kobatuwa, both situated in the uppermost part

of this member, and at Kobatuwa the stone artifacts are associated with fossil vertebrate remains, recovered directly below and above the Wolo Sege Ignimbrite, dated at ~1.02 Ma. There was a considerably gap in the fossil and archaeological record for the period between 1.27 Ma and 1.02 Ma.

In the Sandstone Member, fossil bones and stone tools are mostly concentrated in the lower and middle parts, bracketed by the Pumaso Tephra (PMS) and the Mata Menge Tephra (MMT). Fossil and artifact-bearing layers were discovered at a level ~5 m below MMT and ~12 m below the Piga Tephra 02 (PGT-02) dated at 0.65 Ma. Hominins and animals may have survived in the Soa Basin at ~810–700 ka ago during a time interval of decreasing volcanic events.

Laboratory-based studies were conducted to determine the geochemical and mineralogical compositions of sediments and volcaniclastic deposits and their vertical changes throughout the studied sections. These approaches were applied to reconstruct the palaeoenvironmental settings and climatic changes in the Soa Basin during the Pleistocene. The climatic conditions at between ~1.5 Ma and 1.0 Ma were characteristic for a warm, sub-humid to dry tropical climate, alternating with wetter periods. The past climatic conditions changed to drier and colder around 1.0 Ma, as indicated by a well-developed pedogenic horizon with desiccation structures.

Environmental and climatic settings between ~1.0 Ma and 0.70 Ma reflect a warm and humid tropical climate. A period of drier and cooler conditions is represented during the interval ~15.0–18.0 m that is *ca.* 0.80 Ma ago. In the period between ~0.80 Ma and 0.65 Ma, the calculated variables indicate a warm to hot tropical climate, with alternating dry and wet conditions (monsoonal). A lacustrine environment developed in the entire Soa Basin since ~0.65 Ma ago, corresponding with the interglacial of MIS 17. The climatic setting then remained warm and humid. However, the pollen records suggest evidence that the lake basin has experienced episodes of drying in which lake levels were shallowing.

ACKNOWLEDGEMENTS

I would like to express my gratitude to my supervisors, Prof. Mike Morwood (deceased), Prof. Allan Chivas and Dr. Gert van den Bergh, for their support, patience and professional guidance throughout my candidature and research. Their assistance, intensive support and valuable advice within all aspects of preparation, research, analyses and thesis manuscript are very much appreciated. I also wish to acknowledge for their understanding regarding some aspects of my life that had given an impact on the progress of my thesis. I am deeply indebted to Prof. Mike Morwood and Prof. Fachroel Aziz for providing and encouraging this research and also have shown me about the big picture of hominin evolution since before I commenced my candidature.

I specially acknowledge the following institutions: University of Wollongong (for a University Postgraduate Award scholarship and International Postgraduate Tuition Award scholarship), Centre for Geological Survey-Indonesia (for permit and support during fieldwork), Australian Research Council (for fieldwork and laboratory supports through Discovery Grant "In Search of the first Asian hominins"), QUADLab-Denmark (for processing the argon-argon samples) and Victoria University of Wellington-New Zealand (for facilitating EPMA).

A special thank goes to Assoc. Prof. Brent V. Alloway (Victoria University of Wellington, New Zealand)) for introducing "tephrochronology", help with EPMA and data collection, scientific discussion during fieldwork and research, and constructive comments to this thesis. Prof. Michael Storey and Dr. Stephanie Flude (QUADLab, Denmark) are greatly thanked for valuable argon-argon data and discussions in the field. I would like to acknowledge Assoc. Prof. Paul Carr and Mr. José Abrantes for their assistance with XRF preparation and data collection. Assoc. Prof. Brian Jones is specially thanked for discussion in the field and XRD interpretation. I thank to Dr. Adam Brumm for support and discussion on Archaeology-related topics in the field.

I wish to thank my colleagues: Iwan Kurniawan (Museum Geologi) and Yayan Sopyan (Centre for Geological Survey) for their support and helps during fieldwork. I am grateful for companionship and fruitful discussions of the Indonesian postgraduate students (Dida Yurnaldi, Thomas Sutikna and Mika Puspaningrum). I also thank to other postgraduate students who occupied Room 167 for the positive environment.

Finally, I cannot express how grateful I am to my parent and family, for their patience, support, care and understanding.

I dedicated this research to my father (deceased), Mike (deceased) and my whole family.

TABLE OF CONTENTS

LIST OF FIGURES

a massive structure, is silty-sandy, and represents distal pyroclastic fall deposits (pencil as scale, 14 cm length). (D) Field characteristics of facies Tms, Tmp, Tma and LTmp, which are well-exposed at Wolo Sege (8°41’27.1”S; 121°06’00.0”E). Facies Tms and Tmp formed predominantly by turbulence of a pyroclastic surge. The prominent accretionary lapilli of facies Tma suggests pyroclastic fall deposits produced by a wet eruption. Facies LTmp, pumice-rich, indicates pyroclastic flow deposits (coin diameter is 24 mm).

LIST OF TABLES

LIST OF ABBREVIATIONS AND SYMBOLS

Quaternary

Ar/Ar	Argon-argon
ITCZ	Inter-tropical convergence zone
ITPFT	Isothermal plateau fission track
Ka	Thousand years (1 ka = 1,000 years)
K-Ar	Potasium argon
Ma	Million years (1 Ma = 1,000,000 years)
MIS	Marine isotope stage
OTT	Oldest Toba Tuff

Stratigraphy

AEI	Aesessa ignimbrite
FA	Facies association
Fm	Formation
KLP	Kolopanu tephra
KPW	Kopowatu tephra
KLVC	Keli Lambo Volcanic Complex
LM	Limestone Member
LMI	Lowo Mali ignimbrite
MMT	Mata Menge tephra
NTR	Nata Randang tephra
OK	Ola Kile Formation
PGT	Piga tephra
PMS	Pumaso tephra
SM	Sandstone Member
TM	Tuff Member
TRI	Turekeo ignimbrite
TTL	Tangi Talo tephra
WCC	Welas Caldera Complex
WLB	Wulabara tephra
WLW	Wolowawo tephra
WSI	Wolo Sege ignimbrite

Geochemistry

CIA	Chemical index alteration
EPMA	Electron probe micro analysis
HFSE	High field strength elements
LILE	Large ion lithopile
LREE	Light rare earth elements
n.d	Not determined
NMORB	Normal mid-ocean ridge basalt
PAAS	Post Archean Australian shale
PIA	Plagioclase index alteration
ppm	Parts per million
RGM	Rhyollite Glass Mountain
TTE	Transition trace elements
UCC	Upper continental crust
wt %	Weight percent
XRF	X-ray fluorescence

Mineralogy

Amp	Amphibole
Bt	Biotite
Cal	Calcite
Cbz	Chabazite
Chl	Chlorite
Cpt	Clinoptilolite
Cpx	Clinopyroxene
Hem	Hematite
Hly	Halloysite
Hul	Heulandite
Ilt	Illite
Kfs	K-feldspar
Kln	Kaolinite
I/S	Illite – smectite mixed-layer
Mgh	Maghemite
Ms	Muscovite
Opx	Orthopyroxene
Pl	Plagioclase
Qz	Quartz
S/C	Smectite – chlorite mixed-layer

Sme	Smectite
Stb	Stilbite
XRD	X-ray diffraction

Symbols

%	Parts per hundred
±	An error margin (plus and minus)

Others

c.	(Circa) about
cm	Centimetre (1 cm= 10^{-2} metre)
E	East
mm	Millimetre (1 mm= 10^{-3} metre)
m	Metre (1 m= 100 cm, 1000 mm)
NE	Northeast
NW	Northwest
S	South
SW	Southwest
W	West
yr	Year

CHAPTER ONE
INTRODUCTION

This thesis, titled "*Geoarchaeology of the Soa Basin, Flores, Indonesia: New Considerations on Stratigraphy, Chronology and Palaeoenvironment*", demonstrates the necessity of collaboration between earth and archaeological sciences to address geological questions in archaeological sites. For the past 20 years, geoscience and archaeological science have a prolonged connection as an integrative approach to study prehistoric human antiquities, site formation processes, archaeosedimentary sequences and chronological frameworks (Rapp and Hill, 1998). So much so that, the term *geoarchaeology* has been proposed. Hassan (1979) describes *geoarchaeology* as the contribution from earth sciences to the resolution of geology-related problems in archaeology, including (1) locating archaeological sites, (2) evaluating the geomorphic landscape for site catchment activities and site location, (3) studying regional stratigraphic and microstratigraphic materials for relative dating and recognition of lateral and vertical distribution of activity areas, (4) analyzing sediments for the elucidation of site-forming processes and quantification of microarchaeological (sub-macroscopic) remains, (5) analyzing palaeoenvironments, (6) studying artefacts to determine manufacturing practices, procurement range, trade, and exchange networks, (7) modelling cultural/environmental interactions, (8) conserving archaeological resources, and (9) geochronology.

In the early period of development of archaeology, researchers were primarily concerned with human remains, artefactual materials and their characteristics to understand past hominin behaviours and systems. The scope of archaeology needs other disciplines, particularly earth sciences, which provide the fundamental concepts for understanding archaeological evidence. With

suitable approaches, the dynamic processes within archaeological sites can be recognized, archaeosedimentary features can be observed, palaeoenvironmental conditions can be inferred and the timing of archaeological sequences can be estimated.

Archaeological evidence is mute, in fact archaeologists cannot interpret artefacts and their distributional pattern in terms of cultural or settlement behaviours without understanding site formation processes. *In situ* artefacts considered as primary origin can be influenced by geological processes and should be conceived as having secondary contexts. Artefactual deposits can be transported, eroded, weathered and redeposited in certain environments. Studying the formation of sediments and/or (buried) soils that affect archaeological records is crucial, and supplementary methods to complement the interpretation of sediment/soil occurrences are also essential.

Archaeological archives also provide information on the interaction between human activities and landscape (habitat). The distribution of archaeological evidence tends to reflect the distribution of important resources across the landscape (e.g. food, water, shelter). The characteristics of landscapes, therefore, provide an environmental framework for human activities. Assessing the correlation between landscape features and the distribution of evidence for past human activities forms a significant part of archaeological and/or palaeontological studies. Furthermore, estimating the timing of formation processes associated with archaeological deposits is also a primary task.

Sedimentary features generated by natural processes provide a spatial framework within archaeological sites, while the age of geological deposits and/or archaeological materials will contribute to establish a temporal framework. Collaboration of these two approaches ascertains the entire archaeological sequence. Although direct dating of the fossil materials and artefacts commonly raises particular problems, relative age estimation using

lithostratigraphy, tephrostratigraphy or biostratigraphy can be considered. The principle of stratigraphic methods has been applied to delineate the relationships of artefacts, fossil remains and sediments into historical context (Rapp and Hill, 2006). The fundamentals of stratigraphic law, i.e. 1) original horizontality, 2) lateral distribution, 3) superposition, 4) cross cutting relationships and 5) law of faunal succession, combined with uniformitarian principles, are pivotal tools to understand archaeological records spatially and temporally.

Following Hassan (1979), my research will apply an earth science perspective and methods to establish a chronostratigraphical framework and document the associated environmental changes in the Soa Basin of Flores in the eastern part of Indonesia. Similar studies in Africa have provided good case studies. Work by Stollhofen *et al*. (2008), Blumenschine *et al*. (2012), McHenry (2012), Stanistreet (2012) and Stollhofen and Stanistreet (2012) at Olduvai Gorge, Tanzania, all show the strength of geoarchaeological approaches in archaeological research by documenting the natural processes of deposition, preservation and erosion (taphonomy), the formation of landscape features and changes in palaeoenvironmental conditions, as well as providing a time frame.

Geoarchaeological approaches will be applied to the important archaeological sites in the Soa Basin. Located between the Asian mainland and the Australian continent, Flores has the potential to preserve archaeological evidence of major importance. On the island of Java to the west of Flores, archaeological and palaeoanthropological research has been carried out since the nineteenth century and the findings have made major contributions to world archaeology, palaeoanthropology, hominin evolution, the timing of modern human dispersal and the faunal sequence (Watanabe and Kadar, 1985; Swisher *et al*., 1994; van den Bergh, 1999; Morwood *et al*., 2004, 2005; Westaway *et al*., 2007b).

In contrast to Java, limited archaeological work has occurred in the eastern part of Indonesia. Research in this area only really commenced since the 1950s. However, as in Java, preliminary research projects obtained significant archaeological and palaeontological findings, particularly in the Soa Basin of Central Flores, Liang Bua cave in Western Flores and Timor Island. The intramontane Soa Basin contains abundant assemblages of stone tools and fossil remains occurring in Early to Middle Pleistocene layers (Morwood *et al.,* 1998; Brumm and Moore, 2006; van den Bergh *et al.,* 2009a; Brumm *et al.,* 2010). Previous work has focused on examinations of archaeological and palaeontological materials, site sequences and chronologies. However, in all these examples, problems remain in establishing the depositional history of sites, inter-site correlations, their environmental context and their age, as well as obtaining evidence for palaeoclimatic changes.

This research aimed to explore the geoarchaeological archives of the Soa Basin, Flores, in order to better understand the fauna, hominin and cultural evolution. The objective of this study was specifically to 1) identify, characterize and correlate sedimentary units through the basin sequence to infer depositional environments and their temporal and spatial changes; 2) apply numerical dating techniques to obtain a time frame for archaeological and palaeontological finds, and 3) combine stratigraphical, chronological and palaeoenvironmental records to understand the history of archaeological and faunal occurrences.

This study has focused on several geoarchaelogical approaches, an overview of which is given in Chapter 2. Chapter 3 provides details and context of the study area, the So'a Basin on Flores. The used methodology is described in Chapter 4. The description and geochemistry of tephra units observed and sampled in the field, and their intra-basinal correlations based on these observations and chemical analyses, is described in Chapter 5. Chapter 6 provides a stratigraphic framework of the basin using the new tephrochronology,

and places the various fossil and archaeological sites in a temporal sequence. This chapter also provides a thorough sedimentary facies description and palaeoenvironmental reconstruction of the basin. Chapter 7 discusses the implications for palaeoclimate, provenance and weathering characteristics.

These outcomes will bring new evidence and understanding about geological processes and the occurrence of fossil fauna and archaeological materials in the Soa Basin.

CHAPTER TWO
AN OVERVIEW OF GEOARCHAEOLOGICAL APPROACHES

2.1. Introduction

Chapter One described the background and aims of the research. The main objective of my study is to apply geological techniques to resolve geoarchaeological problems in archaeological sites. This chapter will briefly highlight the principles and application of geological methods and provide several examples from important archaeological sites worldwide. The case study site, the Soa Basin, is a volcanic depression that contains archaeological and palaeontological materials deposited during the Early to Middle Pleistocene.

The geoarchaeological approaches highlighted in this chapter are examples in which earth science techniques have been used in archaeological and palaeontological research in Africa and Southeast Asia. The approaches have been selected on the basis of relevance to my study.

This chapter begins with an outline of methods for identifying strata or horizons. It will then provide a review of depositional environments of geological and/or archaeological deposits, followed by a brief description of methods used to estimate the age of archaeological sequences. Finally, a summary will be presented in the final part of this chapter.

2.2. Stratigraphy: Fundamentals and Application in Archaeological Sites

Stratigraphy is defined as a discipline in the earth sciences with the objective to record strata/layers in order and considering the thickness and description of lithology (Pettijhon, 1975). Stratigraphy deals with all aspects of rocks in a time framework (Nicholls, 2009). In archaeological context, the concept of stratigraphy is used to assess the relationships between sediments and archaeological deposits and to estimate the spatial and temporal distribution of artefact-bearing layers (Rapp and Hill, 2006). The field of

stratigraphy encompasses a number of subfields as described below.

2.2.1. Lithostratigraphy

Lithostratigraphy tends to be a fundamental approach to determine relative time of deposition of archaeological deposits. Lithostratigraphy is defined as a subdiscipline of stratigraphy based on physical characteristics of rocks that can be observed macroscopically, including colour, texture, composition, thickness and geometric boundaries between upper and lower layers, with consideration of their relative stratigraphic positions (Nicholls, 2009; Boggs, 2010). The basic lithostratigraphic unit is the **formation**, which is a distinctive body of sedimentary rock that can be mapped on the surface or subsurface and is laterally traceable (Boggs, 2006). A formation may comprise single and/or multiple types of lithologies and can be defined by considering lithological composition, texture, sedimentary structures and fossil content (Nicholls, 2009). A formation can be divided into **members**, which represent rock bodies of limited lateral extent and with distinct lithological properties within a formation, while the smallest units are called **beds** (Nicholls, 2009; Boggs, 2010).

The principle of lithostratigraphic unit in the archaeological sequence generally follows the law of stratigraphy, i.e. superposition, cross cutting relationships and original horizontality. The law of superposition states that in a stratigraphic column, the lower layer is older than the upper (overlaying) layer (Nicholls, 2009). The artefacts incorporated in the lower layer occur in the older position than in the uppermost horizon. Meanwhile, the law of cross cutting relationship states that a layer cutting across other layers will be younger than the horizons it cuts. Stone artefact assemblages incorporated within channel sediment that truncates underlying palaeosols are deposited later and occupy younger strata in the stratigraphic section. Furthermore, without any disturbance, e.g. tectonic forces, sediment layers will be deposited in horizontal or nearly horizontal beds. Faulting of the artefacts-bearing layer can place the artefact unit slightly tilted to, in rare cases, completely overturned. To avoid

misleading information on the recognition of a stratigraphic unit, it is necessary to determine the pattern of younging order (upward) in the sequence (Nicholls, 2009). By using this stratigraphic law, it will be possible to predict the relative time occurrence of archaeological deposits directly in archaeological sites.

Lithostratigraphy commonly deals with sediments, palaeosols (see subchapter 2.2.2 for details) and tephra deposits (see subchapter 2.2.4 for details). Sediments can be described in the field based on their grain size (Wentworth Scale), such as claystone, siltstone, sandstone *etc*. In the Quaternary context, sediments can be unconsolidated or consolidated materials. Sediments can be divided as clastic and non-clastic sediments. Clastic sediments refer to terrigeneous materials (e.g. conglomerate, sandstone, siltstone, shale) and volcaniclastics (e.g. lapilli, blocks, bombs, ash). While non-clastic sediments include chemical sediments (e.g. carbonate) and oraganic-rich sedimentary deposits (e.g. peat, coal).

An example of the application of lithostratigraphy is provided by a well-known archaeological site in Olduvai Gorge, Tanzania. Recent work by Blumenschine *et al*. (2012) yielded a comprehensive lithostratigraphic framework and palaeoenvironmental reconstruction. Excavation at FLK and FLK NN recovered large assemblages of stone artefacts and the holotype of *Paranthropus boisei*, then known as *Zinjanthropus* (Leakey 1959, cited in Blumenschine *et al*., 2012), dated at 1.845 – 1.839 Ma (Blumenschine *et al*., 2003). Blumenschine *et al*. (2012) identified the land surface as a living floor, occupied by hominids before a volcanic eruption.

2.2.2. Pedostratigraphy

Pedostratigraphy is the study of modern and ancient soils spatially and temporally. Soils are the product of post-depositional processes, such as weathering and alteration, processes that are influenced by the characteristics of parent materials, organisms, landscape, climate and time (Rapp and Hill, 2006).

In the Quaternary, research in pedostratigraphy usually deals with palaeosols, defined as fossil soils that formed in a palaeolandscape. They can be buried, exhumed or remain as relict on the surface (Palmer, 2013). Paleosols represent stable periods in which depositional or erosional processes were slow or absent. Palaeosols have developed to be important tools to ascertain past weathering and pedogenesis, and to reconstruct palaeoclimates and palaeonvironments in broader context. Most common palaeosols include Entisol, Andisol, Inceptisol, Histosol, Vertisol, Aridisol, Alfisol, Ultisol, Oxisol and Spodosol (Mack *et al*., 1993; Retallack, 1993).

Soils can form soil stratigraphic or pedostratigraphic units that need to be defined and described, and their independencies ascertained when deposited through various landscapes (Nettleton *et al*., 2000). Examples of the application of pedostratigraphy in archaeological sites are presented by Potts *et al*. (1999), Wynn (2000) and Bennet *et al*. (2012).

Potts *et al*. (1999) showed the benefit of palaeosols in reconstructing the palaeotopography of hominin habitats. Palaeosol UM1p of the Olorgesailie Formation in Kenya contains large assemblages of bones and stone artefacts. This palaeosol can be traced over 4 km laterally, and suggested the presence of a flat topography with minor channels and depressions. Argon–argon dating of the relevant units provides information on an average sedimentation rate of 0.95 m per thousand years.

Another study by Wynn (2000) combined field characteristics, carbon isotope ratios and measurements of carbonate with depth to estimate the palaeoprecipitation and palaeoecological settings. His research suggested that *Australopithecus anamensis* was able to survive in a dry savannah and open habitat. Similar investigation by Bennet *et al*. (2012) that used qualitative and quantitative analyses on carbonate horizons, provides evidence for palaeoenvironmental instability during a period when *Australopithecus boisei* and *Homo habilis* exploited the ecosystem. The scale of changes in the landscape has influenced the habitat of the hominins. The occurrence of lake flooding

every few thousand years changed the environment, with periodic flooding and withdrawal of the palaeolake affecting the spatial distribution of wetlands, grasslands, and woodlands.

2.2.3. Magnetostratigraphy

The Earth's magnetic field alternates between periods of normal magnetic polarity, which is the field orientation of the present, and reversed magnetic polarity, when the field is reversed, meaning that the 'north' arrow on a magnetic compass would point towards the South Pole. Evidence from measuring the magnetic fields of the past (palaeomagnetism) indicates that these magnetic polarity reversals have occurred at irregular intervals during geological time (Nicholls, 2009). The Matuyama-Brunhes polarity reversal from Reversed to Normal polarity is a well-known chronostratigraphic marker in the Quaternary. However, the age of Matuyama-Brunhes boundary (MBB) has been controversial topics. Several studies yielded different ages of MBB, i.e. 773±1 ka (Channel *et al*., 2010), 770.2±7.3 ka (Suganuma *et al*., 2015) and 783.4±0.6 ka (Mark *et al*., 2017).

The objective of a magnetostratigraphic study is to identify periods of Normal and Reversed magnetic polarity recorded in a rock sequence. Magnetostratigraphy is based on the fact that volcanic rocks and fine-grained sediments preserve the magnetic direction that prevails during their formation. The resulting remanent magnetism of a rock may be generated by a complex mixture of different field orientations resident in different minerals comprising the rock (Nicholls, 2009). The primary magnetic remanence can be affected by chemical weathering process, which can provide a secondary magnetic overprint (Twyman, 2007). Sediments can become magnetised through a process known as post- depositional remanent magnetisation (PDRM), and there is also filtering of the geomagnetic signal (Quidelleur and Valet, 1993).

Magnetic excursions of the Earth's magnetic field during the Quaternary have been used to date events and to correlate the timing of events

around the world, although exceptional local events during the early Quaternary still present a challenge (Twyman, 2007). Palaeomagnetic analysis has been applied to date the holotype of *Australopithecus boisei* that was deposited on Bed I at Olduvai Gorge, Tanzania. Magnetostratigraphic studies have identified a normal polarity interval extending from Lower Bed I through Lower Bed II, and which is now named the Olduvai Subchron, with an age of between 1.945 and 1.778 Ma (Deino, 2012). In Southeast Asia, a detailed magnetostratigraphic analysis has been performed in the Sangiran area, Java, where various *Homo erectus* skulls have been recovered. Lithological sequences of the Bapang Formation display a reverse-to-normal polarity transition and spanned the time interval from 783 ka to 773 ka (Hyodo *et al*., 2011).

2.2.4. Tephrostratigraphy

Tephrostratigraphy is defined as the study of sequences of tephra layers and related deposits and their relative ages. It involves defining, describing, and characterizing tephra sequences using their physical, mineralogical, or geochemical properties and determining the age of tephra units with radiometric or other dating techniques. Tephra may include fall deposits (tephra-fall or tephra fallout) and unconsolidated deposits derived from pyroclastic flows or surges. Tephra can be derived from a very short time period of eruption and/or spread widely over the landscape (Lowe, 2011; Alloway *et al*., 2013; Houghton *et al*., 2015).

Tephra particles range in size from ash (<2 mm) and lapilli (2–64 mm) to blocks (dense, angular) and bombs (vesicular, rounded, >64mm) that may reach several metres in diameter (Cas and Wright, 1987). Densities vary from low-density vesicular pumice and scoria to dense crystals and rock fragments. Materials can be juvenile (formed from magma involved in the eruption) or xenolithic (derived from pre-existing rock or from material beneath the volcano) (Lowe, 2011; Alloway *et al*., 2013; Houghton *et al*., 2015).

The thickness of tephra beds can range from millimetres to

metres depending on the distance from the source. Tephra deposits consist of alternating gradational coarse- to finer-grained layers without sharp bedding in the proximal zone. The upper part of a tephra layer in a terrestrial setting can be weathered and modified by soil-forming processes, then formed in to a palaeosol. Thin (centimetre-thick), distal tephra layers transported by winds over long distances are commonly massive to normal graded and probably affected by bioturbation, soft-sediment deformation, and locally reworked material washing into the site. Lower contacts are generally sharp and planar, whereas the upper contacts can be gradational admixtures of nonvolcanic grains over millimetres to metres up section. Some tephra layers can display tractional sedimentary structures such as trough cross-stratification from reworking in shallow marine and fluvial environments. Tephra can also be deposited in very fine grained layers that are invisible to the naked eye and can only be observed under the microscope. Such tephra deposits are known as cryptotephra (Lowe and Hunt, 2001; Lowe, 2011; Alloway *et al*., 2013).

For correlation purposes, although tephra deposits have different ages, it is essential to determine physical and geochemical properties, to guide detection and identification of the deposits as well as to avoid mistakes in correlating tephras in multiple sequence records. Ferromagnesian mineral assemblages and chemical composition of glass shards can aid in the tracing of source volcanoes and distinguish between individual tephra units in the sequence. Redeposited and/or mixed tephra beds can also be distinguished by glass major-element compositional analysis, which indicates when a glass population most likely represents the mixed products of separate eruptive events (Lowe, 2011; Alloway *et al*., 2013).

Estimating the time of eruption that produced tephra layers can be conducted directly on the materials by applying radiometric dating techniques, for instance fission-track and argon-argon dating. Zircon fission track dating is a common technique; however, problems may arise when dealing with distal tephra units, due to the fine grain size and low abundance of detrital

zircons. Alternatively, dating can be done on volcanic glass by the isothermal plateau fission track (ITPFT) technique. This technique is suitable and reliable for dating rhyolitic distal tephra (Lowe, 2011; Alloway *et al*., 2013; Westgate *et al*., 2013).

The $^{40}Ar/^{39}Ar$ method provides an opportunity to obtain high precision ages on young tephra deposits. Initial $^{40}Ar/^{39}Ar$ studies performed step-heated technique on bulk feldspar and sanidine, and laser fusion analysis on mineral subsamples to obtain age spectra and isochrons. Such studies have shown that an accurate age for some tephra deposits can be assessed only by grain-specific techniques. Because of the small volume of argon, potassium-rich phases are commonly required. This limits its application to calc-alkaline volcanic provenances. Unfortunately, the technique cannot be widely applied to distal tephra beds because of their fine grain size and crystal-poor character (Lowe,2011; Alloway *et al*., 2013).

Indirect dating tephra on the associated materials are also popular if there are no directly datable minerals present. Radiocarbon (^{14}C) dating of charred wood fragments has been the dominant technique for dating tephra layers deposited within the past 50 ka, while thermo-luminescence (TL) or optically stimulated luminescence (OSL) can be an alternative tool to date loess – palaeosol sequences that are interbedded with tephra layers in the time period up to 200 ka (Alloway *et al*., 2013).

Tephrostratigraphy and chronology have been applied to provide ages on early hominins and their activities in eastern Africa and Asia (Feibel, 1999; Larick *et al*., 2001; Tryon and McBrearty, 2002; Woldegabriel *et al*., 2005; Stollhofen *et al*., 2008; Tryon *et al*., 2008; Deino *et al*., 2010). Some eruptions have generated widespread tephra deposits that occurred as a series of dated marker horizons throughout the fossil-bearing deposits of East Africa. Similarly, this technique has long been applied in Southeast Asia, particularly in Sangiran, to date and correlate the tuff layers that are associated with *Homo erectus*

fossils (Swisher *et al*., 2000; Larick *et al*., 2001, Zaim *et al*., 2011).

2.2.5. Chronostratigraphy

Chronostratigraphy is that part of stratigraphy that deals with the relative time relations of rock bodies, and a chronostratigraphic unit is a body of rock that was formed during a specified interval of geological time (Salvador, 1994). A chronostratigraphic horizon or marker is a stratigraphic surface that has the same age everywhere (Salvador, 1994). Although they are theoretically without thickness, in practice the term chronostratigraphic horizon (or chronohorizon) has been applied to very thin and distinctive markers that are essentially the same age over their whole geographic extent (Pillans, 2007b). Examples of chronostratigraphic markers in the Quaternary include tephras, magnetic polarity reversal horizons, and horizons enriched in tektites. Tektites are glassy objects produced from melted crustal rocks that are caused by large meteorite impacts. A large extra-terrestrial impact occurred in Southeast Asia at c. 800 ka, producing tektites which are found over a wide area, including Australia and surrounding oceans (Izett and Obradovich 1992; Kunz *et al*., 1995; Yamei *et al*., 2000, Folco *et al*., 2011). These tektites have become known as Australites or Australasian tektites.

Like tephras, tektites are important chronostratigraphic markers, because they represent almost instantaneous events, and can be directly dated by methods, such as fission-track, K/Ar and $^{40}Ar/^{39}Ar$, and can be correlated over large distances, including both marine and terrestrial deposits (Pillans, 2007a). Tektites can be incorporated in sediments and may have been transported or reworked. In such cases, the presence of tektites provides a maximum age of 800 ka for the enclosing sediment. A good example from South China where Acheulean-like stone tools occurred in association with Australasian tektites, yielded a $^{40}Ar/^{39}Ar$ age of 803±3 ka (Hou *et al*., 2000).

2.3. Depositional Environment of the Archaeological Sequence

2.3.1. Fluvial Environment

Fluvial sediments consist predominantly of channel and overbank deposits (Nicholls, 2009; Boggs, 2010). Channel deposits are dominated by sand and gravel and represent the bed load of rivers. Overbank deposits generally consist primarily of clay, silt, and lesser amounts of very fine to fine sand and represent suspended-load sediments that accumulate on floodplains. Organic sediments such as peat, and chemical sediments, such as carbonate and evaporitic minerals, may also constitute important components in some overbank settings (Aslan, 2013).

Fluvial channels have been subdivided into straight, meandering, and braided More recent classifications also recognize anastomosing channels (Miall, 1985; 1996). Braided rivers are characterized by channel bifurcation around bars or islands and low channel sinuosities, whereas anastomosing channels are separated by larger-scale flood basins (Nicholls, 2009; Boggs, 2010).

Within ancient fluvial deposits, the recognition of different fluvial depositional styles (e.g. braided and meandering channel fill) along with changes in grain size of deposits can be used to reconstruct the palaeogeography and provide evidence of changes through time. It may be expected that a conglomerate deposited by a pebbly braided river will have, downstream of the palaeo-flow direction, equivalent aged sandstone beds deposited in a sandy braided river, and that this may in turn pass to finer grained deposits further downstream with the characteristics of deposition by a meandering river (Aslan, 2013).

One approach to archaeological site formation is the spatial analysis of the artefacts to infer whether their location was influenced by human behaviour as opposed to other natural processes that may have transformed the original record (Rapp and Hill, 2006). A good example comes from Olduvai

Gorge, Tanzania. Petraglia and Potts (1994) studied the distribution of artefacts in Bed I and Bed II at site FLK-22. Leakey (1959) described clay deposits in this site as a living floor, occupied by hominins at c. 1.8 Ma ago. This fine grained sediment represents a low- energy depositional process, and large numbers of small artefacts incorporated in this layer, with only few artefacts showing evidence of rounding by transportation. By contrast, in Bed II, the presence of high-energy depositional processes is obvious as testified by the occurrence of deposited sands, pebbles and gravels. The artefacts that are associated with these deposits were definitely in secondary contexts.

2.3.2. Lacustrine Environments

Lakes have numerous origins, including rift valleys, volcanic and meteorite craters, glacial depressions left by melting ice (kettles) or retreating ice (moraines), alluvial floodplains (oxbows and abandoned channels), or karstic depressions (sinkholes) (Golberg and McPhail, 2006). Generally, lakes are categorized as open lakes or closed lakes. Open lakes (*exorheic*) are those which have an outlet and consequently remain fresh, without concentrations of salts. They also tend to be stable and have shorelines (Boggs, 2010) with only some slight, short-range fluctuations in lake level. Meanwhile, closed lakes (*endorheic*) have no outflow and dissolved solutes are concentrated; in arid and semiarid areas, evapotranspiration generally exceeds any inputs from rivers or springs. In these same areas, lakes can be only temporary features on the landscape (*ephemeral lakes*), where their basins can be filled only for short periods of time, much of the time the lake bottom is dry. In more extreme areas of the landscape, lake bottoms can be seen but are essentially dry for most of the time (*playa lakes*), although in more humid episodes during the Quaternary, they could have been perennial, or at least seasonal features on the landscape (Nicholls, 2009; Boggs, 2010).

In an archaeological context, hominins preferred to occupy places along or close to lake margins (Feibel, 2001). This setting can include not only

the lakeshore itself but also streams and surrounding wetland areas. Stratigraphic sequences in such fluvio-lacustrine settings may include a variety of sedimentary facies and lithologies that can be caused by rising or lowering of the lake level. Such fluctuations can be triggered by tectonic movements within the basin or drainage areas, or by climate changes. Consequently, deposits and archaeological sites in lake-margin settings may be influenced by a variety of depositional and post-depositional factors (Goldberg and McPhail, 2006). A lowering of lake level exposes sediments that were previously deposited at or below water level and may encourage overprinting by pedogenic processes, or may result in coverage of lacustrine sediments or archaeological materials by alluvium, or be eroded if channels migrate over the occupation area.

In contrast, with a slow rise in lake level and high energy beach settings, previous deposits and artefacts can be subjected to erosion, transport, or destruction by wave activity. A rise in lake level is often associated with higher groundwater tables, possibly transforming previously dry areas into swampy, less habitable ones. At the same time, diagenesis becomes more prominent, and depending on the specific environment, can be expressed by increased swampy (reedy) vegetation and rooting, cementation by carbonates, or the formation of iron pans (Goldberg and McPhail, 2006).

Examples of archaeological sites in lacustrine and fluvio-lacustrine settings can be found in the East African Rift (Kenya and Tanzania) and Jordan Valley, which are both associated with prehistoric sites for over the past 1–2 million years (Potts *et al*., 1999; Feibel, 2001; Blumenschine *et al*., 2012). The Lower Palaeolithic site of Ubeidiya is situated on the west bank of the Jordan River in the Central Jordan Rift Valley of Israel, and dates to about 1.4 million years and is the oldest early Acheulean site outside Africa (Bar-Yosef, 1994).

2.4. Dating Marker Beds in Archaeological Sites

As described above, chronostratigraphic markers such as tephra beds and tektites are often also well suited for radiometric dating methods. This section will briefly describe the principle of dating techniques that are suitable for estimating the age of tephra deposits and tektites.

2.4.1. Fission Track Dating

Fission tracks are produced when alpha particles created by spontaneous fission of ^{238}U leave a track of damage across minerals and glass. Samples need to be polished and etched to expose the tracks. Then, the fission tracks are counted under a high magnification microscope. The age of a sample is determined by the number of tracks per unit area, with a higher number of tracks corresponding to older samples (Westgate *et al*., 2013).

Zircon and glass are the most suitable materials for dating Quaternary deposits by fission-track methods, although apatite and sphene may also be useful. The most desirable situation for dating Quaternary sediments is where they are associated with silicic tephra beds because not only can they be reliably dated using their zircon and glass shards, but their widespread distribution and common distinctiveness make tephra beds excellent markers, linking the stratigraphies of isolated sites (Westgate *et al*., 2013).

The mineral or glass to be dated by the FT method must meet several criteria (Faure, 1977; Dumitru, 2000). The U concentration must be sufficient to give a statistically significant age. The tracks must be stable at ambient temperatures and not fully annealed soon after formation. Partial fading of tracks is common in some minerals and glasses, but correction procedures have been developed to account for this condition. Ideally, the material should be free of microlites and other inclusions, defects, and lattice dislocations, which, upon etching, can resemble fission tracks and make track identification and counting difficult (Storzer and Wagner, 1982). The crystal or glass surface area must be large enough to permit an accurate measurement of

the areal track densities. The mineral or glass must be unaltered and form a primary constituent of the rock or sediment being dated. For example, tephra deposits typically contain allochtonous grains or xenocrysts, and grains of detrital origin, which must be avoided during the track-counting operation. This requires use of grain-specific methods for FT counting. As with all geochronologic studies, the stratigraphic, and, in some cases, sedimentological context of the deposit must be well established. Materials that satisfy these criteria are glass (obsidian, tektites, volcanic glass shards, and glasses made by humans), zircon, apatite, and sphene, although the latter two are seldom used to date Quaternary events because of their low U content and their rarity in general (Westgate *et al*., 2013).

The precision of zircon and glass FT ages is similar and lower than the typical precision on K–Ar and $^{40}Ar/^{39}Ar$ ages, which can be a few percent or less, depending on the material dated and the age of the sample (McDougall, 1995). However, one of the advantages of fission tracks is that many tephra beds that do not contain suitable material for K–Ar or $^{40}Ar/^{39}Ar$ dating can be dated by FT using glass and/or zircon (Westgate *et al*., 2013). Furthermore, FT methods are particularly useful for dating K-poor, calc-alkaline volcanics and highly vitric tephra beds. Other favourable attributes include the small sample requirement for glass-FT ages, and the grain-discrete methodologies used, which neutralise the contamination problem (Westgate *et al*., 2013).

An example of FT dating involving the use of glass shards to determine the age is Bed 1 at Olduvai Gorge (Fleischer *et al*., 1965a, b). The FT age of 2.0 ± 0.3 Ma agreed with the K–Ar age of 1.75 ± 0.05Ma, obtained earlier by Leakey *et al*. (1961). Suzuki *et al* (1985) applied fission track on zircon to date the Upper Tuff of the Pohjajar Formation in the Sangiran area on Java, that is associated with a hominin-bearing layer, suggested that hominins occupied that area until 0.25 Ma ago.

2.4.2. Potassium Argon and Argon–Argon Dating

Radiometric dating methods measure the natural decay of radioactive isotopes that will be used to determine the ages of rocks, minerals, and archaeological artefacts. Potassium–argon dating is based on measuring the decay of potassium-40 (^{40}K) to argon-40 (^{40}Ar), a process with a half-life of 1.25 x 10^9 years. This makes the process suitable for dating rocks and minerals ranging from a few tens of thousands to more than 1 billion years in age (Twyman, 2007). Radioactive decay is a nuclear process and is independent of chemical and physical conditions found in geological processes. It has been shown that radioactive decay is constant over the wide range of temperatures and pressures encountered in geological events. Consequently, potassium–argon dating is one of the most widely used geological dating methods.

Argon–argon dating is a derivative method in which samples are bombarded in a fast neutron reactor, converting a proportion of the abundant and stable isotope ^{39}K into ^{39}Ar (McDougall and Harrison, 1999). Corrections must be made for atmospheric argon and for interfering argon isotopes produced by neutron reactions with calcium and other potassium isotopes. If an irradiated sample is completely melted, the argon in the sample is released in a single stage and provides an age comparable to that derived from conventional potassium–argon dating (McDougall and Harrison, 1999). However, the main advantage of the $^{40}Ar/^{39}Ar$ method is that multiple aliquots can be tested from the same sample, usually using either a laser probe or step by step heating in a furnace to release argon samples at progressively higher temperatures that can be collected and analysed separately (Twyman, 2007). Ages calculated for each temperature increment can be plotted on an age spectrum diagram, which for an undisturbed sample will yield a horizontal line (i.e., all ages are the same; Twyman, 2007).

The $^{40}Ar/^{39}Ar$ dating technique is useful for archaeological applications, e.g., assigning approximate ages to archaeological artifacts at sites rich in volcanic rock. An example is the dating of artifacts at Olduvai

Gorge, Tanzania, Africa. Deino (2012) applied the $^{40}Ar/^{39}Ar$ dating technique to refine the previous ages of the widespread tuff marker of Bed I (Tuff 1B), which yielded an age of 1.848 Ma that provided insight in the timing of hominin evolution and paleoclimate histories in East Africa.

Zaim *et al*. (2011) provided a new age for a *Homo erectus*-bearing layer at Sangiran. Their $^{40}Ar/^{39}Ar$ analysis gave an age of 1.58 Ma, which coincided with previous dating results of the Bapang formation by Swisher *et al*. (1994) and Swisher (1997) as well as other $^{40}Ar/^{39}Ar$ ages from the *H. erectus*-bearing interval in Sangiran (Larick *et al*., 2001; Bettis *et al*., 2004).

2.5. Summary

This chapter has highlighted the principles, theory and application of suitable geoarchaeological techniques, complemented by a number of examples from archaeological sites. These approaches will serve as guidance, when employing similar methods for the case study site, the Soa Basin. The following chapter will discuss the geoarchaeology of the Soa Basin.

CHAPTER THREE

GEOARCHAEOLOGY OF THE SOA BASIN, FLORES

3.1. Introduction

Geoarchaeological approaches have been highlighted in Chapter 2. The previous chapter outlined the principles and application of earth sciences in helping to resolve questions at archaeological sites, and provided several examples that illuminated some of the techniques that have been applied in diverse complex archaeological settings with success.

Chapter 3 will outline the geoarchaeological archives of the study area, the Soa Basin in Flores Indonesia. This chapter compiles interdisciplinary data including geology, palaeontology and archaeology that have been obtained from previous studies. A brief description of the geological background, previous dating results and palaeontological and archaeological findings will be provided.

3.2. Regional Tectonic Setting

Early compilations of the geology and tectonic evolution of the Indonesian region were established by van Bemmelen (1949), Katili (1975) and Hamilton (1979). Indonesia is situated in a complex tectonic setting, at the boundary between several major and smaller active tectonic plates such as the Indo–Australia, the Pacific and the Philippines Sea plates (Hamilton, 1979; Hall, 2002; Fig. 3.1). The geology of the Indonesian region shows characteristic sequences resulting from subduction and collision processes (Hamilton, 1979; Hall, 2002). These tectonic processes have created still active volcanic chains, the longest extending continuously from Sumatra in the west, eastward along Java and the Lesser Sunda islands, then bending northward along Banda to the Moluccas. Shorter active volcanic arc or trench segments are located along north Sulawesi and Sangihe islands that bend northward to the southern part of

Philippines and another on the opposite eastern side of the Celebes and Moluccas Seas at Halmahera (Katili, 1975; Hamilton, 1979; Hall, 2002). Four volcanic arcs have been recognized including the Sunda, the Banda, the Halmahera and the Sangihe Arcs, respectively (Hall and Smyth, 2008). The study area, the Soa Basin, is situated in the central part of Flores Island, which is part of the Sunda Arc system.

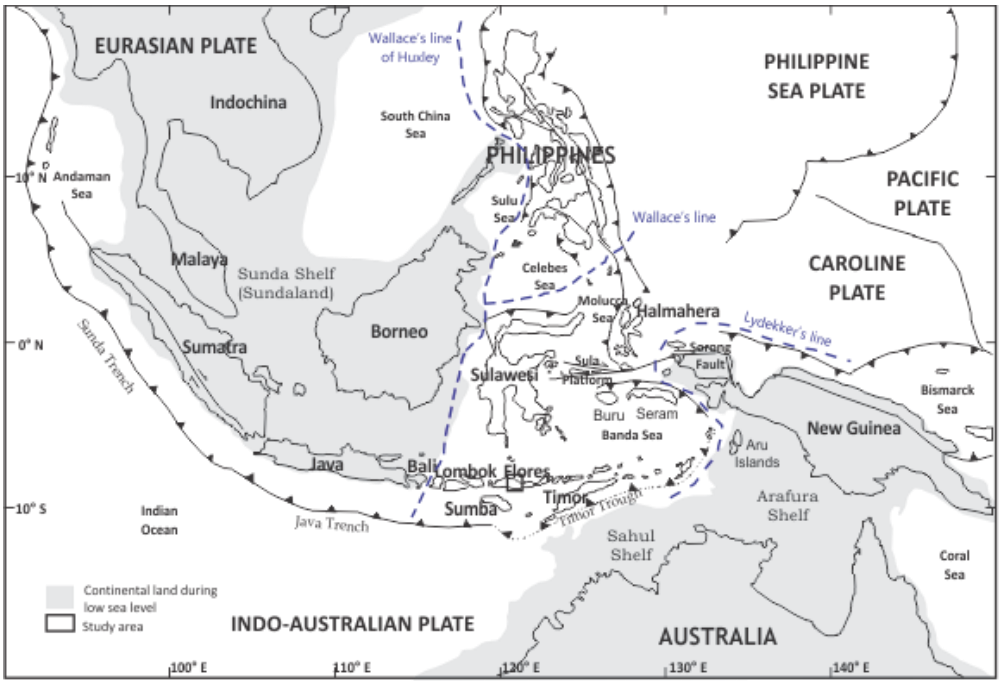

Figure 3.1. General tectonic setting of the Indonesian Archipelago surrounded by actively colliding continental and oceanic plates. Two continental landmasses occurred during periods of low sea level, the Sunda Shelf (Sundaland) in the west, and Sahul Shelf in the east (gray shaded areas).The biogeographic zones of western and eastern Indonesia are separated by Wallace's line, while to the east; the Lydekker's line borders the Sahul biogeographic region (Redrawn from Hall, 2002).

The Sunda Arc comprises a volcanic arc from the continental islands of Sumatra, Java and Bali that continues eastward to a string of volcanic oceanic islands, the lesser Sunda Islands (Lombok, Sumbawa, Flores and smaller islands further east (Katili, 1975, Hamilton, 1979). The latter is also known as the Eastern Sunda Arc (van Bemmelen, 1949). The Sunda–Eastern Sunda Arc is related to the northward subduction of the Australian plate beneath the Eurasian plate (Sundaland). During glacial periods sea level dropped to more than 100 m below present–day sea–level and Sundaland became a large single landmass connecting Sumatra, Java, Borneo and Indochina (Voris, 2000). Magmatism along the western portion of the Sunda Arc started during the Eocene (Hamilton, 1979; Hall, 2002), when the subduction zone bend northwards east of Java passing along West Sulawesi. Subsequently subduction activity along the Sunda Arc was reduced during the Early to Middle Miocene, when collision events of several microcontinental fragments collided with the eastern margin of Sundaland (Macpherson and Hall, 2002). As a result of these collisions the subduction zone of the Eastern Sunda Arc was formed andvolcanism resumed at ca. 5 Ma along the entire Sunda Arc and has continued until the present (Hall and Smyth, 2008). Volcanic activity in the Alor segment of the eastern Sunda Arc is considered to be inactive since ca. 2–3 Ma (Hamilton, 1979; Abbot and Chamalaun, 1981). Silver *et al*. (1983) suggested that it was caused by an intensive collision among continental arcs or due to the absence of underthrusting of lithosphere during that period.

The Sunda–Banda Arc complex that is elongated west to east, is divided into four segments (Fig. 3.2.), i.e. West Java, Bali, Flores and Banda (Hamilton, 1979; Wheller *et al*., 1987). There is an offset between the Flores and Banda sectors, with no volcanic activity between Alor to Wetar islands (Hamilton, 1979).

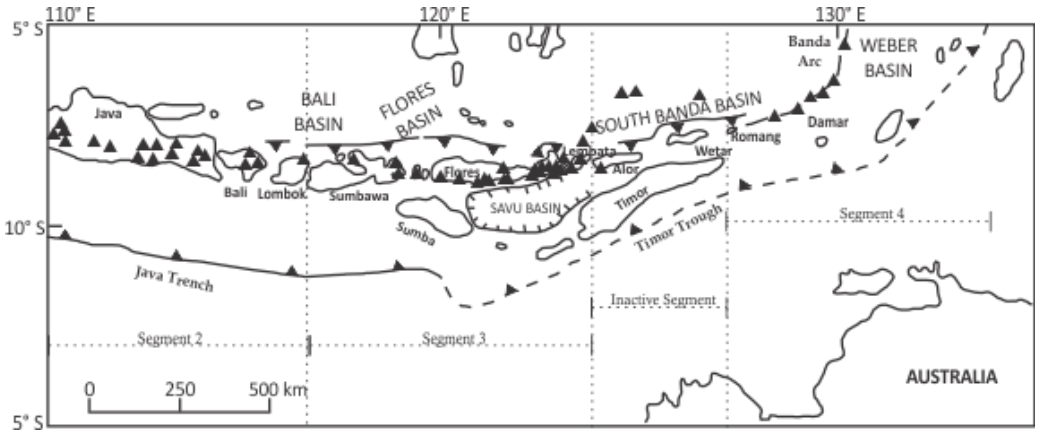

Figure 3.2. The Quaternary volcanic chain within the Sunda–Banda Arc system comprises four segments based on their chemical compositions. Segment 1 (western Java) is not shown in this figure. The study area (square) is situated in Segment 3. The filled triangles represent active volcanoes (Modified from Hamilton, 1979 and Wheller *et al*., 1987).

The Quaternary volcanoes in the Eastern Sunda Arc vary in compositions and isotopic signatures, which controlled by tectonic activities occurred close to the plate margin or arc lithospere (Pacey *et al*., 2013) Magma composition varies from tholeiite to high–K calc–alkaline series (Katili, 1975; Whitford *et al*., 1977; 1979; Varekamp *et al*., 1989) and shoshonitic to leucitic (Wheller *et al*., 1987). Partial melting of the subducting Australian Plate below the volcanic arc is considered to produce the calc–alkaline volcanoes along the Sunda–Banda Arc system (Katili, 1975). The strontium and lead isotope ratios also tend to increase toward the subduction zone as partial melting takes place at increasingly shallower depths (Varekamp *et al*., 1989; Elburg *et al*., 2004).

The structural framework of Flores is also heavily influenced by the subduction of the Australian plate and by the collision between the Sunda–Banda Arc with Australian continental crust. East–west trending of faults or lineaments and volcanoes are parallel to the subduction trench in the south and it has been concluded that these features were formed by northward subduction movements (Hamilton, 1979). Furthermore, Silver *et al*. (1983) suggested that

two major back–arc thrusts, the Flores Thrust in the west and Wetar Thrust in the east were triggered by the collision mechanism. The tectonic shear zone along the back-arc setting changes from normal (Flores) to more oblique (along east Wetar), shows an evolutionary stage of underthrusting across the Wetar back-arc segment that moves eastward (Koulali *et al*., 2016). North–south compression trends have initiated the uplift of coastal terraces along the north coast of Flores, which has been estimated at an average rate of 0.32 mm/yr (Muraoka *et al*., 2002). More detailed evidence available from securely dated uplifted coastal terraces on nearby Sumba and Timor indicates that tectonic uplift continues to the present at rates of between 0.2–0.65 mm/yr (Pirazolli *et al*., 1993; Fortuin *et al*., 1994) and 0.5 mm/yr, respectively (Chappel and Veeh, 1978; de Smet *et al*., 1990).

In the Soa Basin, the structural background is still poorly documented, although it has been mapped geologically. Geological structural investigations have only been carried out in the western and southern part of the Basin in the Bajawa region and adjacent areas in relation with geothermal surveys (Nasution *et al*., 2000; Muraoka *et al*., 2002). In general, the faults and lineaments show NW–SE, NE–SW and N–S trending systems (Nasution *et al*., 2000). The northeast–southwest faults coincide with a regional pattern connected to the northward movement of the active plate in the south. The NE–SW normal faults and N–S strike–slip faults systems are responsible for constructing natural fissures that allow heat flowing from the subsurface to form geothermal manifestations (Nasution *et al*., 2000; Muraoka *et al*., 2002).

3.3. Stratigraphic Sequence

Ehrat (1925) was the first to undertake geological investigations in the Soa Basin. Following the discovery of fossils of *Stegodon*, an extinct elephant species, in 1956 by the *Raja* of Nage Keo (Hooijer, 1957); Hartono in 1961 re–investigated the area and divided the sequence into three stratigraphic

units. A sequence of massive volcanic breccias that form the basement of the basin were named the Ola Kile Formation. The basin was filled in with a sequence of tuffaceous and fluvial deposits capped by lacustrine limestones, the Ola Bula Formation, which is unconformably overlaid by sub–recent volcanic deposits. The Ola Bula Formation comprises three members, from base to top the Tuff, the Sandstone and the Limestone Members (Hartono, 1961; O'Sullivan *et al*., 2001; Suminto *et al*., 2009; Figure 3.3 and 3.4). Meanwhile, geological surveys were also conducted in the adjacent area of the Soa Basin in association with geothermal resource assessments (e.g. Nasution *et al*., 2000 and Muraoka *et al*., 2002). However, they established lithological units that did not consider the named geological formations from previous research. For instance, the "Welas Tuff" is similar to the Ola Kile Formation and Tuff Member of the Ola Bula Formation, while "Aesesa Formation" corresponds to the Sandstone and Limestone Members of the Ola Bula Formation. This thesis will refer to the stratigraphic units as suggested by Hartono (1961) and unit descriptions will be combined with the results of previous geological investigations. Each geological unit will be described below.

3.3.1. The Ola Kile Formation

According to Hartono (1961), the Ola Kile Formation comprises massive andesitic breccias that are locally interbedded with lava flows, tuffaceous siltstone and tuffaceous sandstone. In the northern part of the Soa Basin, this formation reaches a minimum thickness of approximately 75 m and its occurrence was associated with the development of the Welas Caldera (Suminto *et al*., 2009). This formation covers the entire part of the basin and forms the basement for the overlying Ola Bula Formation. The Ola Kile Formation has been tilted to the south–southwest due to tectonic activities in the northern part of the Soa Basin (Suminto *et al*., 2009). The upper part of this formation generally has been truncated or eroded (O'Sullivan *et al*., 2001; Suminto *et al*.,

2009).

The Ola Kile Formation has similar characteristics as compared to The Welas Tuff of Muraoka *et al*. (2000, 2002). The Welas Tuff comprises predominantly pumiceous and scoriaceous tuffs as products of caldera collapse.

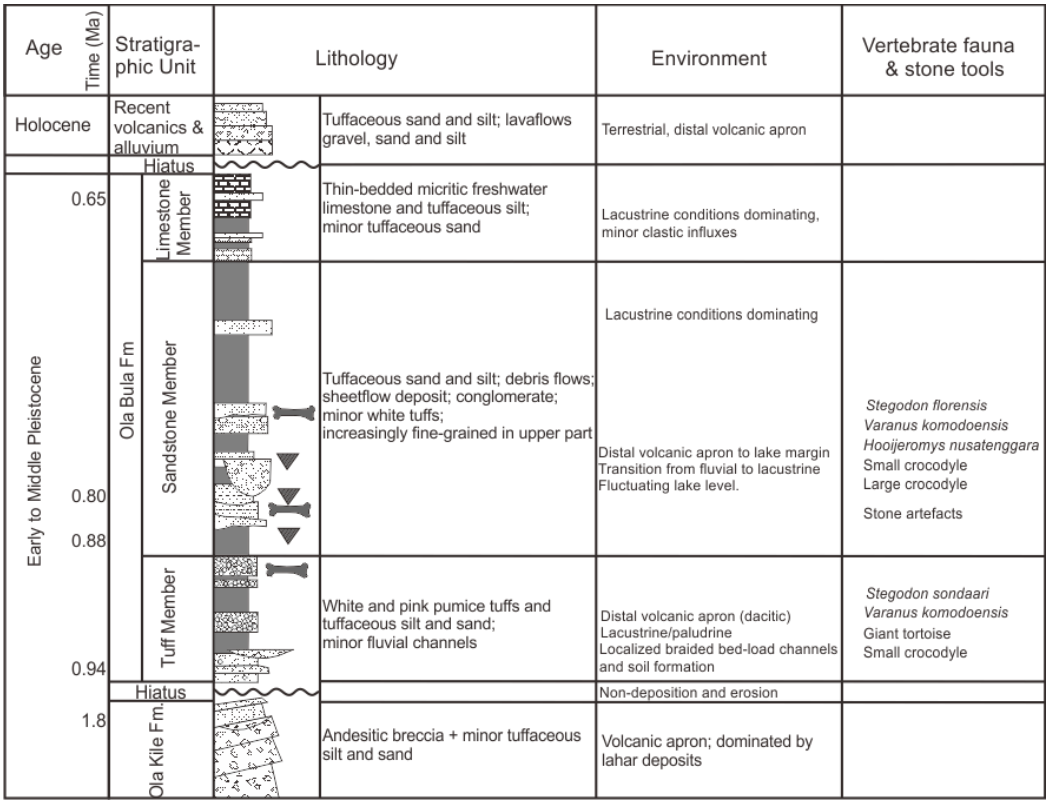

Figure 3.3. General stratigraphic framework of the Soa Basin showing schematic lithological descriptions, chronology and significant palaeontological and archaeological findings. Fossil fauna and stone artefacts are concentrated in the Tuff and Sandstone Members of the Ola Bula Formation. So far, the Ola Kile Formation provides no evidence for animals and/or hominin preservations and activities (From Suminto *et al*., 2009).

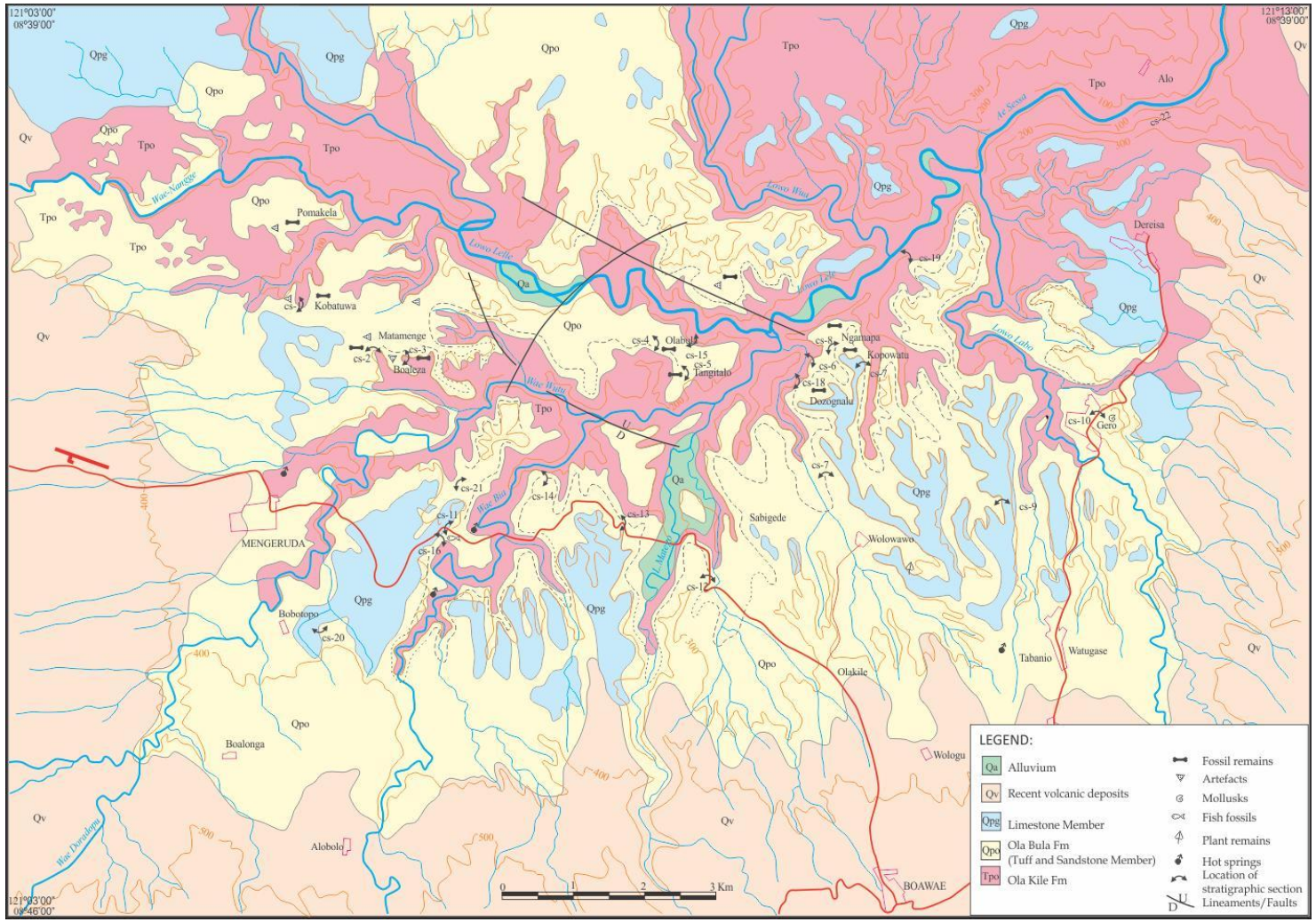

Figure 3.4. The geological map of the Soa Basin, Flores, Indonesia (Modified from Suminto *et al*., 2009).

3.3.2. The Ola Bula Formation

The Ola Bula Formation unconformably overlies the Ola Kile Formation. This formation is up to 100 m in thickness in the central basin area and pinches out toward the margins of the basin. The Ola Bula Formation consists of three Members, i.e. the Tuff, Sandstone and Limestone Members (Hartono, 1961; O'Sullivan *et al*., 2001; Suminto *et al*., 2009; Brumm *et al*., 2016). Each stratigraphic interval will be discussed below.

3.3.2.1. The Tuff Member

The Tuff Member occupies the lower part of the Ola Bula Formation, unconformably overlies the Ola Kile Formation and is composed predominantly of volcanic deposits, which are interbedded with tuffaceous siltstones, and locally developed sandstone and conglomerate lenses (Hartono, 1961; O'Sullivan *et al*., 2001; Suminto *et al*., 2009).

Previous research has documented the presence of pyroclastic flow deposits in the western part of the basin. At the sites Wolo Sege and Mata Menge, an ignimbrite layer has been identified, which commonly overlies well–developed palaeosols (Suminto *et al*., 2009; Brumm *et al*, 2010; Brumm *et al*., 2016). These palaeosols indicate an intensive process of soil formation and a lack of deposition prior to the deposition of the ignimbrite (Suminto *et al*., 2009; Brumm *et al*., 2010).

At the Wolo Sege site, an assemblage of stone tools has been recovered from a conglomerate lens and siltstone layer beneath the ignimbrite layer (Brumm *et al*., 2010). However, fossils are absent.

Another good example of the basal sequence of the Ola Bula Formation can be found at the Tangi Talo site, where fossil–bearing layers are developed at about 8 m above the Ola Bula/Ola Kile boundary. At least 5 horizons can be recognised from the Tangi Talo excavation. Fossil fragments of *Stegodon*, Komodo dragon and giant tortoise are concentrated on Layer IV and the transition between Layer IV and Layer V, which have been described as

tuffaceous siltstone and clast–supported pumiceous siltstone layers, respectively. However, no *in situ* artefacts have been recovered so far (Sondaar *et al*., 1994; van den Bergh, 1999; Aziz *et al*., 2009).

In general, the Tuff Interval becomes thicker towards the eastern and southeastern parts of the Soa Basin. In the western part of the basin near Kobatuwa, in contrast, this interval is absent or has been eroded (Suminto *et al*., 2009). This unit was interpreted to be deposited in a distal volcanic setting with locally low energy fluvial – lacustrine environments (O'Sullivan *et al*., 2001; Suminto *et al*., 2009). In contrast, the Tuff Member was designated as the Welas Tuff and the Aesesa Formation according to Muraoka *et al*. (2002). Their Welas Tuff reportedly contains ash flow tuffs, siltstone lenses and minor clastic deposits; while their Aesesa Unit consist of scoria– and pumice fall deposits, sandstone and thin laminations of siltstone (Muraoka *et al*., 2002).

3.3.2.2. The Sandstone Member

The Sandstone Member conformably overlies the Tuff Unit. This interval was deposited in a fluvio–lacustrine environment (Suminto *et al*., 2009). The sandy interval predominantly comprises tuffaceous siltstones, tuffaceous sandstones and conglomerates. Some sandstone layers preserve sedimentary structures such as scour– and– fill, parallel laminations and cross bedding, but volcanic tuffs and massive mud flow deposits also occur (O'Sullivan *et al*., 2001, Suminto *et al*., 2009). In the middle part of the basin, the Sandstone Interval can reach approximately 60 m in thickness, and individual sandstone layers may reach a maximum thickness of 5.5 m, while in the western margin the unit becomes more thinner (O'Sullivan *et al*., 2001, Suminto *et al*., 2009).

The middle part of this interval contains abundant fossil vertebrate remains and stone artefacts. Excavations carried out near Mata Menge have yielded hundreds of stone tools and fossil bones from two intervals, both with alternating coarse sandstones and fine–grained tuffaceous siltstones from the Sandstone Unit (Morwood *et al*., 1998; Suminto *et al*.,

2009; van den Bergh *et al*., 2009a; Brumm *et al.*, 2016). The upper fossil-bearing interval has also yielded isolated teeth and a mandible fragment of a hominin that is thought to represent the direct ancestor of *Homo floresiensis*, the small-statured Late Pleistocene hominin from Liang Bua (van den Bergh *et al.*, 2016). At the Boa Leza site, fossils and stone artefacts have also been excavated from the Sandstone Member (Morwood *et al*., 2009).

3.3.2.3. The Limestone Member

The Limestone Member occupies the uppermost part of the Ola Bula Formation. Hartono (1961), at first, suggested this unit to be an independent formation, which he named the "Gero Limestone". However, because of gradual contacts, depositional continuity and absence of erosional features with the underlying Sandstone Member, this interval has been included in the Ola Bula Formation as the upper Limestone Member by subsequent authors (O'Sullivan *et al*., 2001, Suminto *et al*., 2009). However, in some places particularly in the northern part of the Soa Basin where the basal members of the Ola Bula Formation are not developed or have been eroded, this limestone interval directly overlies the Ola Kile Formation unconformably (Suminto *et al*., 2009).

The Limestone Member consists of an alternation of micritic limestones, siltstones, volcanic tuffs and sandstones. Alternating limestone and fine–grained sediments display horizontal parallel laminations. Freshwater algae, plants, molluscs, ostracods and fossil fish occur in this member. This Limestone Member has a total thickness of up to 40 m in the eastern part of the Soa Basin, whereas individual limestone beds can reach 30 cm in thickness. In the western margin of the basin, in contrast, this unit is thinner and comprises an intercalation of thinly bedded (1–5 cm) layers, dominated by clay–and silt–sized sediments (O'Sullivan *et al*., 2001, Suminto *et al*., 2009).

The Limestone Member is deposited in a freshwater lacustrine

environment without any influences of marine transgression. Shrinkage cracks commonly occur at the top of the limestone beds, indicating fluctuating levels of lake water (O'Sullivan *et al*., 2001; Suminto *et al*., 2009; Brumm *et al*., 2016).

3.3.3. Recent volcanic deposits and alluvium

The uppermost part of the stratigraphy within the Soa Basin contains young volcanic deposits and alluvium that unconformably overlie the Ola Bula Formation. This unit is about 10 m thick and mainly consists of andesitic and basaltic lavas with minor siltstone, sandstone and conglomerate. The clastic deposits are composed of volcanic fragments that were derived from the adjacent volcanic edifices (Hartono, 1961, O'Sullivan *et al*., 2001; Suminto *et al*., 2009). Muraoka *et al*. (2002) suggested that the basaltic lavas were associated with the development of post–caldera cones that formed lava domes. On the other hand, almost a hundred cinder cones have been recognised in the southern part of the Soa Basin, near Bajawa town. The cinder cone complex showed compositions in basaltic andesite and andesite (Sucipta *et al*., 2006).

Recent active volcanoes in the southern part of the basin, Mt. Inierie, Mt. Ine Lika and Mt. Ambulobo, should also be considered able to produce effusive materials. In addition, alluvium deposits mainly consist of sand, clay and gravel and are associated with the present river system (Hartono, 1961).

3.4. Chronological Framework

Previous research mostly applied fission track dating for establishing a chronological framework. So far, a total of 20 samples taken from the Ola Kile and Ola Bula Formations have been dated. 17 samples have been analysed by fission track dating on zircons (Morwood *et al*., 1998; O'Sullivan *et al*., 2001; Figure 3.5), and subsequently three samples have been examined by argon–argon dating method, dated to single hornblende crystals (Brumm *et al*.,

2010; Brumm *et al*., 2016). Samples were collected from tuffaceous layers beneath fossil and/or artefact-bearing layers, and from associated layers above the fossil and/or artefact-bearing horizons. Two samples from the base and the top of Limestone Member were dated, while one sample was taken from the upper part of the Ola Kile Formation in order to get minimum and maximum ages of the depositional units. The fission track and argon–Argon ages are consistent throughout the sequence, displaying an upward younging trend (Morwood *et al*., 1998; O'Sullivan *et al*., 2001; Suminto *et al*., 2009; Brumm *et al*., 2010).

Fission track dating on the tuff sample from the lowermost part of the Soa Basin sequence (Ola Kile Formation.) provided an age of 1.86 ± 0.12 Ma (O'Sullivan *et al*., 2001). In addition, Muraoka *et al*. (2002) obtained mean ages of 2.52 ± 0.30 Ma and 1.66 ± 0.11 Ma on pumice clasts taken from the Welas Caldera Complex by K–Ar dating. These ages indicate depositional processes within the Soa Basin since the Early Pleistocene (O'Sullivan *et al*., 2001), but the published K-Ar dates should be considered with great care.

On the Tuff Unit of the Ola Bula Fm, zircon fission track dating of the basal layers yielded ages of 0.95 ± 0.09 Ma and 0.94± 0.08 Ma (O'Sullivan *et al*., 2001). Moreover, the zircon fission track age from the Tangi Talo site and the argon–argon age from the Wolo Sege site were 0.90 ± 0.07 Ma and 1.02 ± 0.01 Ma, respectively (O'Sullivan *et al*., 2001, Brumm *et al*., 2010). In this case, the argon–argon dating resulted in a more precise age than the fission track technique. However, fission track ages are still acceptable because the results are still close to the Argon–Argon age. The age results suggested that the Tuff Interval was deposited in the late Early Pleistocene.

Fission track dating on the tuffaceous layers developed just below and above the lower fossil and artefact-bearing interval at the Mata Menge site, yielded ages of 0.88 ± 0.07 Ma and 0.80 ± 0.07 Ma, respectively. Recently published palaeomagnetic evidence has shown that the Brunhess-Matuyama

boundary occurs just below the lower fossil-bearing interval, indicating that the age of the fossils and artefacts is less than 0.78 Ma (Yurnaldi *et al*., 2018). Fission track dating on the Kobatuwa sample provided younger result (0.70 ± 0.07 Ma) and suggested that the depositional time span of the Sandstone Member is ca. 200 ka (Morwood *et al*., 1998; O'Sullivan *et al*., 2001, Suminto *et al*., 2009). Moreover, two samples from the Limestone Interval yielded ages of 0.68 ± 0.07 Ma and 0.65 ± 0.06 Ma, and implied that the deposition of the Ola Bula Formation terminated in the Middle Pleistocene (O'Sullivan *et al*., 2001, Suminto *et al*., 2009). With the exception of the northern part of the basin, which is slightly sloping to the south, the Ola Bula sequence generally is nearly horizontal and elevation can represent the relative age approximately. Fission track ages and previous palaeomagnetic studies appear to be in accordance and confirm the age of the Limestone unit (Sondaar *et al*., 1994, O'Sullivan *et al*., 2001).

There are few age determinations from younger volcanic deposits surrounding the Soa Basin (Muraoka *et al*., 2002). The only age was obtained from the associated layer near Wolo Bobo in the southern region by radiocarbon dating that yielded an age of 10 ka (Nasution *et al*., 2000). It can be assumed that the youngest volcanic deposits were formed during the Holocene.

Potassium–argon dating on volcanic breccias and lavas collected from the Bajawa cinder cone complex on the southwestern margin of the Soa Basin, provided a wide time range. The oldest cones varied between 0.53 and 0.73 Ma, while the youngest groups were dated between 0.0–0.2 Ma (Takashima *et al*., 2002, Sucipta *et al*., 2006). It can be summarized that the deposition of younger volcanic materials commenced in the Late Pleistocene.

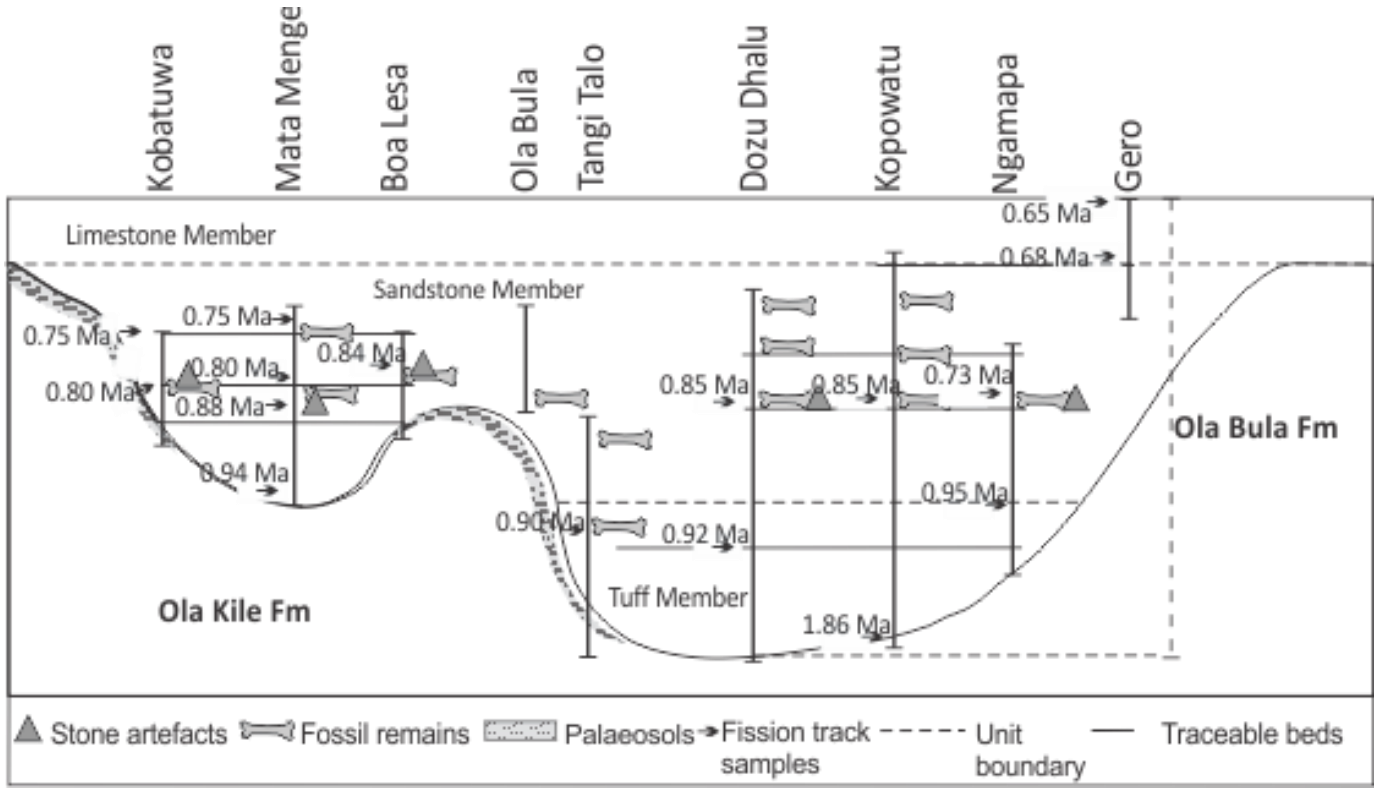

Figure 3.5. The chronological framework of the Soa Basin based on fission track dating (After O'Sullivan *et al*., 2001).

3.5. Palaeoenvironmental Conditions

The Soa Basin is a NE–SW elliptical volcanic depression that trends with the Aesesa River drainage, which leaves the basin to the northeast towards the Flores Sea. The depositional phases in the Soa Basin began during the Late Pliocene with accumulation of volcanic breccias of the Ola Kile Formation to create the basin basement (Suminto *et al*., 2009). The Soa depression was presumably formed during the development of a volcanic complex in the northern part. The volcanic centre of the Welas Caldera is considered to be the main source of the Ola Kile sequence (O'Sullivan *et al*., 2001; Suminto *et al*., 2009). Tectonic activities during the formation of the Ola Kile unit caused its southward dip, but the unconformably overlying younger depositional units form horizontal layers. The uppermost part of the Ola Kile Formation was eroded and then unconformably overlain by the Ola Bula sequence (Suminto *et al*., 2009).

The deposition of the Ola Bula Formation commenced with the accumulation of the volcanic–rich interval of the Tuff Member at 1 Ma ago (O'Sullivan *et al*., 2001; Suminto *et al*., 2009; Brumm *et al*., 2010). Major eruptions produced ignimbrite deposits that are widely distributed throughout the basin. During lulls in volcanic activity, fluvial processes were also active to form conglomeratic lenses, as suggested from the Mata Menge and Wolo Sege sites. Moreover, the pyroclastic flow deposits are commonly associated with red palaeosols particularly in the western part of the basin, indicating stable environments and no or very slow deposition (Suminto *et al*., 2009). Some authors have suggested that the deposition of the Tuff Member may be related to the caldera forming event of the Welas Caldera (Muraoka *et al*., 2002; Suminto *et al*., 2009).

During the accumulation of the Sandstone and Limestone Members at 0.88–0.65 Ma, the Soa Basin became a large shallow lake or series of lakes (O'Sullivan *et al*., 2001; Suminto *et al*., 2009). The lacustrine environment was presumably formed by water ponding when the main drainage

was blocked by volcanic deposits or faulting. Similarly, rising of the lake water level during high intensity rainfall can also create lakes and/or ponds along lowlands (O'Sullivan *et al*., 2001; Suminto *et al*., 2009). The sandy materials of the Sandstone Member were formed when channels were built up and subsequently advanced into the lake (for instance at Mata Menge). Debris–and hyper–concentrated flow mechanisms also interrupted the lake phase caused by flooding from surrounding highlands (Suminto *et al*., 2009). The textural features of tuffaceous sediments also indicate that such deposits also accumulated in the lake, rivers, creeks and waterholes (O'Sullivan *et al*., 2001, Suminto *et al*., 2009; van den Bergh *et al*., 2009a).

The presence of freshwater fossils strongly supports the lacustrine interpretation. Freshwater molluscs, fishes, ostracods as well as plant remains and diatoms occur in the upper two units of the Ola Bula sequence. The associated volcanic tuffs also contain characteristics of lacustrine deposition. In some places, palaeosols separate the lacustrine successions and indicate climatic fluctuations (Suminto *et al*., 2009). The lacustrine stages ceased around 0.65 Ma, when thick limestone beds were formed in the eastern part and thin carbonate layers in the western margin.

Overall, fossil remains and stone artefacts were mostly preserved in the sandy facies and/or fine grained lenses associated with sandy facies (van den Bergh, 1999; Morwood *et al*., 1998; Suminto *et al*., 2009). The sandstone facies is represented by channel fill, sheet flood and mudflow deposits. A taphonomic study of the fossil assemblage excavated at Mata Menge indicated that artefacts and fossil remains have been transported by water although not far from their sources (van den Bergh *et al*., 2009a). Stone tool assemblages frequently were concentrated in the basin margin (e.g. Mata Menge and Wolo Sege) rather than in the deepest part of the lake (e.g. Tangi Talo, Gero). This suggests that lake margin environments provided the most valuable resources for hominin activities (Morwood *et al*., 1998, van

den Bergh, 1999, Suminto *et al*., 2009, van den Bergh *et al*., 2009a).

3.6. Archaeological and Palaeontological Contexts

Palaeontological and archaeological research in the Soa Basin, Flores was pioneered by Father Verhoeven, who undertook large excavations at Ola Bula, Mata Menge and Boa Leza (Hooijer 1957; Verhoeven 1958; Verhoeven 1968; Maringer and Verhoeven, 1970). During the 1990s, joint researches by Indonesian, Dutch and Australian teams provided significant progress on palaeontology, archaeology and geology (Sondaar *et al*., 1994; van den Bergh 1999; van den Bergh *et al*., 1996, 2001; Morwood *et al*., 1997, 1998, 1999; O'Sullivan *et al*., 2001; Morwood and Aziz, 2009a).

Recently, at least 16 palaeontological/archaeological sites have been documented in the Soa Basin (Table 3.2). Fossils/artefacts locations are dispersed along the western and central parts of the basin. Previous interdisciplinary researches have recorded stratigraphic profiles, GPS position, and altitude measurements as well as fossils/artefacts descriptions.

Table 3.1. The list of paleontological and archaeological sites in the Soa Basin, Flores.

No.	Location	Latitude Longitude	Stratigraphic Unit	Age*	Findings	References
1.	Boa Leza	8° 41' 45.8'' S 121° 06' 02.1'' E	Sandstone Member	0.84 ±0.07 Ma	Fossils: *Stegodon florensis*, crocodile, giant rat (*Hooijeromys nusatenggara*) and bird. Stone tools: flakes, hammerstones, cores	1, 3 7, 8, 13, 14
2	Deko Weko	8° 41' 44.8'' S 121° 09' 49.4' E	Sandstone Member	Unknown (Correlative to Mata Menge and Kobatuwa)	Fossils: *Stegodon* Stone tools: none	14
3	Dozu Dhalu	8° 42' 00.1'' S 121° 09' 13.6'' E	Sandstone Member	0.85 ±0.09 Ma	Fossils: *Stegodon florensis*, Komodo dragon, snake (?), giant rat. Stone tools: flakes (?).	3, 7, 8, 14
4	Kobatuwa	8° 41' 18.6'' S 121° 05' 16.4'' E	Sandstone Member	0.70 – 0.80 Ma	Fossils: *Stegodon florensis*, crocodile, giant rat (*Hooijeromys nusatenggara*) and bird. Stone tools (flakes, hammerstones, cores)	8, 14
5	Kopowatu	8° 41' 40.7''S 121° 09' 33.6'' E	Sandstone Member	0.85 ±0.09 Ma	Fossils: *Stegodon florensis*, (skull) Stone tools (flakes?)	8, 14

6	Malahuma	8° 40’ 59.9’’S 121° 08’ 30.3’’ E	Sandstone Member	Unknown	Fossils: *Stegodon* Stone tools (surface)	14
7	Mata Menge/ Lembah Menge	8° 41’ 32.7’’S 121° 05’ 43.9’’ E	Sandstone Member	0.88 – 0.80 Ma	Fossils: *Stegodon florensis*, crocodile, giant rat (*Hooijeromys nusatenggara*) and bird. Stone tools (flakes, hammerstones, cores)	1 – 11, 14, 15, 17, 18
8	Ngamapa	8° 41’ 30.1’’S 121° 09’ 22.5’’ E	Sandstone Member	0.73 ±0.07 Ma	Fossils: *Stegodon* Stone tools (flakes?)	8, 14
9	Ola Bula	8° 41’ 38.0’’S 121° 07’ 59.0’’ E	Sandstone Member	Unknown (Correlative to Ngamapa and Kopowatu)	Fossils: *Stegodon florensis* Stone tools (flakes?; surface only)	1, 14
10	Ola Bula abandoned village	8° 41’ 42.2’’S 121° 08’ 24.3’’ E	Sandstone Member	Unknown (Correlative to Ngamapa and Kopowatu)	Fossils: *Stegodon* Stone tools (flakes?; surface)	1, 14
11	Pauphadhi	8° 41’ 15.0’’S 121° 10’ 06.3’’ E	Sandstone Member	Unknown (Correlative to Kopowatu and Dozu Dhalu)	Fossils: *Stegodon* Stone tools (flakes?)	14
12	Sagala	8° 42’ 42.0’’S 121° 09’ 22.8’’ E	Sandstone Member	Unknown	Fossils: *Stegodon* Stone tools: none	14
13	Tangi Talo	8° 41’ 53.0’’S 121° 08’ 10.6’’ E	Tuff Member	0.90 ±0.07 Ma	Fossils: *Stegodon sondaari*, giant tortoise, Komodo dragon and crocodile. Stone tools: none	2, 3, 5, 6, 7, 8, 9, 12, 14, 18

14	Wolo Keo	8° 42’ 33.3’’S 121° 08’ 59.0’’ E	Sandstone Member	Unknown	Fossils: *Stegodon* Stone tools (flakes?)	14
15	Wolo Sege	8° 41’ 27.1’’S 121° 06’ 00.0’’ E	Tuff Member	1.02 ±0.01 Ma**	Fossils: none Stone tools: flakes	14, 16
16	Wolo Milo	8° 40’ 57.8’’S 121° 08’ 27.2’’ E	Sandstone Member	Unknown (Correlative to Mata Menge and Kobatuwa)	Fossils: *Stegodon* Stone tools (flakes?)	14

Note: All numerical ages (*) were obtained by fission track dating on zircon, except the Wolo Sege site (**) that was dated by $^{40}Ar/^{39}Ar$ dating on hornblende.

1. Maringer and Verhoeven, 1970
2. Sondaar *et al*., 1994
3. van den Bergh *et al*., 1996
4. Morwood *et al*., 1997
5. Morwood *et al*., 1998
6. Morwood *et al*., 1999
7. van den Bergh, 1999
8. O’Sullivan *et al*., 2001
9. van den Bergh *et al*., 2001
10. Brumm *et al*., 2006
11. Moore and Brumm, 2007
12. Aziz *et al*., 2009
13. Morwood *et al*., 2009
14. Suminto *et al*., 2009
15. van den Bergh *et al*., 2009a
16. Brumm *et al*., 2010
17. Brumm *et al*., 2016
18. Yurnaldi *et al*., 2018

The excavations at Tangi Talo have recovered unique fossil remains, including pygmy elephant (*Stegodon sondaari*), giant tortoise (*Geochelone sp*) and Komodo dragon (*Varanus komodoensis*) and a small crocodile. *S. sondaari* and *Geochelone* are not recorded from any other Soa Basin fossil site and document a major faunal turnover in Flores at ca. 900 ka ago (Sondaar *et al*., 1994; van den Bergh *et al*., 1996; Morwood *et al*., 1998, 1999; van den Bergh 1999, O'Sullivan *et al*., 2001, Aziz *et al*., 2009). The pygmy *Stegodon* was replaced by medium to large–bodied *Stegodon florensis,* supposedly a new immigrant to the island, while giant tortoise bacame extinct around the same time. Only Komodo dragons have lived in Flores and the surrounding islands until present times. Due to the absence of stone artefacts, the contribution of early hominins to the extinction of those two species is still unclear and debatable. In fact, at Tangi Talo, all fossils are associated with a volcanic layer suggesting that a volcanic eruption may have been the primary cause for the demise of pygmy *Stegodon* and giant tortoise (Sondaar *et al*., 1994; Morwood *et al*., 1998, 1999; van den Bergh, 1999, O'Sullivan *et al*., 2001, Aziz *et al*., 2009).

The Mata Menge site preserves a faunal assemblage occurring in two stratigraphic intervals separated by ~10 m of deposits and both associated with stone artefacts. The fossil fauna includes *Stegodon florensis*, crocodile, birds and giant rat (*Hooijeromys nusatenggara*), while the upper interval has also yielded *Homo floresiensis*-like hominin remains (Sondaar *et al*., 1994; Morwood *et al*., 1998, 1999; van den Bergh 1999; O'Sullivan *et al*., 2001, van den Bergh *et al*., 2009a; Meijer *et al.*, 2015; Brumm *et al.*, 2016; van den Bergh *et al.*, 2016). *S. florensis* and possibly also the giant rat represent elements that colonized the Soa Basin between 880 – 700 ka ago (). *In situ* stone tools have been found together with fossil remains in the same layers, seemingly indicating that the presence of hominins may have influenced the accumulation of fauna remains by their behaviour (hunting or scavenging),

although unambiguous evidence such as cut marks on bones has not been demonstrated. Alternatively, mammals and birds may have served as food sources for predatory animals (e.g. Komodo, crocodile; Sondaar *et al*., 1994; Morwood *et al*., 1998, 1999; van den Bergh *et al*., 1996; van den Bergh 1999) or they may have died predominantly of old age or disease.

In Liang Bua Cave in western Flores, *ca.* 60 km to the west of the Soa Basin, *Stegodon* bones and teeth accumulated in the well–dated sedimentary sequence associated with large numbers of stone tools (Morwood *et al*., 2004; van den Bergh *et al*., 2009b). They occupied the cave between 95 and 50 ka ago (Westaway *et al*., 2007a, Roberts *et al*., 2009; Sutikna *et al.*, 2016). This *Stegodon*, named *Stegodon florensis insularis*, has similar characteristics and morphologies as compared with *Stegodon florensis* from the Soa Basin, although on average its body size tends to be 30% smaller. *S. florensis* from the Soa Basin is considered to be the ancestor of the pygmy *S. florensis insularis* from Liang Bua (van den Bergh *et al*., 2008; van den Bergh *et al*., 2009b). Micromammal remains are also abundantly present in the Liang Bua deposits. They have been identified as three species of giant rats, two murids of intermediate size and two small–bodied species (Locatelli *et al*., 2012). Two of the giant rats, *Papagomys theodorverhoeveni* and *Spelaeomys florensis*, appear to have become extinct during the Holocene, while *Papagomys armandvillei* still lives on Flores. Morphological description of *Papagomys* suggests that this species shows not many differences with the Middle Pleistocene giant rat (*H. nusatenggara*) from the Soa Basin (Musser, 1981, Locatelli *et al*., 2012). The available evidence suggests that there is no other faunal change since the last faunal turnover at 900 ka ago, and the Flores fauna subsequently demonstrates prolonged phylogenetic continuity (van den Bergh *et al*., 2001; van den Bergh *et al*., 2009b; Meijer *et al*., 2010).

Stegodon florensis most closely matches *Stegodon* species B from the Tanrung Formation in Sulawesi, rather than with *Stegodon*

trigonochepalus from Java (van den Bergh 1999, van den Bergh *et al*., 2001; van den Bergh *et al*., 2009b). *Stegodon* disappeared since *ca.* 120 ka from Java (Westaway *et al*., 2007b), while it survived until the Late Pleistocene (*ca.* 50 ka ago) in Flores (Sutikna *et al.*, 2016). Similarly, *Varanus komodoensis*, seems to be a relic of a once much wider distribution of giant varanids, of which fossils have been found further to the west in Java and the Asian Mainland and to the East in Timor and Australia (Hooijer 1972, Hocknull *et al*., 2009, van den Bergh *et al*., 2009b). Hocknull *et al* (2009) argue that Komodo dragons may be derived from Australian varanids that dispersed all the way towards Java in the Pliocene.

The fossil and recent vertebrate fauna on Flores displays examples of both island dwarfing and gigantism. Large–bodied mammals tend to reduce in size once isolated on relatively small islands, while small mammals such as rats tend to increase size. *Stegodon sondaari*, which stood only around 1 m at the shoulders, is the most extreme known example of island dwarfing in the southeast Asian region. The very limited faunal diversity combined with examples of dwarfing and gigantism clearly indicates that Flores remained isolated throughout the Quaternary and was not connected by land-bridges with the Asian mainland. Only terrestrial animals which had the capabilities of swimming, floating or rafting could reach the island. As mentioned above, *Stegodon florensis* seems to be closely related to *Stegodon* species B from Sulawesi and the *S. florensis* ancestors may have reached Flores from the Philippines via Sulawesi in the north (van den Bergh, 1999; van den Bergh *et al*., 2001; van den Bergh *et al*., 2009b). This model would be in accordance with the dominant surface ocean current patterns with a dominantly north to south flow direction (Kuhn *et al*.,2004), and known as the "Indonesian Throughflow", which has strong currents southward from the Pacific Ocean to the Indian Ocean.

The Soa Basin contains thousands of *in situ* stone artefacts in well–dated sedimentary layers. Stone tool accumulation that is related to fossiliferous layers at Mata Menge reveals that hominins first arrived on Flores at 1.02 Ma ago and then thrived until 700 ka ago (Morwood *et al*., 1998;

O'Sullivan *et al*., 2001; Brumm *et al*., 2010). The oldest site of Tangi Talo preserved only faunal remains and no artefacts. Evidence from the Wolo Sege site pushed back the timing of hominin settlement to ~1.0 Ma ago (Brumm *et al*., 2010). Analyses of the core technology at Mata Menge and Wolo Sege suggests that hominins apparently reduced cobble sized cores and only brought flaked pieces of stone to the sites, where these were subsequently further reduced to produce radial cores and small flakes (Brumm *et al*., 2006; Moore and Brumm, 2007). Radial cores from Mata Menge and Kobatuwa are similar to those found in the Oldowan stone tool assemblages of East Africa, which have a maximum age of ~2.6 Ma ago and are usually ascribed to *Homo habilis* (Brumm *et al*., 2006; Moore and Brumm, 2007). Although hominin remains have not been discovered yet from any sites in the Soa Basin, and stone tools that have been attributed to *Homo erectus* on Java are very rare, it is well known that African *Homo erectus* started with the widespread production of prominent Acheulian handaxes at ~1.8 Ma ago (Brumm *et al*., 2006; Moore and Brumm, 2007; Brumm *et al*., 2009).

The abundance of stone artefacts, recovered from Liang Bua and associated with fossil vertebrate remains and a small–bodied adult hominin skeleton has been attributed to a new species, *Homo floresiensis* (Morwood *et al*., 2004). This small–bodied hominin has a mixture of archaic and advanced morphological characteristics, notably a comparatively small brain size and short stature, some of which is reminiscent of *Australopithecus*, while other traits are more like *Homo sapiens* (Brown *et al*., 2004; Morwood *et al*., 2005; Jungers *et al*., 2009a,b). Despite its small brain size, *Homo floresiensis* had the capability to produce simple flaked artefacts and radial cores. The used technology shows a strong similarity with that known from the Soa Basin (Moore *et al*., 2009), suggesting that the Soa Basin knappers could be ancestral to *Homo floresiensis* (Morwood and Aziz, 2009; Morwood and Jungers, 2009).

3.7. Problems and pitfalls

As mentioned above, the Soa Basin provides significant palaeontological and archaeological findings, which accumulated in a well–described sedimentary sequence and accompanied with an obvious time frame. Previous researchers have recognized a number of palaeontological/ archaeological sites, where fossil/artefact– bearing layers have been described, stratigraphic profiles have been recorded and dating samples have been collected (Morwood *et al*., 1998; Brumm *et al*., 2006; Suminto *et al*., 2009). However, inter–correlation between sites is still difficult to conduct even though there are abundant volcanic layers developed with the potential to represent marker beds. In a complex volcanic setting like the Soa Basin, collaboration of litho– and tephrostratigraphical approaches on excavation sites and adjacent areas should play an important role to establish a relative chronological framework that can be used to monitor the relative position of fossils, artefacts and dating samples throughout the sequence. Identification, physical description and chemical characterization of volcanic (tephra) layers that are associated with fossil remains and artefacts, will be strong tools to understand the processes and timing of palaeontological and archaeological findings.

So far, samples from above and beneath the fossil/artefact–bearing layers have been dated by zircon fission tracks, which tend to have an error margin of up to *ca.* 10%. Previous work noted that fission track samples were taken from syn–eruption volcanic deposits with only minor indications for reworking (Morwood *et al*., 1998; 1999; O'Sullivan *et al*., 2001). However, dated layers seem to display erosional contacts with the basal units and poor to moderately sorted textures, which represent water–supported or hyperconcentrated flow mechanisms, and subsequently should be interpreted as redeposited volcaniclastics (see Figure 4.5–4.12 in van den Bergh *et al*., 2009a; Figure 3.4 in Aziz *et al*., 2009). Plotting of zircon grains on the

radial plot diagram initially showed scattered patterns and dated grains distributed not in a single population, causing high deviations. Dating on zircon from reworked material is unreliable and only represents a maximum age, because zircon is a resistant mineral that can be transported far away from its source. Moreover, the accumulations of zircons on redeposited or epiclastic deposits can be derived from mixed origins, and thus provide inhomogeneity of ages. It is suggested that previous zircon fission track results need to be refined and clarified.

The only precise age was obtained by the $^{40}Ar/^{39}Ar$ dating technique on an ignimbrite layer at Wolo Sege, which yielded an age of 1.02±0.01 Ma (Brumm *et al*., 2010). The pyroclastic deposit contains abundant hornblende crystals that are suitable and reasonable for single grain $^{40}Ar/^{39}Ar$ dating. Because the dated sample is a primary volcaniclastic deposit, the age represents the time of its formation. This approach can be applied to date other volcanic layers that are associated with fossil remains or stone artefacts at various sites within the Soa Basin. Combination between stratigraphic analysis and $^{40}Ar/^{39}Ar$ dating will establish a robust chronological framework.

3.8. Summary

From the paragraphs discussed above, it can be seen that previous research in the Soa Basin has provided a consistent basic stratigraphic framework, but that further detailed work should be done to correlate key marker beds of volcanic origin. So far little attention has been paid to the correlation of palaeosols and the sourcing of volcaniclastic deposits. Chronological methods that have been applied need to be evaluated to avoid misinterpretation.

Litho–and tephrostratigraphical analyses, combined with mineralogical and geochemical analyses and age assessments, will be used in this study to improve the chronological framework and to reconstruct past

environmental and climatic conditions. Overall, this study will demonstrate the vitality of interdisciplinary approaches to answer such problems in the Soa Basin. The results and interpretations of these approaches will be highlighted and discussed in the next two chapters.

CHAPTER FOUR

RESEARCH FRAMEWORK

4.1. Introduction

Chapter Three outlined the results of previous interdisciplinary research in the study area and prominent archaeological findings in the complex Soa Basin system. Data presented in Chapter Three also indicated that the inter-basin correlation among the various archaeological sites is still unclear and needs to be clarified.

Chapter Four aims to highlight analytical methods that are used in this study to address problems mentioned in the previous chapter. First, a brief overview of the research sites will be presented, followed by an outline of sampling strategies and inter-laboratory techniques applied in the present study.

4.2. Study Area

The Soa Basin comprises multifaceted geological features and at least 16 archaeological and palaeontological sites have so far been recognized (see Chapter 3). The present study focuses on improving the stratigraphic and chronological contexts of the Soa Basin and proposes new palaeoenvironmental and paleoclimatic interpretations. To obtain these goals, all well-known sites across the basin were studied and in addition, new areas with the most complete geological sections and/or important new findings were recorded. A detailed overview of the various sites is shown in Figure 4.1 and Table 4.1.

The chosen study sites cover the entire Soa Basin; four laterally equivalent stratigraphic sections were recorded. These sections, some (Wolo Sege and Mata Menge) covering the entire thickness of the basin fill sequence, serve as the basic stratigraphic framework. In addition to these sections, isolated

outcrops with key stratigraphic features, were also recorded and sampled. In the northern part of the basin five spot sites have been selected to obtain geological information related to volcanism and the development of lacustrine phases. Welas, Nata Randang and Kolopanu are representative sites to study explosive volcanic eruptions, while Wulubara provides a 14-metre thick sequence of alternating tephra and lacustrine sediments.

Along the western margin of the basin, sections were recorded at Mata Menge, Wolo Sege and Kobatuwa, covering the entire basin sequence from basement to top. At the Mata Menge site, three sub-units or members of the Ola Bula Formation were recognised. Recording of stratigraphic profiles at the important archaeological excavation sites Kobatuwa and Wolo Sege aimed to complement the Mata Menge section and compare the lateral development of the sequence for palaeo-landscape reconstruction. Research in the western basin area has successfully traced the spatial distribution of a pyroclastic marker unit known as the "Wolo Sege Ignimbrite".

Furthermore, to cover the central part of the basin, the field studies were performed at Tangi Talo, Ola Bula, Lowo Lele, Rata Gawe and Deko Anekoa. Tangi Talo is in the deepest part of the basin and provides a comparatively thick sequence of the lowermost part of the Ola Bula Formation. To compare the lateral development of the Tangi Talo section, stratigraphic logs were also measured at nearby Ola Bula, Lowo Lele, Rata Gawe and Deko Anekoa.

Further to the south, studies were conducted at Wae Bha, Wolo Peti and Matago, while in the eastern part of the basin, surveys were made at Pumaso, Lowo Mali and Gero. At these sites, the investigation is aimed at recording the vertical succession and to identify potential marker beds.

Table 4.1. Selected study sites in the Soa Basin, Flores. The asterisks indicate established archaeological sites.

No.	Study Sites	Latitude/Longitude	Elevation (m)	Remarks	Sample
1	Welas	8° 36′ 03.2″; 121° 04′ 51.4″	433	Outcrop	Yes
2	Nata Randang	8° 36′ 20.7″; 121° 03′ 15.9″	426	Outcrop	Yes
3	Wulabara	8° 39′ 02.3″; 121° 03′ 38.6″	397[b]	Outcrop	Yes
4	Kolopanu	8° 39′ 58.0″; 121° 02′ 29.5″	397	Outcrop	Yes
5	Kobatuwa a. Kobatuwa 1 b. Kobatuwa 3 c. Kobatuwa 4	 8° 41′ 24.7″; 121° 05′ 07.0″ 8° 41′ 24.6″; 121° 05′ 01.1″ 8° 41′ 15.5″; 121° 05′ 02.5″	 340[b] 378 382	 Outcrop Outcrop Outcrop	 Yes Yes Yes
6	Mata Menge*	8° 41′ 32.7″; 121° 05′ 43.9″	367[b]	Outcrop and Trenches	Yes
7	Wolo Sege*	8° 41′ 27.1″; 121° 06′ 00.0″	366[b]	Trenches	Yes
8	Wae Bha	8° 43′ 19.6″; 121° 07′ 11.1″	289	Outcrop	No
9	Wolo Peti	8° 43′ 12.8″; 121° 06′ 40.2″	277	Outcrop	No
10	Rate Gawe	8° 41′ 34.3″; 121° 07′ 52.5″	336[b]	Outcrop	No
11	Deko Anekoa	8° 41′ 37.3″; 121° 07′ 55.7″	291	Outcrop	No
12	Ola Bula	8° 41′ 37.1″; 121° 08′ 08.1″	325[b]	Outcrop	No
13	Tangi Talo*	8° 41′ 53.0″; 121° 08′ 10.6″	279[b]	Outcrop and Trench	Yes
14	Lowo Lele	8° 41′ 26.6″; 121° 08′ 50.8″	190	Outcrop	No
15	Matago	8° 43′ 05.9″; 121° 08′ 18.0″	240	Outcrop	Yes
16	Pumaso	8° 42′ 29.6″; 121° 09′ 36.5″	301[b]	Outcrop and Trench	Yes
17	Kopowatu	8° 41′ 36.6″; 121° 09′ 26.4″	298	Outcrop	Yes
18	Lowo Mali	8° 41′ 29.1″; 121° 10′ 34.1″	257	Outcrop	Yes
19	Gero	8° 41′ 57.8″; 121° 11′ 50.1″	410[b]	Outcrop and Trench	Yes

Note. Asterisks refer to well-known palaeontological and archaeological sites. a. The altitude generally measured with portable GPS (Garmin), except for b that measured with DGPS (Leica).

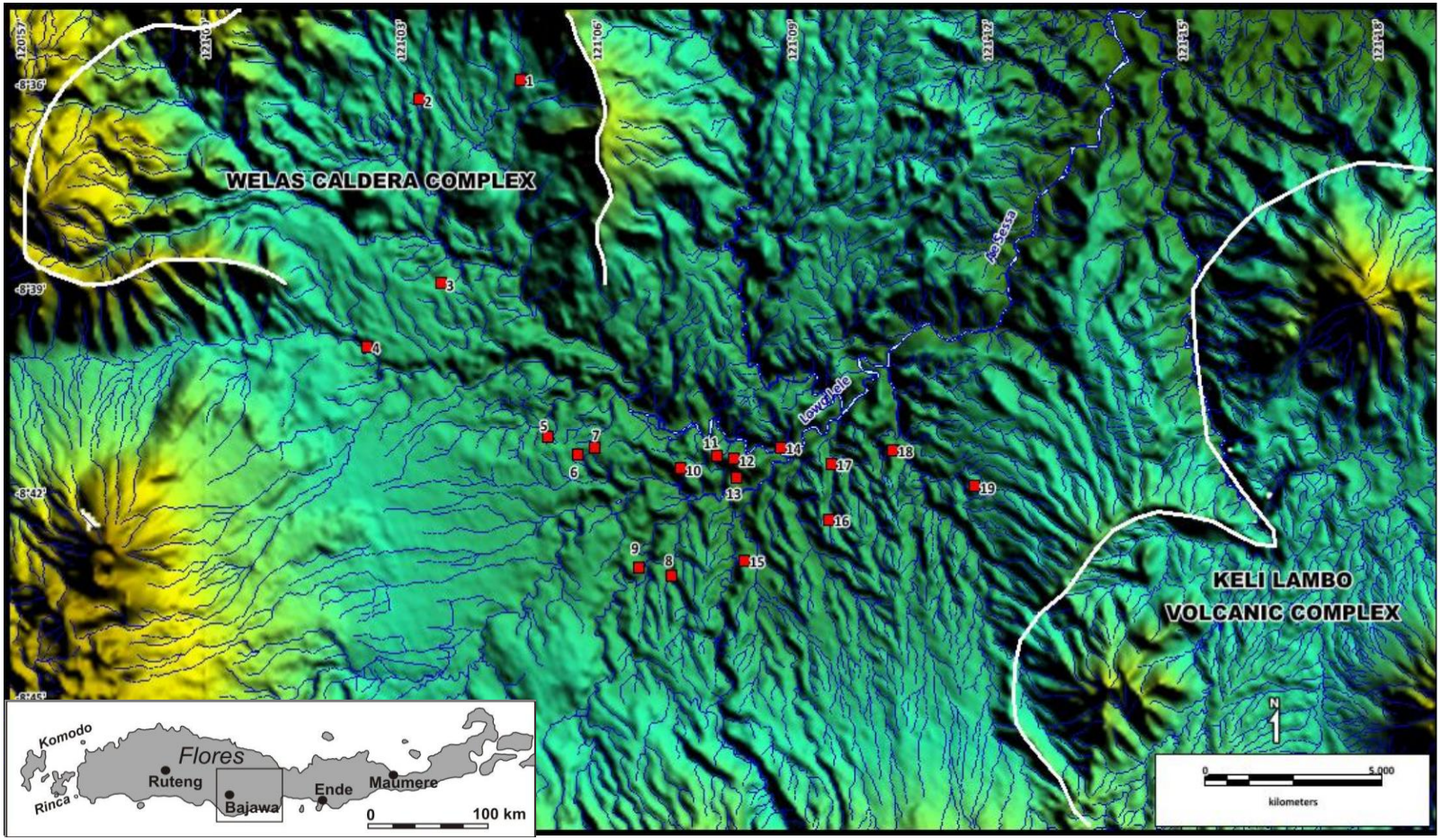

Figure 4.1. Map of the Soa Basin showing the location of sampling sites and sections studied in detail. 1. Welas; 2. Nata Randang; 3. Wulubara; 4. Kolopanu; 5. Kobatuwa; 6. Mata Menge; 7. Wolo Sege; 8. Wae Bha; 9.Wolo Peti; 10. Rata Gawe; 11. Deko Anekoa; 12. Ola Bula; 13. Tangi Talo; 14. Lowo Lele; 15. Matago; 16. Pumaso; 17. Kopowatu; 18. Gero; 19. Lowo Meli. Lowo and Ae are local words for “river”, while Wolo means “hill”.

4.3. Field Observations

Field surveys were conducted across the research area on motorbike and on foot in search for suitable exposures and sections and to record stratigraphic profiles. Because of vegetation cover and locally developed thick soils, 1 m wide step trenches were dug in several key areas, such as at Mata Menge, Wolo Sege, Tangi Talo, Pumaso and Gero. This allowed for the examination of continuous fresh outcrops and the collection of samples not affected by weathering and soil-formation processes and to provide better views of detailed lithological features in vertical section. Each of these trenches was logged in detail, recording aspects of rock type, texture and mineralogy. Sedimentological structures, contacts and other notable features were recorded and photographed in the field, and representative samples were taken for laboratory analyses. Colours were recorded using the standard Munsell Colour Chart.

4.4. Laboratory analysis

4.4.1. Sampling strategy

Samples taken from trenches or exposures were stored in sealed plastic bags and labelled. They were fresh without soil contaminants. Further treatments were carried out depending on the type of laboratory analyses.

Samples were obtained at standard intervals between centimetres to a maximum of a metre through the stratigraphic sections and of representative lithological units of the Ola Bula and Ola Kile Formations. For chemical fingerprinting and correlation, tephra samples were taken from every single tephra layer encountered in exposures or trenches. Larger 100 g sediment samples were also collected and at least every sediment layer was sampled throughout the vertical sections at the main archaeological sites, i.e. Mata Menge, Wolo Sege and Tangi Talo.

4.4.2. Bulk geochemistry by X-ray fluorescence (XRF)

At least 281 samples have been analysed for whole-rock geochemistry using a SPECTRO XEPOS energy-dispersive polarisation X-ray fluorescence (XRF) spectrometer at the University of Wollongong. The laboratory procedures follow the methods as described by Norrish and Hutton (1969) and Norrish and Chappell (1977). Samples were crushed into fine powder using a chrome-steel or tungsten carbide mill. For trace-element analysis, 5 - 5.5 gram of each powdered sample was mixed thoroughly with a PolyVinyl Acetate (PVA) solution in an aluminium cup, and then pressed at ~2000-2500 psi. Pressed pellets were dried overnight in an oven at 65°C before processing in the XRF spectrometer.

Glass buttons were prepared for major-element analysis using a pure metaborate (100 % metaborate) flux for high silica samples, and 12:22 and 57:43 ratio of tetraborate and metaborate fluxes for sediment samples. 400 mg of sediment sample and 300 mg of volcanic sample was added to 2.4 g of each flux. Powdered samples and flux were blended in platinum crucibles and heated from 600°C to 970°C over a period of one hour, with a NH_4I pellet added to reduce viscosity prior to pouring and pressing on a graphite disc. Samples with > 1000 ppm sulfur or 400 ppm Cu as determined from trace element analysis were oxidised prior to fusing through the addition of 5 ml of $LiNO_3$ and dried overnight at 65°C, then heated at 100°C for one hour, then to 600°C by increasing 50°C increments every 20 minutes. Deconvolution of the spectra and conversion of X-ray intensities was performed using Ametex Materials- Analysis Division proprietary software. Accuracy was controlled by calibration of the instrument against a wide range of natural rock standards and synthetic materials. If a sample yielded a poor total percentage, an additional glass pellet of the same sample was prepared and the measurement repeated.

In addition, Loss on ignition (LOI) measurements were carried out before samples were analysed in the XRF spectrometer, in order to determine moisture and organic contents. LOI was calculated by heating ~1 g of powdered

sample in a ceramic crucible at 1050°C for two hours. Afterwards, samples were weighed after slight cooling with the difference in ignitied and initial weight (before heating) converted to loss on ignition as a weight percentage (wt %).

4.4.3. Electron Probe Microanalysis (EPMA)

Electron probe microanalysis on single glass shards was conducted at the University of Victoria, New Zealand under supervision of Associate Prof. Brent V. Alloway. Tephra samples were dried, disaggregated and then fractionated with 125-300 μm sieves. The glass shards were observed under a binocular microscope in order to select fresh shards of coarse grained sizes (250-300 μm), which were mounted in epoxy blocks. Before being analysed under the electron microprobe, the shards were polished to expose fresh internal surfaces and then coated in carbon following the procedure of Froggatt (1992). The analyses were performed using a JEOL JXA-8230 SuperProbe electron probe microanalyser (EPMA), which has five combined wavelength dispersive X-ray spectrometers (WDS). The equipment was operated under 15 kV accelerating voltage, 0.5 nA beam current and 10 - 20 μm defocussed beam. A glass standard, ATHO-G, was analysed simultaneously through the sample measurements to obtain high accuracy and precision results. At least 15-20 shards were analysed within each individual sample.

4.4.4. Mineralogy by X-ray diffraction (XRD)

X-ray diffraction analysis was conducted to recognize the minerals and determine the presence of minerals in selected rock samples. At least 150 selected sediment samples were prepared for this analysis. Samples were powdered, smeared and then processed on a Philips 1150 PW Bragg-Brentano diffractometer at 40 kV and 30 mA, using CuKα radiation. Each sample was scanned at 2° (2θ)/min in the range from 4 to 70° (2θ). This XRD analysis was performed at the University of Wollongong. Diffraction peak patterns were selected using software TRACES 6 and Siroquant ver. 3 (licensed

to University of Wollongong) was applied for mineral identification. Siroquant is a quantitative interpretive software, which is able to determine the relative abundance of crystalline phases. Siroquant uses a Rietveld method, and minerals can be quantified using observed HKL files (Ward and Taylor, 1996; Keeling *et al.*, 2000; Alves and Omotoso, 2009).

4.4.5. Scanning Electron Microscopy (SEM)

SEM analysis employed in this study to identify clay minerals or microfossils in the selected samples. The SEM observation has the capability to look at materials in high magnification range (commonly 10x to 20000x) (Welton, 1984). The minerals were determined by noting their morphological characteristics. A piece of sample was attached to a specimen plug with epoxy or Silpaste and dried overnight in a low temperature oven. The gold coated sample was imaged by SEM at the Faculty of Engineering, University of Wollongong, using a JEOL JX-6870 electron microscope.

4.4.6. Dating Techniques

Two dating techniques, i.e. isothermal plateau fission track (ITPFT) and argon-argon dating, were applied as part of this study. The ITPFT dating was conducted at the University of Toronto on hydrated-volcanic glass shards, following procedures described by Westgate (1989, 2014), Sandhu and Westgate (1995), and Westgate *et al*., (2013).

For selected crystal-rich tephra samples containing feldspars, hornblende and/or biotite, single-grain argon-argon dating techniques were applied. The $^{40}Ar/^{39}Ar$ dating was performed at the QUADLAB, Roskilde University, Denmark, and analytical procedures are given in Storey *et al* (2012) dan Rivera *et al* (2013). Neutron irradiation was conducted at the Oregon State University TRIGA reactor, using Alder Creek age standard/ACs-2 (Nomande *et al*., 2005) for monitoring neutron fluence.

4.4.7. Statistical Analysis

Dealing with large numbers of samples and geochemical data requires statistical analysis in order to understand the data behaviour and distribution of variables. This study applies Factor Analysis to recognize and distinguish the unique factors from the majority of all other factors (Reimann *et al*., 2002). In terms of tephrostratigraphy, this study also uses a similarity coefficient as suggested by Borchardt *et al*. (1971, 1973) to distinguish and correlate numbers of tephra layers.

Bulk geochemical data within rock samples consist of major, minor and trace elements. These analytical data are presented in different units, for instance the major and minor elements are measured in percentages (%), while the trace elements are measured in part per million (ppm). To avoid further problems during factor analysis, all chemical concentrations need to be standardized and transformed into log ratios. Furthermore, outliers commonly occur within large data sets and these need to be reduced. In this study, the outliers were removed prior to analysis. This study uses the strength of centred log ratio (CLR) transformation to detect the outliers and converts the variables into homogeneous variances. The analytical procedures follow those given in Aitchison (1986), Egozcue *et al*., (2003) and Egozcue and Pawlowsky-Glahn (2006).

In order to obtain rapid statistical analysis, this study used the SPSS version 17 software package. The statistical approach complements the geochemical analysis results and assists on chemical fingerprinting between large numbers of samples, provenance studies and stratigraphic correlation.

4.5. Summary

The result of analytical methods discussed above, will be used to ascertain the geological processes occured in the Soa Basin, the timing of deposition and palaeoenvironmental changes. Combined with high-resolution stratigraphic profiles, these data will be used to clarify the key volcanic events that were associated with the occurrence of archaeological and palaeontological deposits and intra-basinal correlations.

CHAPTER FIVE

TEPHROSTRATIGRAPHY, CHRONOLOGY AND GEOCHEMICAL CORRELATION

5.1. Introduction

As described in Chapter Three, there are a number of pyroclastic deposits emplaced in the Soa Basin. The present chapter deals with a detailed characterisation, including geochemical fingerprinting, of the various tephra units recognized mainly in the Ola Bula Formation. The major aim is to establish a tephrochronological framework. Geochemical analyses were performed on whole-rock samples and individual glass shards to distinguish individual tephra layers. Statistical analyses, such as hierarchical cluster and factor analyses are applied to verify the geochemical interpretations. The chapter begins with a summary of tephra nomenclature, followed by a field description of individual tephra units and a presentation of the chemical analyses and statistical approaches. A comparison of the results between grain-discrete glass shard major-element analyses acquired by electron microprobe (EPMA) and whole-rock geochemical analyses via XRF will also be discussed. In addition, all mineralogical analyses mentioned in this chapter are obtained by X-ray diffraction (XRD) technique (Appendix 4).

5.2. Tephra Nomenclature and Description

5.2.1. Tephra Nomenclature

The term “tephra” was firstly defined by Thorarinsson (1944), and originates from the Greek word that it means ashes. Tephras comprise unconsolidated pyroclastic materials that are explosively erupted during a volcanic eruption (Alloway *et al*., 2013). The word “tephra’ in this chapter is only used for primary pyroclastic airfall deposits (or more correctly tephra-fall deposits, see Lowe, 2011). If a pyroclastic layer shows signs of secondary

reworking from a primary tephra unit this will be indicated as such or the term "tephric" will be employed. For convenience of reference, a formal name has been given to the individual tephra layers according to their type locality. In most cases, the format for the tephra name commences with "type location" followed by the word "Tephra". For instance "Kopowatu Tephra" refers to a unique volcanic ash, which is well-exposed at its type locality Kopowatu, but which may have also been recognised in other sections and localities. If there is more than one key tephra layer in a specific type locality; the name of the following tephra adopts the nearest alternative site to that type locality.

For a few pyroclastic deposits, the specific term "ignimbrite" is used. An ignimbrite refers to a pumiceous ash-rich pyroclastic flow deposit. Ignimbrites are the product of hot ash clouds, or "*Nuées ardentes"*. Depending on the original temperature of the ash cloud, ignimbrites can be either welded or nonwelded (Cas and Wright, 1987). Volcanic deposits that are considered ignimbrites will have a formal name consisting of "Type locality" followed by the word "Ignimbrite" (e.g. "Wolo Sege Ignimbrite"). At least 73 discrete pyroclastic layers have been recognised, and they will be described from oldest to youngest. Some closely spaced stratigraphically tephra layers from individual volcanic events have been given additional sequential numbers.

5.2.2. Description of Tephra and Pyroclastic Deposits

A. Aesessa Ignimbrite (AEI)

The Aesessa Ignimbrite (hereafter AEI) is exposed along the Lowo Lele and Aesessa Rivers. It consists of welded pyroclastic deposits, which can be divided in two sub-units, i.e. a pyroclastic fall and pyroclastic flow sub-unit (Figure 5.1). The fall sub-unit is 45-cm thick, and is overlain by the flow sub-unit, which has a thickness of ~26 m. The fall sub-unit is white, has a sharp and irregular base, and displays an agglutinated or welded characteristic. This fall sub-unit is massive to weakly stratified near the top with normal graded and consists of a mixture of fine to medium pumiceous lapilli and fine to coarse

poorly sorted ash. This basal sub-unit overlies a prominent palaeosol. The pyroclastic flow sub unit is white to creamy white, has a sharp depositional boundary with the basal fall sub-unit, consists of medium to very coarse pumiceous lapilli in a fine to coarse ash matrix, and is poorly sorted, normal graded and is massive to weakly stratified. Macroscopically, this sub-unit contains moderate crystal concentrations of plagioclase, quartz, pyroxene, hornblende and biotite. The AEI is derived from one or more hot and dense pyroclastic density currents (PDC), generated by a collapsing caldera associated with an explosive eruption. Accretionary lapilli do not occur and this reflects "a dry eruption", lacking magma and water interaction. The occurrence of two types of pumice (white and grey) with distinct compositions suggests a mixture of rhyolitic and andesitic magma (Figure 5.2). Relatively hot and dense andesitic magma invaded cooler and more viscous rhyolitic magma, increasing the pressure in the magma chamber. The overpressure is responsible for triggering an explosive eruption and a caldera collapse (Cas and Wright, 1987; Roche *et al.*, 2000; Branney and Kokelaar, 2002).

The AEI is interpreted to be the product of a caldera-forming eruption, linking this pyroclastic with the formation of the Welas Caldera Complex (WCC) in the northwestern part of the Soa Basin and dated at 2.52 Ma ago (Muraoka *et al*., 2002). Moreover, the AEI forms the lower part of the Ola Kile Formation.

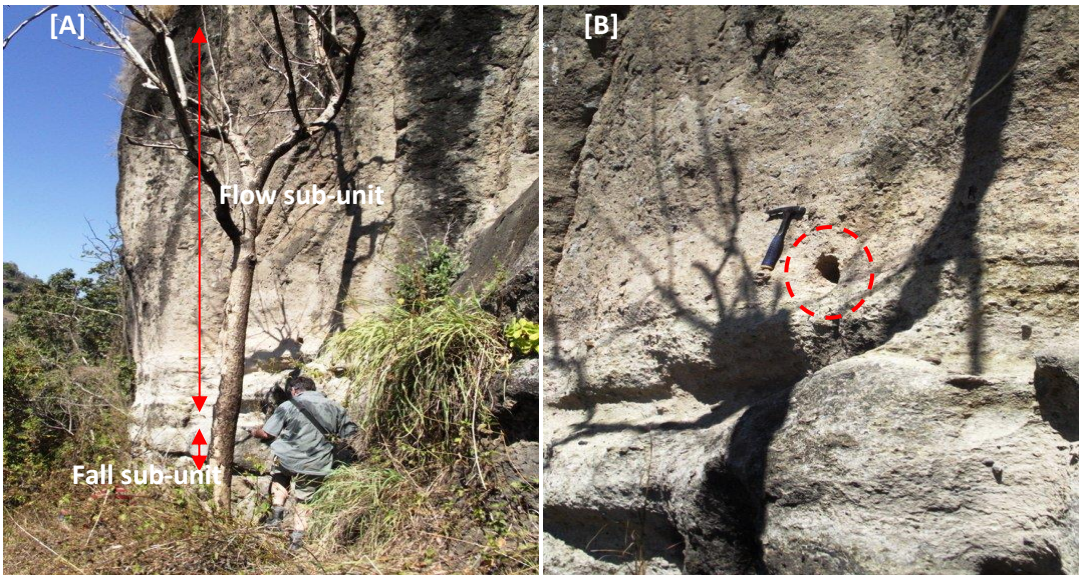

Figure 5.1. Exposures of the Aesessa Ignimbrite (AEI) at the Lowo Lele River (8°41'26.6"S; 121°08'50.8"E). A). The welded fall and flow sub-units of the AEI form a steep cliff along the Lowo Lele River. B) A tree mould within red dash circle originally trapped with in the pyroclastic flow sub-unit (The geological hammer is ~30 cm long).

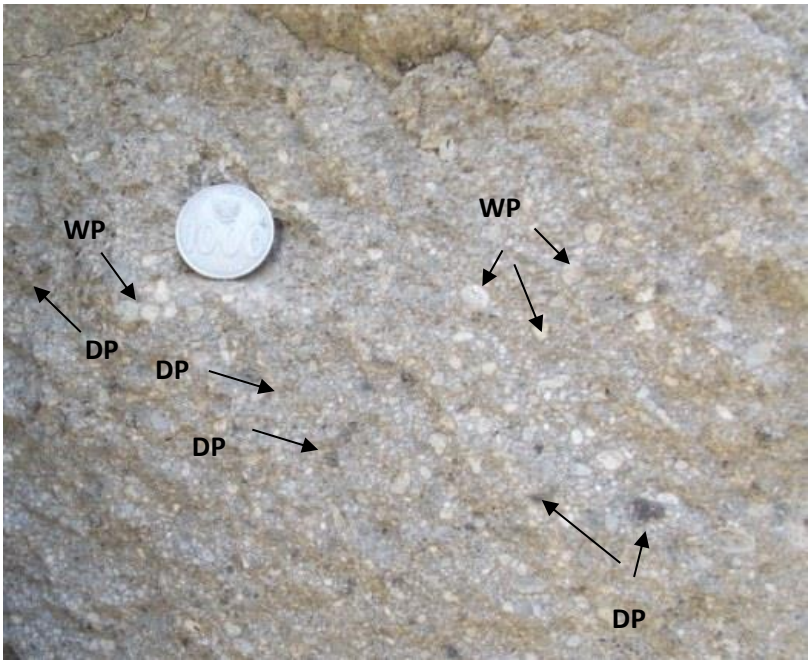

Figure 5.2. The field appearance of the AEI (8°41'57.3"S; 121°08'29.2"E) displays two types of pumice clasts, i.e. white pumice (WP) and dark pumice (DP), suggesting that mixing of basaltic and rhyolitic magma triggered the eruption (The coin for scale is ~24 mm in diameter).

B. Lowo Mali Ignimbrite (LMI)

B.1. Description and Interpretation

The Lowo Mali Ignimbrite (hereafter LMI) is a nonwelded ignimbrite and exposed in the Lowo Mali area. This pyroclastic deposit is stratigraphically above the Aesessa Ignimbrite (AEI). The LMI comprises three sub-units, from base to top 1) tephra-fall, 2) surge and, 3) flow sub-units (Figures 5.3). The basal tephra-fall sub-unit is white and in sharp contact with an underlying palaeosol. This sub-unit shows massive to weakly stratified, normal grading, coarse – very coarse pumiceous lapilli, and contains moderate amounts of crystal components consisting of quartz, plagioclase, and lesser abundance of pyroxene, hornblende and biotite. The tephra-fall sub-unit contains white and pink pumice fragments and is 277 cm thick. The overlying surge sub-unit has a sharp basal contact and planar to low-angle cross bedding, consists of coarse lithic ash with minor amounts of minerals and is 130 cm thick. The upper flow sub-unit is very prominent, with a thickness of 26 m, and a sharp basal contact. It consists of coarse to very coarse lapilli, is poorly sorted, massive to crudely stratified and contains abundant of plagioclase and low amounts of biotite, amphibole, quartz, and pyroxene. The uppermost part of this flow unit has been eroded in its type locality and is covered by a 30 cm-thick palaeosol.

Stratigraphically, the LMI belongs to the Ola Kile Formation. The erosional contact indicates that this pyroclastic deposit is unconformably overlain by the lowermost part of the Tuff Member of the Ola Bula Formation. The LMI is a pyroclastic density current (PDC) deposit that was generated by caldera-forming processes. The LMI initially appears to have been dispersed and deposited across the basin following the ancient topography. The resulting ignimbrites were subsequently partly eroded and covered by younger sediments, and overprinted by soil formation. The LMI probably originated from the Keli Lambo Volcanic Complex (KVC) or old volcano in the southeastern part of the basin.

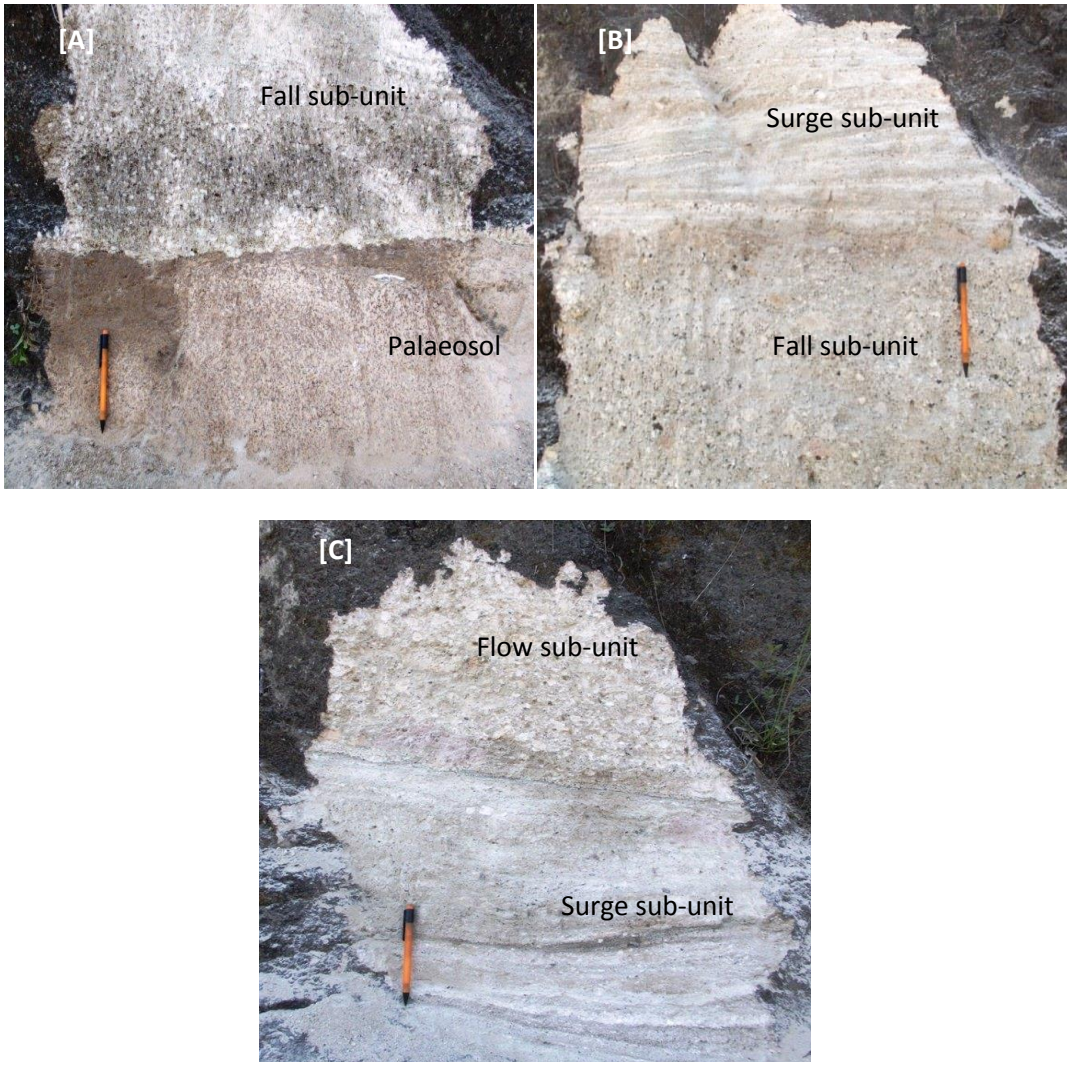

Figure 5.3. Field photographs of the Lowo Mali Ignimbrite at the type section (8°41”27.2”S; 121°10’36.1”E). A) The pyroclastic fall sub-unit directly overlies a palaeosol, and shows a sharp wavy to irregular contact. B) The sharp contact between the surge and tephra-fall sub-units. The surge sub-unit is characterised by planar to low-angle cross bedding. C) The contact between the surge and flow sub-units is a sharp boundary (The pencil is ~14 cm long).

B.2. Geochemistry

Whole-rock chemical analysis by XRF technique was undertaken to obtain the chemical composition of the LMI. Samples were taken from the air-fall and flow sub-units. The major-and trace- element compositions are summarised in Table 5.1. The chemical composition between the air-fall and flow sub-units of the LMI is similar (see Table 5.1). After normalising the total to 100 %, the major-element values of the Upper LMI suggest 63.8–64.0 wt% SiO_2, 0.81–0.84 wt% TiO_2, 17.22–17.47 wt% Al_2O_3, 6.16–6.28 wt% ΣFe_2O_3, 1.62–1.69 wt% MgO, 5.03–5.28 wt% CaO, 3.27–3.30 wt% Na_2O, 1.21–1.29 wt% K_2O and 0.18 wt% P_2O_5 .

Moreover, the trace-element composition of the two sub-units display only small variation and indicate 30 ppm Rb, 238–243 ppm Sr, 140–151 ppm Zr and 246–288 ppm Ba. The silica contents of the air-fall and flow sub-units likely do not reflect the expected values. Field description suggests that the LMI contains white pumice and ash. This ignimbrite likely should have a more silicic (rhyolitic) composition. The low silica content is probably affected by the abundance of minerals in whole-rock samples, such as feldspars, and ferromagnesian minerals.

Table 5.1. Representative major-and trace-element data for the Upper Lowo Mali Ignimbrite, whose samples are taken from Lowo Mali (8°41”27.2”S; 121°10’36.1”E).

Sample	LM-02	LM-03
Unit	Airfall	Flow
Major elements (wt %)		
SiO_2	59.21	59.50
TiO_2	0.78	0.76
Al_2O_3	15.97	16.24
ΣFe_2O_3	5.82	5.72
MnO	0.14	0.14
MgO	1.57	1.51
CaO	4.89	4.67
Na_2O	3.07	3.04
K_2O	1.12	1.20
P_2O_5	0.17	0.16
SO_3	0.01	0.03
LOI	6.29	6.07
Total	99.04	99.04
Trace elements (ppm)		
V	91.4	81.2
Rb	30.3	30.2
Sr	243.0	238.3
Y	37.6	39.0
Zr	139.5	151.0
Nb	2.7	3.1
Ba	246.4	287.5
La	< 2.0	< 2.0
Ce	30.7	12.8
Hf	4.3	5.4
Pb	9.0	10.4
Zn	55.0	57.0
Th	3.4	3.9
U	< 1.0	1.1

Note. Total Fe is expressed as ΣFe_2O_3. LOI = Loss on Ignition.

C. Tangi Talo Tephra (TTL)

C.1. Description and Interpretation

The Tangi Talo Tephra (hereafter TTL) is a series of tephra deposits, consisting of three discrete layers i.e. TTL-T1, TTL-T2, TTL-T4 and TTL-T5, occurring within a vertical interval of ~5 m and separated by other sedimentary facies (Figure 5.4 and 5.5). The complete sequence of the TTL is well-exposed in the main Tangi Talo slot trench. The TTL-T3 is not included because it is definitely a debris flow deposit.

TTL-T1 is a fine grained (clay to silt) vitric ash. It displays white colour, is texturally very well-sorted, massive and has a low crystal content. Thickness of this tephra is approximately 14.5 cm, and it is bracketed by palaeosol horizons with flat but gradationall basal contact. TTL-T2 is a vitric ash, with a white colour, has a low mineral content and is 9-cm thick. This tephra is overlain by a palaeosol and has similar texture to TTL-T1. TTL-T1 and TTL-T2 are separated by a 48-cm-thick palaeosol. It is difficult to observe the mineral assemblages of TTL-T1 and TTL-T2 because of their fine grain size. XRD analysis indicates that both tephras contain low amounts of plagioclase, quartz, biotite, amphibole and pyroxene.

TTL-T4 is a massive vitric ash of whitish colour. This tephra is well sorted, and predominantly composed of volcanic glass in clay to very find sand size and low amounts of minerals. This ash bed is bracketed by laharic deposits. TTL-T4 is up to 4.2 cm-thick, has a sharp and undulating basal boundary and the upper part has been eroded by the overlying laharic deposit. It should be taken into account that the stratigraphic position of TTL-T4 is ~1 m above the laharic layer that contains abundant fossil vertebrate remains.

TTL-T5 is quite distinctive compared to all other pyroclastic deposits encountered in the Soa Basin. This tephra displays a greenish colour, is 54 cm-thick and consists of coarse to very coarse-grained sandy ash, massive to crudely stratified, with a sharp and planar basal contact (Figure 5.5). TTL-T5 is normal-graded, well to moderately sorted, and contains moderate contents of

feldspars and less abundance of quartz, K-feldspar, hornblende, pyroxene and biotite. The upper part shows stratification that indicates redeposition by flowing water. TTL-T5 overlies a laharic deposit and this tephra occurrs ~2-m above the fossil-bearing layers. This TTL-T5 has been dated using the $^{40}Ar/^{39}Ar$ technique and yielded an age of 1.27±0.038 Ma (Stephanie Flude, personal communication). Field characteristics of coarse grain size, normal grading and being crystal-rich suggest that TTL-T5 represents a distal-medial pyroclastic fall deposit.

Because of limited exposures, the spatial distribution of the TTL in the Soa Basin is unclear. So far, the TTL has only been encountered in the Tangi Talo excavation and this ash may have been eroded from the higher basin areas.

C.2. Geochemistry

Whole-rock XRF analysis and electron microprobe analysis (EMPA) of individual glass shards are used to determine the chemical composition of the TTL. The summary of major-and trace-element values is listed in Table 5.2 and 5.3; and the major-element values then are recalculated to 100 % for discussion.

The whole-rock composition of the TTL displays 60.0–95.3 wt% SiO_2, 0.06–0.30 wt% TiO_2, 2.47–17.45 wt% Al_2O_3, 0.92–8.06 wt% ΣFe_2O_3, 0.01–0.18 wt% MnO, 0.58–2.43 wt% MgO, 0.42–6.82 wt% CaO, 0.22–3.36 wt% Na_2O, 0.04–1.40 wt% K_2O, 0.01–0.15 wt% P_2O_5, 21–49 ppm Rb, 152–354 ppm Sr, 65–147 ppm Zr and 147–214 ppm Ba (Table 5.2a). Whole-rock composition indicates that TTL-T4 has the highest SiO_2 content and lowest Al_2O_3 and total alkali contents. TTL-T1 has highest Rb, Sr, Ba, Ce and Th; while TTL-T5 displays highest Al_2O_3, MnO, ΣFe_2O_3, MgO, Sr and Y contents. TTL-T1 and TTL-T2 show small differences in CaO, Zr and La.

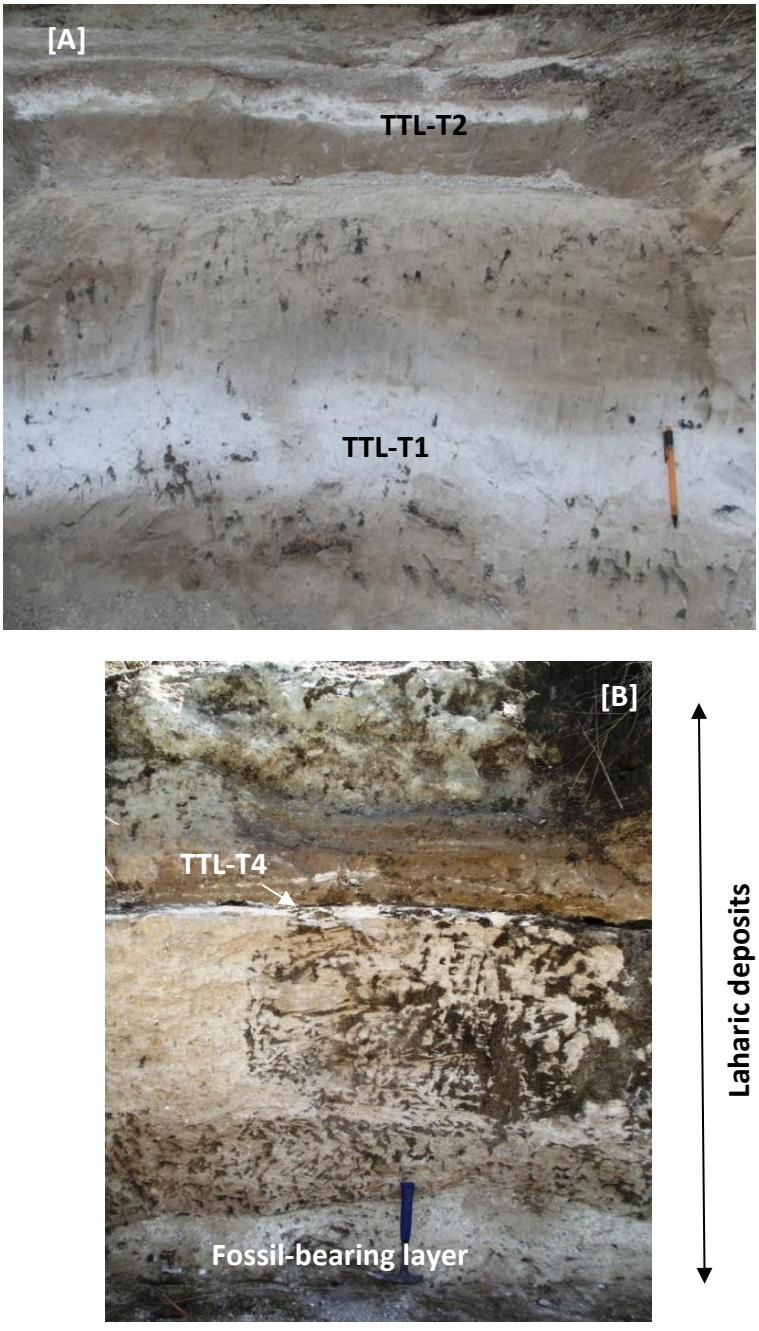

Figure 5.4. Field photographs of the Tangi Talo Tephra that is well-exposed at Tangi Talo (8°41'53.0"S; 121°08'10.6"E); A) Exposure of TTL-T1 and TTL-T2, which indicate that TTL-T1 is bracketed by palaeosols; B) TTL-T4 overlies a laharic deposit, ~1 m above the fossil layer (The pencil is ~14 cm, and the geological hammer is ~30 cm).

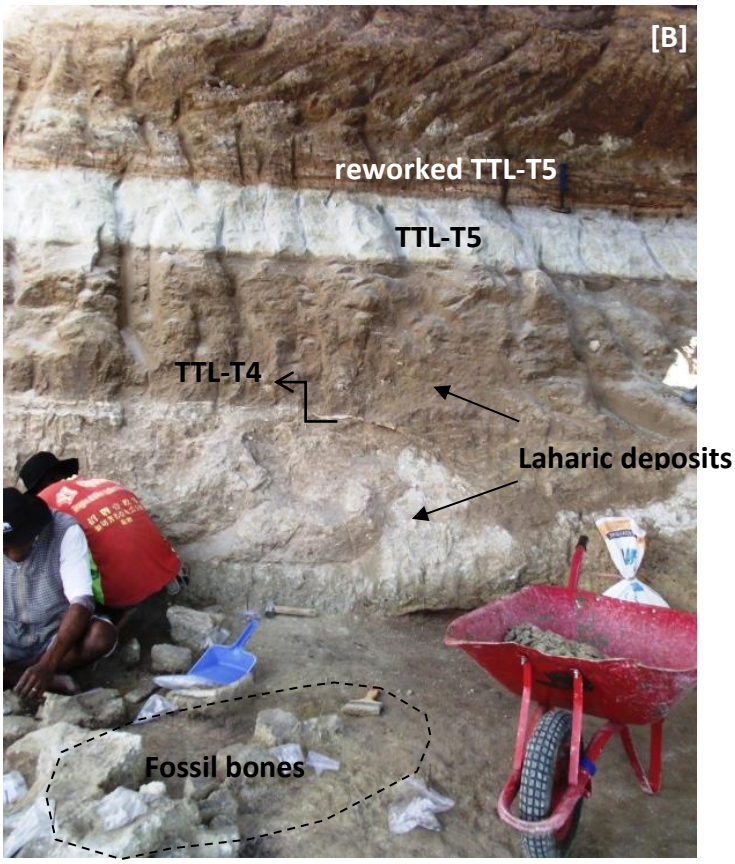

Figure 5.5. Exposure of TTL-T5 at the Tangi Talo excavation (8°41'53.0"S; 121°08'10.6"E); A) The sharp lower boundary and reworked tephra immediately above TTL-T5. B) TTL-T5 overlies two laharic deposits (brownish and whitish colours), of which the lower horizon covers a concentration of fossil remains (The geological hammer is ~30 cm).

Table 5.2. Representative major-and trace-element data for the Tangi Talo Tephra, whose analysed samples are collected from the Tangi Talo site (8°41'53.0"S; 121°08'10.6"E).

Sample	TT-02	TT-04	TT-07	TT-10
Unit	TTL-T1	TTL-T2	TTL-T4	TTL-T5
Major elements (wt %)				
SiO_2	64.88	63.83	88.82	58.50
TiO_2	0.26	0.27	0.06	0.75
Al_2O_3	12.87	13.97	1.82	17.02
ΣFe_2O_3	2.66	3.32	1.06	7.86
MnO	0.05	0.09	0.01	0.16
MgO	2.39	2.88	0.39	2.37
CaO	2.43	2.21	0.42	6.65
Na_2O	0.87	0.74	0.19	3.27
K_2O	1.23	1.23	0.04	0.80
P_2O_5	0.03	0.04	0.01	0.15
S	0.02	0.02	0.02	0.02
LOI	12.05	10.80	6.74	3.03
Total	99.74	99.41	99.57	100.59
Trace elements (ppm)				
V	79.7	202.0	n.d.	191.1
Rb	49.4	21.2	n.d.	21.9
Sr	197.7	152.1	n.d.	354.1
Y	13.7	12.9	n.d.	18.3
Zr	121.1	147.4	n.d.	64.9
Nb	1.8	2.6	n.d.	1.5
Ba	214.3	146.8	n.d.	190.1
La	18.4	18.6	n.d.	10.1
Ce	46.1	22.6	n.d.	26.9
Hf	8.9	5.3	n.d.	1.7
Pb	14.9	21.3	n.d.	5.0
Zn	58.7	71.8	n.d.	24.1
Th	4.2	2.8	n.d.	2.1
U	1.9	1.1	n.d.	< 1.0

Note. Total Fe is presented as ΣFe_2O_3. LOI = Loss on Ignition; and n.d. = not determined.

Table 5.3. Major-element composition of glass shards from the Tangi Talo Tephra collected from the Tangi Talo site (8°41'53.0"S; 121°08'10.6"E).

Sample	TT-02		TT-04		TT-07	
Unit	TTL-T1		TTL-T2		TTL-T4	
n	7		4		4	
SiO_2	74.16	1.34	74.59	0.49	72.88	1.78
TiO_2	0.16	0.04	0.16	0.04	0.27	0.08
Al_2O_3	12.22	0.21	12.09	0.27	9.99	2.05
ΣFeO	1.05	0.08	1.27	0.55	3.86	1.82
MnO	0.09	0.03	0.12	0.07	0.05	0.06
MgO	0.21	0.02	0.45	0.50	0.58	0.21
CaO	1.18	0.13	1.17	0.06	0.87	0.42
Na_2O	2.73	0.43	3.26	0.79	0.99	1.57
K_2O	2.41	0.39	2.41	0.44	0.58	0.70
Cl	0.17	0.02	0.16	0.01	0.06	0.10
Total	94.39	-	95.69	-	90.12	-

Note. Major-element values are expressed in wt % and presented as a mean value (first column) and standard deviation (second column). Total Fe is presented as ΣFeO and *n* is the number of glass shards analysed.

The glass composition of the TTL shows 78.0–83.0 wt% SiO_2, 0.16–0.34 wt% TiO_2, 10.20–12.95 wt% Al_2O_3, 1.11–5.36 wt% ΣFeO, 0.02–0.13 wt% MnO, 0.23–0.77 wt% MgO, 0.75–1.66 wt% CaO, 0.23–3.40 wt% Na_2O and 0.26–2.75 wt% K_2O. TTL-T4 is characterised by the highest SiO_2, TiO_2, ΣFeO and MgO contents; TTL-T2 displays the highest Na_2O content, and TTL-T5 has the highest contents of CaO and K_2O. The major-element composition of TTL-T1 and TTL-T2 are very similar. Both tephras have small differences in the concentration of SiO_2, TiO_2, Al_2O_3, ΣFeO, MnO, MgO, CaO and K_2O. In contrast, TTL-T4 has a distinct composition compared to TTL-T1, TTL-T2 and TTL-T5, displaying the highest values of SiO_2, TiO_2, ΣFeO and MgO; and the lowest amounts of Na_2O and K_2O. TTL-T1 and TTL-T2 have nearly identical chemical composition and these tephra beds are clearly chemically different with TTL-T4 and TTL-T5. It can be presumed

that TTL-T1 and TTL-T2 are derived from the same source volcano or characteristic magma. On the other hand, TTL-T4 and TTL-T5 indicate different volcanic sources.

D. Wolo Wawo Tephra (WLW)

D.1. Description and Interpretation

The Wolo Wawo Tephra (WLW) is a distal tephra-fall deposit of fine-grained vitric ash, silty to sandy, massive, well sorted, with a sharp base and minor crystal content. This tephra is well-exposed near Wolowawo Village, and also found at Tangi Talo, Mata Menge and Pumaso (Figure 5.6). The WLW is bounded by palaeosols in all recorded sections.

The WLW can be traced laterally both in the western (Mata Menge) and eastern (Pumaso) parts of the Soa Basin. The WLW varies in thickness from 4 to 21 cm. The thinnest WLW unit is developed in the lower slot Trench IX at Mata Menge, while the thickest is at Pumaso. The westward thinning may reflect the wind direction from east to west during the eruption. XRD analysis reveals that this tephra consists of moderate content of plagioclase and less abundance of quartz, K-feldspar, biotite, amphibole and pyroxene.

D.2. Geochemistry

The chemical composition of whole-rock samples and glass shards from the WLW is summarised in Table 5.4. The major-element values then are recalculated to 100 % for discussion. The whole-rock composition of this tephra indicates 69.5–74.3 wt% SiO_2, 0.16–0.22 wt% TiO_2, 14.72–18.93 wt% Al_2O_3, 1.89–7.47 wt% ΣFe_2O_3, 0.03–0.07 wt% MnO, 0.79–2.35 wt% MgO, 1.99–2.40 wt% CaO, 0.03–1.92 wt% Na_2O, 0.06–2.17 wt% K_2O, 0.02–0.06 wt% P_2O_3, 6–22 ppm Rb, 97–172 ppm Sr, 74–78 ppm Zr and 94–147 ppm Ba. The analysed samples display small variation in such elements, for instance SiO_2, Al_2O_3, ΣFe_2O_3, Na_2O, K_2O, V, Ba and Sr contents.

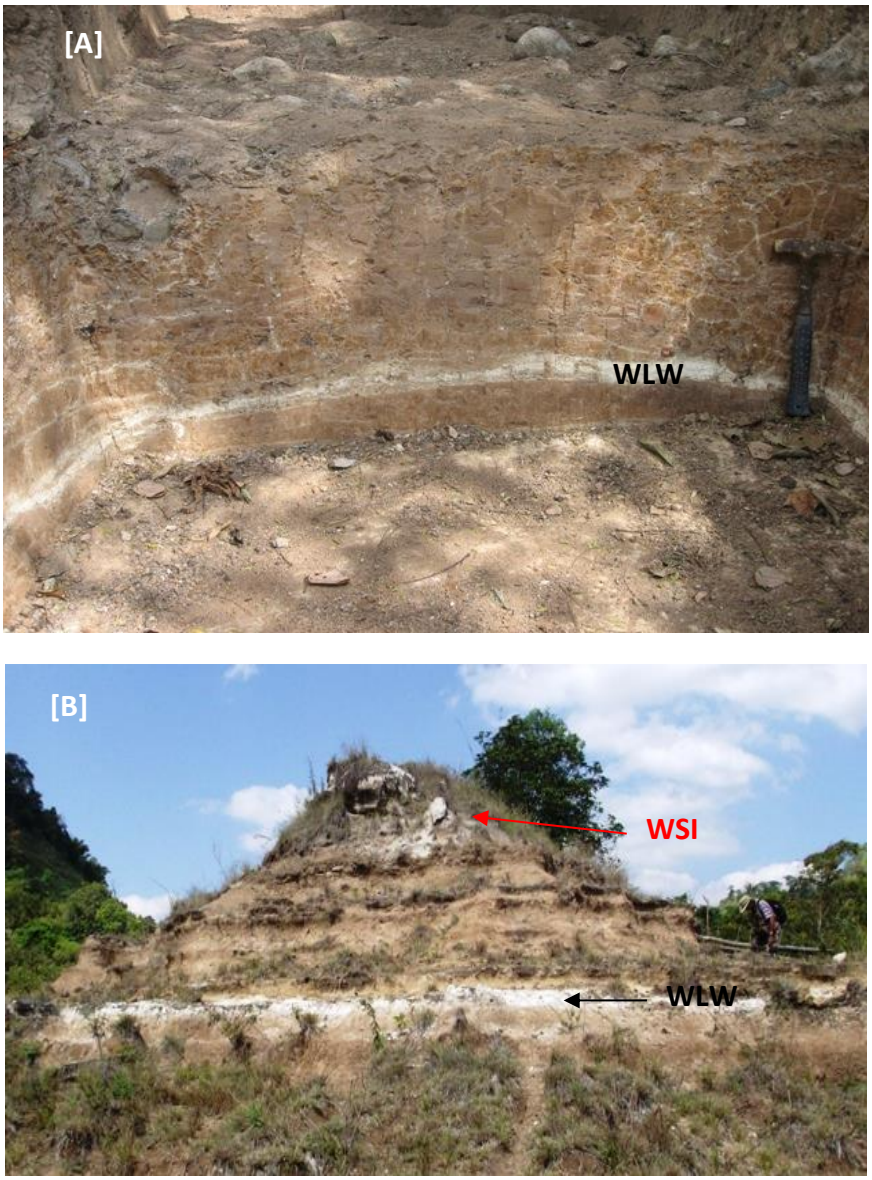

Figure 5.6. Photographs of the Wolo Wawo Tephra. A) The WLW exposed in the lower Trench IX at Mata Menge (8°41'33.8"S; 121°05'44.6"E). B) A part of the stratigraphic section at Pumaso (8°42'30.5"S; 121°09'37.2"E), clearly showing the WLW horizon (black arrow) occurs beneath the Wolo Sege Ignimbrite (red arrow) (The geological hammer is ~30 cm long).

Table 5.4. Representative major-and trace-element data for whole-rock samples and glass shards from the Wolo Wawo Tephra.

Sample	TT-18	MM-03	PM-01		TT-18		PM-01	
Locality	Tangi Talo 8°41'53.0"S 121°08'10.6"E	Mata Menge 8°41'33.8"S 121°05'44.6"E	Pumaso 8°42'30.5"S 121°09'37.2"E		Tangi Talo (n = 11)		Pumaso (n = 18)	
Major elements (wt %)								
SiO_2	60.31	55.17	65.49	SiO_2	74.49	1.48	75.40	0.69
TiO_2	0.52	0.92	0.21	TiO_2	0.15	0.01	0.15	0.01
Al_2O_3	14.20	15.03	16.53	Al_2O_3	12.05	0.40	12.30	0.18
ΣFe_2O_3	4.77	5.93	1.73	ΣFeO	1.02	0.07	1.00	0.07
MnO	0.04	0.03	0.06	MnO	0.08	0.02	0.07	0.02
MgO	1.58	0.63	1.83	MgO	0.23	0.02	0.23	0.01
CaO	2.65	1.58	1.84	CaO	1.18	0.02	1.19	0.02
Na_2O	0.02	< 0.02	1.76	Na_2O	2.52	0.55	3.63	0.35
K_2O	0.29	0.05	1.98	K_2O	2.54	0.56	2.43	0.20
P_2O_5	0.11	0.05	0.02	Cl	0.18	0.01	n.d.	
S	0.05	0.01	0.04					
LOI	16.63	19.91	8.34					
Total	101.16	99.31	99.83		94.44	-	96.40	-
Trace elements (ppm)								
V	170	193	n.d.		n.d.		n.d.	
Rb	22	6	n.d.		n.d.		n.d.	
Sr	172	97	n.d.		n.d.		n.d.	
Y	13	9	n.d.		n.d.		n.d.	
Zr	78	74	n.d.		n.d.		n.d.	
Nb	2	1	n.d.		n.d.		n.d.	
Ba	94	147	n.d.		n.d.		n.d.	
La	2	12	n.d.		n.d.		n.d.	
Ce	2	2	n.d.		n.d.		n.d.	
Hf	4	2	n.d.		n.d.		n.d.	
Pb	12	4	n.d.		n.d.		n.d.	
Zn	75	55	n.d.		n.d.		n.d.	
Th	4.3	1.0	n.d.		n.d.		n.d.	
U	1.0	1.0	n.d.		n.d.		n.d.	

Note. Total Fe is expressed as ΣFe_2O_3 (whole-rock) and ΣFeO (glass shards). Glass composition is presented as a mean value (first column) and standard deviation (second column), n is the number of glass shards analysed, and n.d. = not determined.

Moreover, the glass composition of the WLW suggests 78.2–78.9 wt% SiO_2, 0.15–0.16 wt% TiO_2, 12.74–12.76 wt% Al_2O_3, 1.04–1.08 wt% ΣFe_2O_3, 0.07–0.08 wt% MnO, 0.24 wt% MgO, 1.23–1.25 wt% CaO, 2.62–3.77 wt% Na_2O and 2.52–2.77 wt% K_2O. The major-element values of glass shards analysed show little variation. The chemical composition of whole-rock samples and glass shards from the WLW exhibits differences with respect to SiO_2, Al_2O_3, MgO, CaO and iron oxides. The SiO_2 content of glass shards is higher than the whole-rock samples; however, the other major oxides in whole-rock samples are more abundant than in the glass shards. The occurrence of feldspars and ferromagnesian minerals in whole-rock samples is responsible for those anomalies as confirmed by XRD analysis.

E. Wolo Sege Ignimbrite (WSI)

E.1. Description and Interpretation

The Wolo Sege Ignimbrite (WSI) was first discovered at the archaeological site of Wolo Sege (Brumm et al., 2010), the type locality for this widespread volcanic marker bed (Figure 5.7a and 5.7b). The WSI generally consists of six sub-units that can be grouped into surge (A, B and D), tephra-fall (C) and flow (E and F) sub-units. Sub-unit A near the base of WSI is a fine grained vitric ash, silty-sandy, crystal poor, massive to crudely stratified, very well sorted, with a sharp and undulatory basal surface and a thickness of less than 4 cm. Sub-unit A is interpreted as a pyroclastic surge deposit (base surge), which was formed from the base of a collapsing eruption column.

Sub-unit A is always overlain by sub-unit B, which comprises a pumiceous vitric ash, coarse grained, massive to showing bedding with abundant sand-sized pumice clasts, poorly sorted, has a sharp base and a thickness of 2.5 – 10 cm. This sub-unit represents a pyroclastic surge deposit, which was formed by pyroclastic density currents in which particles were supported mainly by turbulence (see Cas and Wright, 1987; Branney and Kokelaar, 2002). XRD analysis of sub-unit B indicates the presence of plagioclase, K-feldspar, quartz, micas

(biotite and muscovite), amphibole (hornblende, cummingtonite and riebeckite), and pyroxene.

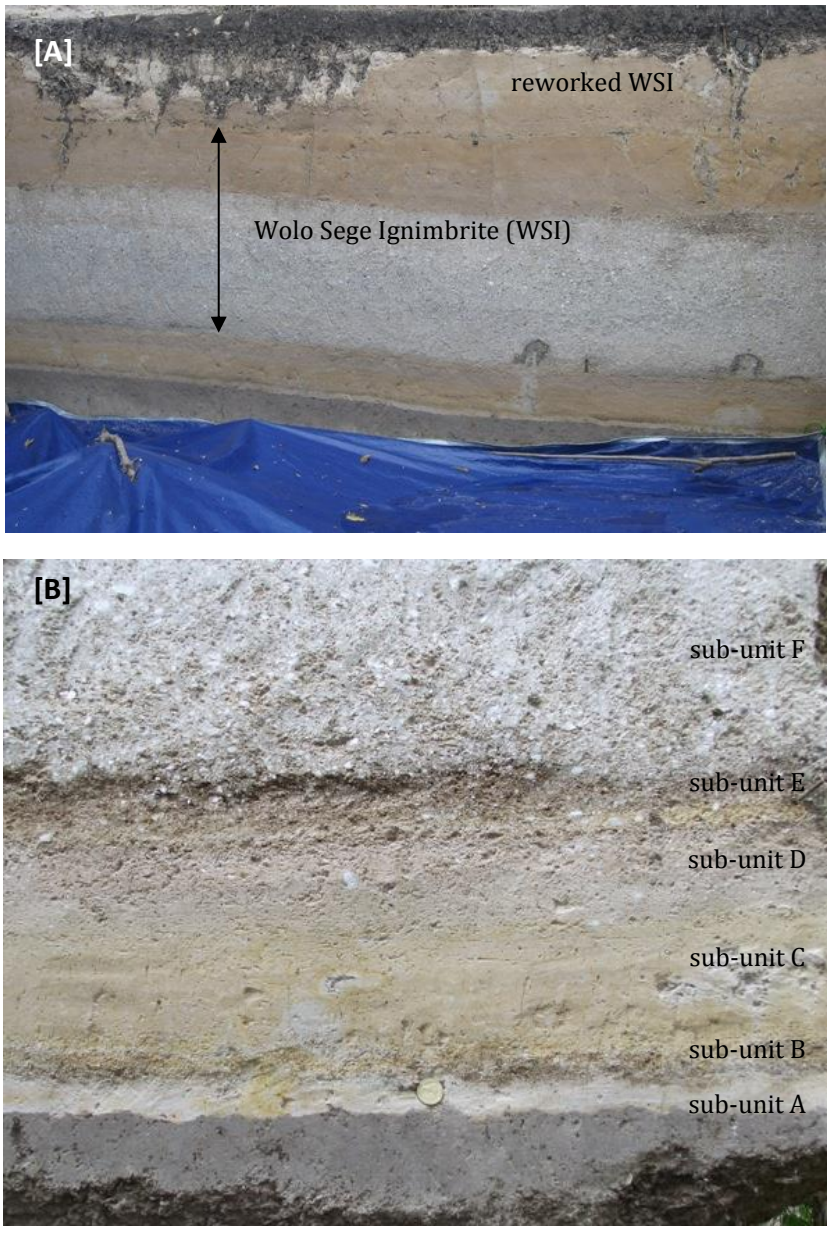

Figure 5.7a. Exposure of the Wolo Sege Ignimbrite at the type section (8°41'27.1"S; 121°06'00.0"E); A) WSI is directly overlain by its reworked materials as exposed in the southern face of the Wolo Sege excavation; B) Detail of WSI consisting of 6 sub-units (The coin is ~24 mm in diameter; the geological hammer is ~30 cm long).

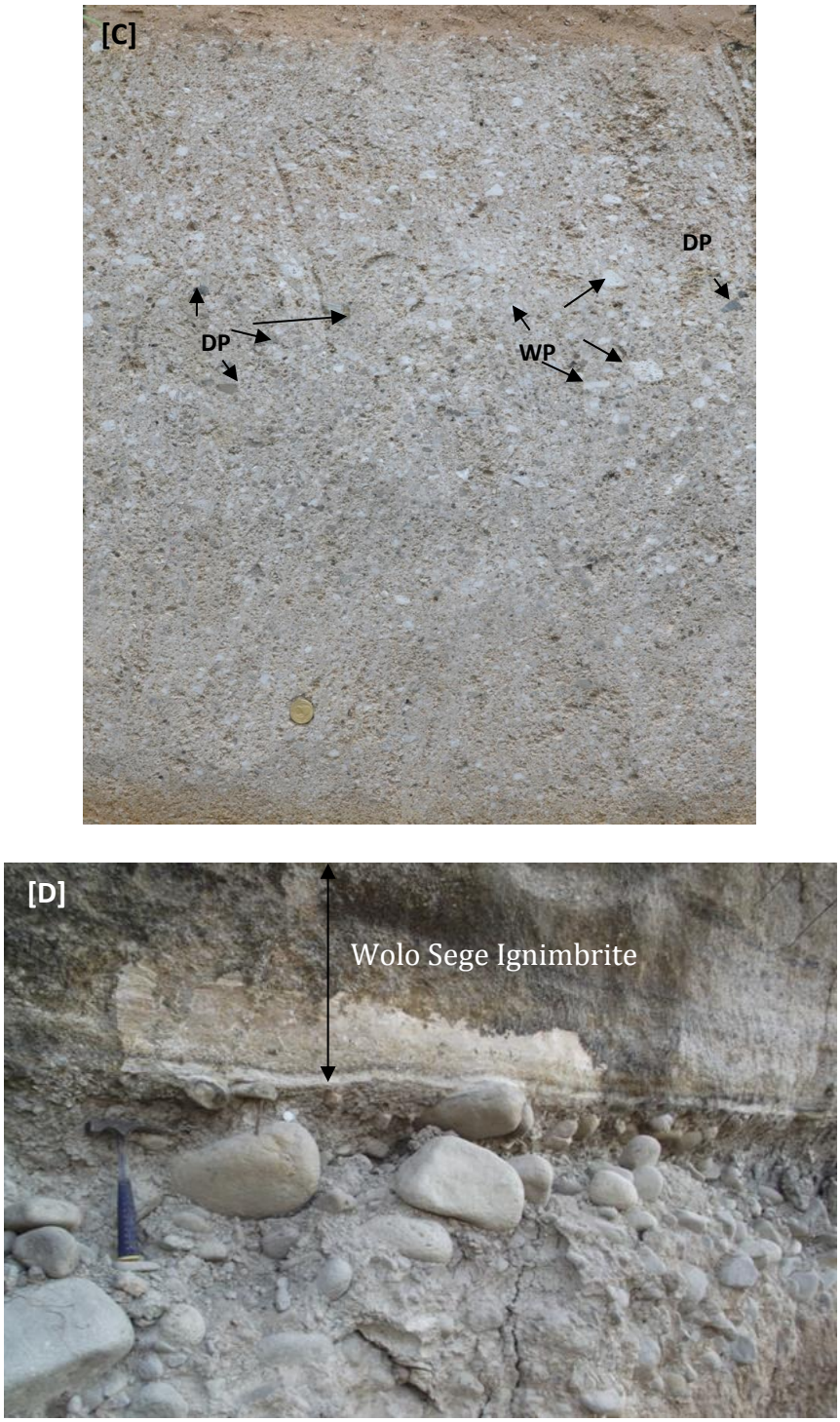

Figure 5.7b. C) Pumice clasts in sub-unit F consist of white pumice (WP) and dark pumice (DP), which indicate magma mixing; and D) WSI overlies a fluvial conglomerate at Matago (8°43'06.5"S; 121°08'18.9"E) (The coin is ~24 mm in diameter; the geological hammer is ~30 cm long).

Sub-unit B is covered by Sub-unit C, which constitutes fine sandy vitric ash, that contains abundant rim-type accretionary lapilli (facies Tma). The texture of Sub-unit C is massive, poorly sorted, has a sharp basal contact and is 11 – 30 cm-thick. The occurrence of accretionary lapilli is a characteristic of a pyroclastic fall deposits, generated from phreatomagmatic eruptions (Cas and Wright, 1987; Morrissey *et al*., 2000). XRD analysis indicates a similar mineral composition as Sub-unit B.

Sub-unit C is overlain by sub-unit D, which consists predominantly of coarse sandy pumiceous ash, rich in sand-sized pumice detritus, massive, poorly sorted, with a sharp lower contact and is 4 – 18.5 cm-thick. Sub-unit D has identical characteristics and mineral composition (XRD) as Sub-unit B, and was formed by turbulence-dominated pyroclastic density currents. Sub-unit E overlies sub-unit D, and this sub-unit comprises fine – coarse pumiceous lapilli, poorly sorted, normally graded, crudely to well bedded, low crystal concentrations, has a sharp base and a thickness ranging from 5 to 22 cm. This sub-unit is a pyroclastic flow deposit, representing a pre-ignimbrite phase. Sub-unit F immediately overlies sub-unit E, constitutes fine to coarse pumiceous lapilli, is normally graded, poorly sorted, composed of white pumice (silicic) and grey pumice (basaltic or andesitic), with a moderate concentration of crystals, poor in lithic fragments, has a sharp base and is 17.5 – 171 cm-thick. XRD analysis shows that Sub-unit F contains plagioclase, K-feldspar, quartz, tridymite, micas (biotite and muscovite), amphibole (hornblende, cummingtonite and riebeckite), and pyroxene.

Sub-units E and F represent non-welded ignimbrites, produced by pyroclastic density currents. The two distinct types of pumice fragments indicate mixing of mafic and felsic magmas in the magma chamber prior to an explosive eruption. The reaction between hot basaltic magma and cooler silicic magma at shallow depth generates extensive gas bubbles, raising pressures in the magma chamber. The increased pressures result in the formation of fractures within volcanoes and subsequently trigger explosive eruptions (Cas and Wright, 1986;

Branney and Kokelaar, 2002). Pyroclastic flow sub-units are commonly overlain by resedimented co-ignimbritic ash, comprising massive-stratified fine grained ash with abundant accretionary lapilli.

The field characteristics indicate that WSI is a product of a single phreatomagmatic eruption and the source is still unknown. The presence of a large grey pumice clast (4 cm x 5.5 cm) incorporated within resedimented ash exposed at Lowo Mali (Figure 5.8), may indicate that the source of WSI more likely originated from the Keli Lambo Volcanic Complex (KLVC) in the eastern part of the study area, rather than the Welas Caldera in the northwest. WSI is widely distributed in the Soa Basin and can be found at many localities. The WSI has been securely dated at 1.02 ± 0.02 Ma (Brumm *et al*., 2010) and is an important stratigraphic marker bed. The WSI commonly covers well-developed palaeosols, which in at least three sites contain *in situ* stone tools (e.g. Wolo Sege, Kobatuwa-04 and Matago).

Figure 5.8. Grey pumice clast within reworked WSI exposed at Lowo Mali (8°41'25.8"S; 121°10'37.2"E). The white bands in the pumice indicate rhyolitic composition, thus this pumice is a product of magma mixing (The coin is ~24 mm in diameter).

D.2. Geochemistry

Whole-rock XRF analysis has been made on representative samples collected from Kobatuwa-4, Mata Menge, Wolo Sege, Wae Bha, Tangi Talo, Matago, Pumaso and Lowo Mali. In addition, glass samples of Wolo Sege and Tangi Talo are also determined for their chemical composition. The geochemical data of the WSI are listed in Table 5.5a and 5.5b, and then the major-element contents of whole-rock samples and glass shards are recalculated to 100 % for discussion.

The whole-rock composition of sub-unit A displays 63.4–76.1 wt% SiO_2, 0.34–0.51 wt% TiO_2, 15.31–19.35 wt% Al_2O_3, 3.10–4.16 wt% ΣFe_2O_3, 0.02–0.21 wt% MnO, 0.01–3.87 wt% MgO, 1.23–2.88 wt% CaO, 0.02–1.98 wt% Na_2O, 0.31–2.61 wt% K_2O, 0.01–0.10 wt% P_2O_3, 13–80 ppm Rb, 146–206 ppm Sr, 113–146 ppm Zr and 157–415 ppm Ba. Sub-unit B comprises 69.1–71.5 wt% SiO_2, 0.37–0.48 wt% TiO_2, 15.31–17.82 wt% Al_2O_3, 3.65–4.73 wt% ΣFe_2O_3, 0.09–0.15 wt% MnO, 0.38–1.29 wt% MgO, 2.72–3.31 wt% CaO, 1.44–2.13 wt% Na_2O, 1.85–2.44 wt% K_2O, 0.04–0.10 wt% P_2O_3, 63–72 ppm Rb, 209–240 ppm Sr, 103–115 ppm Zr and 355–409 ppm Ba.

Chemical analysis of whole-rock samples from sub-unit C and sub-unit D display 66.0–73.0 wt% and 70.0–73.2 wt% SiO_2 respectively, 0.34–0.46 wt% and 0.35–0.40 wt% TiO_2, 15.60–21.10 wt% and 15.50–17.90 wt% Al_2O_3, 3.40–4.14 wt% and 3.21–3.76 wt% ΣFe_2O_3, 0.02–0.19 wt% and 0.10–0.21 wt% MnO, 0.01–4.30 wt% and 0.18–1.82 wt% MgO, 1.08–4.73 wt% and 2.56–2.84 wt% CaO, 0.02–1.98 wt% and 1.33–2.18 wt% Na_2O, 0.40–2.47wt% and 1.96–2.50 wt% K_2O, 0.02–0.17 wt%, 0.04–0.11 wt% P_2O_3, 12–76 ppm and 74–77 ppm Rb, 187–635 ppm and 207–224 ppm Sr, 106–139 ppm and 106–113 ppm Zr, and 96–519 ppm and 397–492 ppm Ba.

The whole-rock samples of sub-unit F constitute 66.8–77.6 wt% SiO_2, 0.23–0.41 wt% TiO_2, 14.26–20.90 wt% Al_2O_3, 1.75–3.80 wt% ΣFe_2O_3, 0.05–0.16 wt% MnO, 0.11–3.77 wt% MgO, 1.56–3.12 wt% CaO, 0.56–2.53 wt% Na_2O, 0.37–2.81 wt% K_2O, 0.02–0.15 wt% P_2O_5, 23–79 ppm Rb, 150–220 ppm Sr, 99–

139 ppm Zr, 191–530 ppm Ba. Moreover, the whole-rock redeposited sub-units (sub-unit G and H) are composed of 66.7–73.2 wt% SiO_2, 0.31–0.45 wt% TiO_2, 16.33–19.70 wt% Al_2O_3, 3.21–4.72 wt% ΣFe_2O_3, 0.09–0.14 wt% MnO, 0.26–3.40 wt% MgO, 2.28–3.14 wt% CaO, 0.75–1.31 wt% Na_2O, 0.62–2.37 wt% K_2O, 0.02–0.15 wt% P_2O_5, 36–77 ppm Rb, 195–237 ppm Sr, 113–142 ppm Zr, and 249–504 ppm Ba.

The glass composition of individual sub-units from the WSI is listed in Table 5.5b. Sub-unit B exhibits 77.5 wt% SiO_2, 0.18 wt% TiO_2, 13.75 wt% Al_2O_3, 1.27 wt% ΣFeO, 1.91 wt% CaO, 2.46 wt% Na_2O and 2.31 wt% K_2O. Sub-unit C has 77.5 wt% SiO_2, 0.18 wt% TiO_2, 13.57 wt% Al_2O_3, 1.23 wt% ΣFeO, 1.90 wt% CaO, 2.79 wt% Na_2O and 2.22 wt% K_2O. The glass content of sub-unit D is composed of 77.3 wt% SiO_2, 0.16 wt% TiO_2, 13.61 wt% Al_2O_3, 1.25 wt% ΣFeO, 1.86 wt% CaO, 3.09 wt% Na_2O and 2.13 wt% K_2O.

The two samples of sub-unit F have 76.7–77.2 wt% SiO_2, 0.17 wt% TiO_2, 13.66–13.68 wt% Al_2O_3, 1.25–1.26 wt% ΣFeO, 0.09 wt% MnO, 0.32–0.33 wt% MgO, 1.85–1.86 wt% CaO, 3.08–3.59 wt% Na_2O, 2.11–2.12 wt% K_2O. In addition, the reworked sub-units (sub-unit G and H) consist of 77.17–77.30 wt% SiO_2, 0.17–0.19 wt% TiO_2, 13.69–13.70 wt% Al_2O_3, 1.25–1.28 wt% ΣFeO, 0.07–0.09 wt% MnO, 0.31–0.33 wt% MgO, 1.84–1.85 wt% CaO, 2.94–3.15 wt% Na_2O, and 2.07–2.16 wt% K_2O.

The whole-rock composition of the primary and reworked sub-units does not display significant differences. The glass composition also confirms that the major-element values of the primary and reworked sub-units are nearly similar. The chemical similarity between the primary and reworked sub-units coincide with the field features that those sub-units were derived from the same source. In addition, the contents of TiO_2, Al_2O_3, MgO, CaO and total iron in whole-rock samples are commonly higher than in the glass shards (see Table 5.5a and 5.5b). The elemental variation is presumably due to the abundance of feldspars and ferromagnesian minerals within whole-rock samples.

Table 5.5a. Representative major-and trace-element compositions of whole-rock samples from the Wolo Sege Ignimbrite.

Sample	KBT04/2	KBT04/3	KBT04/4	MM-09	MM-10	MM-11	WS-07	WS-08	WS-09	WS-10	WS-11	WS-12	WS-13
Sub-unit	A	C	F	B	C	F	A	B	C	D	F	G	H
Locality	Kobatuwa-04 8°41'16.7"S; 121°05'01.6"E			Mata Menge 8°41'33.8"S; 121°05'44.6"E			Wolo Sege 8°41'27.1"S; 121°06'00.0"E						
Major elements (wt %)													
SiO_2	65.07	66.17	68.74	63.23	59.42	68.47	67.56	66.50	67.53	69.16	70.38	65.21	67.49
TiO_2	0.30	0.34	0.27	0.43	0.34	0.20	0.32	0.41	0.37	0.28	0.26	0.34	0.33
Al_2O_3	13.59	14.24	13.09	14.87	17.16	14.47	14.91	15.52	15.19	14.41	14.23	15.40	15.56
ΣFe_2O_3	2.76	3.17	2.44	3.18	2.81	1.55	2.97	3.74	3.43	2.49	2.29	3.15	3.03
MnO	0.08	0.10	0.09	0.02	0.01	0.04	0.08	0.09	0.08	0.20	0.08	0.08	0.10
MgO	0.70	0.77	0.55	< 0.01	< 0.01	0.19	0.27	0.35	0.29	0.07	0.10	0.50	0.68
CaO	2.16	2.42	2.40	1.03	0.88	1.38	2.23	2.90	2.66	2.49	2.46	2.12	2.28
Na_2O	1.76	1.81	2.00	< 0.02	< 0.10	0.74	0.94	1.34	1.13	1.19	1.48	0.93	0.57
K_2O	2.32	2.22	2.18	0.25	0.45	1.23	2.30	2.04	2.28	2.46	2.48	2.13	2.40
P_2O_5	0.03	0.04	0.03	0.04	0.14	0.03	0.09	0.09	0.10	0.11	0.08	0.08	0.10
S	0.03	0.04	0.03	0.07	0.55	0.06	0.01	0.01	0.005	0.01	0.01	0.04	0.14
LOI	10.14	8.32	7.27	16.37	18.55	10.42	8.94	8.13	8.16	8.30	7.76	10.16	9.36
Total	98.91	99.64	99.09	99.51	100.42	98.78	100.62	101.12	101.23	101.17	101.61	100.14	102.04
Trace elements (ppm)													
V	47.8	30.5	12.4	128.1	107.4	36.7	52.2	67.4	61.7	51.9	27.0	70.0	86.3
Rb	80.2	76.3	73.9	12.9	11.8	28.6	72.1	65.1	73.9	76.7	77.8	77.2	72.1
Sr	205.5	219.7	204.8	145.9	635.1	149.5	204.9	237.1	236.1	224.5	217.3	236.9	210.8
Y	15.3	20.1	16.7	5.6	5.9	6.6	16.8	17.5	16.8	16.3	13.5	18.8	16.8
Zr	116.0	110.6	99.2	146.0	105.6	98.6	112.5	103.9	110.2	105.7	102.4	112.5	121.9
Nb	2.9	2.3	2.2	3.6	2.4	2.4	2.4	2.7	2.5	2.6	2.5	2.7	2.6
Ba	413.6	430.5	429.7	208.1	519.4	190.6	414.9	408.5	424.1	492.2	421.6	504.4	472.4
La	21.2	17.0	2.0	12.7	30.0	18.4	6.8	12.2	12.3	11.9	15.6	2.0	35.4
Ce	28.5	38.1	29.5	2.0	54.7	2.0	19.9	22.9	20.4	23.0	2.0	58.7	2.0
Hf	3.9	4.5	5.4	4.2	3.3	2.9	4.2	4.0	3.9	3.2	4.2	3.4	5.0
Pb	9.4	16.3	9.1	34.5	59.0	11.1	12.3	12.4	18.0	15.1	10.5	13.2	14.2
Zn	23.1	54.7	40.2	34.3	26.9	16.8	48.0	51.5	54.7	52.0	41.9	55.4	53.4
Th	7.9	7.1	7.5	4.8	5.3	4.6	7.7	6.7	7.2	7.1	7.7	7.2	8.0
U	2.0	3.1	3.6	1.0	1.0	0.4	1.9	1.5	1.8	1.6	2.3	1.9	1.4

Table 5.5a. Continued.

Sample	WB-01	WB-02	WB-03	TT-25	TT-26	TT-27	MTG-01	MTG-02	MTG-03	MTG-04	MTG-05
Sub-unit	C	F	G	C	F	G	A	B	C	D	F
Locality	Wae Bha 8°43'12.8"S; 121°06'40.2"E			Tangi Talo 8°41'53.0"S; 121°08'10.6"E			Matago 8°43'06.5"S; 121°08'18.9"E				
Major elements (wt %)											
SiO_2	54.84	55.94	57.29	56.05	63.32	65.91	55.84	65.88	61.87	63.06	68.34
TiO_2	0.38	0.36	0.38	0.38	0.32	0.31	0.37	0.40	0.36	0.36	0.27
Al_2O_3	15.81	17.44	16.05	16.58	15.06	14.71	16.04	14.16	14.65	14.64	13.35
ΣFe_2O_3	3.45	3.46	4.28	3.42	2.91	2.89	3.45	3.68	3.35	3.37	2.24
MnO	0.05	0.13	0.09	0.16	0.09	0.08	0.10	0.09	0.08	0.19	0.11
MgO	3.58	3.06	2.81	2.77	1.04	0.86	3.20	0.96	1.73	1.52	0.59
CaO	3.94	2.67	2.47	2.61	2.74	2.38	2.39	3.06	2.46	2.53	2.49
Na_2O	0.80	0.75	0.98	0.02	0.49	0.67	0.80	1.97	1.55	1.73	2.05
K_2O	0.33	0.35	0.67	0.53	1.75	2.11	0.68	2.26	1.74	2.05	2.59
P_2O_5	0.03	0.03	0.04	0.11	0.14	0.14	0.02	0.06	0.04	0.05	0.05
S	0.05	0.02	0.11	0.02	0.01	0.02	0.04	0.10	0.08	0.04	0.08
LOI	16.24	14.86	14.35	19.41	11.17	10.34	16.35	7.62	11.48	10.73	7.1
Total	99.50	99.06	99.51	102.05	99.04	100.43	99.28	100.23	99.39	100.26	99.26
Trace elements (ppm)											
V	235.3	29.4	67.0	206.6	40.8	44.4	77.8	65.3	71.4	54.3	43.9
Rb	11.7	23.3	35.6	20.0	64.7	70.7	30.7	71.9	60.9	73.8	78.5
Sr	187.1	160.7	194.7	188.8	212.2	211.7	166.6	239.5	214.3	206.5	219.7
Y	20.9	27.7	24.6	19.9	15.8	16.8	13.8	15.7	16.1	16.6	15.4
Zr	131.9	139.5	141.5	135.9	114.0	115.0	141.4	103.3	122.5	112.6	107.6
Nb	3.2	3.7	3.3	3.4	3.0	2.6	2.4	2.9	3.0	3.0	2.8
Ba	95.7	198.1	249.2	283.1	326.7	403.2	156.6	390.6	324.3	457.8	529.9
La	15.0	27.9	10.6	8.8	16.8	21.4	15.7	23.7	21.9	12.6	18.0
Ce	26.4	53.0	40.5	36.7	36.3	34.0	29.6	2.0	40.1	35.0	27.6
Hf	5.5	3.3	4.7	2.6			3.3	2.4	2.9	3.0	2.8
Pb	17.8	14.0	16.0	22.3	15.3	12.6	8.0	10.9	16.8	15.1	11.4
Zn	66.2	64.5	63.4	68.8	55.2	50.1	32.4	25.7	37.5	50.9	13.8
Th	7.8	9.85	9.3	9.1	8.2	7.9	8.8	6.8	8.1	7.3	8.0
U	0.8	1.55	1.1	0.6	1.9	1.7	1.0	2.0	1.0	1.4	2.1

Table 5.5a. Continued.

Sample	PM-06	PM-07	PM-08	PM-09	PM-10-12	PM-13	LM-05	LM-06	LM-07	LM-08	LM-09
Sub-unit	A	B	C	D	F	G	A	B	C	D	F
Locality	Pumaso 8°42'30.5"S; 121°09'37.2"E						Lowo Mali 8°41'25.8"S; 121°10'37.2"E				
Major elements (wt %)											
SiO_2	60.55	64.12	61.50	63.42	64.80	63.15	60.26	62.15	64.56	65.00	69.55
TiO_2	0.31	0.34	0.31	0.32	0.30	0.28	0.35	0.43	0.35	0.36	0.21
Al_2O_3	16.54	16.06	16.97	16.22	15.84	16.55	15.22	16.04	14.48	14.05	13.19
ΣFe_2O_3	3.14	3.33	3.03	3.15	2.96	2.92	3.30	4.26	3.39	3.36	1.64
MnO	0.19	0.14	0.11	0.16	0.09	0.08	0.08	0.08	0.08	0.09	0.08
MgO	2.11	1.18	2.35	1.65	1.27	2.48	1.67	1.02	1.15	0.98	0.63
CaO	2.22	2.48	2.25	2.32	2.63	2.06	2.25	2.53	2.44	2.57	2.13
Na_2O	1.21	1.86	1.13	1.54	2.06	1.18	1.23	1.79	1.55	1.98	2.34
K_2O	1.41	1.77	1.38	1.78	1.88	1.66	1.57	1.67	1.97	2.20	2.49
P_2O_5	0.02	0.06	0.02	0.05	0.06	0.02	0.01	0.03	0.04	0.03	0.03
S	0.01	0.03	0.05	0.02	0.02	0.07	0.01	0.05	0.07	0.02	0.01
LOI	12.16	8.45	10.76	9.20	7.89	9.40	12.65	9.47	9.59	8.42	7.32
Total	99.86	99.81	99.85	99.82	99.79	99.86	98.61	99.51	99.66	99.07	99.62
Trace elements (ppm)											
V	n.d.	n.d.	n.d.	n.d.	n.d.	n.d.	53.9	81.4	60.9	58.5	17.7
Rb	n.d.	n.d.	n.d.	n.d.	n.d.	n.d.	53.9	63.0	61.3	74.7	75.2
Sr	n.d.	n.d.	n.d.	n.d.	n.d.	n.d.	195.1	209.2	241.9	220.5	205.1
Y	n.d.	n.d.	n.d.	n.d.	n.d.	n.d.	12.1	16.1	14.0	15.7	13.3
Zr	n.d.	n.d.	n.d.	n.d.	n.d.	n.d.	130.4	114.7	117.5	108.0	110.0
Nb	n.d.	n.d.	n.d.	n.d.	n.d.	n.d.	3.2	3.1	3.1	2.8	3.0
Ba	n.d.	n.d.	n.d.	n.d.	n.d.	n.d.	343.1	355.1	409.9	396.6	423.6
La	n.d.	n.d.	n.d.	n.d.	n.d.	n.d.	12.9	15.8	27.4	25.6	2.0
Ce	n.d.	n.d.	n.d.	n.d.	n.d.	n.d.	2.0	29.8	2.0	31.3	29.2
Hf	n.d.	n.d.	n.d.	n.d.	n.d.	n.d.	3.1	3.4	3.1	3.8	2.4
Pb	n.d.	n.d.	n.d.	n.d.	n.d.	n.d.	13.0	13.6	18.1	16.2	11.0
Zn	n.d.	n.d.	n.d.	n.d.	n.d.	n.d.	59.0	43.0	50.8	48.9	22.3
Th	n.d.	n.d.	n.d.	n.d.	n.d.	n.d.	8.9	7	7.4	6.8	8.5
U	n.d.	n.d.	n.d.	n.d.	n.d.	n.d.	1.1	1.7	1.2	1.8	2.2

Note: Total Fe is expressed as ΣFe_2O_3, LOI = Loss on Ignition, and n.d. = not determined.

Table 5.5b. The glass composition of the Wolo Sege Ignimbrite.

Sample	Locality	Sub-unit	n	SiO_2	TiO_2	Al_2O_3	Σ FeO	MnO	MgO	CaO	Na_2O	K_2O	Cl	Total
WS-04	Wolo Sege	B	15	73.02	0.17	12.95	1.20	0.08	0.30	1.79	2.32	2.17	0.17	94.18
				1.74	0.01	0.58	0.12	0.02	0.03	0.12	0.65	0.19	0.02	-
WS-05	Wolo Sege	C	17	72.47	0.16	12.69	1.15	0.07	0.30	1.78	2.61	2.08	0.18	93.49
				1.85	0.02	1.04	0.17	0.03	0.04	0.13	0.28	0.20	0.02	-
WS-06	Wolo Sege	D	6	73.42	0.16	12.92	1.19	0.08	0.29	1.77	2.93	2.03	0.17	94.95
				0.69	0.00	0.20	0.04	0.02	0.02	0.05	0.34	0.08	0.03	-
WS-07	Wolo Sege	F	15	72.70	0.16	12.87	1.17	0.09	0.30	1.75	2.91	1.99	0.19	94.14
				0.96	0.02	0.28	0.08	0.02	0.01	0.03	0.33	0.13	0.01	-
WS-08	Wolo Sege	G	16	72.86	0.17	12.91	1.21	0.07	0.30	1.75	2.86	1.95	0.18	94.26
				1.05	0.02	0.26	0.07	0.02	0.02	0.03	0.17	0.09	0.01	-
WS-09	Wolo Sege	H	14	73.50	0.16	13.05	1.22	0.07	0.30	1.75	3.00	2.00	0.19	95.25
				0.93	0.02	0.26	0.07	0.02	0.02	0.03	0.29	0.13	0.01	-
TT-26	Tangi Talo	F	19	74.10	0.16	13.18	1.24	0.09	0.31	1.84	3.22	2.20	0.20	96.50
				0.65	0.01	0.16	0.07	0.02	0.02	0.03	0.11	0.08	0.01	-
TT-27	Tangi Talo	G	19	73.46	0.18	12.99	1.21	0.08	0.31	1.81	2.60	2.22	0.19	95.01
				1.07	0.03	0.26	0.07	0.02	0.02	0.07	0.30	0.28	0.01	-

Note. Major-element values are expressed in wt % and presented as a mean value (first row) and standard deviation (second row). Total Fe is presented as ΣFeO and *n* is the number of glass shards analysed. Sub-unit G and H correspond to reworked deposits of the WSI.

F. Turekeo Ignimbrite (TRI)

F.1. Description and Interpretation

The Turekeo Ignimbrite (TRI) represents a pyroclastic density current (PDC) deposit, and generally consists of two sub-units, i.e. the surge sub-unit and the flow sub-unit (Figure 5.9). The TRI is widely distributed in the Soa Basin, and the exposures can be traced continuously across the basin except at places where the TRI has been eroded.

The surge sub-unit comprises coarse-grained (sandy) vitric ash, displays low-angle cross stratification and lithic-fragment lamination, well-moderately sorted, low crystal content, wavy and sharp basal boundary, and is 4 - 90 cm thick. At Wolo Sege and Tangi Talo, scour structures can be recognised. This surge sub-unit contains less abundance of plagioclase, K-feldspar, quartz, micas (biotite and muscovite), amphibole (hornblende, cummingtonite and riebeckite), and pyroxene.

The 12 to 72 cm thick flow sub-unit is typically fine to coarse pumiceous lapilli, is massive, texturally clast supported and poorly sorted, normal grading, low contents of coarse crystals and lithic fragments, and a sharp and wavy basal contact. This flow deposit contains a moderate amount of plagioclase and less abundance of K-feldspar, quartz, micas (biotite and muscovite), amphibole (hornblende, cummingtonite and riebeckite), and pyroxene.

The surge sub-unit of TRI commonly overlies a well-developed palaeosol and the flow sub-unit is commonly covered by reworked ashes. However, at Turekeo and Tangi Talo, the flow sub-unit is overlain by the air-fall sub-unit which comprises silty vitric ash, massive, contains predominantly core-type accretionary lapilli (4-7-mm), and is 28 - 38 cm thick. The presence of accretionary lapilli indicates that the TRI was triggered by a phreatomagmatic eruption that generated a PDC deposit. The large-sized pumice (~3.5 cm x 5.5 cm) and lithic (~3.5 cm x 6 cm) fragments exposed at Alo Rawe in the eastern part of the basin may indicate that TRI was derived from the Keli Lambo Volcanic Complex (KLVC).

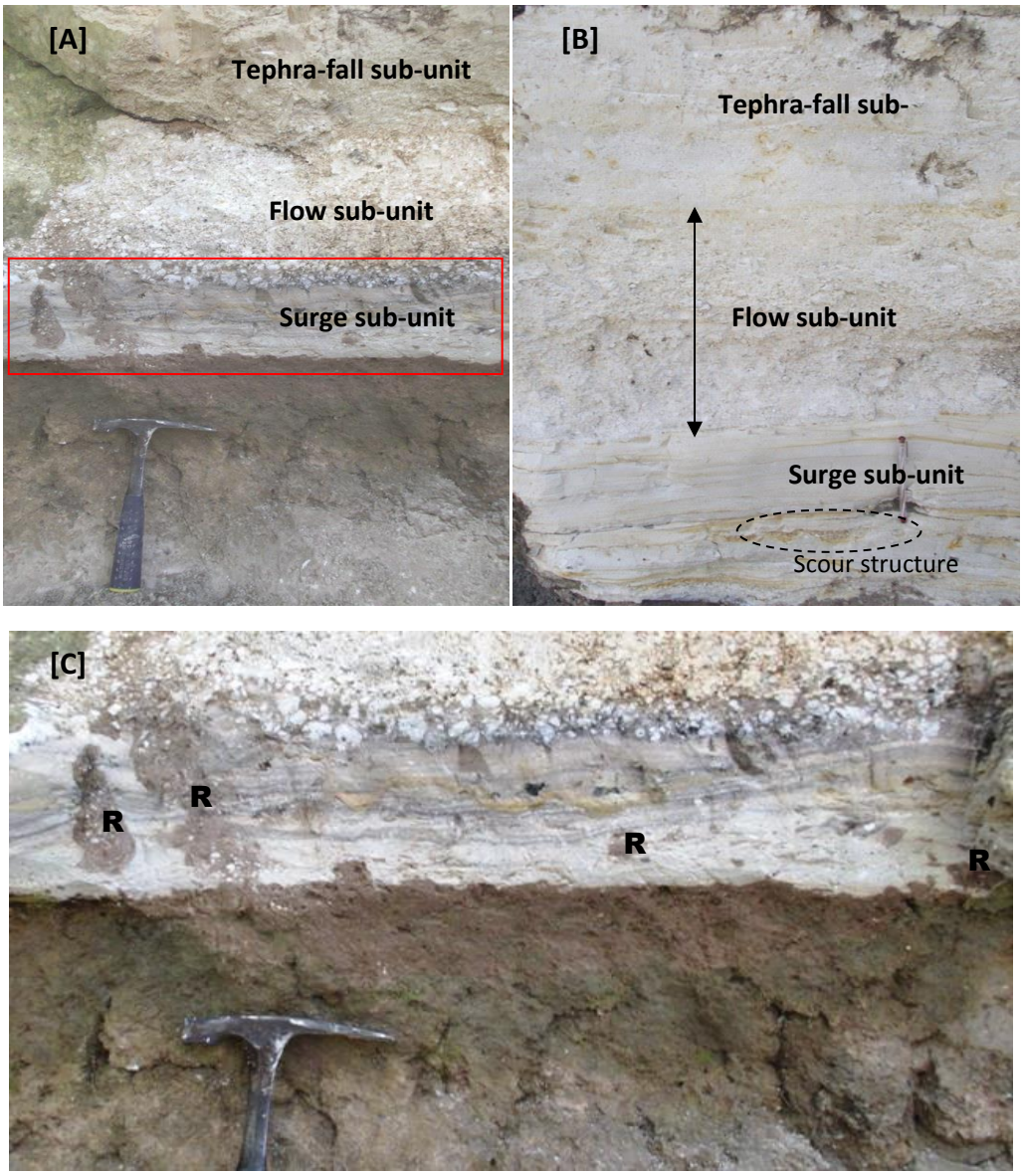

Figure 5.9. Field photographs of the Turekeo Ignimbrite as developed at various sites. A) The TRI exposed at Turekeo (type locality; S: 08° 42' 55.6", E: 121° 07' 43.2"). The thickness of the surge, flow and tephra-fall sub-units is 12-cm, 24-cm and 38-cm, respectively. B) Exposure at Tangi Talo, showing scour features in the surge sub-unit, and the tephra-fall sub-unit on top. C) Detail of the surge sub-unit at Turekeo (red box), which displays rip clasts (R) derived from the underlying palaeosol (The geological hammer is ~30 cm long; the pen is ~ 16 cm long).

F.2. Geochemistry

Whole-rock chemical analysis has been made for representative samples collected from Kobatuwa-03, Kobatuwa-04, Wolo Sege, Turekeo, Tangi Talo, Matago, Pumaso and Lowo Mali. Three representative samples taken from Turekeo, Tangi Talo and Pumaso are analysed to determine their glass compositions. The major-and trace-element data of the TRI are listed in Table 5.6a and 5.6b; and then the major-element values are recalculated to 100 % for discussion.

It can be summarised that whole-rock samples of the surge sub-unit consist of 71.5–76.4 wt% SiO_2, 0.23–0.28 wt% TiO_2, 14.00–16.97 wt% Al_2O_3, 1.76–2.56 wt% ΣFe_2O_3, 0.07–0.10 wt% MnO, 0.01–1.22 wt% MgO, 2.02–2.77 wt% CaO, 0.68–3.23 wt% Na_2O, 2.19–2.90 wt% K_2O, 0.02–0.10 wt% P_2O_5, 63–84 ppm Rb, 165–214 ppm Sr, 117–124 ppm Zr, 339–458 ppm Ba. The glass composition of this sub-unit shows 77.2–77.3 wt% SiO_2, 0.18–0.19 wt% TiO_2, 13.34–13.45 wt% Al_2O_3, 1.23–1.28 wt% ΣFeO, 0.07–0.08 wt% MnO, 0.33–0.35 wt% MgO, 1.75–1.77 wt% CaO, 3.08–3.49 wt% Na_2O and 2.38–2.62 wt% K_2O.

The whole-rock samples of the flow sub-unit comprise 72.4–76.4 wt% SiO_2, 0.21–0.28 wt% TiO_2, 13.93–16.97 wt% Al_2O_3, 1.48–2.56 wt% ΣFe_2O_3, 0.07–0.10 wt% MnO, 0.01–1.22 wt% MgO, 1.95–2.77 wt% CaO, 1.35–3.23 wt% Na_2O, 2.22–2.90 wt% K_2O, 0.03–0.10 wt% P_2O_5, 68–84 ppm Rb, 155–214 ppm Sr, 105–124 ppm Zr, 333–458 ppm Ba. The glass composition of this sub-unit has 75.6–77.1 wt% SiO_2, 0.14–0.18 wt% TiO_2, 13.35–13.54 wt% Al_2O_3, 1.03–1.18 wt% ΣFeO, 0.08–0.13 wt% MnO, 0.11–0.34 wt% MgO, 0.69–1.75 wt% CaO, 3.63–3.65 wt% Na_2O and 2.34–5.13 wt% K_2O.

Table 5.6a. The whole-rock chemical composition of the Turekeo Ignimbrite.

Sample	KBT03/2	KBT03/3	KBT04/5	KBT04/6	WS-18	WS-19	TRK-01	TRK-02	MTG-08	MTG-09	TT-28	TT-29	PM-15	PM-16	LM-11	LM-12
Sub-unit	Surge	Flow	Surge	Flow	Surge	Flow	Surge	Flow	Surge	Flow	Surge	Flow	Surge	Flow	Surge	Flow
Locality	Kobatuwa-03		Kobatuwa-04		Wolo Sege		Turekeo		Matago		Tangi Talo		Pumaso		Lowo Mali	
	8°41'24.6"S 121°05'01.1"E		8°41'16.7"S 121°05'01.6"E		8°41'27.1"S 121°06'00.0"E		08° 42' 55.6"S 121° 07' 43.2"E		8°43'06.5"S 121°08'18.9"E		8°41'53.0"S 121°08'10.6"E		8°42'30.5"S 121°09'37.2"E		8°41'25.8"S 121°10'37.2"E	
Major elements (wt %)																
SiO_2	68.38	66.38	68.06	70.58	70.98	71.11	61.78	65.69	63.56	67.97	66.57	67.56	66.57	68.07	69.64	72.04
TiO_2	0.28	0.23	0.26	0.23	0.23	0.23	0.28	0.25	0.24	0.24	0.29	0.23	0.21	0.20	0.21	0.20
Al_2O_3	16.07	15.44	14.82	13.53	14.07	13.90	15.15	14.62	14.01	13.83	13.86	13.98	15.15	15.07	12.84	13.25
ΣFe_2O_3	2.66	2.33	2.15	1.95	1.62	1.73	2.22	1.99	1.75	2.04	2.39	1.76	1.65	1.69	1.63	1.41
MnO	0.15	0.07	0.19	0.06	0.07	0.07	0.33	0.08	0.08	0.09	0.07	0.07	0.07	0.07	0.07	0.07
MgO	0.57	0.43	0.47	0.40	0.01	0.01	1.57	1.11	1.77	0.59	0.89	1.00	1.03	0.74	0.37	0.36
CaO	2.38	1.78	2.11	1.81	1.87	1.94	1.95	2.41	2.21	2.55	2.51	2.35	2.04	2.00	2.06	2.03
Na_2O	1.84	1.90	1.75	2.23	0.63	1.25	1.28	2.26	1.17	2.38	1.97	2.37	2.02	2.52	2.03	3.07
K_2O	2.45	2.43	2.64	2.06	2.75	2.70	1.89	2.24	2.13	2.59	2.26	2.31	2.24	2.25	2.84	2.64
P_2O_5	0.03	0.03	0.03	0.02	0.10	0.09	0.02	0.03	0.04	0.03	0.04	0.03	0.02	0.04	0.03	0.02
S	0.02	0.02	0.03	0.03	0.01	0.01	0.02	0.02	0.02	0.11	0.03	0.02	0.01	0.01	0.01	0.01
LOI	7.12	8.76	8.36	7.61	8.02	7.18	12.78	8.32	12.43	10.04	8.34	8.44	8.82	7.10	7.17	5.67
Total	101.95	99.78	100.87	100.53	100.35	100.23	99.27	99.02	99.41	102.47	99.21	100.12	99.83	99.78	98.90	100.77
Trace elements (ppm)																
V	1.0	13.8	27.3	26.3	17.1	15.5	62.3	36.4	22.9	27.6	42.5	36.0	n.d.	n.d.	17.8	12.9
Rb	90.4	74.0	87.4	67.7	86.7	84.0	62.6	71.7	72.8	77.2	79.5	75.3	n.d.	n.d.	84.6	77.2
Sr	165.9	154.9	187.9	160.9	174.1	189.2	175.2	201.2	165.4	214.1	208.7	201.8	n.d.	n.d.	190.0	186.4
Y	14.1	15.8	15.2	13.4	15.5	14.7	14.6	14.0	16.2	14.4	16.0	14.9	n.d.	n.d.	13.6	13.1
Zr	119.4	104.6	126.0	107.8	124.0	117.2	144.2	124.0	136.0	112.0	118.3	120.2	n.d.	n.d.	116.9	116.9
Nb	2.3	2.0	3.0	2.4	2.7	2.5	3.0	2.8	3.2	2.9	2.8	3.0	n.d.	n.d.	2.8	2.8
Ba	436.1	405.0	425.2	398.7	459.9	456.1	494.0	333.4	338.8	458.4	377.5	370.4	n.d.	n.d.	412.0	417.2
La	8.2	2.0	26.3	9.8	15.6	2.0	2.0	28.0	28.9	17.5	9.7	24.6	n.d.	n.d.	29.0	21.5
Ce	23.2	2.0	2.0	21.9	30.2	41.9	57.9	44.4	40.9	29.9	2.0	2.0	n.d.	n.d.	29.8	2.0
Hf	1.4	6.5	2.5	3.3	4.5	4.3	2.9	3.0	2.2	2.2	3.3	3.4	n.d.	n.d.	1.7	1.5
Pb	10.1	10.3	12.1	9.3	13.3	12.0	14.1	11.1	13.9	12.7	11.9	11.5	n.d.	n.d.	11.1	10.7
Zn	46.8	40.3	20.0	1.0	52.6	42.5	38.4	16.5	50.8	21.8	28.0	21.2	n.d.	n.d.	25.8	17.8
Th	7.1	6.8	7.9	6.3	7.2	6.9	8.9	7.6	8.6	6.6	6.8	7.4	n.d.	n.d.	6.8	7.4
U	2.7	2.3	2.1	2.5	2.3	1.7	0.9	2	1.1	1.7	1.5	1.7	n.d.	n.d.	1.9	2.2

Note: Total Fe is expressed as ΣFe_2O_3, LOI = Loss on Ignition, and n.d. = not determined.

Table 5.6b. The glass composition of the Turekeo Ignimbrite.

Sample	Locality	Sub-unit	n	SiO_2	TiO_2	Al_2O_3	ΣFeO	MnO	MgO	CaO	Na_2O	K_2O	Cl	Total
TRK-01	Turekeo	Surge	20	73.31	0.18	12.65	1.21	0.07	0.31	1.66	2.92	2.48	n.d.	94.80
				0.89	0.03	0.22	0.10	0.02	0.02	0.07	0.37	0.34		-
TRK-02		Flow	18	74.01	0.18	12.88	1.17	0.08	0.33	1.68	3.45	2.27	n.d.	96.05
				0.66	0.02	0.17	0.07	0.02	0.02	0.05	0.25	0.13		-
TT-28	Tangi Talo	Surge	18	73.71	0.17	12.79	1.18	0.07	0.32	1.68	3.33	2.27	n.d.	95.51
				0.53	0.02	0.11	0.08	0.02	0.02	0.04	0.16	0.09		-
TT-29		Flow	15	74.17	0.17	12.84	1.14	0.07	0.33	1.68	3.51	2.25	n.d.	96.16
				0.68	0.02	0.14	0.06	0.02	0.03	0.08	0.17	0.06		-
TT-30		Airfall	18	73.71	0.17	12.76	1.12	0.07	0.31	1.63	3.14	2.40	n.d.	95.32
				0.75	0.02	0.19	0.07	0.03	0.03	0.08	0.38	0.22		-
PM-15	Pumaso	Surge	18	73.15	0.18	12.75	1.19	0.08	0.33	1.68	3.13	2.31	n.d.	94.80
				1.49	0.01	0.23	0.04	0.02	0.04	0.05	0.49	0.14		-

Note. Major-element values are expressed in wt % and presented as a mean value (first row) and standard deviation (second row). Total Fe is presented as ΣFeO and *n* is the number of glass shards analysed.

The whole-rock and glass compositions of the analysed samples from the surge and flow sub-units are indistinguishable, and these chemical similarities indicate that the surge and flow sub-units were derived from the same source, which agree with the field characteristics. In addition, whole-rock samples display higher values compared to the glass shards in term of the major-element composition. The greater contents of TiO_2, Al_2O_3, MgO, CaO and total iron in whole-rock samples are caused by the occurrence of feldspars and ferromagnesian minerals within whole-rock samples.

G. Kopowatu Tephra (KPW)

G.1. Description and Interpretation

The 7 – 9-cm thick Kopowatu Tephra (KPW) is a distal pyroclastic fall deposit, which comprises fine grained vitric ash (silty to very fine sandy), is massive to weakly normal grading, well sorted, with low crystal contents. This ash contains less abundance of plagioclase, K-feldspar, micas (biotite and muscovite), apatite, amphibole (hornblende, cummingtonite and riebeckite), and pyroxene.

The type locality of this tephra is situated near Kopowatu (8° 41’ 36.6” S; 121° 09’ 26.4” E) at ~50-m distance to the southeast from the 1999 excavation (conducted by a team of the GRDC and the University of New England). At this location, the 13-cm thick KPW overlies a palaeosol horizon and is covered by well-cemented tuffaceous sandstone.

The KPW is widely distributed and has been recognised in many exposures across the Soa Basin. However, this ash layer has probably been eroded at some localities, such as Kobatuwa and Pumaso. The KPW commonly overlies and is covered by well-developed palaeosols (Figure 5.10). The fission track dating on this tephra yielded an age of 0.90±0.07 Ma (Brumm *et al*., 2016).

Figure 5.10. The Kopowatu Tephra is well-exposed in the stratigraphic slot trench at Wolo Sege ((8°41'27.1"S; 121°06'00.0"E), and this whitish ash is bracketed by palaeosols (The bar is ~10 cm).

G.2. Geochemistry

Four representative samples have been prepared for whole-rock chemical analysis, and two representative samples have been prepared to determine their glass compositions. The chemical composition of KPW is summarised in Table 5.7. The major-element values of whole-rock samples and glass shards are recalculated to 100 % for discussion.

The whole-rock samples of KPW comprise 71.5–73.8 wt% SiO_2, 0.22–0.27 wt% TiO_2, 14.90–17.09 wt% Al_2O_3, 1.85–2.45 wt% ΣFe_2O_3, 0.13–0.14 wt% MnO, 0.11–1.89 wt% MgO, 0.85–1.74 wt% CaO, 1.31–2.31 wt% Na_2O, 3.72–4.98 wt% K_2O, 0.003–0.10 wt% P_2O_5, 62–196 ppm Rb, 128–166 ppm Sr, 115–235 ppm Zr, 357–1426 ppm Ba and 3.4–43.1 ppm Th. The glass composition of the KPW suggests 75.6–77.1 wt% SiO_2, 0.14–0.18 wt% TiO_2, 13.35–13.54 wt% Al_2O_3, 1.03–1.18 wt% ΣFeO, 0.08–0.13 wt% MnO, 0.11–0.34 wt% MgO, 0.69–1.75 wt% CaO, 3.63–3.65 wt% Na_2O and 2.34–5.13 wt% K_2O.

The KPW has distinct chemical composition, which is characterised by high contents of potassium, barium and thorium. In the case of TiO_2, Al_2O_3 and ΣFe_2O_3, the chemical values between whole-rock samples and glass shards exhibit small differences. The higher values of these elements in whole-rock samples are possibly affected by the presence of feldspars and ferromagnesian minerals.

H. Pumaso Tephra (PMS)

H.1. Description and Interpretation

The Pumaso Tephra (PMS) corresponds to a PDC deposit, which comprises sandy vitric ash, well to moderately sorted, abundant dark crystals suggestive of hornblende, is massive to normally graded, and is 13.5 – 190-cm thick. The base of this layer is commonly sharp. In the eastern part of the Soa Basin, this tephra is much coarser in grain size, consists of medium to very coarse pumiceous vitric ash, moderately–poorly sorted, massive–stratified and contains large accretionary lapilli and abundant hornblende. The presence of accretionary lapilli suggests that the PMS was generated by a phreatomagmatic eruption and may have been derived from volcanic edifices in the east, probably the Keli Lambo Volcanic Complex. XRD analysis suggests that PMS contains moderate contents of hornblende and plagioclase, and less abundance of K-feldspar, quartz, tridymite, cummingtonite, riebeckite, and pyroxene. The $^{40}Ar/^{39}Ar$ dating has been conducted on a PMS sample collected from Mata Menge, which gives an age of 0.81±0.04 Ma (Brumm *et al*., 2016).

Table 5.7. Representative major-and trace-element compositions of whole-rock samples and glass shards from the Kopowatu Tephra.

Sample	WS23	MM201	KPW-01	LM-13	Sample	KPW-01		LM-13	
Locality	Wolo Sege	Mata Menge	Kopowatu	Lowo Mali	Locality	Kopowatu		Lowo Mali	
	8°41'27.1"S	8°41'31.5"S	8°41'36.6"S	8°41'26.4"S	n	18		18	
	121°06'00.0"E	121°05'44.3"E	121°09'26.4"E	121°10'45.5"E					
Major elements (wt %)					*Major elements (wt %)*				
SiO_2	68.99	66.62	67.94	62.69	SiO_2	73.24	0.85	72.86	1.09
TiO_2	0.24	0.20	0.23	0.24	TiO_2	0.14	0.01	0.15	0.01
Al_2O_3	15.01	15.36	13.72	14.99	Al_2O_3	13.11	0.33	13.42	0.48
ΣFe_2O_3	2.32	1.68	1.82	1.80	ΣFeO	0.99	0.08	1.03	0.13
MnO	0.13	0.12	0.13	0.12	MnO	0.13	0.02	0.14	0.02
MgO	0.11	0.19	0.33	1.66	MgO	0.11	0.05	0.11	0.02
CaO	1.65	0.77	1.17	1.50	CaO	0.67	0.10	0.76	0.14
Na_2O	1.24	1.53	2.13	1.46	Na_2O	3.52	0.35	3.59	0.33
K_2O	4.57	4.37	4.59	3.27	K_2O	4.97	0.21	5.02	0.41
P_2O_5	0.09	0.003	0.02	0.01	Cl	n.d.		n.d.	
S	0.01	0.02	0.02	0.01					
LOI	7.06	8.41	7.26	11.57					
Total	101.41	99.27	99.34	99.32	Total	96.87	-	97.08	-
Trace elements (ppm)									
V	62.2	79.7	33.7	137.6					
Rb	185.0	61.6	195.7	194.8					
Sr	127.7	129.1	150.0	165.6					
Y	23.5	12.2	23.6	20.1					
Zr	151.6	114.6	187.4	235.4					
Nb	10.5	1.9	11.7	10.8					
Ba	1088.0	357.2	1426.0	1142.0					
La	52.4	2.0	60.6	66.1					
Ce	74.6	35.5	138.4	93.8					
Hf	5.3	3.6	5.2	4.8					
Pb	25.6	9.2	27.7	28.4					
Zn	45.4	48.0	20.4	46.9					
Th	35.3	3.4	38.1	43.1					
U	7.0	0.9	7.5	5.0					

Note. Total Fe is expressed as ΣFe_2O_3 (whole-rock) and ΣFeO (glass shards). The glass composition is presented as a mean value (first column) and standard deviation (second column). *n* is the number of glass shards analysed, and n.d. = not determined.

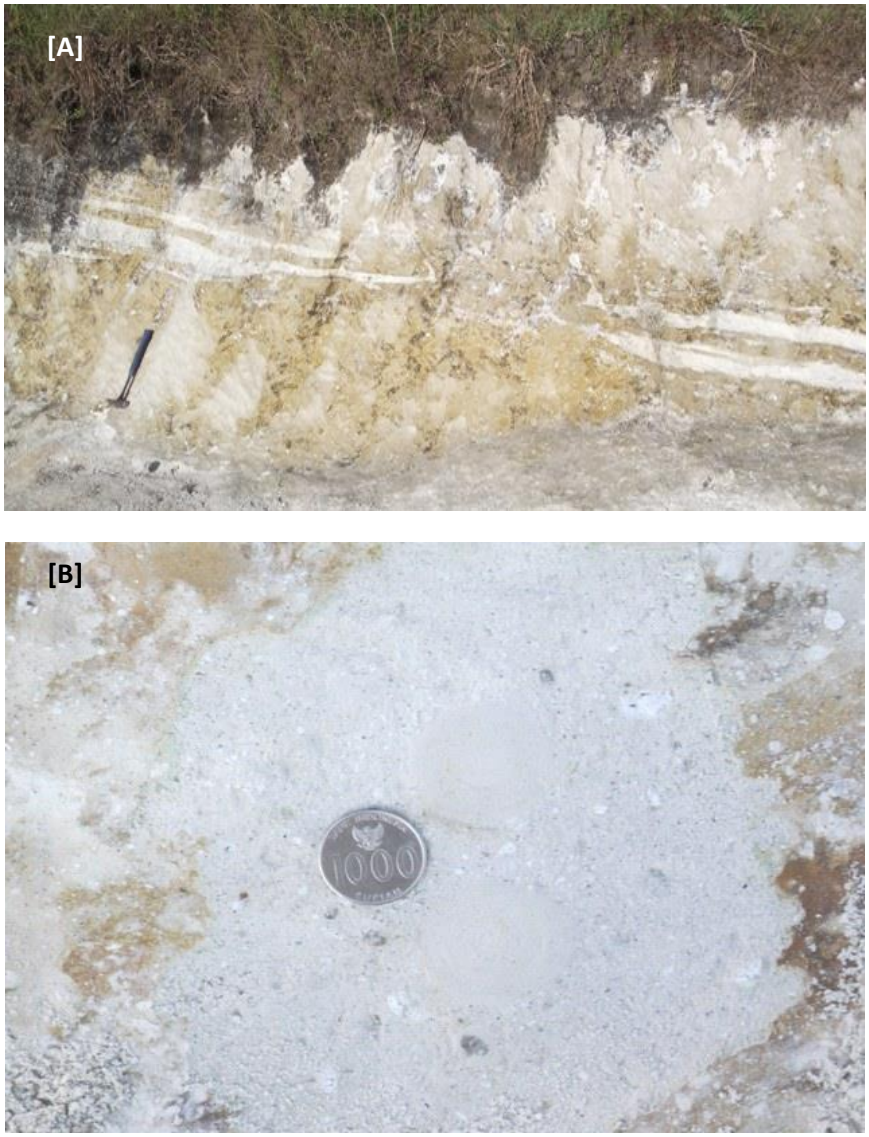

Figure 5.11. The exposure of Pumaso Tephra (PMS) at Lowo Mali (8°41'26.4"S; 121°10'45.5"E). A) Massive vitric ash with parallel pumice beds indicating traction mechanism; and B) Detailed picture of concentric accretionary lapilli incorporated within massive ash (The hammer is ~30 cm long, and the coin is ~24 mm in diameter).

H.2. Geochemistry

Three representative samples taken from Wolo Sege, Pumaso and Lowo Mali were prepared for whole-rock chemical analysis and two samples (Pumaso and Lowo Mali) were analysed to determine their glass compositions. The chemical data of the PMS are summarised in Table 5.8.

After recalculating the total to 100 %, the major-element composition of whole-rock samples from the PMS display 68.4–71.8 wt% SiO_2, 0.40–0.65 wt% TiO_2, 14.75–15.57 wt% Al_2O_3, 3.33–4.62 wt% ΣFe_2O_3, 0.10–0.17 wt% MnO, 1.01–1.64 wt% MgO, 3.39–4.21 wt% CaO, 2.58–2.76 wt% Na_2O, 1.93–2.34 wt% K_2O, 0.10–0.18 wt% P_2O_5. The major-element values of glass shards analysed from the PMS suggests 76.8–77.0 wt% SiO_2, 0.22 wt% TiO_2, 13.62–13.68 wt% Al_2O_3, 1.37–1.40 wt% ΣFeO, 0.09–0.10 wt% MnO, 0.39 wt% MgO, 1.80–1.85 wt% CaO, 2.90–3.48 wt% Na_2O and 2.24–2.46 wt% K_2O. Moreover, the trace-element content of the PMS comprises 50–66 ppm Rb, 251–348 ppm Sr, 112–131 ppm Zr and 309–385 ppm Ba.

The whole-rock samples of the PMS have less compositional variability with respect to the major-element composition. The major-element contents of the glass shards analysed also display similarity. In terms of the trace-element concentration, the studied samples exhibit relatively wide variation in the contents of V, Rb, Ba, La and Ce. Sample MM-201 has the lowest content of these elements compared to the other samples, which these differences are controlled by the variable proportion of mineral assemblages within the analysed samples. Moreover, regarding the major-element composition, whole-rock samples display higher values compared to the glass shards. The higher TiO_2, Al_2O_3, CaO and total iron contents in whole-rock samples are affected by the occurrence of feldspars and ferromagnesian minerals within whole-rock samples.

Table 5.8. Representative major-and trace-element compositions of whole-rock samples and glass shards from the Pumaso Tephra.

Sample	WS25	PM-18	LM-14	Sample	PM-18		LM-14	
Locality	Wolo Sege 8°41'27.1"S 121°06'00.0"E	Pumaso 8°42'30.5"S 121°09'37.2"E	Lowo Mali 8°41'26.4"S 121°10'45.5"E	Locality n	Pumaso 18		Lowo Mali 18	
Major elements (wt %)				*Major elements (wt %)*				
SiO_2	66.67	66.28	65.41	SiO_2	72.25	1.25	72.79	0.88
TiO_2	0.37	0.62	0.56	TiO_2	0.21	0.01	0.20	0.02
Al_2O_3	13.69	14.34	14.89	Al_2O_3	12.84	0.35	12.91	0.30
ΣFe_2O_3	3.09	4.12	4.42	ΣFeO	1.31	0.07	1.30	0.05
MnO	0.10	0.17	0.10	MnO	0.09	0.02	0.10	0.02
MgO	0.94	1.32	1.56	MgO	0.36	0.03	0.37	0.03
CaO	3.15	3.88	4.02	CaO	1.74	0.05	1.71	0.06
Na_2O	2.56	2.46	2.61	Na_2O	2.73	0.62	3.30	0.53
K_2O	2.17	1.84	1.92	K_2O	2.31	0.37	2.12	0.24
P_2O_5	0.09	0.16	0.13	Cl	n.d.		n.d.	
S	0.02	0.02	0.02					
LOI	6.46	5.26	4.6					
Total	99.31	100.47	100.25	Total	93.83	-	94.80	-
Trace elements (ppm)								
V	30.1	n.d.	92.1					
Rb	65.7	n.d.	49.9					
Sr	250.9	n.d.	348.4					
Y	19.3	n.d.	23.1					
Zr	130.8	n.d.	111.8					
Nb	2.0	n.d.	2.3					
Ba	384.9	n.d.	308.8					
La	30.4	n.d.	2.0					
Ce	42.8	n.d.	34.5					
Hf	2.1	n.d.	2.7					
Pb	1.0	n.d.	9.4					
Zn	10.5	n.d.	21.9					
Th	5.1	n.d.	3.9					
U	5.4	n.d.	1.3					

Note. Total Fe is expressed as ΣFe_2O_3 (whole-rock) and ΣFeO (glass shards). The glass composition is presented as a mean value (first column) and standard deviation (second column). *n* is the number of glass shards analysed, and n.d. = not determined.

I. Mata Menge Tephra (MMT)

I.1. Description and Interpretation

The Mata Menge Tephra (MMT) is a distal pyroclastic tephra-fall deposit that is well-exposed at Mata Menge in western part and Gero in the eastern part of the Soa Basin. This 16-25-cm thick tephra consists of fine to coarse sandy ash, grey to dark grey in colour, is massive, normal graded, and displays irregular and sharp lower base (Figure 5.12). At Gero, the MMT contains abundant pumice clasts and is overlain by its reworked materials (~40 cm), while this tephra is finer and covered by a palaeosol at Mata Menge. Due to the lack of outcrops in the middle part of the Soa Basin, the lateral distribution of the MMT cannot be estimated. The source volcano of this tephra is still unclear, however, the variation of grain size may indicate westward wind direction, and thus the MMT was erupted from a volcano in the east. This discrete tephra consists of a moderate content of plagioclase and less abundance of K-feldspar, quartz, apatite, micas (biotite and muscovite), amphibole (hornblende and cummingtonite), and pyroxene, as determined by XRD analysis.

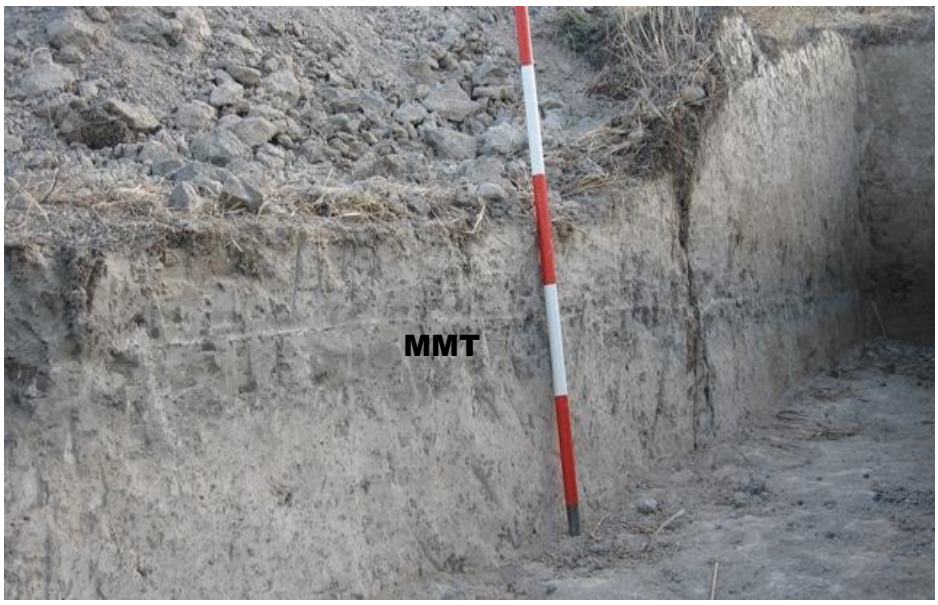

Figure 5.12. The discrete Mata Menge Tephra is well-exposed at Mata Menge (8°41'29.1"S; 121°05'36.4"E) (The bar is ~10 cm).

I.2. Geochemistry

Two representative samples collected from Mata Menge and Gero were analysed for the whole-rock chemical composition (Table 5.9). Furthermore, the major-element values of the whole-rock samples are recalculated to 100 %. The MMT is composed of 60.5–63.8 wt% SiO_2, 0.63–1.02 wt% TiO_2, 17.26–19.06 wt% Al_2O_3, 6.29–8.04 wt% ΣFe_2O_3, 0.10–0.19 wt% MnO, 1.90–2.06 wt% MgO, 5.92–6.33 wt% CaO, 1.63–3.07 wt% Na_2O, 0.71–0.99 wt% K_2O, and 0.22–0.25 wt% P_2O_5. Moreover, the trace-element content of MMT comprises 20–48 ppm Rb, 341–390 ppm Sr, 92–116 ppm Zr and 203–393 ppm Ba (see Table 5.9. for details). The two analysed samples generally display minor compositional variability.

J. Piga Tephra (PGT)

J.1. Description and Interpretation

The Piga Tephra (PGT) is a series of mm to cm thick pyroclastic air-fall deposits, interbedded with lacustrine deposits of the Limestone Member of The Ola Bula Formation (Figure 5.13). The PGT consists of at least 58 macroscopically visible tephra layers and the individual ash layers are subsequently numbered as PGT-01, PGT-02, etc. The sequence of this tephra is well-exposed at Mata Menge, Pumaso and Gero.

Table 5.9. The major-and trace-element compositions of the whole-rock samples from Mata Menge Tephra.

Sample	MM-42	GR-01
Locality	Mata Menge 8°41'29.1"S 121°05'36.4"E	Gero 8°41'57.8"S 121°11'50.1"E
Major elements (wt %)		
SiO_2	54.61	60.55
TiO_2	0.92	0.60
Al_2O_3	17.19	16.38
ΣFe_2O_3	7.25	5.96
MnO	0.09	0.18
MgO	1.86	1.80
CaO	5.71	5.61
Na_2O	1.47	2.92
K_2O	0.89	0.67
P_2O_5	0.22	0.21
S	0.52	0.01
LOI	8.79	5.19
Total	99.52	100.08
Trace elements (ppm)		
V	210.6	18.5
Rb	47.9	20.3
Sr	340.5	390.4
Y	23.1	30.1
Zr	116.2	92.1
Nb	5.7	1.6
Ba	392.6	202.8
La	17.5	11.2
Ce	59.2	49.1
Hf	3.7	0.7
Pb	9.0	1.0
Zn	20.8	10.6
Th	6.3	1
U	1.0	0.7

Note. Total Fe is expressed as ΣFe_20_3; LOI = Loss on Ignition.

The PGT comprises coarse to very coarse-grained crystal ashes, massive, well sorted, ungraded or normal graded, has a horizontal and sharp lower boundary, and the thickness varies from mm up to 12 cm. The PGT displays dark and light colours, which indicate different compositions, varying from basalt to rhyolite. The PGT generally contains abundant plagioclase and less abundant K-feldspar, quartz, apatite, micas (biotite and muscovite), amphiboles (hornblende, cummingtonite and riebeckite), and pyroxenes (diopside and enstatite).

A sample of PGT-02 from Mata Menge has been dated by $^{40}Ar/^{39}Ar$ dating technique and yielded an age of 0.65±0.02Ma (Brumm *et al*., 2016).

J.2. Geochemistry

Twenty six samples of the PGT have been prepared for whole-rock chemical analysis, sampled from slot trench XII at Matamenge. The major-and trace-element values of the PGT are listed in Table 5.10. After recalculating the total to 100 %, the major-element composition of the PGT is 50.9–67.7 (average 57.3) wt% SiO_2, 0.63–1.10 (0.78) wt% TiO_2, 16.16–26.45 (19.70) wt% Al_2O_3, 4.45–12.67 (9.51) wt% ΣFe_2O_3, 0.02–0.77 (0.19) wt% MnO, 0.01–6.21 (2.96) wt% MgO, 2.81–10.62 (7.15) wt% CaO, 0.11–3.59 (1.57) wt% Na_2O, 0.16–0.81 (0.40) wt% K_2O and 0.04–2.07 (0.19) wt% P_2O_5.

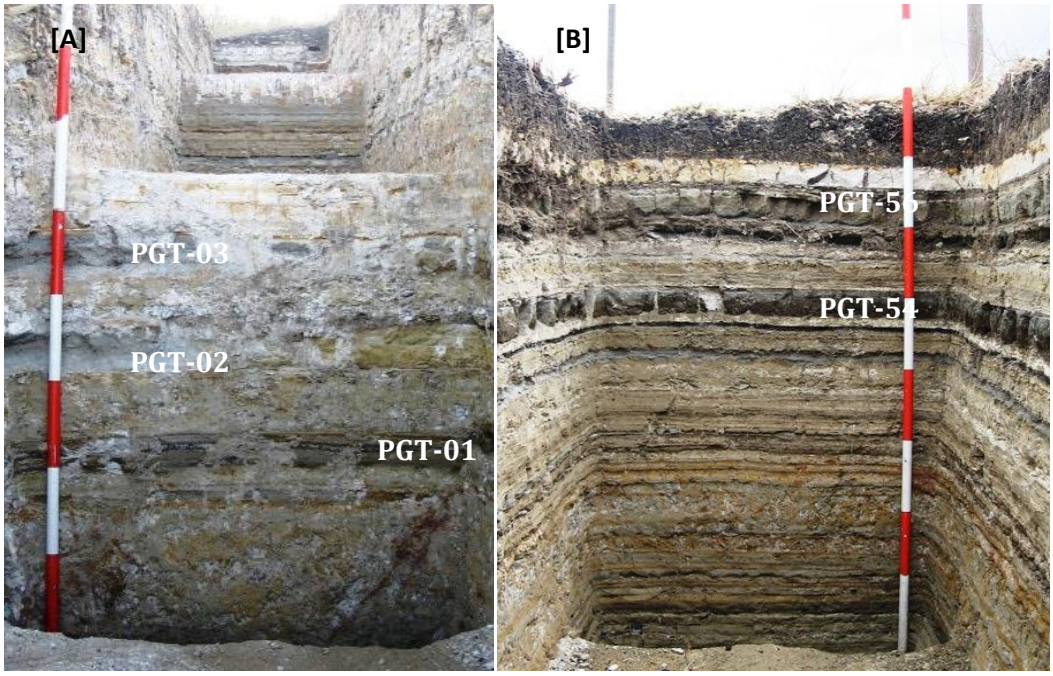

Figure 5.13. Exposures of the Piga Tephra in the trench at Mata Menge (A and B) (8°41'29.1"S; 121°05'36.4"E), which horizontally interbedded with lacustrine claystones (The bar is 10 cm).

The trace-element composition of the PGT displays 92–371 (average 214) ppm V, 6–24 (13) ppm Rb, 88–497 (229) ppm Sr, 12–30 (17) ppm Y, 12–89 (39) ppm Zr, 0.1–4 (1) ppm Nb, 79–440 (184) ppm Ba, 1–24 (6) ppm La, 2–51 (11) ppm Ce, 0.3–4 (2) ppm Hf, 1–6 (3) ppm Ta, 0.4–18 (5) ppm Pb, 0.1–3.5 (1.4) ppm Th, and 0.3–6.6 (1.1) ppm U.

The chemical composition of the PGT shows a wide range from basaltic to dacitic composition (~51–68 wt% SiO_2). This tephra is also characterised by low K_2O content. The abundance of minerals may affect the concentration of such elements. The Al_2O_3, CaO, Sr and Ba contents display moderate to high values, which can be associated with the occurrence of feldspars. The enrichment of ΣFe_2O_3 and MgO are probably related to the presence of amphibole and pyroxene within whole-rock samples.

Table 5.10. The major-and trace-element compositions of whole-rock samples from the Piga Tephra collected from Mata Menge (8°41'29.1"S; 121°05'36.4"E).

Sample Layer	MM54 PGA-01	MM56 PGA-02	MM59 PGA-03	MM64 PGA-04	MM69 PGA-06	MM72 PGA-08	MM78 PGA-12	MM81 PGA-16	MM83 PGA-17	MM85 PGA-18	MM89 PGA-21	MM91 PGA-22	MM92 PGA-23
Major elements (wt %)													
SiO_2	51.71	52.22	52.38	49.45	49.88	49.81	49.94	52.04	54.58	54.93	49.79	53.26	52.13
TiO_2	0.78	0.89	0.62	0.62	0.83	0.74	0.70	0.69	0.69	0.83	0.68	0.79	0.79
Al_2O_3	18.22	17.57	20.19	19.81	19.30	18.45	18.26	18.52	16.42	16.88	18.75	19.93	18.23
ΣFe_2O_3	7.91	12.10	9.15	10.15	12.42	9.30	11.81	10.64	10.54	6.44	10.72	10.04	10.20
MnO	0.13	0.31	0.26	0.19	0.22	0.16	0.19	0.17	0.16	0.17	0.73	0.18	0.19
MgO	0.97	4.12	3.59	2.22	5.57	3.50	5.38	5.80	4.98	0.81	3.94	4.21	3.54
CaO	8.67	8.74	9.63	3.64	8.29	3.86	8.43	4.78	3.50	4.80	9.28	7.69	7.87
Na_2O	2.36	1.70	1.25	0.14	1.24	0.68	1.14	0.40	0.10	0.75	1.17	1.38	1.12
K_2O	0.43	0.21	0.23	0.15	0.15	0.28	0.17	0.22	0.24	0.38	0.16	0.23	0.23
P_2O_5	0.13	0.10	0.16	0.05	0.10	0.13	0.04	0.10	0.09	0.15	0.06	0.10	0.06
S	0.01	0.03	0.08	0.0004	0.19	1.05	0.05	0.01	0.05	0.01	0.01	0.01	0.01
LOI	9.50	1.80	3.78	12.64	3.90	11.03	3.64	7.75	10.19	12.87	4.11	4.20	5.59
Total	100.82	99.80	101.32	99.07	102.09	98.98	99.76	101.13	101.52	99.01	99.40	102.02	99.96
Trace elements (ppm)													
V	220.8	153.6	91.9	111.5	293.4	240.3	266.8	265.5	260.0	190.1	267.2	255.2	245.7
Rb	14.8	7.8	7.7	5.8	6.3	10.6	6.1	7.9	9.6	16.9	6.6	8.7	8.8
Sr	350.3	242.4	251.5	91.5	238.0	269.4	202.4	124.7	88.0	208.8	176.4	163.5	158.1
Y	13.6	20.8	17.7	12.6	14.4	14.3	12.4	12.6	12.7	12.5	27.9	14.6	14.7
Zr	45.0	17.2	17.2	14.9	12.4	24.6	15.7	23.1	26.4	62.5	17.8	24.9	26.7
Nb	1.6	0.2	0.3	0.2	1.0	1.0	0.4	0.1	0.2	3.1	1.0	< 0.2	1.0
Ba	184.2	81.2	109.6	89.9	80.8	140.6	89.1	147.2	166.2	226.7	229.7	144.6	162.7
La	2.0	9.6	2.0	11.0	16.0	11.7	2.0	2.0	2.0	2.0	2.0	< 2.0	5.9
Ce	2.0	2.0	2.0	38.5	2.0	2.0	2.0	2.0	2.0	2.0	7.8	< 2.0	10.5
Hf	2.9	2.4	2.0	n.d	n.d	1.6	0.5	2.3	n.d	3.7	1.5	2.5	2.3
Pb	2.5	1.8	1.0	1.0	1.0	1.0	1.0	3.2	4.8	6.3	2.6	< 1.0	4.4
Zn	5.4	1.2	2.3	1.7	0.4	1.6	1.1	1.7	1.5	9.1	1.0	2.0	3.3
Th	1.3	1.0	1.0	0.5	1.0	1.0	1.0	1.0	1.0	2.3	0.4	< 1.0	1.0
U	0.7	1.1	0.7	0.5	0.9	0.8	6.6	1.2	1.0	1.4	1.0	0.8	0.5

Table 5.10. Continued.

Sample	MM94	MM95	MM96	MM97	MM103	MM105	MM108	MM118	MM121	MM123	MM124	MM129	MM130	MM131	MM132
Layer	PGA-24	PGA-25	PGA-26	PGA-27	PGA-29	PGA-31	PGA-33	PGA-47	PGA-48	PGA-49	PGA-50	PGA-54	PGA-56	PGA-57	PGA-58
Major elements (wt %)															
SiO_2	60.70	61.03	50.71	61.12	55.91	49.18	60.23	52.27	53.06	52.86	54.39	54.02	51.12	54.96	50.43
TiO_2	0.59	0.59	0.78	0.58	0.74	0.70	0.58	0.69	0.71	0.83	0.85	0.68	0.67	0.59	0.86
Al_2O_3	15.70	15.65	18.12	15.47	15.18	16.69	15.02	19.22	22.68	19.83	19.29	21.32	18.74	17.63	20.88
ΣFe_2O_3	6.78	6.78	11.60	6.71	10.70	8.37	6.70	9.97	6.29	7.96	6.88	6.67	10.55	7.66	3.52
MnO	0.11	0.12	0.19	0.10	0.19	0.23	0.11	0.17	0.12	0.11	0.10	0.10	0.19	0.11	0.02
MgO	1.14	1.21	4.02	0.76	2.96	1.58	1.31	4.50	1.27	1.89	1.77	1.79	3.88	1.45	0.01
CaO	4.18	4.33	6.02	2.97	6.43	6.46	4.45	9.40	10.36	9.54	7.92	9.28	9.43	6.33	2.22
Na_2O	1.94	2.03	1.20	1.82	1.40	1.96	1.68	0.88	2.36	2.98	3.43	2.53	1.20	1.76	0.58
K_2O	0.62	0.63	0.30	0.61	0.39	0.55	0.74	0.26	0.52	0.54	0.71	0.54	0.19	0.31	0.30
P_2O_5	0.12	0.12	0.06	0.11	0.06	1.81	0.15	0.10	0.15	0.12	0.13	0.21	0.06	0.10	0.13
S	0.01	0.01	0.12	0.01	0.01	0.96	0.51	0.01	0.01	0.01	0.02	0.01	0.01	0.01	0.84
LOI	8.43	7.67	7.12	9.54	4.87	10.68	8.10	2.80	4.41	3.52	4.57	3.18	2.45	7.83	17.74
Total	100.32	100.17	100.23	99.80	98.84	99.18	99.59	100.26	101.94	100.18	100.08	100.31	98.49	98.74	97.54
Trace elements (ppm)															
V	106.5	109.8	270.6	108.3	237.4	323.9	162.2	279.0	179.8	235.2	205.6	194.4	371.4	201.7	144.7
Rb	20.7	21.1	8.9	20.4	14.3	19.0	21.6	8.4	18.2	17.8	23.9	22.4	7.8	11.5	21.3
Sr	123.9	129.2	154.9	103.9	144.4	367.9	138.6	190.0	487.3	460.2	418.9	496.5	204.7	171.9	240.9
Y	27.5	27.7	14.5	26.4	26.0	14.7	30.2	12.2	13.0	16.3	16.1	16.3	15.2	21.4	11.6
Zr	61.0	61.0	26.8	65.3	42.8	46.4	64.0	22.8	46.7	49.1	57.0	53.4	20.3	45.5	89.2
Nb	0.4	0.3	1.0	0.5	0.2	1.8	0.4	0.1	2.6	3.0	3.2	3.8	0.1	0.5	4.0
Ba	248.5	244.3	244.6	185.5	103.4	320.8	129.2	103.9	243.0	234.3	319.9	253.5	78.7	139.8	439.7
La	16.0	12.4	0.9	24.1	2.0	4.0	2.0	2.8	2.0	2.0	9.7	2.0	12.7	15.0	2.0
Ce	<2	2.0	7.4	29.7	17.0	2.0	18.2	2.0	44.0	2.0	2.0	50.7	11.6	19.0	24.3
Hf	2.7	3.3	0.3	3.3	n.d	1.3	3.6	n.d	2.5	3.4	3.7	1.7	n.d	n.d	n.d
Pb	2.6	2.4	1.7	3.1	1.7	5.5	3.4	1.0	1.6	2.3	2.0	3.4	5.2	1.0	4.9
Zn	8.0	7.3	2.0	5.6	3.1	6.2	5.9	1.8	8.6	8.0	9.4	8.4	2.7	5.6	18.1
Th	< 1.0	1.0	1.0	1.0	1.0	1.7	1.0	1.0	2.4	2.7	2.7	3.2	1.0	0.1	3.5
U	1.0	0.6	1.0	0.8	1.0	1.0	1.0	0.6	0.6	0.3	0.5	1.0	1.0	0.5	1.5

Note. Total Fe is presented as ΣFe_2O_3, LOI = Loss on Ignition (%) and n.d. = not determined.

K. Other Pyroclastic Deposits

K.1. Description and Interpretation

There are three pyroclastic layers, whose stratigraphic positions are still unclear relative to the before mentioned tephras. These tephra deposits are well-exposed in the Welas Caldera Complex in the northwestern part of the Soa Basin. These tephra beds have been informally named as the Nata Randang Tephra, Wulubara Tephra and Kolopanu Tephra.

The Nata Randang Tephra (NTR) is a thick pyroclastic surge deposit with a thickness of up to 40 m. The surge unit consists of coarse sandy pumiceous ash, moderately to poorly sorted, displaying low-angle cross stratification and lithic fragment laminations, and has a sharp basal surface (Figure 5.14). XRD analysis of this tephra indicates abundant plagioclase, moderate content of muscovite, and less abundance of quartz, tridymite, K-feldspar, biotite, pyroxene and amphibole (cummingtonite and riebeckite) (see Appendix 6).

The Wulabara Tephra (WLB) represents a pyroclastic fall deposit, consist ing of four distinct layers (Figure 5.15). WLB-T1 and WLB-T2 are thin basaltic tephra layers (1 and 2-cm, respectively), coarse to very coarse sandy ash with normal grading, is massive, well-moderately sorted, abundant in crystals, and displaying a sharp lower boundary. WLB-T3 is a pumiceous tephra-fall, massive, shows a fining upward sequence, moderately sorted, angular to sub-angular clasts, has a sharp basal contact, and the thickness is 50-cm. WLB-T4 indicates a distal vitric ash, white in colour, silty to coarse sandy in grain size, is massive, displays normal grading (fining-upward), has a sharp basal surface and is 1.16-m thick. This ash layer contains iron stains at the lowermost part. WLB-T4 contains moderate content of plagioclase and low contents of K-feldspar, quartz, tridymite, K-feldspar, muscovite, pyroxene and amphibole (hornblende, cummingtonite and riebeckite) (see Appendix 4).

Figure 5.14. The exposure of a thick surge deposit of the Nata Randang Tephra exposed at Nata Randang (8°36'20.7"S; 121°05'15.9"E) in the Welas Caldera Complex. The inset shows low-angle or horizontal lithic/heavy minerals stratifications (The coin is ~24 mm).

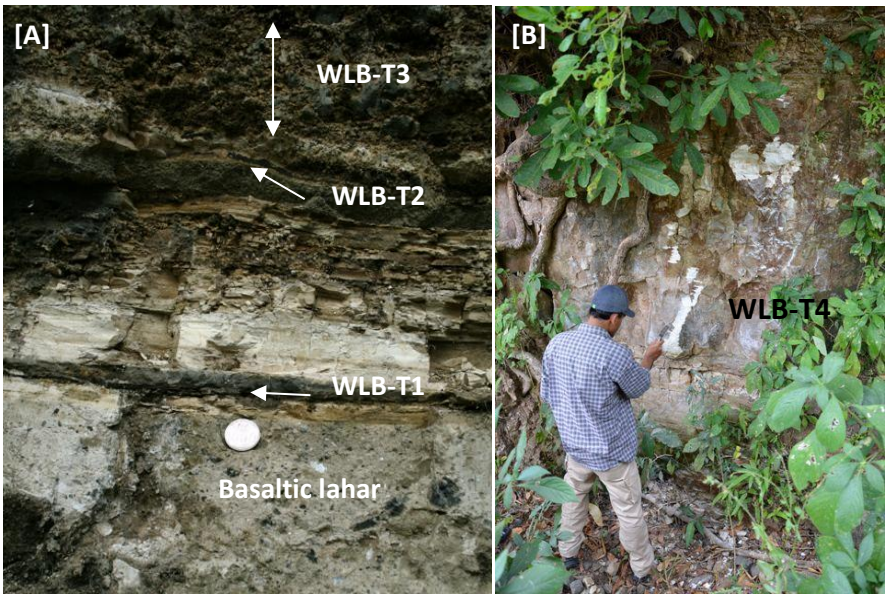

Figure 5.15. Photographs of the WLB tephra at Wulabara (8°39'02.3"S; 121°03'38.6"E); A) WLB-T1 overlies a basaltic lahar, and B) the outcrop of WLB-T4 (The coin is ~24 mm).

The Kolopanu Tephra (KLP) has typical characteristics of a pyroclastic flow unit (Figure 5.16). This tephra is exposed at Kolopanu, displays moderate to strong weathering and the thickness reaches up to 3.4 m. This tephra overlies a palaeosol and comprises pumiceous lapilli, is massive, clast supported, poorly sorted, and contains a mixture of white and grey pumice clasts (~10 cm) and few medium-sized lithics fragments.

Figure 5.16. The expsoure of the Kolopanu Tephra at Kolopanu (8°39'58.0"S; 121°02'29.5"E), which displays a weathered condition (The hammer is ~30 cm).

K.2. Geochemistry

The geochemical analysis has been conducted on whole-rock samples of NTR and WLB-T4, and glass shards of the KLP, NTR and WLB-T4. The major-and trace-element compositions of these tephras are summarised in Table 5.11. Furthermore, the major-element values of whole-rock samples and glass shards are recalculated to 100 % for discussion.

The whole-rock chemical composition indicates that the NTR and WLB-T4 display compositional variability. The NTR is characterised by higher contents of SiO_2, K_2O, V, Sr, Zr and Ba; while WLB-T4 has the greater contents of TiO_2, Al_2O_3, ΣFe_2O_3, MgO, CaO, Na_2O, and La.

The glass composition suggests that the analysed samples show small variation. The KLP has the highest values of TiO_2, Al_2O_3, MgO, CaO and K_2O; the NTR is characterised by the highest amounts of ΣFeO, MgO, Na_2O; and the WLB-T4 has the highest SiO_2 content.

The elemental variation of the KLP, NTR and WLB-T4 may indicate that these tephras were derived from different source volcanoes. In addition, the major-oxide values of whole-rock samples and volcanic glasses are different in some elements. The TiO_2, Al_2O_3, MgO, CaO and total iron contents are higher in whole-rock samples than glass shards due to the occurrence of plagioclase and ferromagnesian minerals in bulk samples

Table. 5.11. Major-and trace-element compositions of whole-rock samples and glass shards from the Wulabara (WLB-T4), Nata Randang and Kolopanu Tephras.

Sample	WLB-01	NTR-01		WLB-01		NTR-01		KLP-01	
Layer	WLB-T4	NTR		WLB-T4 (n=18)		NTR (n=18)		KLP (n=14)	
Locality	Wulabara	Nata Randang		Wulabara 8°41'29.1"S 121°05'36.4"E		Nata Randang 8°41'29.1"S 121°05'36.4"E		Kolopanu 8°41'29.1"S 121°05'36.4"E	
	Whole-rock			Glass shards					
Major elements (wt %)									
SiO_2	66.50	61.08	SiO_2	73.41	1.03	73.46	1.00	71.57	0.59
TiO_2	0.47	0.77	TiO_2	0.32	0.02	0.27	0.04	0.39	0.02
Al_2O_3	14.26	14.91	Al_2O_3	12.22	0.26	12.03	0.16	13.09	0.14
ΣFe_2O_3	2.82	5.74	ΣFeO	1.66	0.07	2.48	0.13	2.14	0.07
MnO	0.10	0.18	MnO	0.06	0.02	0.13	0.03	0.08	0.01
MgO	0.57	1.20	MgO	0.37	0.02	0.25	0.05	0.47	0.03
CaO	2.96	4.39	CaO	1.86	0.04	1.77	0.10	2.11	0.10
Na_2O	2.61	3.17	Na_2O	3.66	0.31	3.75	0.34	3.15	0.71
K_2O	1.55	1.35	K_2O	1.70	0.06	1.30	0.06	1.90	0.07
P_2O_5	0.10	0.14	Cl	n.d.		n.d.		n.d.	
S	0.02	0.02							
LOI	7.53	6.1							
Total	99.48	99.05	Total	95.27	-	95.44	-	94.89	-
Trace elements (ppm)									
V	220.8	153.6							
Rb	14.8	7.8							
Sr	350.3	242.4							
Y	13.6	20.8							
Zr	45.0	17.2							
Nb	1.6	0.2							
Ba	184.2	81.2							
La	2.0	9.6							
Ce	2.0	2.0							
Hf	2.9	2.4							
Ta	2.5	1.8							
Pb	5.4	1.2							
Th	1.3	1.0							
U	0.7	1.1							

Note. Total Fe is expressed as ΣFe_2O_3 (whole-rocks) and ΣFeO (glass shards); the glass composition is presented as a mean value (first column) and standard deviation (second column); *n* is the number of glass shards analysed; and n.d. = not determined.

5.3. Geochemical Correlation

The chemical analysis of tephra deposits can be a powerful tool to understand magma composition, discriminate individual tephra layers and delineate volcanic sources (Alloway *et al*., 2007; Lowe, 2008; 2011). Here the analysis of multi datasets were employed, including stratigraphic position, geochemical signatures (major- and trace-elements) on both whole-rock samples and glass shards, in order to distinguish and correlate individual tephra layers. This study is largely restricted to discrete tephra layers in the Tuff and Sandstone Members of the Ola Bula Formation that are macroscopically visible. Previous sub-chapters have highlighted the field characteristics and chemical compositions of tephras, exposed at a number of localities and stratigraphic slot trenches across the Soa Basin. Stratigraphic position indicates that the AEI and LMI belong to the oldest exposed unit in the Soa Basin, the Ola Kile Formation. The tephra layers of the Tuff Member comprise the TTL, WLW, WSI, TRI, KPW and PMS. The MMT is the only studied ash deposit from the Sandstone Member, while the series of PGT occur in the lacustrine sequence of the Limestone Member. The stratigraphic positions of three tephras (KLP, NTR and WLB-T4) are unclear.

Several tephra layers recognised in the Tuff and Sandstone Members of the Ola Bula Formation are important for stratigraphic correlation because of their wide spread distributions across the Soa Basin. Some of these are deposited in association with fossil-and/or artifact-bearing layers and these play significant roles for intra-basinal correlations of faunas and palaeoenvironmental reconstructions. The application of two geochemical methods, i.e. XRF and EPMA, for geochemical fingerprinting of tephra layers is tested. For correlation purposes, the major-element values of whole-rock samples and glass shards have been recalculated to 100 %.

5.3.1. Geochemical correlation based on whole-rock composition (XRF)

The whole-rock chemical composition (major-and trace-elements) of tephra layers from the Tuff and Sandstone Members varies between 59.98–95.27 wt% SiO_2, 0.04 –4.98 wt% K_2O, 0.08–7.30 wt% total alkali ($Na_2O + K_2O$), 6–196 ppm Rb, 97–390 ppm Sr, 94–1426 ppm Ba and 1–30 ppm Th. Plotting the SiO_2 versus Na_2O+K_2O contents of the tephras on the Total Alkali Silica (TAS) diagram, it can be seen how the various tephras fall into various chemical suites, ranging from andesite to rhyolite (Figure 5.17). The diagram shows that TTL-T4, TRI, KPW, and NTR have a rhyolitic composition; LMI, TTL-T1, TTL-T2, WLW, PMS and WLB-T4 display a dacitic composition; while TTL-T5 has an andesitic composition. The WSI has an intermediate dacitic to rhyolitic composition and the MMT has an andesitic to dacitic composition.

The SiO_2 *versus* K_2O diagram is used to further characterise and distinguish the analysed tephras. This data demonstrate that tephra layers can be separated into four main groups (Figure 5.18): TTL-T1 and TTL-TT4 correspond to the tholeiite series; the WSI, reworked WSI, WLW, MMT and PGT fit into the tholeiite – calk-alkaline series. The LMI, TTL-T2, TTL-T5, TRI, reworked TRI, PMS, NTR and WLB all fall into the calk-alkaline series, and the KPW is the only tephra correponding to the high-K calk-alkaline series.

The silica-based diagrams (Harker diagrams) suggest that the major-element compositions of the tephras display a wide compositional variability and several distinct populations can be observed (Figure 5.19). Some tephras show scattered trends and display inconsistent chemical populations. The wide spread of some major elements in some cases cause problems in characterising the tephras. However, grouping of the tephras can be most clearly observed from the SiO_2 *versus* K_2O diagram, suggesting that at least five distinct clusters are present. The TTL-T1, TTL-T2 and WLW are similar (Group 1 hereafter); LMI, TTL-T5, and MMT are closely related to each other (Group 3) and the WSI, reworked WSI, TRI, reworked TRI and PMS display chemical similarities (Group 4). The TTL-T4 and KPW are separated from the majority of populations

and forms two distinct clusters (Group 2 and 5, respectively). The diagram further shows that the WLB-T4 and NTR, both of uncertain stratigraphic position, are compositionally relatively close to Group 1 and Group 4, respectively.

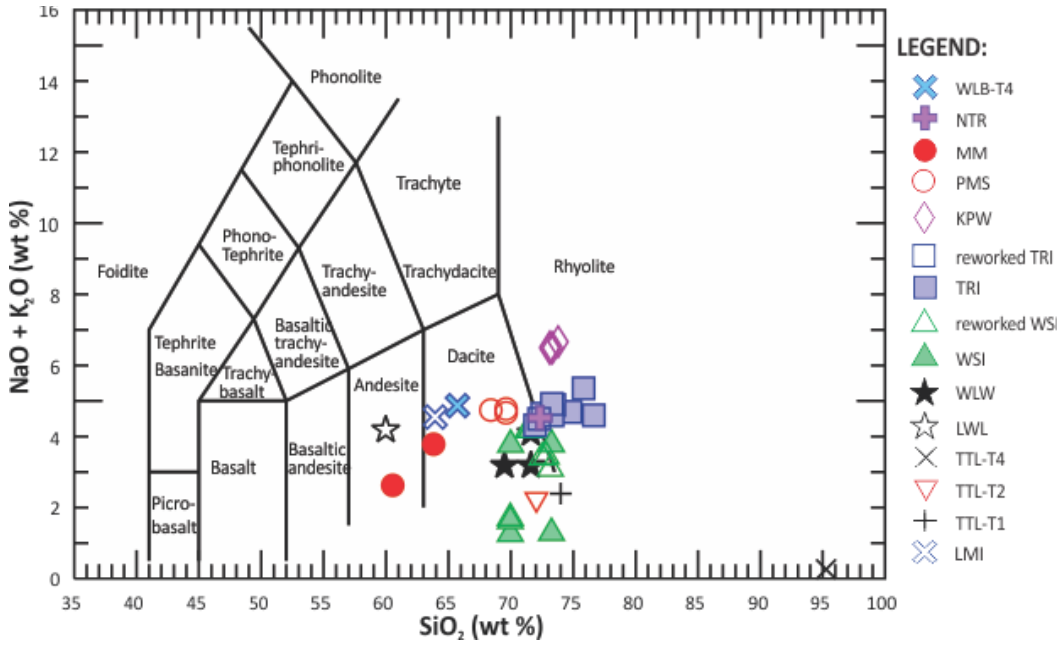

Figure 5.17. The whole-rock composition of discrete tephra layers from the Tuff and Sandstone Members of the Ola Bula Formation. The LMI (Ola Kile Formation) and stratigraphically unknown tephra beds of NTR and WLB-T4 are also plotted for comparison. Legend indicates pyroclastic samples in stratigraphic order. The TAS diagram is suggested by LeBas *et al*. (1986).

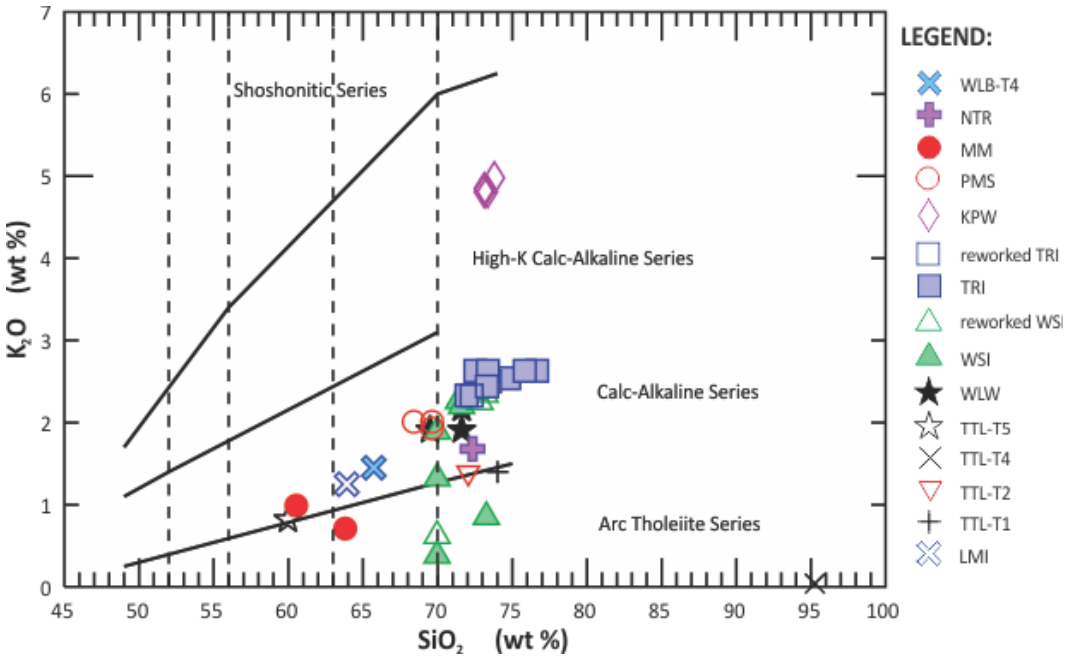

Figure 5.18. The compositional variation of whole-rock samples of discrete tephra layers from the Tuff and Sandstone Members of the Ola Bula Formation. The LMI (Ola Kile Formation) and stratigraphically unknown tephra beds of NTR and WLB-T4 are also plotted for comparison. Legend indicates pyroclastic samples in stratigraphic order. Compositional fields are from Peccerillo and Taylor (1976).

Some studies have used the ΣFeO, CaO and K_2O contents for fingerprinting multiple tephra layers (e.g. Alloway *et al*., 2004, 2005). In whole-rock samples, total iron is expressed as ΣFe_2O_3, thus the ΣFeO value is replaced by ΣFe_2O_3 for this analysis. The biplot diagrams of ΣFe_2O_3 *versus* CaO and K_2O *versus* CaO are shown in Figure 5.20. The studied tephras can be grouped into 3 to 8 populations. In the ΣFe_2O_3 *versus* CaO diagram (Figure 5.20A), 3 clusters have been identified with one cluster consisting of several tephras that have similar ΣFe_2O_3 and CaO contents. However, considering the CaO/K_2O ratios, a large group of tephras is difficult to assign to a particular group with unique chemical characteristics (Figure 5.19).

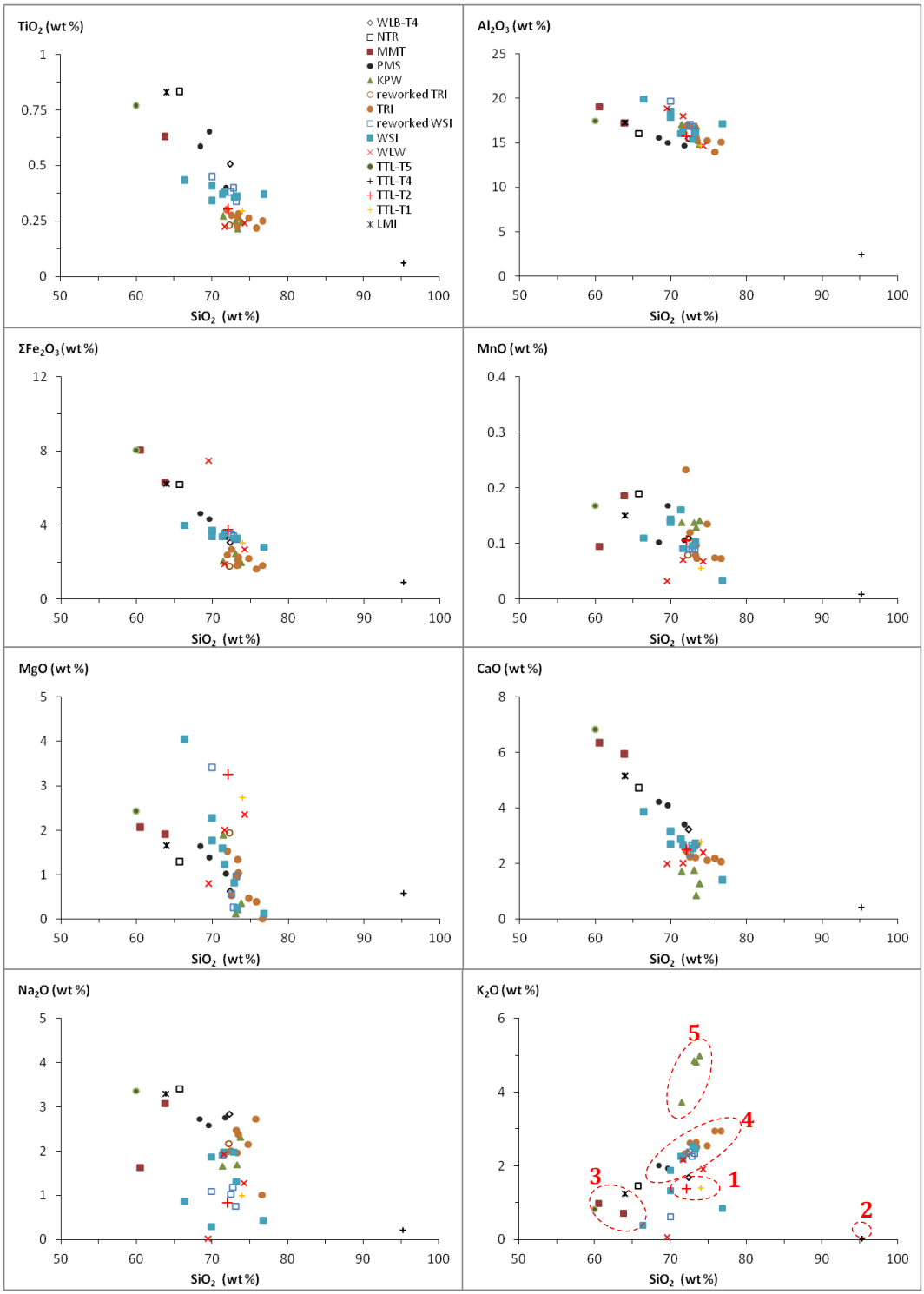

Figure 5.19. Harker diagrams of whole-rock samples from tephra deposits of the Tuff and Sandstone Members (Ola Bula Formation). The LMI (Ola Kile Formation) and two tephras of unknown stratigraphic position (NTR and WLB-T4) are also plotted for comparison. Legend indicates pyroclastic samples in stratigraphic order.

Despite the wide scatter of K_2O *versus* CaO ratios (Figure 5.20B), it is clear that TTL-T1 and TTL-T2 are chemically similar to each other; the LMI and TTL-T5 show a close relation; and the WLW, WSI, reworked WSI, TRI, reworked TRI and PMS constitute a chemically similar grouping. However, three samples of the WSI have strongly distinct K/Ca ratio, possibly due to abundant crystal concentrations. The TTL-T4, KPW, MMT, NTR and WLB-4 do not match with any of other groups and show a wide scatter pattern. The K_2O *versus* CaO ratio seems to provide more a clear result discriminating the studied tephras compared to the ΣFe_2O_3 *versus* CaO ratio. The K/Ca ratio further seems to single out some individual tephras that do not seem to have an affinity with any of the groupings, such as MMT and TTL-T4.

For comparison purposes and to facilitate the correlation of the studied tephras, the major-and trace-element compositions are normalised to N-type mid oceanic basalt (NMORB) and Rhyolite Glass Mountain (RGM). Normalised to NMORB, the major-element values of whole-rock samples from the analysed tephra layers display similar patterns, with the exception of TTL-T4 (Figure 5.21A).

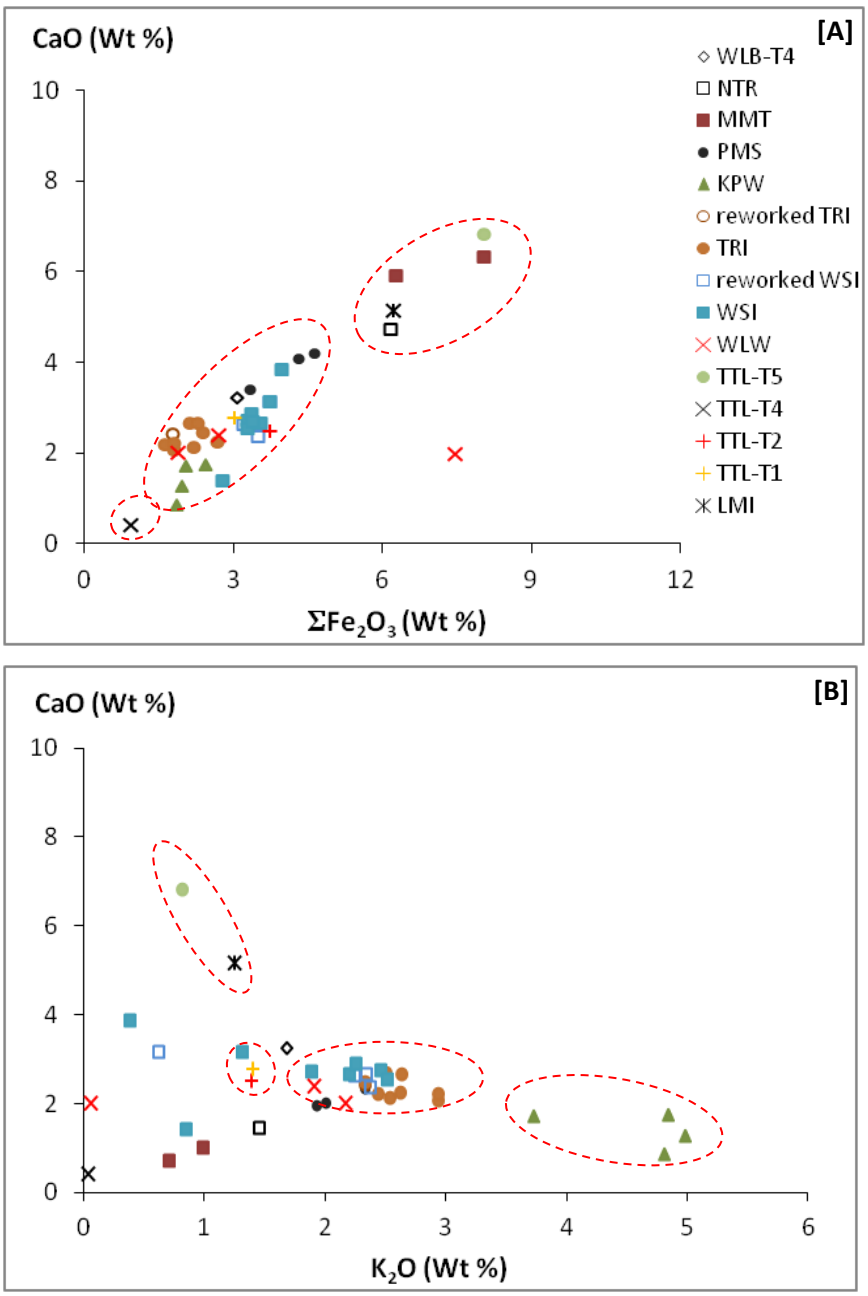

Figure 5.20. A) The ΣFe_2O_3 *versus* CaO and B) K_2O *versus* CaO diagrams of the studied tephra layers from the Tuff and Sandstone Members of the Ola Bula Formation based on the whole-rock chemical composition. The Upper LMI (Ola Kile Formation) and two stratigraphically unknown tephras of NTR and WLB-T4 are also plotted for comparison. Legend indicates pyroclastic samples in stratigraphic order.

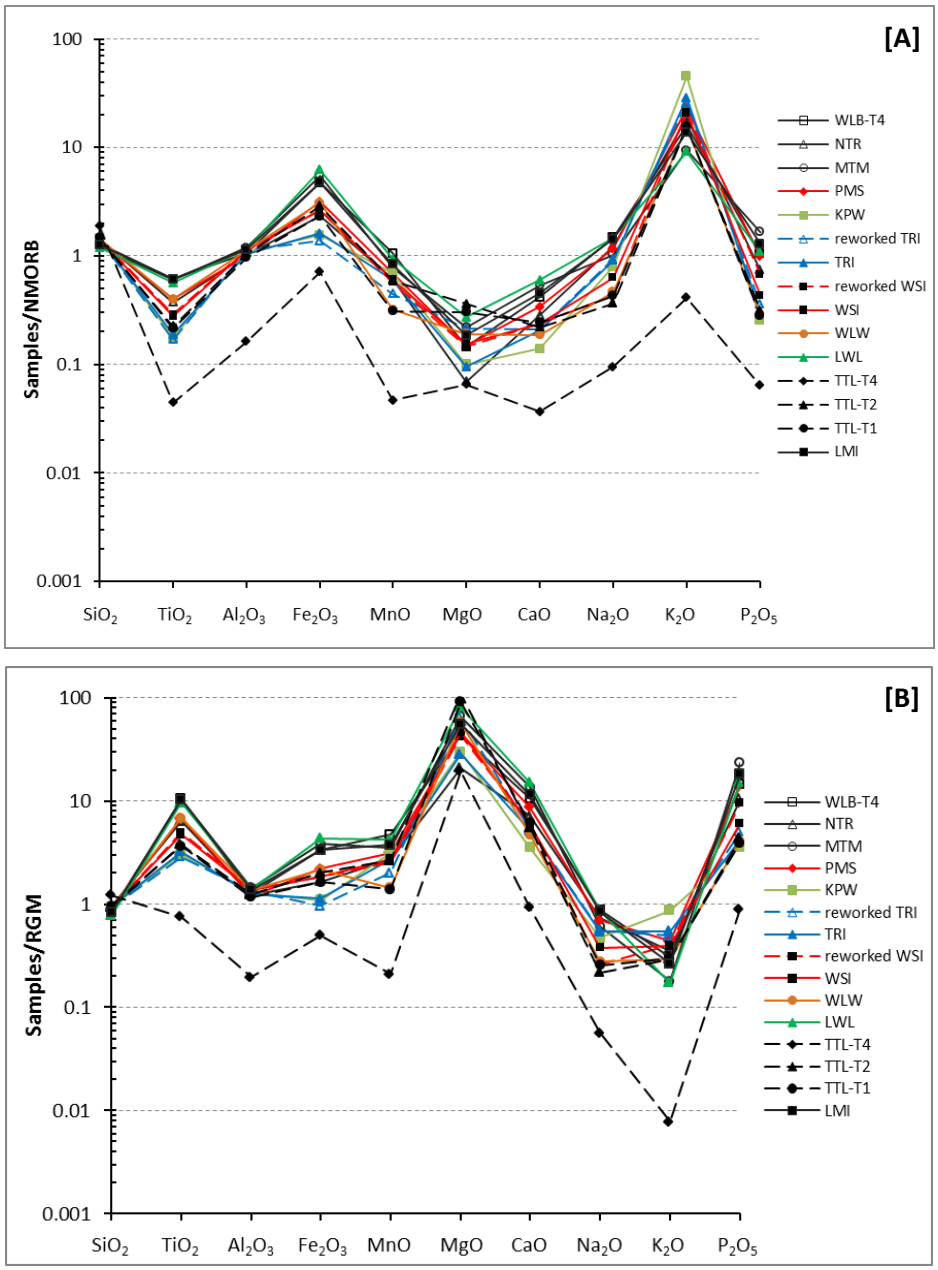

Figure 5.21. The variation of major-element composition of whole-rock samples from the studied tephra layers; A) normalised to the NMORB composition (Sun and McDonough, 1989), and B) normalised to the RGM composition (Noble *et al.*, 1972; and USGS (1995) for the ΣFe_2O_3 content). The major-element values are presented as mean values and have been recalculated to 100 %. Legend indicates pyroclastic samples in stratigraphic order.

The normalised major-element diagram generally displays depletion of TiO_2, MnO, MgO, CaO and P_2O_5; and slight enrichment of SiO_2, Al_2O_3, ΣFe_2O_3 and strong enrichment of the K_2O content. The TTL-T4 sample has a distinct pattern compared to the other tephras with most major-elements depleted and showing the strongest enrichment in the SiO_2 content. In addition, KPW also displays a unique trend, having the strongest enrichment of K_2O and the largest depletion in CaO. It can also be seen at a glance that the WSI and TRI show indistinguishable patterns compared to their reworked deposits. The WSI, TRI and PMS have nearly similar normalised values relative to NMORB.

In the case of the major-element RGM normalisation, most tephra layers generally display comparable patterns with strong enrichments of MgO; slight enrichments of TiO_2, Al_2O_3, ΣFe_2O_3, MnO, CaO and P_2O_5 and depletions of SiO_2, Na_2O and K_2O (Figure 5.21B). Compared to the other tephras, TTL-T4 again demonstrates a distinct pattern, in line with the NMORB normalised diagram. This tephra is enriched in SiO_2 and MgO and depleted in TiO_2, Al_2O_3, ΣFe_2O_3, MnO, CaO and P_2O_5. Apart from SiO_2 it has the lowest negative anomaly for all other major elements. From the RGM-normalised diagram, the WSI and TRI exhibit identical trends with their reworked deposits. The LMI and MMT have nearly similar normalised-value and the TTL-T1 and TTL-T2 display nearly similar patterns.

In term of trace-element composition, whole-rock samples of tephras generally show similar trends compared to NMORB, but tend to be more variable (Figure 5.22A). Few tephras have a distinct trend regarding Nb, La, Ce and Zr contents. Samples of WSI, reworked WSI and TRI have enrichment of Nb. The WSI and reworked WSI display identical patterns. The KPW has a significantly higher enrichment of Sr, Ba and Th compared to all other tephras; while the NTR has a distinct pattern, displaying the lowest negative anomalies of Nb and Zr.

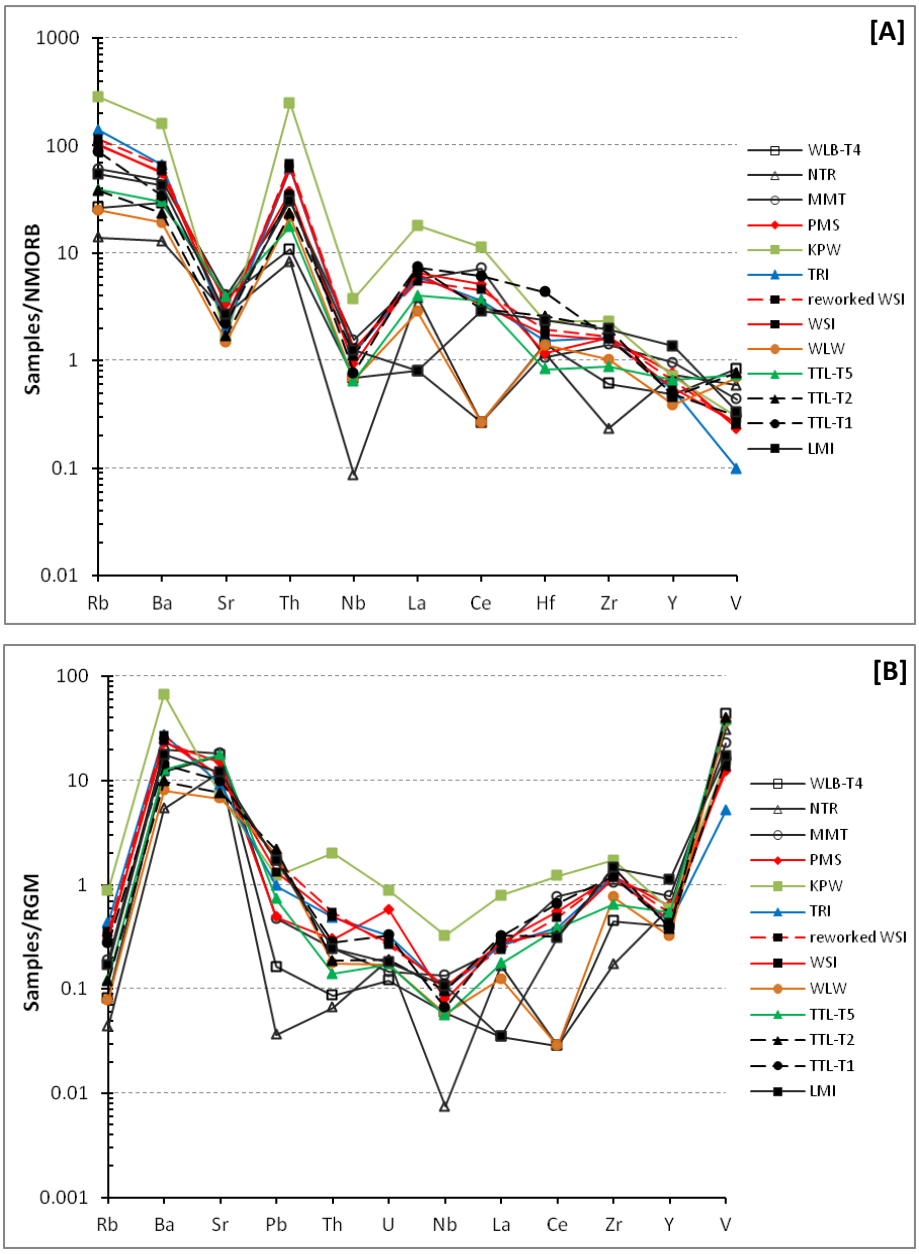

Figure 5.22. The variation of trace-element composition of whole-rock samples from the studied tephra layers; A) normalised to the NMORB composition (Sun and McDonough, 1989), and B) normalised to the RGM composition (Noble *et al*., 1972; and USGS (1995) for Ta, Th and U contents). The trace-element values are presented as mean values. Legend indicates pyroclastic samples in stratigraphic order.

Regarding the normalised trace-elements to the RGM values, the analysed tephra samples mostly have indistinguishable trends, which show strong positive anomalies of Ba, Sr and V, low positive anomalies of Pb and Zr and negative anomalies of Rb, Th, U, Nb, La, Ce and Y (Figure 5.22B). Few tephra deposits, such as the LWL, TRI, PMS, MMT, NTR and WLB-T4 are enriched in Pb. Moreover, the WSI and reworked WSI display identical trends; and the KPW has a unique pattern with Th and Ce contents enriched and having the highest value of Ba and U compared to the other tephras.

Both the TAS and the normalised-diagrams reveal that some tephra layers have identical chemical affinities, suggestive of a common source volcano. The LMI and MMT could be derived from the same volcano. The WSI, TRI and PMS also possibly originated from the same volcano. The TTL-T4 and KPW have unique characteristics that do not match any other studied tephra.

Another method commonly applied to classify and distinguish tephra layers, based on their major-element composition, by plotting some combinations of major oxides in a ternary diagram. Here we use a triplot diagram of K_2O-CaO-ΣFe_2O_3 (K-Ca-Fe) is used in this study to chemically fingerprint the studied tephra deposits and further to confirm the groupings suggested in the previous diagrams. The K-Ca-Fe diagram (Figure 5.23) enables to characterise 5 (five) distinct populations, nearly matching the five groupings distinguished based on the SiO_2 *versus* K_2O diagram (Figure 5.19). However, the current characterisation is slightly different from the K_2O *versus* CaO diagram (Figure 5.20B). The triplot diagram indicates that TTL-T1, TTL-T2 and PMS group together (Group 1); TTL-T5 and MMT display chemical similarity with LMI (Group 3); and WSI, reworked WSI, TRI, reworked TRI and WLW are closely associated (Group 4). Moreover, the composition of TTL-T4 and KPW cannot be correlated with any other tephras, and these two tephra deposits consistently form two unique outliers (Group 2 and 5, respectively), that are significantly separated from all other tephra populations. In the ternary diagram, NTR and WLB-T4 are compositionally closer to Group 1 and 3, respectively, unlike the suggested

grouping derived from the TAS diagram. The PMS, WLW, NTR and WLB-T4 also group differently compared to their SiO_2 *versus* K_2O diagram (Figure 5.19).

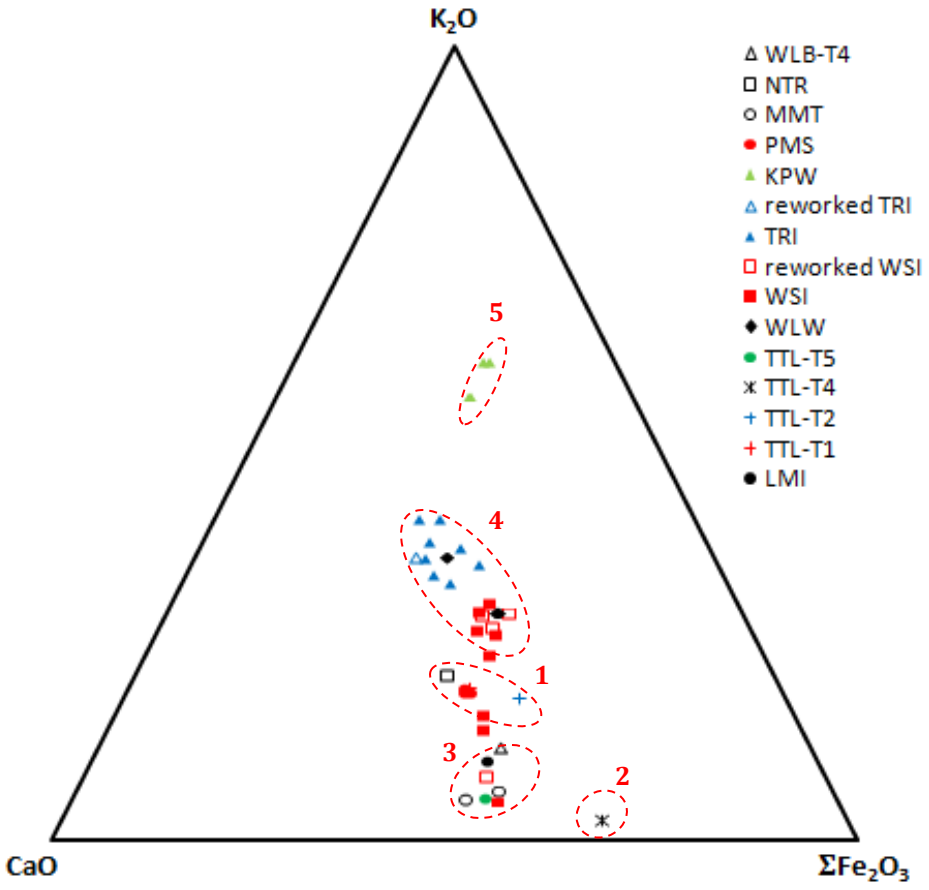

Figure 5.23. The K_2O-CaO-ΣFe_2O_3 diagram of whole-rock samples from the studied tephra deposits of the Ola Bula Formation. The LMI (Ola Kile Formation) and stratigraphically unknown tephra layers of NTR and WLB-T4 are also plotted for comparison. Legend indicates pyroclastic samples in stratigraphic order.

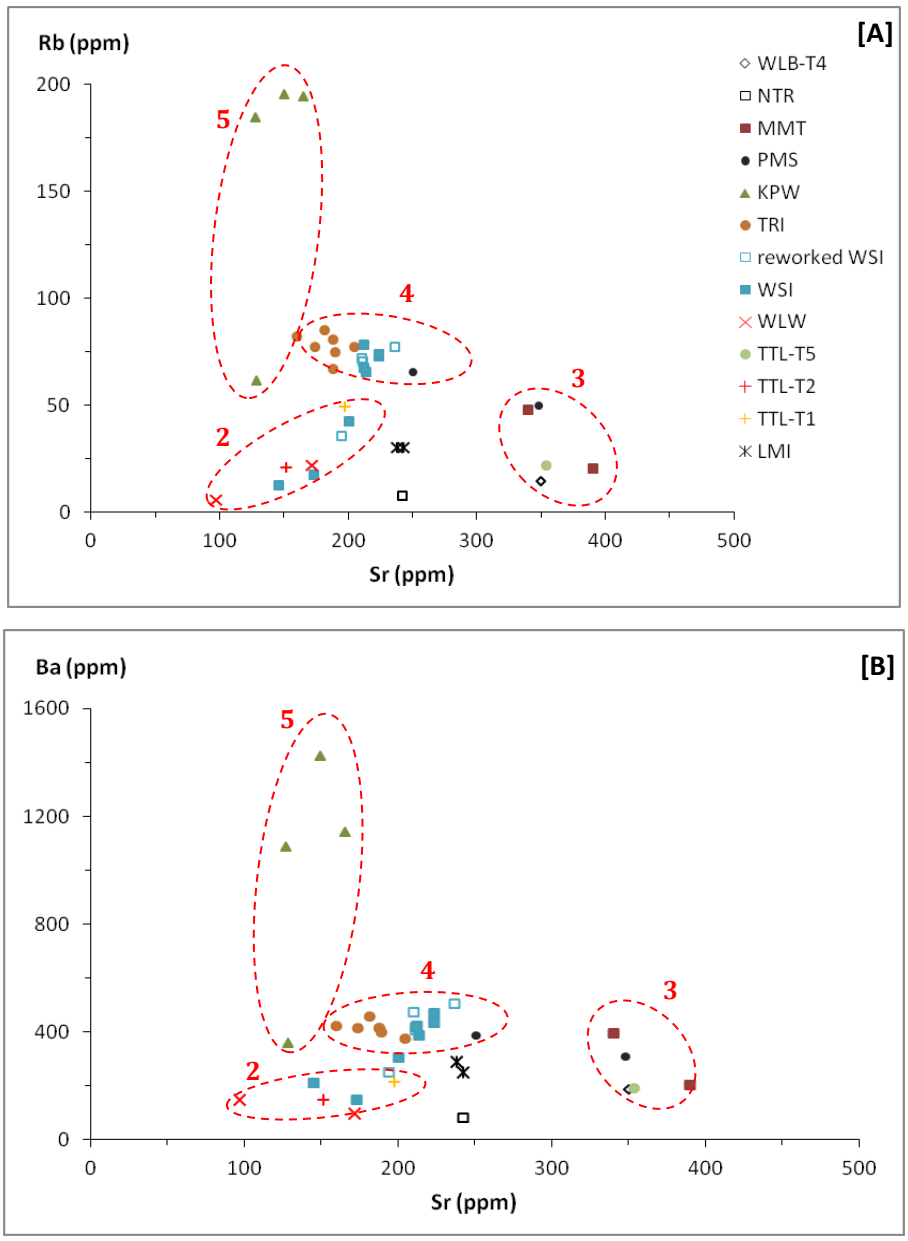

Figure 5.24. The variation of selected trace-element compositions of whole-rock samples from the studied tephra deposits of the Ola Bula Formation. The LMI (Ola Kile Formation) and stratigraphically unknown tephra layers of NTR and WLB-T4 are also plotted for comparison. Legend indicates pyroclastic samples in stratigraphic order. The groupings follow the K-Ca-Fe composition and are given the same numbers here.

Using the major-element composition, the analysed tephra samples can be distinguished and some can be shown to have close affiliation with other tephras. In addition, some studies use the trace-element composition for correlating tephra deposits derived from different source volcanoes (e.g., Pearce *et al*., 2002; Begét and Keskinen, 2003; Kuehn *et al*., 2009). It is shown that trace-element concentration of whole-rock samples from tephra layers generally show large variations in Rb, Sr and Ba contents. The Rb, Sr and Ba values of analysed tephras, therefore, are plotted in biplot diagrams of Rb and Sr *versus* Ba (Figure 5.23). These show that trace-element values enable to distinguish four major populations. LMI and NTR do not match with the four major groups and form a separate group, between Group 2 and Group 4. It also should be noted that the WLB-T4 is compositionally closer to Group 3, the same group with it matches in the K-Ca-Fe diagram. The KPW is widely separated from all other groups, as in the binary diagrams of the major-element values (Figure 5.18, 5.19 and 5.20B) and the K-Ca-Fe diagram (Figure 5.23).

Summarising, the whole-rock composition of the studied tephra layers from the Soa Basin show large compositional variability and can be separated into distinct groupings based on their major-and trace-element compositions. The binary plot of SiO_2 *versus* K_2O, K_2O *versus* CaO, Sr *versus* Rb and Sr *versus* Ba as well as the K_2O-CaO-ΣFe_2O_3 diagram provide useful tools for chemically fingerprinting most tephra samples. The analysed tephras of the Tuff and Sandstone Members can be discriminated into 5 (five) main groups:

1) TTL-T1, TTL-T2 and WLW (Group 1);
2) TTL-T4 (Group 2);
3) TTL-T5 and MMT (Group 3);
4) WSI, reworked WSI, TRI, reworked TRI and the PMS (Group 4); and
5) KPW (Group 5).

In addition, LMI (the Ola Kile Formation) has relatively identical major-element composition with TTL-T5 and MMT. However, its trace-element concentrations, particularly Rb, Sr and Ba are different from those two tephra beds and also do not match with other tephra layers. The analysis also indicates that NTR and WLB-T4, both of uncertain stratigraphic position, are relatively close in chemical composition to Group 2 and Group 3, respectively.

5.3.2. Geochemical correlation based on volcanic glass composition (EPMA)

Electron microprobe analysis has been conducted on glass shards of several discrete tephra layers from the Tuff Member (the Ola Bula Formation) and three prominent tephra beds whose stratigraphic positions are still unclear. The major-element composition of glass shards show less variability than the whole-rock composition, ranging from 75.05–82.05 wt% SiO_2, 0.14–0.41 wt% TiO_2, 10.20–13.83 wt% Al_2O_3, 1.03–5.36 wt% ΣFeO, 0.02–0.14 wt% MnO, 0.11–0.77 wt% MgO, 0.69–2.23 wt% CaO, 0.23–3.92 wt% Na_2O, 0.26–5.17 wt% K_2O. The major-element values have been recalculated to 100 % on a water free-basis. Two discrete tephra deposits, i.e. TTL-T4 and KPW, are important to note because of their unique chemical properties. The TTL-T4 is shown to have the highest SiO_2 value, while the KPW has the highest K_2O value.

As mentioned before, SiO_2 and total alkalis (Na_2O + K_2O) element concentrations are good parameters to characterize products of volcanic eruptions (Rollinson, 1993; LeBas *et al*., 1986; Alloway *et al*., 2007). Plotting these parameters in a Total Alkali Silica (TAS) diagram denotes that all tephra layers fall into the rhyolite fields with three distinct populations (Figure 5.25). The TTL-T4 and KPW have the lowest and highest total alkalis and the highest and lowest SiO_2 content, respectively. In addition, the SiO_2 *versus* K_2O diagram (Figure 5.26) allows the tephra samples to be classified into 3 volcanic suites: 1) TTL-T4 and NTR represent the tholeiite series; 2) TTL-T1, TTL-T2, TTL-T5, WLW, WSI, TRI, PMS and WLB-T4 correspond to the calk-alkaline series; and 3) KPW fits into the high-K calk-alkaline series.

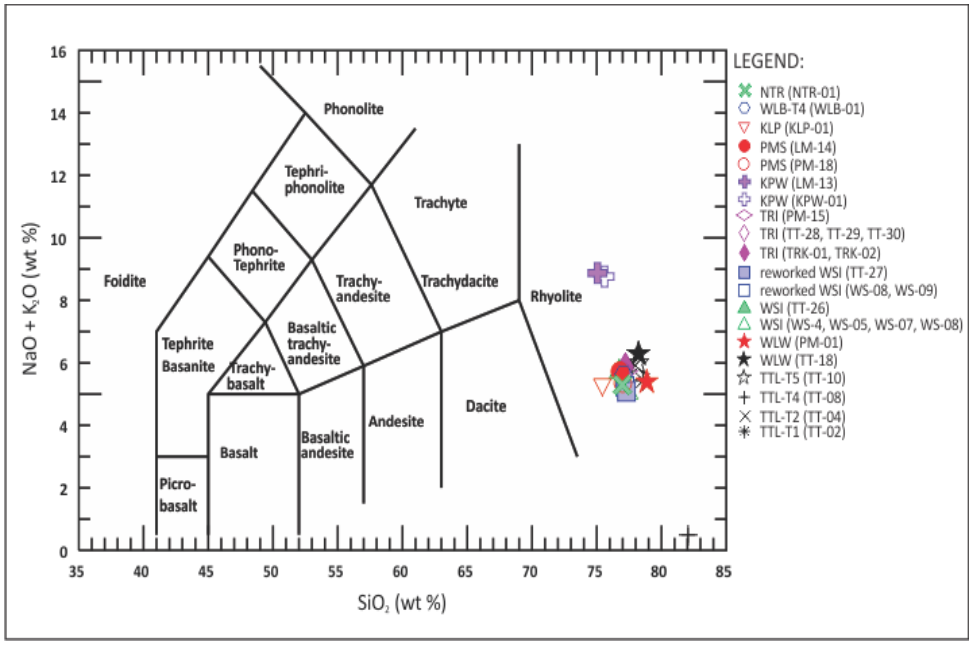

Figure 5.25. The glass composition of tephra deposits from the Tuff Member of the Ola Bula Formation and stratigraphically unknown tephra beds of WLB-T4, NTR and KLP. The TAS diagram is adopted from LeBas *et al*. (1986). The major-element values are presented as mean values and have been recalculated to 100%. Legend indicates pyroclastic samples in stratigraphic order, while parentheses indicate the sample number. Abbreviation: LM=Lowo Mali, KLP= Kolopanu, KPW=Kopowatu, MM=Mata Menge, NTR= Nata Randang; PM= Pumaso, TT= Tangi Talo, WLB= Wulabara, WS= Wolo Sege.

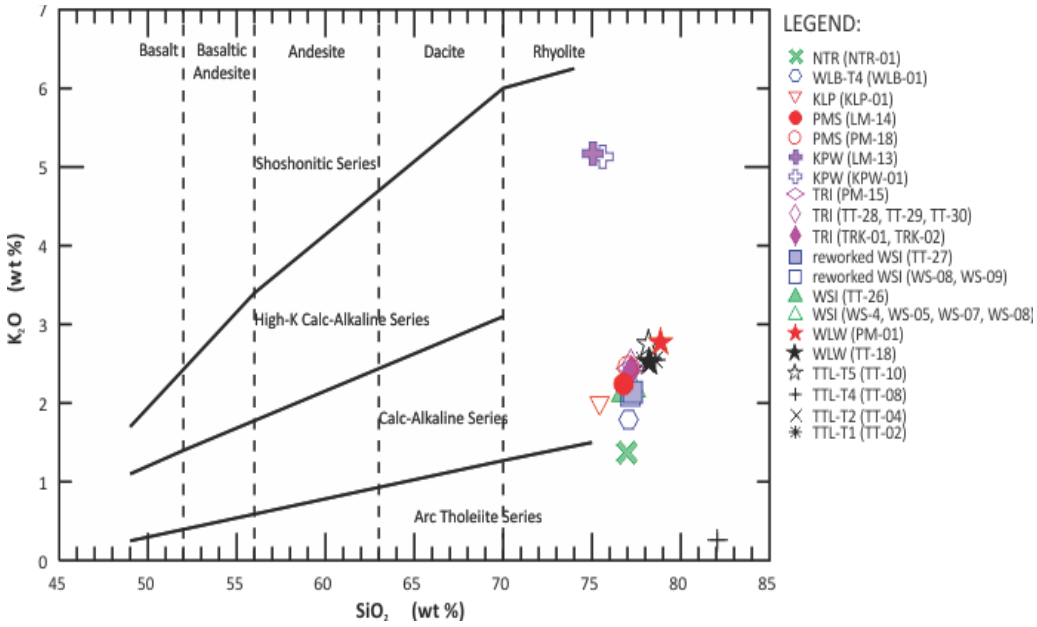

Figure 5.26. The compositional variation of glass shards from discrete tephra layers of the Tuff Member (Ola Bula Formation) and stratigraphically unknown tephra beds of WLB-T4, NTR and KLP. The compositional field follows Peccerillo and Taylor (1976). Parentheses indicates the sample number, while legend and abbreviations follow Figure 5.25.

Figure 5.27 shows the major-element composition of glass shards in Harker diagrams. All samples display limited variation for TiO_2, Al_2O_3, ΣFeO, MnO and Na_2O *versus* SiO_2, but a wider separation into distinct clusters can be observed in the MgO and CaO *versus* SiO_2 diagrams. Considering these ratios, the tephras can be grouped into two large clusters and four small populations, while five distinct groups can be recognised in the SiO_2 *versus* K_2O diagram. In the SiO_2 *versus* MgO diagram, TTL-T1, TTL-T5 and WLW show identical ratios (Group 1); TTL-T2 and the WLB-T4 are closely matching (Group 2); and WSI, reworked WSI, TRI and PMS are chemically indistinguishable (Group 4). Moreover, TTL-T4, KPW and KLP represent separate distinct populations (Groups 3, 5 and 6, respectively).

In addition, the SiO_2 *versus* CaO diagram suggests that tephra samples can be discriminated in six clusters; however, the tephra populations are slightly different from the SiO_2 *versus* MgO diagram. In this biplot diagram, TTL-T2 displays compositional similarity with TTL-T1 and WLW (Group 1). The WLB-T4 is closer to Group 4; and TTL-T5 is separated from the most populations and forms an independent cluster (Group 2). Moreover, TTL-T4, KPW and KLP consistently do not match any groups and represent three very distinct groups.

As shown in the SiO_2 *versus* K_2O diagram (Figure 5.27), the tephras display less heterogeneity and only three tephra populations can be observed with Groups 1, 4 and 6 plotting closely together. The members of Group 2 from the SiO_2 *versus* CaO diagram (TTL-T2 and WLB-T4) and the SiO_2 *versus* MgO diagram (TTL-T5) are chemically closer to the member of Group 1 (TTL-T1 and WLW) in the SiO_2 *versus* K_2O diagram. The other tephras plot in the same group as in the SiO_2 *versus* CaO and SiO_2 *versus* MgO diagrams with the WSI, reworked WSI, TRI, PMS, NTR and are compositionally identical (Group 4); while TTL-T4 and KPW are widely separated from the main clusters (Groups 3 and 5, respectively).

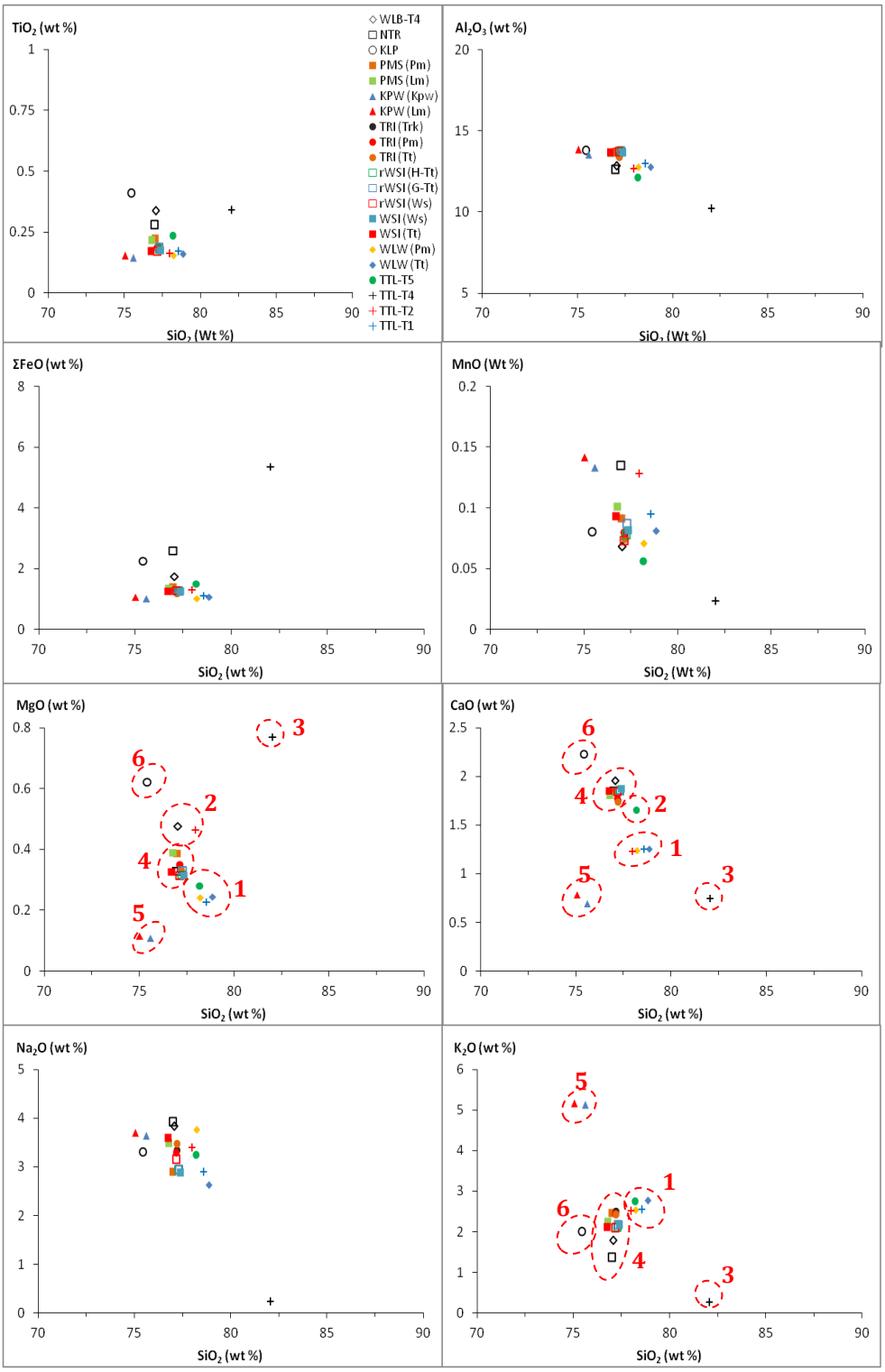

Figure 5.27. The variation of major-element composition of glass shards from discrete tephra beds in the Tuff Member of the Ola Bula Formation and stratigraphically unknown tephra layers of WLB-T4, KLP and NTR. Parentheses indicate the sample location and "r" means reworked (rWSI= reworked WSI). Abbreviations: Kpw = Kopowatu; Lm = Lowo Mali; Pm = Pumaso; Trk = Turekeo; Tt = Tangi Talo; Ws = Wolo Sege. Legend indicates pyroclastic samples in stratigraphic order.

The ΣFeO *versus* CaO and CaO *versus* K_2O diagrams (Figure 5.28) permit five groups:

1) TTL-T1, TTL-T2 and WLW (Group 1)
2) TTL-T4 (Group 2)
3) TTL-T5, WSI, reworked WSI, TRI and PMS (Group 3)
4) KPW (Group 4)
5) KLP, NTR and WLB-T4 (Group 5)

The TTL-T5 matches with tephras of Group 1 in the Harker diagram, but it exhibits similar composition with Group 3 in the biplot diagrams of ΣFeO *versus* CaO and CaO *versus* K_2O contents. The ΣFeO and CaO *versus* K_2O diagrams further indicate that KLP, NTR and WLB-T4 chemically disperse and do not have a close affinity with any of the other tephra groupings. Therefore, these tephras of unknown stratigraphic position (KLP, NTR and WLB-T4) cannot be correlated with any of the other prominent tephra layers of the Tuff Member (the Ola Bula Formation).

The K_2O content of the analysed tephras ranges between 0.26–5.17 wt%, except for the KPW which has the highest potassium content (~ 5 wt% K_2O) and it is the only tephra that can be classified as belonging to the high-K calk-alkaline series (Figure 5.26). This distinctive characteristic suggests that it probably originated from a distant volcano with a high-potassium magma. Numerous studies indicate that the deposits of Toba eruptions are characterised by a high K_2O content (Chesner and Rose, 1991; Dehn *et al*., 1991; Chesner, 1998, Lee *et al*., 2004; Chesner and Luhr, 2010; Pattan *et al*., 2010).

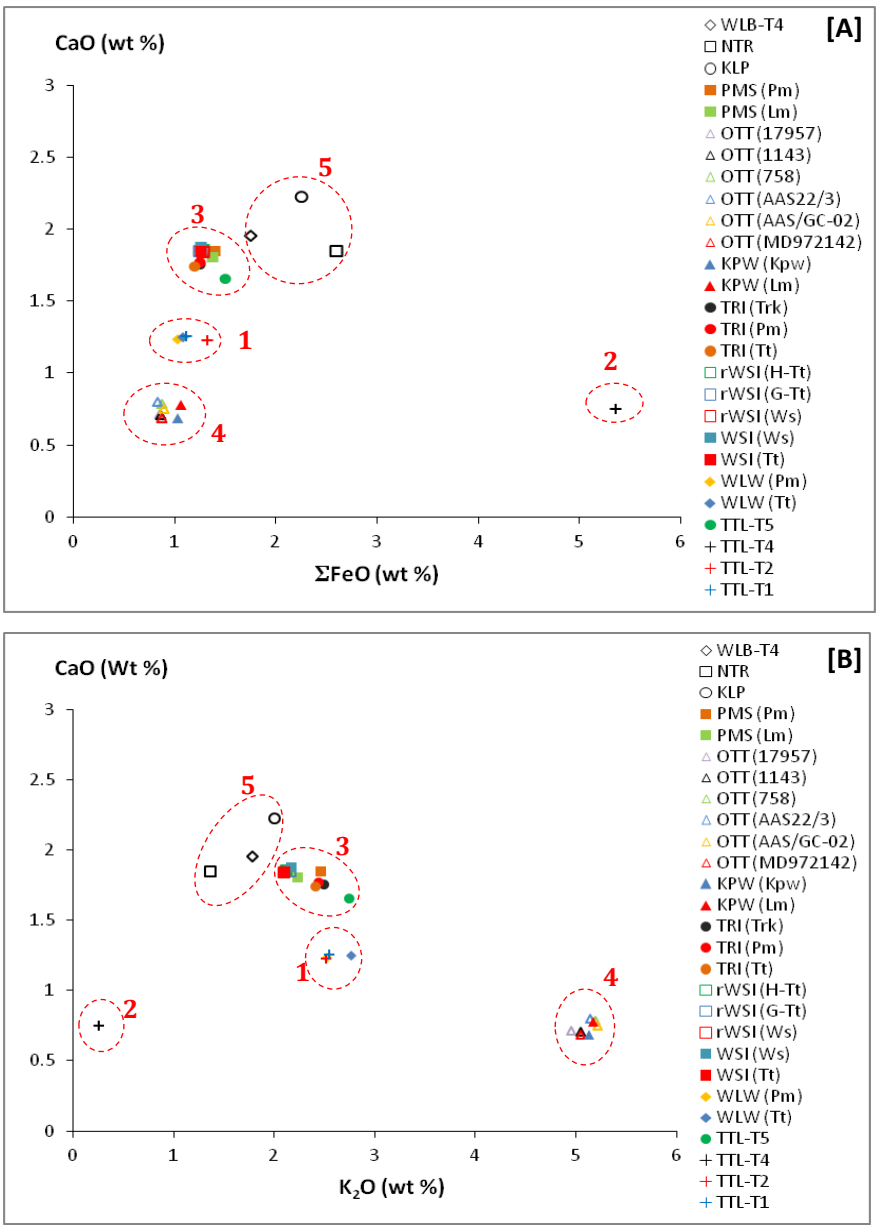

Figure 5.28. A) The ΣFeO *versus* CaO and B) K_2O *versus* CaO diagrams of discrete tephra beds from the Tuff Member of the Ola Bula Formation and stratigraphically unknown tephra layers of WLB-T4, KLP and NTR. Legend indicates pyroclastic deposits in stratigraphic order, and parentheses refer to the sample location. Samples of the oldest Toba Tuff (OTT) taken from marine cores are also plotted for reference. The OTT data of core 758 is from Dehn *et al.*, (1991); cores 17957, 1143, and MD972142 are from Lee *et al.* (2004); while the OTT composition of cores AAS22/3 and AAS/GC-02 are from Pattan *et al.*, (2010).

The stratigraphic position of KPW ~3-4 m above WSI, which was Ar/Ar dated at 1.02 Ma, combined with the similar K_2O content suggests that the KPW can be correlated to the oldest Toba Tuff (OTT), which was ejected between 840 and 780 ka ago (Diehl *et al*., 1987; Hall and Farrell, 1995; Lee *et al*, 2004). Published average glass compositions of the OTT range between 4.95 to 5.21 wt% K_2O (Dehn *et al*., 1991; Lee *et al*., 2004; Pattan *et al*., 2010). To further investigate the chemical similarities between the KPW and the OTT, the published concentrations of K_2O, ΣFeO and CaO from several Toba samples collected from marine cores (e.g. Dehn *et al*., 1991; Lee *et al*., 2004; Pattan *et al*., 2010) are compared with KPW in the ΣFeO *versus* CaO and CaO *versus* K_2O diagrams (Figure 5.28). In these two diagrams, KPW and OTT are compositionally indistinguishable and these tephras represent a unique and discrete cluster. Combined with its age estimate, the geochemical data strongly suggest that KPW represents the OTT.

To further explore the affinities of the Soa tephra beds, the major-element values of the analysed glass shards are normalised to the NMORB and RGM compositions for comparison. Relative to NMORB, all tephra samples generally demonstrate a similar pattern: they are enriched in SiO_2, Na_2O and K_2O; and depleted in TiO_2, Al_2O_3, ΣFeO, MnO, MgO and CaO (Figure 5.29A). TTL-T4 is the only tephra with a very distinct pattern, having the lowest values of MnO, CaO and Na_2O, and only a minor enrichment of K_2O. The highest enrichment of the K_2O content is found in KPW and OTT.

The KPW and OTT have indistinguishable trends relative to NMORB. In the case of the MgO value, three samples of OTT from deep sea cores 17957, 758 and 1143 indicate strong depleted anomalies relative to the KPW and other samples of OTT. In the case of Na_2O, KPW and most OTT samples display enrichments, however, a sample of OTT from core AAS/GC-02 demonstrates an opposite pattern, showing a minor depletion of Na_2O (Figure 5.29A).

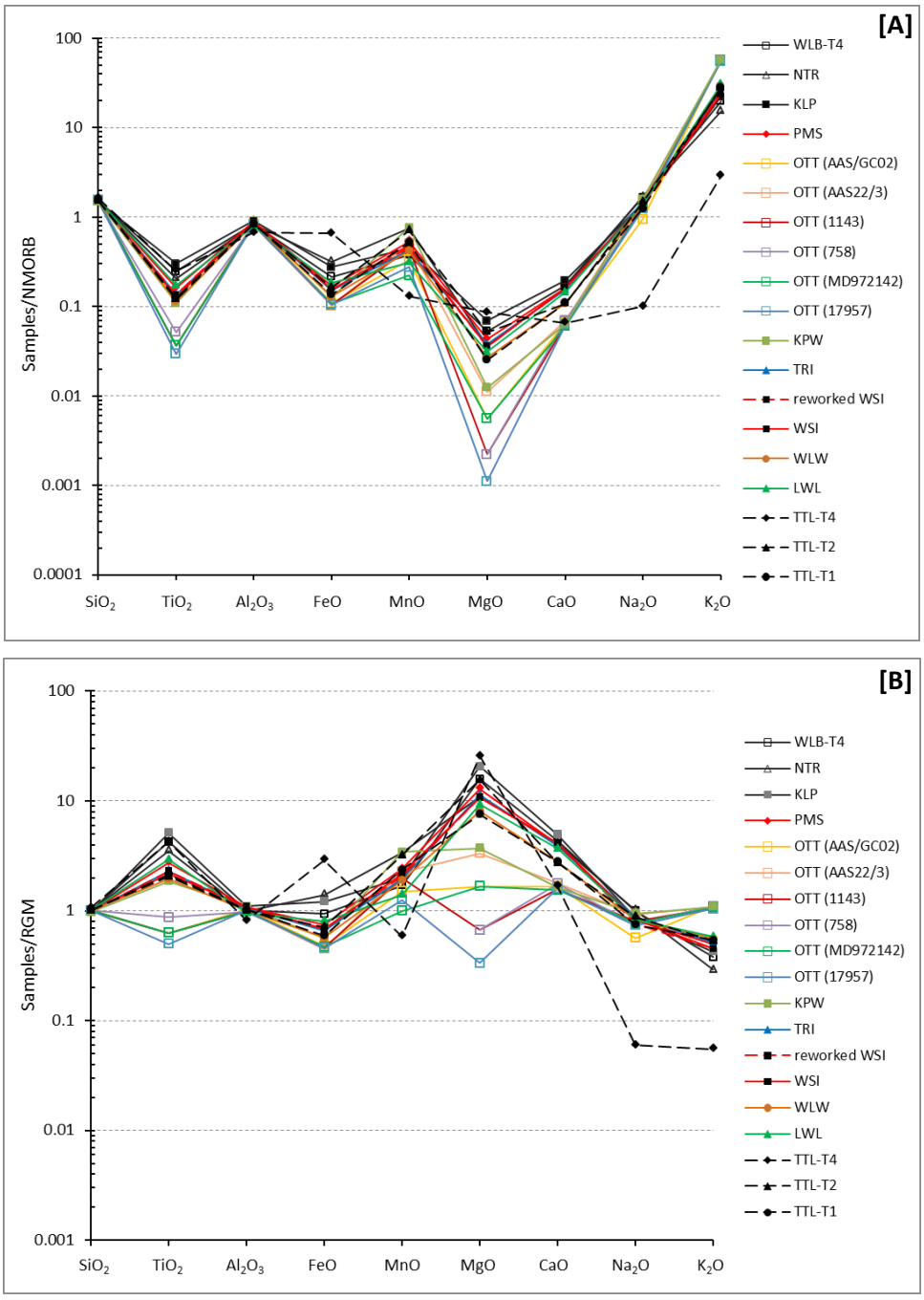

Figure 5.29. The variation of major-element composition of glass shards from the studied tephra layers; A) normalised to the NMORB composition (Sun and McDonough, 1989), and B) normalised to the RGM composition (Nobel *et al.*, 1972; and USGS (1995) for the ΣFeO content). The major-element oxides are presented as mean values and have been recalculated to 100 %. Legend indicates pyroclastic deposits in stratigraphic order. The OTT samples are also plotted for comparison.

In the RGM-normalised diagram, the majority of the analysed tephras demonstrate nearly identical trends with the exception of TTL-T4 that displays a very distinct pattern (Figure 5.29B). Most samples are enriched in TiO_2, MnO, MgO and CaO contents, and depleted in ΣFeO, Na_2O and K_2O. The SiO_2 and Al_2O_3 values of the tephras are similar to the RGM composition. The TTL-T4 with its unique characteristic compared to the other tephras, has the strongest enrichment of ΣFeO and the strongest depletion of Na_2O and K_2O. It should be noted from this normalised-diagram that the KPW and some published OTT concentrations are dissimilar with respect to the TiO_2, Al_2O_3 and MgO contents, where the KPW is enriched in these elements while three of six OTT samples are depleted relative to RGM. Despite having marked differences in TiO_2 and MgO between KPW and some of OTT compositions, they are chemically very similar.

The ternary diagram of K_2O-CaO-ΣFeO (K-Ca-Fe) is applied to further distinguish and correlate tephra layers of the Tuff Member and three tephras that are stratigraphically unknown. This ternary diagram suggests that the analysed tephra layers can be discriminated into six distinct populations (Figure 5.30). The clustering differs slightly from the biplot diagrams (compared to Figures 5.27 and 5.28). However, the K-Ca-Fe diagram is able to distinguish tephras of Group 5 (KLP, NTR and WLB-T4; see Figure 5.28), KLP and WLB-T4 show the closest similarities and NTR plots as an independent point. The tephra groupings are mostly similar within the ΣFeO *versus* CaO and CaO *versus* K_2O diagrams (Figure 5.28). Again TTL-T4 and KPW are consistently separated from the majority of populations as two unique clusters (Groups 2 and 4, respectively). The chemical values of the OTT are also plotted (Figure 5.30), indicating KPW and OTT are compositionally very homogeneous ensuring that KPW is very likely correlated to OTT. In addition, TTl-T1, TTl-T2 and WLW show strong chemical similarities (Group 2) and also WSI, reworked WSI, TRI and PMS show identical composition (Group 3). The KLP and WLB-T4 are chemically indistinguishable (Group 5) and NTR does not match any of the other groupings (Group 6).

The glass compositions of the analysed tephras reveal the similar compositional heterogeneity compared to the whole-rock analysis, showing two discrete tephra layers that have unique chemical signatures. In case of KPW, it is very likely that this tephra represents as the OTT.

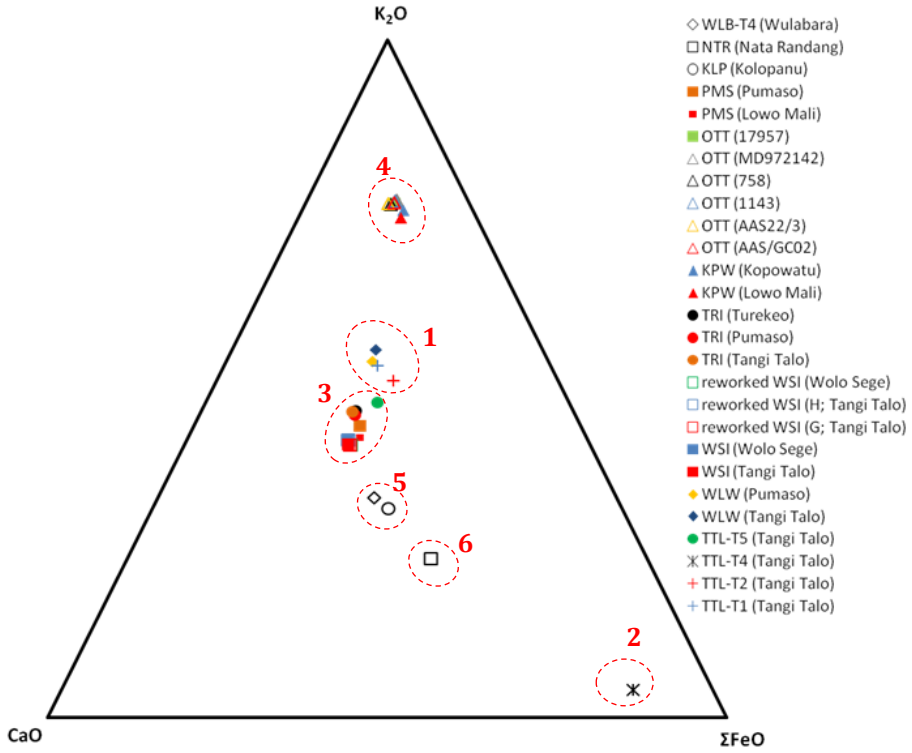

Figure 5.30. The variation of K_2O-CaO-ΣFeO contents of glass shards from tephra layers of the Tuff Member (Ola Bula Formation) and stratigraphically unknown tephra beds of the KLP, NTR and WLB-T4. Legend indicates pyroclastic deposits in stratigraphic order, and parentheses refer to the sample location. The OTT samples are also plotted for comparison.

5.4. Whole-rock samples versus glass shards

The summary of average major-element composition obtained from whole-rock analysis (XRF) and individual glass shards (EMPA) is listed in Table 5.12. The TiO_2, Al_2O_3, MgO and CaO contents of whole-rock samples are higher than in glass shards. In whole-rock samples, these major elements are enriched 1-4 times compared to glass shards. The total Fe content in whole-rock samples is even up to 6 times greater than in glass shards. In contrast, the values of SiO_2, Na_2O and K_2O are commonly higher in glass shards.

The compositional variability of whole-rock samples from the Soa Basin is controlled by the abundance of mineral assemblages. The major-element composition can be affected by phenocryst contents and/or micro-phenocryst phases (Rollinson, 1993; Shane, 2000). In the Soa Basin samples, TTL-T5 is a good example because this tephra represents a crystal-rich tephra-fall deposit. Compared to its glass composition, the whole-rock composition of TTL-T5 indicates lower values of SiO_2 and K_2O; and higher TiO_2, Al_2O_3, MnO, MgO, CaO and total iron contents. Lower proportions of glass shards during sample preparation and analysis clearly result in lower amount of SiO_2, and by contrast, free crystals of minerals increase the abundance several major elements.

It has been noted that the mineral contents in whole-rock samples can cause considerable variation in the concentration of major-elements of the same tephra deposit sampled from different localities (Pearce *et al.*, 2004). This can be seen when comparing the bulk samples of the WSI from different localities and/or levels within the tephra layer itself. The samples of the WSI taken from various localities demonstrate that some major-element values display significant variation, for instance 2.74 wt% for SiO_2, 1.54 wt% for Al_2O_3 and 1.20 wt% for MgO. These differences are associated with the variable distribution of minerals.

Table. 5.12. Comparison of the major-element composition of selected tephra layers obtained from two different methods.

Major-element composition of whole-rock samples (XRF)

Tephra	SiO_2	TiO_2	Al_2O_3	ΣFe_2O_3	MnO	MgO	CaO	Na_2O	K_2O	P_2O_5
TTL-T1	74.01	0.29	14.68	3.03	0.06	2.73	2.77	0.99	1.40	0.04
TTL-T2	72.05	0.30	15.77	3.75	0.11	3.25	2.49	0.84	1.39	0.04
TTL-T4	95.27	0.06	2.47	0.92	0.01	0.58	0.42	0.22	0.04	0.01
LWL	59.98	0.77	17.45	8.06	0.17	2.43	6.82	3.36	0.82	0.15
WLW	71.80	0.54	17.24	4.02	0.06	1.71	2.13	1.07	1.38	0.04
WSI	71.54	0.38	17.08	3.45	0.11	1.38	2.68	1.45	1.86	0.06
reworked WSI	72.12	0.39	17.50	3.47	0.10	1.30	2.69	1.01	1.90	0.10
TRI	73.89	0.26	15.75	2.10	0.11	0.85	2.33	2.09	2.59	0.04
KPW	72.80	0.24	16.36	2.02	0.13	0.90	1.60	1.83	4.09	0.04
PMS	69.95	0.55	15.13	4.09	0.13	1.34	3.89	2.69	2.09	0.14
NTR	72.34	0.51	15.51	3.07	0.11	0.62	3.22	2.84	1.68	0.10
WLB-T4	65.73	0.83	16.05	6.17	0.19	1.29	4.73	3.41	1.45	0.15

Major-element composition of glass shards (EPMA)

Tephra	SiO_2	TiO_2	Al_2O_3	ΣFeO	MnO	MgO	CaO	Na_2O	K_2O
TTL-T1	78.56	0.17	12.95	1.11	0.09	0.23	1.25	2.89	2.55
TTL-T2	77.97	0.16	12.64	1.32	0.13	0.46	1.23	3.40	2.52
TTL-T4	82.05	0.34	10.20	5.36	0.02	0.77	0.75	0.23	0.26
LWL	78.18	0.23	12.11	1.50	0.06	0.28	1.66	3.24	2.75
WLW	78.54	0.16	12.75	1.06	0.08	0.24	1.24	3.19	2.65
WSI	77.06	0.17	13.66	1.26	0.09	0.32	1.86	3.23	2.14
reworked WSI	77.29	0.18	13.72	1.27	0.08	0.32	1.86	2.94	2.14
TRI	77.19	0.18	13.40	1.23	0.08	0.34	1.76	3.37	2.45
KPW	75.32	0.15	13.68	1.04	0.14	0.11	0.74	3.67	5.15
PMS	76.89	0.22	13.65	1.39	0.10	0.39	1.83	3.19	2.35
NTR	76.97	0.28	12.61	2.60	0.13	0.33	1.85	3.92	1.37
WLB-T4	77.06	0.34	12.82	1.75	0.07	0.47	1.96	3.84	1.79

Note: Major-element values are presented as mean values, and have been recalculated to 100 %.

In the case of a distal vitric ash, glass shards and small-and light pumice clasts are the dominant constituents and crystals of minerals are much less abundant. However, whole-rock chemical analysis still provides chemical ambiguity due to the presence of impurities, such as xenocrysts, xenoliths and inclusions on glass shards or very fine-grained crystals (Shane, 2000). The TTL-T1 and TTL-T2 are two discrete distal ashes, and both macroscopically comprise predominantly glass shards and small pumice fragments. The major-element values, however, are significantly different with TiO_2, Al_2O_3, MnO, MgO, CaO and total iron contents of whole-rock samples displaying enrichments compared to glass shards contents. These disparities are caused by the presence of tiny crystals of feldspars and ferromagnesian minerals in the whole-rock samples that not visible in the field.

Another distal ash is KPW, comprising fine-grained ash (clay to very fine sand). Similarly with TTL-T1 and TTL-T2, the major-element values of the whole-rock samples from KPW are commonly higher than in glass shards. Besides micro-inclusions in glass shards, the occurrence of fine-grained minerals should also be considered. During sieving and hand-picking prior to electron microprobe measurement, micro-phenocrysts (mostly biotite) could be recognised in the KPW samples (Brent V. Alloway, pers. comm).

The chemical analysis of whole-rock samples from pyroclastic surge or pyroclastic flow deposits emplaced in the proximal to distal zones, can also be affected by lithic fragments, present in variable proportions and grain sizes. A good example for this case can be seen in the major-element composition of NTR. The NTR is showing typical characteristics of a pyroclastic surge deposit and field observation revealed the presence of thin laminations of lithic fragments (see section 5.2.2K). The abundance of lithic fragments can reduce significantly the silica content.

This study uses the grain-discrete method to determine the major-element composition of glass shards from individual analysed tephras. This technique is able to characterise separate populations of glass shards within the

same sample, which cannot be identified by whole-rock chemical analysis (Hunt and Hill, 1993; Shane, 2000). A potential problem can emerge regarding the grain morphology of glass shards. A tephra deposit may contain very small or pumiceous shards with a thin-bubble wall texture. In this context, a defocussed beam (usually 10-20 μm in diameter) of the electron microprobe does not fit to the even surface of glass shards and the measurement can provide unreliable or irrepresentative geochemical data (Hunt and Hill, 1993; Shane, 2000).

In general, geochemical analysis on individual glass shards using an electron microprobe provides much better and reliable elemental compositions compared to XRF analysis on whole-rock samples. Despite its disadvantages, the XRF technique can be the first step for filtering and discriminating numbers of tephra beds, because the method is faster and requires less preparation. As shown in the few examples above, the whole-rock composition commonly displays lower SiO_2 content compared to glass shards and, accordingly, the SiO_2 content should not be used as a parameter to characterise the analysed tephras, particularly in the volcanic-rock classification (the TAS diagram). Alternatively, plotting such major-elements of whole-rock samples in the binary diagrams of ΣFe_2O_3 or K_2O versus CaO and the ternary diagram of K_2O–CaO–ΣFe_2O_3 is effective to distinguish and correlate the tephra layers. Some tephras contain multimodal glass compositions, which could not be distinguished using XRF (whole-rock). However, it will be detected when analysing individual glass shards. In case of WSI, two types of pumices are present, caused by mixing of two magmas, but for the glass composition only the white pumices were selected for analysis. A combination of whole-rock and glass compositions is a powerful tool for discriminating and fingerprinting tephra deposits in the study area.

5.5. Statistical Analysis

The application of multivariate statistical analysis has been broadly used for facilitating discrimination and correlation of tephra layers derived from different source volcanoes (e.g. Preece *et al*., 2000; Jordan *et al*., 2006; Hillenbrand *et al*., 2008; Brendryen *et al*., 2010). The binary and ternary diagrams of major-element values, as well as the biplot diagrams of trace-element values presented in the previous sections have distinguished the studied tephras into 3 to 6 populations. A few tephra samples appear to form outliers that cannot be grouped with the other clusters.

In order to assess the validity of tephra clusters distinguished by the multi-element diagrams, a combination between hierarchical cluster analysis and factor analysis was employed to discriminate compositionally heterogeneous tephra units of the Tuff Member (the Ola Bula Formation) and of tephra beds of unknown stratigraphic position, and published major-element compositon of the OTT glass shards were also included in the analysis. The statistical analyses were performed using the major-element data as variables. As noted in the previous section (5.4), major-element contents of glass shards are more reliable as than the whole-rock compositions. Concerning the compositional nature of geochemical data, statistical analyses are conducted within a centred log-ratio framework to overcome misinterpretation arising from the effect of non-independent variables and other effects imposed by the normalisation of the major-element values (Aitchison, 1986; Aitchison and Egozcue, 2005). The centred log-ratio is defined as:

$$\mathbf{z} = \mathrm{clr}(\mathbf{x}) = \left[\ln\left(\frac{x_1}{g(\mathbf{x})}\right), \ln\left(\frac{x_2}{g(\mathbf{x})}\right), \ldots, \ln\left(\frac{x_D}{g(\mathbf{x})}\right)\right]. \qquad (5.1)$$

where $g(\mathbf{x}) = [\mathbf{x}_1 * \mathbf{x}_2 * \ldots * \mathbf{x}_D]^{1/D}$ is the geometric mean of the composition **x** (Aitchison, 1986). The centred log-ratio transformation has the advantage that all of the variables are preserved although the data array shows high complexity (Buccianti *et al*., 2006).

Hierarchical cluster analysis is intended to gain information on the geochemical characteristics of each tephra unit. Ward's method is used and the squared Euclidean distance is applied for the criterion of dissimilarity. Templ *et al*., (2008) provide a good example of the application of this method in cluster analysis when large geochemical datasets are considered as variables. In addition, factor analysis is aimed to reproduce a correlation matrix with a small number of orthogonal factors (Aitchison, 1986; Reimann *et al*., 2002). Factors reflect underlying processes that create the correlation between variables. In this study, the principal component method was used for factor extraction and the Varimax method with Kaiser Normalisation for factor rotation was applied. The Varimax method is usually employed in factor analysis dealing with geochemical data (Reimann *et al*., 2002). Both hierarchical cluster and factor analyses were performed using the SPSS 17 package.

The dendrogram resulting from the cluster analysis is illustrated in Figure 5.31. The tephra samples can be classified into two major groups, indicating compositional similarities. One group (Group A) includes the majority of tephras, but this group can be split into three sub-groups: 1) WSI, rWSI, TRI and PMS (Group A1); 2) a large sub-group of TTL-T1, TTL-T2, TTL-T5, WLW, KLP, NTR and WLB-T4 (Group A2); and 3) TTL-T4 (Group A3). The TTL-T4 is compositionally quite distinct from other all tephras. The other major group (Group B) only includes KPW from the Soa Basin, which clusters together with the various OTT samples from deep-sea cores in the South China Sea and Indian Ocean.

The summary of statistical description of factor analysis is shown in Table 5.13. This study uses the term "factors" instead of "components" that is usually used in principal component analysis (PCA). The first two factors (F1 and F2) account for 96.55 % and 2.65 % of the overall data variation and the rotated factors denote 53.94 % and 37.83 % of the variation of the data. Eigenvalues provide indications of the significance of derived principal components (Buccianti *et al*., 2006). This means that the undertaken factor analysis is robust.

The result of Varimax rotation applied to principal component extraction is listed in Table 5.14. The first factor (F1) displays positive scores in all tephra samples and is highly loaded on KPW and OTT. The scores of KPW and OTT are nearly similar and these tephras have the highest scores compared to the other tephras. The variation of the first factor also suggests that the scores of WSI, rWSI, TRI and PMS are within close ranges. Moreover, the second factor (F2) exhibits positive scores in most tephras. TTL-T4 has the highest positive score relative to the other samples. The third factor (F3) is positively loaded in all samples, and the highest scores can be observed in TRI and WLB-T4. A few tephra samples are negatively loading in the fourth factor (F4). The F4 is a residue of the other major factor extraction and only accounts for 0.16 % of the total data variation and this factor is considered negligible for the analysis. In all factors, TTL-T4 shows uniqueness with its factor loadings highly distinct from all other tephra samples.

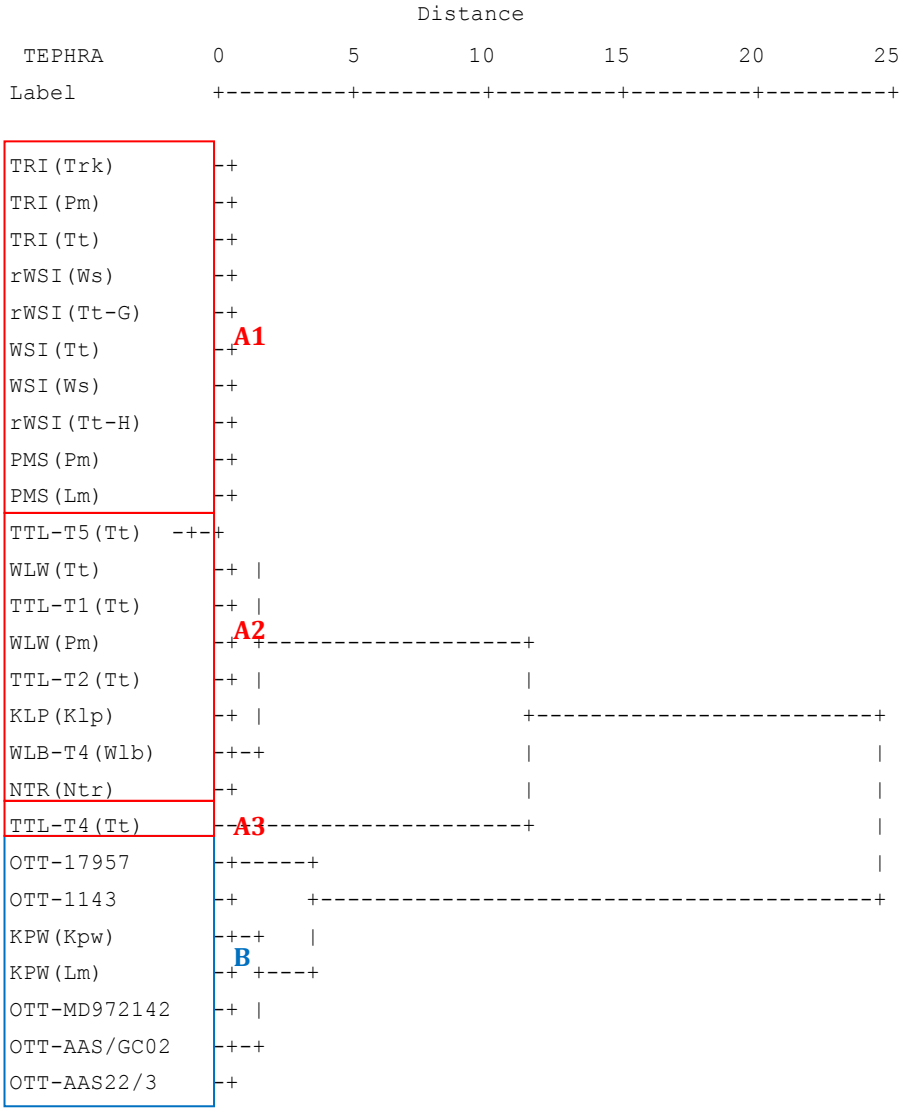

Figure 5.31. Dendrogram displaying the presence of tephra groups determined by cluster analysis (Ward's method) using log–ratio transformed variables of major-element values. Parentheses refer to the sample location. Abbreviation: Kpw = Kopowatu; KLP= Kolopanu; Lm = Lowo Mali; Ntr= Nata Randang; Pm = Pumaso; Trk = Turekeo; Tt = Tangi Talo; WLb= Wulabara; Ws = Wolo Sege, and "r" means reworked (rWSI= reworked WSI).

Table 5.13. The description of factor analysis using the major-element data of the studied tephras.

Factor	Initial Eigenvalues			Extraction Sums of Squared			Rotation Sums of Squared		
	Total	% of Variance	Cumulative %	Total	% of Variance	Cumulative %	Total	% of Variance	Cumulative %
1	25.10	96.55	96.55	25.10	96.55	96.55	14.02	53.94	53.94
2	.69	2.65	99.19	.69	2.65	99.19	9.84	37.83	91.77
3	.12	.46	99.65	.12	.46	99.65	2.05	7.88	99.65
4	.04	.16	99.81	.04	.16	99.81	.04	.16	99.81
5	.02	.09	99.90						
6	.02	.07	99.97						
7	.01	.03	100						

Factor analysis produces a correlation matrix that displays relationships among samples and the correlation coefficients of the sample (Table 5.15). Some tephra samples display highly significant positive correlation with each other (bold font in Table 5.15). TTL-T1 is significantly correlated to WLW; WSI, rWSI, TRI and PMS have significant relations to each other, and KLP exhibits a strong correlation with the WLB-T4. TTL-T2 can be correlated to WLW, rWSI and PMS; while TTL-T5 has a stronger relation with TRI and PMS. TTL-T4, KPW and NTR do not have a strong correlation with any of other tephra units. In the case of KPW, however, this tephra is clearly correlated with the OTT samples, albeit with slightly lower significance. It should be noted, however, that tephra layers ascribed to the OTT, only two are significantly correlated with each other. The TTL-T4 and NTR do no show any strong correlation with the other tephra deposits because their correlation values are mostly below the significance boundary of compositional similarity (0.995).

Table. 5.14. Factor loadings (F) of tephra samples from the Tuff Member, stratigraphically unknown tephra layers (KLP, NTR and WLB-T4) and the oldest Toba Tuff (OTT), using log-transformed variables of major-element values.

Tephra	F1	F2	F3	F4
WLB-T4	.626	.703	.330	.056
NTR	.671	.686	.247	.088
KLP	.605	.733	.305	.043
PMS (Pm)	.691	.654	.308	-.003
PMS (Lm)	.694	.644	.323	.003
KPW (Kpw)	.854	.472	.206	-.037
KPW (Lm)	.854	.473	.209	-.030
OTT-1143	.898	.404	.162	.054
OTT-17957	.898	.401	.147	.099
OTT-MD972142	.844	.481	.230	.003
0TT-AAS22/3	.846	.457	.262	-.060
OTT-AAS/GC02	.856	.475	.197	-.016
TRI (Trk)	.703	.632	.326	.005
TRI (Pm)	.698	.635	.329	-.000005
TRI (Tt)	.700	.629	.336	.005
WSI (Ws)	.692	.645	.324	.019
WSI (Tt)	.696	.644	.316	.007
rWSI (Ws)	.693	.648	.316	.016
rWSI (G-Tt)	.697	.643	.315	.011
rWSI (H-Tt)	.704	.627	.331	.013
WLW (Pm)	.735	.596	.322	-.002
WLW (Tt)	.739	.609	.285	-.026
TTL-T5	.699	.646	.298	.040
TTL-T4	.298	.954	.023	-.029
TTL-T2	.712	.622	.313	-.080
TTL-T1	.747	.602	.280	-.011

Table 5.15. Correlation matrix of tephra samples from the Tuff Member (Ola Bula Formation), stratigraphically unknown tephras (KLP, NTR and WLB-T4) and the oldest Toba Tuff (OTT).

Tephra	KLP	NTR	WLB-T4	PMS (Pm)	PMS (Lm)	KPW (Kpw)	KPW (Lm)	TRI (Trk)	TRI (Pm)	TRI (Tt)	WSI (Ws)	WSI (Tt)	rWSI (Ws)	rWSI (G-Tt)	rWSI (H-Tt)	WLW (Pm)	WLW (Tt)	LWL	TTL-T4	TTL-T2	TTL-T1	OTT-17957	OTT-MD972142	OTT-1143	0TT-AAS22/3	OTT-AAS/GC02
KLP	1																									
NTR	.984	1																								
WLB-T4	**.999**	.987	1																							
PMS (Pm)	.991	.986	.992	1																						
PMS (Lm)	.989	.988	.993	**.999**	1																					
KPW (Kpw)	.925	.945	.934	.961	.962	1																				
KPW (Lm)	.926	.947	.936	.963	.964	**1.00**	1																			
TRI (Trk)	.988	.985	.992	**.999**	**.999**	.965	.966	1																		
TRI (Pm)	.988	.984	.992	**.999**	**1.00**	.963	.965	**1.00**	1																	
TRI (Tt)	.988	.984	.992	**.999**	**.999**	.964	.965	**1.00**	**1.00**	1																
WSI (Ws)	.990	.988	.993	**.999**	**1.00**	.960	.962	**1.00**	**1.00**	**.999**	1															
WSI (Tt)	.988	.987	.991	**1.00**	**1.00**	.962	.963	**.999**	**.999**	**.999**	**1.00**	1														
rWSI (Ws)	.990	.988	.992	**1.00**	**1.00**	.960	.962	**.999**	**.999**	**.999**	**1.00**	**1.00**	1													
rWSI (G-Tt)	.988	.987	.991	**1.00**	**.999**	.962	.963	**.999**	**.999**	**.999**	**1.00**	**1.00**	**1.00**	1												
rWSI (H-Tt)	.985	.988	.990	.998	**.999**	.964	.965	**.999**	**.999**	**.999**	**.999**	**.999**	**.999**	**.999**	1											
WLW (Pm)	.980	.982	.986	.996	.997	.977	.978	.998	.998	.998	.996	.996	.996	.996	**.997**	1										
WLW (Tt)	.980	.980	.983	.997	.997	.979	.980	.998	.997	.997	.996	.997	.996	.997	.996	**.998**	1									
TTL-T5	.991	.983	.994	.997	.995	.962	.963	.997	.996	.996	.996	.995	.996	.995	.993	.995	.994	1								
TTL-T4	.885	.856	.862	.837	.828	.710	.710	.820	.822	.817	.828	.829	.831	.828	.815	.795	.809	.830	1							
TTL-T2	.977	.979	.980	.993	.995	.969	.969	.994	.994	.994	.993	.994	.993	.993	.995	.995	.995	.986	.814	1						
TTL-T1	.977	.983	.982	.996	.996	.981	.982	.997	.996	.996	.995	.996	.996	.996	.996	**.998**	**.999**	.993	.803	.994	1					
OTT-17957	.886	.922	.897	.928	.929	.982	.983	.934	.931	.932	.930	.931	.931	.932	.934	.946	.948	.934	.651	.926	.953	1				
OTT-MD972142	.935	.950	.943	.968	.968	.994	.995	.973	.971	.972	.968	.969	.968	.969	.971	.981	.982	.972	.716	.970	.983	.985	1			
OTT-1143	.890	.926	.902	.934	.936	.989	.990	.940	.937	.938	.936	.937	.936	.938	.941	.953	.955	.938	.655	.937	.959	**.999**	.989	1		
0TT-AAS22/3	.923	.943	.933	.964	.966	.992	.993	.969	.968	.968	.964	.966	.964	.966	.969	.978	.979	.961	.696	.975	.980	.976	.995	.984	1	
OTT-AAS/GC02	.926	.944	.932	.963	.963	.994	.995	.967	.965	.965	.963	.964	.963	.965	.965	.975	.979	.964	.714	.966	.980	.988	**.998**	.992	.995	1

Note: The bold numbers indicate significant correlation between the sample pairs.

For correlation purposes, the first, second and third factor loadings are plotted in the biplot diagrams. The first factor (F1) is very important for correlation because this factor represents ~96 % of total data variation. The first factor is plotted against the second and third factors (Figure 5.32). The two binary diagrams indicate that all samples are plotted in the same quadrant and both diagrams provide similar sample populations. The analysed samples can be clustered into six groups: 1) TTL-T1 and WLW (Group 1); 2) TTL-T2, TTL-T5, WSI, TRI and PMS (Group 2); 3) TTL-T4 (Group 3), 4) KPW (Group 4), 5) KLP and WLB-T4 (Group 5) and 6) NTR (Group 6). In the case of TTL-T4 and KPW display distinct clusters, both tephras are widely separated from all other populations and appear as two independent groups. Both diagrams suggest that KPW is closely associated with OTT (Group 4). The NTR (Group 6) does not match any tephra samples and likely has no corelatives amongst the studied samples.

The application of hierarchical cluster and factor analyses using the major-element compositions of glass shards as variables for discriminating tephra units is tested in this study. The hierarchical cluster analysis distinguishes the studied tephras as four clusters (see Figure 5.31), while factor analysis using principal component extraction and Varimax rotation produces a better result in terms of compositional fingerprinting, significantly identifying six tephra populations. Tephras with identical composition but stratigraphically superposed are certainly derived from the same volcano. The statistical analyses suggest that nine tephra layers of the Tuff Member and three stratigraphically unknown tephra deposits were originated from at least six different volcanoes, and confirm the groupings based on the TAS and the Harker diagram in the previous sections.

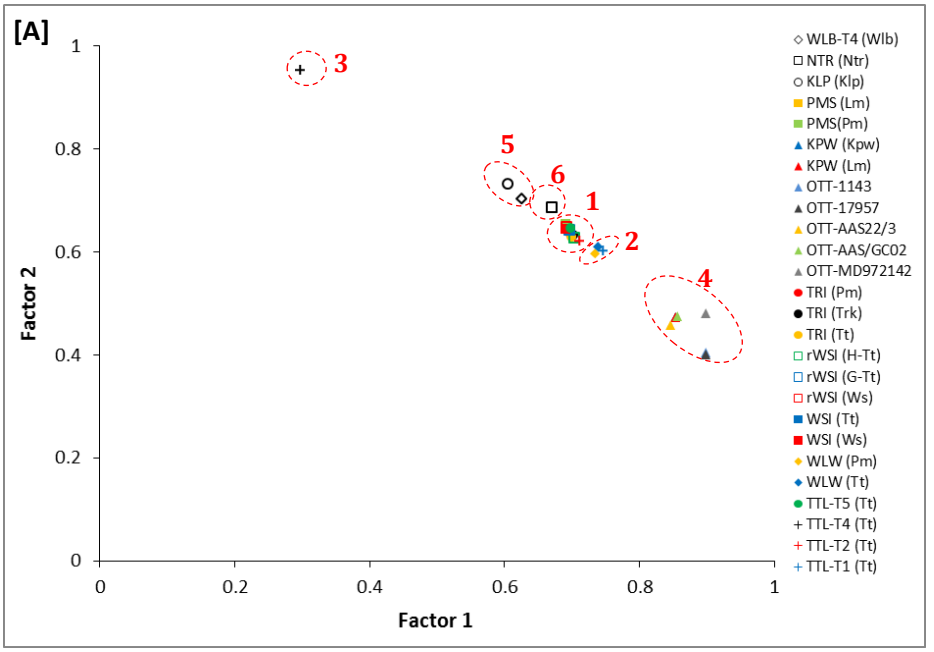

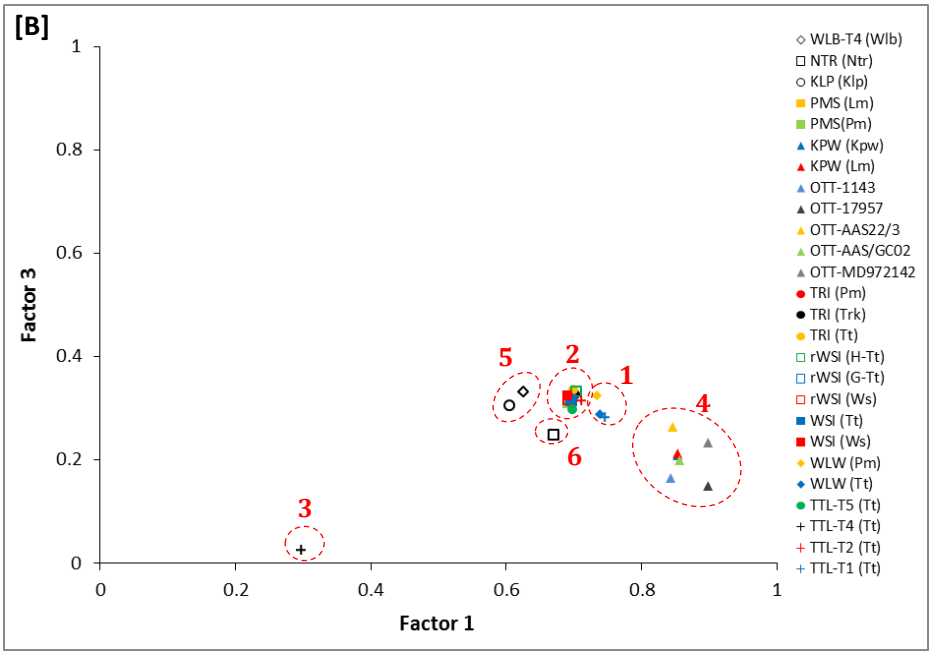

Figure 5.32. A) The F1 vs. F2 and B) F1 vs. F3 biplot diagrams of tephra deposits from the Tuff Member and stratigraphically unknown tephra beds (the KLP, NTR and WLB-T4). Samples of the oldest Toba Tuff (OTT) collected from several marine cores are also plotted for reference. Lettercodes between parentheses refer to the sample location. Abbreviation: Kpw = Kopowatu; KLP= Kolopanu; Lm = Lowo Mali; Ntr= Nata Randang; Pm = Pumaso; Trk = Turekeo; Tt = Tangi Talo; WLb= Wulabara; Ws = Wolo Sege, and "r" means reworked (rWSI= reworked WSI).

5.6. New tephrostratigraphy and potential source volcanoes

At least 73 prominant tephra layers have been identified in the various sections of the Soa Basin, and most tephras are identifiable on the basis of their field characteristics and geochemical composition combined with their stratigraphic positions. For most tephras, the whole-rock compositions have been determined and the glass compositions of a few tephra layers have also been analysed. The tephra deposits in the study area can be classified into pyroclastic tephra-fall, pyroclastic surge and pyroclastic density current (PDC) deposits. A total of 65 macroscopically visible distal tephra-fall deposits were recognised in the basin, which vary in composition from mafic to felsic. Two PDC deposits (AEI and LMI) that were formed in relation to caldera forming events of adjacent volcanic centres are widely distributed. In addition, two PDC deposits (WSI and TRI) have widespread distributions across the basin, displaying rhyolitic compositions and relating to voluminous explosive eruptions from local volcanic vents. The occurrence of a thick-rhyolitic surge deposit (NTR) also provides evidence of another large explosive event derived from a local volcanic edifice.

Based on the field data and chemical fingerprinting of tephras employed in this study, a tephrostratigraphy for the Soa Basin is proposed as shown in Figure 5.33. This composite tephrostratigraphy is not completely developed in any one section, but composed from several key stratigraphic sections, such as Lowo Lele, Lowo Mali, Mata Menge, Pumaso, Tangi Talo and Wolo Sege.

The ~26-m-thick welded PDC deposit of the Aesessa Ignimbrite (AEI) and the ~30-m-thick non-welded PDC deposit of the Lowo Mali Ignimbrite (LMI) occupy the lowermost part of sequence. They are both included in the Ola Kile Formation, and the LMI has an unconformable upper boundary. Despite these two PDC deposits displaying similar chemical compositions (rhyolite) and representing the products of caldera formation, their geochemical composition suggest that they originated from different volcanoes. The AEI is exposed in the middle and western part of the basin along the Lowo Lele and Aesessa Rivers,

and this welded PDC deposit is presumably derived from the Welas Caldera Complex (WCC), which was formed *ca*. 2.5 Ma ago according to Muraoka *et al*. (2002). The non-welded LMI is mostly exposed in the eastern part of the basin close to the Keli Lambo Volcanic Complex (KLVC) and possibly represents one of a series of large eruptions from the KLVC, which produced LMI. The Ola Kile Formation is unconformably overlain by the Tuff Member of the Ola Bula Formation. In most localities, the Ola Kile Formation and the Tuff Member of the Ola Bula Formation are separated by thick-prominent palaeosols, signifying prolonged periods of landscape stability and absense of depositional processes.

The Tuff Member of the Ola Bula Formation consists of nine rhyolitic tephra deposits, which can be classified into pyroclastic tephra-fall (six layers) and PDC deposits (three layers). The lower part of the Tuff Member comprises four distal tephra-fall units, the Tangi Talo Tephra (TTl-T1, TTL-T2, TTL-T4 and TTL-T5) that all indicate a rhyolitic composition. These tephra units are exposed at the Tangi Talo depocentre with deepest sections. Lower tephras may have been eroded subsequently in the more marginal areas of the Soa Basin.

There is only one tephra layer in the middle part of the Tuff Member corresponding to a rhyolitic tephra-fall deposit, the Wolo Wawo Tephra (WLW). An ~8-m-thick sequence of sediments, mostly palaeosol deposits separate WLW from the upper tephra units. The upper part of the Tuff Member contains two PDC deposits, including the Wolo Sege Ignimbrite (WSI) and Turekeo Ignimbrite (TRI), and two tephra-fall units consist of Pumaso Tephra (PMS) and Kopowatu Tephra (KPW). The glass composition of the upper tephra sequence displays a rhyolitic composition.

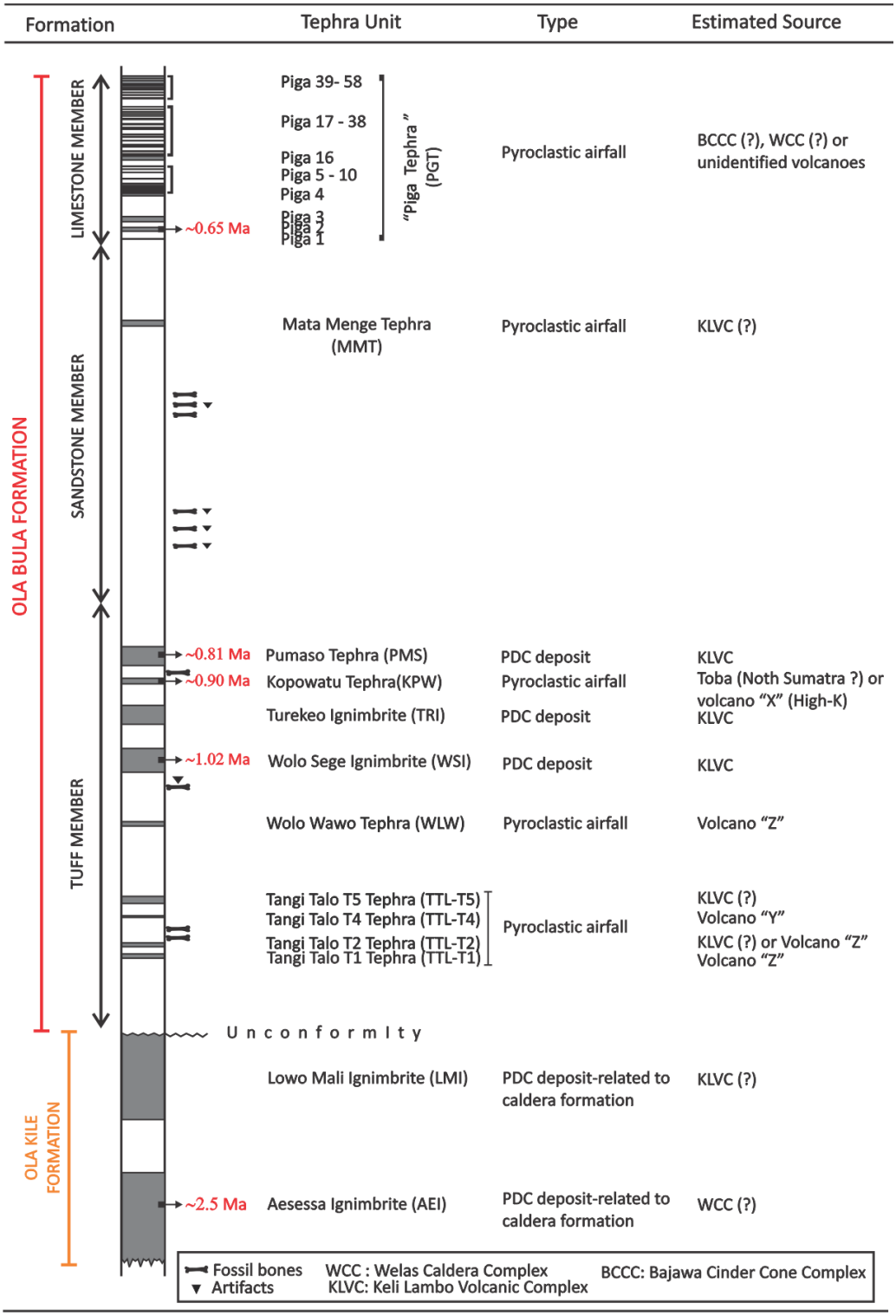

Figure 5.33. Reconstruction of the new tephrochronological framework of the Soa Basin. The KLP, NTR and WLB-T4 are not included due to unclear stratigraphic positions. Relative positions of artifacts and fossil bones are also plotted. The age of the oldest Toba Tuff (OTT) is presented as the mean age obtained from Diehl *et al.*, 1987; Hall and Farrel, 1995; and Lee *et al.*, 2004; the age of WSI is from Brumm *et al.*, 2010, 2016; the ages of KPW, PMS and Piga 2 are from Brumm *et al.*, 2016 (note that KPW is referred to as 'T3' in Brumm *et al.*, 2016); and the K-Ar age of AEI is suggested by Muraoka *et al.*, 2002.

The ages of some pyroclastic units of the Tuff Member have been determined using the $^{40}Ar/^{39}Ar$ dating technique. The TTL-T5 has an age of 1.27±0.03 Ma (Stephanie Flude, unpubl. data, pers. comm), while WSI is dated at 1.01±0.02 Ma ago (Brumm *et al*., 2010; 2016). In addition, the $^{40}Ar/^{39}Ar$ analysis on feldspars from the fossil-bearing layer at Tangi Talo (~80-cm below TTL-T4) yielded an age of 1.43±0.018 Ma (Stephanie Flude, unpubl. data, pers. comm). This age can be used to estimate the maximum age of TTL-T4, which could not be dated due to the lack of sufficiently large crystals. Based on its stratigraphic position between TTL-T5 and the dated laharic deposit below, TTL-T4 must have been deposited between 1.35 and 1.40 Ma ago.

A distal pyroclastic tephra-fall unit of the Mata Menge Tephra (MMT) is preserved in the middle succession of the Sandstone Member. This tephra displays unique field and geochemical characteristics with an andesitic composition. The MMT is exposed in the western and eastern part of the Soa Basin (Mata Menge and Gero, respectively) with a trend of decreasing grain size to the west. The distinct MMT is conformably separated by a ~22-m thick of sediments from the uppermost tephra unit of the Tuff Member (PMS), which has been dated at 0.81±0.04 Ma (Brumm *et al.*, 2016). The Limestone Member that conformably covers sediments of the Sandstone Member comprises 58 closely spaced tephra beds of dominantly basaltic composition, named as PGT. The PGT from the lowermost part sequence of the Limestone Member has been dated at 0.65±0.02 Ma ago (Brumm *et al.*, 2016).

Although most tephra deposits in the study area can be sequentially reconstructed, there are few tephras whose positions are still uncertain. These tephra layers are exposed inside the Welas Caldera Complex (WCCC) located in the northwestern part of the Soa Basin. They are Kolopanu Tephra (KLP), Nata Randang Tephra (NTR) and Wulabara Tephra (WLB). The KLP displays the typical characteristic of a pyroclastic flow deposit and the glass composition of this tephra suggests a rhyolitic composition. In addition, this tephra contains white and grey pumice fragments that indicate the mixing of two

magmas. The NTR is a pyroclastic surge deposit showing a rhyolitic composition, while WLB comprises a series of pyroclastic tephra-fall deposits with three units in the lowermost part (WLB-T1, WLB-T2 and WLB-T3) displaying basaltic composition, and one tephra in the uppermost part (WLB-T4) with a rhyolitic composition. The KLP, NTR and WLB probably originated from the WCCC. However, their chemical compositions do not match or group with any of the other tephras, and they may be much younger than the Soa Basin tephras.

Tephra layers with compositional similarity were probably derived from the same source. As potential tephra sources, three volcanic provinces should be considered, namely the Bajawa Cinder Cone Complex (BCCC), the Keli Lambo Volcanic Complex (KLVC) and the Welas Caldera Complex (WCC), given their geographic proximity to the Soa Basin. Some distal tephras with highly distinctive compositions, such as KPW and TTL-T4 likely have an extrabasinal source.

With respect to the tephra sequence of the Tuff Member, the majority of tephra layers show similar composition (rhyolite), however, they are still distinguishable on the basis of their field characteristics, stratigraphic positions and major-element values of volcanic glasses, in particular CaO, ΣFeO and K_2O contents that can discriminate them into several tephra populations (see Figures 5.28 and 5.30). The geochemical data indicate that discrete tephra deposits of the Tuff Member derive from at least four volcanoes. The Keli Lambo Volcanic Complex (KLVC) is the major volcano depositing five tephra units, the TTL-T2, TTL-T5, WSI, TRI and PMS. The large-scale eruptions of the KLVC generated the voluminous PDC deposits of the WSI, TRI and PMS that blanketed the entire basin. In addition, TTL-T1 is nearly similar in composition with WLW and both tephras are distal tephra-fall units that most likely erupted from the same volcano. Two tephra units have unique characteristics, which compositionally do not match any other tephra units of the Tuff Member. The high-silica tephra of TTL-T4 represents a very distal tephra-fall deposit that was produced by a strong explosive eruption from a distant volcanic province.

Another distal ash, the KPW, is characterised by a very high potassium content, and has a geochemical similarity with the oldest Toba Tuff (OTT). The Toba volcano is situated ~3000 km to the west from the Soa Basin.

Concerning the provenance of TTL-T1 and WLW, both very similar in chemical composition, this study cannot identify their source, due to the lack of a geochemical database of pyroclastic deposits from surrounding volcanoes across Flores Island. Therefore, TTL-T1 and WLW are informally given the source name of Volcano "Z". Similarly, the source of the TTL-T4 is designated as Volcano "X". With respect to TTL-T2, this tephra can be derived from either the KLVC or Volcano "Z" according to its chemical similarity with tephra units produced from the KLVC, but also with two tephra layers assigned to Volcano "Z". The discrimination diagrams using CaO, ΣFeO and K_2O contents of glass shards suggest that TTL-T2 is compositionally close to the products of Volcano "Z" (TTL-T1 and WLW) (see Figure 5.28 and 5.30), while statistical analyses reveal that TTL-T2 shows chemical affiliation with the KLVC deposits (see Figure 5.32). The field characteristic of TTL-T2 is similar to TTL-T1 and WLW indicating a distal tephra-fall deposit. Thus, this study presumes that TTL-T2 derives from Volcano "Z".

During deposition of the Sandstone Member, volcanic activity in the Soa Basin became less intensive. The andesitic Mata Menge Tephra (MMT) is the only pyroclastic tephra-fall deposit identified and it occurrs in the middle of sequence. The thickness and grain size of MMT suggest a westward ash dispersion and, accordingly, it probably derived from the KLVC. If so, the magma composition of the KLVC significantly changed from rhyolitic to basaltic. The relative stratigraphic position of the MMT indicates that this tephra was deposited in the mid Middle Pleistocene. This inferred age is in agreement with the palaeomagnetic analyses on overlying and underlying sediments with all samples displaying a normal polarity that suggests the Brunches subchron (Dida Yurnaldi, pers. comm).

After the relative volcanic quiescence over *ca*. 100 thousand years, nearby volcanic activity increased again, generating a total of 58 closely-spaced tephra layers (the Piga Tephra/PGT) that show compositional heterogeneity from basaltic to dacitic composition. The lowermost layer of Piga Tephra has been dated at 0.65±0.02 Ma ago (Brumm *et al.*, 2016). The PGT were deposited in a lacustrine environment and individual tephra layers are separated by lacustrine claystone and limestone layers. Whole-rock samples of PGT predominantly consisting of basaltic-andesitic ashes that can be correlated to eruptions of either the BCCC in the south-eastern part of the Soa Basin or the younger domes inside the WCC. Sucipta *et al*., (2006) reported several mafic volcanic cones (basaltic andesite–andesite) that formed from 0.73 Ma to 0.20 Ma. Considering the age of PGT, the basaltic layers of PGT may have a correlation with the eruptions of the BCCC. However, the source of the felsic Piga Tephras has not been identified yet, due to the paucity of volcanological data from the surrounding volcanoes of the Soa Basin.

The tephra records in the study area provide important information regarding the history of eruptions sourced either from local or regional volcanic provinces, and some tephra deposits are obvious, distinct and potential as stratigraphic marker beds. This will be discussed in the following section.

5.7. The stratigraphic marker beds: Linking archaeological sites and revising their ages

It has been pointed out that previous studies undertaken in the Soa Basin were unable to link several important archaeological and palaeontological sites dispersed across the basin, although the stratigraphic succession of the excavation sites have been well-documented and chronological determinations have been performed using zircon fission-track (ZFT) dating on samples associated with fossil and/or artifact - bearing layers (see Chapter 3).

The occurrence of prominent pyroclastic deposits provides good opportunities to assess inter-site correlations. Moreover, the widespread pyroclastic layers can be isochronous beds and thus fossil remains and archaeological materials can be chronologically ordered. The compositional data, stratigraphic considerations, together with chronological evidence suggest that the Wolo Sege Ignimbrite (WSI) and the Turekeo Ignimbrite (TRI) are good candidates for stratigraphic marker beds, connecting archaeological sites throughout the Soa Basin. These two tephra deposits occur in the lithological sequence of four main archaeological sites, namely Kobatuwa, Mata Menge, Tangi Talo and Wolo Sege. The WSI and TRI represent conspicuous PDC emplacements with clear field characteristics, enabling their easy tracing in the field.

With respect to WSI, this ignimbrite has been securely dated at 1.01±0.02 Ma (Brumm *et al*., 2010; 2016) and it can be used as an isochronous tie-line. At Matago and Wolo Sege, stone artifacts were recovered just beneath the WSI, while fossil assemblages occurr ~20-m below it at Tangi Talo. In the case of the Tangi Talo site, this tephrostratigraphical study has refined the age of the main fossil layers, indicating a much older age of 1.42 Ma than the previous ZFT age (~0.90 Ma, suggested by O'Sullivan *et al*., 2001). Moreover, fossil remains and artifacts at Kobatuwa were accumulated within volcaniclastic deposits dated at ~0.80 to 0.75 Ma ago (O'Sullivan *et al*., 2001). In contrast, this study notes that those ages must be older because the finds originated in sediments just beneath and above the WSI.

Excavations at Mata Menge have recovered an abundance of fossil remains and stone artifacts (Morwood *et al*., 1998; Brumm *et al*., 2007; van den Bergh *et al*., 2009; Brumm *et al.*, 2016) and zircon fission track dating analyses on samples taken from the fossil layers and overlying sediments suggested a depositional time span of 0.88 Ma to 0.80 Ma for the main (lower) fossil-bearing interval (Morwood *et al*., 1998; O'Sullivan *et al*., 2001). Detailed stratigraphic assessments at the Mata Menge site indicate that the relative positions of fossil

and artifact-bearing layers are most likely stratigraphically above the Pumaso Tephra (PMS). In addition, during a revisit to the Dozu Dhalu site, PMS could be identified, and here fossil accumulations occur at ~8-m above PMS. This new information definitely contradicts the former fission track ages (0.92–0.85 Ma; Sullivan *et al.*, 2001). According to the occurrence of PMS, this site should be considered younger than 0.81 Ma. Moreover, palaeomagnetic data indicate that the lower fossil-bearing interval at Mata Menge is younger than the Brunhess-Matuyama boundary at 0.78 Ma (Yurnaldi *et al.*, 2018). These two cases demonstrate that PMS can be an additional marker horizon for correlating archaeological sites in the study area due to its wide spatial distribution.

The geochemical characterisation indicates that the Kopowatu Tephra (KPW) is compositionally similar with the oldest Toba Tuff (OTT) generated by a supereruption of Toba Volcano in North Sumatra. The wide geographic dispersion and the reliable age of OTT suggest that this tephra can be employed for establishing a regional chronostratigraphic marker bed. Trace elemental compositions of glass shards from the KPW, recently published in Brumm *et al.*, (2016), suggest that the KPW can not be related to any of the known Toba tephras. However, it is potentially an important link between the Soa Basin sequence and other regional sequences, such as archaeological sites in Sangiran, Java.

The chosen stratigraphic markers can significantly contribute to inter-site correlation and provide isochrons at basin and regional scales. The tephra deposits can also be used as relative chronologies and secure benchmarks for evaluating the ages of fossil and/or artifact-bearing layers, depositional rates, soil-formation processes and other palaeoenvironmental parameters.

5.8. Summary

The identification of tephra layers in the Soa Basin provides the first stage in establishing a tephrostratigraphic framework in the eastern part of Indonesia. The field investigation and geochemical analyses on the basis of whole-rock samples and glass shards are able to characterise and group the studied tephra units. The individual tephra layers indicate different eruptive events and give a broader picture in understanding the eruption history of volcanic provinces surrounding the study area. Two caldera-forminggenic eruptions successively occurred in the beginning of the Early Pleistocene. These are the Aesessa Ignimbrite and the Lowo Mali Ignimbrite, which were followed by an erosional phase leading to an unconformity in the sequence. Furthermore two large-scale explosive episodes generating voluminous pyroclastic density current deposits that are recognised in the Soa Basin occurred in the late Early Pleistocene. These are the Wolo Sege Ignimbrite, dated at 1.01 Ma, the Turekeo Ignimbrite, and the Pumaso Tephra, dated at 0.81 Ma.

Major-element analyses of glass shards, multi-element diagrams and statistical analyses have provided useful tools for fingerprinting tephra deposits and estimating the source volcanoes. Indeed, tracing the provenance of tephra deposits can be misinterpreted without being accompanied by reliable chronological data. In further research, age determinations should be conducted on the dateable tephra units throughout the whole sequence in order to reconstruct a robust tephrochronological framework.

Three prominent tephra layers blanket the entire basin and facilitate inter-site correlations and provide accurate age controls for palaeontological and archaeological materials in the Soa Basin. Moreover, the occurrence of a very distal ash (the Kopowatu Tephra, dated at 0.90 Ma) may be valuable for synchronisation of regional sediment records, fossil remains and artifact assemblages in many key archaeological sites across the Indonesian region. In addition, a regional database is still required to futher improve this tephrochronological study and its application across the Indonesian region.

CHAPTER SIX

THE STRATIGRAPHY OF THE SOA BASIN: CURRENT STUDY

6.1. Introduction

The general stratigraphic framework of the Soa Basin has been highlighted in Chapter Three. The Soa Basin sequence comprises three main rock formations: the Ola Kile, Ola Bula and Quaternary deposits. The Ola Bula Formation consists of Tuff, Sandstone and Limestone Members. Even though previous studies have recognised vertical and lateral variations of each of these stratigraphic units, a detailed analysis of the spatial facies distribution has never been undertaken, and therefore the facies characteristics of the basin sequence are still poorly documented. This study applies facies classification to characterise the lithological succession of the Soa Basin sequence, particularly the Ola Kile Formation and Ola Bula Formation, and to assist on establishing a correlation between the archaeological sites and provide an interpretation of the depositional processes that formed the sequence.

This chapter begins with lithofacies descriptions and facies associations based on representative stratigraphic sections from selected sites in the Soa Basin, followed by an account of the lateral and vertical lithofacies distribution, correlation between stratigraphic profiles and depositional environments. Detailed stratigraphic sections including thickness and lithological descriptions are listed in Appendix 1. The sedimentary facies nomenclature uses the classification suggested by Miall (1985, 1996) and the description of the volcaniclastic facies follows the definitions of Cas and Wright (1987) and McPhie *et al*. (1993). The proposal for a new stratigraphic framework will be outlined at the end of this chapter.

6.2. Lithofacies Description and Facies Association

Lithofacies units were studied in exposed outcrops or in trenches specifically dug for that purpose. Based on optimal outcrop conditions and ensuring that all areas of the Soa Basin were covered, a number of sites and sections were selected as representative of the various geological environments throughout the basin. Determination of facies association and inferred depositional settings are based on characteristics of lithology, lithological sequence, sedimentary structures and associated features. The basin sequence can be divided into nine facies associations, consisting of: I) primary volcaniclastic deposits, II) redeposited volcaniclastic deposits, III) effusive volcanic bodies, IV) lahar and mudflow deposits, V) channel deposits, VI) sheetflood deposits, VII) floodplain deposits, and VIII) lacustrine deposits. All of these facies associations are locally overprinted by soil-formation processes (facies association IX).

6.2.1. Primary volcaniclastic deposits: Facies Association I

A. Description

Primary volcaniclastic deposits (Figure 6.1) constitute massive ash (Tm), massive ash with pumice clasts (Tmp), massive-crudely stratified ash (Tms), stratified ash (Ts), massive ash with accretionary lapilli (Tma) and massive pumiceous lapilli (LTmp). This study has identified at least 73 primary volcaniclastic layers in the Soa Basin, their detailed characteristics and chemical compositions have been outlined in Chapter Five.

Massive ash (Tm) shows well sorted, very fine to coarse ash, vitric to vitric crystal ash, minor lithic fragments, is silty to sandy (Wentworth scale), massive, ungraded to normally graded, either welded or non-welded, and may contain an abundance of hornblende (e.g. Pumaso Tephra, see Chapter Five). The thickness of the Tm varies between 0.3 cm and 277 cm. The upper surface is mostly flat and sharp, while the basal contact is sharp, non-erosive and flat to undulating and fills pre-existing relief.

Massive ash (Tm) with pumice clasts (Tmp) is composed of pumiceous vitric ash, is medium to very coarse grained, has medium to very coarse sand (Wentworth scale), normal grading, is massive to crudely stratified, and is 2.8–18.5 cm in thickness. The upper and lower surfaces are sharp and plain to irregular.

The massive-crudely stratified ash facies (Tms) refers to fine-medium vitric ash, 1–5 cm-thick, is silty-sandy, massive-crudely stratified, well sorted, ungraded, contains rip up clasts in some places, and has a sharp and non-erosional base.

Stratified ash (Ts) consists of 10–130 cm thick layers, comprises fine to coarse ash, fine to coarse sand (Wentworth scale), vitric ash, is well to moderately sorted, has a parallel to low-angle cross stratification, and it is common to have heavy minerals or lithic fragment concentrations occurring as thin laminations. At Nata Randang, in the northern part of the basin where Ts is situated in the proximal zone of Welas Caldera Complex, this facies reaches up to ~40 m in thickness. The basal surface is sharp, wavy or irregular and non-erosional, while the upper surface is flat and sharp.

Massive ash with accretionary lapilli (Tma) contains fine to medium grained ash, fine to medium sand (Wentworth scale), vitric ash, is poorly sorted, massive, normally graded, and rim-type accretionary lapilli are dispersed with an average diameter of 4 mm. This lithofacies has a maximum thickness of between 11 cm and 25 cm. The basal surface shows a sharp, plain and non-erosional contact, while the upper contact is sharp and flat to slightly irregular.

Massive pumiceous lapilli (LTmp) comprises fine to coarse pumiceous lapilli, coarse sand to cobble size (Wentworth scale), vitric ash but commonly with few sand sized-crystals and lithic fragments, is clast supported, poorly sorted, dominated by pumice clasts that are in a sandy coarse ash matrix, can be welded or non-welded, displays normal grading, is stratified in the lower part and has a thickness between 11 cm and 30 m. The basal contact is sharp, flat

to irregular and non- or slightly erosional, while the upper contact is sharp and plain.

B. Interpretation

Massive ash (Tm) displaying ungraded and normally graded textures and an absence of cross stratification are the typical characteristics of pyroclastic air-fall deposits (see Cas and Wright, 1987; Houghton *et al*., 2000). Massive ash is deposited in a distal setting and mostly overlies palaeosols or pedogenically altered sediments (Facies P).

Massive ash with pumice clasts (Tmp) may occur as a result of a turbulent pyroclastic density current (PDC) with tractional grain segregation (see Branney and Kokelaar, 2002). Facies Tma, which contains accretionary lapilli, results from a PDC that was produced by a phreatomagmatic eruption. The presence of rim-type accretionary lapilli indicates wet or moisture-rich co-surge ash clouds (Cas and Wright, 1987; Morrissey *et al*., 2000).

Massive-crudely stratified ash (Tms) and stratified ash (Ts) is characterised by parallel to low angle cross stratification and multiple ash and mineral or lithic grain laminations. At Wolo Sege, this lithofacies contains abundant lithic fragment concentrations at 20 cm from the base that form thin laminations. Texture and structure of this stratified ash are typical of pyroclastic surge deposits. The intercalation between ash, crystal or lithic laminations and bedforms, and the fluctuation in thickness is due to a series of pulses from multiple vent explosions, and are probably generated by a single-eruption column (Cas and Wright, 1987, Branney and Kokelaar, 2002). This interpretation is also supported by the scarcity of pyroclastic fall deposits within this lithofacies.

Massive pumiceous lapilli (LTmp) contains abundant pumice clasts, stratified in the lower part and with normal grading. This facies is welded in one locality (Lowo Lele) and may contain preserved wood remains. This lithofacies is interpreted as consisting of pyroclastic flow deposits. The massive texture, poor and non-erosional basal contacts indicate rapid deposition from a PDC without

tractional grain segregation by turbulence (see Branney and Kokelaar, 2002). The welded features are due to a high temperature during a PDC emplacement.

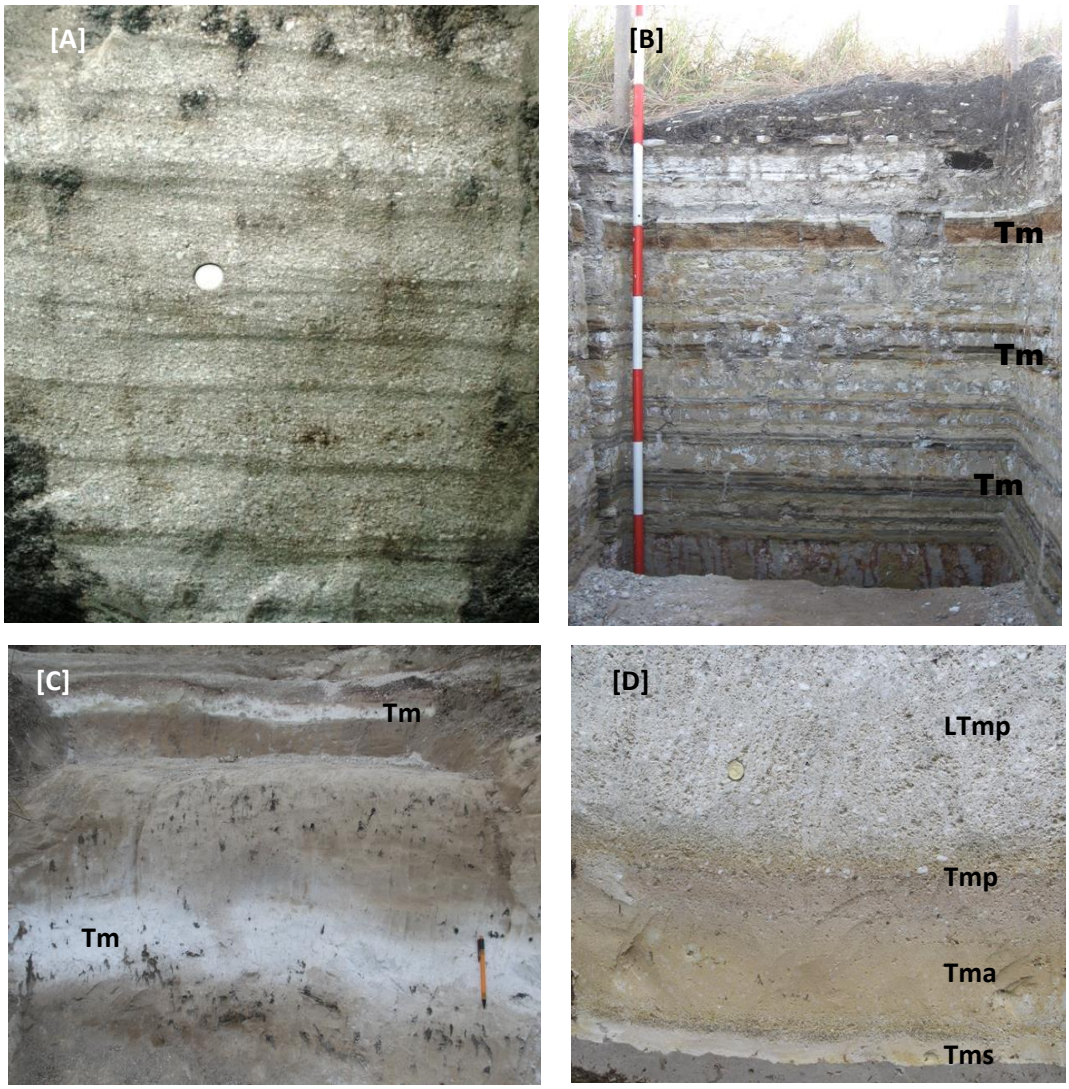

Figure 6.1. Field photographs of primary volcaniclastic facies. (A) Facies Ts, which displays low-angle cross stratification with dark bands representing lithic fragment assemblages, indicates a pyroclastic surge deposit, exposed at Nata Randang (8°36'20.7"S; 121°05'15.9"E) (coin for scale, 24 mm in diameter). (B) Crystal vitric ash (dark layers, facies Tm) interbedded with lacustrine sediments (light colour) that are well-exposed at Mata Menge (8°41'29.1"S; 121°05'36.4"E), suggests a typical pyroclastic fall deposit (Scale bar is 10 cm). (C) The outcrop of vitric ash (facies Tm) at Tangi Talo (8°41'53.0"S; 121°08'10.6"E), shows a massive structure, is silty-sandy, and represents distal pyroclastic fall deposits (pencil as scale, 14 cm length). (D) Field characteristics of facies Tms, Tmp, Tma and LTmp, which are well-exposed at Wolo Sege (8°41'27.1"S; 121°06'00.0"E). Facies Tms and Tmp formed predominantly by turbulence of a pyroclastic surge. The prominent accretionary lapilli of facies Tma suggests pyroclastic fall deposits produced by a wet eruption. Facies LTmp, pumice-rich, indicates pyroclastic flow deposits (coin diameter is 24 mm).

6.2.2. Re-deposited volcaniclastic sediments: Facies Association II

A. Description

The redeposited volcaniclastic (Tr) facies association comprises massive redeposited ash (Trm), massive redeposited ash with accretionary lapilli (Trma), laminated to cross-stratified redeposited ash (Trs) and massive redeposited lapilli (LTrm). Massive redeposited ash (Trm) refers to fine to coarse ash, moderately to poorly sorted, there are floated pumice clasts of granule to pebble-size in some outcrops, ungraded and with random pumice alignments. The basal surface is gradational to sharp, undulating and commonly erosional, but a non-erosive surface occurs in some localities (Wolo Sege, Kobatuwa-04, Pumaso and Lowo Mali).

Massive redeposited ash with accretionary lapilli (Trma) is composed of fine to coarse ash with accretionary lapilli in random orientations. The accretionary lapilli are derived from underlying primary air-fall deposits. The basal surface is usually gradational, planar and non-erosional. Laminated to cross-stratified redeposited ash (Trs) is constituted of fine to very coarse ash, is moderately to poorly sorted, has thin laminations to cross stratification and a sharp, irregular and erosional basal contact. Massive redeposited lapilli (LTrm) comprises fine to very coarse lapilli, contains granule to pebble-sized pumice clasts, is clast supported, has moderate to poor sorting, is sharp to indistinct, planar to irregular and has an erosional basal surface. However, in some localities (Wolo Sege), this facies has a non-erosional base.

Re-deposited volcaniclastics (Figure 6.2) generally overlie the primary volcaniclastic deposits. These redeposited materials are unconsolidated with a maximum thickness of up to 3.5 m.

B. Interpretation

Based on the stratigraphic position of the re-deposited volcaniclastic sediments overlying primary volcaniclastics, and the lack of a

depositional hiatus between primary and re-deposited volcaniclastics as indicated by soil formation processes or bioturbation, it follows that the re-sedimented volcaniclastic facies were deposited shortly after the deposition of primary volcaniclastic deposits. Neither hyperconcentrated flow deposits by *en masse* sedimentation nor stream flow deposits generated by bed-load transport (see Smith and Lowe, 1991) result in massive, ungraded, poorly sorted deposits, displaying lamination, cross stratification and inter-dispersed with pumice alignments. The occurrence of concentrated pumice layers and a non-erosive base instead suggest rapid sedimentation from highly concentrated and laminar flows that are less turbulent and lacking sufficient solid particle segregation within the flow (Cas and Wright, 1987; Branney and Kokelaar, 2002).

In contrast, the products of hyperconcentrated flow mechanisms are often set above conglomeratic or sandy channel deposits (Facies Gm, Gl or Gs) and can be found in almost all studied sections. This suggests that volcaniclastic deposits were emplaced fluvial environments with many channels and water-lodged topographic lows.

In addition, gas escape pipes were found in some massive redeposited ash layers (Trm) and massive redeposited ash with accretionary lapilli (Trma), with lengths of up to 3 m. These gas escape pipes are filled with coarser materials than the surrounding original deposits. These features present at three localities: Wolo Sege, Pumaso and Lowo Mali, and indicate that the resedimented volcaniclastic deposits were either in a hot or warm state during accumulation, or may even have been transported by hyperconcentrated flows.

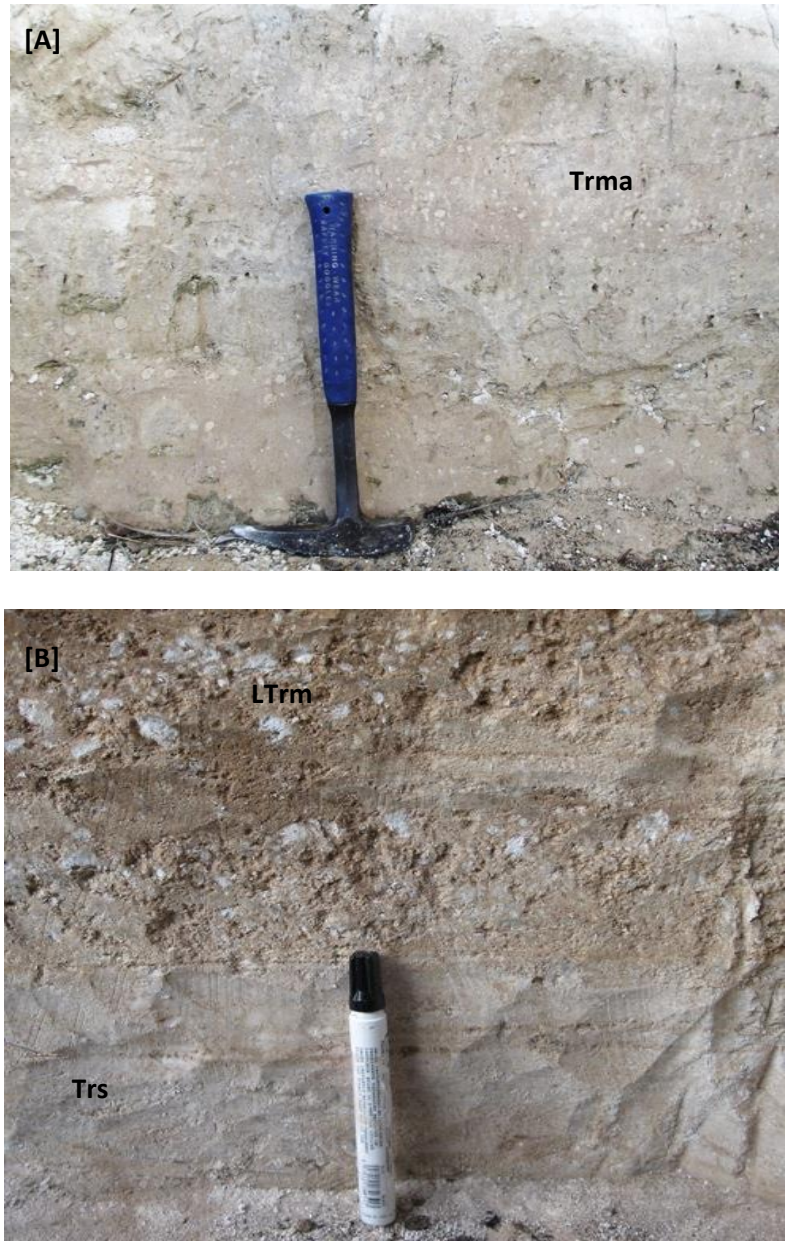

Figure 6.2. Field photographs of redeposited volcaniclastic facies exposed at Wolo Sege (8°41'27.1"S; 121°06'00.0"E). (A) Facies Trma contains abundant accretionary lapilli and displays a gradational contact (geological hammer is ~30 cm long); and (B) the exposures of Facies Trs and LTrm (the marker pen is ~15 cm long).

6.2.3. Effusive volcanic bodies: Facies Association III

A. Description

This facies association (Figure 6.3) consists of lava flows, with two lava bodies cropping out near Welas and Kolopanu in the Welas Caldera Complex in the northern part of the Soa Basin, and one lava flow deposit exposed near Gero in the eastern part of the basin. Lava flows described in this sub-chapter refer to extrusive phases of Pleistocene volcanism with the exception of lava bodies originating from recent eruptions of surrounding volcanic edifices (e.g. Mt. Inielika, Mt. Ebulobo), which unconformably covered the Ola Bula sequence.

These lava bodies generally appear grey-dark grey, are massive, jointed, form a simple shape (sheet), are aphanitic-porphyritic, contain phenocrysts of plagioclase with minor pyroxene and other mafic minerals, are bounded by a groundmass of microcrystalline plagioclase and glassy minerals, are blocky in style without columnar joints, and the thickness varies between 2 m and 6 m. The lava body exposed near Gero displays a vesicular texture and is crudely flow banded. This flow banding feature is formed during cooling, and therefore does not necessarily represent the flow direction (Kilburn, 2000; Lockwood and Hazlett, 2010).

B. Interpretation

The absence of columnar joints suggests that the lava bodies did not have any contact with water, and may have occurred in subaerial environments associated with lava domes. At Kolopanu, the basaltic lava is covered by ~2–4 m-thick pyroclastic flow deposits, representing the effusive phase before an explosive eruption. The two lava flows in the northern part of the basin are associated with the development of lava domes within the Welas Caldera Complex. The presence of the banded lava flow near Gero is from a different source than those at the Welas Caldera Complex, and instead originated from a local volcanic dome.

Figure 6.3. Field photographs of lava flows. Massive-blocky lava flows exposed at (A) Welas (8°36'03.2"S; 121°04'51.4"E) and (B) Kolopanu (8°39'58.0"S; 121°02'29.5"E). (C) Banded lava flow and (D) its vesicular texture exposed at Gero (8°41'59.3"S; 121°11' 38.1"E) (scale indicators: the man is ~160-cm in height, and the geological hammer is ~30-cm in length).

6.2.4. Lahar deposits: Facies Association IV

A. Description

This facies association (Figure 6.4) comprises mudflow and debris/ hyperconcentrated flow deposits, including tuffaceous siltstone (Fmm), tuffaceous sandstone (Smm) and volcanic breccia (Bv).

Tuffaceous siltstone is massive, ungraded, contains predominantly randomly orientated pumice, is moderately-poorly sorted, matrix supported, 10–195 cm-thick, sharp, undulating and has an erosional base. Tuffaceous sandstone

is massive-crudely stratified, ungraded, pumice-rich, moderate to poor sorting, is clast-supported, sharp, irregular and has an erosional contact, and the thickness varies between 14 cm and 35 cm.

Volcanic breccias consist of basalt, andesite, pumice fragments, is massive, clast supported, poorly sorted, ungraded, with sharp and erosive surfaces, and a bedding thickness ranging from 74 cm to > 5 m. In some exposures, scoria clasts predominantly occurred that incorporated into a coarse sandy tuffaceous matrix.

B. Interpretation

'Lahar' is an Indonesian word referring either to a fast flowing volcaniclastic mudflow or the deposit that results from such a mass-flow. Lahars contain a mixture of volcanic rock debris and water, other than a normal streamflow from a volcanic edifice (Smith and Fritz; 1989, Smith and Lowe; 1991). According to Vallance and Iverson (2015), lahars can be hyperconcentrated flows or debris flows (see also Smith, 1986; Lavigne and Suwa, 2004).

Facies Smm and Bv, which are characterised by being massive, ungraded, clast supported and poorly sorted, can be categorised as hyperconcentrated flow deposits. Facies Fmm on the other hand, tends to be generated by a debris flow.

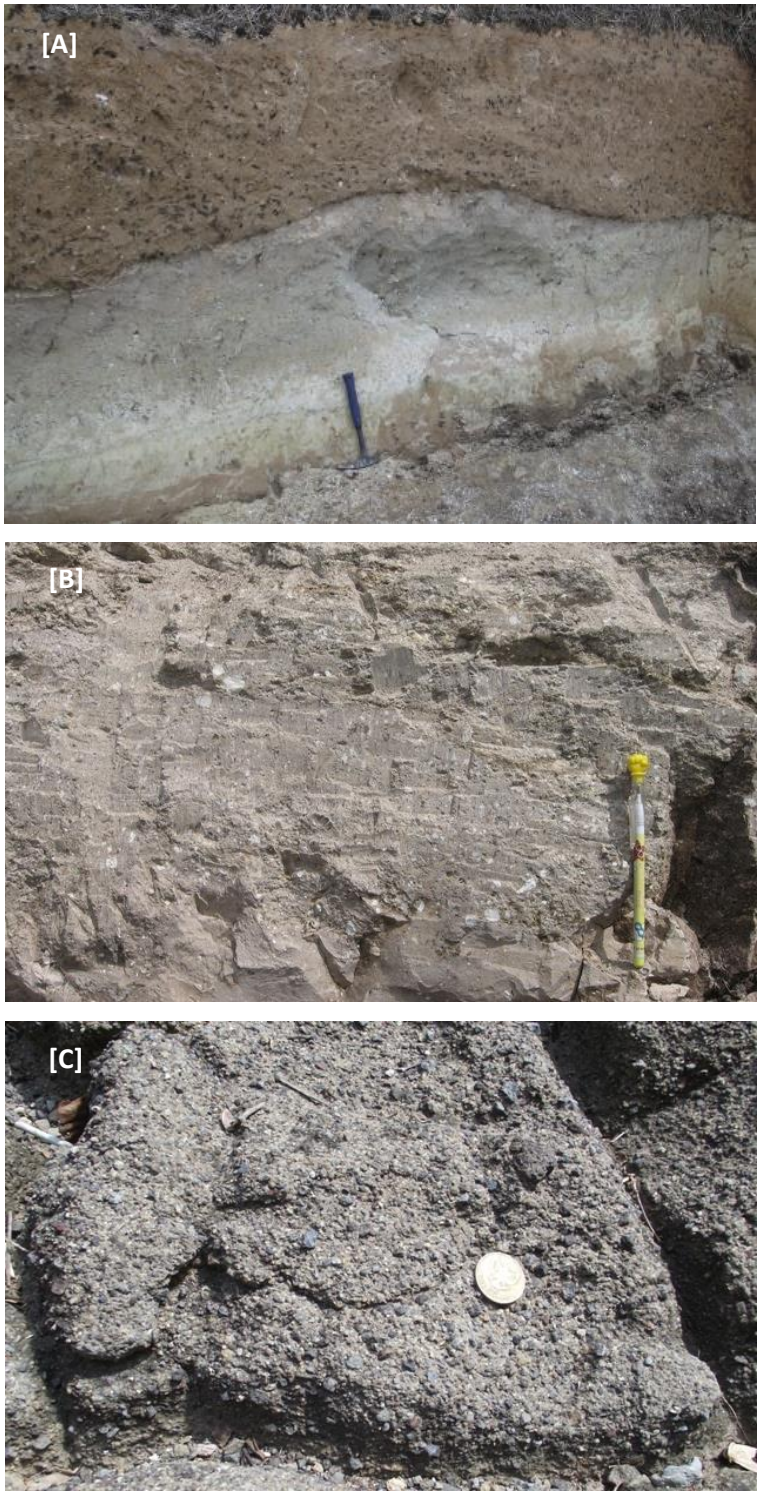

Figure 6.4. Field photographs of lahar deposits. (A) Two distinct diamictons, well exposed at Tangi Talo (8°41'53.0"S; 121°08'10.6"E). The massive brown lahar truncates the massive light grey lahar, and remains erosional contact (geological hammer is ~30 cm long). (B) Field characteristic of facies Smm at Mata Menge (8°41'33.8"S; 121°05'44.6"E), which is massive, clast supported and poorly sorted (pencil is ~15 cm). (C) Polymict volcanic breccias outcrop at Tangi Talo (coin is 24 mm in diameter).

6.2.5. Channel deposits: Facies Association V

Facies association V (Figure 6.5.) includes cross stratified sandstone (Sl and Ss), horizontal laminated sandstone (Sh), well-cemented stratified sandstone (Scl) and conglomerate (Gm and Gl). Sub facies Sl comprises of fine to coarse sandstone, well–moderately sorted, of normal grading , has horizontal to low-angle cross bedding, and a sharp and erosional lower boundary. This sub-facies occurs at Mata Menge, Tangi Talo, Ola Bula and Pumaso, with individual layer thicknesses varying from 5 cm to 140 cm. At Pumaso in particular, this facies alternates with palaeosols (facies P) to form a 406 cm-thick deposit. Sub facies Ss refers to pebbly coarse sandstone which is poorly sorted, has normal grading, cross bedding, a scouring surface, and the thickness varies between 27 cm and 154 cm. This sub-facies is well exposed at Mata Menge, Wae Bha and Ola Bula.

Fine grained sandstone with horizontal parallel lamination (sub facies Sh) and a sharp and erosional lower contact, is only exposed in the upper sequence of the Mata Menge section. This sub-facies constitutes well-cemented stratified sandstone (Scl), is medium–coarse grained, well–moderately sorted, of normal grading, has low-angle cross bedding, cut-and-fill structures, a sharp and erosional basal surface, is 91–160 cm-thick, and is composed of quartz, feldspar, pumice and lithic grains. This sub facies is well exposed at Kobatuwa 4, Mata Menge, Wolo Sege, Tangi Talo and Gero. At Mata Menge, leaf fossils are preserved in this sub facies, while at Tangi Talo, this facies is characterised by a few centimetres of conglomeratic tuffaceous sandstone bed in the lowermost part.

Figure 6.5. Field photographs of channel facies association. (A) Pebbly sandstone (Ss) truncates a prominent palaeosol at Mata Menge (8°41'33.5"S; 121°05'44.2"E). (B) Horizontal fine grained sandstone (Sh) shows lens geometry at the Mata Menge upper section (8°41'30.7"S; 121°05'48.5"E). (C) Massive conglomerate at Matago (8°43' 06.5"S; 121°08'18.9"E), representing the widest braided channel deposits in the Soa Basin (Extensive channel width is up to ~30-m). (D) Cross stratified conglomerate at Wolo Sege (8°41'27.1"S; 121°06'00.0"E), overlain by palaeosol and volcaniclastic deposits (geological hammer is ~30-cm long; scale bar is ~10-cm; the stick is ~1-m).

Conglomerate facies types encompass both massive conglomerate (Gm) and cross-stratified conglomerate (Gl). Sub-facies Gm comprises subrounded to rounded clasts composed predominantly of basalt and andesite, rounded clasts of pebble-cobble size, a coarse sand matrix, is massive, with normal grading, poorly sorted, has an erosional scouring base, and is 8–150 cm-thick. The geometry of conglomerate layers is ribbon-shaped. This sub-facies crops out at Matago, where it extends laterally over 20-m in width, and near Wae Bha, where it shows a width of ~5 m. In addition, sub-facies Gm is also exposed at some localities displaying a narrow channel width that is less than 50 cm thick, (i.e. Kobatuwa 4 and Mata Menge). Sub-facies Gl refers to cross stratified conglomerate that is poorly sorted, clast supported, clasts are composed of basalt and andesite of a granule to pebble size, has a coarse sandy matrix, is 40–70 cm-thick, and well exposed at Wolo Sege, Wae Bha and Gero. In all exposures, the conglomerate sub-facies is covered by palaeosols (facies P).

B. Interpretation

Facies association V is interpreted to represent fluvial channel deposits, of streams with predominantly bedload sediments as demonstrated by the appearance of cross-bedding structures, cut and fills and erosional bases. Overall, this facies association represents shallow braided channels with low sinuosity and a strong (seasonal?) fluctuation of discharge (Miall, 1985, 1996). High discharge will favour coarse grained sub-facies emplacement (Gm, Gl and Ss), while low discharge will allow for a sandy sediment emplacement (Sl). An exception to this is at Tangi Talo, where the sub facies Sl shows an intensive cross stratification together with cut and fill structures, and this is thought to be due to a high-energy channel process occurring during a catastrophic flood. At one locality (Pumaso), this facies shows upward interbedding features with palaeosols (facies P).

Horizontal beds of fine grained sandstone that are only exposed at Mata Menge reflect deposition by a high-energy sheet flood that inundated a

relatively low-relief topographic environment, probably a flood plain (see Miall, 1996). Field observations indicate that in all localities, the conglomerate facies types are commonly overlain by palaeosols (facies P). These characteristics suggest that the channels did not exist for a long period of time, as the discharge decreases over time, and may therefore only have developed during high rare precipitation events, and can therefore be attributed to an ephemeral fluvial system or in frequent avulsions.

Sub-facies Scl contains sand-sized pumice clasts and fine to coarse ash. These volcaniclastic deposits have a high silica content, and leaching of volcanic glass during transport and after deposition can fill the interstitial pore space of the sand grains, and result in solid and well cemented characteristics. The local presence of leaf fossils and poorly fossilised woody trunks (usually only preserved as cylindrical cavities) incorporated within this sub-facies suggests that high-energy flows were able to transport fallen leaves and vegetal matter from the floodplain during major floods.

6.2.6. Sheetflood deposits: Facies Association VI

A. Description

This facies association (Figure 6.6) is composed of sub-facies massive sandstone (Sm) and well cemented massive sandstone (Scm). Sub-facies Sm refers to a fine to coarse sandstone which is tuffaceous, massive, shows normal grading, is well to moderately sorted, with a base that is sharp, flat, and either non- erosive or erosive. This sub-facies occurs at Mata Menge, Wolo Sege and Gero, with a thickness range of between 20 cm and 128 cm. The sandstone beds usually have a sheet-like geometry and overlie palaeosols (Facies P) in all exposures. Sub-facies Scm represents medium to coarse-grained, moderately sorted, well cemented, massive sand layers with a sharp, flat-irregular base, up to 263-cm thick, and is composed of quartz, feldspar, lithic fragments and sand-sized pumice grains.

B. Interpretation

The flat, tabular geometry and the lack of sedimentary structures suggest that this facies association was formed by rapid, unconfined sheet floods. Water bodies run down along the slope of the volcanic flanks with a high velocity during periods of heavy rainfall or extreme run off, bringing fine to coarse grained, readily available loose materials in to suspension and deposit the clastic material following pre-existing channels or across a floodplain (see Miall, 1996; North and Davidson, 2012). The presence of volcaniclastic detritus within sub-facies Scm indicates that the sediments were derived from the adjacent volcanic highland.

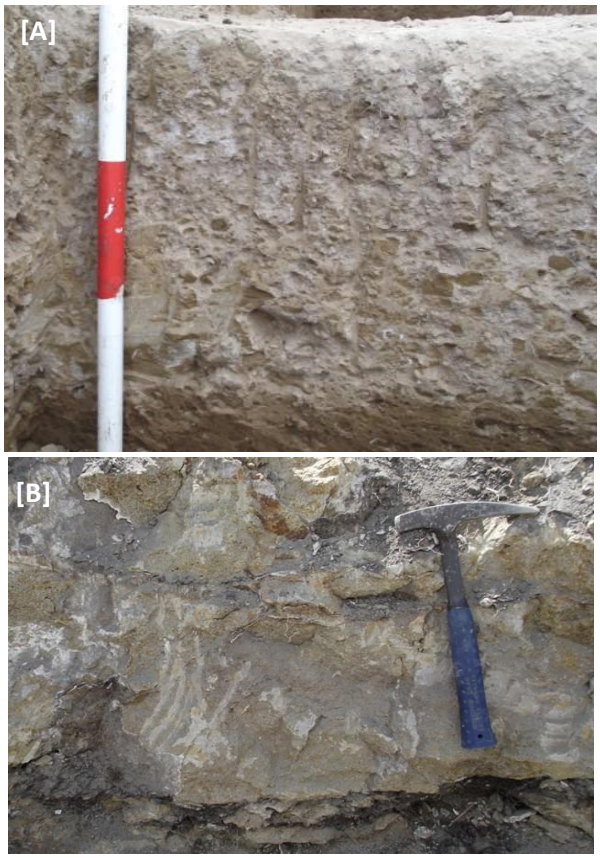

Figure 6.6. Field photographs of sheetflood deposits (Sm). A yellowish massive coarse sandstone generated by unconfined sheetflow (A) at Wolo Sege (8°41'27.1"S; 121°06'00.0"E) and (B) at Gero (8°43'23.5"S; 121°13' 16.4"E) (scale bar is ~10-cm; geological hammer is ~30-cm long).

6.2.7. Floodplain deposits: Facies Association VII

A. Description

This facies association (Figure 6.7) refers to massive claystone (Fm). Facies Fm is dark grey–brownish grey, massive, very well sorted, a sharp and flat basal surface and in some cases are silty. The thickness ranges from 3 cm to 202 cm.

B. Interpretation

Massive claystone composed of very fine-grained detritus suggests a low-energy flow regime. This facies type accumulated from suspension in low-energy environments (floodplain) during waning flood stages (Nichols, 2009). The absence of desiccation cracks suggests that the floodplain was water saturated.

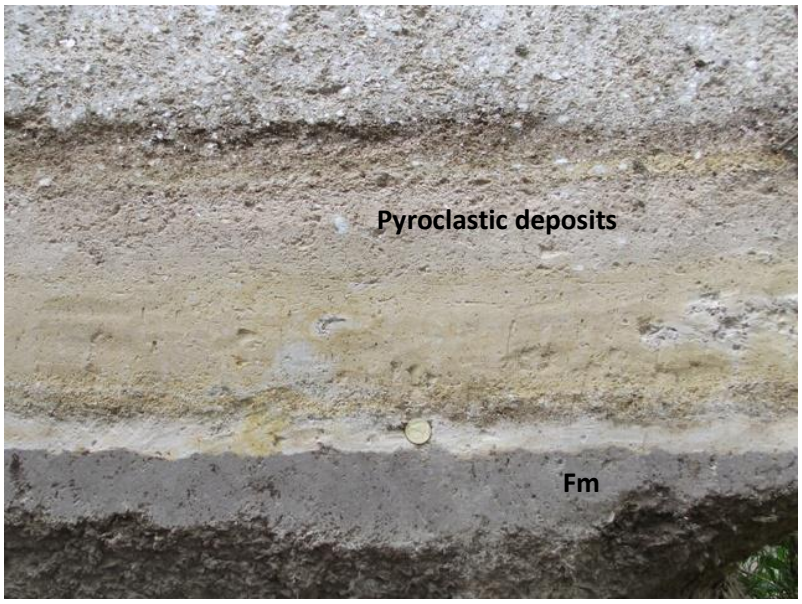

Figure 6.7. A massive claystone deposited in a wet floodplain environment, which is exposed at Wolo Sege (8°41'27.1"S; 121°06' 00.0"E) (coin is ~24 mm in diameter).

6.2.8. Lacustrine Deposits: Facies Association VIII

A. Description

This facies association (Figure 68.) consists of an alternation of regularly flat-bedded sheets of claystone (Fh) and limestone (Lm). Facies Fh is calcareous and diatomaceous, waxy, and light grey to pale brown in colour, with parallel laminations, very well sorted, and the uncommon presence of darker coloured organic-rich laminations, and sharp, flat and non-erosional basal surfaces. Individual layers vary between 2 cm and 40 cm.

Facies Lm refers to a micritic limestone that is tuffaceous, fine grained, clay-fine and sand-size, massive-laminated, with a sharp, plain and non-erosional base, and individual layers are 1.5–10 cm-thick. These facies alternate with pyroclastic fall deposits (facies Tm) to form an interbedded sequence of up to 5.1 m in thickness, which is well exposed at Mata Menge, Wulubara, Pumaso and Gero.

B. Interpretation

Facies Fh and Lm, which denote laminated structures and non-erosive bases, are indicative of a suspension load in a standing body of water, typically occurring in lacustrine environments. Many pyroclastic air-fall deposits are interbedded with the lacustrine facies types, indicating common disruption of normal tranquil lacustrine deposition by volcanic events. The presence of diatoms incorporated within facies Fm and/or Lm, and freshwater molluscs within facies Lm, suggests shallow lacustrine settings. Pennate diatoms of *Achnanthes* sp. and *Achnanthidium* sp. are the most abundant, while centric diatoms of *Paralia* sp. occur sparsely in the lower part of the lacustrine sequence. These diatoms also indicate a shallow water environment (Smol and Stoermer, 2001). Two prominent lacustrine claystones display intensive oxidation in the upper part and root penetration that indicate periods of subaerial exposures.

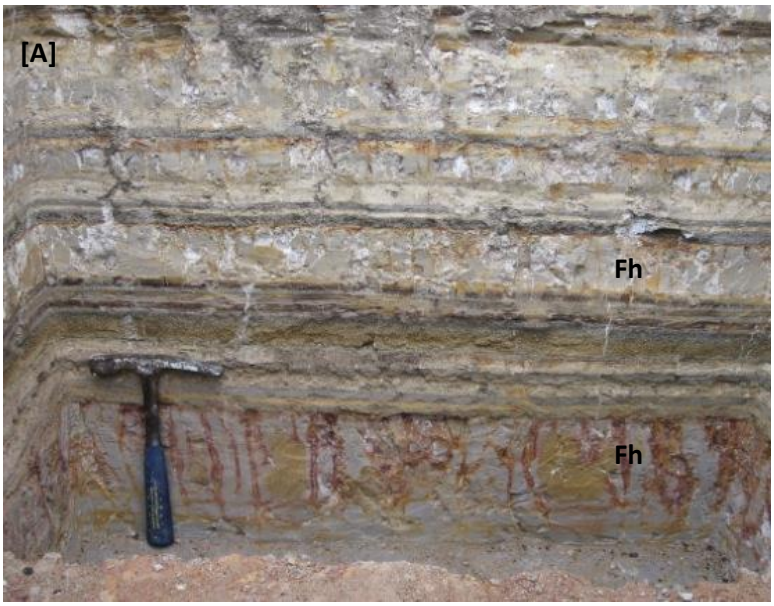
[A]
Fh
Fh

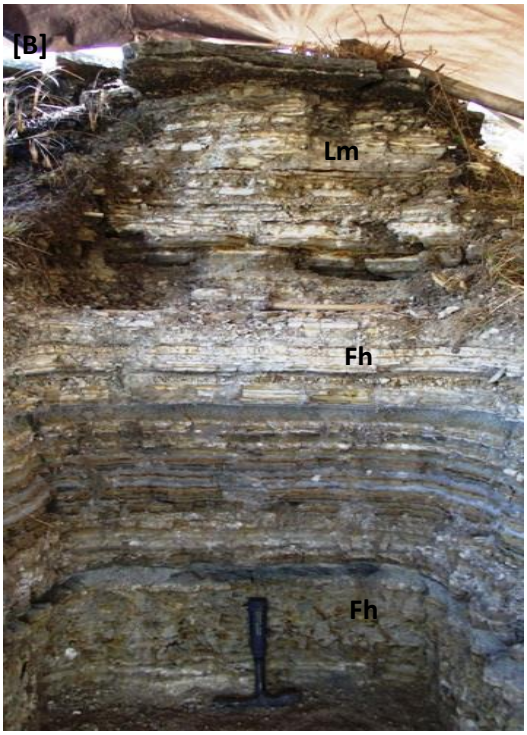
[B]
Lm
Fh
Fh

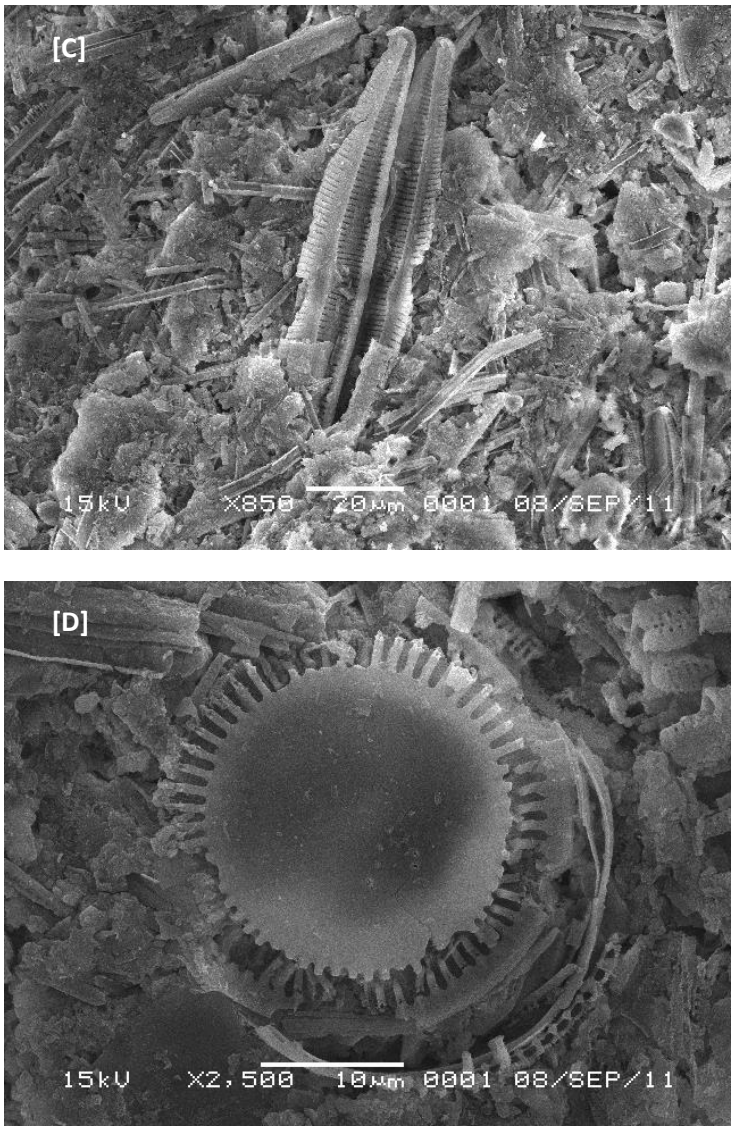

Figure 6.8. Interbedded sequences of facies Fh and Lm (light colours) with facies Tm (dark colours) expsoed at (A) Mata Menge and (B) Pumaso. (A) The exposure of horizontal claystones (facies Fh) at Mata Menge (8°41'30.7"S; 121°05'48.5"E), displaying reddish in colour due to oxidation, and the oxidation patterns are seemingly parallel to the root traces, indicating a period of subaerial exposure, where the lake dried. (B) Massive limestones are well developed in the lacustrine sequence at Pumaso (8°42'23.5"S; 121°09'29.6"E). SEM photographs of lacustrine claystone collected from Mata Menge, showing the presence of (C) mostly broken-pennate and (D) broken-centric diatom frustules.

6.2.9. Pedogenically-altered deposits: Facies Association IX

A. Description

This facies association (Figure 6.9) corresponds to palaeosol deposits, which according to the standard Soil Taxonomy (Soil Survey Staff, 1999), can be divided to sub-facies Pv and sub facies-Pa. Sub-facies Pa commonly is pale brown to brown in colour (10YR 5/3–6/3), is weakly to strongly developed, with upward increasing intensity. The original sedimentary structures are obliterated and the facies type has a massive appearance with a medium to coarse blocky structure, root traces and various degrees of mottling. This sub-facies is 26–371 cm in thickness and commonly has overprinted pyroclastic fall, redeposited volcaniclastic and lahar deposits.

Sub-facies Pv is generally light grey to grey (10YR 6/1–7/1), is weakly to strongly developed, massive, contains intensive cracks, has root traces and is mottled, displays a medium-coarse blocky structure, and is 5.5–140 cm-thick. This type of palaeosol usually develops above facies Gm or Gl and is overlain by pyroclastic surge or flow deposits. In the upper part of the Mata Menge sequence, this sub-facies contains carbonate nodules (calcrete or caliche).

B. Interpretation

Palaeosols reflect a relatively stable landscape, where sedimentation processes are slow and irregular and erosion is minimal whereas pedogenic processes (leaching and clay translocation) are dominant (Kraus, 1999, Retallack, 2001). The appearance of carbonate nodules in sub-facies Pv indicates a lack of sediment input over prolonged periods and suggest a strong seasonality with evaporation of groundwater during dry seasons (Retallack, 2001). Pedogenically overprinted facies can be traced across many exposures and are predominantly developed in floodplain environments.

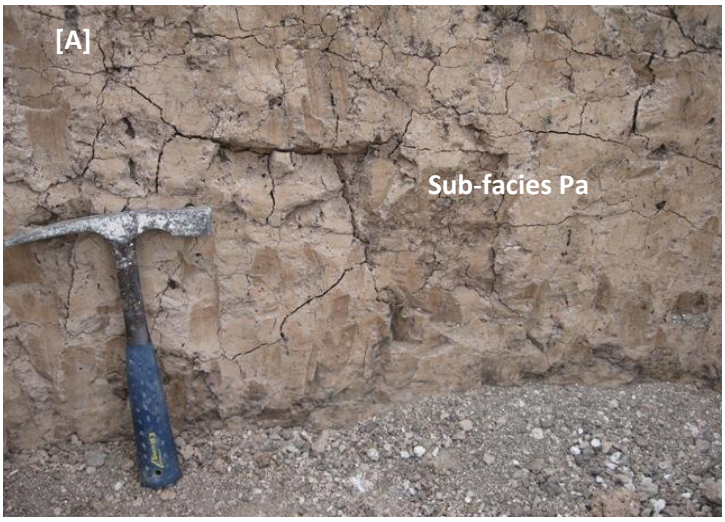
[A]
Sub-facies Pa


[B]
Ts
Sub-facies Pa

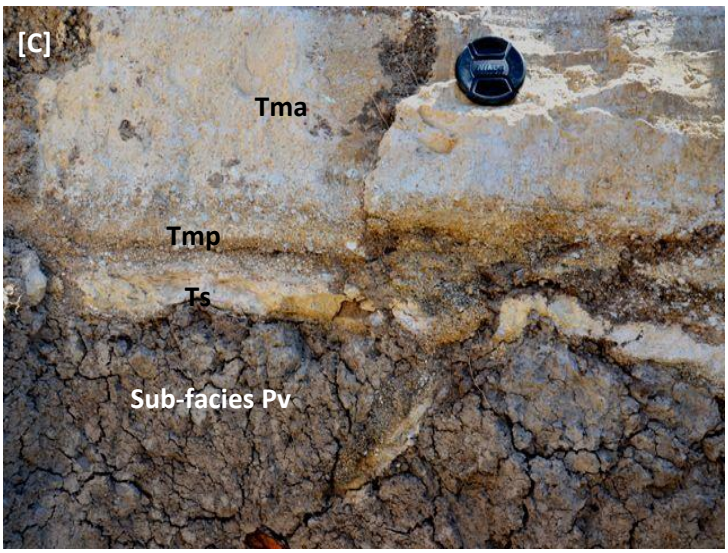
[C]
Tma
Tmp
Ts
Sub-facies Pv

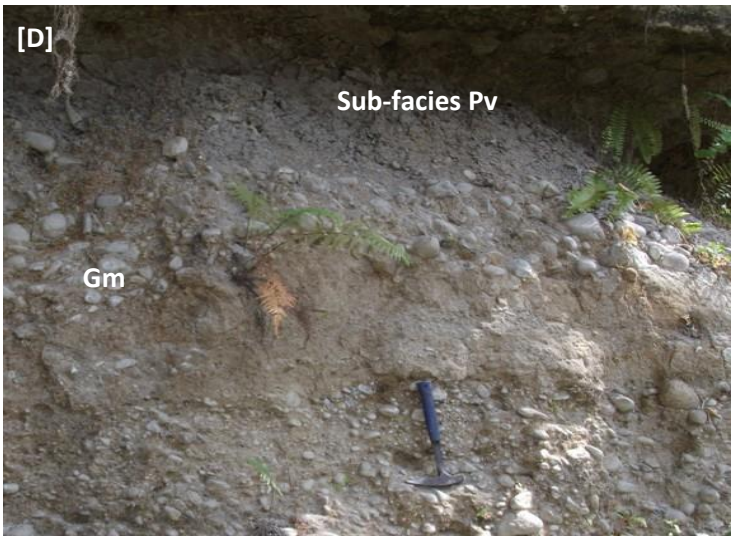

Figure 6.9. Field photographs of palaeosols. (A) Weakly developed sub-facies Pa at Tangi Talo (8°41'53.0"S; 121°08'10.6"E). (B) Strongly developed sub-facies Pa at Wolo Sege (8°41'27.1"S; 121°06' 00.0"E), directly overlain by a pyroclastic surge deposit (facies Ts). (C) Cracks within sub-facies Pv, filled by volcanic ash (facies Ts and Tmp) at Pumaso (8°42'23.5"S; 121°09'29.6"E) (photographed by B.V. Alloway). (D) sub-facies Pv development on massive conglomerate (facies Gm) at Matago (8°43' 06.5"S; 121°08'18.9"E) (geological hammer is ~30 cm long; lens cap is ~7.7 cm in diameter).

6.3. Facies Distribution

6.3.1. Vertical distribution

In the Soa Basin, a distinction can be made between primary volcaniclastic deposits that directly resulted from volcanic eruptions, and post-eruption deposits that resulted from either reworking of primary volcaniclastics or the transport and accumulation of sediments under stable conditions. The recognition of several primary volcanic deposits throughout the basin allow for basin-wide correlation of marker beds. However, not all recognised primary volcanic marker beds are preserved in all measured sections, as some may have been totally eroded or were overprinted by soil formation processes and thus difficult to identify. The vertical distribution of these primary volcaniclastic

marker beds is shown in the composite section of Figure 5.33 (see Chapter 5). This composite section provides a temporal framework for the infill history of the basin and a record of volcanic activity in the surroundings of the basin. During periods of volcanic quiescence deposition, was relatively slow and soil formation processes were dominant.

The general tephrostratigraphic framework of the Soa Basin is used to define the boundary of the sediment succession. The Aesessa Ignimbrite (AEI) is thought to form the basement of the basin, the Pumaso Tephra (PMS) marks the barrier between the Tuff and Sandstone Members, while the Piga Tephra (PGT) characterised the Limestone Member.

The oldest and deepest deposits from the basin infill are preserved in the Lowo Lele section in the east-central part of the basin. Evidence from this section shows that the welded pyroclastic deposits overlies palaeosols and channel deposits. The ~30 m thick AEI is only preserved in the east-central part of the basin, suggesting that the hot descending ash clouds either followed a pre-existing palaeovalley or that these ignimbritic deposits were subsequently eroded in higher areas of the palaeo-topography. At Lowo Mali, the pyroclastic deposit has been truncated and is covered by palaeosols, which indicates a prolonged depositional break following this major volcanic event. In the lowermost part of basin sequence, facies association I (FA–I) and FA–III are tilted in a S-SW direction, and form a low angle-unconformity. During the deposition of this sequence tectonic uplift and tilting was active. This tectonic activity is thought to have created a series of normal faults, as observed in some localities. Moreover, the welded pyroclastic deposits in the lowermost part (corresponds to the AEI in Lowo Lele section) caused the initial basin infill and created the basin morphology.

The lower sequence of the Soa Basin (the part previously designated as the lower Tuff Member) is dominated by primary volcaniclastics (FA–I), resedimented volcaniclastics (FA–II), lahar deposits (FA–IV), and minor channel deposits (FA–V), floodplain deposits (FA–VII) and palaeosols (FA–IX).

Palaeosols (FA–IX) are mostly separate products of eruptive events and reflect sedimentation hiatuses during lulls in volcanic activity. It indicates that after the explosive eruptions, which deposited FA–I, resedimentation processes of the primary volcaniclastic deposits were limited; otherwise pedogenic transformations would be more abundant. Several FA–I (the Wolo Sege Ignimbrite/WSI and Turekeo Ignimbrite/TRI) are covered by reworked volcaniclastic deposits (FA–II), exhibit emplacement aftermath the eruptions, and indicate that erosional processes rapidly took place in the higher parts of the western basin area. In addition, lahar deposits occurred in limited areas. Lahars are either triggered by heavy rainfall during or shortly after volcanic eruptions or by mixture of water from crater lakes with eruptive materials.

In the middle sequence (tentatively corresponding to the Sandstone Member), the occurrence of FA–I and FA–VII is less abundance; FA–IV, FA–V and FA–IX become more dominant in this interval, and there is a limited presentation of FA–VI and FA–VIII. The channel deposits (FA–V) still show braided characteristics, and there are no significant changes to the palaeodrainage pattern. Palaeosols (FA–IX) are commonly developed suggesting low influxes of volcaniclastic and/or siliciclastic debris to the basin. As there is only one layer of preserved pyroclastic deposit, this indicates decreasing eruption intensities.

Lacustrine deposits (FA–VIII) are well developed in the uppermost part of the Soa basin sequence (refers to the Limestone Member), and are interbedded with pyroclastic air-fall deposits (FA–I). The standing water environments were probably induced by either excess inputs of volcaniclastic or lahar deposits that disturbed or blocked the main basin outlet, or due to high intensity precipitation that inundated a number of depressions.

6.3.2. Spatial (Lateral) Distribution

The lateral facies distributions in the Soa Basin as recorded in a number of lithological logs are shown in Figures 6.10 and 6.11. As can be seen in both figures, several lithofacies are widely distributed throughout the basin, and will be discussed in this section. A few of the variations in the lateral facies have been presumably caused by local sedimentation processes, and display some discontinuities in the correlation.

The deposits of FA–I generally exhibits lateral continuity. Pyroclastic layers are missing in some of the localities (for instance the Mata Menge trenches) and this was probably induced by erosion in association with debris flows or channel fills, and the subsequent lack of exposure. In the northern part of the Soa Basin, thick FA–I deposits (predominantly lithofacies Ts and LTmp) are developed at Nata Randang and Kolopanu, respectively. Furthermore, effusive volcanic bodies (FA–III) also occurred in this region, and are well-exposed at Welas and Kolopanu. It can be noted that these areas reflect the proximal zones, and subsequently correspond to the Welas Caldera Complex.

The FA–I deposits generally display only very limited lateral changes in bed thickness. As mentioned above, this facies usually envelops palaeosols without any erosional contacts. The basin-scale distribution and relatively uniform thickness of this facies and underlying palaeosol deposits imply that the pyroclastic density currents blanketed the entire palaeosurface of the Basin's substrate topography. As with the FA–I deposits, palaeosols (FA–IX) can also be traced across the basin. The vertical distributions show that this facies occurred repeatedly. Vertical variation and lateral continuity of this facies indicates relatively low sediment input into the basin during volcanic quiescence.

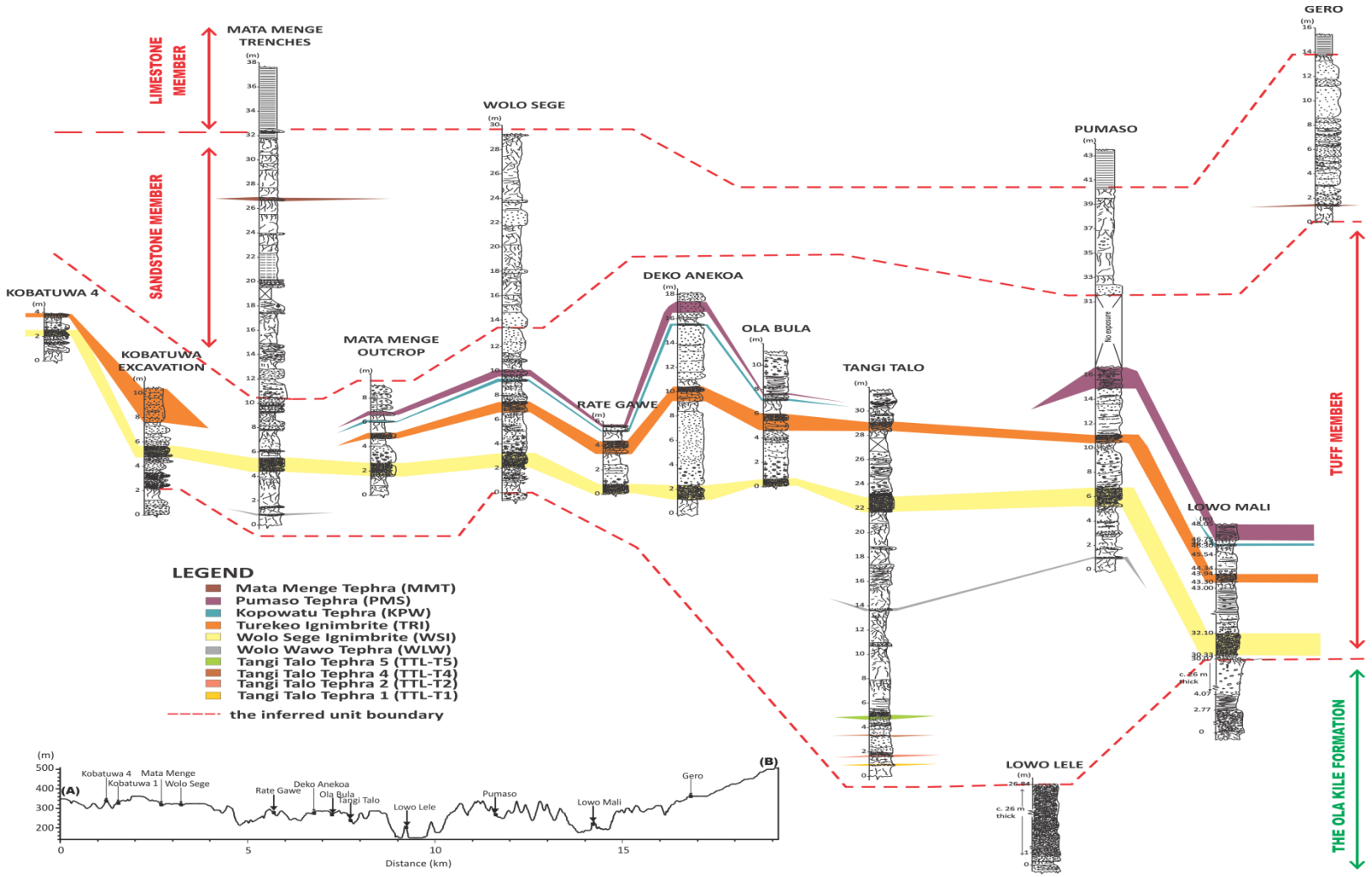

Figure 6.10. West-East correlation (Section A-B) of lithofacies units, showing three pyroclastic deposits (Wolosege Ignimbrite, Turekeo Ignimbrite and Pumaso Tephra) that can be traced across the basin and will be potentially used as the stratigraphic marker beds.

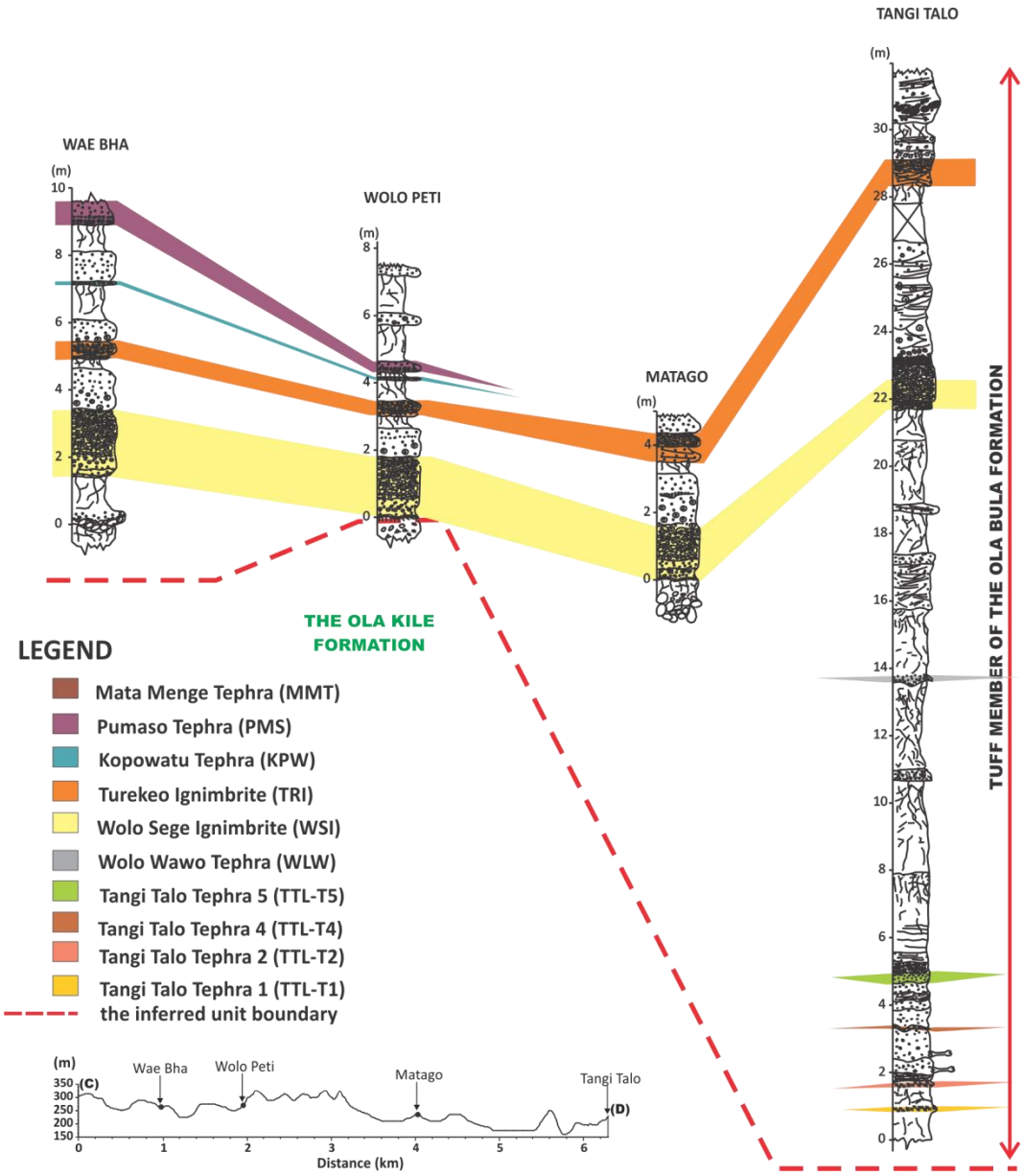

Figure 6.11. Lithofacies correlation in the southern part of the Soa Basin (Section C-D) exhibits lateral continuities of some primary volcaniclastic deposits and palaeosols.

The alternating nature of the laharic (FA–IV) and channel (FA–V) deposits is present in both the western and eastern part of the basin. The lithofacies, however, differ slightly. In the western part of the Basin, the channel deposits are dominated by lithofacies Sl and Ss, while lithofacies Gl dominates the eastern part. Furthermore, the size of the clasts are coarser in the eastern part. It is likely that the sources of the bed load sediments are different. That is,

the gravels in the eastern part probably derived from the volcanic highland in the east, while sediments deposited in the western channel system were likely sourced from the western or northern volcanic aprons. Lahars tended to be largely confined by the pre-existing fluvial channels.

In addition, the lacustrine deposits (FA–VIII) are present in both the western and eastern part of the Soa Basin. Tectonic events generated normal faults during the early stage of the basement configuration, and which subsequently form either isolated or partly interconnected depocentres (sub-basins). During the wet season, depressions develop into pools or ponds, and therefore suspended sediments accumulate.

This study recognises that the relief of the basin topography was deepest towards the central part of the basin in the surroundings of the Tangi Talo site. This deep incised topography is inferred as being due to the impact of the NE-SW normal faults with variable displacements. These incipient faults occurred during periods of post eruptive sedimentation, and thereby generated laharic deposits. This is confirmed by elevation measurements taken from a number of localities where the laharic deposits occupied high altitudes. On the other hand, intensive erosional processes were also responsible for deepening topography in the central part of the basin.

6.4. Proposal of a new stratigraphic framework

Previous investigations have documented the spatial and temporal distribution of the lithological units in the Soa Basin during the Early-Middle Pleistocene (Hartono, 1961; Suminto *et al*., 2009). This study has been able to obtain new information regarding the changes to the lithofacies throughout the basin. In combination with the previous work, this study will propose a new stratigraphical framework for the Soa Basin. The detailed description of each stratigraphical formation is discussed below and the composite stratigraphy is shown in Figure 6.12.

6.4.1. The Ola Kile Formation

The Ola Kile Formation occupies the basement of the Soa Basin infill sequence. This formation is predominantly composed of primary volcaniclastic deposits (FA–I), lahar deposits (FA–IV), channel deposits (FA–V), palaeosols (FA–IX) and localised effusive volcanic bodies (FA–III). The volcanic bodies refer to lava flows occurring in the northern part of the Soa Basin, suggesting a proximal source to the north of the basin. Although this study has not focussed on detailed stratigraphic analysis of the Ola Kile Formation, it is thought that the former volcanic centre that once occupied the location of the Welas Caldera structure has been the major source of the primary Ola Kile volcaniclastics.

This formation consists of thick pyroclastic density current deposits, involving the Aesessa Ignimbrite (AEI) and the Lowo Mali Ignimbrite (LMI). The AEI is traceable along the Lowo Lele and Ae Sessa rivers in the middle part of the basin and exhibits distinct welding textures. These pyroclastic deposits overlie prominently developed palaeosols. Cross stratified channel-fill sandstones that are locally developed below the AEI suggest that small streams were cutting down the generally stabilised land surface at some places during this stage.

The lahar deposits in this formation correspond to massive, up to ~6 m thick layers of volcanic breccias (facies Bv) composed of andesite, basalt, scoria and pumice clasts, and which commonly envelop (or enclose) the PDC deposits. This Ole Kile Formation has a total thickness of 100–200 m and shaped the early landscape relief. This formation is tilted at a low angle (5–15°) in a S–SW direction, and marks an unconformity with the overlying deposits.

6.4.2. The Tuff Member of the Ola Bula Formation

The basal Tuff Member of the Ola Bula Formation unconformably overlies the Ola Kile Formation. At Lowo Lele River in the middle of the basin, it can be seen clearly that the tilted Ola Kile deposits covered relatively horizontal

layers of the Ola Bula sequence as an angular unconformity. However, the boundary between the Ola Kile Formation and the basal unit of the Tuff Member in the western area is difficult to recognise. We interpret the presence of palaeosols among the Ole Kile and the Tuff Member deposits as the unconformity, because palaeosols indicate absence or minimum sedimentation processes (hiatus).

The Tuff Member has a maximum thickness of 50–60 m in the central basin area (Tangi Talo section), but is much thinner in the western marginal basin area (e.g. near Mata Menge, Kobatuwa). It consists in descending abundance order of the following facies associations: palaeosols (FA IX), primary volcaniclastics (FA–I), resedimented volcaniclastics (FA–II), laharic deposits (FA–IV), channel deposits (FA–V), and locally floodplain deposits (FA–VII).

This member comprises nine primary silicic pyroclastic deposits from base to top: the Tangi Talo Tephra (TTL-T1, TTL-T2, TTL-T4 and TTL-T5), Wolo Wawo Tephra (WLW), Wolo Sege Ignimbrite (WSI), Turekeo Ignimbrite (TRI), Kopowatu Tephra (KPW) and Pumaso Tephra (PMS). The field characteristics and textures of the volcaniclastic deposits indicate pyroclastic density current (PDC) deposits, except TTL, WLW and KPW, which are considered to be distal pyroclastic fall deposits (facies Tm). The volcaniclastic deposits commonly cover palaeosol deposits, and the reworking material (FA–II) has occurred following the emplacement of the Wolo Sege Ignimbrite and the Turekeo Ignimbrite.

The lahar deposits (FA–IV) constitute tuffaceous siltstone (facies Fmm) and tuffaceous sandstone (Smm). This facies association is well-developed in the western part of the basin, and is significantly associated with channel deposits. The latter consist of conglomerates (facies Gl and Gm), well cemented sandstone (Scm), stratified sandstone (Sl) and cross stratified pebbly sandstone (Ss). The floodplain deposits (FA–VII) refer to massive silty claystone (facies Fm), which has a localised occurrence in the western part of the basin.

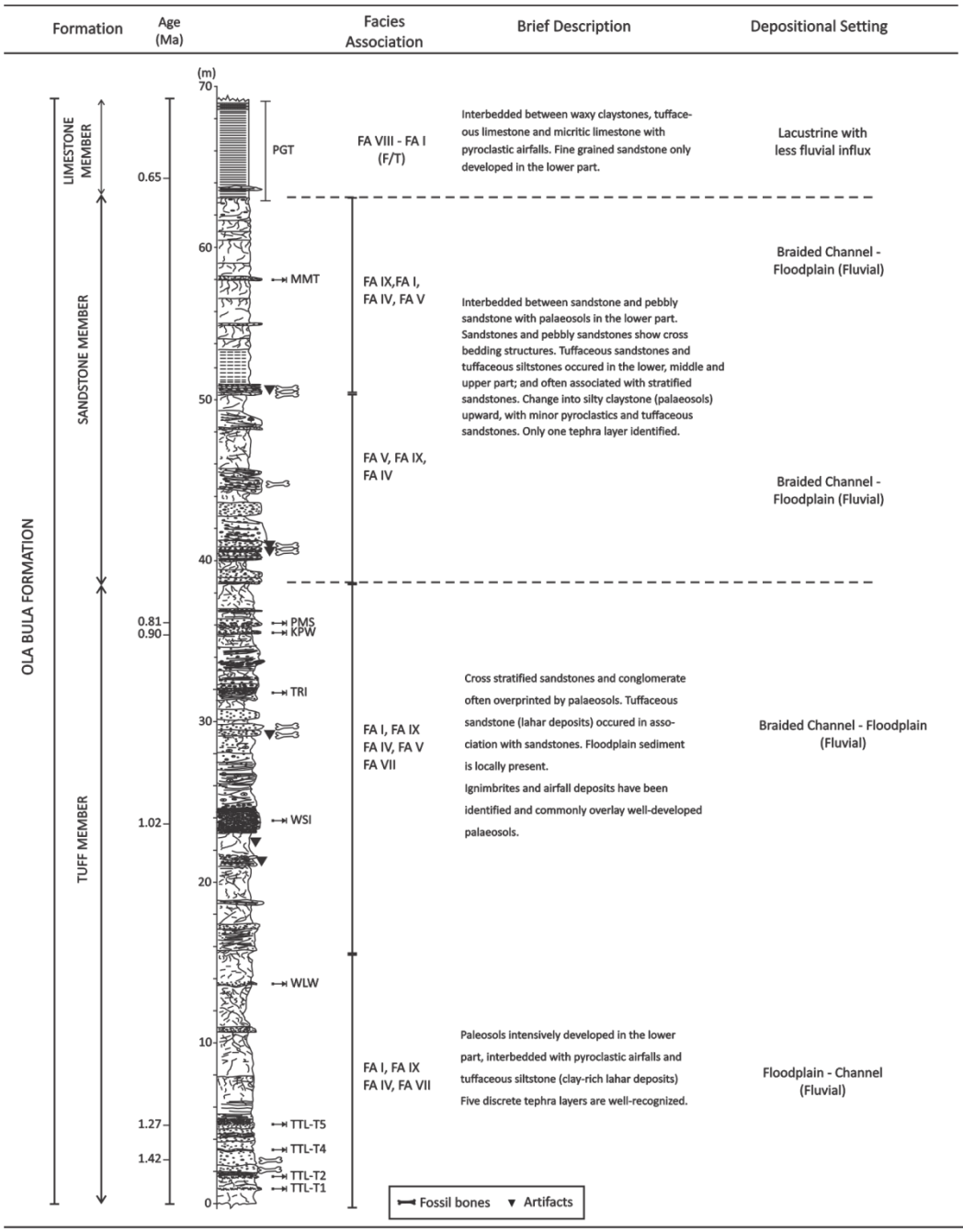

Figure 6.12. The general composite stratigraphy of the Ola Bula sequence of the Soa Basin based on lithological descriptions and sections mentioned in this chapter and Appendix 1. The position of primary tephra layers, stone artefacts and fossil remains are also shown.

6.4.3. The Sandstone Member of the Ola Bula Formation

The Sandstone Member conformably overlies the Tuff Member but there is no sharp transition between the two members. For convenience, we place the boundary between the two members at the top of the Turekeo Ignimbrite (TRI), or at the top of redeposited TRI (FA–II). This member predominantly consists of channel deposits (FA–V) and palaeosols (FA–IX), with minor pyroclastic deposits (FA–I), lahars (FA–IV), sheet flood (FA–VI) and floodplain (FA–VII). Palaeosols are intensively developed upwards in the sequence. The channel deposits comprise conglomerates (Gl), stratified sandstone (Sl), cross stratified pebbly sandstone (Ss) and occasionally well cemented sandstone (Scm). The lahar deposits correspond to tuffaceous siltstone (Fmm) and tuffaceous sandstone (Smm), while the sheet flood deposits are represented by massive sandstone (Sm).

The Sandstone Member is well-exposed at Gero in the east, and Mata Menge in the west. At Gero, the upper part of this member comprises alternating channel deposits (facies Gl) and lahar deposits (facies Fmm and Smm). At Mata Menge, the uppermost part of this sequence is predominantly composed of palaeosols. There is only one pyroclastic deposit occurring in the middle of the sequence, which has been identified as pyroclastic fall deposits (facies Tm) and subsequently formally named the Mata Menge Tephra (MMT). The total thickness of this Sandstone Member is ~20–30 m.

6.4.4. The Limestone Member of the Ola Bula Formation

Previous research has noted that the Limestone Member consists of micritic limestone (Hartono 1961; Suminto *et al*., 2009). In addition to this observation, this study also recognises that this member comprises an interbedding of limestone (facies Lm), horizontal claystone (facies Fh) and pyroclastic deposits (facies Tm), which were deposited in a lacustrine environment (FA–VIII). The individual lacustrine deposits vary in thickness between 2–30 cm, while the thickness of volcaniclastic deposits ranges from 2

mm to 12 cm. The volcaniclastic materials are identified as pyroclastic air-fall deposits (facies Tm), which exhibit basaltic to rhyolitic compositions and may indicate different sources. The Limestone Member conformably (uniformly) overlies the underlying unit of the Sandstone Member, and has a thickness of up to 10 m.

6.4.5. Artefacts and fossil-bearing layers

Stone tools and fossil remains have been found exclusively in the top of the Tuff Member and throughout the Sandstone Member of the Ola Bula Formation, and are absent from the Ola Kile Formation and the Limestone Member of the Ola Bula Formation. In the Tuff Member, fossil bones are accumulated within lahar deposits and occur in a channel fill, while stone artefacts are incorporated within the channel deposits (conglomerate), lahars and palaeosols, with their oldest occurrence directly below the WSI. The only fossil accumulations documented are at the Tangi Talo site, and these include pygmy stegodon, giant turtle, crocodile, and Komodo dragon (Sondaar *et al*., 1994; van den Bergh, 1999; Aziz *et al*., 2009). These fossil-bearing layers are described as tuffaceous siltstones, which in fact represent clay-rich diamictons (lahar deposits). The Tangi Talo fossil layer is 16 m below the 1 Ma old Wolo Sege Ignimbrite, and thus must be older than the ~0.9 Ma it was initially assumed to be based on Zircon Fission Track ages published in Morwood *et al.*, (1998) and O'Sullivan *et al.*, (2001). An unpublished single crystal K-feldspar argon-argon age of ~1.27 is now available for TTL-T5, which is 2 m above the fossil bed (Flude, pers.comm.), thus supporting the age in excess of 1 Ma for the Tangi Talo fauna. This surprisingly pushes back the timing of the faunal turnover in the Soa Basin, which had been previously thought to have occurred at ~900 ka (Morwood *et al*., 1997, 1998; van den Bergh, 1999; Morwood *et al*., 2009).

Large assemblages of artefacts and fossil bones have also accumulated in the lahar deposits at the Mata Menge site. Excavation at the Wolo Sege site recovered stone tools, which are concentrated by reworking in

the channel fills (conglomerate), and other *in situ* artefacts occur in the siltstones overprinted by palaeosols above the conglomerate (Brumm *et al*., 2010; this study). The artefact bearing layers are capped by Wolo Sege Ignimbrite (WSI), which is dated at 1.02 Ma using the argon-argon technique on hornblende crystals (Brumm *et al*., 2010). Moreover, few stone tools were also preserved in the palaeosols underlying the WSI at Matago and excavation at Kobatuwa-4 (unpublished data). This indicates that hominins occupied the Soa Basin by one million years ago.

Fossil bones and stone artefacts are randomly distributed within the Sandstone Member. Large concentrations have been recovered in the lower part, while fewer assemblages have been excavated from the middle and top intervals of the sandstone member. The best example of this comes from the Mata Menge site, where thousands of fossil bones and stone tools have been recovered from the lowermost part of the Sandstone Member during the 2010-2014 excavations. Zircon fission track dating yielded an age of between 880 and 800 ka for the main artefact and fossil-bearing interval at Mata Menge (O'Sullivan *et al*., 2001). However, this research suggests that the fossil layers should be considered younger than 800 ka, based on relative positions of fossil layers compared to the stratigraphic levels of WSI, PMS and PGT-02 (see Figure 6.12), and supported by palaeomagnetic data (Yurnaldi *et al*., 2018). In the middle part of the Sandstone Member, large abundance of vertebrate remains, including hominin fossils, are also preserved within a sandstone layer (channel deposits) and lahar deposits at a level 12 m below PGT-02. The Limestone Member has not yielded any vertebrate remains, but this lacustrine interval may document a valuable record of climatic parameters and local and interregional volcanic activity during the Middle Pleistocene.

6.5. Depositional History

6.5.1. pre-Stage 1

The initial environmental condition of the Soa Basin was dominated by fluvial settings as indicated by the presence of braided channel systems. Numerous effusive phases of volcanic activity produced lava flows that were deposited in subaerial environments during the Late Pliocene (~2.96 Ma; Muraoka *et al*., 2002). O'Sullivan *et al*. (2001) also reported a FT age of 1.86 Ma for a tuff layer occurring at the top of the Ola Kile Formation. This therefore indicates that the early step of basin deposition occurred from the Late Pliocene to Early Pleistocene.

The braided river systems are overprinted by prominent palaeosols that are subsequently developed when erosion or sedimentation induced by hyperconcentrated or stream flows are minimal. The characteristic of the palaeosols suggests overall dry conditions.

6.5.2. Stage 1: the Ola Kile Formation

A huge explosive volcanic eruption occurred at ~2.52 Ma, sourced probably from the Welas volcano in the northern part of the Basin (Muraoka *et al*., 2000, 2002; Nasution *et al*., 2000). This explosive event generated voluminous pyroclastic deposits and remained as a 9 km x 18 km caldera, which has been named the Welas Caldera Complex. This sudden deposition of pyroclastic density current materials implies a levelling of a pre-existing topography created by volcanic edifices and fault systems. The welded Aesessa Ignimbrite (AEI) covered prominent palaeosols, and this indicates that the volcanic products covered the pre-existing stable palaeosurface. Environmental changes occurred after caldera forming processes, including the development of lacustrine environments within the Welas Caldera Complex.

After the cessation of volcanic activity, sudden volcaniclastic inputs generated clay-rich mudflow, debris and hyperconcentrated flow deposits that were emplaced throughout the basin. Palaeosols and/or pedogenically

altered sediments subsequently developed again, representing a sedimentation hiatus. A major eruption produced the Lowo Mali Ignimbrite (LMI) overlaying the palaeo-landscape. The climate changed into a wet season with heavy rainfalls, which generated lahar deposits, carrying lava and volcaniclastic debris derived from the neighbouring volcanic highlands. Zircon fission track dating suggests that these lahar deposits occurred until 1.86 Ma (Morwood *et al*., 1998; O'Sullivan *et al*., 2001). The deposition of diamictons was then followed by active tectonic events, developing W-E and NE-SW trending normal fault segments. The tectonic forces also tilted the basin floor in a S-SW direction. These inferred normal faults systems were probably the main factors in the formation of multiple depocentres or sub-basins, such as in the western, middle and eastern part of the Soa Basin. On the other hand, major erosional processes during a prolonged period of volcanic quiescence preceding the LMI were also responsible for creating the basin topography. The stratigraphic sequence and the lower elevation of the Tangi Talo section suggest that this area was the deepest depocentre, displaying the morphology of a palaeovalley system and accommodating the early stages of sediment accumulation in the basin. The individual sub-basins were then filled by primary volcaniclastic deposits (FA–I), localised effusive bodies (FA–III), lahar deposits (FA–IV), channel deposits (FA–V), and palaeosols (FA–IX).

Sedimentation fluctuated with abrupt pulses of volcanic inputs triggered by eruptive events causing rapid accumulation, followed by periods of intense reworking levelling the topography and reaching a landscape stability as indicated by the development of soil formation.

6.5.3. Stage 2: the Tuff Member of the Ola Bula Formation

After a period of low volcanic activity, when palaeosols and channel deposits became the dominant facies association, volcanism was reactivated resulting in intermittent silicic pyroclastic fall deposits (facies Tm) at *ca*. 1.86–1.27 Ma by the deposition of the Tangi Talo Tephra (TTL-T1, TTL-T2,

TTL-T4 and TTL-T5). Following the deposition of TTL-T5, the basin is likely to have been in a comparatively stable condition, during which thick-multi layers of palaeosols developed upwards. Multi-eruptive phases generated silicic pyroclastic deposits, including the Wolo Wawo Tephra (WLW), Wolo Sege Ignimbrite (WSI), Turekeo Ignimbrite (TRI), Kopowatu Tephra (KPW) and Pumaso Tephra (PMS), which occurred from ~1.20 Ma to 0.81 Ma. The WSI represents the first large explosive event that resulted in the generation of a widespread marker bed at ~1.02 Ma, which also deposited and preserved in the higher reaches of the basin. Each eruptive event was separated by a pause when the accumulation of channel, laharic and palaeosol deposits prevailed. The occurrence of cross- stratified sandstone with intensive cut-and-fill structures (at the Tangi Talo section) suggest that a catastrophic flood occurred in this place after the deposition of WLW. The sandstone is overlain by thick palaeosols, suggesting no eruptions and/or sediment accumulation.

Inter-eruption episodes continued after the emplacement of WSI, accumulating pyroclastic deposits of TRI, KPW and PMS, which occurred from ~1.0 Ma to 0.81 Ma. A depositional hiatus then interrupted these eruptive stages, and followed by the development of a relatively stable palaeolandscape. At three localities, Wolo Sege, Kobatuwa and Matago, the WSI is underlain by stone tool assemblages.

The chronological data and the presence of key volcanic beds such as TTL-T5, WSI, TRI, KPW and PMS, suggest that Stage 2 occurred between ~1.86 Ma and 0.81 Ma (Early Pleistocene). Fission track dating from near the top of the Tuff Member yields a maximum depositional age of 0.88 Ma (O'Sullivan *et al*., 2001; Suminto *et al*., 2009). However, evidence from Mata Menge section, where the fossil bearing layers truncate PMS suggests a younger age and that it is more likely that the deposition of the Tuff Member ceased at ~0.80 Ma.

6.5.4. Stage 3: the Sandstone Member of the Ola Bula Formation

The Sandstone Member consists predominantly of inter-eruption deposits, indicating that a period of volcanic quiescence occurred. During this stage, the Soa Basin was dominated by fluvial environments, particularly braided channel systems. During the early period, the climate was likely strongly seasonal, developing braided channels and generating mudflows. The strong seasonality with dry and wet seasons probably tended to shift, which is indicated by the interbedding of fluvial sandstone and palaeosols.

In the western and middle part of the basin, the channel subsequently terminated and multi-stacked palaeosols developed, while the braided system still continue to develop in the east. After long periods without or with only limited volcanic activity, estimated to have lasted ~100 ka, an explosive eruption produced an andesitic pyroclastic fall deposit, known as the Mata Menge Tephra (MMT), which blanketed the entire basin. Volcanism then ceased once more and allowed the accumulation of laharic and channel deposits as well as palaeosol development.

The previous fission track ages indicate that this stage occurred at ~0.88–0.68 Ma (O'Sullivan *et al*., 2001; Suminto *et al*., 2009). Based on the tephrostratigraphic framework, the Sandstone Member is bracketed by two prominent pyroclastic layers, i.e. PMS and PGT. Considering positions of those volcanic markers and new Ar/Ar ages, it can be concluded that the Sandstone Member (Stage 3) were deposited at ~0.80–0.65 Ma ago.

6.5.5. Stage 4: the Limestone Member of the Ola Bula Formation

During this stage, a combination of climatic change and tectonic processes probably took place, changing the depositional setting from a fluvial to a lacustrine environment. Evidence from the Mata Menge, Pumaso and Gero sequences suggest that the lacustrine facies overlies a palaeosol. These indicate a climatic change to wetter conditions and subsequently the isolated or inter connected sub-basins changed into a single lake. On the other hand, blocking the

main outlet in the northeastern part of the basin by resedimented volcaniclastics, lava flows or lahars could also trigger the development of lacustrine environments. The diatom and pollen records indicate shallow lacustrine environments.

Inter eruptive events occurred commonly, and exhibit alternating clastic sediments (facies Fh and Lm) and pyrocalstic fall deposits (facies Tm). The pyroclastic fall deposits formally referred to as the Piga Tephra (PGT) show a variation in composition from basalt to dacite. In total 58 layers can be recognised evenly distributed within the Limestone Member, indicating that volcanic activities remained prevalent. The source of the multiple Piga Tephra is still not clear, but younger domes inside the Welas Caldera and Bajawa Cinder Cone Complex are likely candidates, in particular with regard to the basaltic tephras. As a crater lake was present in the caldera at this time, basaltic eruption from these centres may have become explosive leading to widely distributed airfall deposits.

Zircon fission track dates for samples from the Limestone Member initially indicated that this stage developed between 0.68 and 0.65 Ma (O'Sullivan *et al*., 2001). The new hornblende argon-argon age of 0.65 Ma for PGT-02, taken from the basal part of the lacustrine sequence, is in agreement with the ZFT ages, and places the commencing time for the development of the lake phase at ~0.65 Ma. Ultimately, it can be concluded that the deposition of the Limestone Member (Stage 4) began at ~0.65 Ma ago.

6.6. Summary

This chapter has described the application of lithostratigraphy and tephrostratigraphy, combined with argon-argon dating and by adding fission track dating (glass, zircon), which provide the general chronological framework of the Soa Basin. This study also involves the application of lithofacies analyses for understanding the sedimentation processes and palaeoenvironmental settings, and to identify the spatial and temporal distribution of the artefact-and

fossil-bearing layers. Furthermore, by applying these various approaches, this study contributes to the refinement of the stratigraphical framework of the Soa Basin.

As highlighted above, the Soa Basin preserves large assemblages of stone artefacts and fossil remains. Sedimentological and stratigraphical approaches have enabled an understanding of the transformation processes of the archaeological and palaeontological materials. The basin-wide distributions of several volcaniclastic deposits play a significant part in facilitating intra–basinal correlation and linking some key archaeological and palaeontological sites.

CHAPTER SEVEN

FACIES COMPOSITION: IMPLICATIONS FOR PALAEO-WEATHERING, PROVENANCE AND PALAEOCLIMATE

7.1. Introduction

In the Chapter 6, I have outlined facies types of the Soa Basin sequence, their field characteristics, and their spatial and temporal distributions. This study combines the sedimentary facies architectures and analytical techniques on sedimentary rocks in terms of geochemical and mineralogical compositions, in order to understand the palaeoenvironment and palaeoclimatic conditions during deposition.

In this chapter, I highlight the geochemical signatures of volcaniclastic deposits and sedimentary rocks of the Ola Bula Formation. The geochemical signatures on individual facies associations are determined by whole-rock XRF analysis. The raw geochemical data are listed in Appendix 2. The mineral assemblages were determined by XRD analysis on whole-rock samples and the results are summarised in Appendix 4. The mineral identifications were used to support the XRF analyses and establish the provenance of the sedimentary rocks and possible fluctuations in source materials in the Soa Basin during the Early and Middle Pleistocene. It must be noted, however, that the XRD analyses, in particular those of the clay minerals, should be considered as tentative, since no additional tests have been performed to verify the presence of certain clay minerals. In addition, considering the frequent occurrence of pumice fragments in reworked sediments, it is assumed that a significant proportion of the clay fraction may consist of amorphous glass, which cannot be detected by XRD. It is also not possible to distinguish halloysite from kaolinite without additional tests (Churchman and Lowe, 2012; Churchman *et al.*, 2016), and therefore the possible presence of these two clay mineral is reported as

'halloysite/kaolinite'. Another clay mineral that is likely to be present in the Soa Basin but can not be detected by XRD is allophane, a nanocrystalline mineral that tends to form in well-drained tephra deposits (Parfitt *et al*., 1984; Singleton *et al*., 1989).

The chapter commences with the detailed descriptions of geochemical characteristics from individual facies associations in all stratigraphic units of the Ola Bula Formation, starting from the oldest unit (the Tuff Member) towards the youngest unit (the Limestone Member). Factors controlling the variation of geochemical characteristics in the studied samples are also discussed.

7.2. Geochemical Composition

The geochemical data for whole-rock analysis are summarised in Appendix 2. The major-element composition used in this section has been normalised to 100 %. The major-and trace element compositions of lithofacies associations from the Ola Bula Formation will be discussed below.

7.2.1. Lahar Deposits (Facies Association IV/FA–IV)

A. Major elements and mineralogy

In general, the major-oxide values of lahar deposits display narrow ranges in samples of the Tuff Member (TM) and the Sandstone Member (SM). The analysed samples from the TM have relatively higher mean values of SiO_2 (62 wt%), Al_2O_3 (22.60 wt%), TiO_2 (0.85 wt%), K_2O (0.61 wt%) and P_2O_5 (0.11 wt%). The average compositions of ΣFe_2O_3 (8.26 wt%), MnO (0.15 wt%), MgO (2.02 wt%), CaO (7.06 wt%) and Na_2O (1.95 wt%) are much more abundant in samples of the SM.

The lahar deposits predominantly contain plagioclase and clay minerals. Quartz, micas, amphibole, pyroxene and iron oxides are present in small amounts. Interestingly, hematite is only present in the TM, whereas maghemite only occurs in the SM.

In order to recognise the chemical characteristics of the studied sediments, the mean values of major oxides were normalised to the post-Archean Australian Shale (PAAS) composition (Figure 7.1A). Lahar deposits of the TM and SM have nearly similar values with PAAS regarding SiO_2, Al_2O_3 and ΣFe_2O_3 contents. The majority of analysed samples exhibit slight enrichments of Al_2O_3 and CaO. The analysed samples are depleted in TiO_2, MgO, K_2O and P_2O_5. Samples of the TM and SM show opposite trends in MnO and Na_2O; these oxides are enriched in samples of the SM.

Elemental ratios of lahar deposits in all stratigraphic units are outlined in Table 7.1. The major-element ratios display small variation in all samples. The ratios of TiO_2/Al_2O_3, $\Sigma Fe_2O_3/Al_2O_3$ and Na_2O/Al_2O_3 are nearly similar with PAAS. Moreover, SiO_2/Al_2O_3, K_2O/Al_2O_3 and K_2O/Na_2O in the studied samples are lower than PAAS, while in contrast, the CaO/Al_2O_3 ratio is higher than PAAS.

B. Trace elements

The proportions of large ion lithopile elements (LILE; Rb, Ba, Sr, Th, U), high field strength elements (HFSE; Y, Zr, Nb, Hf, Ta, Pb), transition trace elements (TTE; V, Zn) and light rare earth elements (LREE; La, Ce) in lahar deposits from the TM and SM demonstrate small variations. Samples of the TM have the highest mean values of V (348 ppm), Zn (81 ppm), Zr (81 ppm) and Rb (30 ppm), while samples of the SM display greater average contents of Sr (267 ppm) and Ba (249 ppm). The concentrations of other elements in both units are nearly similar.

Compared to PAAS (Figure 7.1B), all samples display slight depletions of Zn, Y, Zr, Ce, Hf, Pb and U; and strong depletions of Rb, Nb and Th contents. The V, Sr and Ta values in the analysed samples are nearly similar with PAAS. In addition, the ratios of Sr/Rb, Sr/Ba, Zr/Rb, La/Th, and La/Rb in most samples are higher than in PAAS, while Th/U is lower than PAAS. Samples of the

TM show higher Sr/Rb and Th/U ratios relative to samples of the SM, the other trace-element ratios in all units exhibit narrow ranges.

7.2.2. Channel and sheetflood deposits (Facies Association V and VI/FA–V and FA–VI)

A. Major elements and mineralogy

The major-element composition of sandstones (FA–V and FA–VI) in all stratigraphic units displays small variations (Appendix 2). After the major-element values have been normalised to 100 %, sandstones of the TM have relatively higher mean values of SiO_2 (59.4 wt%), TiO_2 (1.10 wt%) and ΣFe_2O_3 (9.63 wt%). The Al_2O_3 and P_2O_5 contents are more abundant in the LM (25.36 wt% and 0.19 wt% respectively). Fluvial sandstones (FA–V) of the SM have the highest contents of MnO (0.22 wt%), MgO (3.30 wt%) and K_2O (0.82 wt%). Massive sandstones (FA–VI) of the SM have the highest CaO (7.78 wt%) and Na_2O (2.05 wt%) contents.

Based on XRD analysis, the mineral assemblages of the fluvial sandstones of the Tuff Member (TM) predominantly contain from most to less abundant: plagioclase, zeolites, I/S, halloysite/kaolinite, S/C, quartz and amphibole. Plagioclase tends to be even more abundant in the sandstones from the Sandstone Member (SM), which also tends to contain small amounts of pyroxene.

XRD analysis of fluvial sandstone samples of the TM display the greatest contents of quartz, amphibole, iron oxide minerals and S/C. Sandstones of the SM have the highest abundance of plagioclase and pyroxene. In contrast, halloysite/kaolinite, I/S and zeolites show the highest proportions in sandstones of the LM compared to the other units. K-feldspar was only detected in the SM and LM; while mica, amphibole and pyroxene are absent in the LM. Quartz and iron oxides are commonly present in low amounts. Kaolinite has a less abundance and displays little variation in all the samples.

Massive sandstones of FA–VI generally have similar mineral compositions as the fluvial sandstones of FA–V. FA–VI is only found in the Sandstone Member (SM). This sandstone is predominantly composed of plagioclase, followed by zeolites, halloysite/kaolinite, illite-smectite, amphibole, and smectite-chlorite. In addition, traces of quartz, pyroxene, iron oxide minerals and kaolinite are present.

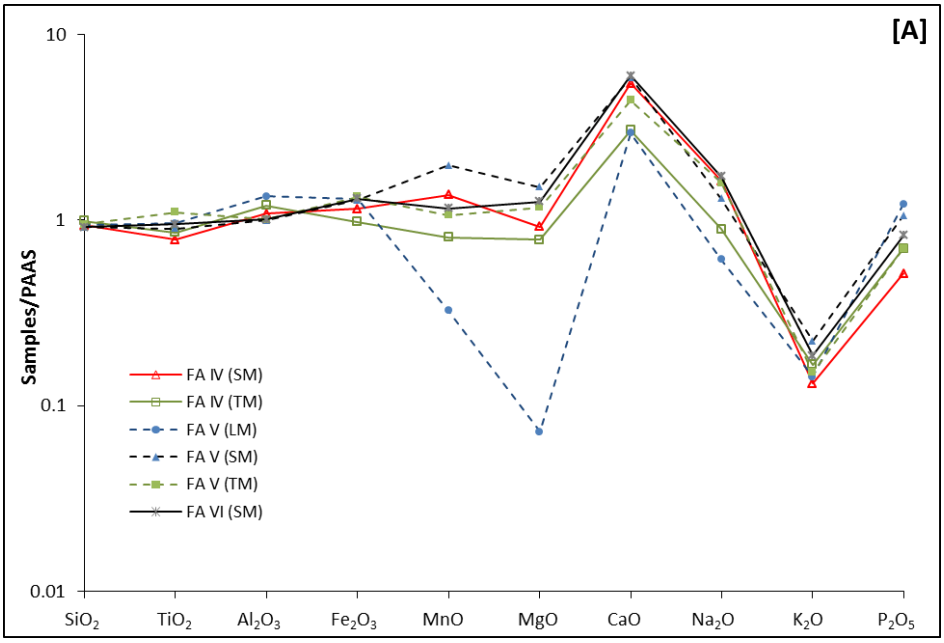

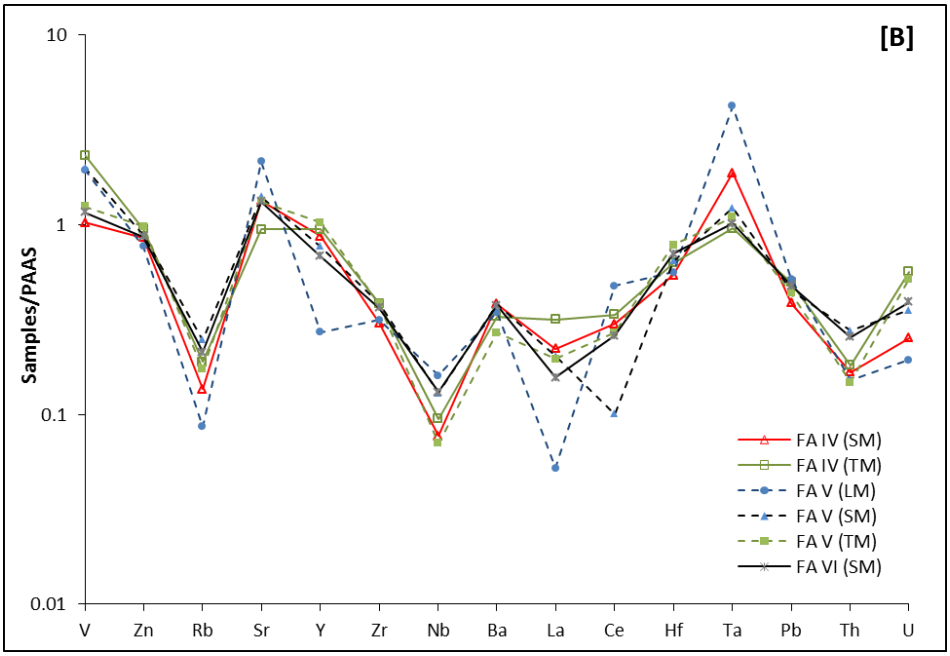

Figure 7.1. (A) The major-element composition of lahar (FA-IV), channel (FA-V) and sheetflood (FA-VI) deposits from the Tuff, Sandstone and Limestone Members, normalised to PAAS (Taylor and McLennan, 1985). The major-element values have been recalculated to 100 %. (B) The variation of selected trace-element composition of whole-rock samples from individual facies associations normalised to PAAS (Taylor and McLennan, 1985; and Barth *et al*. (2000) for Na, La and Ta values).

Compared to PAAS, all sandstones display enrichments of CaO, slight enrichment of ΣFe_2O_3 and depletions of K_2O (Figure 7.1A). The contents of SiO_2, TiO_2 and Al_2O_3 are nearly similar with PAAS. Samples of the LM show distinctive patterns with depletions of MnO, MgO and Na_2O, while in contrast these elements are enriched in all other samples form different facies associations. Moreover, samples of FA–V from the SM and LM are enriched in P_2O_5, while this element is depleted in samples of FA–V and FA–VI from the TM and SM, respectively.

Table 7.1. Average elemental ratios of the various facies associations from three members of the Ola Bula Formation (Tuff, Sandstone and Limestone Members). Elemental ratios of a single palaeosol (FA–IX) from the Ola Kile Formation and PAAS are also listed for comparison. The PAAS composition is from Taylor and McLennan (1985) and Barth *et al*. (2000) for the La content.

	FA IV		FA V			FA VI	FA VII	FA VIII			FA IX			PAAS
	Fmm, Smm		Sl, Scl	Sl, Ss, Scl	Sh	Sm	Fm	Fh		Lm	P			
Unit	**TM**	**SM**	**TM**	**SM**	**LM**	**SM**	**TM**	**SM**	**LM**	**LM**	**TM**	**SM**	**OK**	
SiO_2/Al_2O_3	2.74	2.88	3.13	3.06	2.32	3.02	3.87	3.07	3.04	3.11	3.35	3.05	6.17	3.32
TiO_2/Al_2O_3	0.04	0.04	0.06	0.05	0.04	0.05	0.03	0.04	0.04	0.04	0.04	0.04	0.04	0.05
$\Sigma Fe_2O_3/Al_2O_3$	0.31	0.40	0.51	0.49	0.37	0.49	0.29	0.35	0.42	0.47	0.34	0.45	0.49	0.38
CaO/Al_2O_3	0.17	0.35	0.30	0.40	0.15	0.41	0.14	0.26	0.59	8.29	0.14	0.38	0.17	0.07
Na_2O/Al_2O_3	0.05	0.10	0.10	0.08	0.03	0.11	0.06	0.05	0.04	0.26	0.05	0.06	0.06	0.06
K_2O/Al_2O_3	0.03	0.02	0.03	0.04	0.02	0.04	0.03	0.02	0.02	0.02	0.04	0.02	0.02	0.20
K_2O/Na_2O	0.57	0.25	0.29	0.53	0.72	0.33	0.47	0.34	0.47	0.09	0.75	0.29	0.35	3.08
Sr/Rb	6.23	12.26	9.56	7.11	31.09	7.78	4.26	5.89	9.88	13.04	4.67	7.25	8.01	1.25
Sr/Ba	0.88	1.07	1.51	1.13	1.91	1.08	0.93	1.25	0.90	0.69	0.73	0.88	0.52	0.31
Zr/Rb	2.68	2.92	2.90	2.06	4.79	2.26	3.33	2.26	3.55	3.16	2.62	2.94	3.41	1.31
La/Th	4.58	3.51	3.49	1.93	0.91	1.61	4.97	2.79	3.90	3.50	3.26	3.03	5.00	2.63
La/Rb	0.40	0.39	0.27	0.20	0.14	0.18	0.74	0.22	0.41	0.98	0.41	0.34	0.14	0.24
Th/U	1.52	3.11	1.34	3.67	3.67	3.08	4.62	4.20	1.30	0.81	3.53	3.46	0.40	4.71
CIA	75-93	65-83	69-90	76-94	91	72-77	84	84-88	67-99	44-68	61-100	76-99	83	72
PIA	76-94	66-85	70-92	77-95	92	74-78	85	85-90	68-100	43-69	64-100	77-100	84	82

Note. The Fe content is expressed as ΣFe_2O_3; n.d.=not determined; CIA=Chemical Index Alteration; PIA=Plagioclase Index Alteration; LM=Limestone Member; SM=Sandstone Member; TM=Tuff Member; OK=Ola Kile Formation. The major-element ratios use the normalised values (recalculated to 100%).

Major-oxide ratios (Table 7.1) indicate that the analysed samples show insignificant differences and the ratio of TiO_2/Al_2O_3 and Na_2O/Al_2O_3 are nearly similar with PAAS. All sandstones have identical ratios of TiO_2/Al_2O_3 and K_2O/Al_2O_3. Regarding SiO_2/Al_2O_3, $\Sigma Fe_2O_3/Al_2O_3$, CaO/Al_2O_3 and Na_2O/Al_2O_3 ratios, sandstones of the TM and SM have similar ratios, while sandstone of the LM exhibits the lowest ratios. In addition, samples of the LM demonstrate the highest K_2O/Na_2O. Moreover, all samples have lower SiO_2/Al_2O_3, $\Sigma Fe_2O_3/Al_2O_3$, K_2O/Al_2O_3 and K_2O/Na_2O ratios relative to PAAS, while CaO/Al_2O_3 and Na_2O/Al_2O_3 in the analysed samples are higher than PAAS.

B. Trace elements

The trace-element concentration of sandstones in all units displays small variations (Appendix 2). Samples of the TM have the greatest average values of Zn (298 ppm), Y (298 ppm) and Zr (298 ppm). Sandstones of FA–V from the SM have highest values of V (298 ppm), Rb (298 ppm), Zr (298 ppm), Ba (298 ppm) and Th (298 ppm), while Zn and Y are more abundant in the TM samples (83 ppm and 28 ppm, respectively). The sandstones of FA V from the TM have greatest Rb and Ba (39 ppm and 247 ppm); and the highest Sr and Ce contents (429 ppm and 38 ppm) can be found in sandstone of the LM. The concentrations of Nb, La, Hf, Ta, Pb, and U in all samples show narrow ranges.

The PAAS normalised diagram (Figure 7.1B) indicates that most samples have slight enrichments of V and Sr, and depletions of Zn, Rb, Zr, Nb, Ba, La, Ce, Hf, Pb, Th and U. Sandstones of the TM are strongly depleted in Nb, and sandstone of the LM is strongly depleted in La. Regarding the Y content, sandstones of the TM have similar values with PAAS, while the other sandstones are depleted compared to PAAS. The analysed samples from the TM and SM have nearly similar Ta contents, while this element is slightly enriched in samples of the LM.

The trace-element ratios (Table 7.1) suggest that some ratios are greater than PAAS, such as Sr/Rb, Sr/Ba and Zr/Rb. By contrast, the Th/U ratio is

lower than PAAS. The ratio of Sr/Rb in fluvial sandstone of the LM displays significantly the highest ratio compared to other samples and PAAS. Concerning La/Th and La/Rb ratios, these ratios in samples of the TM are greater than PAAS, while the other samples are lower than PAAS. Samples of the TM displays the highest Zr/Rb compared to other units, and fluvial sandstones of the SM and LM show the greatest Th/U ratio.

7.2.3. Floodplain deposit (Facies Association VII/FA–VII)

A. Major elements and mineralogy

Floodplain sediments have relatively high concentration of SiO_2, moderate value of Al_2O_3 and low values of TiO_2, Fe_2O_3, MgO, MnO, CaO, Na_2O, K_2O and P_2O_5 (Table 7.1). Compared to PAAS, the analysed samples display nearly similar values in SiO_2, Al_2O_3 and MgO, and a slight enrichment of CaO, depletions of TiO_2, ΣFe_2O_3, MnO, Na_2O, and P_2O_5, and a strong depletion of K_2O (Figure 7.2A). Moreover, major-oxide ratios (Table 7.1) reveal that this sediment has higher SiO_2/Al_2O_3 and CaO/Al_2O_3, and lower $\Sigma Fe_2O_3/Al_2O_3$, K_2O/Al_2O_3 and K_2O/Na_2O ratios relative to PAAS. The ratios of TiO_2/Al_2O_3 and Na_2O/Al_2O_3 are similar to PAAS.

Only one sample of floodplain claystone from the Tuff Member (TM) was analysed with XRD. It predominantly contains illite-smectite and zeolites. Smectite-chlorite and halloysite/kaolinite are present in moderate concentrations, while trace amounts of plagioclase, quartz, mica, amphibole, maghemite and kaolinite were detected. K-feldspar, amphibole and pyroxene were not detected.

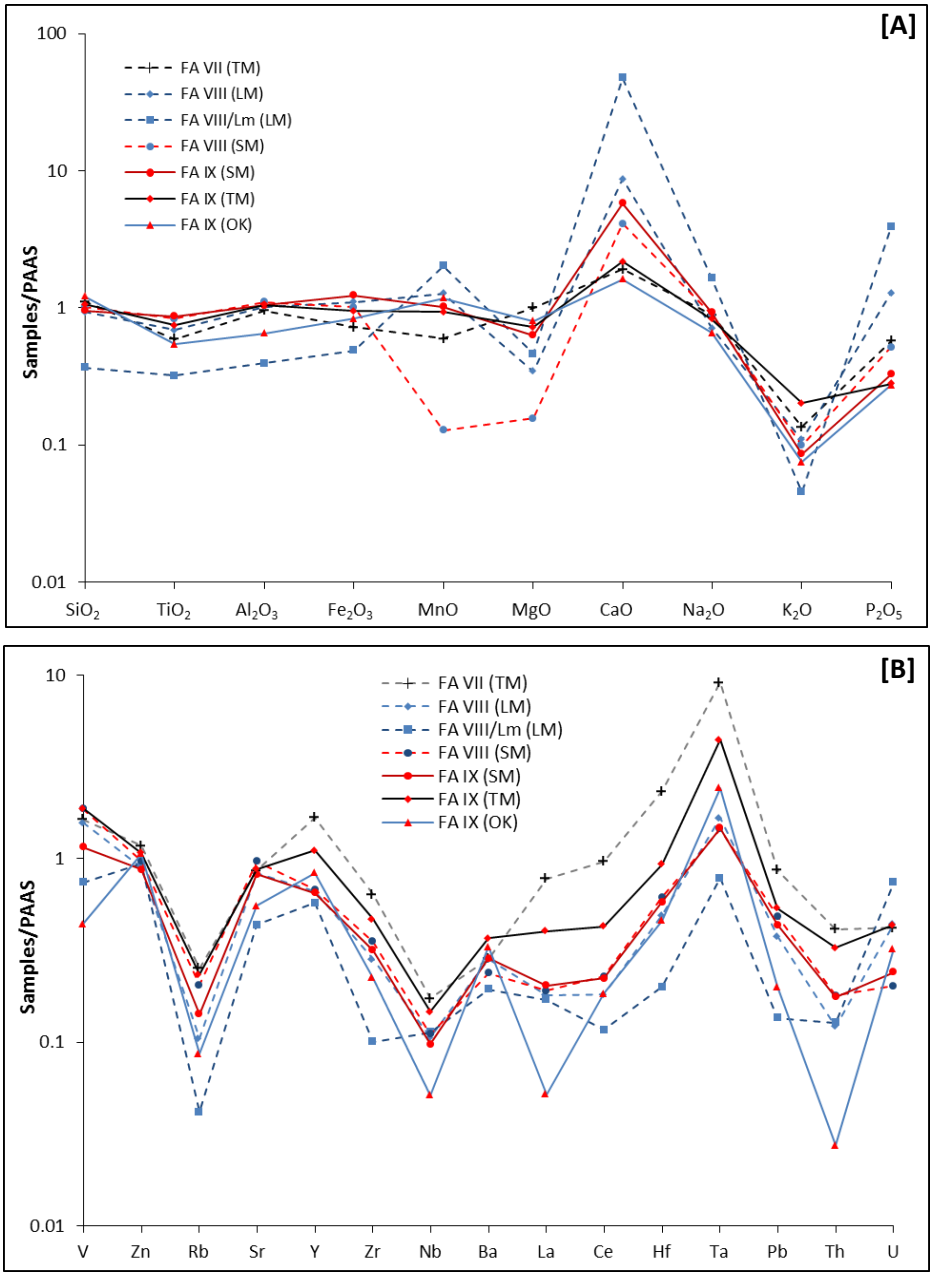

Figure 7.2. (A) The major-element composition of floodplain (FA-VII) and lacustrine (FA-VIII) deposits, and palaeosol (FA-IX) deposits from the Tuff, Sandstone and Limestone Members, and one sample of palaeosol (FA-IX) from the Ola Kile Formation, normalised to PAAS (Taylor and McLennan, 1985). The major-element values have been recalculated to 100 %. (B) The variation of selected trace-element composition of whole-rock samples from individual facies associations normalised to PAAS (Taylor and McLennan, 1985; and Barth *et al.* (2000) for Na, La and Ta values).

B. Trace elements

The trace-element concentration of floodplain sediment shows enrichments of Hf and Ta, depletions of Rb, Sr, Zr, Nb, Ba, La, Pb, Th, while the contents of and V, Zn, Y and Ce are nearly similar with PAAS. Compared to PAAS, this sediment has higher ratios of Sr/Rb, Sr/Ba, Zr/Rb, La/Th and La/Rb, and lower Th/U ratio (Figure 7.2B).

7.2.4. Lacustrine deposit (Facies Association VIII/FA–VIII)

A. Major elements and mineralogy

The chemical composition of lacustrine sediments with respect to facies Fh in the SM and LM shows small differences, with the exception of SiO_2 and CaO (Table 7.1). Claystones of the SM have higher average values of SiO_2 (63.9 wt%), TiO_2 (0.83 wt%) and Al_2O_3 (20.79 wt%); while claystone samples of the LM display greater contents in ΣFe_2O_3 (7.99 wt%) and K_2O (0.44 wt%). Tuffaceous limestone (Lm) of the LM has higher MnO (0.22 wt%), MgO (1.01 wt%), CaO (61.64 wt%), Na_2O (1.96 wt%) and P_2O_5 (0.62 wt%) contents as compared to claystone samples.

The PAAS normalised diagram (Figure 7.2A) suggests that claystones of the SM and LM have nearly similar values with PAAS regarding the contents of SiO_2, Al_2O_3 and ΣFe_2O_3. The analysed samples are enriched in CaO, depleted in TiO_2, MgO and Na_2O, and strongly depleted in K_2O. With respect to MnO and P_2O_5 contents, samples of the SM and LM demonstrate opposite trends; these elements are enriched in claystones of the LM. Moreover, limestone samples from the LM display enrichments of MnO, Na_2O and P_2O_5; and depletions of TiO_2, Al_2O_3, ΣFe_2O_3 and MgO. The limestones are also strongly enriched in CaO and greatly depleted in K_2O.

All samples of FA–VIII have lower ratios of SiO_2/Al_2O_3, K_2O/Al_2O_3 and K_2O/Na_2O relative to PAAS, and higher CaO/Al_2O_3 ratio. The ratios of TiO_2/Al_2O_3 and K_2O/Al_2O_3 are similar to PAAS. The Na_2O/Al_2O_3 ratios of claystones of the SM and LM are identical with PAAS, while in limestones of the

LM, these ratios are higher than PAAS. Samples of claystones and limestones from the LM have greater Fe_2O_3/Al_2O_3 compared to other samples and PAAS.

XRD samples of lacustrine claystones from the Limestone Member (LM) contain in decreasing order illite-smectite , calcite, zeolites, plagioclase, halloysite/kaolinite, S/C and amphibole. The zeolites occur in the majority of samples without much variation. Quartz and kaolinite occur in trace amounts, while traces of K-feldspar, mica, pyroxene and iron oxides were identified in some samples from the LM.

The XRD analysis on tuffaceous limestone of the LM indicates, not surprisingly, an abundance of calcite. Halloysite/kaolinite, plagioclase and smectite-chlorite (S/C) are present in moderate amounts, while Illite-smectite (I/S) was only detected in one sample. Zeolites are present in trace amounts.

B. Trace elements

The trace-element compositions of all samples show narrow ranges, except the V and Sr contents (Table 7.1). Samples of the SM have the highest concentrations of V (280 ppm), Zn (82 ppm), Rb (33 ppm), Sr (193 ppm), Zr (74 ppm), Ce (18 ppm), Pb (10 ppm) and Th (2.6 ppm); while claystones and limestones of the LM have the greatest Ba and U contents respectively (183 ppm and 2.3 ppm). The Y, Nb, La, Hf and Ta contents in all samples are broadly similar.

Relative to PAAS, the most samples display depletions of Sr, Y, Zr, Ba, La, Ce, Hf, Pb, Th and U; and strong depletions of Rb and Nb. The Zn content in the analysed samples is nearly similar with PAAS (Figure 7.2B). Claystones of the SM and LM are slightly enriched in V and Ta. In contrast, V, Ta and Rb contents show negative anomalies in limestone samples of the LM.

Regarding trace-element ratios, the majority of samples have higher Sr/Rb, Sr/Ba, Zr/Rb and La/Th and lower Th/U ratios relative to PAAS. Compared to other Members, claystones of the SM exhibit highest ratios of Sr/Ba and Th/U; claystone samples of the LM have highest Zr/Rb and La/Th ratios; while limestones of the LM display greatest Sr/Rb and La/Rb ratios.

7.2.5. Palaeosols and pedogenically altered deposits (Facies Association IX/FA–IX)

A. Major elements and mineralogy

Samples of FA–IX have been taken from the TM and SM, and one sample from the Ola Kile Formation (OK) for comparison. Comparing samples from the TM and SM, palaeosols of the SM have an higher abundance of SiO_2 (66.4 wt%), MgO (1.58 wt%) and K_2O (0.75 wt%). Palaeosols of the SM have also greater values of TiO_2 (0.86 wt%), ΣFe_2O_3 (8.87 wt%) and CaO (7.52 wt%) (see Appendix 2). The Al_2O_3, MnO, Na_2O and P_2O_5 contents in both units are similar. In addition, the palaeosol from the Ola Kile Formation shows higher contents of SiO_2 (76 wt%) and MgO (1.76 wt%) compared to samples of the TM and SM (Ola Bula Formation).

The normalised diagram of major-elements (Figure 7.2A) indicates that SiO_2 and MnO contents in the analysed samples are similar to PAAS. Palaeosols show positive anomalies of CaO, negative anomalies of TiO_2, MgO, Na_2O and P_2O_5, and strong depletions of K_2O. Regarding Al_2O_3 and ΣFe_2O_3 contents, palaeosols of the TM and SM have similar values with PAAS, while this element is depleted in the sample from the OK.

Major-element ratios in the analysed samples generally show little variation (Table 7.1). The ratios of TiO_2/Al_2O_3, Na_2O/Al_2O_3 and K_2O/Al_2O_3 in all samples are similar. The palaeosol of the OK has the highest SiO_2/Al_2O_3 and $\Sigma Fe_2O_3/Al_2O_3$ ratios; while palaeosols of the TM and SM have highest K_2O/Na_2O and CaO/Al_2O_3 ratios, respectively. Compared to PAAS, TiO_2/Al_2O_3 and Na_2O/Al_2O_3 ratios of all samples are similar with PAAS, and the majority of palaeosols have higher CaO/Al_2O_3 and lower K_2O/Al_2O_3 and K_2O/Na_2O. In the case of $\Sigma Fe_2O_3/Al_2O_3$, this element ratio is higher in samples of the OK and SM (relative to PAAS), while samples of the TM have similar ratios with PAAS.

XRD analysis indicates that FA–IX of the Tuff Member (TM) contains in decreasing order of abundance illite-smectite, smectite-chlorite, plagioclase (in highly variable amounts), zeolites, halloysite/kaolinite and amphibole (see Appendix4). Quartz, iron oxide minerals and kaolinite occur in

trace amounts. Traces of K-feldspar and pyroxene were only detected in a few samples.

Samples of FA–IX from the Sandstone Member (SM) show the presence of illite-smectite, plagioclase (again in highly variable amounts), zeolites, halloysite/kaolinite and smectite-chlorite. Traces of quartz, amphibole and kaolinite were detected, while mica and iron oxides (mostly maghemite) occur randomly in the studied samples. K-feldspar and pyroxene were not detected in most samples. In addition, calcite is present in a few samples.

Illite-smectite (I/S) and zeolites are the dominant constituents of the analysed palaeosol from the Ola Kile Formation. Halloysite and S/C are present in lower amounts, while quartz and kaolinite were recognised only in trace amounts. Calcite, K-feldspar, mica, amphibole, pyroxene and iron oxides were absent from the analysed sample.

Compared to all other palaeosol samples, the palaeosol of the Ola Kile Formation tends to have the highest concentrations of I/S, S/C and zeolites. Plagioclase and amphibole are more abundant in the SM samples; while samples of the TM have the greatest proportion of halloysite/kaolinite.

B. Trace elements

Palaeosols of the TM have the highest values of V (280 ppm), Zn (91 ppm), Rb (37 ppm), Sr (175 ppm), Y (30 ppm), Zr (98 ppm), Ba (239 ppm), La (15 ppm), Ce (34 ppm), Pb (11 ppm) and Th (4.8 ppm). The concentrations of Nb, Hf, Ta and U in the most samples are broadly similar (Appendix 2).

Most palaeosols display negative anomalies of Rb, Sr, Zr, Nb, Ba, La, Ce, Hf, Pb, Th and U relative to PAAS (Figure 7.2B). The OK has distinctive depletions of Nb, La, and Th. Samples of the TM and SM are enriched in the V content, while the sample of the OK shows a negative anomaly of this element. Regarding the Zn content, the palaeosols of the OK and TM have similar values compared to PAAS; while samples of the SM are depleted in this element.

The trace-element ratios (Table 7.1) suggest that all palaeosols have greater Sr/Rb, Sr/Ba, Zr/Rb and La/Th ratios and a lower Th/U ratio relative to PAAS. With respect to La/Rb, samples of the TM and SM display a higher ratio, while the sample of the OK has a lower ratio than in PAAS. Compared to all other samples, the palaeosol of the OK has the highest Sr/Rb and La/Th ratios. Palaeosols of the TM have the highest ratios of La/Rb and Th/U, and palaeosols of the SM have the highest ratios of Sr/Ba and Zr/Rb.

7.3. Influence of mineral assemblages on the geochemical composition

The mineralogical and chemical compositions of continental sediments are influenced by many factors, including depositional processes (e.g. transportation and sorting), parent/source materials, climate and weathering intensity (Nesbitt and Young, 1984, 1989; McLennan, 1989; Condie *et al*., 1993; Cox *et al*., 1995; and Fedo *et al*., 1995, 1997). It has been summarised in previous sections that the major components of all studied samples are plagioclase, zeolites and clay minerals. Quartz, K-feldspar, micas, amphibole, pyroxene and iron oxide minerals are much less abundant and occur at random. The clay mineral assemblages in all facies association are dominated by halloysite/kaolinite, illite-smectite (I/S) and smectite-chlorite (S/C); while kaolinite, illite and montmorillonite are rarely present.

A. Quartz and Feldspars

Quartz can be found in the majority of lithofacies (excluding lithofacies Lm) and this mineral is always present in only low amounts. Volcanic quartz or tridymite only occurs in facies Fh and P see Appendix 4). Quartz and tridymite in sediments and lahar deposit is derived from the erosion of felsic volcanic rocks or direct input from volcanic airfall. The low amounts of quartz and tridymite indicate that the parent materials are poor in these minerals. This interpretation corroborates the field observations that volcanic rocks in the

study area are dominated by basaltic– andesitic lavas and rhyolitic pyroclastic deposits.

Most samples contain plagioclase, but its presence varies from fairly high amounts to only traces. The lowest abundances occur in lithofacies Lm. Plagioclase is commonly abundant in mafic or ultramafic volcanic rocks. There are mafic lavas and basaltic cones surrounding the Soa basin, and these volcanic rocks are the likely source of plagioclase. On the other hand, rhyolitic pyroclastic deposits in the study area may have also contributed to the distribution of plagioclase in sediments or volcaniclastic deposits. XRD analysis of tephra samples records the presence of plagioclase in low to high abundances.

K-feldspar occurs in trace amount (2.4–5.1 %) and is randomly distributed in a few lithofacies. The low concentration of K-feldspar is due to low content of this mineral in source rocks. K-feldspar is commonly abundant in felsic igneous rocks. It must be noted that pyroclastic deposits with a rhyolitic composition are well-distributed in the study area. However, these pyroclastic materials are always dominated by volcanic glass and pumice clasts, with minerals present in only small amounts. XRD analysis on samples of pyroclastic deposits confirms a low abundance of K-feldspar (see Appendix 4).

B. Carbonate mineral

The major carbonate mineral present in sediments of the Soa Basin is calcite. Calcite occurs in lacustrine sediments (FA–VIII) and few palaeosol samples in various proportions. The occurrence of calcite in a lacustrine setting can be influenced by a variety of mechanisms, such as a photosynthetic uptake of CO_2, pH, temperature, evaporation and supply of dissolved calcium in water sources (Tucker and Wright, 1990; Verrecchia, 2007; Gierlowski-Kordesch, 2010).

The presence of some organisms can be important in the formation of carbonate. A palynological study indicates that several claystones contain algae and plant matter (W.A. van der Kaars, pers. comm) and oogonia of green algae (characaea) are present in the micritic limestone facies (van den

Bergh, 1999). The production of micritic carbonate therefore seems to be related to the respiration–photosynthesis balance of aquatic algae and plants (Tucker and Wright, 1990; Gierlowski-Kordesch, 2010). Furthermore, tuffaceous limestones and fluvial sandstones contain freshwater gastropods, which precipitated carbonate. In the sandstones the gastropods invariably occur as molds, but dissolution of the carbonate may have taken place during the erosional phase by percolating groundwater. Calcareous sediments of the Limestone Member alternate with pyroclastic airfall deposits, which contain Ca-bearing minerals, such as plagioclase and pyroxene. The weathering process of these calcium-rich volcanic layers in the lacustrine environment and also in the catchment area may have supply dissolved calcium to the lake water in sufficient quantities to allow for carbonate precipitation (Gierlowski-Kordesch, 2010).

The presence of calcite in some palaeosols can be associated with pedogenesis. Some palaeosols in the Soa Basin show the typical characteristics of vertisols, characterised by prominent cracks (shrinking and swelling features). Field evidence suggests that calcite is present as nodules, cement and in filling of cracks. Precipitation, temperature, pH and the supply of Ca are the main factors controlling the accumulation of calcite in palaeosols (Retallack 2001; Retallack 2005; Nordt *et al*., 2006).

C. Micas, Amphiboles and Pyroxenes

Similar as with K-feldspars; micas and amphiboles are important constituents in either felsic or mafic volcanic deposits. On the other hand, pyroxene is usually present only in mafic igneous rocks. The presence of micas, amphiboles and pyroxenes can be observed in most lithofacies with the exception of lithofacies Lm. Micas consist of biotite and muscovite, which are randomly present in trace amounts. Rhyolitic pyroclastic deposits are a potential source for those minerals, due to the low content of micas within these pyroclastic deposits.

Amphiboles predominantly consist of hornblende and riebeckite, while traces of cummingtonite were encountered rarely. Either of these minerals commonly displays low abundances. The pyroclastic deposits are again considered as a potential contributing source in the supply of amphiboles to sediments and/or lahar deposits. In fact, the Wolo Sege Ignimbrite (WSI) comprises crystals of hornblende up to 2 mm, and this mineral has been used for argon-argon dating (see Chapter 5; Brumm *et al*., 2010; 2016).

Pyroxenes were only encountered in some sandstones in low amounts. Pyroxenes in sediments can be sourced from mafic volcanic rocks.

D. Iron oxide minerals

Hematite and maghemite are the dominant iron oxide minerals that are recognised amongst the studied samples. These minerals are present irregularly but are mostly associated with palaeosols (FA–IX) in trace amounts. Hematite and maghemite are secondary products of the alteration of magnetite during pedogenesis. Magnetite can be a primary constituent of mafic tephras, but magnetite was not identified in the Soa basin tephras (Chapter 5). Magnetite can also be formed via inorganic or organic (bacteria) mediated pathways. The oxidation process of magnetite at soil temperature enables the transformation of magnetite into maghemite (Fassbinder *et al*., 1993). Maghemite can also originate from ferrihydrite that was transformed to maghemite, and then to hematite in an oxidizing environment (Barrón and Torrent, 2002; Torrent *et al*., 2006). Maghemite is a common mineral in weathered volcanic rocks and volcanic soils (Da Costa *et al*., 1999; Otake *et al*., 2010).

E. Zeolite minerals

Zeolites (chabazite, heulandite, stilbite and clinoptilolite) have been identified in all facies in variable concentrations throughout the stratigraphic sequence. Individual zeolites are generally present in low amounts. The occurence of zeolites can be related to hydrothermal processes or post

depositional diagenesis (Moncure *et al*., 1981; Hernandes *et al*., 1993; de Pablo-Galan and Chávez-García, 1996). Most pyroclastic deposits in the Soa Basin contain abundant volcanic glass and have a rhyolitic composition (Chapter 5). Felsic volcanic glass is less reactive than intermediate and basaltic glasses. However, high temperature, water composition and acidic environments play important roles to modify acidic volcanic glasses to become altered into zeolites (de'Gennaro *et al*., 2000).

During volcanic eruptions, the authigenic zeolite minerals can be formed and inherited in pyroclastic fall and flow deposits and lahars as the products of reaction between volcanic glasses with fluids (hydrothermal process; Dill *et al*., 2012). Alternatively, zeolites can be formed during weathering and soil-forming process, and the silicic pyroclastic deposits are suitable parent materials. The interaction among sediments and meteoric waters at high temperature alters volcanic glass of the parent materials (de Pablo-Galan and Chávez-García, 1996; de'Gennaro *et al*., 2000).

F. Clay minerals

The clay minerals mainly constitute kaolin, and the smectite and illite groups. Mixed-layer phases of illite–smectite (I/S) and smectite–chlorite (S/C) also occur in the majority of samples. The kaolin group consists of kaolinite and halloysite. Kaolinite and halloysite commonly co-exist but can not be distinguished from each other without additional tests. The weathering of volcanic glass is considered to be the main process to produce those minerals (Shoji *et al*., 1993; Duzgoren-Aydin *et al*., 2002).

Smectites are only represented by montmorillonite, which is limited to a few samples. The mixed-layers of I/S and S/C are present in the majority of facies, displaying moderate to high amounts. Under moderate conditions where the temperature fluctuates seasonally, smectite can transform to I/S and S/C (Chamley, 1989; Velde and Meunier, 2008). With regard to chlorite, this mineral may have been derived from the alteration of mafic

minerals (Chamley, 1989; Velde and Meunier, 2008). Finally, illite is very rare and was only encountered in one sample of facies Fh. The weathering of feldspar is probably responsible for the formation of kaolinite and illite (Chamley, 1989; Velde and Meunier, 2008).

The clay mineral assemblages in the Soa Basin samples can possibly originate from prolonged weathering of parent rocks. Basaltic volcanic rocks and rhyolitic pyroclastic deposits are considered as the most likely source materials. Sandstones (FA–V and FA–VI), lahar deposits (FA–IV) and lacustrine sediments (FA–VIII) may contain detrital clay minerals. The erosion of clay-rich parent materials could have contributed to the formation of detrital clay minerals within those lithologies.

The sandstones throughout the stratigraphic sequence represent fluvial (braided channel) and sheet flood deposits (Chapter 6). The basin settings suggest a proximal depositional environment relative to the source region, so that transport process probably had a low impact on the transformation of clay minerals. The authigenic formation of clay minerals within sediments of the Soa basin can directly originate from pyroclastic deposits, transported by wind or water (run off or meteoric water) and/or due to pedogenic processes. The variable abundances of clay minerals are controlled by pre-weathering conditions of the parent materials and the intensity of weathering.

Palaeosol deposits (FA–IX) mostly overlie pyroclastic deposits, suggesting that the clay contents in this facies were formed by pedogenetic alteration of tephra deposits. Summarising, clay minerals occur in the majority of samples throughout the sequence, indicating continuous deposition or supply from parent materials. The occurrence of clay minerals in the Soa Basin sediments was to a large extent influenced by climatic conditions, weathering and/or contemporaneous volcanic activity during deposition.

7.4. Palaeoweathering and Provenance

7.4.1. Introduction

Several weathering indices have been commonly used to investigate the weathering history of sediments and volcaniclastic deposits (Nesbitt and Young, 1984; 1989; Fedo *et al*., 1995; Nesbitt *et al*., 1996). The Chemical Index of Alteration (CIA) and the Plagioclase Index of Alteration (PIA) are two kinds of weathering indices that are widely applied. The CIA was proposed by Nesbitt and Young (1982), calculated using the following equation:

$$CIA= [Al_2O_3/ (Al_2O_3+CaO^*+Na_2O+K_2O)] \times 100 \quad (7.1)$$

On the other hand, the PIA was developed by Fedo *et al.* (1995) and determined using the following formula:

$$PIA= [(Al_2O_3 - K_2O)/ (Al_2O_3+CaO^*+Na_2O-K_2O)] \times 100 \quad (7.2)$$

In these equations, the CaO* value represents the Ca content in the silicate phases, and all utilised major oxides are in molecular proportions (Nesbitt and Young, 1982; 1984; Fedo *et al.*, 1995). The CIA value for unweathered rocks is 50 and the CIA values for average shales range from 70 to 75 (of a possible 100), which reflects the compositions of muscovites, illites and smectites. Moreover, strongly weathered rocks yield the mineral compositions trending towards kaolinite or gibbsite and a corresponding CIA value approaches 100 (Taylor and McLennan, 1985; Nesbitt and Young, 1982; 1984; Fedo *et al*., 1995).

On the other hand, the PIA value shows a positive correlation with the chemical weathering intensity, therefore, Fedo *et al*. (1995) classified the degree of chemical weathering into low (PIA < 60), moderate (PIA 60–80) and extreme (PIA > 80). PIA is used to monitor and quantify the alteration of feldspars to clay minerals (Fedo *et al*., 1995). The PIA value of sediments suggests intense destruction of feldspars during the course of source weathering,

transport, sedimentation and diagenesis. During the initial stages of weathering of feldspar-bearing parent material, Ca leaches more rapidly than Na and K. When weathering process is more intense, the total alkali content (K_2O + Na_2O) will decrease, otherwise the K_2O/Na_2O ratio will increase. This is due to destruction of feldspars wherein plagioclase is preferentially removed before K-feldspars (Nesbitt and Young, 1984; 1989).

In this study, because the concentration of $CaCO_3$ on representative samples that are used for estimating the degree of chemical weathering is not measured; the CaO* value is determined using a formula as suggested by Honda and Shimizu (1998). The equation is

$$CaO^* = [0.35 \times 2\ (Na_2O)]/62 \qquad (7.3)$$

This equation assumes that plagioclase contents in sediments show no significant differences with the upper continental crust composition (UCC). Thus, the ratio between Ca and Na in plagioclase will be 1:3 in molar proportions (Honda and Shimizu, 1998).

This study will estimate the degree of chemical weathering (CIA and PIA) of sediments from the Ola Bula Formation including the Tuff, Sandstone and Limestone Members; and to determine the weathering history through the basin sequence. Factors controlling the variation of weathering intensity on the Soa sediments will also be discussed in the following section.

7.4.2. Weathering Intensity

The weathering indices have been determined on samples taken from the Ola Bula sequence, including Tuff, Sandstone and Limestone Members (Table 7.1). A well-developed palaeosol deposit in the Ola Kile Formation is also collected as representing the nature of chemical weathering intensity prior the deposition of the Ola Bula Formation.

The sediments of the Tuff Member have CIA values ranging between 61 and 100 (average 82), which indicate moderate to intense weathering (Nesbitt and Young, 1982, 1984; Taylor and McLennan, 1985). The CIA values of Facies P (FA–IX) range from 61 to 100; The range for facies Fmm-Smm (FA–IV) is 75–84; for facies Sl-Scl (FA–V) 69–81, and facies Fm (FA–VII) has a CIA value of 84.

The PIA values of sediments of the Tuff Member also show similar trends with CIA, ranging between 64 and 100 (average 83). The PIA also suggests that the analysed samples display moderate to extreme weathering (Fedo *et al*., 1995, 1997). The CIA and PIA values of samples from the Sandstone Member display the variability of chemical weathering. Facies Fmm-Smm (FA–IV), Sl-Ss (FA–V) and P (FA–IX) have CIA values ranging from 65–83, 76–94 and 76–99, respectively; and demonstrate intermediate to intense weathering. The CIA values of sandstones as reflected from facies Scl (FA–V) and Sm (FA–VI), reveal 78–79 and 72–77, respectively; and suggest moderate weathering intensities. Facies Fh (FA–VIII) has been intensively weathered with the CIA value ranging between 84 and 88.

Moreover, the PIA value also reflects various degrees of weathering. Facies Fmm-Smm (FA–IV), Sl-Ss-Scl (FA–V), Sm (FA–VI) and P (FA–IX) have PIA values ranging from 66–85, 77–95, 74–78 and 77–100, respectively; and indicate moderate to strong weathering. The PIA of facies Fh is a suggestive of strong weathering (85–90).

The CIA values of sediments from the Limestone Member suggest weak to intense weathering. Facies Fh (FA–VIII) has a range of CIA from 67 to 99 and the CIA values of facies Sh (FA–V) is 91. In addition, the CIA values of facies Lm yield 44–68, represent unweathered to weakly weathered. On the other hand, the PIA values display indistinguishable results with CIA values. The PIA values of facies Fh (FA–VIII), Lm (FA–VIII) and Sh (FA–V) are 68–100, 43–69 and 92, respectively. The PIA of facies Fh and Sh are suggestive of moderate to

extreme weathering; while few samples of facies Lm are relatively fresh and the others exhibit low weathering.

The weathering indices of the studied samples (CIA and PIA) reveal that most samples demonstrate higher CIA and PIA values than the UCC value (51) and denotes that chemical weathering in various intensities has affected the analysed sediments. In addition, some samples are in the range of PAAS, suggesting similar weathering characteristics with PAAS samples There are only two samples of limestones (facies Lm, FA VIII) for which the weathering indices indicate absence of chemical weathering. The high CaO content probably affects the calculation of weathering indices.

7.4.3. The A-CN-K Diagram

The Al_2O_3–CaO*+Na_2O–K_2O (A–CN–K) diagram is usually used to examine the weathering trends and the nature of source rocks because the upper crust is dominated by plagioclase and K-feldspar-rich rocks and their weathering products. The major oxides are expressed in molar proportions and the CaO* value represents the CaO content incorporated in the silicate fraction only (Nesbitt and Young, 1984, 1989; Fedo *et al*., 1995). Similar with the CIA and PIA calculations, the CaO* value is determined using the formula from Honda and Shimizu (1998).

The A-CN-K diagram reveals that most facies of the Tuff Member (TM) are parallel to the A-CN line (Figure 7.3A). Facies P (FA–IX) exhibits scattered trends, with two samples close to the A-K join. The ternary plot also exhibits three distinct groups with respect to the ascending CIA values; correspond to moderate to intense weathering. Some samples of facies P (FA–IX) have CIA values of almost 100, which reflect very strong (extreme) weathering.

Plotting samples of the sandstone Member (SM) on the A-CN-K diagram (Figure 7.3B) displays uniform trends, which all samples closely parallel to the A-CN apex. Regarding the CIA values, moderate to intense weathering has

affected sediments of the SM. Most facies P (FA–IX) of the SM yield CIA values near 100, indicative of extreme weathering.

On the other hand, the analysed samples of the Limestone Member (LM) are plotted in parallel arrays with the A-CN line (Figure 7.3C). Facies Fh (FA–VIII) and Sh (FA–V) of the LM display moderate to strong weathering. A unique pattern can be seen with respect to facies Lm (FA–VIII). Two samples of facies Lm are close and below the plagioclase-K-feldspar line, respectively. These indicate that chemical weathering is absent in those samples. However, one sample of facies Lm occupies an intermediate weathering region according its CIA value.

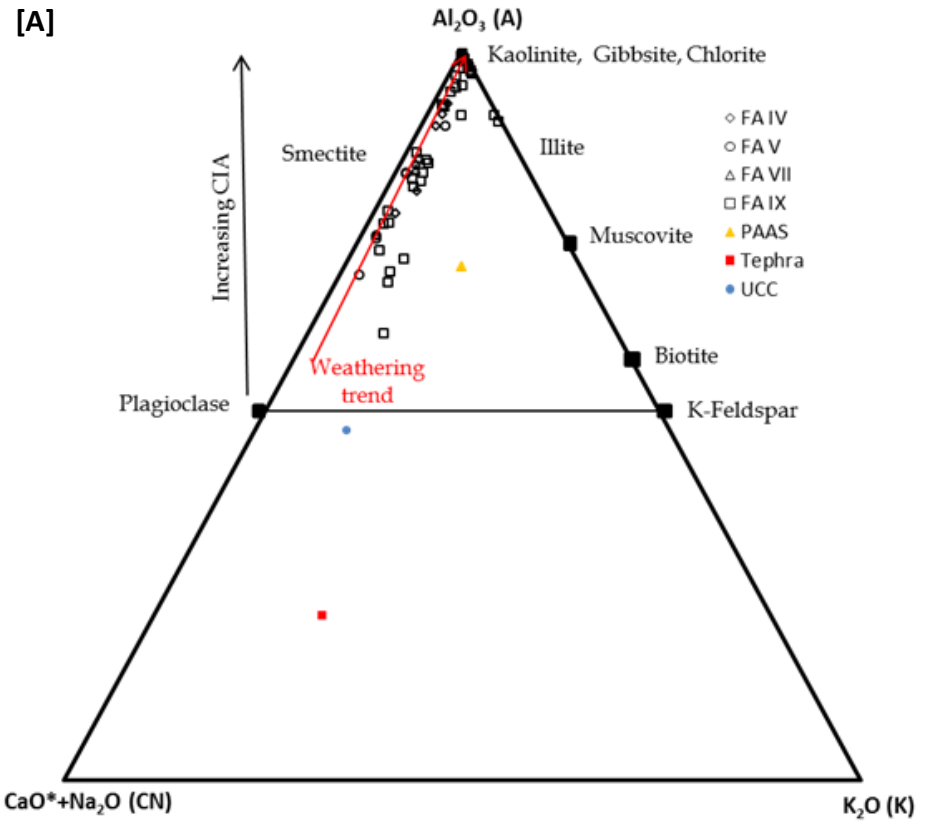

Figure 7.3. The A-CN-K diagrams (after Nesbitt and Young, 1984, 1989) of facies association (FA) from (A) the Tuff Member, (B) the Sandstone Member and (C) the Limestone Member. The average tephra, PAAS and UCC compositions are also plotted for reference. The PAAS and UCC values are from Taylor and McLennan (1985). The major-element values are in molar proportions. The red arrow indicates the inferred weathering trend.

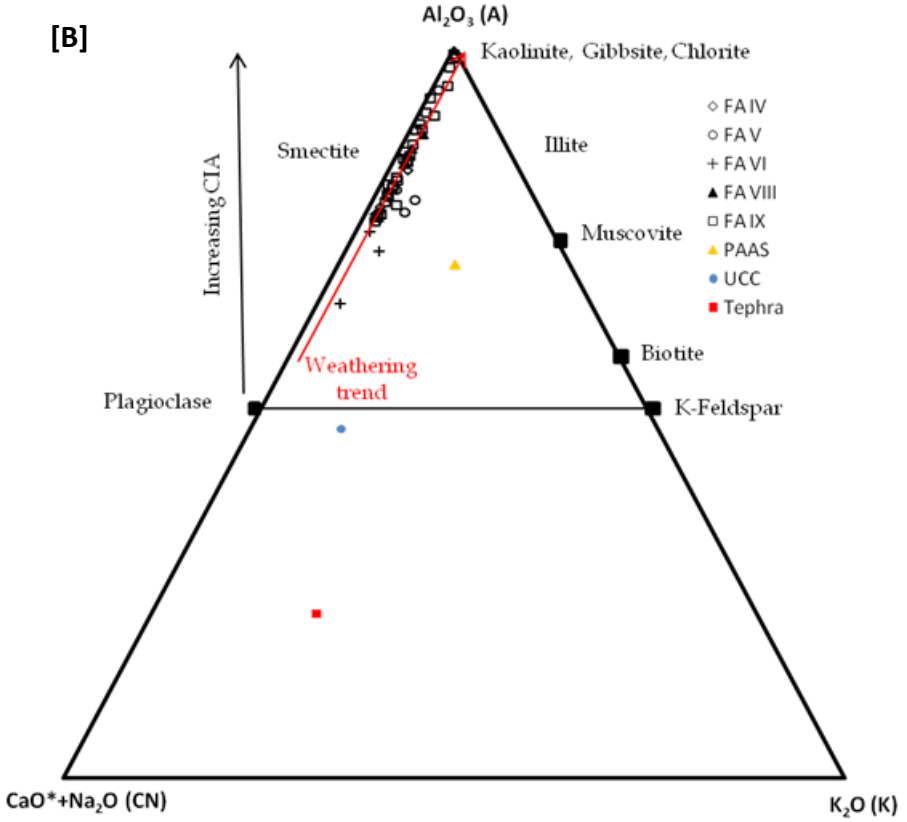

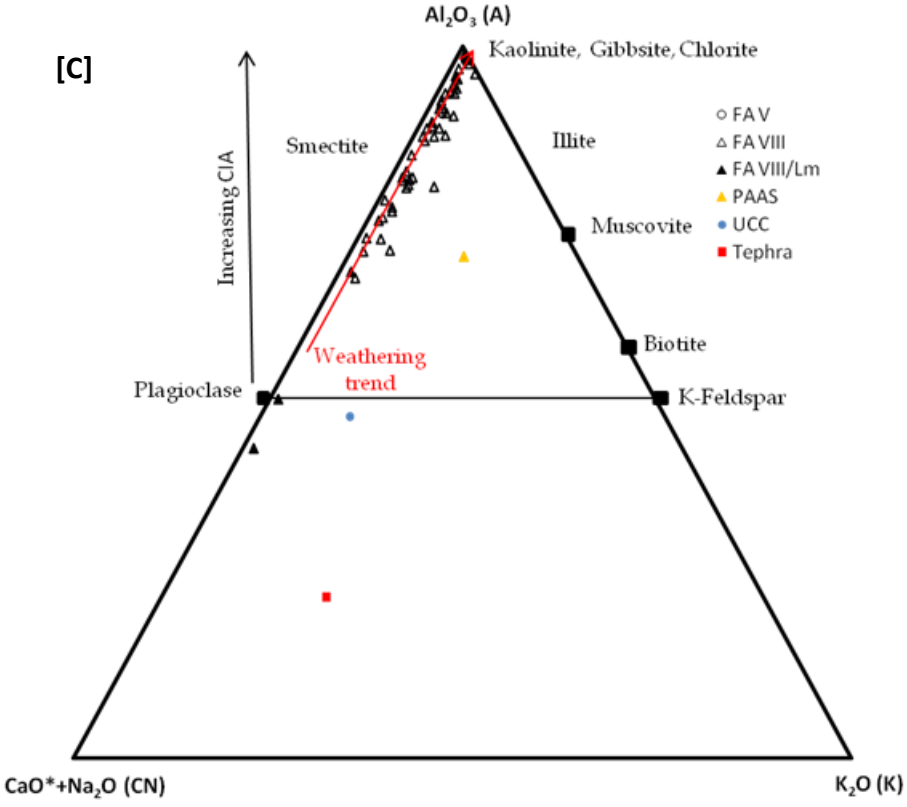

Figure 7.3. Continued.

The studied samples are generally closely parallel to the A-CN line and they do not show scattered plots and are relatively homogeneous in the A-CN-K diagram. The majority of analysed samples fall into the fields of plagioclase and smectite, and smectite and kaolinite. The main trends of silicate weathering in most sediments exhibit preferential leaching of CaO, Na_2O and K_2O; and increasing Al_2O_3 contents during the formation of clay minerals through moderate to intense chemical weathering (see Nesbitt and Young, 1984, 1989; Fedo *et al*., 1995).

As shown in Figure 7.3A, two samples of palaeosols (TT01 and TT03) from the TM are closely linearly parallel to the A-K joint. It may have been caused by K-metasomatism (Fedo *et al*., 1995). The enrichment of K_2O in those samples is probably related to the clay mineral assemblages or post depositional diagenesis; and therefore they plot in the illite and kaolinite region.

Figure 7.3C shows that two samples of facies Lm (MM 122 and MM128) plot closely below the plagioclase and K-feldspar boundary; which suggest the absence of chemical weathering, or unweathered conditions. Facies Lm corresponds to tuffaceous micritic limestone, where calcite is the major constituent and clay minerals are present in moderate proportions. On the other hand, one sample of facies Lm (MM 125) plots in the moderate weathering area. The calcite concentration in this sample is lower than MM 122 and MM 128; however, the plagioclase and clay mineral contents are higher than in the other samples; which suggests leaching of such major elements (CaO, Na_2O and K_2O) was more intense within sample MM125 leading to an increased CIA value and therefore plotting in the A-CN-K ternary diagram region indicative for intermediate weathering.

The alternative reason is associated with the high calcite contents (> 60 %) in samples of MM 122 and MM128, which directly enriched the CaO content (69.77 and 77.15 wt %, respectively).

7.4.4. Discussion: palaeoweathering and provenance

The degree of chemical weathering of source rocks is controlled by the composition of parent materials, duration of weathering process, climatic conditions and intensity of tectonic uplift of the source area (Condie, 1993; Cox, 1993; Johnsson, 1993, Rollinson, 1993). Therefore, chemical weathering will affect the major-and trace-element compositions of sediments. The weathering indices are good indicators to understand the intensity of chemical weathering of source rocks (Nesbitt and Young, 1984, 1989; Fedo *et al*., 1995). This study uses Chemical Index of Ateration (CIA, Nesbitt and Young, 1982) and Plagioclase Index of Alteration (PIA, Fedo *et al*., 1995) to determine the degree of chemical weathering of source materials, and the results have been highlighted in the previous section.

It can be summarised that sediments of the Tuff Member (TM) have wide ranges of CIA and PIA values from 61–100 and 64–100 respectively. Sandstones of the TM display moderate to high CIA and PIA values (69–90 and 70–92 respectively), which Indicate intermediate to strong chemical weathering. The weathering indices of lahar deposits reveal 75–93 CIA and 76–94 PIA and suggest moderate to intense chemical weathering. Claystone of the TM has high CIA and PIA values (84 and 85) that reflect strong weathering processes. Moreover, the CIA and PIA values of palaeosols from the TM suggest moderate to strong pedogenesis (61–100 CIA and 64–100 PIA).

The CIA and PIA values of sediments from the Sandstone Member (SM) show variability ranging from 65–99 and 66–100 respectively. Sandstones of the SM have 72–94 CIA and 74–95 PIA, which indicative of intermediate to intense chemical weathering. The weathering indices of lahar deposits from the SM display medium to high values (65–83 CIA and 66–85 PIA) suggesting moderate to strong chemical weathering. Lacustrine claystones of the SM demonstrate strong weathering (84–88 CIA and 85–90 PIA); while palaeosols have CIA and PIA values varying from 76 to 99 and 77 to 100 respectively, indicating moderate to strong pedogenic processes.

The lacustrine sediments of the Limestone Member (LM) have wide ranges of CIA and PIA values from 67–99 and 68–100 respectively; while sandstone has high CIA and PIA values (91 and 92). These values indicate that moderate to strong chemical weathering occurred in the sediments of the SM. In addition, two samples of tuffaceous limestone have CIA values below 50 (44) suggestive of unweathered samples or that chemical weathering is minimal.

The weathering indices of sediments from all stratigraphic units do not show significant differences and all samples generally display moderate to strong weathering of the source areas. There are only two samples of limestones (facies Lm) that represent unweathered rocks. These characteristics coincide with the trends in the A-CN-K diagram, with the majority of samples plotting in tight groups and the weathering trends generally parallel to the A-CN lines. These facts imply that most samples are not subjected to potassium metasomatism. However, two samples of palaeosols are close to the A-K apex, which suggests these samples are probably affected by K-metasomatism or due to redistribution of potassium during pedogenesis (Fedo *et al*., 1995).

On the other hand, it is difficult to trace the provenance of the analysed sediments due to a lack of geochemical data for older rocks near the study area. According to regional geological map (Koesoemadinata *et al*., 1994; Muraoka *et al*., 2002), there are volcanic rocks and limestone developed close to the Soa Basin. Previous studies suggested that andesitic-basaltic lavas (Wangka Andesite and Mere Basalt) and pyroclastic deposit (Welas Tuff) are the dominant constituents in the western and northern part of the basin, while coral reef limestone (Matale limestone) is only distributed in the northern part of the basin. These lithologies were occurred during Pliocene (Koesoemadinata *et al*., 1994; Muraoka *et al*., 2002). This study assumes that the Pliocene deposits are the main source for sediments and volcaniclastic deposits in the Soa Basin.

To investigate the source material and the weathering intensity of the source region, this study employs the elemental ratios of selected major-and trace elements from sandstones, lahar deposits and suspended sediments

(lacustrine and floodplain claystones). The average elemental ratios of individual facies associations have been outlined in Table 7.1. In fresh igneous rocks, Al_2O_3, CaO and Na_2O reside mainly in feldspars, TiO_2 and ΣFe_2O_3 are more abundant in mafic and iron oxides minerals; and K_2O is in K-feldspar. In addition, La and Th are more abundance in felsic volcanic rocks than mafic volcanic rocks (Taylor and McLennan, 1985; Condie, 1993; Rollinson, 1993).

During initial weathering of parent materials, Al_2O_3 and TiO_2 are relatively immobile. Al_2O_3 occurs mainly in clay minerals, feldspars and micas; while TiO_2 is essential constituent of clay and mafic minerals. In contrast, CaO, Na_2O and K_2O are mobile during weathering of fresh rocks (Nesbitt and Young, 1984, 1989, Fedo *et al*., 1995). In addition, Rb and U contents are easily removed during diagenesis compared to other elements (Sr, Ba, Zr, La and Th). The ratio of mobile-immobile elements is a useful tool to ascertain the weathering of source rocks (Nesbitt and Young, 1984; 1989; Fedo *et al*., 1995).

Sandstones of the Tuff Member (TM) are characterised by enrichments of TiO_2, ΣFe_2O_3, MgO, CaO, Na_2O and Sr; and depletions of K_2O, Rb, Ba, Zr, La, Hf, Th and U relative to PAAS. Lahar deposits and floodplain claystones display positive anomalies of CaO and negative anomalies of TiO_2, ΣFe_2O_3, Rb, Sr, Ba, Zr, La, Hf, Th and U. The ratios TiO_2/Al_2O_3 and Na_2O/Al_2O_3 in all samples are nearly similar with PAAS (0.03–0.07 and 0.02–0.15 respectively); $\Sigma Fe_2O_3/Al_2O_3$, CaO/Al_2O_3, Sr/Rb, Sr/Ba, Zr/Rb, and La/Rb are mostly higher than PAAS (6.43–12.30, 0.04–0.38, 3.42–12.31, 0.43–1.78, 1.87–3.70, and 0.06–1.13 respectively). The TiO_2, ΣFe_2O_3 and MgO contents reside in ferromagnesian minerals (e.g. pyroxene, amphibole, biotite and iron oxide minerals). CaO, Na_2O, Rb, Sr and Ba are constituents of feldspar, while La, Zr and Th are incorporated within volcanic glass rather than zircon. The concentrations of La, Zr and Hf are depleted in sandstones that indicate the effect of sorting is minimal. The feldspar assemblage is more abundant in sandstones as noticed by enrichment of Sr relative to lahar and floodplain deposits.

According to the chemical characteristics and elemental ratios, it can be interpreted that sediments of the TM are derived from felsic source materials which probably correspond to rhyolitic pyroclastic deposits of Welas Tuff. The A-CN-K diagram (Figure 7.3) shows that samples of the TM are plotted in the smectite field and this supports the previous interpretation. Smectite is mainly formed by alteration of felsic volcanic glass. In addition, with respect to sandstones, less influence of mafic volcanic rocks (basaltic-andesitic) should be considered as shown by enrichments of TiO_2, ΣFe_2O_3 and MgO. The palaeocurrent measurements on several fluvial exposures at Kobatuwa 4, Wolo Sege, Matago and Tangi Talo reveal that the palaeochannels generally have NW–SE and W–E directions and the flow escaped to the Flores Sea. Andesitic and basaltic lavas in the western and north-western part of the basin are responsible for the enrichment of ferromagnesian minerals and thus increase the TiO_2, ΣFe_2O_3 and MgO values.

Sandstones and lahar deposits of the Sandstone Member (SM) are enriched in ΣFe_2O_3, MnO, MgO, CaO, Na_2O and Sr; and depleted in TiO_2, K_2O, Rb, Sr, Ba, Zr, La, Hf, Th and U relative to PAAS. Similarly with sediments of the TM, the analysed samples of the TM have nearly similar TiO_2/Al_2O_3 and Na_2O/Al_2O_3 ratios with PAAS; and the ratios $\Sigma Fe_2O_3/Al_2O_3$, CaO/Al_2O_3, Sr/Rb, Sr/Ba, Zr/Rb, and La/Rb are mostly higher than PAAS (5.77–31.91, 0.13–2.93, 2.33–48.75, 0.25–2.58, 1.71–11.02 and 0.06–3.02 respectively). These geochemical data indicate that the source rocks of sediments from the TM are dominantly felsic volcanic rocks. The enrichments of ΣFe_2O_3, MnO and MgO that are controlled by the presence of ferromagnesian and iron oxide minerals are suggestive of inpits from mafic igneous rocks. The palaeochannels suggest NW–SE and W–E directions, and accordingly andesitic and basaltic lavas in the western and north-western part of the basin provide significant contribution of ferromagnesian and iron oxide minerals and these minerals will increase the ΣFe_2O_3, MnO and MgO values.

Sandstone of the Limestone Member (LM) is characterised by enrichments of Al_2O_3, ΣFe_2O_3, CaO and Sr; and depletions of MnO, Na_2O, K_2O, Rb, Ba, Zr, La, Hf, Th and U compared to PAAS. The enrichments of Al_2O_3, CaO and Sr are clearly indicative of the influence of plagioclase; ferromagnesian minerals affect the enrichment of ΣFe_2O_3; while depletions of Zr, La and Hf reflect minor contribution of zircon. The ratios $\Sigma Fe_2O_3/Al_2O_3$, CaO/Al_2O_3, Sr/Rb, Sr/Ba and Zr/Rb are greater than PAAS (9.75, 0.15, 31.09, 1.91 and 4.79). Compared to sandstones from the Tuff and Sandstone Member, sandstone of the TM has the lowest La/Th, suggesting less influence of felsic volcanic rocks. The occurrence of ferromagnesian minerals is clearly indicative of inputs from mafic igneous rocks. This sandstone also shows high clay content. These facts suggest that sandstone of the LM was derived from multiple sources. The clay minerals probably originated from clay-rich parent materials such as palaeosols of the older units (TM and SM) that contain an abundance of clay minerals, and weathering of pyroclastic deposits and/or mafic volcanic rocks (Wangka Andesite and Mere Basalt).

In addition, lacustrine claystones of the LM exhibit positive anomalies of ΣFe_2O_3 and MnO, strong enrichment of CaO; and negative anomalies of MgO, Na_2O, K_2O, Rb, Sr, Ba, Zr, La, Hf, Th and U relative to PAAS. The enriched CaO corresponds to the presence of calcite. ΣFe_2O_3 and MnO are tightly held in ferromagnesian minerals. The ratios $\Sigma Fe_2O_3/Al_2O_3$, CaO/Al_2O_3, Sr/Rb, Sr/Ba, Zr/Rb, La/Th and Th/U are higher than PAAS (8.85, 0.26, 6.01, 1.25, 2.28, 2.65 and 5.12 respectively). The source of the lacustrine claystones is seemingly from felsic volcanic rocks with minor contribution from mafic lavas. Concerning the occurrence of calcite, this mineral is likely a biogenic origin.

In the case of palaeosols, the chemical composition of palaeosols from the TM and SM are nearly identical, display enrichments of CaO, and depletions of TiO_2,MgO, Na_2O, K_2O, Rb, Sr, Ba, Zr, La, Hf, Th and U compared to PAAS. Regarding ΣFe_2O_3 and MnO contents, these elements are enriched in samples of the SM, while depleted in samples of the TM. Palaeosols of the TM

and SM are similar to PAAS, and have higher $\Sigma Fe_2O_3/Al_2O_3$ and CaO/Al_2O_3 (9.27–11.86 and 5.64–17.09; 0.13–3.63 and 0.05–0.40, respectively) than PAAS. All palaeosol samples also show higher trace-element ratios Sr/Rb, Sr/Ba, Zr/Rb, La/Th and La/Rb (3.72–24.41 and 2.01–25.32; 9.27–11.86 and 0.42–2.10; 9.27–11.86 and 1.28–26; 9.27–11.86 and 0.28–26.63; 9.27–11.86 and 0.03–3.28 respectively). The variation of chemical values relative to PAAS and elemental ratios indicate a major influence of felsic parent materials. This fact is in agreement with lithostratigraphic analyses where palaeosols mostly overlie rhyolitic pyroclastic deposits. Concerning palaeosols of the SM, the parent materials are likely more complexes and the field and geochemical data suggest that fluvial sandstone, lahar deposit and basaltic tephra are the main source rocks. Sandstone and basaltic tephra that contain mafic minerals are responsible for enriching ΣFe_2O_3 and MnO contents.

Geochemical studies performed on sediments of the Soa Basin to infer their geochemical characteristics, source composition and weathering of source rocks reveal that the analysed sediments are characterised by moderate to strong weathering and the influence of felsic volcanic rocks are more dominant than mafic igneous rocks. The contribution of carbonate source rocks gradually increases toward the uppermost part of the basin sequence (the Limestone Member).

7.5. Reconstructing palaeoclimate using geochemical data

Some geochemical studies document the application of elemental ratios for reconstruction of palaeoenvironment and palaeoclimate in terrestrial records, such as palaeosol deposits (Sheldon *et al*., 2002; Bokhorst *et al*., 2009; Sheldon and Tabor, 2009) and lacustrine successions (Ng and King, 2004; Das *et al*., 2006; Roy *et al*., 2010). According to literatures, the Na_2O, K_2O and CaO contents are largely removed and by contrast, TiO_2 and Al_2O_3 are relatively retained during weathering and diagenesis of the parent rocks (Nesbitt and

Young, 1984, 1989; Condie, 1993; Fedo *et al*., 1995; Nesbitt *et al*., 1996). The ratios of mobile and immobile elements are good indicators to determine the degree of chemical weathering and intensity of erosion. These two parameters are mainly a function of climate (Sheldon *et al*., 2002; Bokhorst *et al*., 2009; Sheldon and Tabor, 2009).

Regarding TiO_2 and ΣFe_2O_3, these two elements display significant variation in different types of igneous rocks (basalt compared to granite), and the ratios TiO_2/Al_2O_3 and $\Sigma Fe_2O_3/Al_2O_3$ are useful proxies for provenance studies, that are concerned with the input of terrigenous materials through fluvial and/or eolian processes. These elemental ratios can represent the palaeoenvironment or source materials of the catchment (Zabel *et al*., 2001; Li *et al*., 2003; Sheldon and Tabor, 2009). The CaO content commonly resides in silicate minerals such as plagioclase, pyroxene, amphibole and biotite, all of which are susceptible to weathering (Nesbitt and Young, 1984, 1989; Fedo *et al*., 1995). CaO is also the major constituent of carbonate minerals (e.g. calcite) (Nesbitt and Young, 1984, 1989). The carbonate accumulation particularly in palaeosols occurs in relation with post-pedogenic formation and represents a function of rainfall. Palaeosol deposits containing carbonate concretions and cements as well as calcareous rhizomorphs may reflect relatively colder or drier conditions (Royer, 1999; Retallack, 2001). Accordingly, the ratio CaO/Al_2O_3 can be used to detect periods of low precipitation (dry or arid condition) (Ding *et al*., 2001; Yang *et al*., 2004).

The alkali elements Na_2O and K_2O are mainly held in feldspars and micas, and both of these are susceptible to weathering. During intense chemical weathering of feldspar-bearing source materials, K_2O becomes mostly incorporated in clay minerals and therefore a higher K_2O/Na_2O ratio indicates a stronger degree of weathering. On the other hand, Na_2O is mobile during strong chemical weathering and a low Na_2O/Al_2O_3 ratio mirrors relatively dry palaeoclimatic conditions (Nesbitt and Young, 1984, 1989; Fedo *et al*., 1995).

In order to reconstruct fluctuations in climatic or weathering conditions through the time, the Chemical Index of Alteration (CIA) proposed by

Nesbitt and Young (1984) was applied to determine the degree of the source weathering in the Soa Basin. This CIA represents transformation of feldspars and volcanic glass to secondary clay minerals (e.g. kaolinite, halloysite, illite, smectite) relative to fresh source rocks. A low CIA value means near absence of chemical weathering, which can be suggestive of cold and/or arid environments (Nesbitt and Young, 1984, 1989; Fedo *et al*., 1995). The CIA values were calculated and sequentially plotted against the stratigraphic profiles, together with a number of indices.

These include the ratios Sr/Rb and of Sr/Ba, to document palaeoclimatic changes in the Soa Basin. Sr is commonly concentrated in Ca-bearing minerals such as plagioclase, pyroxene, amphibole and carbonate minerals, while Rb and Ba predominantly occur in micas and K-feldspar. Sr is mobile while Rb and Ba are relatively immobile during weathering or pedogenesis (Nesbitt and Young, 1984; Fedo *et al*., 1995; Gallet *et al*., 1996; Sheldon and Tabor, 2009). Therefore, Sr/Rb and Sr/Ba ratios can be used to monitor the intensity of chemical weathering, with low ratios mirrorring strong chemical weathering (Gallet *et al*., 1996; Bokhorst *et al*., 2009; Sheldon and Tabor, 2009).

In a tropical environment, chemical weathering is primarily controlled by rainfall, while temperature varies less strongly and can be considered nearly constant (Metcalfe and Nash, 2012; Penny, 2012). The elemental ratios TiO_2/Al_2O_3, $\Sigma Fe_2O_3/Al_2O_3$, Na_2O/Al_2O_3, CaO/Al_2O_3, K_2O/Na_2O, Sr/Rb and Sr/Ba, combined with CIA can serve as proxy indicators of variation in precipitation under a monsoonal climate with warm and humid periods alternating with colder, drier and less humid periods (e.g. Gallet *et al*., 1996; Wei *et al*., 2004; Liu *et al*., 2007; Bokhorst *et al*., 2009; Roy *et al*., 2010).

In this study, the combination of elemental ratios of sediments and lithofacies successions in all stratigraphic units of the Ola Bula Formation, will be applied to describe and interpret the palaeoclimatic fluctuations in the Soa Basin during the Pleistocene. The variation of geochemical proxies in

stratigraphic profiles provides past environmental and/or climatic changes, spanning from 1.5 Ma to 0.65 Ma. The main stratigraphic sections measured at three key archaeological sites (Mata Menge, Tangi Talo and Wolo Sege) were used for palaeoenvironmental and palaeoclimatic reconstructions. The Tangi Talo section documents the continuous litho-sequence of the Tuff Member of the Ola Bula Formation that was deposited at ~1.5–1.0 Ma. The sedimentation processes between ~1.0 Ma and 0.70 Ma can be recognised in the Wolo Sege section. This section records the lithological characteristics of the Sandstone Member of the Ola Bula Formation, and marks lithofacies changes of the Tuff and Sandstone Members.

The Mata Menge section provides the complete sequence of the Sandstone and Limestone Members of the Ola Bula Formation, and this stratigraphic profile reflects basin deposition at ~0.80 – 0.65 Ma. The interpretation of palaeoenvironment and palaeoclimate of the Soa Basin using geochemical ratios on these key stratigraphic sections will be discussed in the following sections in chronological order. Discrete tephra layers occurring in the stratigraphic profiles are used as relative time markers.

7.5.1. The Early Pleistocene (~1.50 – 1.0 Ma)

The Tangi Talo section records the most complete lower and middle sequence of the Tuff Member, deposited at ~1.50 – 1.0 Ma. This section is dominated by palaeosols (FA–IX) and substantial occurrence of volcaniclastic deposits (FA–I and FA–II), lahar deposits (FA–IV), fluvial sandstones (FA–V) and floodplain claystone (FA–VII). The samples of palaeosol deposits from the Tangi Talo section comprise 0.49–1.03 wt % (average 0.82 wt%) TiO_2, 17.40–22.20 wt% (19.90 wt%) Al_2O_3, 4.67–9.97 wt% (7.68 wt%) ΣFe_2O_3, 2.31–6.61 wt% (3.54 wt%) CaO, 0.02–2.31 wt% (0.51 wt%) Na_2O, 0.24–1.59 wt% (0.52 wt%) K_2O, 164–258 ppm (202 ppm) Sr, 10–63 ppm (27 ppm) Rb, 95–457 ppm (216 ppm) Ba, and 68–98 (92) CIA. In order to visualize the interpretations, representative geochemical

indices and weathering index are plotted in the chemostratigraphic profiles as illustrated in Figure 7.4.

The lower part of the Tangi Talo section (interval 0.0–5.0 m) consists of palaeosol, volcaniclastic–, lahar–and floodplain deposits, whereas the lower part of section is marked by the Tangi Talo T5, dated at 1.27±0.03 Ma (S. Flude, pers. Comm). In the lower section, the elemental ratios display some variability, with the exception of K_2O/Na_2O and Sr/Rb. The latter being relatively constant upsection and below the mean values. Palaeosol horizons in the lowermost part display no significant differences with respect to the elemental ratios and clay minerals. The ratios TiO_2/Al_2O_3, $\Sigma Fe_2O_3/Al_2O_3$, K_2O/Na_2O, Sr/Rb and Sr/Ba are lower than the mean values, while CaO/Al_2O_3 and Na_2O/Al_2O_3 ratios are higher than the average values with minor fluctuations. The contents of immobile components (TiO_2 and ΣFe_2O_3) show similar trends. The mobile elements of CaO and Na_2O also demonstrate identical patterns. In addition, K_2O/Na_2O and CIA indicate moderate chemical weathering.

As shown in Figure 7.4, the ratios TiO_2/Al_2O_3, $\Sigma Fe_2O_3/Al_2O_3$, CaO/Al_2O_3, Na_2O/Al_2O_3 and Sr/Ba in the lower section exhibit similar trends, where they increase in the mid section (interval ~2.0–3.0 m) and subsequently decrease near the top (interval ~4.0–5.0 m). The increasing trends of TiO_2/Al_2O_3, $\Sigma Fe_2O_3/Al_2O_3$, CaO/Al_2O_3, Na_2O/Al_2O_3 and Sr/Ba ratios suggest elemental inputs related to physical erosion of the catchment rocks. The TiO_2/Al_2O_3 and $\Sigma Fe_2O_3/Al_2O_3$ ratios are associated with detrital mafic minerals and these ratios can indicate the weathering intensity of parent rocks (Zebel *et al.*, 2001; Sheldon and Tabor, 2009). The CaO/Al_2O_3, Na_2O/Al_2O_3 and Sr/Ba ratios are controlled by the presence of feldspars and clay minerals. This interpretation is in concordance with the lithology that corresponds to lahar deposits. These lahar deposits were probably derived from erosion of nearby volcanic hinterlands during warm and wet condition.

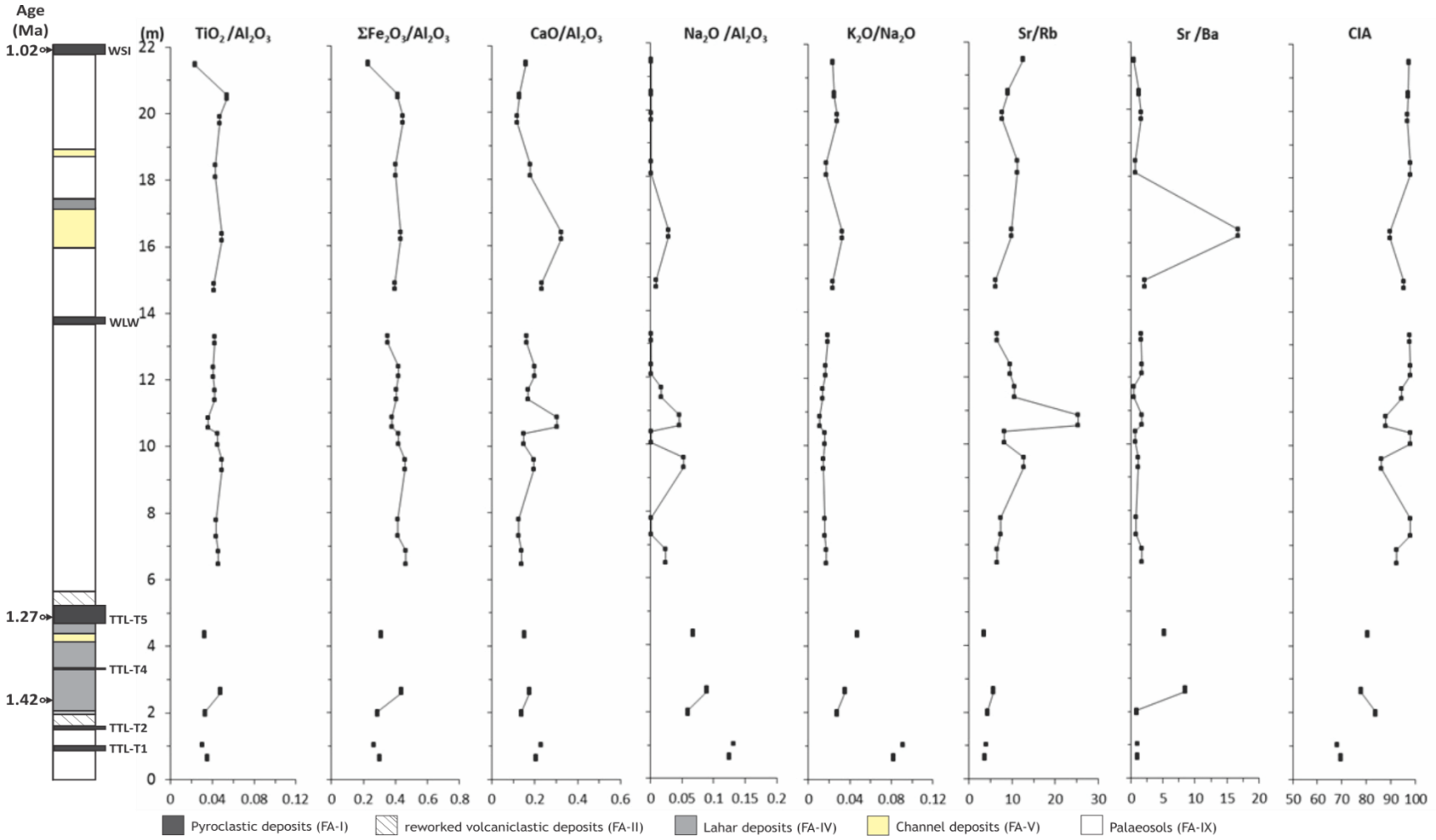

Figure 7.4. The variation of geochemical ratios through the depth profile of the Tuff Member within the Tangi Talo section. Abbreviations: FA = facies association; CIA = Chemical Index of Alteration; TTL T1-T5 = Tangi Talo Tephra (T1-T5); WLW = Wolo Wawo Tephra; WSI = Wolo Sege Ignimbrite.

The middle interval of the Tangi Talo section is characterised by a thick-palaeosol bounded by the Tangi Talo T5 (TTL-T5) at the base and the Wolo Wawo Tephra (WLW) at the top. The TiO_2/Al_2O_3 and $\Sigma Fe_2O_3/Al_2O_3$ ratios show identical trends, no noticeable changes can be observed and these ratios are close to the mean values. The K_2O/Na_2O ratio demonstrates strong oscillations, while the CIA values display small variations. The K_2O/Na_2O and CIA suggest strong pedogenesis. An abrupt change occurs at the interval between 10.0 m and 11.0 m, reflected by increasing CaO/Al_2O_3, Na_2O/Al_2O_3 and Sr/Rb. The higher K_2O/Na_2O ratio are mainly influenced by higher clay mineral contents, rather than the presence of K-feldspar and micas.

Regarding the positive shift of CaO/Al_2O_3, Na_2O/Al_2O_3 and Sr/Rb (interval 10.0–11.0 m), these anomalies reflect strong leaching during pedogenesis and are usually associated with extensive water runoff that can result in the dissolution of detrital feldspar (see Gallet *et al*., 1996; Zabel *et al*., 2001; Bokhorst *et al*., 2009; Sheldon and Tabor, 2009). A wet period in the catchment may have enhanced the water supply to the basin.

The upper part of the Tangi Talo section predominantly comprises palaeosols, sandstones, lahar deposit and pyroclastic deposit. The Wolo Sege Ignimbrite (WSI) marks top of this upper interval. The elemental ratios of palaeosols generally demonstrate small variations and decreasing patterns toward the top of section, with the exception of K_2O/Na_2O and Sr/Rb. The K_2O/Na_2O and CIA suggest intense weathering during soil formation. The K_2O/Na_2O ratio significantly increases upsection and Sr/Rb is slightly increasing upward. Trends in the TiO_2/Al_2O_3 ratio parallel the $\Sigma Fe_2O_3/Al_2O_3$ ratio, with both ratios decreasing toward the upper boundary. The CaO/Al_2O_3 and Na_2O/Al_2O_3 ratios display similar patterns, decreasing up section.

In the upper sequence of the studied section, high ratios of CaO/Al_2O_3, Na_2O/Al_2O_3 and Sr/Ba can be recognised at the interval 16.0–17.0 m, which correspond to strong material input to the study site. Lithofacies analysis suggests that a coarse sandstone with multiple cross stratification showing cut

and fill structures occurs at this interval. The sandstone contains a high proportion of feldspar, which is certainly responsible for the increase in CaO/Al_2O_3, Na_2O/Al_2O_3 and Sr/Ba ratios. The occurrence of cross-stratified sandstone is interpreted as a major flood during a high rainfall event in the watershed, and the patterns of CaO/Al_2O_3, Na_2O/Al_2O_3 and Sr/Ba support this interpretation.

In general, the palaeosol samples through the whole section do not show significant differences, except in the middle interval where notable oscillations of CaO/Al_2O_3, Na_2O/Al_2O_3, Sr/Ba, and CIA can be recognised. The elements TiO_2 and ΣFe_2O_3 are considered as common immobile chemical components during *in situ* weathering process. The TiO_2/Al_2O_3 and $\Sigma Fe_2O_3/Al_2O_3$ ratios commonly remain constant in the soil horizons with different weathering degrees (Nesbitt and Young, 1984, 1989; Fedo *et al*., 1995). In the studied section, TiO_2/Al_2O_3 and $\Sigma Fe_2O_3/Al_2O_3$ shows a similar trend, indicating palaeosols were derived from the same source.

The lithofacies analysis indicates that the sequence of the Tangi Talo section was generally deposited in fluvial environments, where palaeosols preferentially formed in floodplain and/or on abandoned channels. The palaeochannel was likely developed intermittently when wetter seasons occurred. The positive deflections of such elemental ratios in particular CaO/Al_2O_3, Na_2O/Al_2O_3 and Sr/Rb denote several periods with wet conditions. The overall elemental ratios in the entire section suggest that palaeoclimatic condition at ~1.50 – 1.0 Ma were warm, subhumid and dry tropical, alternating with wetter periods. The past climatic condition of the studied basin changed to more drier and colder conditions at ~1 Ma, as indicated by a well-developed vertisol horizon showing intensive shrinkage cracks (see Chapter 6).

7.5.2. The late Early Pleistocene to early Middle Pleistocene (~ 1.0 – 0.70 Ma)

The Wolo Sege section documents the upper part of the Tuff Member and the lower and middle parts of the Sandstone Member, spanning between *ca.* 1.02 Ma and 0.70 Ma. In this section, the upper part of the Tuff Member is dominated by pyroclastic deposits (FA–I) and reworked volcaniclastic deposits (FA–II) with subordinate lahar deposits (FA–IV). Palaeosols are overprinted on fluvial conglomerates (FA–V) and separate reworked and primary volcaniclastic deposits or occur between two primary pyroclastic deposits. The sequence of the Sandstone Member predominantly consists of palaeosols (FA–IX) and massive sandstones (FA–VI), while a lahar deposit (FA–IV) occurs in the top of the section.

The palaeosol deposits of the Tuff Member are composed of 0.39–0.85 wt % (average 0.68 wt%) TiO_2, 15.22–21.48 wt% (19.39 wt%) Al_2O_3, 3.35–9.13 wt% (7.08 wt%) ΣFe_2O_3, 3.15–7.31 wt% (4.94 wt%) CaO, 0.39–2.61 wt% (1.56 wt%) Na_2O, 0.76–2.20 wt% (1.10 wt%) K_2O, 32–64 ppm (35 ppm) Rb, 182–265 ppm (220 ppm) Sr, 230–413 ppm (325 ppm) Ba, and 61–91 (78) CIA.

The palaeosol deposits of the Sandstone Member constitute 0.74–1.06 wt % (average 0.92 wt%) TiO_2, 18.03–22.83 wt% (20.33 wt%) Al_2O_3, 7.24–10.96 wt% (9.39 wt%) ΣFe_2O_3, 3.29–6.81 wt% (5.22 wt%) CaO, 0.50–2.07 wt% (1.50 wt%) Na_2O, 0.07–0.73 wt% (0.36 wt%) K_2O, 7–41 ppm (26 ppm) Rb, 54–256 ppm (177 ppm) Sr, 47–694 ppm (215 ppm) Ba, and 76–93 (82) CIA.

The elemental ratios, CIA and clay mineral contents of palaeosols are plotted with the stratigraphic profile, and combined with the lithology and the chemical and clay mineral compositions of the other lithofacies (Figure 7.5). Palaeosol horizons in the lower part of section corresponding to the Tuff Member display no remarkable changes upward with respect to the elemental ratios and clay minerals. The ratios TiO_2/Al_2O_3, $\Sigma Fe_2O_3/Al_2O_3$, CaO/Al_2O_3, Na_2O/Al_2O_3, Sr/Rb and Sr/Ba are mostly lower than the mean values, while K_2O/Na_2O are higher than the average values. The K_2O/Na_2O and CIA demonstrate lowering trends toward the top, and indicate that the weathering

intensity gradually changes from strong to moderate. Regarding the clay content, kaolin minerals and I/S are present in nearly similar proportions, with S/C is in a low amount. The fluctuations of Sr/Rb and Sr/Ba near the boundary between the Tuff Member and Sandstone Member are related to the variable proportions of feldspars and clay mineral contents within palaeosols and lahar deposits.

In the case of the Sandstone Member, the lower sequence (interval ~13.60–21.90 m) is dominated by palaeosols and massive sandstones. The TiO_2/Al_2O_3 ratio is parallel to $\Sigma Fe_2O_3/Al_2O_3$ and these ratios are relatively constant upward and close to the mean values. The CaO/Al_2O_3 and Na_2O/Al_2O_3 ratios display identical trends, with these ratios decreasing at the interval ~15.0–18.0 m and subsequently constant upward. The Sr/Rb and Sr/Ba ratios demonstrate considerable variation with overall values decreasing upsection. The CIA values indicate moderate to strong weathering during soil formation.

Moreover, palaeosols in the middle sequence of the Sandstone Member (interval ~21.90–29.50 m) show a large variation of Sr/Rb and Sr/Ba toward the top of the section, while the other elemental ratios are relatively constant. The increasing patterns of Sr/Rb and Sr/Ba ratios indicate gradual changes of leaching intensity during pedogenesis. The clay minerals do not show remarkable variations upward and the contents are relatively close to the average values. The CIA value exhibits a decreasing trend upward that indicates the change of weathering intensity from strong to moderate.

The temporal variation of elemental ratios and clay minerals in the whole section is in agreement with the lithology. The shifts of elemental ratios and clay minerals are mainly associated with reworked sediments (sandstones and lahar deposits). In addition, the clay fraction of sandstones is primarily composed of kaolin minerals, whereas I/S and S/C are absent. This suggests that that the source of sandstones contains high amounts of feldspars and kaolin minerals or alternatively kaolin minerals occurred from the alteration of feldspars during post-depositional weathering.

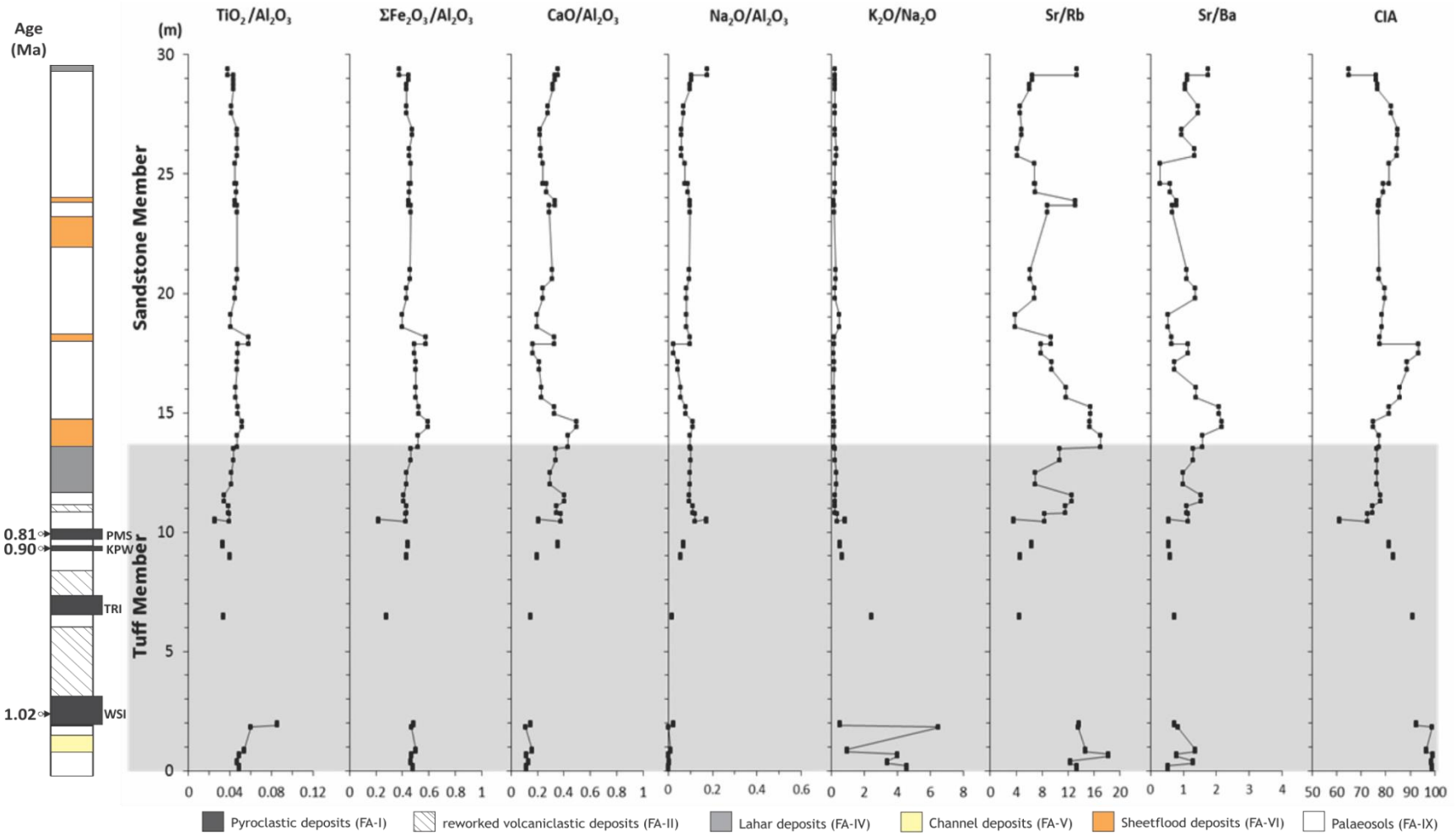

Figure 7.5. The variation of elemental ratios through the sequence of the Tuff Member (shaded interval) and the Sandstone Member (unshaded interval) recorded at the Wolo Sege section. Abbreviations: FA = facies association; CIA = Chemical Index of Alteration; WSI = Wolo Sege Ignimbrite; TRI = Turekeo Ignimbrite; KPW = Kopowatu Tephra; PMS = Pumaso Tephra.

The palaeosol samples in the studied section do not show any significant changes toward the top of section with respect to TiO_2/Al_2O_3, $\Sigma Fe_2O_3/Al_2O_3$ and K_2O/Na_2O. These ratios are nearly similar with the mean values and may suggest stable climatic conditions. The interval 15.0–18.0 m should be noticed regarding the increasing trend of Illite-smectite which is parallel to the decreasing trends of CaO/Al_2O_3, Na_2O/Al_2O_3, Sr/Rb, Sr/Ba and kaolin minerals. The palaeoclimate possibly changed to a drier setting with less moisture at the time of deposition.

The overall elemental ratios and clay mineral assemblages through the Wolo Sege section, spanning from ~1.0 to 0.70 Ma, reflect a warm, humid and dry tropical climate. A period of drier and colder conditions occurred at the interval ~15.0–18.0 m equivalent to *ca*. 0.80 Ma ago.

7.5.3. The Middle Pleistocene (~0.80 – 0.65 Ma)

The continuous sequence of the Sandstone and Limestone Members is recorded in the Mata Menge section, which was deposited at ~0.80 – 0.65 Ma. In this section, the Sandstone Member predominantly comprises palaeosols (FA–IX) that occur in the middle and upper part. The lower part consists of lahar deposits (FA–IV), and fluvial deposits (FA–V). A pyroclastic fall deposit of the Mata Menge Tephra (FA–I) marks the top of middle interval of this section.

The palaeosol deposits of the Sandstone Member composed of 0.48–0.94 wt % (average 0.80 wt%) TiO_2, 12.05–23.26 wt% (19.09 wt%) Al_2O_3, 5.14–9.80 wt% (8.33 wt%) ΣFe_2O_3, 3.19–43.80 wt% (11.44 wt%) CaO, 0.03–1.62 wt% (0.79 wt%) Na_2O, 0.09–0.49 wt% (0.31 wt%) K_2O, 3–30 ppm (20 ppm) Rb, 69–232 ppm (150 ppm) Sr, 38–284 ppm (151 ppm) Ba, and 81–99 (89) CIA.

In addition, lacustrine deposits of the Sandstone Member comprise 0.69–0.95 wt % (average 0.83 wt%) TiO_2, 20.27–21.50 wt% (20.79 wt%) Al_2O_3, 6.97–7.77 wt% (7.29 wt%) ΣFe_2O_3, 4.63–7.05 wt% (5.36 wt%) CaO, 0.85–

1.27 wt% (1.07 wt%) Na_2O, 0.32–0.45 wt% (0.37 wt%) K_2O, 27–36 ppm (33 ppm) Rb, 175–209 ppm (193 ppm) Sr, 150–160 ppm (155 ppm) Ba, and 84–88 (86) CIA.

The plotting of elemental ratios and clay minerals through the stratigraphic profile is shown in Figure 7.6. The major elemental ratios of the Sandstone Member display little variability upsection and the ratios are mostly close to the mean values. The ratios TiO_2/Al_2O_3, $\Sigma Fe_2O_3/Al_2O_3$, Na_2O/Al_2O_3 and K_2O/Na_2O from samples of lacustrine claystones and palaeosols are relatively constant toward the top boundary. The shift of CaO/Al_2O_3 at ~30 m depth is due to a significant amount of carbonate mineral (calcite is up to 31.70 %). The Sr/Rb, Sr/Ba and CIA fluctuate strongly upward. The Sr/Rb and CIA generally show increasing trends and these ratios are nearly similar with the average values. In addition, the Sr/Ba ratio is mostly greater than the mean values and displays oscillations from the bottom part to the top part. The variability of Sr/Ba indicates the degree of leaching under different weathering intensities, and indeed also reflects the hydrolysis process. In addition, the CIA value suggests that palaeosol deposits display moderate to strong weathering. Palaeosols in the upper part of the Sandstone Member show unique characteristics, containing various proportions of calcite, which are suggestive of dry periods. The lithofacies analysis in the studied section indicates that the sediments of the Sandstone Member were deposited in a fluvial environment.

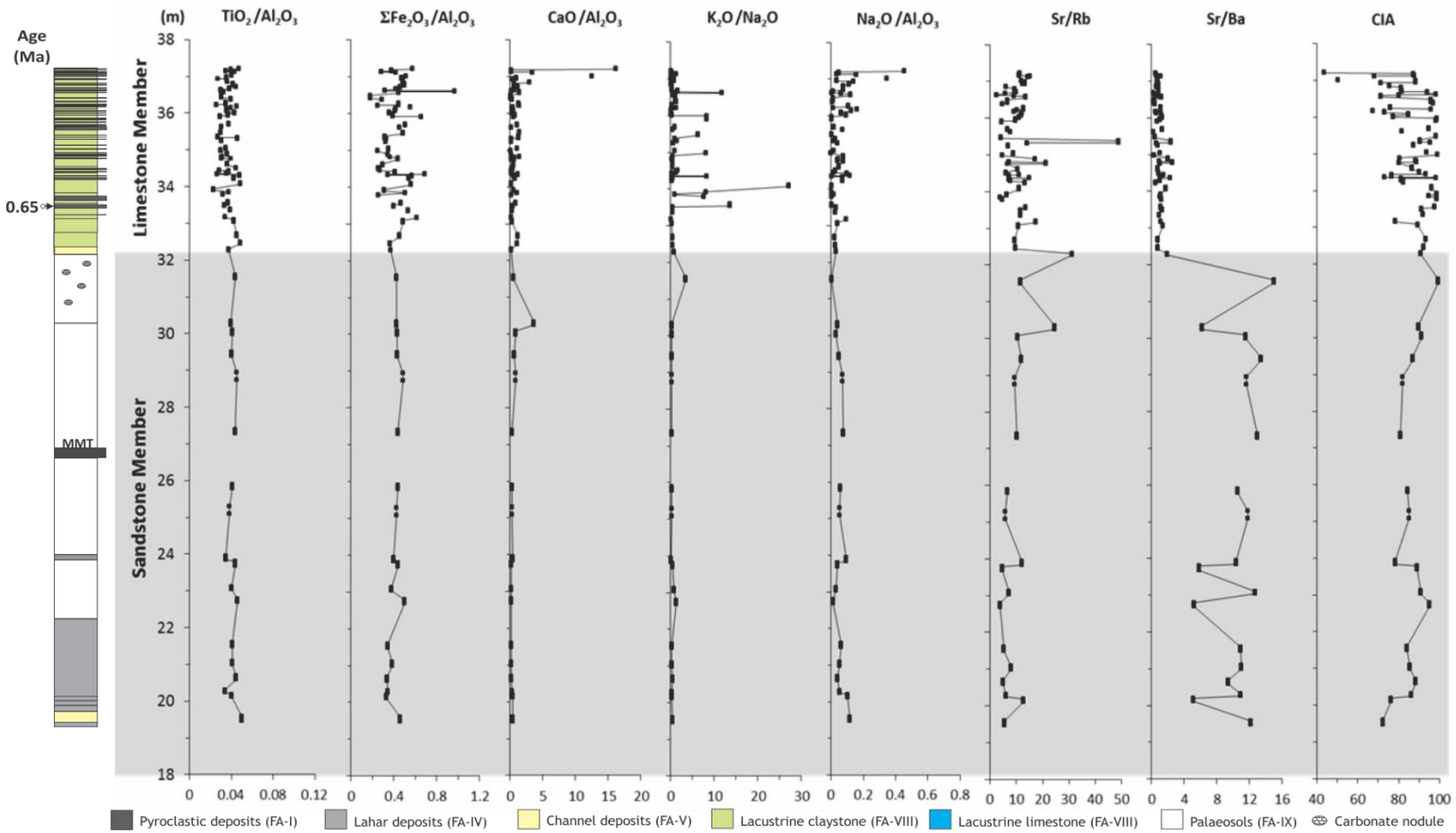

Figure 7.6. The variation of elemental ratios through the sequence of the Sandstone Member (shaded interval) and the Limestone Member (unshaded interval) from the Mata Menge section. Abbreviations: FA = facies association; CIA = Chemical Index of Alteration; MMT = Mata Menge Tephra.

The uppermost part of the Mata Menge section documents the continuous sediment deposition of the Limestone Member that formed in a lacustrine environment (Figure 7.6). This succession consists of interbedded of claystones (FA–VIII/Fh) and mm-to dm-thick pyroclastic airfall deposits (FA–I). Tuffaceous limestone and micritic limestone (FA VIII/Lm) occur in the middle and upper parts. The lacustrine claystones are composed of 0.42–1.14 wt % (average 0.69 wt%) TiO_2, 12.25–27.77 wt% (19.21 wt%) Al_2O_3, 4.13–17.46 wt% (7.99 wt%) ΣFe_2O_3, 3.05–35.96 wt% (11.27 wt%) CaO, 0.02–2.92 wt% (0.86 wt%) Na_2O, 0.17–1.31 wt% (0.40 wt%) K_2O, 8–33 ppm (17 ppm) Rb, 45–405 ppm (165 ppm) Sr, 59–517 ppm (183 ppm) Ba, and 67–99 (88) CIA.

The geochemical ratios TiO_2/Al_2O_3, CaO/Al_2O_3, Na_2O/Al_2O_3 and Sr/Rb display small but frequent fluctuations toward the top of section. The low ratio and less variability of TiO_2/Al_2O_3 indicate a stable lacustrine environment in which streamflow or run-off was weak and consequently the allochthonous input to the lacustrine system was minimal. The sharp peaks of CaO/Al_2O_3 and Na_2O/Al_2O_3 in the top of the section are associated with carbonate minerals and clay minerals, respectively. The CaO/Al_2O_3 ratio matches the trend of calcite content whereas the highest CaO/Al_2O_3 coincides with the highest amount of calcite, and corresponds to the formation of tuffaceous micritic limestone, which developed only in the upper part of the studied section. The relatively stable pattern of CaO/Al_2O_3 in the lower-and middle parts, with a ratio near the mean value, significantly increases near the top, in conjunction with the small variation of calcite, which also greatly increases near the top; these facts reflect gradual climatic change. In the early stage of lacustrine development, the palaeoclimate was warm and wet, favouring clastic sediment supply as indicated by the occurrence of horizontally laminated sandstone, and the clay mineral input to the lacustrine environment. The strong shift of K_2O/Na_2O is associated with the erosion of deep weathered soil profiles in the catchment (see Fedo *et al*., 1995; Zabel *et al*., 2001; Bokhorst *et al*., 2009; Roy *et al*., 2010). Furthermore, the past climate changed into warm and dry as well as the lake level was shallowing,

which governed the formation of abundant carbonate mineral. The occurrence of carbonate minerals in the lacustrine setting is controlled by the availability of calcium and organisms whereas these factors have a correlation with climate (Verrecchia 2007; Gierlowski-Kordesch, 2010).

In addition, the $\Sigma Fe_2O_3/Al_2O_3$ ratio displays considerable variation toward the top of the section. The fluctuation of this ratio is correlated to the degree of weathering and redox conditions. Macroscopical observations suggest that claystones have a reddish to brownish colour that could indicate oxidation of the sediments during periods of oxygenated waters, corresponding with shallow lake levels. In the section, two major events of strong oxidation regimes can be observed at intervals of 32.71–33.16 m and 34.52–34.75 m. The 32.71–33.16 m range is bounded by the deposition of the Piga Tephra 01 (PGT-01), which has a basaltic composition and records the early stage of active volcanism near the Soa Basin after thousands of years of quiescence. Moreover, the interval 34.52–34.75 m is marked by the presence of PGT-08 in the bottom and PGT-09 in the top.

The ratios of Sr/Rb and Sr/Ba display distinct patterns. The Sr/Ba ratio is constant upward and the ratio is below the mean value, while Sr/Rb shows marked oscillations. The variation of Sr/Rb is affected by the clay mineral content and this ratio reflects hydrological variability of the watershed. In addition, The CIA values of claystones reflect moderate to strong chemical weathering of the catchment rocks.

The temporal variation of elemental ratios throughout the section exhibits distinct patterns between the SM and the LM. The obvious differences can be observed in the ratios $\Sigma Fe_2O_3/Al_2O_3$, K_2O/Na_2O, Sr/Rb, Sr/Ba and clay minerals. The $\Sigma Fe_2O_3/Al_2O_3$ ratio is relatively stable in the SM and shows oscillations in the LM. This fact indicates the variability of oxidation processes, which are more intense in the LM. Although K_2O/Na_2O of the SM and LM is generally similar and low, a few strong positive shifts occur in the LM, due to the abundance of kaolin minerals.

The Sr/Rb ratio of the SM displays an increasing trend upsection, while this ratio denotes considerable variation in the LM. This elemental ratio is controlled by the proportions of clay minerals. In addition, the pattern of the Sr/Ba ratio shows uniqueness where this ratio in samples of the SM is mostly greater than the mean values, while Sr/Ba of the LM is mostly lower than the average values. The ratio of Sr/Ba in palaeosols and lacustrine sediments reflects the variability of leaching and hydrological processes. The lacustrine claystones of the SM have higher Sr/Ba, which may indicate considerable influence of material inputs by streamflow or run-off entering the lake system.

The overall data indicate a warm to hot tropical climate, with alternating dry and wet conditions (monsoonal). In the late pahses of deposition of the SM, the climatic conditions displayed a drier environment, reflected by the formation of pedogenic carbonate. The blocking of major outlets by lava flows, mudflows or pyroclastic deposits together with a warm and wet climatic condition, have led the development of lacustrine environment at ~0.65 Ma ago. The climatic setting remained warm and humid during the Middle Pleistocene. Several regressive periods of lake-level in relation to drier conditions are detected as characterised by subaerial exposures, oxidation processes and carbonate precipitation. The pollen analysis on the claystones of the LM confirms the interpretation of low lake level, which denotes the presence of *Poaceae*, *Cyperaceae* and *Pteridophyta*, indicating a shallow lake and dry savanna-type vegetation of the adjacent areas (W.A. van der Kaars, pers. comm).

The climate variability in the Soa Basin during the period of ~1.50–0.65 Ma, shown by the lithological successions and chemostratigraphic profiles, was likely influenced by the Australian monsoon circulation. The monsoon system is characterised by the movement of the Intertropical Convergence Zone (ITCZ), which is situated north of the equator during the dry season (Australian winter) and migrates to the south during the wet season (Australian summer) (Hobbs, 1998; Spooner *et al*., 2005).

7.6. Summary

This study provides the first detailed multi-element geochemical analysis of the Soa Basin sequence, in order to investigate chemical weathering and provenance of sediments through time, and to try to understand the palaeoclimatic conditions and fluctuations of the Soa Basin, spanning from ~1.50 – 0.65 Ma.

The geochemical data suggest that the analysed samples are predominantly derived from felsic volcanic rocks (rhyolite, dacite) with minor contributions from mafic volcanic rocks (andesitic–basaltic) and carbonate rocks. The weathering indices suggest that the source generally experiences moderate to extremely intense chemical weathering and the indices also reflect moderate to strong pedogenesis, in accordance with field observations. The A-CN-K diagram reveals that the majority of samples from all stratigraphic units are parallel to the A-CN line and were not subjected to potash-metasomatism during diagenesis or pedogenesis.

The elemental ratios and weathering indices have been used to understand the climatic control on the Soa Basin sequence. To obtain this objective, the sedimentary records of three important sections were evaluated. The temporal variation of the dataset from the Tangi Talo section suggests climatic conditions during the Early Pleistocene (~1.50 – 1.0 Ma), represented a warm and dry tropical climate, with several short periods of warm and wet conditions.

The Wolo Sege section documents a continuous sequence, spanning from the Early to Middle Pleistocene (~1.0 – 0.70 Ma), which palaeoclimatic conditions reflected a general warm and dry setting. On the other hand, Mata Menge sequence recorded the climatic condition between ~0.80 Ma and 0.65 Ma. At *ca*. 0.65 Ma ago, a lacustrine environment was developed that triggered by the damming processes of the basin outlets and wetter climatic conditions. The palaeoclimatic fluctuations occurred since 0.65 Ma, showing the alternation of dry and wet conditions, and therefore a shallow lake was formed.

CHAPTER EIGHT

CONCLUSIONS AND SUGGESTIONS FOR FUTURE RESEARCH

8.1. Introduction

This study has used an interdisciplinary approach, integrating field and laboratory analyses, to examine geoarchaeological archives of the Soa Basin. The multi-datasets obtained in the field and laboratory were used to solve the objectives of this study. Firstly, since the stratigraphic framework was still problematic, this study performed detailed investigations on temporal and spatial distributions of the lithological units in the Soa Basin by using lithofacies analysis and tephrostratigraphy. The tephra study has provided pivotal information regarding the eruptive events of volcanic centres near the study area and several volcanic layers can be used as stratigraphic marker beds, which correlate key archaeological and palaeontological localities, and define relative chronological data. Secondly, the presence of volcanic deposits is crucial in terms of establishing a chronostratigraphical framework. The $^{40}Ar/^{39}Ar$ dating have been incorporated employed to obtain reliable ages and using some volcanic layers as isochronous tie points that have been proven to be very important for intrabasinal correlations. The stratigraphic analysis, on the other hand, facilitated the refinement of temporal levels of stone artefacts and fossil fauna that were recovered during intensive excavations. These first and second aims were outlined in Chapter 5 and Chapter 6, respectively.

Moreover, laboratory-based studies were conducted to determine the geochemical and mineralogical compositions of sediments and volcaniclastic deposits and their vertical changes throughout the studied sections. The combination of facies analysis and temporal variation of chemical signatures and mineral contents was shown to be a useful method to elaborate on the other objective of this study, namely to reconstruct the palaeo-environmental settings

and climatic changes in the Soa Basin during the Pleistocene. The overviews of depositional environment and palaeoclimatic condition have been highlighted in Chapter 6 and Chapter 7.

This final chapter will outline the implication of geoarchaeological archives and the contribution of this study to answer questions and problems in the Soa Basin. The main conclusions of this study will be drawn in the following sections and suggestions for further research will be discussed in the final part of this chapter.

8.2. Conclusions

8.2.1. New tephrostratigraphy and volcanic sources

This study has established a new tephrostratigraphic framework for the Soa Basin, which provides significant information regarding explosive activities from local or distant volcanoes, and provides important isochronous markers. By combining stratigraphy, geochemical composition, new chonological data and statistical approaches, this study was able to confirm that there are multiple eruption units preserved in the Soa basin sequence and their origin could be hypothesized. In addition, discrete tephra layers identified throughout the Ola Bula Formation, particularly in the Tuff and Sandstone Members, play important roles as stratigraphic controls for archaeological and palaeontological resources. The tephra records and chronological data demonstrate new considerations with regard to stratigraphic positions and the time of accumulation of artefacts and fossils. The new tephrosequence also permits correlation of several important archaeological and/or palaeontological sites (e.g. Kobatuwa, Mata Menge, Wolo Sege and Tangi Talo), which could not be performed by previous studies.

A total of 73 prominent pyroclastic units have been identified from various outcrops and stratigraphic sections in the Soa Basin, which can be identified as pyroclastic airfall, pyroclastic surge and pyroclastic density current deposits. The oldest Ola Kile Formation contains two pyroclastic density current

(PDC) deposits, the Aesessa Ignimbrite (AEI) and Lowo Mali Ignimbrite (LMI), representing two major events of caldera-forming processes, derived from the Welas Caldera Complex (WCC) and the Keli Lambo Volcanic Complex (KLVC), respectively. These volcanic deposits suggest the initial phases of volcanic activity at nearby volcanoes were responsible for creating a palaeolandscape that facilitated further basin accumulations.

The Tuff Member of the Ola Bula Formation consists of nine rhyolitic pyroclastic deposits, including six pyroclastic airfall and three Pyroclastic Density Current (PDC) deposits. The lower part of the Tuff Member comprises four distal airfall units, which belong to the Tangi Talo Tephra (TTl-T1, TTL-T2, TTL-T4 and TTL-T5). These tephra units are well-exposed at Tangi Talo, and TTL-T2 and TTL-T4 bracket the fossil layers developed here. The Wolo Wawo Tephra (WLW) is the only ash layer in the middle of the sequence. The upper part of the Tuff Member constitutes three PDC deposits, including the Wolo Sege Ignimbrite (WSI), Turekeo Ignimbrite (TRI) and Pumaso Tephra, and a chemically unique airfall deposit named Kopowatu Tephra (KPW).

Collected samples were send to Quadlab in Denmark for single grain $^{40}Ar/^{39}Ar$ dating. This method has been applied to plagioclase crystals from TTL-T5 and to hornblende crystals from PMS, and has yielded ages of 1.27±0.03 Ma and 0.81±0.04 Ma, respectively (See Figure 5.33). In addition, isothermal plateau fission track (ITPFT) dating of glass shards was applied to date the KPW at 0.90±0.07 Ma (Brumm *et al.*, 2016). The WSI has been dated by $^{40}Ar/^{39}Ar$ dating on hornblende crystals at 1.02±0.02 Ma, as reported by Brumm *et al*. (2010; 2016) These dated pyroclastic deposits can be placed in the global climate perspective, which TTL-T5, WSI and PMS are good isochronous layers to underpin volcanic eruptions occurring during MIS 39-38, MIS 29-28 and MIS 21-20, respectively.

Except TTL-T5, continuous lateral distribution of WSI, TRI and PMS are considered to be prominent stratigraphic markers for correlating the tuff sequence across the Soa Basin and other age-equivalent successions in Flores.

Although its lateral occurrence is poorly documented, the TTL-T5 is also an important ash layer that marked the accumulation of fossil remains in the lower part of the Tuff Member, because the fossil layers are situated at a level 2 m below TTL-T5.

There is only one distal pyroclastic airfall deposit recognised in the middle succession of the Sandstone Member, known as the Mata Menge Tephra (MMT). This tephra displays unique field and geochemical characteristics, is dark grey in colour with an andesitic composition. The MMT lies approximately 8 m above the uppermost fossil horizons of the Sandstone Member. Unfortunately, the numerical age of this ash has not been determined, and this should be a priority for further research. The MMT can be a potential stratigraphic constraint, being the upper age boundary of the fossil and artefact resources that accumulated in the Sandstone Member.

The youngest tephra succession of the Ola Bula Formation is well-preserved in the lacustrine succession of the Limestone Member, which comprises at least 58 closely spaced sandy ash layers of dominantly basaltic composition, named the Piga Tephra (PGT). The PGT from the lowermost part of the Limestone Member has been dated at 0.65±0.02 Ma ago (Brumm *et al.*, 2016), which is ascribed to MIS 17-16. This age coincides with the commencement of a series of intensive explosive eruptions occurring in the Soa Basin, and which are derived from either local or distant volcanic fields. Further studies are necessary to determine their geochemical characteristics, mineralogical contents and chronology to understand the eruptive history and to investigate the provenance of PGT.

Although most tephra deposits in the study area can be sequentially ordered, there are few pyroclastic deposits whose stratigraphic positions are still uncertain. They include the Kolopanu Ignimbrite (KLP), Nata Randang surge deposit (NTR) and Wulabara Tephra (WLB). All of these pyroclastic units have similarly rhyolitic compositions and derive from the Welas Caldera Complex (WCC). According to their geochemical signatures, this study

infers that KLP, NTR and WLB are younger than PGT. This interpretation should be confirmed by additional research, in order to provide chronological and spatial information for these pyroclastic deposits.

This study has provided geochemical analyses of whole-rock samples and volcanic glasses, and conducted statistical methods using major-element values as variables, and these approaches were used to assess compositional variability of the studied pyroclastic deposits. Geochemical similarities and differences have been subsequently employed to review potential volcanic sources.

With respect to pyroclastic materials of the Tuff Member, the major pyroclasts have a similar composition (rhyolite). However, they are still distinguishable on the basis of their field characteristics, stratigraphic positions and major-element values of volcanic glasses, particularly CaO, ΣFeO and K_2O contents that can discriminate them into several populations. The geochemical data indicates that pyroclastic deposits of the Tuff Member are derived from at least four volcanoes. The Keli Lambo Volcanic Complex (KLVC) is the major volcano depositing five pyroclastic units, TTL-T2, TTL-T5, WSI, TRI and PMS. The large-scale eruptions of the KLVC generated the voluminous PDC deposits of WSI, TRI and PMS that blanketed the entire basin. In addition, TTL-T1 is similar in composition to WLW and both tephras are distal airfall units that most likely erupted from the same volcano. Two tephra units have unique characteristics, which compositionally do not match with any other pyroclastic units of the Tuff Member. The high-silica tephra TTL-T4 represents a very distal airfall deposit that was produced by a strong explosive eruption from a distant volcanic province. Another distal ash, the KPW, is characterised by a very high potassium content, and has a geochemical similarity with the oldest Toba Tuff (OTT). The KPW could potentially originate from the Toba volcano, ~3000 km to the west of the Soa Basin, or possibly from another unknown high-K volcano.

Due to the lack of a geochemical database of pyroclastic deposits from surrounding volcanoes across Flores Island, the sources of TTL-T1 and WLW

are informally given as Volcano "Z", while the TTL-T4 is designated as Volcano "X". With respect to TTL-T2, this tephra can be derived from either the KLVC or Volcano "Z". The discrimination diagrams using CaO, ΣFeO and K_2O contents of glass shards suggest that TTL-T2 is compositionally close to the products of Volcano "Z", similar with TTL-T1 and WLW. By contrast, statistical analyses reveal that TTL-T2 shows chemical affiliation with the KLVC deposits. According to the field characteristics of TTL-T2 being similar to TTL-T1 and WLW suggesting a distal airfall deposit, it can be concluded that TTL-T2 derived from Volcano "Z".

During deposition of the Sandstone Member, the volcanic activity in the Soa Basin became less intense. The andesitic Mata Menge Tephra (MMT) is the only pyroclastic airfall deposit identified and it occurs in the middle of sequence. The thickness and grain size of the MMT suggest a westward ash dispersion and accordingly it is probably derived from the KLVC.

After volcanic quiescence over *ca*. 100 thousand years, volcanic activities generated a total of 58 closely-spaced thin-bedded tephra layers, known as the Piga Tephra (PGT), which were deposited in a lacustrine environment. Whole-rock samples of PGT predominantly consisting of basaltic-andesitic ashes that can be correlated to eruptions of either the BCCC in the south-eastern part of the Soa Basin or the younger domes inside the WCC. However, the source of the felsic Piga Tephras have not been identified yet, due to the paucity of volcanological data from the surrounding volcanoes of the Soa Basin.

8.2.2. New stratigraphic framework of the Soa Basin

By using detailed lithofacies analysis in several stratigraphic columns, this study has added new information about lithological variation of the Ola Bula Formation and improved the general stratigraphy of the Soa Basin. The oldest formation of the basin, the Ola Kile Formation, consists of primary volcaniclastic deposits (FA–I), lahar deposits (FA–IV), channel deposits (FA–V), palaeosols (FA–IX) and localised effusive volcanic bodies (FA–III). This formation

contains two prominent pyroclastic density current deposits, i.e. the Aesessa Ignimbrite (AEI) and the Lowo Mali Ignimbrite (LMI), which were generated by caldera eruptions of the Welas and Keli Lambo, respectively. The overall sequence is dominated by volcanic breccias (laharic deposits) and minor palaeosols and cross-stratified sandstones. The Ola Kile Formation has a total thickness of 100–200 m and was deposited until 1.86 Ma (O'Sullivan *et al*., 2001) in a terrestrial (fluvial) environment.

The Ola Kile Formation is overlain by the Ola Bula Formation and the contact between these two formations indicates an angular unconformity. The overall Ola Bula sequence is relatively horizontal and the maximum total thickness is *ca*. 100–120 m in the central part of the basin near Tangi Talo. The lowermost Member of the Ola Bula Formation, The Tuff Member, consists of (in descending abundance order) palaeosols (FA IX), primary volcaniclastics (FA–I), resedimented volcaniclastics (FA–II), laharic deposits (FA–IV), channel deposits (FA–V), and locally floodplain deposits (FA–VII).

Nine rhyolitic pyroclastic deposits are recognised, including the Tangi Talo Tephra (TTL-T1, TTL-T2, TTL-T4 and TTL-T5), Wolo Wawo Tephra (WLW), Wolo Sege Ignimbrite (WSI), Turekeo Ignimbrite (TRI), Kopowatu Tephra (KPW) and Pumaso Tephra (PMS). The WSI and TRI correpond to pyroclastic density current (PDC) deposits, while TTL, WLW and KPW are interpreted as pyroclastic fall deposits. The general sequence of the Tuff Member predominantly displays an alternation between palaeosols and pyroclastic materials, whereas palaeosols suggest a "time break" of sedimentation and relatively stable palaeolandscape that occurred after the emplacement of volcanic materials.

The presence of several prominent pyroclastic layers is very useful for linking the Tuff sequence, recorded in several stratigraphic profiles throughout the Soa Basin. The WSI, TRI and PMS are good marker beds for intra-basinal correlation, while the KPW that has a unique geochemical composition is a potential candidate for inter-regional correlation. Combining previous fission

track ages and new $^{40}Ar/^{39}Ar$ data, the Tuff Member was deposited at ~1.86–0.81 Ma in fluvial settings and has a maximum total thickness of ~50–60 m in the central part of the basin, but thinning out towards the basin margins.

The Sandstone Member of the Ola Bula Formation conformably overlies the Tuff Member but there is no sharp transition between these two members, except in the Mata Menge section. This member predominantly consists of channel deposits (FA–V) and palaeosols (FA–IX), with minor pyroclastic deposits (FA–I), lahars (FA–IV), sheet flood (FA–VI) and floodplain (FA–VII) facies. The majority of sediments, with a total thickness of ~20–30 m, were deposited in a fluvial environment at a period between 0.81 and 0.65 Ma. A pyroclastic fall deposit, the Mata Menge Tephra (MMT), has been identified in the middle of the sequence and this ash marked the upper boundary of vertebrate-bearing fossil layers.

The youngest member of the Ola Bula Formation, the Limestone Member, has a thickness of up to 10 m and comprises an interbedding of micritic limestones, claystones and basaltic–rhyolitic pyroclastic airfall deposits. This Limestone Member lies conformably on the Sandstone Member. Sediments of this member were deposited in a lacustrine environment, which developed since ~0.65 Ma ago.

8.2.3. Artefact and fossil-bearing layers

Detailed stratigraphic determination, the occurrence of pyroclastic deposits and new ages in this study has confirmed the stratigraphic position of stone tools and fauna remains. Fossil vertebrate remains occur in the lower part of the Tuff Member and throughout the Sandstone Member of the Ola Bula Formation, and are absent from the Ola Kile Formation and the Limestone Member of the Ola Bula Formation (Morwood *et al*., 1997, 1998; O'Sullivan *et al*., 2001; Morwood *et al*., 2009). Stone artefacts occur in the upper part of the Tuff Member and throughout the Sandstone Member.

In the Tuff Member, two main fossil layers have been documented. The oldest fossil beds that contain pygmy stegodon, giant turtle, crocodile, and Komodo dragon are only found at Tangi Talo and no artefacts have been recovered from this site. Previous research reported that a faunal turnover event occurred at ~900 ka based on palaeomagnetic data and a series of zircon fission track dates (Morwood *et al*., 1997, 1998; van den Bergh, 1999; Morwood *et al*., 2009), some of which have now proven to be erroneous. All fossils accumulated in clay-rich laharic deposits stratigraphically below the WSI marker dated at 1.02±0.2 Ma (Brumm *et al.*, 2010). The unpublished $^{39}Ar/^{40}Ar$ ages that were obtained at Quadlab for the fossil-bearing laharic layer (~1.42 Ma) and TTL-T5 situated ~2 m above the fossil-bearing layer (~1.27 Ma) now confirm the much older age of the Tangi Talo fauna at half a million years older than previously envisaged. The TTL-T5 can be used for a stratigraphic marker, below which no stone artefacts have been recovered to date.

Stone artefacts occurring in the Tuff Member are well-preserved at Wolosege, where they are not associated with preserved fauna, and at Kobatuwa, where they occur with fossil vertebrate remains. Both layers are situated in the uppermost part of the Tuff Member. Stone tools and fossil bones have been recovered just below and above the Wolo Sege Ignimbrite, dated at ~1.02 Ma. From the identified layers, there was a considerable time gap in terms of hominin occupation and fauna habitation in the Soa Basin at ~1.27–1.02 Ma ago. The absence of fossil remains in the middle part of the Tuff Member, marked by the Wolo Wawo Tephra (WLW), is probably due to taphonomic factors.

In the Sandstone Member, fossil bones and stone tools accumulated primarily in the lower and middle parts, bracketed by the Pumaso Tephra (PMS) and the Mata Menge Tephra (MMT). The new fossil and artefact layers were found in Trench XII at Mata Menge, which are situated at a level ~5 m below MMT and ~12 m below the 0.65 Ma old Piga Tephra 02 (PGT-02) that was emplaced near the contact between the Sandstone Member and the

Limestone Member. Fission track dating yielded an age of between 880 and 800 ka for the main artefact and fossil-bearing interval at Mata Menge (O'Sullivan *et al*., 2001). However, comparing relative positions of fossil layers with the stratigraphic levels of PMS and PGT-02, and newly obtained palaeomagnetic evidence (Yurnaldi *et al*., 2018), it can be concluded that this lower fossil and artefact-bearing interval must have a maximum age of 0.78 Ma, and that hominins and animals lived in the Soa Basin until at least 0.7 Ma ago, during a the time interval of reduced volcanic activity.

8.2.4. Palaeoenvironment and climatic conditions

This study has employed geochemical analyses of sediments of the Ola Bula Formation in an attempt to interpreting past climatic conditions. Chemical composition, elemental ratios, and Chemical Index Alteration (CIA) were chosen as parameters and they are combined with lithofacies successions from selected stratigraphic profiles (Mata Menge, Wolosege and Tangi Talo) to determine and infer palaeoenvironmental and climatic changes in the Soa Basin during 1.50 Ma to 0.65 Ma.

The Tangi Talo sequence documents a continuous litho-sequence of the Tuff Member, which was deposited between ~1.5 Ma and 1.0 Ma. The lithological sequence of the Tangi Talo section was generally deposited in fluvial environments, where palaeosols preferably formed in floodplain and/or on abandoned channels. The palaeochannel was likely developed intermittently when wetter conditions occurred. The positive deflections of such elemental ratios in particular CaO/Al_2O_3, Na_2O/Al_2O_3 and Sr/Rb denote several periods with wet conditions. The overall elemental ratios and CIA values throughout the section suggest palaeoweathering is moderate to strong and the condition at ~1.50–1.0 Ma were warm, sub-humid tropical climate, alternating with wetter periods. The past climatic condition changed to drier and cooler at ~1.0 Ma, as indicated by a well-developed pedogenic horizon with desiccation structures.

Environmental and climatic changes between ~1.0 Ma and 0.70 Ma can be recognised from the Wolo Sege section. The weathering intensity is generally moderate to strong, and the climatic conditions reflected a warm, humid tropical climate. A period of drier and cooler conditions coincided with the interval ~15.0–18.0 m, which is equivalent to *ca*. 0.80 Ma ago.

The Mata Menge section provides the complete sequence of the Sandstone and Limestone Members of the Ola Bula Formation, and corresponds to depositional process that occurred from ~0.80 ma to 0.65 Ma. The overall data indicate a warm to hot tropical climate, with alternating dry and wet conditions (monsoonal). Just before ~0.65 Ma ago, the climatic conditions displayed a drier environment, reflected by the formation of pedogenic carbonates. The blocking of major river outlets by lava flows, mudflows or pyroclastic deposits together with wetter climatic condition, may have led to the development of lacustrine environments since ~0.65 Ma ago, and corresponds to the interglacial event of MIS 17. The climatic setting then remained warm and humid.

8.3. Suggestions for future research

This study has provided significant contributions to answer research problems in the Soa Basin, providing constraints on stratigraphy, palaeoenvironment and chronology. However, further investigations are needed in the context of the Soa Basin itself. So far, the lowermost fossil horizons of the Tuff Member, are only recorded in the Tangi Talo sequence. The vertebrate remains in this level are very important, contain pygmy elephants and giant turtles not found in any fossil level in the Sandstone Member. No stone tools have been recovered and the Tangi Talo fossil layers are the key components for understanding hominin settlement and faunal evolution in the Soa Basin. Fieldwork and extended excavations should be conducted in the other parts of the Soa Basin that preserve a similar age-sequence as the Tangi Talo stratigraphy. The stratigraphic marker of the TTL-T5 can be used to recognise new fossil layers.

Geoarchaeological research has been focused on the lowermost unit of the Tuff Member, to obtain evidence of the arrival of hominins and faunal changes. Such investigations should also be undertaken in the upper part of the Sandstone Member, through to the youngest finding horizons, to obtain a more complete story of hominin settlement and fauna habitation in the Soa Basin.

In addition, geochemical analyses for determining trace-element composition of volcanic glasses on all pyroclastic units identified throughout the Tuff Member and the Sandstone Member, are useful to confirm the conclusion of this study concerning the provenance of those pyroclastic deposits. The well-preserved airfall deposits in the lacustrine succession of the Limestone Member, record multiple explosive eruptions. The timing of events and volcanic sources should be taken into account as well as impacts of those eruptions upon the favourable conditions for occupation.

This study has proven the strength of interdisciplinary approaches, including lithostratigraphy, geochemical analyses and tephrochronology in order to place archaeological and palaeontological resources in chronological order and thereby suggests the benefits of stratigraphic markers for establishing accurate age controls. This research design can be applied in other key archaeological localities across the Indonesian archipelago, where most Early-Middle Pleistocene sites contain pyroclastic deposits or volcanic ashes (e.g. Watanabe and Kadar, 1985). The presence of regional marker beds will be valuable to connect various archaeological sites and to provide a constructive picture of palaeogeographical settings that will be useful to confirm evolutionary hypotheses concerning hominin and other species in Indonesia and Southeast Asia.

REFERENCES

Abbott, M.J., Chamalaun, F.H., 1981. Geochronology of some Banda Arc volcanics. In: Barber, A.J., and Wiryosujono, S., (Eds), The Geology and Tectonics of Eastern Indonesia. Geological Research and Development Centre Bandung, Indonesia, Special Publication 2, pp. 253–268.

Aitchison, J., 1986. The Statistics Analysis of Compositional Data. Chapman and Hall, London, UK., 416 p.

Aitchison, J., Egozcue, J.J., 2005. Compositional data analysis: where are we and where should we be heading? Mathematical Geology 37 (7), pp. 829–850.

Alloway, B.V., Lowe, D.J., Larsen, G., Shane, P.A.R., Westgate, J.A., 2013. Tephrochronology. In: Elias, S.A., Mock, C.J. (Eds.), The Encyclopedia of Quaternary Science, 2nd Edition, vol. 4, Elsevier, Amsterdam, pp. 277–304.

Alloway, B.V., Westgate, J., Pillans, B., Pearce, N., Newnham, R.M., Bryami, M., Aarburg, S., 2004. Stratigraphy, age and correlation of middle Pleistocene silicic tephras in the Auckland region, New Zealand: a prolific distal record of Taupo Volcanic Zone volcanism. New Zealand Journal of Geology and Geophysics 47, pp. 447–479.

Alloway, B.V., Pillans, B.J., Carter, L., Naish, T.R., Westgate, J.A., 2005. Onshore-offshore correlation of Pleistocene rhyolitic eruptions from New Zealand: implications for TVZ eruptive history and paleoenvironmental construction. Quaternary Science Reviews 24, pp. 1601–1622.

Alves, M.E., Omotoso, O., 2009. Improving Rietveld-based clay mineralogic quantification of oxisols using Siroquant. Soil Science Society of America Journal 73, pp. 2191–2197.

Aslan, A., 2013. Fluvial environments (Sediments). In: Elias, S.A., Mock, C.J. (Eds.), The Encyclopedia of Quaternary Science, 2nd Edition, vol. 1, Elsevier, Amsterdam, pp. 663–675.

Aziz, F., van den Bergh, G.D., Morwood, M.J., Hobbs, D.R., Kurniawan, I., Collins, J. Jatmiko, 2009. Excavations at Tangi Talo, central Flores, Indonesia. In: Aziz, F., Morwood, M.J., van den Bergh, G.D. (Eds.), Pleistocene geology, palaeontology and archaeology of the Soa Basin, Central Flores. Centre for Geological Survey, Ministry of Energy and Mineral Resources, Republic of Indonesia, Special Publication No. 36, pp. 41–58.

Barth, M.G., McDonough, W.F., Rudnick, R.L., 2000. Tracking the budget of Nb and Ta in the continental crust. Chemical Geology 165, pp. 197–213.

Barron, V., Torrent, J., 2002. Evidence for a simple pathway to maghemite in Earth and Mars soils. Geochemica et Cosmochemica Acta 66, pp. 2801–2806.

Bar-Yosef., O., 1994. The Lower Paleolithic of the Near East. Journal of World Prehistory 8, pp. 211–265.

Begét, J.E., Keskinen, M.J., 2003. Trace-element geochemistry of individual glass shards of the Old Crow tephra and the age of the Delta glaciation, central Alaska. Quaternary Research 60, pp. 63–69.

Bennett, C.E., Marshall, J.D., Stanistreet, I.G., 2012. Carbonate horizons, paleosols, and lake flooding cycles: Beds I and II of Olduvai Gorge, Tanzania. Journal of Human Evolution 63, pp. 328–341.

Bettis III, E.A., Zaim, Y., Larick, R.R., Ciochon, R.L., Suminto, Rizal, Y., Reagan, M., Heizler, M., 2004. Landscape development preceding Homo erectus immigration into central Java, Indonesia: the Sangiran formation lower lahar. Palaeogeography Palaeoclimatology Palaeoecology 206, pp. 115–131.

Blumenschine, R.J., Masao, F.T., 1991. Living sites at Olduvai Gorge, Tanzania? Preliminary landscape archaeology results in the basal Bed II lake margin zone. Journal of Human Evolution 21, pp. 451–462.

Blumenschine, R.J., Peters, C.R., 1998. Archaeological predictions for hominid land use in the paleo-Olduvai Basin, Tanzania, during lowermost Bed II times. Journal of Human Evolution 34, pp. 565–607.

Blumenschine, R.J., Stanistreet, I.G., Masao, F.T., 2012. Olduvai Gorge and the Olduvai Landscape Paleoanthropology Project. Journal of Human Evolution 63, pp. 247–250.

Boggs, S., 2006. Principles of Sedimentology and Stratigraphy. Fourth Edition, Pearson Prentice Hall, 662p.

Boggs, S., 2010. Principles of Sedimentology and Stratigraphy. Fifth Edition, Pearson Education, 585p.

Bokhorst, M.P., Beets, C.J., Marković, S.B., Gerasimenko, N.P., Matviishina, Z.N., Frechen, M., 2009. Pedo-chemical climate proxies in Late Pleistocene

Serbian–Ukranian loess sequences. Quaternary International 198, pp. 113–123

Borchardt, G.A., Harward, M.E., Schmitt, R.A., 1971. Correlation of volcanic ash deposits by activation analysis of glass separates. Quaternary Research 1, pp. 247–260.

Borchardt, G.A., Norgren, J.A., Harward, M.E., 1973. Correlation of ash layers in peat bogs of eastern Oregon. Geological Society of America Bulletin 84, pp. 3101–3108.

Branney, M.J., Kokelaar, B.P., 2002. Pyroclastic Density Currents and the Sedimentation of Ignimbrites. Geological Society of. London Memoir 27, 143p.

Brendryen, J., Haflidason, H., Sejrup, H.P., 2010. Norwegian Sea tephrostratigraphy of marine isotope stages 4 and 5: prospects and problems for tephrochronology in the North Atlantic region. Quaternary Science Reviews 29, pp. 847–864.

Brown, P., Sutikna, T., Morwood, M.J., Soejono, R.P., Jatmiko, Saptomo, E.W., Awe Due, R., 2004. A newsmall-bodied hominin fromthe Late Pleistocene of Flores, Indonesia. Nature 431, pp. 1055–1061.

Brumm, A., Aziz, F., van den Bergh, G.D., Morwood, M.J., Moore, M.W., Kurniawan, I., Hobbs, D.R., Fullagar, R., 2006. Early stone technology on Flores and its implications for Homo floresiensis. Nature 441, pp. 624–628.

Brumm, A., Moore, M.W., Kurniawan, I., Suyono, R.S., Jatmiko,MorwoodM.J., Aziz, F., 2009. Early Pleistocene stone technology at Mata Menge, central Flores, Indonesia. In: Aziz, F., Morwood, M.J., van den Bergh, G.D. (Eds.), Pleistocene geology, palaeontology and archaeology of the Soa Basin, Central Flores. Centre for Geological Survey, Ministry of Energy and Mineral Resources, Republic of Indonesia, Special Publication No. 36, pp. 119–137.

Brumm, A., Jensen, G.M., van den Bergh, G.D., Morwood, M.J., Kurniawan, I., Aziz, A., Storey, M., 2010. Hominins on Flores, Indonesia, by one million years ago. Nature 464, pp. 748–752.

Brumm, A., van den Bergh, G.D., Storey, M., Kurniawan, I., Alloway, B.V., Setiawan, R., Setiyabudi, E., Grün, R., Moore, M.W., Yurnaldi, D., Puspaningrum, M.R., Wibowo, U.P., Insani, H., Sutisna, I., Westgate, J.A., Pearce, N.J.G., Duval, M., Meijer,H.J.M., Aziz, F., Sutikna, T.,vander Kaars,

S., Flude, S.,Morwood, M.J., 2016. Age and context of the oldest known hominin fossils from Flores. Nature 534, pp. 249–253.

Buccianti A, Mateu-Figueras G, Pawlowsky-Glahn V, 2006. Compositional data analysis in the geosciences: from theory to practice. Geological Society of London Special Publication 264, 212p.

Cas, R.A.F., Wright, J.V., 1987. Volcanic Successions: Modern and Ancient. Allen & Unwin, 544p.

Chamley, H., 1989. Clay Sedimentology. Springer, Berlin, 623p.

Channell, J.E.T., Hodell, D.A., Singer, B.S., Xuan, C., 2010. Reconciling astrochronological and $^{40}Ar/^{39}Ar$ ages for the Matuyama-Brunhes boundary and late Matuyama Chron. Geochemistry Geophysic and Geosystem 11, Q0AA12, doi:10.1029/2010GC003203.

Chappell, J., Veeh, H.H., 1978. Late Quaternary tectonic movements and sea-level changes at Timor and Atauro Island. Geological Society of America Bulletin 89, pp. 356–368.

Chesner, C.A., Rose, W.I., 1991. Stratigraphy of the Toba Tuffs and the evolution of the Toba caldera complex, Sumatra, Indonesia. Bulletin of Volcanology 53, pp. 343–356.

Chesner, C.A., 1998. Petrogenesis of the Toba Tuffs, Sumatra, Indonesia. Journal of Petrology 29 (3), pp. 397–438.

Chesner, C.A., Luhr, J.F., 2010. A melt inclusion study of the Toba Tuffs, Sumatra, Indonesia. Journal of Volcanology and Geothermal Research 197, pp. 259–278.

Churchman, G.J., Lowe, D.J., 2012. Alteration, formation, and occurrence of minerals in soils. In Huang, P.M., Li, Y., Sumner, M.E. (Eds), Handbook of Soil Sciences, 2nd Edition, Volume 1: Properties and Processes. CRC Press, Boca Raton, FL., pp. 20.1–20.72.

Churchman, G.J.,Pasbakhsh, P., Lowe, D.J., Theng, B.K.G., 2016. Unique but diverse: some observations on the formation, structure and morphology of halloysite. Clay Minerals 51, pp. 395–416.

Condie K.C., 1993. Chemical composition and evolution of the upper continental crust: contrasting results from surface samples and shales. Chemical Geology 104, pp. 1–37.

Cox, R., Low, D.R., Cullers, R.L., 1995. The influence of sediment recycling and basement composition on evolution of mudrock chemistry in the southwestern United States. Geochimica et Cosmochimica Acta 59, pp. 2919–2940.

Cullers, R.L., 1995. The controls on the major- and trace-element evolution of shales, siltstones and sandstones of Ordovician to Tertiary age in wet mountains region, Colorado, USA. Chemical Geology 123, pp. 107–131.

Cullers, R.L., 2000. The geochemistry of shales, siltstones and sandstones of Pennsylvanian–Permian age, Colorado, USA: Implications for provenance and metamorphic studies. Lithos 51, pp. 181–203.

de'Gennaro, B., Cappelletti, P., Langella. A., Perotta, A., Scarpati, C., 2000. Genesis of zeolites in the Neapolitan Yellow Tuff: geological, volcanological and mineralogical evidence. Contributions to Mineralogy and Petrology 139, pp. 17–35.

de Pablo-Galan, L., Chávez-García, M., 1996. Diagenesis of Oligocene vitric tuffs to zeolites, Mexican Volcanic Belt. Clays and Clay Minerals 44, pp. 324–338.

Da Costa A. C. S., Bigham J. M., Rhoton F. E. and Traina S. J., 1999. Quantification and characterization of maghemite in soils derived from volcanic rocks in Southern Brazil. Clays Clay Mineralogy 47, pp. 466–473.

Das, B.K., Al-Mikhlafi, A.S., Kaur, P., 2006. Geochemistry of Mansar Lake sediments, Jammu, India: Implication for source-area wethaering, provenance and tectonic setting. Journal of Asian Erath Sciences 26, pp. 649–668.

Dehn, J., Farrell, J.W., Schmincke, H.-U., 1991. Neogene tephrochronology from Site 758 on northern Ninetyeast Ridge: Indonesian arc volcanism of the past 5 Ma. In: Weissel, J., Peirce, J., Taylor, E., Alt, J., et al. (Eds.), Proceedings Ocean Drilling Program: Scientific Results 121, pp. 273–295.

Deino, A.L., Scott, G.R., Saylor, B., Alene, M., Angelini, J.D., Haile-Selassie, Y., 2010. $^{40}Ar/^{39}Ar$ dating, paleomagnetism, and tephrochemistry of Pliocene strata of the hominid-bearing Woranso-Mille area, west-central Afar Rift, Ethiopia. Journal of Human Evolution 58, pp. 111–126.

Deino, A., 2012. $^{40}Ar/^{39}Ar$ dating of Bed I, Olduvai Gorge, Tanzania, and the chronology of early Pleistocene climate change. Journal of Human Evolution 63, pp. 251–273.

De Smet, M.E.M., Fortuin, A.R., Troelstra, S.R., van Marle, L.J., Karmini, M., Tjokrosapoetro, S., Hadiwisatra, S., 1990. Detection of collision-related vertical movements in the outer Banda arc (Timor, Indonesia) using related micropaleontology data. Journal of Southeast Asian Earth Sciences 4, pp. 337–356.

Diehl, J.F., Onstott, T.C., Chesner, C.A., Knight, M.D., 1987. No short reversals of Brunhes age recorded in the Toba tuffs, north Sumatra, Indonesia. Geophysical Research Letters 14, pp. 753–756.

Dill, H.G., Techmer, A., Botz, R., Dohrmann, R., Kaufhold, S., 2012. Hypogene and supergene alteration of the zeolite-bearing pyroclastic deposits at Tell Rimah, Jordan, and rift-related processes along the Dead-Sea-Transform Fault System during the Quaternary. Journal of Volcanology and Geothermal Research 239–240, pp. 49–68.

Ding, Z.L., Sun, J.M., Yang, S.L., Liu, T.S., 2001. Geochemistry of the Pliocene red clay formation in the Chinese Loess Plateau and implications for its origin, source provenance and paleoclimate change. Geochimica et Cosmochimica Acta 65, pp. 901–913.

Dumitru, T.A., 2000. Fission-track geochronology. In: Noller J.S., Sowers J.M., Lettis, W.R. (Eds.), American Geophysical Union Reference Shelf. Quaternary Geochronology: Methods and Applications, Washington, DC: American Geophysical Union, pp. 131–155.

Duzgoren-Aydin, N.S., Aydin, A., Malpas, J., 2002. Distribution of clay minerals along a weathered pyroclastic profile, Hongkong. Catena 50, pp. 17–41.

Egozcue, J.J., Pawlowsky-Glahn,V., Mateu-Figueras, G.,Barcelo´ Vidal, C., 2003. Isometric logratio transformations for compositional data analysis. Mathematical Geology 35(3), pp. 279–300.

Egozcue, J.J., Pawlowsky-Glahn,V., 2006. Simplicial geometry for compositional data. In: Buccianti,A., Mateu-Figueras,G., Pawlowsky-Glahn,V.(Eds.),Compositional Data Analysis in the Geosciences: From Theory to Practice, vol.264, Geological Society London Special Publications, pp. 145–160.

Ehrat, H. 1925. Geologische Mijnbouwkundige onderzoekingen op Flores, Jaarboek v.h. Mijnwezen in N.O.1 Verhandelingen Geologische Schetskaart 250,000.

Elburg, M.A., van Bergen, M.J., Foden, J.D., 2004. Subducted upper and lower continental crust contributes to magmatism in the collision sector of the Sunda-Banda Arc, Indonesia. Geology 32, pp. 41–44

Faure, G., 1986. Principles of Isotope Geology, Second edition. Wiley, New York, 608p.

Fedo, C.M., Nesbitt, H.W., Young, G.M., 1995. Unraveling the effects of potassium metasomatism in sedimentary rocks and paleosols, with implications for weathering conditions and provenance. Geology 23, pp. 921–924.

Feibel, C.S., Brown, F.H., McDougall, I., 1989. Stratigraphic context of fossil hominids from the Omo Group deposits: northern Turkana Basin, Kenya and Ethiopia. American Journal of Physical Anthropology 78, pp. 595-622.

Feibel, C.S., 1999. Tephrostratigraphy and geological context in paleoanthropology. Evolutionary Anthropology 8, pp. 87-100.

Feibel, C.S., 2001. Archaeological sediments in lake margin environments. In: Stein, J.K., Farrand, W.R. (Eds.), Sediments in Archaeological Context, University of Utah Press, Salt Lake City, pp. 127–148.

Fleischer, R. L., Price, P. B., Walker, R. M., 1965a. Effects of temperature, pressure and ionization on the formation and stability of fission tracks in minerals and glasses. Journal of Geophysical Research 70, pp. 1497–1502.

Fleischer, R. L., Price, P. B., Walker, R. M., Leakey, L. S. B., 1965b. Fission track dating of Bed I, Olduvai Gorge. Science 149, pp. 383–393.

Fortuin, A.R., Roep, T.B., Sumosusastro, P.A., 1994. The Neogene sediments of East Sumba, Indonesia - products of a lost arc?. Journal of Southeast Asian Earth Sciences 9, pp. 67–79.

Froggatt, P.C., 1992. Standardization of the chemical analysis of tephra deposits. Report of the ICCT working group. Quaternary International 13-14, pp. 93–96.

Galán, E., 2006. Chapter 14: Genesis of Clay Minerals. Developments in Clay Science Vol. 1, pp. 1129–1162.

Gallet, S., Jahn, B., Torii, M., 1996. Geochemical characterization of the Luochuan loess-paleosol sequence, China, and paleoclimatic implications. Chemical Geology 133, pp. 67–88.

Gansecki, C. A., Mahood, G. A., McWilliams, M., 1998. New ages for the climactic eruptions of Yellowstone: single-crystal $^{40}Ar/^{39}Ar$ dating identifies contamination. Geology 26, pp 343–346.

Gierlowski-Kordesch, E.H., 2010. Chapter 1: Lacustrine carbonates. In: Alonso-Zarza, A.M., Tanner, L.H., Carbonate in Continental Settings: Facies, Environment and Processes. Developments in Sedimentology Vol. 61, pp. 1–101.

Goldberg, P., Macphail, R.I., 2006. Practical and Theoretical Geoarchaeology. Blackwell Science Ltd, 454p.

Hall, C.H., Farrell, J.W., 1995. Laser $^{40}Ar/^{39}Ar$ ages of tephra from Indian Ocean deep-sea sediments: tie points for the astronomical and geomagnetic polarity time scales. Earth and Planetary Science Letters 133, pp. 327–338.

Hall, R., 2002. Cenozoic geological and plate tectonic evolution of SE Asia and the SW Pacific: computer-based reconstructions, model and animations. Journal of Asian Earth Sciences 20, pp. 353–431.

Hall, R., Smyth, H.R., 2008. Cenozoic arc processes in Indonesia: Identification of the key influences on the stratigraphic record in active volcanic arcs. Geological Society of America Special Paper 436, pp. 27–54.

Hamilton, W., 1979, Tectonics of the Indonesian region. U.S. Geological Survey Professional Paper 1078, 345p.

Hassan, F. A. 1979. Geoarchaeology: the geologist and archaeology. American Antiquity 44: pp. 267–70

Hartono, H.M.S., 1961. Geological Investigation at Olabula, Flores. Djawatan Geologi Bandung, Indonesia, 40p.

Hernandes, J.E.G, Del Pino, J.S.N, Martin, M.M.G, Reguera, F.H., Losada, J.A.R., 1993. Zeolites in pyroclastic deposits in southern Tenerife (Canary Islands). Clays and Clay Minerals 41, pp. 521–526.

Hillenbrand, C.-D., Moreton, S.G., Caburlotto, A., Pudsey, C.J., Lucchi, R.G., Smellie, J.L., Benetti, S., Grobe, H., Hunt, J.B., Larter, R.D., 2008. Volcanic timemarkers for Marine Isotopic Stages 6 and 5 in Southern Ocean sediments and Antarctic ice cores: implications for tephra correlations between palaeoclimatic records. Quaternary Science Reviews 27, pp. 518–540.

Hobbs, J.E., Lindesay, J.A., Bridgman, H.A., 1998. Climates of the Southern Continents: Present, Past and Future. Wiley, New York, 297p.

Hocknull, S.A., Piper, P.J., van den Bergh, G.D., Due, R.A., Morwood, M.J., Kurniawan, I., 2009. Dragon's paradise lost: palaeobiogeography, evolution and extinction of the largest-ever terrestrial lizards (Varanidae). PLoS ONE 4 (9), 7241. http://dx.doi.org/10.1371/journal.pone.0007241.

Honda, M., Shimizu, H., 1998. Geochemical, mineralogical and sedimentological studies on the Taklimakan Desert sands. Sedimentology 45, pp. 1125–1143.

Hooijer, D.A., 1957. Three giant prehistoric rats from Flores, Lesser Sunda Islands. Zoologische Mededelingen 35 (21), pp. 128–133.

Hooijer, D.A., 1972. Varanus (Reptilia, Sauria) from the Pleistocene of Timor. Zoologische Mededelingen 47: pp. 445–448.

Houghton, B.F., Carey, R.J., 2015. Pyroclastic fall deposits. In: Sigurdsson, H., Houghton, B., McNutt, S., Rymer, H., Stix, J. (Eds.), Encyclopedia of Volcanoes. Academic Press, Elsevier, pp. 599–616.

Hunt, J.B., Hill, P.G., 1993. Tephra geochemistry: a discussion of some persistent analytical problems. The Holocene 3, pp. 271–278.

Hyodo, M., Matsu'ura, S., Kamishima, Y., Kondo, M., Takeshita, Y., Kitaba, I., Danhara, T., Aziz, F., Kurniawan, I., Kumai, H., 2011. High-resolution record of the Matuyama-Brunhes transition: Constrains the age of Javanese Homo erectus in the Sangiran dome, Indonesia. Proceedings of the National Academy of Sciences 108, pp. 19563–19568.

Johnsson, M.J., 1993. The system controlling the composition of clastic sediments. In: Johnsson, M.J., Basu, A. (Eds.), Processes Controlling the Composition of Clastic Sediments. Geological Society of America Special Paper 284, pp. 1–19.

Jones, R.T., Jordan, J.T., 2007. Tephrochronology. In: Elias, S.A. (Ed.), Encyclopaedia of Quaternary Science. Elsevier, London, pp. 1320–1336.

Jordan, B.R., Sigurdsson, H., Carey, S.N., Rogers, R., Ehrenborg, J., 2006. Geochemical correlation of Caribbean Sea tephra layers with ignimbrites in Central America. Geological Society of America Special Papers 402, pp. 175–208.

Jungers, W.L., Harcourt-Smith, W.E.H., Wunderlich, R.E., Tocheri, M.W., Larson, S.G., Sutikna, T., Awe Due, R., Morwood, M.J., 2009a. The foot of Homo floresiensis. Nature 459, pp. 81–84.

Jungers, W.L., Larson, S.G., Harcourt-Smith, W., Morwood, M.J., Sutikna, T., Awe Due, R., Djubiantono, T., 2009b. Descriptions of the lower limb skeleton of Homo floresiensis. Journal of Human Evolution 57, pp. 538–554.

Katili, J.A., 1975. Volcanism and plate tectonics in the Indonesian island arcs. Tectonophysics, v. 26, pp. 165–188.

Keeling, J.L., Raven, M.D., Gates, W.P., 2000. Geology and characterization of two hydrothermal nontronites from weathered metamorphic rocks at the Uley graphite mine, South Australia. Clay and Clay Minerals 48, pp. 537-548.

Kilburn, C.R.J., 2000. Lava flows and flow fields. In: Sigurdsson, H., Houghton, B., McNutt, S., Rymer, H., Stix, J. (Eds.), Encyclopedia of Volcanoes. Academic Press, San Francisco (CA), pp. 291–306.

Koesoemadinata, S., Noya, Y., Kadarisman, D., 1994. Geological Map of the Ruteng Quadrangle, Nusa Tenggara. Geological Reserach and Development Centre, Bandung.

Koulali, A., Susilo, S., McClusky, S., Meilano, I., Cummins, P., Tregoning, P., Lister, G., Efendi, J., Syafi'I, M.A., 2016. Crustal strain partitioning and the associated earth-quake hazard in the eastern Sunda–Banda Arc. Geophysical Research Letters 43, pp. 1943–1949.

Kraus, M.J., 1999. Paleosols in clastic sedimentary rocks: their geologic applications. Earth-Science Reviews 47, pp. 41–70.

Kuehn, S.C., Froese, D.G., Carrara, P.E., Foit Jr., F.F., Pearce, N.J.G., Rotheisler, P., 2009. Major- and trace-element characterization, expanded distribution, and a new chronology for the latest Pleistocene Glacier Peak tephras in western North America. Quaternary Research 71, pp. 201–216.

Kuhnt, W., Holbourn, A., Hall, R., Zuvela, M., Käse, R., 2004. Neogene history of the Indonesian Throughflow. In: Clift, P., Hayes, D., Kuhnt, W., Wang, P. (Eds.), Continent-Ocean Interactions in the East Asian Marginal Seas, American Geophysical Union Monograph 149, pp. 299–320.

Larick, R., Ciochon, R.L., Zaim, Y., Sudijono, Rizal, Y., Aziz, F., Reagan, M., Heizler, M., 2001. Early Pleistocene $^{40}Ar/^{39}Ar$ ages for bapang formation hominins,

Central Jawa, Indonesia. Proceedings of the National Academy of Sciences 98, pp. 4866–4871.

Laurenzi M.A., Bigazzi G., Balestrieri M.L., Bouska V., 2003. $^{40}Ar/^{39}Ar$ laser probe dating of the Central European tektite-producing impact event. Meteorite and Planetary Science 38, pp. 887–893.

Laurenzi, M. A., Balestrieri M.L., Bigazzi G., Neto, J.C.H., Lunes, P.J., Norelli, P., Oddone, M., Osorio Araya, A.M., Viramonte, J.G., 2007. New constraints on ages of glasses proposed as reference materials for fission-track dating. Geostandard and Geoanalytical Research 31, pp. 105–124.

Lavigne, F., Suwa, H., 2004. Contrasts between debris flows, hyperconcentrated flows and stream flows at a channel of Mount Semeru, East Java, Indonesia. Geomorphology 61, pp. 41–58.

Leakey, L.S.B., Evernden, J.F., Curtis, G.H., 1961. The age of Bed I, Olduvai Gorge, Tanzania. Nature 191, pp. 478–479.

Leakey, L.S.B., 1959. A new fossil skull from Olduvai. Nature 184, pp. 91–493.

LeBas, M.J., LeMaitre, R.W., Streckeisen, A., and Zanettin, B., 1986. A chemical classification of volcanic rocks based on the total alkali-silica diagram: Journal of Petrology 27, pp. 745–750.

Lee, M., Chen, C., Wei, K., Iizuka, Y., Carey, S.N., 2004. First Toba supereruption revival. Geology 32, pp. 61–64.

Li, X.,Wei, G., Shao, L., Liu, Y., Liang, X., Jain, Z., Sun, M.,Wang, P., 2003. Geochemical and Nd isotopic variations in sediments of the South China Sea: a response to Cenozoic tectonism in SE Asia. Earth and Planetary Science Letters 211, pp. 207–220.

Liu, Z., Colin, C., Huang, W., Le, K.P., Tong, S., Chen, Z., Trentesaux, A., 2007. Climatic and tectonic controls on weathering in South China and the Indochina Peninsula: clay mineralogical and geochemical investigations from the Pearl, Red, and Mekong drainage basins. Geochemistry, Geophysics, Geosystems 8, Q05005. doi:10.1029/2006GC001490**.**

Liu, Z., Zhao, Y., Colin, C., Siringan, F.P., Wu, Q., 2009. Chemical weathering in Luzon, Philippines from clay mineralogy and major-element geochemistry of river sediments. Applied Geochemistry 24, pp. 2195–2205.

Locatelli, E., Awe Due, R., van den Bergh, G.D., van den Hoek Ostende, L.W., 2012. Pleistocene survivors and Holocene extinctions: the giant rats from Liang Bua (Flores, Indonesia). Quaternary Internasional 281, pp. 47–57.

Lockwood, J., Hazlett, R., 2010. Volcanoes: global perspectives. Wiley, 552p.

Lowe, D.J., Hunt, J.B., 2001. A summary of terminology used in tephra-related studies. Les Dossiers de l'Archeo-Logis 1, pp. 17–22.

Lowe, D.J., 2008. Globalisation of tephrochronology e new views from Australasia. Progress in Physical Geography 32, pp. 311–335.

Lowe, D.J., 2011. Tephrochronology and its application: a review. Quaternary Geochronology 6, pp. 107–153.

Mack, G.H., James, W.C., Monger, H.C., 1993. Classification of paleosols. Geological Society of America Bulletin 105, pp. 129–136.

Macpherson, C.G., Hall, R., 2002. Timing and tectonic controls in the evolving orogen of SE Asia and the western Pacific and some implications for ore generation. In Blundell, D.J., *et al*.,(Eds), The Timing and Location of Major Ore Deposits in an Evolving Orogen. Geological Society London Special Publication 204, pp. 49–67.

Maringer, J., and Verhoeven, T. 1970. Die Steinartefake aus der Stegodon-fossilschicht von Mengeruda auf Flores, Indonesien. Anthropos 65, p. 229–247.

McDougall, I., Harrison, T. M., 1999. Geochronology and Thermochronology by the $^{40}Ar/^{39}Ar$ Method. Second Edition. Oxford University Press, New York, 288p.

McLennan, S.M., 1993. Weathering and global denudation. Journal of Geology 101, pp. 295–303.

McLennan, S.M., Hemming, D.K., Hanson, G.N., 1993. Geochemical approaches to sedimentation, provenance and tectonics. Geological Society of America Special Paper 284, pp. 21–40.

McPhie, J., Doyle, M., Allen, R., 1993. Volcanic Textures: A Guide to the Interpretation of Textures in Volcanic Rocks. Center for Ore Deposits and Exploration Studies. Tasmania University, Tasmania, 198p.

Meijer, H.J.M., van den HoekOstende, L.W., van den Bergh, G.D., de Vos, J., 2010. The fellowship of the Hobbit: the fauna surrounding Homo floresiensis. Journal of Biogeography 37, pp. 995–1006.

Meijer, H.J.M., Kurniawan, I., Setyabudi, E., Brumm, A., Sutikna, T., Setiawan, R., van den Bergh, G.D., 2015. Avian remains from the Early/Middle Pleistocene of the So'a Basin, central Flores, Indonesia, and their palaeoenvironmental significance. Palaeogeography, Palaeoclimatology, Palaeoecology 440, pp 161–171.

Metcalfe, S.E., Nash, D.J., 2012. Introduction. In: Metcalfe, S.E., Nash, D.J. (Eds), Quaternary Environmental Change in the Tropics. Wiley-Blackwell, pp. 3–33.

Miall A.D., 1985. Architectural-element analysis: a new method of facies analysis applied to fluvial deposits. Earth Science Reviews 22, pp. 261–308.

Miall, A.D., 1996. The Geology of Fluvial Deposits. Springer-Verlag, Berlin, 582p.

Moncure, G.K., Surdam, R.C., McKague, H.L., 1981. Zeolite diagenesis below Pahute Mesa, Nevada Test Site. Clays and Clay Minerals 29, pp. 385–396.

Moore, D.M., Reynolds, R.C., 1997. X-ray Diffraction and the Identification and Analysis of Clay Minerals. Second Edition, Oxford University Press, Oxford, 378p.

Moore, M.W., Brumm, A., 2007. Stone artifacts and hominins in island Southeast Asia: new insights from Flores, eastern Indonesia. Journal of Human Evolution 52, pp. 85–102.

Morrisey, M., Zimanowski, B., Wohletz, K.H., Buettner, R., 2000. Phreatomagmatic fragmentation. In: Sigurdsson, H., Houghton, B., McNutt, S., Rymer, H., Stix, J. (Eds.), Encyclopedia of Volcanoes. Academic Press, San Francisco (CA), pp. 431–445.

Morwood, M.J., Aziz, F., van den Bergh, G.D., Sondaar, P.Y. & J. de Vos. 1997. Stone artefacts from the 1994 excavation at Mata Menge, West Central Flores, Indonesia. Australian Archaeology 44: 26-34.

Morwood, M.J., O'Sullivan, P., Aziz, F., Raza, A., 1998. Fission track age of stone tools and fossils on the east Indonesian island of Flores. Nature 392, pp. 173–176.

Morwood, M.J., Aziz, F., O'Sullivan, P., Nasruddin, Hobbs, D.R., and Raza, A. 1999, Archaeological and palaeontological research in central Flores, east Indonesia: Results of fieldwork, 1997–98. Antiquity, v. 280, p. 273–286.

Morwood, M.J., Soejono, R.P., Roberts, R.G., Sutikna, T., Turney, C.S.M., Westaway, K.E., Rink, W.J., Zhao, J.-x., van der Bergh, G.D., Awe Due, R., Hobbs, D.R., Moore, M.W., Bird, M.I., Fifield, L.K., 2004. Archaeology and age of a new hominin from Flores in eastern Indonesia. Nature 431, 1087–1091.

Morwood, M.J., Brown, P., Jatmiko, Sutikna, T., Saptomo, E.W., Westaway, K.E., Awe Due, R., Roberts, R.G., Maeda, T., Wasisto, S., Djubiantono, T., 2005. Further evidence for small-bodied hominins from the Late Pleistocene of Flores, Indonesia. Nature 437, pp. 1012–1017.

Morwood, M.J., Aziz, F., 2009. Introduction: Palaeontology and archaeology of the Soa Basin, Central Flores, Indonesia. In: Aziz, F., Morwood, M.J., van den Bergh, G.D. (Eds.), Pleistocene geology, palaeontology and archaeology of the Soa Basin, Central Flores. Centre for Geological Survey, Ministry of Energy and Mineral Resources, Republic of Indonesia, Special Publication No. 36, pp. 1–18.

Morwood, M.J., Aziz, F., Nasruddin, Hobbs, D.R., van den Bergh, G.D., 2009. Archaeological and palaeontological excavations at Boa Lesa, central Flores, Indonesia. In: Aziz, F., Morwood, M.J., van den Bergh, G.D. (Eds.), Pleistocene geology, palaeontology and archaeology of the Soa Basin, Central Flores. Centre for Geological Survey, Ministry of Energy and Mineral Resources, Republic of Indonesia, Special Publication No. 36, pp. 95–104.

Morwood, M.J., Jungers, W.L., 2009. Conclusions: implications of the Liang Bua excavations for hominin evolution and biogeography. Journal of Human Evolution 57, pp. 640–648.

Morwood, M.J., Aziz, F., Nasruddin, Hobbs, D.R., van den Bergh, G.D., 2009. Archaeological and palaeontological excavations at Boa Lesa, central Flores, Indonesia. In: Aziz, F., Morwood, M.J., van den Bergh, G.D. (Eds.), Pleistocene geology, palaeontology and archaeology of the Soa Basin, Central Flores. Centre for Geological Survey, Ministry of Energy and Mineral Resources, Republic of Indonesia, Special Publication No. 36, pp. 95–104.

Muraoka, H., Nasution, A., Urai, M., Takahashi, M., Takashima, I., Simanjuntak, J., Sundhoro, H., Aswin, D., Nanlohy, F., Sitorus, K., Takahashi, H., Koseki, T., 2002. Tectonic, volcanic and stratigraphic geology of the Bajawa geothermal field, central Flores, Indonesia. Bulletin of the Geological Survey of Japan 53, pp. 109–138.

Musser, G.G., 1981. The giant rat of Flores and its relatives east of Borneo and Bali. Bulletin of the American Museum of Natural History 169, pp. 67–176.

Nasution, A., Takashima, I., Muraoka, H., Takahashi, H., Matsuda, K., Akasako, H., Futagoishi, M., Kusnadi, D., Nanlohi, F., 2000. The geology and geochemistry of Mataloko-Nage-Bobo geothermal areas, central Flores, Indonesia. Proceedings World Geothermal Congress, pp. 2165–2170.

Nesbitt, H.W., Young, G.M., 1982. Early Proterozoic climates and plate motions inferred from major element chemistry of lutites. Nature 54, pp. 2015–2050.

Nesbitt, H.W., Young, G.M., 1984. Prediction of some weathering trends of plutonic and volcanic rocks based on thermodynamic and kinetic consideration. Geochimica et Cosmochimica Acta 48, pp. 1523–1534.

Nesbitt, H.W., Young, G.M., 1989. Formation and diagenesis of weathering profiles. Journal of Geology 97, pp. 129–147.

Nettleton W.D., Olson, C.G., Wysocki, D.A., 2000. Paleosol classification: problems and solutions. Catena 41, pp. 61–92.

Nichols, G., 2009. Sedimentology dan Stratigraphy. Second Edition, Wiley-Blackwell, Oxford, 419p.

Ng, S.L., King, R.H., 2004. Geochemistry of lake sediments as a record of environmental Change in a high Arctic watershed. Chemie der Erde 64, pp. 257–275.

Nobel, D.C., Korringa, M.K., Hedge, C.E., Riddle, G.O., 1972. Highly differentiated subalkaline rhyolite from Glass Mountain, Mono County, California. G 83, Geological Society America Bulletin 83, pp. 1179–1184.

Nomade, S., Renne, P.R., Vogel, N., Deino, A.L., Sharp, W.D., Becker, T.A., Jaouni, A.R., Mundil, R., 2005. Alder Creek sandidine (ACs-2): a Quaternary $^{40}Ar/^{39}Ar$ dating standard tied to the Cobb Mountain geomagnetic event. Chemical Geology 218, pp. 315–338.

Nordt, L., Orosz, M., Driese, S., Tubbs, J., 2006. Vertisol carbonate properties in relation to mean annual precipitation: implications for paleoprecipitation estimates. Journal of Geology 114, pp. 501–510.

Norish, K., Chappel B.W., 1977. X-ray fluorescence spectrometry. In Zussman, J. (Eds). Physical methods in determine mineralogy, Acdemic, New York, pp. 201–272.

Norish, K., Hutton, J.T., 1969. An acurate X-ray spectrographic method for the analysis of a wide range of geological samples. Geochemica et. Cosmochemica Acta 33, pp. 431–453.

North, C.P., Davidson, S.K., 2012. Unconfined alluvial flow processes: recognition and interpretation of their deposits, and the significance for palaeogeographic reconstruction. Earth Science Reviews 111, pp. 199–223.

O'Sullivan, P.B., Morwood, M.J., Hobbs, D., Aziz, F., Suminto, M.S., Raza, A., Maas, R., 2001. Archaeological implications of the geology and chronology of the Soa Basin, Flores, Indonesia. Geology 29 (7), pp. 607–610.

Otake, T., Wesolowski, D.J., Anovitz, L.M., Allard, L.F., Ohmoto, H., 2010. Mechanisms of iron oxide transformations in hydrothermal systems. Geochemica et Cosmochemica Acta 74, pp. 6141–6156.

Pacey, A., Macpherson, C.G., McCaffrey, K.J.W., 2013. Linear volcanic segments in the central Sunda Arc, Indonesia, identified using Hough Transform analysis: implications for arc lithosphere control upon volcano distribution. Earth Planetary Science Letters 369–370, pp. 24–33

Pattan, J.N., Prasad, M.S., Babu, E.V.S.S.K., 2010. Correlation of the oldest Toba Tuff to sediments in the central Indian Ocean Basin. Journal of Earth Systems Science 119, pp. 531–539.

Pearce, N.J.G., Eastwood, W.J., Westgate, J.A., Perkins, W.T., 2002. Trace-element composition of single glass shards in distal Minoan tephra from SW Turkey. Journal of the Geological Society 159, pp 545–557.

Pearce, N.J.G., Westgate, J.A., Perkins, W.T., Preece, S.J., 2004. The application of ICPMS methods to tephrochronological problems. Applied Geochemistry 19, pp. 289–322.

Peccerillo, A., Taylor, S.R., 1976, Geochemistry of eocene calc-alkaline volcanic rocks from the Kastamonu area, northern Turkey. Contributions to Mineralogy and Petrology 58, pp. 63-81.

Penny, D., 2012. China and Southeast Asia. In: Metcalfe, S.E., Nash, D.J. (Eds), Quaternary Environmental Change in the Tropics. Wiley-Blackwell, pp. 207–235.

Peters, C.R., Blumenschine, R.J., 1995. Landscape perspectives on possible land use patterns for early hominids in the Olduvai Basin. Journal of Human Evolution 29, pp. 321–362.

Petraglia, M.D., Potts, R., 1994. Water flow and the Formation of Early Pleistocene Artifact site in Olduvai Gorge, Tanzania. Journal of Anthropological Archaeology 13, pp. 228–254.

Pettijohn, F.J., 1975. Sedimentary Rocks. Third Edition. Harper and Row Publishers, New York, 628p.

Pirazzoli, P.A., Radtke, U., Hantoro, W.S., Jouannic, C., Hoang, C.T., Cause, C., Best, M.B., 1993. A one million-year-long sequence of marine terraces on Sumba island. Indonesia. Marine Geology 109, pp. 221–236.

Potts, R., Behrensmeyer, A.K., Ditchfield, P., 1999. Paleolandscape variation and early Pleistocene hominid activities: Members 1 and 7, Olorgesailie Formation, Kenya. Journal of Human Evolution 37, pp. 747–788.

Preece, S.J., Westgate, J.A., Alloway, B.V., Milner, M.W., 2000. Characterization, identity, distribution, and source of late Cenozoic tephra beds in the Klondike district of the Yukon, Canada. Canadian Journal of Earth Sciences 37, pp. 983–996.

Quidelleur, X., and Valet, J. P., 1994. Paleomagnetic records of excursions and reversals: possible biases caused by magnetization artefacts. Physics of the Earth and Planetary Interiors 82, pp. 27–48.

Rapp, G., and Hill, C.L., 2006. Geoarchaeology : the earth-science approach to archaeological interpretation. Second Edition. New Haven: Yale University Press, 339p.

Reimann, C., Filzmoser, P., Garret, R.G., 2002. Factor analysis applied to regional geochemical data: problems and possibilities. Applied Geohemistry 17, pp. 185–206.

Retallack, G. J., 2001. Soils of the Past: An introduction to Paleopedology. Second Edition. Blackwell Science Ltd., Oxford, 404p.

Retallack, G.J., 2005. Pedogenic carbonate proxies for amount and seasonality of precipitation in paleosols. Geology 33, pp. 333–336.

Rivera, T. A., Storey, M., Schmitz, M. D., Crowley, J. L., 2013. Age intercalibration of $^{40}Ar/^{39}Ar$ sanidine and chemically distinct U/Pb zircon populations from the Alder Creek Rhyolite Quaternary geochronology standard. Chemical Geology 345, pp. 87–98.

Roberts, R.G., Westaway, K.E., Zhao, J.-X., Turney, C.S.M., Rink, W.J., Bird, M.I., Fifield, K., 2009. Geochronology of cave deposits in Liang Bua and river terraces in the Wae Racang valley, western Flores, Indonesia. Journal of Human Evolution 57, pp. 484–502.

Roche, O., Druitt, T.H., Merle, O., 2000. Experimental study of caldera formation. Journal of Geophysical Research 105, pp. 395–416.

Roche, O., Phillips, J.C., Kelfoun, K., 2013. Pyroclastic density currents. In: Fagents, S.A., Gregg, T.K.P., Lopes, R.M.C. (Eds.), Modeling Volcanic Processes: The Physics and Mathematics of Volcanism. Cambridge University Press, pp. 203–229.

Rollinson, H.R., 1993. Using Geochemical Data: Evaluation, Presentation, Interpretation. Longman Scientific and Technical, Essex, 352p.

Roy, P.D., Caballero, M., Lozano, R., Ortega, B., Lozano, S., Pi, T., Israde, I., Morton, O., 2010. Geochemical record of Late Quaternary paleoclimate from lacustrine sediments of paleo-lake San Pelipe, western Sonora Desert, Mexico. Journal of South American Earth Sciences 29, pp. 586–596.

Royer, D.L., 1999. Depth to pedogenic carbonate horizon as a paleoprecipitation indicator? Geology 27, pp. 1123–1126.

Salvador A.,1994. International Stratigraphic Guide: A Guide to Stratigraphic Classification, Terminology and Procedure, 2nd Edition, The International Union of Geological Sciences and The Geological Society of America, 214p.

Sandhu, A. S., Westgate, J. A., 1995. The correlation between reduction in fission-track diameter and areal track density in volcanic glass shards and its

application in dating tephra beds. Earth and Planetary Science Letters 131, pp. 289–299.

Silver, E.A., Reed, D., McCaffrey, R., Joyodiwiryo, Y., 1983. Back arc thrusting in the eastern Sunda arc, Indonesia: a consequence of arc–continent collision. Journal of Geophysical Research 88, pp. 7429–7448.

Shane, P.A.R., 2000. Tephrochronology: a New Zealand case study. Earth-Science Reviews 49, pp. 223–259.

Sheldon, N.D., Retallack, G.J., Tanaka, S., 2002. Geochemical climofunctions from North America soils and application to paleosols across the Eocene–Oligocene boundary in Oregon. Journal of Geology 110, pp. 687–696.

Sheldon, N.D., Tabor, N.J., 2009. Quantitative paleoenvironmental and paleoclimatic reconstruction using paleosols. Earth-Science Reviews 95, pp. 1–52.

Shoji, S., Nanzyo, M., Dahlgren, R.A., 1993. Volcanic ash soils: genesis, properties and utilization. Development in Soil Science: 21. Elsevier, 288p.

Smith, G.A., 1986. Coarse-grained nonmarine volcaniclastic sediment: terminology and depositional process. Geological Society of America Bulletin 97, pp. 1 –10.

Smith, G. A., Fritz, W. J., 1989. Volcanic influences on terrestrial sedimentation. Geology 17, pp. 375–376.

Smith, G.A., 1991. Facies sequences and geometries in continental volcaniclastic sediments. In: Fisher, R., Smith, G. (Eds.), Sedimentation in Volcanic Settings. SEPM Special Publication, Vol. 45, pp. 109–121.

Smith, G.A., Lowe, D.R., 1991. Lahars: volcano-hydrologic events and deposition in the debris flow-hyperconcentrated flow continuum. In: Fisher, R.V., Smith, G.A. (Eds), Sedimentation in Volcanic Settings. SEPM Special Publication, Vol. 45, pp. 59–70.

Spooner, M.I., Barrows, T.T., De Deckker, P., Paterne, M., 2005. Palaeoceanography of the Banda Sea, and Late Pleistocene Initiation of the Northwest Monsoon. Global and Planetary Change 49, pp. 28–46.

Sondaar, P.Y., van den Bergh, G.D., Mubroto, B., Aziz, F., de Vos, J., and Batu, U.L. 1994. Middle Pleistocene faunal turn-over and colonisation of Flores

(Indonesia) by Homo erectus: Paris, Acade mie des Sciences Comptes Rendus, Vol. 319, pp. 1255–1262.

Stoermer, E.F., Smol, J.P., 2001. The Diatoms: Applications for the Environmental and Earth Sciences. Cambridge University Press, 469p.

Stollhofen, H., Stanistreet, I.G., McHenry, L.J., Mollel, G.F., Blumenschine, R.J., Masao, F.T., 2008. Fingerprinting facies of the Tuff IF marker, with implications for early hominin palaeoecology, Olduvai Gorge, Tanzania. Palaeogeography Palaeoclimatology Palaeoecology 259, pp. 382-409.

Storey, M., Roberts, R. G., Saidin, M., 2012. Astronomically calibrated $^{40}Ar/^{39}Ar$ age for the Toba supereruption and global synchronization of late Quaternary records. Proceedings of the National Academy of Science 109, pp. 18684–18688.

Sucipta, I G.B.E, Takashima, I., Muraoka, H., 2006. Morphometric age and petrological characteristics of volcanic rocks from the Bajawa Cinder Cone Complex, Flores, Indonesia. Journal of Mineralogical and Petrological Sciences 101, pp. 48-68.

Suganuma, Y., Okada, M., Horie, K., Kaiden, H., Takehara, M., Senda, R., Kimura, J.-I., Kawamura, K., Haneda, Y., Kazaoka, O., Head, M.J., 2015. Age of Matuyama-Brunhes boundary constrained by U-Pb zircon dating of a widespread tephra. Geology 43 (6), pp. 491–494.

Suminto, Morwood, M.J., Kurniawan, I., Aziz, F., van den Bergh, G.D., Hobbs, D.R., 2009. Geology and fossil sites of the Soa Basin, Flores. In: Aziz, F., Morwood, M.J., van den Bergh, G.D. (Eds.), Pleistocene geology, palaeontology and archaeology of the Soa Basin, Central Flores. Centre for Geological Survey, Ministry of Energy and Mineral Resources, Republic of Indonesia, Special Publication No. 36, pp. 19–40.

Sun S.S., McDonough, W.F., 1989. Chemical and isotopic systematics of oceanic basalts: implications for mantle composition and processes. In: Saunders A.D., Norry, M.J (Eds), Magmatism in the ocean basins. Geological Society Special Publications 42, pp. 313–345.

Suzuki M, Wikarno, Budisantoso, Saefudin I, Itihara M., 1985. Fission track ages of pumice tuff. Eds Watanabe N, Kadar D. Quaternary Geology of the Hominid Fossil Bearing Formations in Java. Geological Research and Development Centre, special publication, pp. 309–357.

Swisher, C.C., Curtis, G.H., Jacob, T., Getty, A.G., Suprijo, A.,Widiasmoro, 1994. Age of the earliest known Hominids in Java, Indonesia. Science 263, pp. 1118–1121.

Swisher, C.C., 1997. A revised geochronology for the Plio-Pleistocene hominid bearing strata of Sangiran Java, Indonesia. Journal of Human Evolution 32, A23.

Takashima, I., Nasution, A. and Muraoka, H., 2002. Thermoluminescence dating of volcanic and altered rocks in the Bajawa geothermal area, central Flores Island, Indonesia. Bulletin of the Geological Survey of Japan 53, pp. 139-146.

Taylor S.R., McLennan S.M., 1985. The continental crust: its composition and evolution. Blackwell Scientific Publication, Carlton, 312 p.

Templ, M., Filzmoser, P., Reimann, C., 2008. Cluster analysis applied to regional geochemical data: problems and possibilities. Applied Geochemistry 23 (8), pp. 2198–2213.

Thorarinsson, S., 1944. Tefrokronologiska studier pa Island; Thjorsardalur och dess foeroedelse; Tephrochronological studies in Iceland. Geografiska Annaler 1–2, pp. 1–217.

Torrent, J., Barrón, V., Liu, Q.S., 2006. Magnetic enhancement is linked to and precedes hematite formation in aerobic soil. Geophysical Research Letters 33, L02401. doi:10.1029/2005GL024818.

Tryon, C.A., McBrearty, S., 2002. Tephrostratigraphy and the Acheulian to Middle Stone Age transition in the Kapthurin Formation, Kenya. Journal of Human Evolution 42, pp. 211–235.

Tryon, C.A., Roach, N.T., Logan, M.A.L., 2008. The Middle Stone Age of the northern Kenyan Rift: age and context of new archaeological sites from the Kapedo Tuffs. Journal of Human Evolution 55, pp. 652–664.

Tucker, M.E., Wright, V.P., 1990. Carbonate Sedimentology. Blackwell Scientific Publications, Oxford, 482p.

Twyman, R., M., 2007. Geomagnetic excursions and secular variations. In: Elias, S.A. (Ed.), Encyclopaedia of Quaternary Science. Elsevier, London, pp. 717-720.

United States Geological Survey (USGS), 1995. https://crustal.usgs.gov/geochemical_reference_standards/rhyolite.html#top

van den Bergh, G.D., B. Mubroto, F. Aziz, P.Y. Sondaar, J. de Vos, 1996. Did Homo erectus reach the island of Flores? In: Bellwood, P. (Eds.), Indo-Pacific prehistory Association Bulletin 14, pp. 27-36.

van den Bergh, G.D. 1999. The late Neogene elephantoid-bearing fauna of Indonesia and their palaeozoogeographic implications: a study of the terrestrial fauna succession of Sulawesi, Flores and Java, including evidence for early hominid dispersal east of Wallace's Line. Scripta Geologica 117, 419p.

van Bergh, G.D. van den, J. de Vos, F. Aziz, M.J. Morwood, 2001. Elephantoidea in the Indonesian region: new Stegodon findings from Flores. 1st Int. Congress "The World of Elephants", October 16-20, 2001, Rome. In: G. Cavarretta, P. Gioia, M. Mussi, M.R. Palombo (Eds.): The World of Elephants. Consiglio Nazionale delle Ricerche, Roma, pp. 623-627.

van den Bergh, G.D., Awe Due, R., Morwood, M.J., Sutikna, T., Jatmiko, Saptomo, E.W., 2008. The youngest Stegodon remains in Southeast Asia from the Late Pleistocene archaeological site Liang Bua, Flores, Indonesia. Quaternary Internasional 182, pp. 16–48.

van den Bergh, G.D., Aziz, F., Kurniawan, I., Morwood, M.J., Lentfer, C.J., Suyono, Setiawan R., 2009a. Environmental reconstruction of the Middle Pleistocene archaeological and palaeontological site of Mata Menge, Central Flores, Indonesia. In: Aziz, F., Morwood, M.J., van den Bergh, G.D. (Eds.), Pleistocene geology, palaeontology and archaeology of the Soa Basin, Central Flores. Centre for Geological Survey, Ministry of Energy and Mineral Resources, Republic of Indonesia, Special Publication No. 36, pp. 58–94.

an den Bergh, G.D., Meijer, H.J.M., Awe Due, R., Morwood, M.J., Szabo, K., van den Hoek Ostende, L.W., Sutikna, T., Saptomo, E.W., Piper, P.J., Dobney, K.M., 2009b. The Liang Bua faunal remains: a 95 k.yr. sequence from Flores, East Indonesia. Journal of Human Evolution 57, pp. 527–537.

van den Bergh, G.D., Kaifu, Y., Kurniawan, I., Kono, R.T., Brumm, A., Setiyabudi, E., Aziz, F., Morwood, M.J., 2016. Homo floresiensis-like fossils from the early Middle Pleistocene of Flores. Nature 534, pp. 245–248

van Bemmelen, R.W., 1949, The Geology of Indonesia: Nijhoff, The Hague, Government Printing Office, 732p.

Vallance, J.W., Iverson, R.M., 2015. Chapter 37: Lahars and their deposits. In: Sigurdsson, H., Houghton, B., McNutt, S., Rymer, H., Stix, J. (Eds.), Encyclopedia of Volcanoes. Academic Press, Elsevier, pp. 649–664.

Varekamp, J.C., van Bergen, M.J., Vroon, P.Z., Porter, R.P.E., Wirakusumah, A.D., Erfan, R., Suharyono, K., Sriwana, T., 1989. Volcanism and tectonics in the eastern Sunda Arc, Indonesia. Netherlands Journal of Sea Research 24, pp. 303–312.

Velde, B., Meunier, A., 2008. The Origin of Clay Minerals in Soils and Weathered Rocks. Springer, London, 406p.

Verhoeven, Th., 1958. Pleistozane funde in Flores. Anthropos 53, pp. 264-65.

Verhoeven. Th., 1968. Pleistozane funde auf Flores, Timor and Sumba. In Anthropica, Gedenkschrift zum 100. Geburtstag von P.W. Schmidt, Studia Instituti Anthropos 21, pp. 393-403.

Verrecchia, E.P., 2007. Lacustrine and palustrine geochemical sediments. In: Nash,D.J., McLaren, S.J. (Eds). Geochemical Sediments and Landscapes. Blackwell Publishing, Malden, USA, pp. 298–329.

Voris, H.K., 2000. Maps of Pleistocence sea levels in Southeast Asia: shorelines, river systems and time durations. Journal of Biogeography 27, pp. 1153-1167.

Walker, M., 2005. Quaternary dating methods. John Wiley and Sons Ltd., 286p.

Ward, C.R., C.W., Taylor, J.C., 1996. Quantitative mineralogical analysis of coals form the Callide Basin, Queensland, Australia using X-ray diffractometry and normative interpretation. International Journal of Coal Geology 30, pp. 211-229.

Watanabe, N., Kadar, D. (Eds.), 1985. Quaternary Geology of the Hominid Fossil Bearing Formations in Java. Geological Research and Development Centre, Special Publication no. 4, 378p.

Wei, G., Liu, Y., Li, X., Shai, L., Fang, D., 2004. Major and trace element variations of the sediments at ODP Site 1144, South China Sea, during the last 230 ka and their paleoclimate implications. Palaeogeography Palaeoclimatology Palaeoecology 212, **pp.** 331–342.

Welton, J.E., 1984. SEM petrology atals. Methods in Exploration Series, the American Association of Petroleum Geologists, 235p.

Westaway, K.E., Morwood, M.J., Roberts, R.G., Zhao, J.-X., Sutkina, T., Saptomo, E.W., Rink, W.J., 2007a. Establishing the time of initial human occupation of Liang Bua, western Flores, Indonesia. Quaternary Geochronology 2, 337–343.

Westaway, K.E., Morwood, M.J., Roberts, R.G., Rokhus, A.D., Zhao, J.-X., Storm, P., Aziz, F., van den Bergh, G., Hadi Jatmiko, P., de Vos, J., 2007b. Age and biostratigraphic significance of the Punung rainforest fauna, East Java, Indonesia, and implications for Pongo and Homo. Journal of Human Evolution 53, pp. 709–717.

Westgate, J. A., 1998. Isothermal plateau fission-track ages of hydrated glass shards from silicic tephra beds. Earth and Planetary Science Letters 95, pp. 226–234.

Westgate, J. A., 2014. Fission track dating of volcanic glass. In: Rink, W. J., Thompson, J., (Eds.), Encyclopedia of Scientific Dating Methods, Springer Dordrecht, pp. 1–60.

Westgate, J.A., Naeser, N.D., Alloway, B.V., 2013. Fission-track dating. In: Elias, S.A., Mock, C.J. (Eds.), Encyclopaedia of Quaternary Science, 2nd Edition, vol. 1, Elsevier, Amsterdam, pp. 643–662.

Wheller, G.E., Varne, R., Foden, J.D., Abbott, M.J., 1987. Geochemistry of Quaternary volcanism in the Sunda-Banda arc, Indonesia, and three component genesis of island-arc basaltic magmas. Journal of Volcanology and Geothermal Research 32, pp. 137-160.

White, J.D.L., Houghton, B., 2000. Surtseyan and related phreatomagmatic eruptions. In: Sigurdsson, H., Houghton, B., McNutt, S., Rymer, H., Stix, J. (Eds.), Encyclopedia of Volcanoes. Academic Press, New York, pp. 495–512.

Whitford, D.J., Compston, W., Nichols, I.A., Abbott, M.J., 1977. Geochemistry of late Cenozoic lavas from eastern Indonesia: role of subducted sediments in petrogenesis. Geology 5, pp. 571-575.

Whitford, D.J., Nichols, I.A., Taylor, S.R., 1979. Spatial variations in the geochemistry of Quaternary lavas across the Sunda Arc in Java and Bali. Contributions to Mineralogy and Petrology 70, pp. 341-356.

Whitney, D.L., Evans, B.E., 2010. Abbreviations for names of rock-forming minerals. American Mineralogist 95, pp. 185–187.

WoldeGabriel, G., Hart, W.K., Katoh, S., Beyene, Y., Suwa, G., 2005. Correlation of Plio-Pleistocene tephra in Ethiopian and Kenyan rift basins: temporal calibration of geological features and hominid fossil records. Journal of Volcanology and Geothermal Research 147, pp. 81–108.

Wynn, J.G., 2000. Paleosols, stable carbon isotopes, and paleoenvironmental interpretation of Kanapoi, Northern Kenya. Journal of Human Evolution 39, pp. 411–432.

Yang, S.Y., Li, C.X., Yang, D.Y., Li, X.S., 2004. Chemical weathering of the loess deposits in the lower Changjiang Valley, China and paleoclimatic implications. Quaternary International 117, pp. 27–34.

Yurnaldi, D., Setiawan, R., Patriani, E.Y., 2018. The Magnetostratigraphy and the Age of Soa Basin Fossil-Bearing Sequence, Flores, Indonesia. Indonesian Journal on Geoscience 5 (3), pp 221–234.

Zabel, M., Schneider, R.R., Wagner, T., Adegbie, A.T., deVries, U., Kolonic, S., 2001. Late Quaternary climate changes in Central Africa as inferred from terrigenous input to the Niger Fan. Quaternary Research 56, pp. 207–217.

Zaim Y, Ciochon, R.L., Polanski, J.M., Grine, F.E., Bettis III, E.A., Rizal, Y., Franciscus, R.G., Larick, R.R., Heizler, M., Aswan, Eaves, K.L., dan Marsh, H.E., 2011. New 1.5 million-year-old Homo erectus maxilla from Sangiran (Central Java, Indonesia). Journal of Human Evolution 61, pp. 363–376.

APPENDIX 1. STRATIGRAPHIC SECTIONS AND LITHOFACIES DESCRIPTIONS

Appendix 1.1. KOBATUWA

1.1.1. Kobatuwa 1 (Outcrop)

Depth (m)		Thickness (m)	Facies	Description
From	To			
0.00	0.74	0.74	Bv	Volcanic breccias, poorly sorted, clast supported, massive, major component of scoria, pumice, basalt and andesite fragments.
0.74	0.82	0.08	Pv	Palaeosol, silty claystone, strongly developed, massive, rootlets and mottled, medium-coarse blocky structure.
0.82	0.85	0.03	Tms	Stratified ash, fine grained vitric ash, silt- very fine sand sized, massive, well sorted, sharp basal surface. (WSI)
0.85	0.875	0.025	Tmp	Pumiceous ash, coarse sandy vitric ash, sand-sized pumice clasts, massive, poorly sorted, sharp contact. (WSI)
0.875	1.07	0.195	Tma	Fine sandy vitric ash, abundance of rim type accretionary lapilli, massive, poorly sorted. (WSI)
1.07	1.12	0.05	Tmp	Pumiceous ash, coarse sandy vitric ash, sand-sized pumice clasts, massive – crudely stratified, poorly sorted, sharp contact. (WSI)
1.12	1.295	0.175	LTmp	Fine to coarse lapilli, pumiceous, massive, stratified at lower part, clast supported, normal grading, vitric, few crystals and lithics, poorly sorted, *p*max 2 x 1.4 cm, sharp basal contact. (WSI)
1.295	1.775	0.48	Trma	Reworked ash with many accretionary lapilli, poorly sorted, massive, fine to medium sandy.
1.775	2.775	1.00	Trm	Reworked ash, coarse sandy, massive, well sorted.
2.775	3.145	0.37	Pa	Palaeosol, silty claystone, strongly developed, massive, rootlets and mottled, medium - coarse blocky structure, strongly developed, strength colouring (10YR 5/2).
3.145	4.045	0.90	Ts	Stratified ash, coarse sandy vitric ash, low angle cross stratification, lithic laminations sharp basal boundary. (TRI)
4.045	4.060	0.15	LTmp	Fine to coarse lapilli, pumiceous, massive, clast supported, normal grading, vitric, few crystals and lithics, poorly sorted, *p*max 2 x 1.2 cm. (TRI)
4.060	4.90	0.84	Trma	Reworked ash with accretionary lapilli, massive-crudely stratified, fine grained, well-moderately sorted.
4.90	5.70	0.80	Pa	Palaeosol, silty claystone, strongly developed, massive, rootlets and mottled, medium - coarse blocky structure, strongly developed, (10YR 5/2).
5.70	5.90	0.20	Tm	Vitric ash, fine grained, contains hornblende, massive, well sorted (PMS).

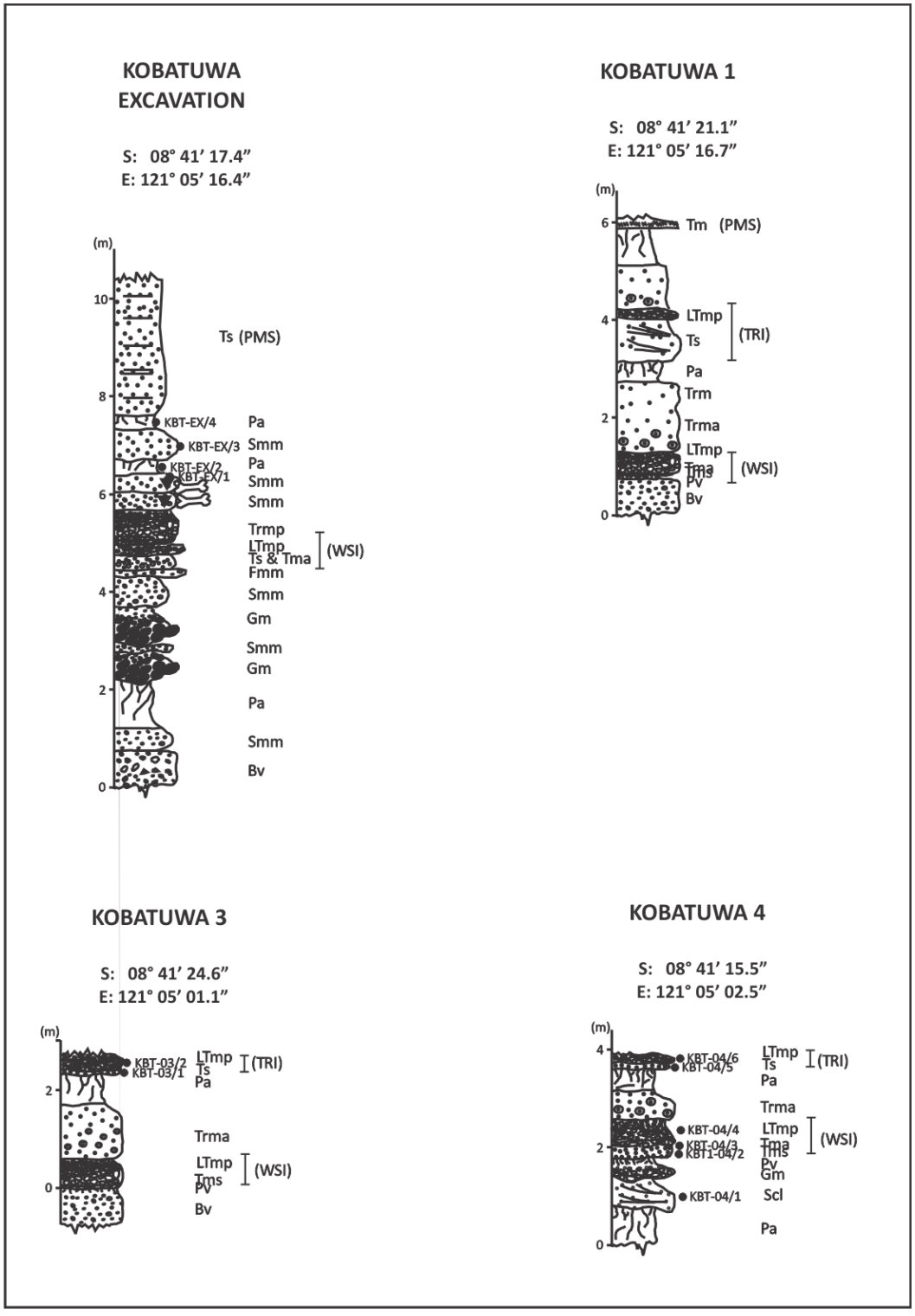
KOBATUWA EXCAVATION
S: 08° 41' 17.4"
E: 121° 05' 16.4"
(m)
10
8
6
4
2
0
Ts (PMS)
KBT-EX/4
KBT-EX/3
KBT-EX/2
KBT-EX/1
Pa
Smm
Pa
Smm
Smm
Trmp
LTmp
Ts & Tma
Fmm
Smm
Gm
Smm
Gm
Pa
Smm
Bv
(WSI)
KOBATUWA 1
S: 08° 41' 21.1"
E: 121° 05' 16.7"
(m)
6
4
2
0
Tm (PMS)
LTmp
Ts
Pa
Trm
Trma
LTmp
Tma
Tms
Pv
Bv
(TRI)
(WSI)
KOBATUWA 3
S: 08° 41' 24.6"
E: 121° 05' 01.1"
(m)
2
0
KBT-03/2
KBT-03/1
LTmp
Ts
Pa
Trma
LTmp
Tms
Pv
Bv
(TRI)
(WSI)
KOBATUWA 4
S: 08° 41' 15.5"
E: 121° 05' 02.5"
(m)
4
2
0
KBT-04/6
KBT-04/5
KBT-04/4
KBT-04/3
KBT-04/2
KBT-04/1
LTmp
Ts
Pa
Trma
LTmp
Tma
Tms
Pv
Gm
Scl
Pa
(TRI)
(WSI)

2.1.2. Kobatuwa 3 (Outcrop)

Depth (m)		Thickness (m)	Facies	Description
From	To			
-	-	-	Bv	Volcanic breccias, poorly sorted, clast supported, massive, angular-subangular, sandy matrix, major component of scoria, pumice, basalt and andesite fragments; covered by palaeosol, silty claytone, massive.
0.00	0.04	0.04	Tms	Stratified ash, fine grained vitric ash, silt- very fine sand sized, massive, well sorted, sharp basal surface. (WSI)
0.04	0.60	0.56	LTmp	Fine to coarse lapilli, pumiceous, massive, stratified at lower part, clast supported, crudely stratified in the base, normal grading, vitric, few crystals and lithics, poorly sorted, sharp basal contact. (WSI)
0.60	1.80	1.20	Trma	Reworked ash contains accretionary lapilli in the lower part, poorly sorted, massive, fine to medium sandy.
1.80	2.45	0.65	Pa	Palaeosol, silty claystone, strongly developed, massive, rootletss and mottled, medium - coarse blocky structure, strongly developed, strength colouring (10YR 5/2).
2.45	2.55	0.10	Ts	Stratified ash, coarse sandy vitric ash, low angle cross stratification, lithic laminations sharp basal boundary. (TRI)
2.55	2.85	0.30	LTmp	Fine to coarse lapilli, pumiceous, massive, clast supported, normal grading, vitric, few crystals and lithics, poorly sorted, *p*max 2 x 1.2 cm. (TRI)

1.1.3. Kobatuwa 4 (Outcrop)

Depth (m)		Thickness (m)	Facies	Description
From	To			
0.00	1.20	1.20	Pa	Palaeosol, silty claystone, strongly developed, massive, rootletss and mottled, medium-coarse blocky structure, brown (10YR 5/3).
1.20	2.45	1.25	Scl	Sandstone, medium-coarse grained, moderately – poorly sorted, cemented, composed of quartz, feldspars and sand-sized pumice.
2.45	2.75	0.30	Gm	Conglomerate, clast supported, poorly sorted, coarse sand matrix, composed of basalt and andesite fragments, pebble to cobble sized.
2.75	2.805	0.055	Pv	Palaeosol, silty claystone, strongly developed, massive, rootletss and mottled, medium-coarse blocky structure, light grey – grey (10YR 6/1 – 10YR 7/1).
2.805	2.830	0.025	Tms	Fine grained vitric ash, silt- very fine sand sized, massive, well sorted, sharp basal surface. (WSI)
2.830	2.858	0.028	Tmp	Pumiceous ash, coarse - very coarse sandy vitric ash, sand-sized pumice clasts, massive, poorly sorted, sharp contact. (WSI)
2.858	2.993	0.135	Tma	Fine sandy vitric ash, abundance of rim type accretionary lapilli, massive, poorly sorted. (WSI)

2.993	3.178	0.185	Tmp	Pumiceous ash, coarse – very coarse sandy vitric ash, sand-sized pumice clasts, massive – crudely stratified, poorly sorted, sharp contact. (WSI)
3.178	3.542	0.364	LTmp	Fine to coarse lapilli, pumiceous, massive, stratified at lower part, clast supported, normal grading, vitric, few crystals and lithics, poorly sorted, *p*max 2.8 x 1.6 cm, sharp basal contact. (WSI)
3.542	4.132	0.59	Trma	Reworked ash with many accretionary lapilli, poorly sorted, massive, fine to medium sandy.
4.132	4.592	0.46	Pa	Palaeosol, silty claystone, strongly developed, massive, rootletss and mottled, medium - coarse blocky structure, strongly developed and coloured (10YR 5/2).
4.592	4.712	0.12	Ts	Stratified ash, coarse sandy vitric ash, low angle cross stratification, lithic laminations sharp basal boundary. (TRI)
4.712	4.897	0.185	LTmp	Fine to coarse lapilli, pumiceous, massive, clast supported, normal grading, vitric, few crystals and lithics, poorly sorted. (TRI)

1.1.4. Kobatuwa Excavation

Depth (m)		Thickness (m)	Facies	Description
From	To			
0.00	0.80	0.80	Bv	Basaltic lahar, clast supported, angular-subangular, poorly sorted, consists of scoria, basalt, pumice, lithic in sandy matrix, maximum clast 22 x 18 cm.
0.80	1.25	0.45	Smm	Tuffaceous sandstone, poorly sorted, clast supported, contains fragments of basalt and andesite, average size 1-2 cm, in coarse sandy matrix.
1.25	2.25	1.00	Pa	Palaeosols, silty claystone, mottled, rootletss, medium-coarse blocky structure, strongly developed, (10YR 5/3).
2.25	2.9	0.65	Gm	Conglomerate, clast supported, poorly sorted, rounded – subrounded, dominantly basaltic and andesitic clasts, maximum size 38 x 58 cm, in coarse sandy matrix.
2.9	3.1	0.20	Smm	Tuffaceous sandstone, coarse-very coarse, poorly sorted, clast supported, comprises pumice and lithics in coarse sandy matrix.
3.1	3.9	0.80	Gm	Conglomerate, clast supported, poorly sorted, rounded – subrounded, dominantly basaltic and andesitic clasts, maximum size 22 x 33 cm, in coarse sandy matrix.
3.9	4.52	0.62	Smm	Pumiceous sandstone, coarse-very coarse grained, moderately sorted, sandy ash matrix.
4.52	4.64	0.12	Fmm	Pumiceous siltstone (lahar/mudflow), clast supported, poorly sorted, polymict, comprises fragments of basalt, andesite, pumice, and claystone.
4.64	4.93	0.29	Ts & Tma	Vitric ash (Ts) and massive ash with accretionary lapilli (Tma), considered as surge and airfall deposits, respectively. (WSI)
4.93	5.07	0.14	LTmp	Pumiceous lapilli (Pyroclastic flow), clast supported,

				moderately sorted, comprises pumice in coarse sandy ash matrix. (WSI)
5.07	5.77	0.70	Trmp	Redeposited pumiceous lapilli, crudely stratified, clast supported, rip up clasts, comprises pumice in coarse sandy ash matrix.
5.77	6.17	0.40	Smm	Tuffaceous sandstone, clast supported, poorly sorted, coarse-very coarse grained, massive, polymict, comprises pumice, basalt, andesite and claystone.
6.17	6.53	0.36	Smm	Tuffaceous sandstone, fine grained, well sorted, massive, contains silicified root.
6.53	6.83	0.30	Pa	Palaeosols, massive, moderately developed, mottled, medium-coarse blocky structure.
6.83	7.43	0.60	Smm	Tuffaceous sandstone, fine grained, well sorted, massive, contains silicified root.
7.43	7.79	0.36	Pa	Palaeosols, massive, moderately developed, mottled, medium-coarse blocky structure.
7.79	10.37	2.58	Ts	Vitric ash, massive-laminated, well sorted, very fine-fine grained. (TRI)

Appendix 1.2. MATA MENGE

1.2.1. Mata Menge Outcrop

Depth (m)		Thickness (m)	Facies	Description
From	To			
0.00	0.80	0.80	Pa	Palaeosol, silty claystone, well developed upward, massive, rootlets and mottled, medium-coarse blocky structure, brown – pale brown (10YR 5/3-6/3).
0.80	1.60	0.80	Pv	Palaeosol, silty claystone, strongly developed, massive, rootlets and mottled, medium-coarse blocky structure, light grey – grey (10YR 6/1 – 10YR 7/1).
1.60	2.65	1.05	LTmp	Fine to coarse lapilli, pumiceous, massive, stratified at lower part, clast supported, normal grading, vitric, few crystals and lithics, poorly sorted, sharp basal contact. 4 cm volcanic ash in the bottom, silty-sandy, well sorted, suggests as surge deposit. (WSI)
2.65	3.88	1.23	Trma	Reworked ash with many accretionary lapilli, poorly sorted, massive, fine to medium sandy.
3.88	4.54	0.66	Pa	Palaeosol, silty claystone, strongly developed, massive, rootlets and mottled, medium - coarse blocky structure, strongly developed and coloured (10YR 5/2).
4.54	4.62	0.08	Ts	Stratified ash, coarse sandy vitric ash, low angle cross stratification, lithic laminations sharp basal boundary. (TRI)
4.62	4.88	0.26	LTmp	Fine to coarse lapilli, pumiceous, massive, clast supported, normal grading, vitric, few crystals and lithics, poorly sorted. (TRI)
4.88	5.75	0.87	Pa	Palaeosol, silty claystone, massive, rootlets and mottled, medium - coarse blocky structure, strongly developed, (10YR 5/2).

5.75	5.91	0.16	Tm	Fine grained vitric ash, silt- very fine sand sized, massive, well sorted, sharp basal surface. (KPW)
5.91	6.31	0.40	Pa	Palaeosol, silty claystone, strongly developed, massive, rootlets and mottled, medium-coarse blocky structure, brown (10YR 5/3).
6.31	6.61	0.30	Tm	Fine grained vitric ash, silt- very fine sand sized, massive, well sorted, sharp basal surface, hornblende rich (PMS).
6.61	6.81	0.20	Pa	Palaeosol, silty claystone, massive, rootlets and mottled, medium - coarse blocky structure, (10YR 5/2).
6.81	7.21	0.40	Smm	Tuffaceous sandstone, coarse-very coarse grained, moderately sorted, massive.
7.21	7.71	0.50	Sm	Sandstone, coarse grained, poorly sorted, massive.
7.71	8.13	0.42	Smm	Tuffaceous sandstone, coarse-very coarse grained, moderately sorted, massive.
8.13	8.71	0.58	Fmm	Tuffaceous siltstone, moderately sorted, massive.

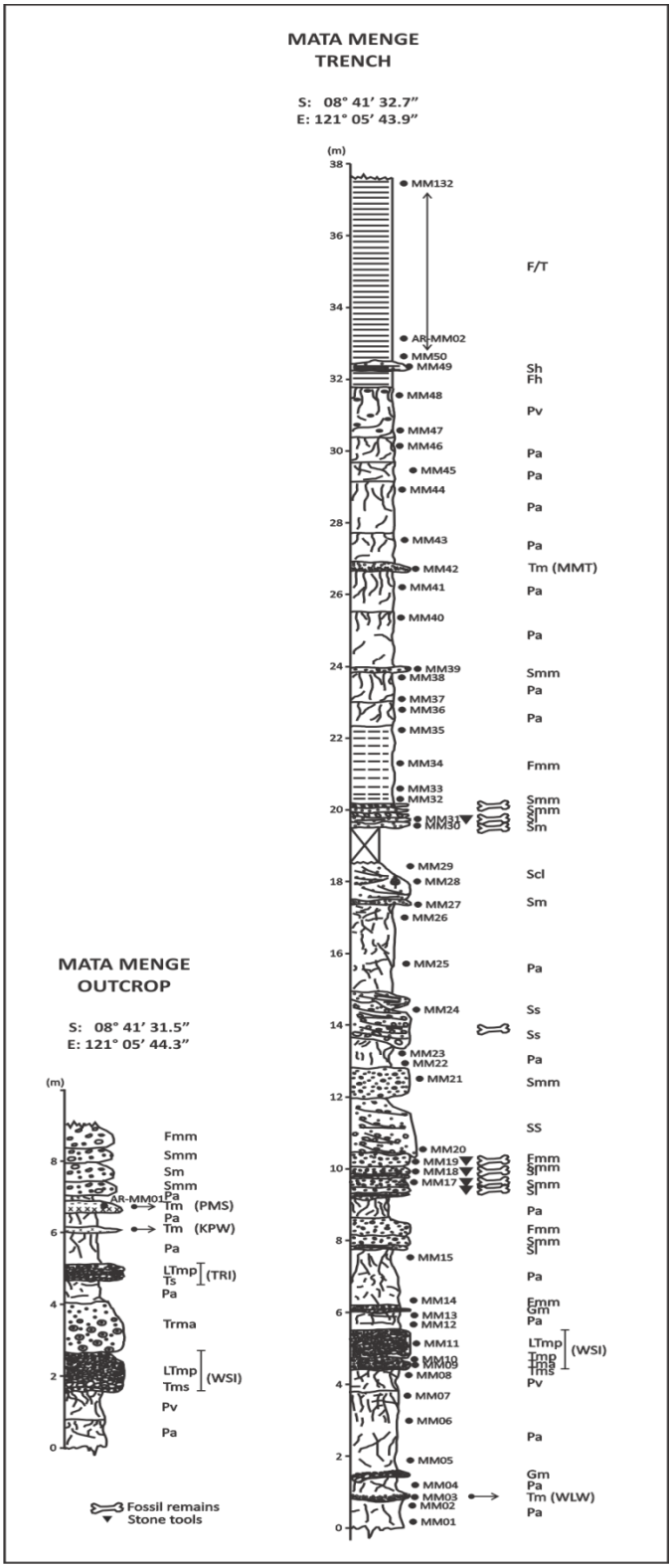
MATA MENGE
TRENCH
S: 08° 41′ 32.7″
E: 121° 05′ 43.9″
(m)
MM132
AR-MM02
MM50
MM49
MM48
MM47
MM46
MM45
MM44
MM43
MM42
MM41
MM40
MM39
MM38
MM37
MM36
MM35
MM34
MM33
MM32
MM31
MM30
MM29
MM28
MM27
MM26
MM25
MM24
MM23
MM22
MM21
MM20
MM19
MM18
MM17
MM15
MM14
MM13
MM12
MM11
MM10
MM09
MM08
MM07
MM06
MM05
MM04
MM03
MM02
MM01
F/T
Sh
Fh
Pv
Pa
Tm (MMT)
Smm
Sm
Fmm
Scl
Ss
SS
Gm
Tm (WLW)
LTmp
Tmp
Tms
(WSI)
MATA MENGE
OUTCROP
S: 08° 41′ 31.5″
E: 121° 05′ 44.3″
AR-MM01
Tm (PMS)
Tm (KPW)
Ts
(TRI)
Trma
Fossil remains
Stone tools

1.2.2. Mata Menge Trench

Depth (m)		Thickness (m)	Facies	Description
From	To			
0.00	0.80	0.80	Pa	Palaeosol, silty claystone, moderately developed, massive, rootlets and mottled, medium-coarse blocky structure, intensive cracks, brown (10YR 5/3).
0.80	0.82	0.02	Tm	Fine grained vitric ash, silt- very fine sand sized, massive, well sorted, sharp basal surface. (WLW)
0.82	1.27	0.45	Pa	Palaeosol, silty claystone, moderately developed, massive, rootlets and mottled, medium-coarse blocky structure, brown (10YR 5/3).
1.27	1.45	0.18	Gs	Conglomerate, clast supported, sandy matrix, dominated by fragments of basalts and andesite, rounded – subrounded, scour and fills, erosional contact.
1.45	3.65	2.20	Pa	Palaeosol, silty claystone, strongly developed upward, massive, rootlets and mottled, medium-coarse blocky structure, brown (10YR 5/3).
3.65	4.28	0.63	Pv	Palaeosol, silty claystone, strongly developed, massive, rootlets and mottled, medium-coarse blocky structure, light grey – grey (10YR 6/1 – 10YR 7/1).
4.28	4.30	0.02	Tmp	Pumiceous ash, coarse sandy vitric ash, sand-sized pumice clasts, massive, poorly sorted, sharp contact, overlies ~1 cm vitric ash (Tms), massive-crudely stratified, silty-sandy.(WSI)
4.30	4.42	0.12	Tma	Fine sandy vitric ash, abundance of rim type accretionary lapilli, massive, poorly sorted. (WSI)
4.42	4.54	0.12	Tmp	Pumiceous ash, coarse sandy vitric ash, sand-sized pumice clasts, massive – crudely stratified, poorly sorted, sharp contact. (WSI)
4.54	5.32	0.78	LTmp	Fine to coarse lapilli, pumiceous, massive, stratified at lower part, clast supported, normal grading, vitric with less abundant of crystals and lithics, poorly sorted, *p*max 3 x 2 cm, stratified in the lower part, sharp basal contact. (WSI)
5.32	5.82	0.50	Pa	Palaeosol, silty claystone, weakly developed, massive, rootlets, reddish colour- intensive oxidation in the upper part, (10YR 6/1-6/2).
5.82	5.90	0.08	Gm	Conglomerate, clast supported, sandy matrix, dominated by fragments of basalts and andesite, rounded – subrounded, erosional contact.
5.90	6.00	0.10	Fmm	Tuffaceous siltstone, mud supported, poorly sorted, pumice dispersed.
6.00	7.64	1.64	Pa	Palaeosol, silty claystone, weakly developed, massive, rootlets and mottled, brown (10YR 5/3).
7.64	7.76	0.12	Sl	Sandstone, coarse grained, moderately sorted, crudely low angle cross bedding, erosional contact.
7.76	8.04	0.28	Smm	Tuffaceous sandstone, coarse grained, poorly sorted, contains dispersed pumice, quartz and feldspars, and erosional base.
8.04	8.46	0.42	Fmm	Tuffaceous siltstone, mud supported, poorly sorted,

				contains dispersed pumices.
8.46	9.06	0.60	Pa	Palaeosol, silty claystone, weakly developed, massive, rootlets and mottled, brown (10YR 5/3).
9.06	9.24	0.18	Sl	Sandstone, coarse grained, moderately sorted, crudely low angle cross bedding, erosional contact.
9.24	9.39	0.15	Smm	Tuffaceous sandstone, coarse grained, poorly sorted, contains dispersed pumice, quartz and feldspars, and erosional base.
9.39	9.67	0.28	Smm	Tuffaceous sandstone, coarse grained, poorly sorted, contains dispersed pumice, quartz and feldspars, and erosional contact.
9.67	9.77	0.10	Sl	Sandstone, coarse grained, moderately sorted, low angle cross bedding, erosional contact.
9.77	9.97	0.20	Smm	Tuffaceous sandstone, coarse grained, poorly sorted, contains dispersed pumice, quartz and feldspars.
9.97	10.38	0.41	Fmm	Tuffaceous siltstone, mud supported, poorly sorted, dispersed pumice, fossils and stone tools accumulation.
10.38	11.92	1.54	Ss	Sandstone, coarse grained, pebbly, moderately-poorly sorted, planar cross bedding, erosional lower boundary.
11.92	12.77	0.85	Smm	Tuffaceous sandstone, coarse grained, poorly sorted, contains dispersed pumices, quartz and feldspars, and erosional base.
12.77	16.51	0.74	Pa	Palaeosol, silty claystone, weakly developed, massive, rootlets and mottled, brown (10YR 5/3).
16.51	14.60	1.09	Ss	Sandstone, coarse grained, pebbly, moderately-poorly sorted, planar cross bedding, erosional lower boundary, contains fossil bones.
14.60	14.87	0.27	Ss	Sandstone, coarse grained, pebbly in the base, well-moderately, planar cross bedding, erosional lower boundary.
14.87	17.27	2.40	Pa	Palaeosol, silty claystone, weakly developed, massive, rootlets and mottled, brown (10YR 5/3).
17.27	17.43	0.16	Sm	Sandstone, fine grained, well sorted, erosional lower boundary.
17.43	18.47	1.04	Scl	Sandstone, coarse grained, well cemented, moderately sorted, planar cross bedding, erosional lower boundary.
				c. 1 m with no exposure.
19.47	19.59	0.12	Sm	Sandstone, fine grained, well sorted, massive-crudely stratified, undulatory and erosional contact.
19.59	19.87	0.28	Sl	Sandstone, coarse grained, pebbly in the base, well-moderately, planar cross bedding, erosional lower boundary, contains fossil remains.
19.87	20.02	0.15	Smm	Pumiceous sandstone (lahar), poorly sorted, massive, contains abundant pumice clasts and fossil remains.
20.02	20.14	0.12	Sm	Sandstone, coarse grained, massive-crudely stratified, poorly sorted, and contains molluscs.
20.14	20.25	0.11	Smm	Pumiceous sandstone (lahar), poorly sorted, massive, contains abundant pumice clasts and fossil remains.
20.25	22.27	2.02	Fmm	Silty claystone (lahar), massive, waxy, moderately

				sorted.
22.27	22.97	0.70	Pa	Palaeosol, silty claystone, weakly developed, massive, rootlets and mottled, brown – pale brown (10YR 5/3-6/3).
22.97	23.80	0.83	Pa	Palaeosol, silty claystone, weakly developed, massive, rootlets and mottled, brown – pale brown (10YR 5/3-6/3).
23.80	23.94	0.14	Smm	Tuffaceous sandstone, coarse grained, poorly sorted, massive, irregular base.
23.94	25.29	1.35	Pa	Palaeosol, silty claystone, weakly developed, massive, rootlets and mottled, brown – pale brown (10YR 5/3-6/3).
25.29	26.44	1.15	Pa	Palaeosol, silty claystone, weakly developed, massive, rootlets and mottled, brown – pale brown (10YR 5/3-6/3).
26.44	26.69	0.25	Tm	Vitric ash, massive, coarse grained, dark grey, sharp base, basaltic composition. (MTM)
26.69	27.49	0.80	Pa	Palaeosol, silty claystone, weakly developed, massive, rootlets and mottled, brown – pale brown (10YR 5/3-6/3).
27.49	29.49	2.00	Pa	Palaeosol, silty claystone, weakly developed, massive, rootlets and mottled, brown – pale brown (10YR 5/3-6/3).
29.49	30.17	0.68	Pa	Palaeosol, silty claystone, weakly developed, massive, rootlets and mottled, brown – pale brown (10YR 5/3-6/3).
30.17	31.67	1.50	Pv	Palaeosol, silty claystone, cracked, moderately developed, massive, rootlets and mottled, carbonate concretion, greenish grey - grey (10YR 6/1-10Y 6/1).
31.67	32.11	0.44	Fh	Horizontal claystone, waxy, carbonate cemented.
32.11	32.31	0.20	Sh	Sandstone, fine grained, well sorted, parallel lamination, erosional contact.
32.31	37.465	5.155	F/T	Interbedded horizontal claystone (Facies Fh) and tephra (facies Tm), and tuffaceous limestone (Lm) developed in the upper part. Claystone (Fh) displays parallel lamination, waxy, very well sorted. Tephra (Tm) refers to vitric crystal ash, coarse to very coarse, composed of sand-sized pumice, feldspars and mafic minerals.

Appendix 1.3. WOLO SEGE (Trench)

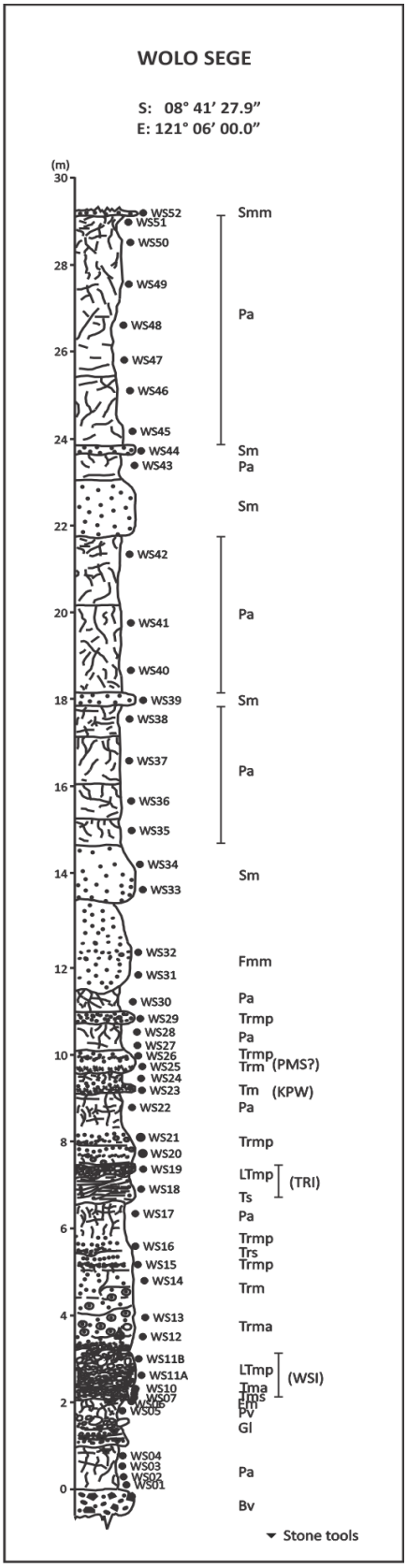

Depth (m)		Thickness (m)	Facies	Description
From	To			
-	-	-	Bv	Volcanic breccias, poorly sorted, clast supported, massive, angular-subangular, sandy matrix, major component of pumice, basalt and andesite fragments.
0.00	1.00	1.00	Pa	Palaeosol, silty claystone, strongly developed, massive, rootlets and mottled, medium-coarse blocky structure, brown (10YR 5/3).
1.00	1.70	0.70	Gl	Conglomerate, clast supported, sandy matrix, dominated by fragments of basalts, rounded – subrounded, cross bedding and cut and fill structures.
1.70	2.08	0.38	Pv	Palaeosol, silty claystone, strongly developed, massive, rootlets and mottled, medium-coarse blocky structure, light grey – grey (10YR 6/1 – 10YR 7/1).
2.08	2.11	0.03	Fm	Silty claystone, massive.
2.11	2.14	0.03	Tms	Fine grained vitric ash, silt- very fine sand sized, massive, well sorted, sharp basal surface. (WSI)
2.14	2.18	0.04	Tmp	Pumiceous ash, coarse sandy vitric ash, sand-sized pumice clasts, massive, poorly sorted, sharp contact. (WSI)
2.18	2.29	0.11	Tma	Fine sandy vitric ash, abundance of rim type accretionary lapilli, massive, poorly sorted. (WSI)
2.29	2.38	0.09	Tmp	Pumiceous ash, coarse sandy vitric ash, sand-sized pumice clasts, massive – crudely stratified, poorly sorted, sharp contact. (WSI)
2.38	3.29	0.91	LTmp	Fine to coarse lapilli, pumiceous, massive, stratified at lower part, clast supported, normal grading, vitric with less abundant of crystals and lithics, poorly sorted, *p*max 3 x 2 cm, stratified in the lower part, sharp basal contact. (WSI)
3.29	5.23	1.94	Trma	Reworked ash with many accretionary lapilli, poorly sorted, massive, fine to medium sandy ash, gradational contact.
5.23	5.29	0.06	Trm	Reworked ash, massive, coarse grained, fining upward.
5.29	5.34	0.05	Trmp	Reworked ash, pumiceous, massive, coarse grained, poorly sorted.
5.34	5.56	0.21	Trs	Reworked ash, ash, coarse grained with thin lamination of very fine grained.
5.56	5.65	0.09	Trm	Reworked ash, massive, coarse grained.
5.65	6.10	0.45	Trmp	Reworked ash, pumiceous, massive, coarse grained, poorly sorted, pumice bed in the lower part.
6.10	6.60	0.50	Pa	Palaeosol, silty claystone, strongly developed, massive, rootlets and mottled, medium - coarse blocky structure, strongly coloured (10YR 5/2).
6.60	7.28	0.68	Ts	Stratified ash, coarse sandy vitric ash, low angle cross stratification, lithic laminations sharp basal boundary. (TRI)
7.28	7.40	0.12	LTmp	Fine to coarse lapilli, pumiceous, massive, clast supported, normal grading, vitric, few crystals and lithics, poorly sorted., *p*max 3 x 2 cm. (TRI)
7.40	7.585	0.185	Trmp	Reworked ash, pumiceous, massive, coarse grained,

				poorly sorted, high concentration crystals in the uppermost part. *p*max 4 x 2 cm.
7.585	7.925	0.34	Trmp	Reworked ash, pumiceous, massive, coarse grained, poorly sorted, *p*max 2 x 1.8 cm.
7.925	8.085	0.16	Trs	Reworked ash, ash, coarse grained with thin lamination of very fine grained.
8.085	8.175	0.09	Trmp	Reworked ash, pumiceous, massive, coarse grained, poorly sorted.
8.175	8.20	0.025	Trm	Reworked ash, massive, medium - coarse grained, well sorted.
8.20	8.32	0.12	Trmp	Reworked ash, pumiceous, massive, coarse grained, poorly sorted, erosional contact (channel fill).
8.32	9.15	0.83	Pa	Palaeosol, silty claystone, strongly developed, massive, rootlets and mottled, medium-coarse blocky structure, brown – dark yellowish brown (10YR 5/3 – 4/6).
9.15	9.34	0.19	Tm	Vitric ash, massive, well sorted, normal grading (KPW).
9.34	9.60	0.26	Pa	Palaeosol, silty claystone, strongly developed, massive, rootlets and mottled, medium-coarse blocky structure, brown – dark yellowish brown (10YR 5/3 – 4/6).
9.60	9.90	0.30	Trm	Reworked ash, massive, medium - coarse grained, poorly sorted, erosional base.
9.90	10.03	0.13	Trmp	Reworked ash, pumiceous, massive, coarse grained, poorly sorted, sharp lower boundary.
10.03	10.75	0.72	Pa	Palaeosol, silty claystone, strongly developed, massive, rootlets and mottled, medium-coarse blocky structure, brown – dark yellowish brown (10YR 5/3 – 4/6).
10.75	11.05	0.30	Trmp	Reworked ash, pumiceous, massive, coarse grained, poorly sorted, sharp and erosional lower boundary.
11.05	11.65	0.50	Pa	Palaeosol, silty claystone, strongly developed, massive, rootlets and mottled, medium-coarse blocky structure, brown – dark yellowish brown (10YR 5/3 – 4/6).
11.65	13.60	1.95	Fmm	Tuffaceous siltstone, moderately sorted, pumice floats, pumice concentrations in the middle, gradational - undulatory base.
13.60	14.74	1.14	Sm	Sandstone, coarse grained, massive, well sorted, irregular/undulatory base, light grey (10YR 7/1).
14.74	15.35	0.61	Pa	Palaeosol, silty claystone, strongly developed, massive, rootlets and mottled, medium-coarse blocky structure, brown – dark yellowish brown (10YR 5/3 – 4/6).
15.35	16.17	0.82	Pa	Palaeosol, silty claystone, strongly developed, massive, rootlets and mottled, medium-coarse blocky structure, pale brown (10YR 6/3).
16.17	17.24	1.07	Pa	Palaeosol, silty claystone, strongly developed, massive, rootlets and mottled, medium-coarse blocky structure, brown – dark yellowish brown (10YR 5/3 – 4/6).
17.24	17.98	0.74	Pa	Palaeosol, silty claystone, strongly developed, massive, rootlets and mottled, medium-coarse blocky structure, pinkish grey (7.5YR 7/2).

17.98	18.28	0.30	Sm	Sandstone, coarse grained, massive, undulatory base, yellowish brown (10YR 5/8).
18.28	20.30	2.02	Pa	Palaeosol, silty claystone, strongly developed, massive, rootlets and mottled, medium-coarse blocky structure, very pale brown (10YR 7/3).
20.30	21.90	1.60	Pa	Palaeosol, silty claystone, strongly developed, massive, rootlets and mottled, medium-coarse blocky structure, dark yellowish brown (10YR 6/4).
21.90	23.18	1.28	Sm	Sandstone, coarse grained, massive, undulatory base, yellowish brown (10YR 5/8).
23.18	23.78	0.60	Pa	Palaeosol, silty claystone, strongly developed, massive, rootlets and mottled, medium-coarse blocky structure, brown – dark yellowish brown (10YR 5/3 – 4/6).
23.78	23.98	0.20	Sm	Sandstone, coarse grained, massive, undulatory base, yellowish brown (10YR 5/8).
23.98	25.54	1.56	Pa	Palaeosol, silty claystone, strongly developed, massive, rootlets and mottled, medium-coarse blocky structure, brown – dark yellowish brown (10YR 5/3 – 4/6).
25.54	29.25	3.71	Pa	Palaeosol, silty claystone, strongly developed, massive, rootlets and mottled, medium-coarse blocky structure, light grey – light brownish grey (10YR 7/2 – 6/2).
29.25	29.50	0.25	Smm	Tuffaceous sandstone, coarse grained, pumice rich, poorly sorted, massive, irregular base.

Appendix 1.4. RATE GAWE (Outcrop)

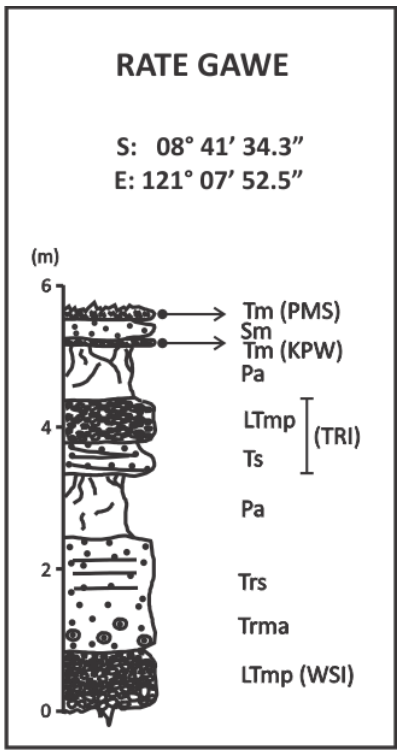

Depth (m)		Thickness (m)	Facies	Description
From	To			
0.00	0.85	0.85	LTmp	Fine to coarse lapilli, pumiceous, massive, stratified at lower part, clast supported, normal grading, vitric, few crystals and lithics, poorly sorted, *p*max 2.8 x 1.6 cm, sharp basal contact. (WSI)
0.85	2.45	1.60	Trma	Reworked ash with many accretionary lapilli, poorly sorted, massive, fine to medium sandy. Thin lamination of very fine grained ash in the upper part (Trs), gradational contact.
2.45	3.35	0.90	Pa	Palaeosol, silty claystone, strongly developed, massive, rootlets and mottled, medium - coarse blocky structure, strength colouring (10YR 5/3).
3.35	3.80	0.45	Ts	Stratified ash, coarse sandy vitric ash, low angle cross stratification, lithic laminations sharp basal boundary. (TRI)
3.80	4.40	0.60	LTmp	Fine to coarse lapilli, pumiceous, massive, clast supported, normal grading, vitric, few crystals and lithics, poorly sorted. (TRI)
4.40	5.18	0.78	Pa	Palaeosol, silty claystone, strongly developed, massive, rootlets and mottled, medium - coarse blocky structure, strongly coloured (10YR 5/3).
5.18	5.28	0.10	Tm	Vitric ash, white to very pale brown, fine grained, sandy, well sorted, massive. (KPW)
5.28	5.54	0.26	Sm	Coarse sandstone, moderately sorted, massive.
5.54	5.69	0.15	Tm	Vitric ash, white, fine grained, sandy, well sorted, massive, hornblende rich. (PMS)

Appendix 1.5. OLA BULA (Outcrop)

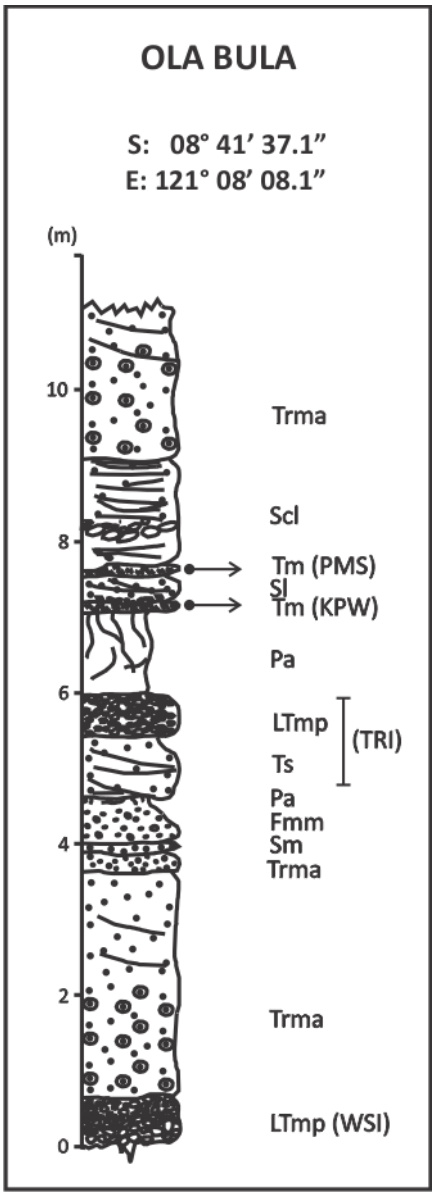

Depth (m)		Thickness (m)	Facies	Description
From	To			
0.00	0.85	0.85	LTmp	Fine to coarse lapilli, pumiceous, massive, stratified at lower part, clast supported, normal grading, vitric, few crystals and lithics, poorly sorted. (WSI)
0.85	3.85	3.00	Trma	Reworked ash with many accretionary lapilli, poorly sorted, massive, fine to medium sandy.
3.85	4.11	0.26	Trmp	Reworked ash, pumiceous, massive, coarse grained, poorly sorted.
4.11	4.23	0.12	Sm	Sandstone, coarse grained, moderately sorted, massive.
4.23	4.73	0.50	Fmm	Tuffaceous siltstone, mud supported, pumiceous, poorly sorted.
4.73	4.84	0.11	Pa	Palaeosol, silty claystone, strongly developed, massive, rootlets and mottled, medium - coarse blocky structure, strongly coloured (10YR 5/3).
4.84	5.64	0.80	Ts	Stratified ash, coarse sandy vitric ash, low angle cross stratification, lithic laminations sharp basal boundary. (TRI)
5.64	6.14	0.50	LTmp	Fine to coarse lapilli, pumiceous, massive, clast supported, normal grading, vitric, few crystals and lithics, poorly sorted. (TRI)
6.14	7.24	1.10	Pa	Palaeosol, silty claystone, weakly developed, massive, pale brown (10YR 6/3).
7.24	7.38	0.14	Tm	Vitric ash, white, massive, well sorted (KPW).
7.38	7.71	0.35	Ss	Conglomeratic sandstone, coarse to very coarse grained, scour and fill structures, erosional contact.
7.71	7.845	0.135	Tm	Vitric ash, white, massive, well sorted (PMS?).
7.845	9.245	1.40	Ss	Sandstone, coarse-very coarse grained, planar cross bedding, cut and fills structures, erosional contacts, composed of pumice, quartz, feldspars.
9.245	11.245	2.00	Trma	Reworked ash with many accretionary lapilli, poorly sorted, massive to crudely stratified, medium to coarse sandy.

Appendix 1.6. DEKO ANEKOA (Outcrop)

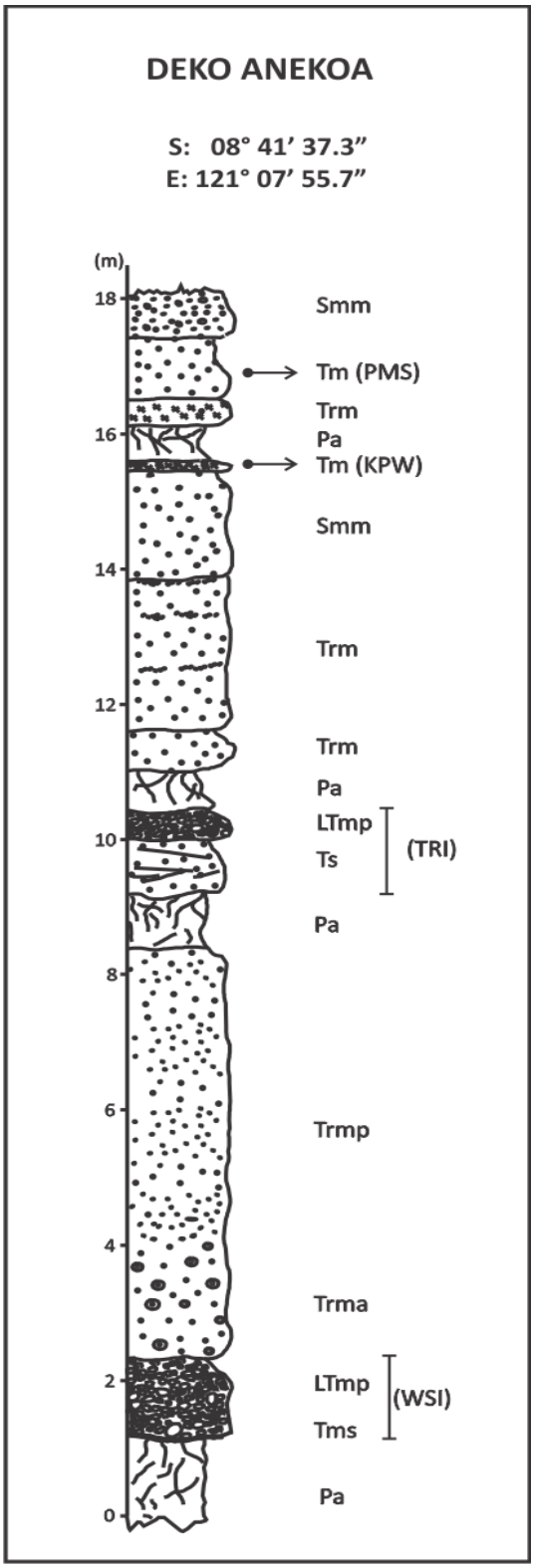

Depth (m)		Thickness (m)	Facies	Description
From	To			
0.00	1.20	1.20	Pa	Palaeosol, silty claystone, strongly developed, massive, rootlets and mottled, medium - coarse blocky structure, strongly coloured (10YR 5/3).
1.20	1.225	0.025	Tms	Fine grained vitric ash, silt- very fine sand sized, massive, well sorted, sharp basal surface. (WSI)
1.225	1.252	0.027	Tmp	Pumiceous ash, coarse sandy vitric ash, sand-sized pumice clasts, massive, poorly sorted, sharp contact. (WSI)
1.252	1.402	0.15	Tma	Fine sandy vitric ash, abundance of rim type accretionary lapilli, massive, poorly sorted. (WSI)
1.402	1.497	0.095	Tmp	Pumiceous ash, coarse sandy vitric ash, sand-sized pumice clasts, massive – crudely stratified, poorly sorted, sharp contact. (WSI)
1.497	2.342	0.845	LTmp	Fine to coarse lapilli, pumiceous, massive, stratified at lower part, clast supported, normal grading, vitric with less abundant of crystals and lithics, poorly sorted, *p*max 3.5 x 1.6 cm, stratified in the lower part, sharp basal contact. (WSI)
2.342	4.142	1.80	Trma	Reworked ash with many accretionary lapilli, poorly sorted, massive, fine to medium sandy.
4.142	4.842	0.70	Trmp	Reworked ash, pumiceous, massive, coarse grained, poorly sorted.
4.842	4.912	0.07	Trm	Reworked ash, massive, coarse grained.
4.912	6.112	1.20	Trmp	Reworked ash, pumiceous, massive, coarse grained, poorly sorted.
6.112	7.312	1.20	Trmp	Reworked ash, pumiceous, massive, coarse grained, poorly sorted.
7.312	8.412	1.10	Trmp	Reworked ash, pumiceous, massive, coarse grained, poorly sorted.
8.412	9.212	0.80	Pa	Palaeosol, silty claystone, strongly developed, massive, rootlets and mottled, medium - coarse blocky structure, strongly coloured (10YR 5/3).
9.212	10.112	0.90	Ts	Stratified ash, coarse sandy vitric ash, low angle cross stratification, lithic laminations sharp basal boundary. (TRI)
10.112	10.562	0.45	LTmp	Fine to coarse lapilli, pumiceous, massive, clast supported, normal grading, vitric, few crystals and lithics, poorly sorted., *p*max 3 x 2 cm. (TRI)
10.562	11.182	0.62	Pa	Palaeosol, silty claystone, strongly developed, massive, rootlets and mottled, medium - coarse blocky structure, strength colouring (10YR 5/3).
11.182	11.742	0.56	Trm	Reworked ash, massive, coarse grained.
11.742	13.942	2.20	Trm	Reworked ash, massive, coarse grained, well sorted.
13.942	15.542	1.60	Smm	Tuffaceous sandstone, massive, coarse-very coarse grained, moderately sorted, contains pumice clasts.
15.542	15.692	0.15	Tm	Vitric ash, massive, fine grained, (KPW).
15.692	16.192	0.50	Pa	Palaeosol, silty claystone, strongly developed, massive, rootlets and mottled, medium - coarse blocky structure, strongly coloured (10YR 5/3).
16.192	16.592	0.40	Trm	Reworked ash, massive, sandy, well sorted, fine to medium grained.
16.592	17.472	0.88	Tm	Vitric ash, white, massive, fine grained, sandy,

				contains hornblende. (PMS)
17.472	18.142	0.67	Fmm	Tuffaceous sandstone, massive, moderately sorted, undulatory base.
			Fh	150 m to the northwest, there is 30 cm thick, horizontal claystone, massive, waxy, contains diatoms; covered by palaeosol and tuffaceous sandstone with fossil fragments.

Appendix 1.7. MATAGO (Outcrop)

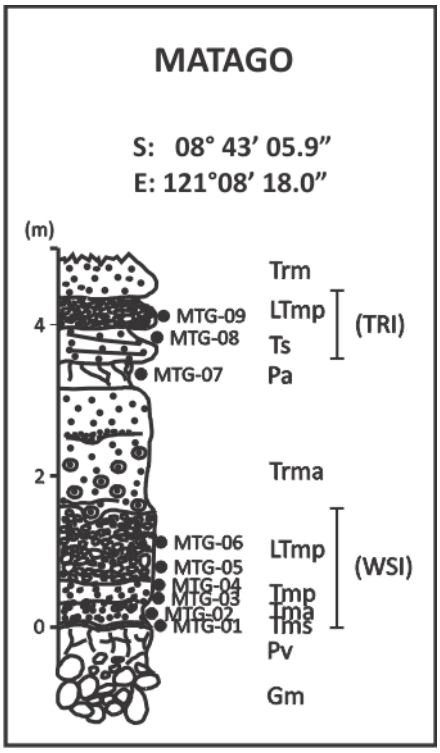

Depth (m)		Thickness (m)	Facies	Description
From	To			
-	-	-	Gm	Conglomerate, massive – crude cross bedding, clast imbrications, granule – cobble, clast supported, composed of basalt, and andesite. c. 2 m, width c. 30 m. Covered by palaeosol (Pv). silty claystone, massive, strongly developed, medium –coarse blocky structure, max thickness 1.40 m.
0.00	0.04	0.04	Tms	Fine grained vitric ash, silt- very fine sand sized, massive, well sorted, sharp basal surface. (WSI)
0.04	0.09	0.05	Tmp	Pumiceous ash, coarse sandy vitric ash, sand-sized pumice clasts, massive, poorly sorted, sharp contact. (WSI)
0.09	0.22	0.13	Tma	Fine sandy vitric ash, abundance of rim type accretionary lapilli, massive, poorly sorted. (WSI)
0.22	0.26	0.04	Tmp	Pumiceous ash, coarse sandy vitric ash, sand-sized pumice clasts, massive – crudely stratified, poorly sorted, sharp contact. (WSI)
0.26	1.81	1.53	LTmp	Fine to coarse lapilli, pumiceous, massive, stratified at lower part, clast supported, normal grading, vitric with less abundance of crystals and lithics, poorly sorted, *p*max 3 x 2 cm, stratified in the lower part, sharp basal contact. (WSI)
1.81	3.21	1.40	Trma	Reworked ash with many accretionary lapilli, poorly sorted, massive, fine to medium sandy.
3.21	3.56	0.35	Pa	Palaeosol, silty claystone, strongly developed, massive, rootlets and mottled, medium - coarse blocky structure, strongly coloured (10YR 5/3).
3.56	4.01	0.45	Ts	Stratified ash, coarse sandy vitric ash, low angle cross stratification, lithic laminations sharp basal boundary. (TRI)
4.01	4.41	0.40	LTmp	Fine to coarse lapilli, pumiceous, massive, clast supported, normal grading, vitric, few crystals and lithics, poorly sorted. (TRI)
4.41	4.91	0.50	Trm	Reworked ash, well sorted, massive, medium to coarse sandy.

Appendix 1.8. WAE BHA (Outcrop)

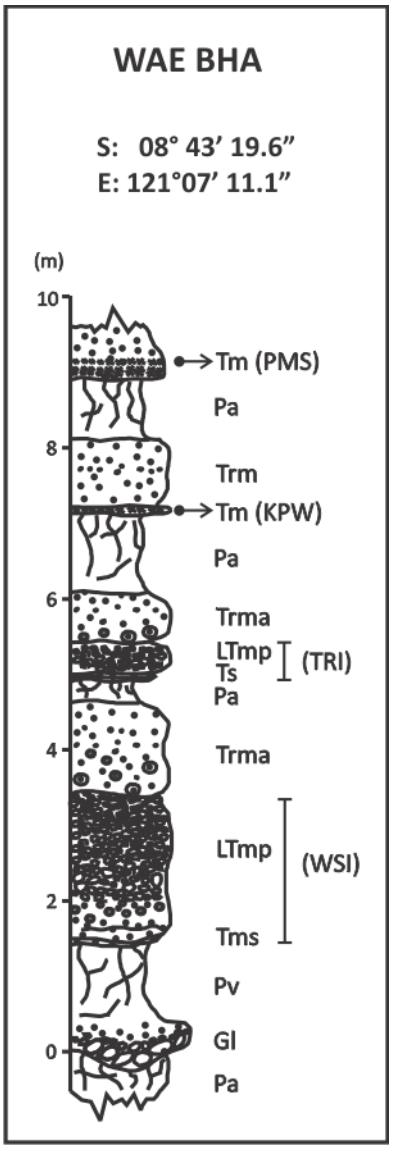

Depth (m)		Thickness (m)	Facies	Description
From	To			
-	-	1.80 plus	Pa	Palaeosol, silty claystone, strongly developed, massive, rootlets and mottled, medium - coarse blocky structure, brown (10YR 5/3).
0.00	0.40	0.40	Gl	Conglomerate, stratified, clast imbrications, granule – cobble, clast supported, composed of basalt, and andesite.
0.40	1.45	1.05	Pv	Palaeosol, silty claystone, strongly developed, massive, rootlets and mottled, medium - coarse blocky structure, brown (10YR 5/3).
1.45	3.56	2.11	Tms, Tmp, Tma, LTmp	Vitric ash, massive, pumiceous – accretionary lapilli. Fine to coarse lapilli, pumiceous, massive, stratified at lower part, clast supported, normal grading, vitric with less abundance of crystals and lithics, poorly sorted, stratified in the lower part, sharp basal contact. (WSI)
3.56	4.76	1.20	Trma	Reworked ash with many accretionary lapilli, poorly sorted, massive, fine to medium sandy.
4.76	5.06	0.30	Pa	Palaeosol, silty claystone, strongly developed, massive, rootlets and mottled, medium - coarse blocky structure, strongly coloured (10YR 5/3).
5.06	5.16	0.10	Ts	Stratified ash, coarse sandy vitric ash, low angle cross stratification, lithic laminations sharp basal boundary. (TRI)
5.16	5.58	0.42	LTmp	Fine to coarse lapilli, pumiceous, massive, clast supported, normal grading, vitric, few crystals and lithics, poorly sorted. (TRI)
5.58	6.38	0.80	Trm	Reworked ash, poorly sorted, massive, fine to medium sandy, pumice clasts dispersed.
6.38	7.28	0.90	Fmm	Tuffaceous siltstone, massive, mud supported, pumice floats, moderately sorted.
7.28	7.36	0.08	Tm	Vitric ash, fine grained, silty – fine sandy, massive, well sorted. (KPW)
7.36	8.26	0.90	Trm	Reworked ash, poorly sorted, massive, fine to medium sandy, pumice clasts dispersed, gas escape structures.
8.26	9.06	0.80	Pa	Palaeosol, silty claystone, weakly developed, massive, rootlets and mottled, medium - coarse blocky structure, (10YR 5/3).
9.06	9.76	0.70	Tm	Fine grained vitric ash, massive, well sorted, hornblende rich. (PMS)

Appendix 1.9. WOLO PETI (Outcrop)

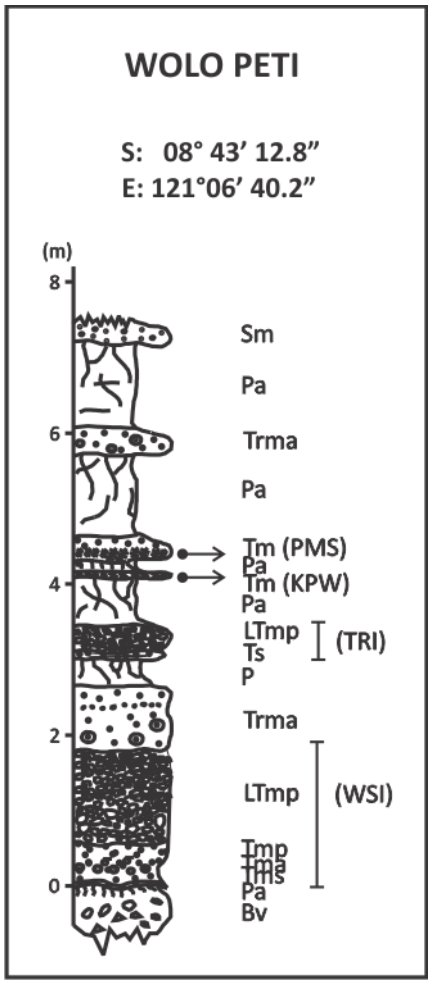

Depth (m)		Thickness (m)	Facies	Description
From	To			
-	-	4.00 plus	Bv	Volcanic breccia, clast supported, poorly sorted, coarse sand matrix,
0.00	0.04	0.04	Tms	Fine grained vitric ash, silt- very fine sand sized, massive, well sorted, sharp basal surface. (WSI)
0.04	0.115	0.075	Tmp	Pumiceous ash, coarse sandy vitric ash, sand-sized pumice clasts, massive, poorly sorted, sharp contact. (WSI)
0.115	0.415	0.30	Tma	Fine sandy vitric ash, abundance of rim type accretionary lapilli, massive, poorly sorted. (WSI)
0.415	0.485	0.07	Tmp	Pumiceous ash, coarse sandy vitric ash, sand-sized pumice clasts, massive – crudely stratified, poorly sorted, sharp contact. (WSI)
0.485	1.695	1.21	LTmp	Fine to coarse lapilli, pumiceous, massive, stratified at lower part, clast supported, normal grading, vitric with less abundance of crystals and lithics, poorly sorted, stratified in the lower part, sharp basal contact. (WSI)
1.695	2.555	0.86	Trma	Reworked ash with many accretionary lapilli, poorly sorted, massive, fine to medium sandy.
2.555	2.915	0.36	Pa	Palaeosol, silty claystone, strongly developed, massive, rootlets and mottled, medium - coarse blocky structure, strongly coloured (10YR 5/3).
2.915	3.025	0.11	Ts	Stratified ash, coarse sandy vitric ash, low angle cross stratification, lithic laminations sharp basal boundary. (TRI)
3.025	3.345	0.32	LTmp	Fine to coarse lapilli, pumiceous, massive, clast supported, normal grading, vitric, few crystals and lithics, poorly sorted. (TRI)
3.345	3.945	0.60	Pa	Palaeosol, silty claystone, weakly developed, massive, rootlets and mottled, medium - coarse blocky structure, (10YR 5/3).
3.945	4.015	0.07	Trm	Vitric ash, fine grained, silty – fine sandy, massive, well sorted (KPW).
4.015	4.165	0.15	Pa	Palaeosol, silty claystone, strongly developed, massive, rootlets and mottled, medium - coarse blocky structure, (10YR 5/3).
4.165	4.485	0.32	Tm	Fine grained vitric ash, massive, well sorted, hornblende rich (PMS).
4.485	5.585	1.10	Pa	Palaeosol, silty claystone, strongly developed, massive, rootlets and mottled, medium - coarse blocky structure, (10YR 5/3).
5.585	5.935	0.35	Trma	Reworked ash, with accretionary lapilli, poorly sorted, massive, fine to medium sandy.
5.935	7.055	1.12	Pa	Palaeosol, silty claystone, strongly developed, massive, rootlets and mottled, medium - coarse blocky structure, (10YR 5/3).
7.055	7.325	0.27	Sm	Sandstone, coarse-very coarse grained, massive, moderately sorted.

Appendix 1.10. LOWO LELE (Outcrop)

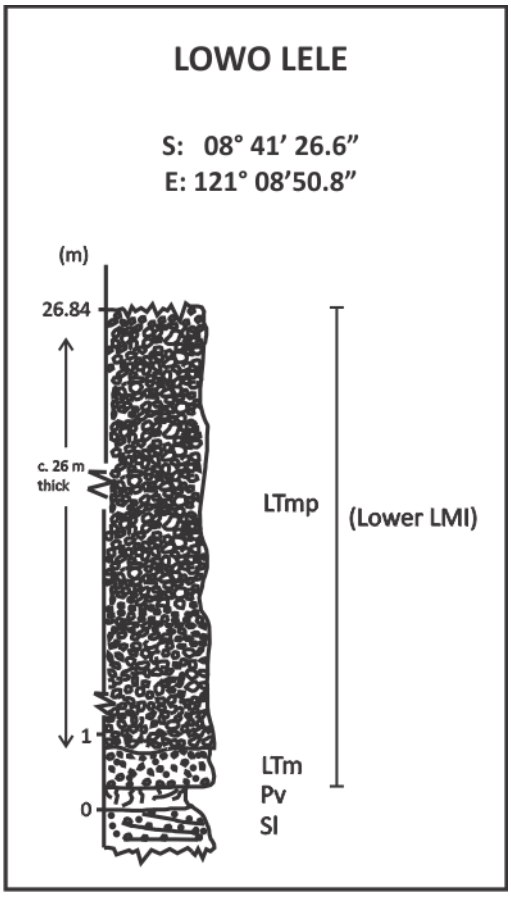

Depth (m)		Thickness (m)	Facies	Description
From	To			
-	-	-	Sl	Sandstone, coarse grained, planar cross bedding, moderately sorted.
0.00	0.30	0.30	Pv	Palaeosol, silty claystone, strongly developed, massive, rootlets and mottled, medium - coarse blocky structure, (10YR 6/2).
0.30	0.84	0.54	LTm	Fine to medium grained pumiceous lapilli, welded, massive, normal grading, stratified upward (AEI).
0.84	26.84	26	LTmp	Coarse to very coarse pumiceous lapilli, welded, crudely stratified, poorly sorted, wood remains.

Appendix 1.11. TANGI TALO (Trench and Outcrop)

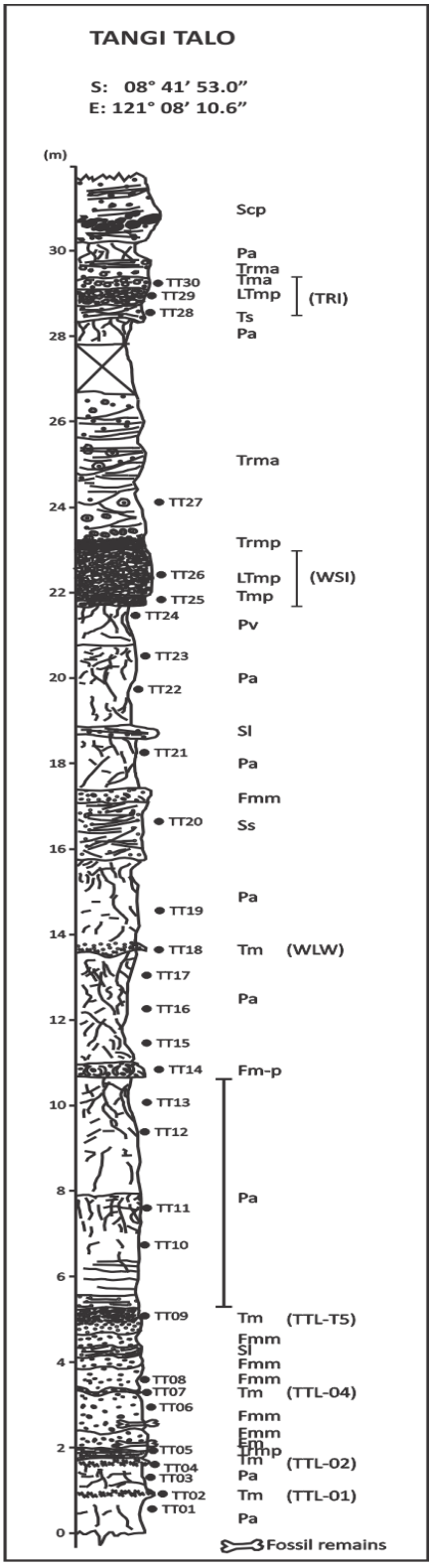

Depth (m)		Thickness (m)	Facies	Description
From	To			
0.00	0.88	0.88	Pa	Palaeosol, silty claystone, strongly developed, massive, rootlets and mottled, medium - coarse blocky structure, (10YR 6/3).
0.88	1.025	0.145	Tm	Vitric ash, silty-sandy, massive, white, well sorted, sharp contact. (TTL-01)
1.025	1.505	0.48	Pa	Palaeosol, silty claystone, strongly developed, massive, rootlets and mottled, medium - coarse blocky structure, (10YR 6/3).
1.505	1.595	0.09	Tm	Vitric ash, silty-sandy, massive, white, well sorted, sharp contact. (TTL-02)
1.595	1.935	0.34	Trmp	Reworked pumiceous ash, poorly sorted, coarse ash matrix, sharp and undulatory base.
1.935	2.035	0.10	Fm	Silty claystone, very well sorted, massive.
2.035	2.395	0.36	Fmm	Tuffaceous siltstone, moderately sorted, mud supported, pumice dispersed, erosional contact, contains fossil remains. near the boundary with underlying bed. (Lahar deposit)
2.395	3.135	0.90	Fmm	Tuffaceous siltstone, mud supported, well-moderately sorted, pumice dispersed, erosional contact, contains fossil bones. (Lahar deposit)
3.135	3.175	0.04	Tm	Vitric ash, silty-sandy, massive, white, well sorted, sharp contact. (TTL-04)
3.175	3.705	0.53	Fmm	Tuffaceous siltstone, mud supported, moderately-poorly sorted, pumice dispersed, erosional contact. (Lahar deposit)
3.705	3.965	0.26	Fmm	Tuffaceous siltstone, mud supported, moderately-poorly sorted, pumice dispersed, erosional contact. (Lahar deposit)
3.965	4.205	0.24	Sl	Sandstone, medium-coarse grained, tuffaceous, cross stratificaction.
4.205	4.505	0.30	Fmm	Tuffaceous siltstone, mud supported, moderately-poorly sorted, pumice dispersed, erosional contact. (Lahar deposit)
4.505	5.045	0.54	Tm	Vitric crystal ash, coarse-very coarse grained, well – moderately sorted, reverse grading, massive-crudely stratified, composed of feldspars, sand sized pumice and mafic minerals. (TTL-T5)
5.045	5.465	0.42	Trm	Reworked ash, horizontal stratification,
5.465	7.765	2.30	Pa	Palaeosol, silty claystone, strongly developed in the top, massive, rootlets and mottled, medium - coarse blocky structure, (10YR 5/3).
7.765	10.565	2.80	Pa	Palaeosol, silty claystone, strongly developed in the upper part, massive, rootlets and mottled, medium - coarse blocky structure, gradational colour changes (10Y 6/3 – 5Y 7/4-8/4 - 10YR 5/3).
10.565	10.865	0.30	Fm-p	Sandy Siltstone, pedogenically altered, massive, spheroidal weathering, rootlets. (10YR 6/2).
10.865	13.515	2.65	Pa	Palaeosol, silty claystone, well developed, massive, rootlets and mottled, medium - coarse blocky structure, (10YR 5/3).
13.515	13.715	0.20	Tm	Vitric ash, silty-sandy, massive, well sorted. (WLW)
13.715	15.785	2.07	Pa	Palaeosol, silty claystone, well developed upward, massive, rootlets and mottled, medium - coarse

				blocky structure, (10YR 5/3-6/3).
15.785	16.985	1.20	Ss	Sandstone, coarse-very coarse grained, well-moderately sorted, cross bedding and cut and fill structures, rip up clasts, high energy currents, catastrophic flood (?).
16.985	17.285	0.30	Fmm	Tuffaceous siltstone, massive, mud supported, poorly sorted, basaltic clasts.
17.285	18.555	1.27	Pa	Palaeosol, silty claystone, poorly developed (10YR 5/3-6/3).
18.555	18.775	0.22	Sl	Silty sandstone, well sorted, fine grained, low angle cross bedding.
18.775	19.675	0.90	Pa	Palaeosol, silty claystone, well developed, massive, rootlets and mottled, medium - coarse blocky structure, (10YR 8/2).
19.675	20.675	1.00	Pa	Palaeosol, silty claystone, well developed, massive, rootlets and mottled, medium - coarse blocky structure, (10YR 7/3).
20.675	21.635	0.96	Pa	Palaeosol, silty claystone, well developed, massive, rootlets and mottled, medium - coarse blocky structure, (10Y 7/1).
21.635	21.855	0.22	LTmp	Pumiceous lapilli, crudely stratified, poorly sorted, clast supported, sharp base. (WSI)
21.855	22.665	0.81	LTmp	Pumiceous lapilli, massive-crudely stratified, poorly sorted, clast supported, predominantly composed of pumice with few crystals and lithics, *p*max 2.5 x 1.8 cm., sharp base. (WSI)
22.665	22.975	0.31	Trmp	Reworked pumiceous ash, horizontal stratification, poorly sorted, clast supported.
22.975	26.475	3.50	Trma	Reworked ash, abundance of accretionary lapilli, parallel lamination of very fine grained ash.
				c. 1.10 m with no exposure.
27.575	28.055	0.48	Pa	Palaeosol, silty claystone, strongly developed, massive, rootlets and mottled, medium - coarse blocky structure, strength colouring (10YR 5/2).
28.055	28.375	0.32	Ts	Vitric ash, coarse sandy, low angle cross stratification, load structures, wavy sharp basal contact. (TRI)
28.375	28.745	0.37	LTmp	Pumiceous lapilli, massive, poorly sorted, clast supported, normal grading, predominantly composed of pumice with few crystals and lithics, *p*max 2.5 x 1.8 cm., sharp base. (TRI)
28.745	29.025	0.28	Tma	Vitric ash with core-type accretionary lapilli, massive. (TRI)
29.025	29.395	0.37	Trma	Reworked ash, massive, poorly sorted.
29.395	29.795	0.40	Pa	Palaeosol, silty claystone, well developed, massive, rootlets and mottled, medium - coarse blocky structure, (10YR 5/3).
29.795	31.395	1.60	Scl	Tuffaceous sandstone, well cemented, very coarse grained, cross bedding, well-moderately sorted, conglomeratic in the lower part.

Appendix 1.12. PUMASO (Outcrop)

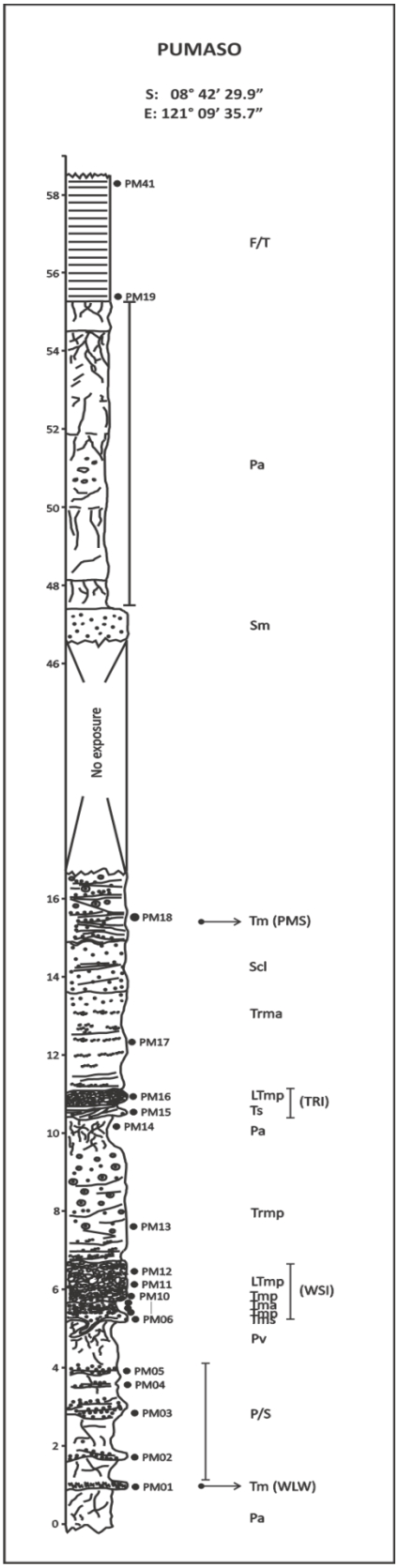

Depth (m)		Thickness (m)	Facies	Description
From	To			
0.00	1.00	1.00	Pa	Sandstone, coarse grained, planar cross bedding, moderately sorted.
1.00-	1.21	0.21	Tm	Vitric ash, silty-sandy, massive, well sorted. (WLW)
1.21	4.51	3.30	P/S	Interbedded palaeosols (Pa) and sandstone (Sl). Sandstone (Sl) displays coarse-very coarse grained, sharp and erosional contact. Palaeosols (Pa) comprise silty claystone, massive, strongly developed upward, medium-coarse blocky structure, rootlets and mottled.
4.51	5.17	0.66	Pa	Palaeosol, silty claystone, strongly developed, massive, rootlets and mottled, medium - coarse blocky structure, 15 x 6 cm crack filled by volcanic ash, 10YR 6/1-6/2.
5.17	5.22	0.05	Tms	Fine grained vitric ash, silt- very fine sand sized, massive, well sorted, sharp basal surface, filled the crack. (WSI)
5.22	5.32	0.10	Tmp	Pumiceous ash, coarse sandy vitric ash, sand-sized pumice clasts, massive, poorly sorted, sharp contact. (WSI)
5.32	5.50	0.18	Tma	Fine sandy vitric ash, abundance of rim type accretionary lapilli, massive, poorly sorted. (WSI)
5.50	5.63	0.13	Tmp	Pumiceous ash, coarse sandy vitric ash, sand-sized pumice clasts, massive – crudely stratified, poorly sorted, sharp contact. (WSI)
5.63	7.34	1.71	LTmp	Fine to coarse lapilli, pumiceous, massive, stratified at lower part, clast supported, normal grading, vitric with less abundanceof crystals and lithics, poorly sorted, *p*max 2.5 x 1.8 cm, stratified in the lower part, sharp basal contact. (WSI)
7.34	9.54	2.20	Trma	Reworked ash with many accretionary lapilli, poorly sorted, massive, fine to medium sandy, gas pipes.
9.54	10.54	1.00	Pa	Palaeosol, silty claystone, strongly developed, massive, rootlets and mottled, medium - coarse blocky structure, strongly developed in the top, pinkish grey (7.5YR 6/2).
10.54	10.82	0.28	Ts	Stratified ash, fine to coarse sandy vitric ash, low angle cross stratification, lithic laminations sharp wavy basal boundary. (TRI)
10.82	11.18	0.36	LTmp	Fine to coarse lapilli, pumiceous, massive, clast supported, normal grading, vitric, few crystals and lithics, poorly sorted, *p*max 7 x 6 cm (TRI)
11.18	13.80	2.62	Trmp	Reworked ash, coarse, pumiceous, massive to crudely stratified.
13.80	15.05	1.25	Scl	Sandstone, massive, well cemented, coarse-very coarse, moderately sorted, tuffaceous, irregular contact.
15.05	16.95	1.90	Tm	Vitric ash, massive – crudely stratified, well sorted, hornblende rich. (PMS)
				c. 30 m covered or no exposure.
46.95	47.75	0.80	Sm	Sandstone, yellowish, coarse-very coarse grained, poorly sorted, massive.
47.75	48.50	0.75	Pa	Palaeosol, silty claystone, strongly developed, massive, rootlets and mottled, medium - coarse

				blocky structure, (10YR 5/3).
48.50	54.88	6.38	Pa	Palaeosol, silty claystone, strongly developed in the upper part, massive, rootlets and mottled, medium - coarse blocky structure, (10YR 5/2- 5/3).
54.88	55.64	0.76	Pa	Palaeosol, silty claystone, strongly developed, massive, rootlets and mottled, medium - coarse blocky structure, (10YR 5/3).
55.64	58.86	3.22	F/T	Interbedded horizontal claystone (Facies Fh) and tephra (facies Tm), and tuffaceous limestone (Lm) developed in the upper part. Claystone (Fh) displays parallel lamination, waxy, very well sorted. Tephra (Tm) refers to vitric crystal ash, coarse to very coarse, composed of sand-sized pumice, feldspars and mafic minerals.

Appendix 1.13. LOWO MALI (Outcrop)

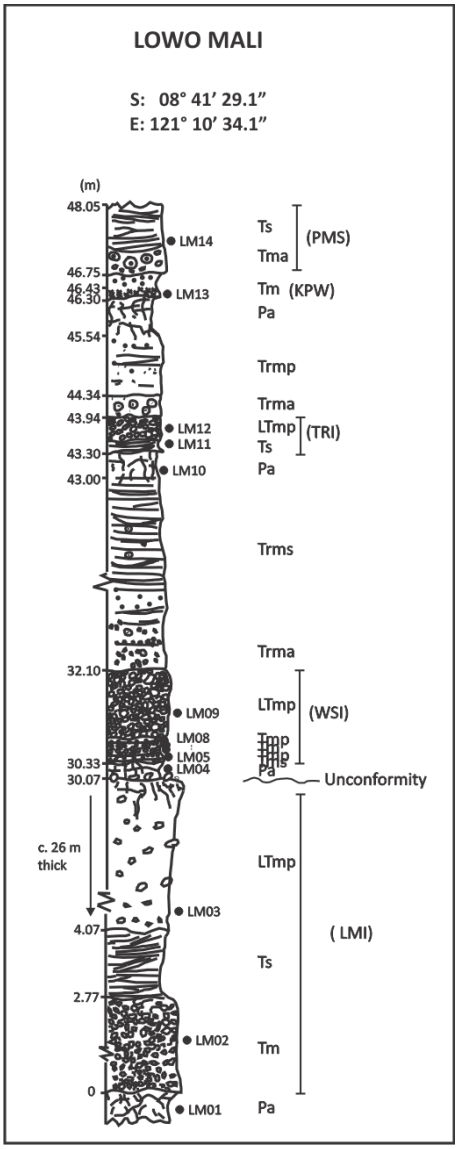

Depth (m)		Thickness (m)	Facies	Description
From	To			
-	-	0.78	Pa	Palaeosol, silty claystone, strongly developed, massive, rootlets and mottled, medium - coarse blocky structure., 10YR 4/3-5/3.
0.00	2.77	2.77	LTm	Fine to coarse pumiceous lapilli, massive, normal grading, pink pumice clats. (LMI)
2.77	4.07	1.30	Ts	Coarse sandy vitric ash, low angle cross stratification, lithic thin lamination. (LMI)
4.07	30.07	26	LTmp	Fine to coarse pumiceous lapilli, massive-crudely stratified, clast supported, poorly sorted. (LMI)
30.07	30.33	0.26	Pa	Fine grained vitric ash, silt- very fine sand sized, massive, well sorted, sharp basal surface, filled the crack. (WSI)
30.33	30.40	0.07	Tms	Fine grained vitric ash, silt- very fine sand sized, massive, well sorted, sharp basal surface, filled the crack. (WSI)
30.40	30.49	0.09	Tmp	Pumiceous ash, coarse sandy vitric ash, sand-sized pumice clasts, massive, poorly sorted, sharp contact. (WSI)
30.49	30.74	0.25	Tma	Fine sandy vitric ash, abundant of rim type accretionary lapilli, massive, poorly sorted. (WSI)
30.74	30.80	0.06	Tmp	Pumiceous ash, coarse sandy vitric ash, sand-sized pumice clasts, massive – crudely stratified, poorly sorted, sharp contact. (WSI)
30.80	32.10	1.30	LTmp	Fine to coarse lapilli, pumiceous, massive, stratified at lower part, clast supported, normal grading, vitric with less abundant of crystals and lithics, poorly sorted, *p*max 2.5 x 1.8 cm, stratified in the lower part, sharp basal contact. (WSI)
32.10	43.00	10.90	Trma, Trms	Reworked ash with many accretionary lapilli, poorly sorted, massive, fine to medium sandy, gas pipes.
43.00	43.30	0.30	Pa	Palaeosol, silty claystone, strongly developed, massive, rootlets and mottled, medium - coarse blocky structure, brown (10YR 5/3).
43.30	43.49	0.19	Ts	Stratified ash, fine to coarse sandy vitric ash, low angle cross stratification, lithic laminations sharp wavy basal boundary. (TRI)
43.49	43.94	0.45	LTmp	Fine to coarse lapilli, pumiceous, massive, clast supported, normal grading, vitric, few crystals and lithics, poorly sorted, *p*max 7 x 6 cm. (TRI)
43.94	44.34	0.40	Trma	Reworked ash with many accretionary lapilli, poorly sorted, massive, fine to medium sandy, gas pipes.
44.34	45.54	1.20	Trm	Reworked ash, moderately sorted, massive, fine to medium sandy, pumice dispersed.
45.54	46.30	0.76	Pa	Palaeosol, silty claystone, strongly developed, massive, rootlets and mottled, medium - coarse blocky structure (10YR 5/2- 5/3).
46.30	46.43	0.13	Tm	Vitric ash, massive well sorted, hornblende rich. (KPW)
46.43	46.75	0.32	Sm	Sandstone, coarse - very coarse grained, well - moderately sorted, erosional contact.
46.75	48.05	1.30	Tm	Vitric ash, coarse – very coarse, massive – cross stratified, poorly sorted, cm-dm cross bedding, concentration of accretionary lapilli in the lower part (max 3 x 3.5 cm), hornblende rich. (PMS)

Appendix 1.14. GERO (Trench)

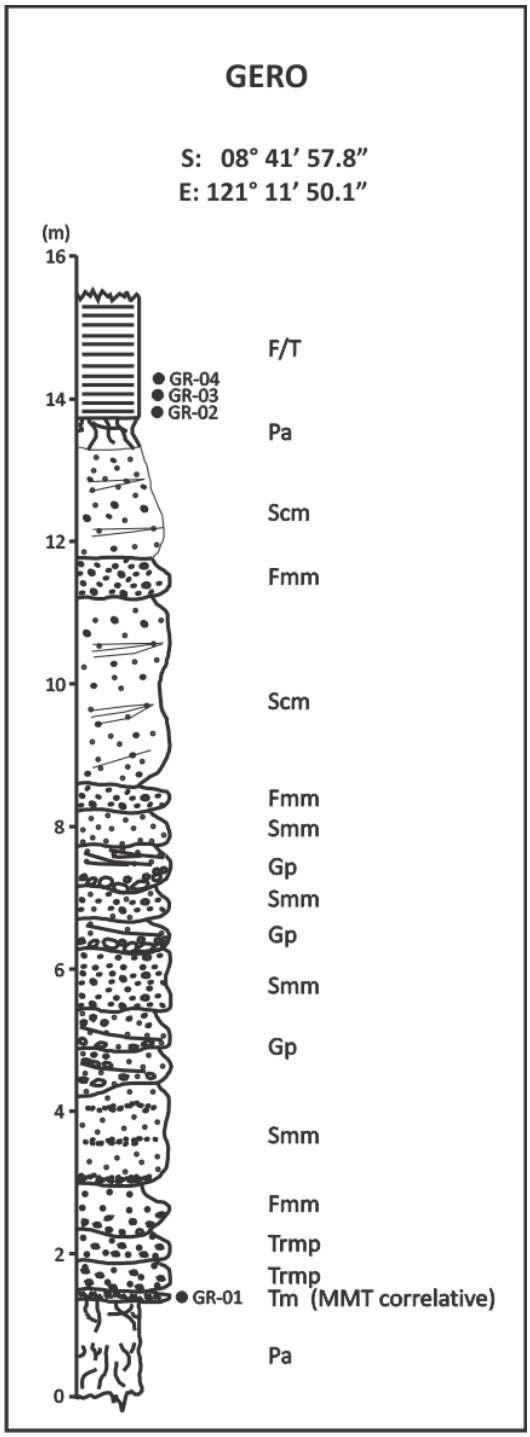

Depth (m)		Thickness (m)	Facies	Description
From	To			
0.00	1.36	1.36	Pa	Palaeosol, silty claystone, strongly developed upward, massive, rootlets and mottled, medium - coarse blocky structure, 10YR 6/3-5/3.
1.36	1.52	0.16	Tm	Vitric ash, pumiceous, coarse-very coarse sandy, dark grey, massive, normal grading, sharp base, andesitic/basaltic composition. (MMT)
1.52	1.92	0.40	Trmp	Reworked ash, pumiceous, coarse grained, massive-crudely stratified, irregular and erosional contact.
1.92	2.30	0.38	Trmp	Reworked ash, pumiceous, coarse grained, massive-crudely stratified, irregular and erosional contact.
2.30	2.95	0.65	Fmm	Tuffaceous siltstone, mud supported, pumiceous, moderately sorted, pumice concentration in the lower part.
2.95	3.24	1.29	Smm	Tuffaceous sandstone, pumiceous, poorly sorted, pumice imbrications, coarse-very coarse grained, HCF deposits, undulatory contact.
3.24	3.76	0.52	Gl	Sandy conglomerate, matrix supported, coarse sand matrix, poorly sorted, crudely cross bedding, erosional surface, rounded-subrounded, contains basalt, andesite fragments.
3.76	4.20	0.54	Gl	Sandy conglomerate, matrix supported, coarse sand matrix, poorly sorted, crudely cross bedding, erosional surface, rounded-subrounded, contains basalt, andesite fragments.
4.20	5.05	0.85	Smm	Tuffaceous sandstone, coarse-very coarse grained, massive, irregular and erosional contact.
5.05	5.48	0.43	Gl	Sandy conglomerate, matrix supported, coarse sand matrix, poorly sorted, cross bedding, erosional surface, rounded-subrounded, contains basalt, andesite fragments.
5.48	5.94	0.46	Smm	Tuffaceous sandstone, coarse-very coarse grained, massive, irregular and erosional contact.
5.94	6.50	0.56	Gl	Sandy conglomerate, matrix supported, coarse sand matrix, poorly sorted, cross bedding, erosional surface, rounded-subrounded, contains basalt, andesite fragments.
6.50	7.01	0.51	Smm	Sandstone, coarse grained, massive, moderately sorted, undulatory contact.
7.01	7.475	0.465	Fmm	Tuffaceous siltstone, mud supported, pumice dispersed, moderately sorted, erosional contact.
7.475	10.105	2.63	Scm	Sandstone, well-cemented, coarse-very coarse grained, occasionally pebbly, pumice scattered, moderate-poorly sorted, planar cross bedding, yellowish grey.
10.105	10.65	0.545	Fmm	Tuffaceous siltstone, mud supported, pumice dispersed, moderately sorted, irregular contact.
10.65	12.71	1.52	Scm	Sandstone, well-cemented, coarse-very coarse grained, occasionally pebbly, pumice scattered, moderate-poorly sorted, planar cross bedding, yellowish grey.
12.71	13.175	0.465	Pa	Palaeosol, silty claystone, strongly developed, massive, rootlets and mottled, medium - coarse blocky structure, (10YR 5/2- 5/3).

13.175	15.445	1.695	F/T	Interbedded horizontal claystone (Facies Fh) and tephra (facies Tm), tuffaceous marl (Mm) and tuffaceous limestone (Lm) developed in the upper part. Claystone (Fh) displays parallel lamination, waxy, very well sorted. Tephra (Tm) refers to vitric crystal ash, coarse to very coarse, composed of sand-sized pumice, feldspars and mafic minerals.

Appendix 1.15. WULUBARA (Outcrop)

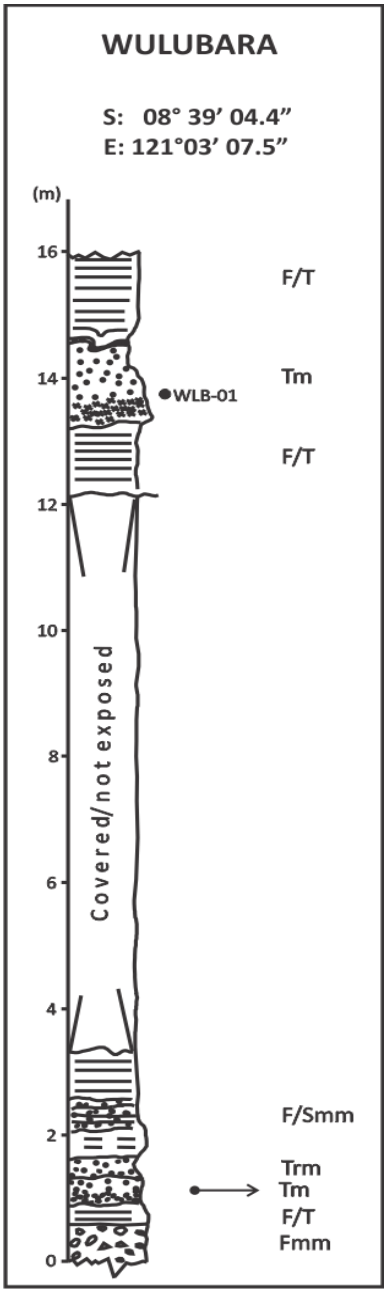

Depth (m)		Thickness (m)	Facies	Description
From	To			
0.00	0.64	0.64	Bv	Basaltic breccia, poorly sorted, matrix and mud supported, composed of basaltic clasts and pumice, *p*max 4 x 4 cm, angular-subrounded. (Lahar deposit)
0.64	0.93	0.29	F/T	Interbedded horizontal claystone (Facies Fh) and tephra (facies Tm). Claystone (Fh) displays parallel lamination, waxy, very well sorted. Tephra (Tm) refers to vitric crystal ash, coarse to very coarse, composed of sand-sized pumice, feldspars and mafic minerals.
0.93	1.43	0.50	Tm	Vitric ash, coarser in the bottom, fining upward, moderately sorted, contains pumice and lithics. (WLB-T1)
1.43	1.63	0.20	Trm	Reworked ash, coarse sandy ash, massive, fine-medium lapilli scattered.
1.63	3.33	1.70	Fh	Claystone, waxy, horizontal bedding, very well sorted. Iin the middle part, scour and fill structure of 10-30 cm, tuffaceous sandstone (Smm/Lahar), rip up clasts, strongly bedded.
				c. 8.8 m covered or no exposure.
12.13	13.17	1.04	F/T	Interbedded horizontal claystone (Facies Fh) and tephra (facies Tm). Claystone (Fh) displays parallel lamination, waxy, very well sorted. Tephra (Tm) refers to vitric crystal ash, coarse to very coarse, composed of sand-sized pumice, feldspars and mafic minerals.
13.17	14.33	1.16	Tm	Vitric ash, massive, silty-coarse sandy ash, normal grading, iron stain at the base, fining upward. (WLB-T2)
14.33	14.48	0.15	Trm	Reworked ash, cross stratified, mm-cm lamination in the top, bioturbation (worm burrow) at the upper part,
14.48	15.98	1.50	F/T	Interbedded horizontal claystone (Facies Fh) and tephra (facies Tm). Claystone (Fh) displays parallel lamination, waxy, very well sorted. Tephra (Tm) refers to vitric crystal ash, coarse to very coarse, composed of sand-sized pumice, feldspars and mafic minerals.

APPENDIX 2. THE RAW GEOCHEMICAL COMPOSITION OF WHOLE-ROCK SAMPLES BY X-RAY FLUORESCENCE ANALYSIS

Table A2.1. Major-and trace-element composition of samples from the Welas Caldera Complex.

Sample	NTR-01	WLB-01	WLS-01	WLS-02
Facies	Ts	Tm	Lv	Lv
Locality	Nata Randang	Wulubara	Welas	Kolopanu
Major elements (Wt %)				
SiO_2	61.08	66.50	51.49	54.75
TiO_2	0.77	0.47	0.98	1.08
Al_2O_3	14.91	14.26	18.59	17.09
Fe_2O_3	5.74	2.82	9.56	9.04
MnO	0.18	0.10	0.17	0.15
MgO	1.20	0.57	3.78	3.53
CaO	4.39	2.96	10.54	8.77
Na_2O	3.17	2.61	2.59	3.14
K_2O	1.35	1.55	0.65	0.61
P_2O_5	0.14	0.10	0.17	0.17
SO_3	0.02	0.02	0.01	0.01
LOI	6.1	7.53	1.42	2.28
Total	99.05	99.48	99.94	100.62
Trace elements (ppm)				
Cl	812	561	477	167
V	90	63	178	218
Cr	3	4	134	6
Co	28	30	70	59
Ni	7	5	20	6
Cu	16	13	69	40
Zn	49	40	81	93
Ga	15	14	18	19
Ge	2	< 1	1	1
As	3	10	24	1
Se	< 1	< 1	1	1
Br	4	2	1	1
Rb	32	45	22	17
Sr	215	181	296	251
Y	35	64	24	33
Zr	135	170	71	88
Nb	3	3	2	2
Mo	< 1	< 1	1	1
Cd	< 2	< 2	1	< 1
Sn	< 3	< 3	3	1
Sb	< 3	< 3	3	< 3
Cs	< 4	< 4	4	< 4
Ba	266	361	152	180
La	< 2	17	6	14
Ce	40	48	27	43
Hf	5	6	2	4
Ta	< 0.9	< 2	1	< 1
W	109	94	5	201
Hg	< 1.0	< 0.5	2	< 1
Pb	9	13	5	3
Bi	< 1	< 1	1	1
Th	3.2	5.4	2.7	2.4
U	< 1	2.5	1.4	2.2

Table A2.2. Major-and trace-element composition of samples from Kobatuwa.

Sample	KBT03/1	KBT03/2	KBT04/1	KBT04/2	KBT04/3	KBT04/4	KBT04/5	KBT04/6
Facies	Ts	LTmp	Scl	Ts	Tma	LTmp	Ts	LTmp
Locality	Kobatuwa 03		Kobatuwa 04					
Major elements (Wt %)								
SiO_2	68.38	66.38	55.30	65.07	66.17	68.74	68.06	70.58
TiO_2	0.28	0.23	1.18	0.30	0.34	0.27	0.26	0.23
Al_2O_3	16.07	15.44	16.18	13.59	14.24	13.09	14.82	13.53
Fe_2O_3	2.66	2.33	9.52	2.76	3.17	2.44	2.15	1.95
MnO	0.15	0.07	0.12	0.08	0.10	0.09	0.19	0.06
MgO	0.57	0.43	2.51	0.70	0.77	0.55	0.47	0.40
CaO	2.38	1.78	5.37	2.16	2.42	2.40	2.11	1.81
Na_2O	1.84	1.90	2.37	1.76	1.81	2.00	1.75	2.23
K_2O	2.45	2.43	0.54	2.32	2.22	2.18	2.64	2.06
P_2O_5	0.03	0.03	0.12	0.03	0.04	0.03	0.03	0.02
SO_3	0.02	0.02	0.07	0.03	0.04	0.03	0.03	0.03
LOI	7.12	8.76	6.16	10.14	8.32	7.27	8.36	7.61
Total	101.95	99.78	99.43	98.91	99.64	99.09	100.87	100.53
Trace elements (ppm)								
Cl	812	886	256	779	900	1026	800	811
V	1	5	160	48	31	12	27	26
Cr	10	1	11	5	1	1	3	7
Co	23	9	39	42	< 5	< 5	35	49
Ni	3	1	9	3	2	1	6	4
Cu	12	9	55	12	17	6	13	14
Zn	49	42	91	23	55	40	20	< 1
Ga	14	12	17	12	14	11	14	11
Ge	2	1	1	2	2	1	2	3
As	11	8	20	4	13	7	4	3
Se	1	1	1	< 1	1	1	< 1	< 1
Br	1	1	1	3	1	1	2	3
Rb	84	82	25	80	76	74	87	68
Sr	193	164	229	206	220	205	188	161
Y	16	15	37	15	20	17	15	13
Zr	110	115	80	116	111	99	126	108
Nb	2	2	1	3	2	2	3	2
Mo	1	1	1	< 1	1	1	< 1	< 1
Cd	1	3	1	< 2	1	10	< 2	< 2
Sn	5	5	3	4	3	3	3	3
Sb	3	3	3	< 3	3	3	< 3	< 3
Cs	4	4	4	< 4	4	4	< 4	< 4
Ba	409	426	183	414	431	430	425	399
La	2	14	13	21	17	2	26	10
Ce	35	34	25	29	38	30	< 2	22
Hf	2	4	5	4	5	5	3	3
Ta	1	3	< 1	3	< 1	2	< 2	7
W	3	2	5	187	2	2	154	230
Hg	1	2	1	< 1.0	< 1	1	0	< 1.0
Pb	11	11	6	9	16	9	12	9
Bi	2	1	1	< 1	2	1	< 1	< 1
Th	6.4	6.9	0.7	7.9	7.1	7.5	7.9	6.3
U	2.7	2.4	1.8	2.0	3.1	3.6	2.1	2.5

Table A2.3. Major-and trace-element composition of samples from Mata Menge.

Sample	MM01	MM02	MM03	MM04	MM05	MM06	MM07	MM08	MM09	MM10
Facies	Pa	Pa	Tm	Pa	Pa	Pa	Pa	Pa	Tmp	Tma
Major elements (Wt %)										
SiO_2	55.17	56.67	55.17	45.95	51.42	50.23	47.61	50.59	63.23	59.42
TiO_2	0.92	1.03	0.92	1.02	0.92	0.69	1.09	1.01	0.43	0.34
Al_2O_3	15.03	15.95	15.03	18.55	18.93	18.05	21.45	18.17	14.87	17.16
Fe_2O_3	5.93	9.50	5.93	10.54	8.84	7.63	10.33	7.45	3.18	2.81
MnO	0.03	0.03	0.03	0.04	0.04	0.04	0.04	0.05	0.02	0.01
MgO	0.63	< 0.01	0.63	0.80	0.73	1.30	0.54	1.56	< 0.01	< 0.01
CaO	1.58	1.21	1.58	1.37	1.14	1.42	1.02	1.54	1.03	0.88
Na_2O	< 0.02	< 0.02	< 0.02	< 0.02	< 0.02	< 0.02	< 0.02	< 0.02	< 0.02	< 0.10
K_2O	0.05	0.08	0.05	0.05	0.07	0.05	0.05	0.05	0.25	0.45
P_2O_5	0.05	0.06	0.05	0.02	0.04	0.04	0.03	0.04	0.04	0.14
S	0.01	0.03	0.01	< 0.01	0.02	0.02	0.02	0.02	0.07	0.55
LOI	19.91	17.40	19.91	20.83	19.49	20.65	19.87	21.13	16.37	18.55
Total	99.31	102.00	99.31	99.20	101.65	100.14	102.05	101.64	99.51	100.42
Trace elements (ppm)										
Cl	156	104	33	78	35	72	10	65	98	219
V	193	264	249	184	170	281	208	128	107	37
Cr	n.d.	n.d.	n.d.	n.d.	n.d.	n.d.	n.d.	n.d.	n.d.	n.d.
Co	21	9	19	11	5	9	< 4.1	< 3.3	< 3.0	< 3.0
Ni	n.d.	n.d.	n.d.	n.d.	n.d.	n.d.	n.d.	n.d.	n.d.	n.d.
Cu	97	85	107	67	75	60	64	16	15	7
Zn	55	85	100	119	112	88	90	34	27	17
Ga	15	13	17	16	17	17	15	12	13	12
Ge	3	3	2	1	3	3	2	1	2	1
As	36	83	90	53	20	80	25	30	39	14
Se	0.3	0.3	0.3	0.2	0.2	0.3	0.2	0.3	0.6	0.3
Br	< 0.5	0.3	< 0.5	< 0.5	0	< 0.1	< 0.5	1	1	0.1
Rb	6	10	7	9	6	6	4	13	12	29
Sr	97	96	71	74	86	61	78	146	635	150
Y	9	8	9	5	2	3	8	6	6	7
Zr	74	76	75	64	71	78	99	146	106	99
Nb	1	1	1	2	2	2	3	4	2	2
Mo	< 1.0	< 0.2	< 1.0	< 1.0	< 1.0	< 1.0	< 1.0	< 1.1	< 1.0	< 1.2
Cd	< 0.1	n.d.	< 2.4	< 2.0	< 0.3	< 0.1	n.d.	< 2.0	< 2.0	< 0.1
Sn	1	< 3.0	< 3.0	< 3.0	1	< 3.0	3	3	1	5
Sb	< 3.0	< 3.0	< 3.0	< 3.0	< 3.0	< 3.0	< 3.0	< 3.0	< 3.0	< 3.0
Cs	< 4.0	< 4.0	< 4.0	< 4.0	< 4.0	< 4.0	< 4.0	< 4.0	< 4.0	< 4.0
Ba	147	175	100	108	78	75	55	208	519	191
La	12	< 2.0	7	< 2.0	< 2.0	7	< 2.0	13	30	18
Ce	< 2.0	21	< 2.0	21	< 2.0	18	23	< 2.0	55	< 2.0
Hf	2	n.d.	2	3	2	2	n.d.	4	3	3
Ta	2	< 1.6	< 1.0	< 1.0	< 1.0	< 1.3	4	1	1	< 1.0
W	5	1	2	< 1.0	< 1.0	1	4	1	1	1
Hg	0.4	1	1	1	1	1	1	1	< 1.0	1
Pb	4	6	5	5	3	6	10	35	59	11
Bi	n.d.	n.d.	n.d.	n.d.	n.d.	n.d.	n.d.	n.d.	n.d.	n.d.
Th	< 1.0	0.4	1.5	2.8	1.4	4.6	1.8	4.8	5.3	4.6
U	< 1.0	< 1.0	< 1.0	< 0.5	< 1.0	< 1.0	< 1.0	< 1.0	1	0.4

Table A2.3. Continued.

Sample	MM11	MM12	MM13	MM14	MM15	MM16	MM17	MM18	MM19	MM20
Facies	LTmp	Pa	Pa	Pa	Pa	Pa	Smm	Smm	Fmm	Sl
Major elements (Wt %)										
SiO_2	60.81	65.14	63.85	53.44	52.02	51.29	56.68	55.86	57.90	50.58
TiO_2	0.25	0.27	0.24	0.76	0.73	0.74	0.77	0.79	0.72	0.78
Al_2O_3	15.36	16.59	15.85	20.72	18.41	16.86	18.94	19.04	20.16	19.74
Fe_2O_3	1.99	3.13	4.03	7.63	7.65	7.48	7.01	6.47	6.33	8.44
MnO	0.02	0.05	0.05	0.03	0.02	0.10	0.11	0.09	0.10	0.03
MgO	< 0.01	< 0.01	< 0.01	< 0.01	0.54	0.80	1.85	2.21	2.09	1.47
CaO	0.97	1.27	1.19	1.04	1.67	2.07	5.32	7.17	7.35	3.34
Na_2O	< 0.02	< 0.02	< 0.02	< 0.02	0.23	< 0.07	0.50	1.02	1.16	0.36
K_2O	0.38	1.61	1.38	0.41	0.34	0.23	0.41	0.46	0.49	0.19
P_2O_5	0.03	0.08	0.03	0.04	0.03	0.02	0.07	0.11	0.08	0.03
S	0.02	0.04	0.01	0.01	0.01	0.01	0.01	0.01	0.01	0.02
LOI	19.69	12.11	12.93	18.31	18.21	18.77	10.83	7.26	6.30	17.64
Total	99.54	100.32	99.57	102.42	99.86	98.45	102.49	100.48	102.68	102.62
Trace elements (ppm)										
Cl	515	472	384	51	92	45	126	175	169	31
V	95	89	344	479	416	313	271	300	195	743
Cr	n.d.	n.d.	n.d.	n.d.	n.d.	n.d.	n.d.	n.d.	n.d.	n.d.
Co	< 3.4	5	< 3.0	< 4	26	27	29	23	26	15
Ni	n.d.	n.d.	n.d.	n.d.	n.d.	n.d.	n.d.	n.d.	n.d.	n.d.
Cu	18	16	17	61	72	71	41	33	38	86
Zn	51	46	48	100	104	95	84	72	76	92
Ga	11	11	10	15	17	16	16	16	17	17
Ge	1	3	1	5	2	2	< 0.5	3	< 0.5	5
As	34	21	23	23	12	7	6	6	7	12
Se	0.4	0.5	0.4	0.3	< 0.1	< 0.1	0.3	0.4	0.4	0.3
Br	2	2	1	0.2	< 0.5	< 0.5	< 0.5	1	< 0.5	< 0.5
Rb	58	55	49	36	31	26	21	24	23	16
Sr	142	143	118	112	115	120	233	268	286	175
Y	12	11	9	7	63	17	24	23	15	11
Zr	99	106	85	79	66	66	65	55	54	59
Nb	2	2	2	2	2	2	1	1	1	1
Mo	< 1.4	< 1.0	< 1.0	< 1	< 1.0	< 1	< 1.0	< 1.0	< 1.0	< 1.0
Cd	< 2.0	< 0.3	< 0.1	n.d.	< 0.2	n.d.	n.d.	< 0.4	n.d.	< 2.7
Sn	2	2	4	1	1	< 3	1	< 3.0	1	2
Sb	< 3.0	< 3.0	< 3.0	< 3	< 3.0	2	< 3.0	< 3.0	< 3.0	< 3.0
Cs	< 4.0	< 4.0	< 4.0	n.d.	< 4.0	n.d.	< 4.0	< 4.0	< 4.0	< 4.0
Ba	263	260	253	123	95	128	162	188	195	77
La	11	< 2.0	17	26	20	< 2	17	11	< 2.0	19
Ce	< 2.0	24	< 2.0	< 2	65	30	31	< 2.0	28	< 2.0
Hf	4	3	3	3	5	4	n.d.	3	n.d.	2
Ta	1	1	1	< 1	< 1.0	< 1	< 1.5	3	< 1.0	< 1.5
W	1	1	1	< 1	2	1	< 1.0	< 1.0	< 1.0	< 1.0
Hg	< 0.3	< 1.0	1	< 1	1	1	2	< 1.0	2	2
Pb	14	14	7	7	9	10	7	4	5	7
Bi	n.d.	n.d.	n.d.	n.d.	n.d.	n.d.	n.d.	n.d.	n.d.	n.d.
Th	6.4	5.7	5.0	2.8	2.8	2.3	2.1	1.6	2.0	1.8
U	1.6	0.7	2.1	0.8	0.9	< 1.0	< 0.5	0.7	1.3	< 0.5

Table A2.3. Continued.

Sample	MM21	MM22	MM23	MM24	MM25	MM26	MM27	MM28	MM29	MM30
Facies	Smm	Pa	Pa	Ss	Pa	Pa	Sm	Scl	Scl	Sm
Major elements (Wt %)										
SiO_2	55.76	54.67	50.35	54.54	54.98	51.95	52.65	55.54	56.30	54.69
TiO_2	0.62	0.66	0.73	0.77	0.41	0.87	0.92	0.91	0.84	0.85
Al_2O_3	16.60	14.96	16.74	20.15	11.86	19.24	22.68	16.42	18.23	17.10
Fe_2O_3	6.27	6.64	7.71	7.96	4.88	8.53	8.46	9.93	8.13	7.83
MnO	0.29	0.11	0.18	0.08	0.06	0.20	0.14	0.30	0.26	0.10
MgO	0.54	0.84	0.68	2.19	0.80	0.70	2.28	4.22	3.45	2.11
CaO	4.60	2.20	2.20	6.42	8.34	5.13	8.39	7.90	8.05	7.31
Na_2O	1.02	< 0.02	0.11	1.52	< 0.02	1.60	1.89	1.14	1.47	1.98
K_2O	0.44	0.13	0.14	0.52	0.10	0.32	0.48	1.03	1.07	0.94
P_2O_5	0.10	0.02	0.02	0.09	0.04	0.03	0.15	0.18	0.17	0.11
S	<0.01	0.01	0.02	0.01	0.02	0.01	< 0.01	0.02	0.01	0.004
LOI	12.81	19.94	20.72	8.51	19.67	11.88	4.24	3.26	3.65	6.50
Total	99.06	100.18	99.59	102.77	101.19	100.46	102.27	100.86	101.63	99.52
Trace elements (ppm)										
Cl	111	20	24	211	35	73	158	303	311	358
V	175	241	239	199	277	199	199	376	282	187
Cr	n.d.	n.d.	n.d.	n.d.	n.d.	n.d.	n.d.	n.d.	n.d.	n.d.
Co	38	14	25	17	10	23	21	26	30	19
Ni	n.d.	n.d.	n.d.	n.d.	n.d.	n.d.	n.d.	n.d.	n.d.	n.d.
Cu	46	61	72	54	41	63	75	40	46	54
Zn	66	72	83	71	49	84	84	78	69	72
Ga	14	14	16	17	9	18	19	15	18	17
Ge	2	2	4	< 0.5	2	3	< 0.5	4	< 0.1	1
As	14	9	13	14	10	13	5	32	20	20
Se	0.4	0.2	0.3	0.3	0.2	0.4	0.2	1	1	0.4
Br	0.2	< 1	< 0.5	< 0.5	1	1	1	2	1	1
Rb	27	12	16	26	13	20	17	51	53	49
Sr	226	130	136	290	104	261	368	269	284	268
Y	40	12	16	16	10	21	21	21	21	22
Zr	61	51	67	70	37	80	68	89	98	100
Nb	1	1	2	2	1	2	1	2	3	3
Mo	n.d.	< 1	< 1.0	< 1.0	< 1.0	< 1.0	< 1.0	< 1.0	< 1.0	< 1.0
Cd	n.d.	n.d.	n.d.	< 0.2	< 2.0	n.d.	< 2.0	< 2.0	< 2.0	< 2.0
Sn	< 3	1	1	2	2	0.4	< 3.0	< 3.0	< 3.0	1
Sb	< 3	< 3	< 3.0	< 3.0	< 3.0	< 3.0	< 3.0	< 3.0	< 3.0	< 3.0
Cs	< 4	n.d.	n.d.	< 4.0	< 4.0	n.d.	< 4.0	< 4.0	< 4.0	< 4.0
Ba	425	157	241	134	108	201	214	241	305	242
La	7	17	< 2.0	9	< 2.0	7	< 2.0	4	13	6
Ce	29	33	32	< 2.0	< 2.0	27	15	< 2.0	< 2.0	24
Hf	n.d.	2	n.d.	2	3	n.d.	3	3	2	2
Ta	5	4	< 1.0	< 1.0	4	< 1.0	< 1.6	< 1.8	< 1.0	< 1.6
W	2	< 1	2	0.4	< 1.0	1	< 1.0	1	3	1
Hg	1	2	0.4	3	2	1	1	< 1.0	2	1
Pb	7	6	9	8	4	10	9	9	11	12
Bi	n.d.	n.d.	n.d.	n.d.	n.d.	n.d.	n.d.	n.d.	n.d.	n.d.
Th	1.9	1.7	2.5	2.6	1.9	3	2.6	5.2	5.4	5.3
U	0.8	< 1.0	< 0.5	0.4	0.8	< 1.0	< 1.0	1.2	1.2	1.6

Table A2.3. Continued.

Sample	MM31	MM32	MM33	MM34	MM35	MM36	MM37	MM38	MM39	MM40
Facies	Sl	Fm	Fm	Fm	Fm	Pa	Pa	Pa	Smm	P
Major elements (Wt %)										
SiO_2	54.52	52.04	53.20	55.79	55.66	50.69	52.84	52.30	52.49	54.70
TiO_2	0.75	0.57	0.80	0.72	0.74	0.70	0.84	0.75	0.66	0.63
Al_2O_3	18.45	16.82	18.03	17.43	18.25	15.29	20.68	17.09	18.91	16.46
Fe_2O_3	6.13	5.73	6.03	6.69	6.32	7.62	7.79	7.50	7.47	7.04
MnO	0.07	0.01	0.01	0.01	0.01	0.05	0.05	0.05	0.08	0.05
MgO	2.06	0.01	0.46	0.01	0.70	0.44	1.17	0.32	1.32	0.31
CaO	7.50	5.80	4.20	4.07	4.04	2.48	4.45	3.44	7.35	4.31
Na_2O	1.88	0.86	0.72	0.95	1.11	0.20	0.58	0.66	1.76	0.90
K_2O	0.43	0.28	0.38	0.28	0.31	0.26	0.44	0.27	0.31	0.32
P_2O_5	0.30	0.10	0.03	0.05	0.10	0.03	0.08	0.03	0.04	0.03
S	0.02	0.02	0.02	0.02	0.06	0.02	0.08	0.02	0.001	0.01
LOI	7.25	18.70	16.03	13.72	14.79	20.38	13.70	18.01	8.48	14.67
Total	99.36	100.93	99.90	99.74	102.09	98.15	102.70	100.43	98.89	99.44
Trace elements (ppm)										
Cl	244	205	116	182	140	16	150	33	315	88
V	686	288	243	285	303	220	212	253	186	206
Cr	n.d.	n.d.	n.d.	n.d.	n.d.	n.d.	n.d.	n.d.	n.d.	n.d.
Co	52	28	18	13	20	23	14	24	23	21
Ni	n.d.	n.d.	n.d.	n.d.	n.d.	n.d.	n.d.	n.d.	n.d.	n.d.
Cu	40	52	67	55	65	67	58	66	43	59
Zn	79	80	88	78	85	89	80	103	75	71
Ga	15	17	18	16	18	15	17	16	15	15
Ge	<1	2	1.1	<1	2	2	3	2	< 0.5	1
As	12	14	11	15	11	6	18	9	8	9
Se	0.4	0.3	0.2	0.2	0.3	< 1	0.2	0.4	0.2	0.3
Br	<1	1	2	1	2	< 1	1	2	0	1
Rb	24	33	35	27	36	30	29	30	19	30
Sr	304	197	175	209	190	111	201	138	230	175
Y	59	18	19	19	18	21	16	24	22	15
Zr	59	72	79	71	75	74	87	78	46	64
Nb	1	2	2	1	2	2	2	2	1	1
Mo	<1	<1	<1	<1	<1	n.d.	< 1.0	< 1.0	< 1.0	n.d.
Cd	<2	5	<2	<2	14	n.d.	n.d.	n.d.	n.d.	n.d.
Sn	1	3	2	0.1	2	< 1	4	< 3.0	1	< 1
Sb	2	< 3.0	< 3.0	< 3.0	< 3.0	2	< 3.0	< 3.0	< 3.0	1
Cs	< 4.0	< 4.0	< 4.0	< 4.0	< 4.0	< 3	< 4.0	< 4.0	< 4.0	< 3
Ba	227	158	160	150	151	99	284	126	151	146
La	<2	11	<2	<2	14	< 2	< 2.0	2	< 2.0	14
Ce	<2	<2	50	<2	19	35	24	17	< 2.0	< 2
Hf	5	3	3	3	3	4	n.d.	n.d.	n.d.	4
Ta	5	4	< 1.0	2	< 1.4	2	5	1	5	8
W	1	< 1.0	1	< 1.0	1	1	< 0.7	< 1.0	< 1.0	< 1
Hg	2	1	1	3	1	2	2	2	2	3
Pb	7	9	12	8	10	10	11	10	8	10
Bi	n.d.	n.d.	n.d.	n.d.	n.d.	n.d.	n.d.	n.d.	n.d.	n.d.
Th	2.3	2.9	2.8	2	3	3	3	2	2	3
U	0.7	0.3	< 1.0	< 0.5	1	< 1.0	< 1.0	< 1.0	< 0.5	1

Table A2.3. Continued.

Sample	MM41	MM42	MM43	MM44	MM45	MM46	MM47	MM48	MM49	MM50	MM51
Facies	Pa	Tm	Pa	Pa	Pa	Pa	Pa	Pv	Sh	Fh	Fh
Major elements (Wt %)											
SiO_2	52.73	54.61	51.37	47.61	50.45	43.22	24.25	42.53	48.14	38.45	36.49
TiO_2	0.72	0.92	0.80	0.66	0.61	0.55	0.32	0.66	0.78	0.68	0.60
Al_2O_3	17.61	17.19	18.42	14.51	15.16	13.46	7.98	15.14	20.73	14.09	13.30
Fe_2O_3	7.69	7.25	8.09	7.05	6.53	5.77	3.40	6.43	7.62	5.14	6.06
MnO	0.07	0.09	0.07	0.06	0.05	0.05	0.19	0.01	0.03	0.02	0.08
MgO	0.87	1.86	1.28	1.41	0.23	0.88	0.59	0.92	0.13	0.64	0.97
CaO	4.66	5.71	5.76	12.12	9.47	11.71	28.99	8.61	3.12	14.64	15.57
Na_2O	1.03	1.47	1.42	1.03	0.74	0.42	0.30	0.02	0.60	0.36	0.29
K_2O	0.36	0.89	0.36	0.30	0.23	0.13	0.08	0.07	0.43	0.16	0.14
P_2O_5	0.02	0.22	0.05	0.06	0.06	0.05	0.09	0.03	0.16	0.05	0.07
S	0.02	0.52	0.02	0.02	0.05	0.02	0.06	0.01	1.34	0.07	0.08
LOI	13.49	8.79	11.71	15.11	16.31	22.39	33.80	25.45	18.47	25.43	25.88
Total	99.25	99.52	99.34	99.95	99.90	98.65	100.04	99.87	101.55	99.73	99.52
Trace elements (ppm)											
Cl	100	485	116	114	55	39	1	19	112	61	50
V	157	211	182	163	136	161	126	225	292	188	194
Cr	n.d.	n.d.	n.d.	n.d.	n.d.	n.d.	n.d.	n.d.	n.d.	n.d.	n.d.
Co	25	19	16	14	11	10	9	12	12	6	15
Ni	n.d.	n.d.	n.d.	n.d.	n.d.	n.d.	n.d.	n.d.	n.d.	n.d.	n.d.
Cu	67	101	65	50	45	51	26	38	44	60	74
Zn	74	69	77	63	68	57	32	56	65	60	67
Ga	16	16	17	13	13	12	8	13	18	15	13
Ge	2	1	2	3	< 1	< 0.5	< 0.5	< 1	< 1	< 0.5	2
As	13	15	20	15	11	10	6	18	55	32	42
Se	0.2	1	0.3	1	0.3	0.4	1	1	1	1	2
Br	< 0.5	3	1	2	1	4	3	2	2	8	10
Rb	29	48	23	19	15	11	3	6	14	11	10
Sr	186	341	232	175	173	118	71	69	429	103	94
Y	18	23	18	15	13	10	11	5	7	4	7
Zr	68	116	74	65	59	49	24	57	66	63	56
Nb	1	6	2	1	2	1	2	2	3	3	2
Mo	< 1.0	< 1.0	< 1.0	< 1.0	n.d.	< 1.0	< 1.0	< 1	< 1	< 1.0	< 1.0
Cd	< 2.3	< 0.1	12	< 0.1	n.d.	< 2.0	< 2.0	n.d.	n.d.	< 0.4	< 2.0
Sn	< 3.0	2	< 3.0	0.4	< 1	2	< 3.0	< 3	0.2	3	< 3.0
Sb	< 3.0	< 3.0	< 3.0	< 3.0	1	< 3.0	< 3.0	< 3	< 3	< 3.0	< 3.0
Cs	< 4.0	< 4.0	< 4.0	< 4.0	< 3	< 4.0	< 4.0	n.d.	n.d.	< 4.0	< 4.0
Ba	200	393	213	170	168	88	128	38	224	129	125
La	10	18	24	< 2.0	< 2	5	8	13	< 2	32	< 2.0
Ce	33	59	< 2.0	17	< 2	< 2.0	< 2.0	32	38	27	< 2.0
Hf	5	4	3	3	3	1	< 1.0	2	3	3	2
Ta	2	9	3	1	4	< 1.0	< 1.0	5	5	3	3
W	0.4	1	< 0.7	< 1.0	1	< 0.7	1	< 1	< 1	< 1.0	< 1.0
Hg	2	1	1	< 1.0	2	1	< 1.0	1	1	0.4	< 1.0
Pb	11	21	9	6	7	7	4	9	10	9	8
Bi	n.d.	n.d.	n.d.	n.d.	n.d.	n.d.	n.d.	n.d.	n.d.	n.d.	n.d.
Th	2	6	3	3	2	2	1	2	2	3	2.3
U	1	< 1.0	0.3	1	1	0.3	< 0.5	< 1.0	< 0.6	< 1.0	< 1.0

Table A2.3. Continued.

Sample	MM52	MM53	MM54	MM55	MM56	MM57	MM58	MM59	MM60	MM61
Facies	Fh	Fh	Tm	Fh	Tm	Fh	Fh	Tm	Fh	Fh
Major elements (Wt %)										
SiO_2	44.67	46.39	51.71	48.33	52.22	50.69	43.45	52.38	62.48	40.76
TiO_2	0.72	0.65	0.78	0.68	0.89	0.58	0.51	0.62	0.46	0.46
Al_2O_3	16.97	19.03	18.22	17.41	17.57	17.42	13.88	20.19	14.16	12.22
Fe_2O_3	8.21	11.71	7.91	9.32	12.10	6.91	6.45	9.15	3.63	6.19
MnO	0.05	0.25	0.13	0.14	0.31	0.09	0.09	0.26	0.01	0.13
MgO	0.02	0.01	0.97	1.12	4.12	1.91	1.17	3.59	0.33	0.92
CaO	4.63	3.90	8.67	5.53	8.74	7.77	11.56	9.63	2.77	12.66
Na_2O	0.63	1.80	2.36	0.46	1.70	0.52	0.02	1.25	0.02	0.18
K_2O	0.23	0.20	0.43	0.24	0.21	0.24	0.27	0.23	0.15	0.18
P_2O_5	0.11	0.21	0.13	0.61	0.10	0.10	0.19	0.16	0.06	0.16
S	0.43	0.01	0.01	0.10	0.03	0.05	0.52	0.08	0.02	0.08
LOI	22.29	16.59	9.50	17.91	1.80	15.91	21.96	3.78	17.55	25.15
Total	98.97	100.74	100.82	101.85	99.80	102.20	100.07	101.32	101.65	99.09
Trace elements (ppm)										
Cl	59	66	205	50	292	139	76	329	49	194
V	348	303	221	229	154	193	262	92	250	221
Cr	n.d.	n.d.	n.d.	n.d.	n.d.	n.d.	n.d.	n.d.	n.d.	n.d.
Co	13	37	21	18	19	< 4.5	8	19	5	5
Ni	n.d.	n.d.	n.d.	n.d.	n.d.	n.d.	n.d.	n.d.	n.d.	n.d.
Cu	82	85	59	57	7	32	42	12	60	47
Zn	73	66	62	156	78	88	92	72	81	83
Ga	17	15	16	16	14	13	12	16	12	11
Ge	< 1	< 0.5	< 0.5	< 1	< 0.1	< 0.1	< 0.5	< 1	< 0.2	1
As	125	174	176	56	33	76	71	36	75	68
Se	2	1	1	1	0.3	1	1	1	7	4
Br	1	< 0.2	1	1	0.2	4	7	1	2	3
Rb	15	10	15	14	8	10	15	8	17	16
Sr	157	176	350	158	242	120	200	252	80	61
Y	7	7	14	41	21	12	12	18	6	9
Zr	76	51	45	82	17	46	54	17	61	64
Nb	3	2	2	2	< 0.2	1	2	0	1	2
Mo	< 1	< 1.0	< 1.0	< 1	< 1.0	< 1.0	< 1.0	< 1	< 6.9	<1
Cd	n.d.	< 2.0	< 2.0	n.d.	< 2.0	n.d.	n.d.	n.d.	7	<2
Sn	< 3	< 3.0	< 3.0	< 3	< 3.0	< 3.0	1	< 3	4	2
Sb	< 3	< 3.0	< 3.0	< 3	< 3.0	< 3.0	< 3.0	< 3	< 3.0	< 3.0
Cs	n.d.	< 4.0	< 4.0	n.d.	< 4.0	< 4.0	< 4.0	n.d.	< 4.0	< 4.0
Ba	114	155	184	163	81	94	174	110	65	59
La	< 2	< 2.0	< 2.0	11	10	19	15	< 2	< 2.0	6
Ce	6	36	< 2.0	24	< 2.0	< 2.0	33	< 2	18	<2
Hf	2	1	3	4	2	n.d.	n.d.	< 2	3	3
Ta	6	5	3	< 1	< 1.8	< 1.0	< 1.0	< 1	< 1.0	< 1.0
W	< 1	< 0.8	1	< 1	< 1.0	< 1.0	< 1.0	1	< 1.0	< 1.0
Hg	1	< 1.0	1	1	1	1	< 1.0	1	1	< 1.0
Pb	11	4	5	13	1	5	6	2	3	3
Bi	n.d.	n.d.	n.d.	n.d.	n.d.	n.d.	n.d.	n.d.	n.d.	n.d.
Th	2.2	1.4	1.3	4.1	< 1.0	< 0.2	1.4	< 1.0	1.5	2.1
U	< 1.0	< 1.0	0.7	1.0	1.1	0.9	1.1	0.7	1.1	0.8

Table A2.3. Continued.

Sample	MM62	MM63	MM64	MM65	MM66	MM67	MM68	MM69	MM70	MM71
Facies	Fh	Fh	Tm	Fh	Fh	Fh	Fh	Tm	Fh	Fh
Major elements (Wt %)										
SiO_2	43.71	50.58	49.45	45.54	54.22	42.41	53.38	49.88	59.01	57.45
TiO_2	0.40	0.75	0.62	0.64	0.63	0.32	0.55	0.83	0.62	0.57
Al_2O_3	17.50	15.45	19.81	15.23	13.07	12.09	15.36	19.30	16.39	20.02
Fe_2O_3	5.47	8.67	10.15	8.18	7.41	4.17	10.62	12.42	6.71	5.43
MnO	0.02	0.05	0.19	0.53	0.08	0.06	0.09	0.22	0.13	0.08
MgO	0.89	0.46	2.22	0.91	1.11	0.51	0.87	5.57	1.34	1.32
CaO	9.52	3.27	3.64	11.02	6.66	14.55	3.43	8.29	4.26	3.60
Na_2O	0.02	0.02	0.14	1.06	0.94	0.02	1.81	1.24	1.58	0.34
K_2O	0.16	0.54	0.15	0.26	0.38	0.17	0.59	0.15	0.50	0.45
P_2O_5	0.11	0.16	0.05	0.16	0.13	0.06	0.23	0.10	0.09	0.16
S	0.12	0.21	0.0004	0.28	0.08	0.12	1.88	0.19	0.04	0.58
LOI	24.22	19.22	12.64	15.22	15.45	25.08	12.56	3.90	9.79	12.17
Total	102.14	99.39	99.07	99.04	100.15	99.55	101.36	102.09	100.45	102.18
Trace elements (ppm)										
Cl	158	152	n.d.	280	307	188	444	251	422	383
V	275	314	112	287	263	265	197	293	142	141
Cr	n.d.	n.d.	n.d.	n.d.	n.d.	n.d.	n.d.	n.d.	n.d.	n.d.
Co	<4	9	12	65	10	6	14	21	18	4
Ni	n.d.	n.d.	n.d.	n.d.	n.d.	n.d.	n.d.	n.d.	n.d.	n.d.
Cu	45	58	13	44	33	27	45	13	37	40
Zn	103	121	73	95	66	70	103	119	63	69
Ga	13	17	14	12	12	10	13	15	14	13
Ge	<1	0.6	2	<1	<1	1.7	1	1	< 0.5	2
As	83	117	29	80	89	14	82	19	37	34
Se	1	1	1	2	1	1	11	8	5	9
Br	2	2	< 0.1	2	2	9	1	< 0.5	1	2
Rb	13	33	6	12	18	15	20	6	20	18
Sr	81	360	92	160	133	107	295	238	142	194
Y	9	13	13	33	24	17	23	14	22	20
Zr	60	106	15	35	50	39	41	12	47	47
Nb	2	3	< 0.2	0.3	1	1	<1	< 1.0	1	1
Mo	<1	<1	< 12	<1	<1	<1	<1	< 1.0	< 2.4	< 1.0
Cd	<2	17	n.d.	<2	<2	<2	<2	n.d.	4	n.d.
Sn	0.3	2	< 1.3	< 3.0	< 3.0	5	< 3.0	< 3.0	1	2
Sb	< 3.0	< 3.0	< 1.2	< 3.0	< 3.0	4	< 3.0	< 3.0	< 3.0	< 3.0
Cs	< 4.0	< 4.0	< 6.3	< 4.0	< 4.0	< 4.0	< 4.0	< 4.0	< 4.0	< 4.0
Ba	73	208	90	320	122	100	128	81	120	130
La	<2	11	< 11	<2	<2	<2	6	16	< 2.0	< 2.0
Ce	20	28	39	<2	<2	<2	18	< 2.0	15	< 2.0
Hf	2	3	n.d.	3	2	3	2	n.d.	2	n.d.
Ta	6	2	< 1.0	< 1.0	< 1.5	3	< 1.0	< 1.0	< 1.4	< 1.0
W	< 1.0	< 1.0	< 0.7	1	1	< 1.0	< 1.0	< 1.0	< 1.0	0
Hg	1	< 0.5	4	1	0.4	< 1.0	< 0.5	1	2	< 1.0
Pb	4	22	2	4	6	2	4	< 0.4	6	3
Bi	n.d.	n.d.	n.d.	n.d.	n.d.	n.d.	n.d.	n.d.	n.d.	n.d.
Th	1.5	4.8	< 0.5	< 1.0	< 0.2	1.1	< 1.0	< 1.0	< 1.0	< 1.0
U	< 0.5	0.3	< 0.5	1.7	1.9	0.4	< 1.0	0.9	1.6	2.2

Table A2.3. Continued.

Sample	MM72	MM73	MM74	MM75	MM76	MM77	MM78	MM79	MM80	MM81
Facies	Tm	Fh	Fh	Fh	Fh	Fh	Tm	Fh	Fh	Tm
Major elements (Wt %)										
SiO_2	49.81	54.20	46.63	57.57	41.58	37.06	49.94	55.62	47.58	52.04
TiO_2	0.74	0.75	0.63	0.67	0.48	0.38	0.70	0.63	0.66	0.69
Al_2O_3	18.45	16.92	17.54	16.85	15.87	12.19	18.26	17.71	21.86	18.52
Fe_2O_3	9.30	4.31	5.18	7.40	6.93	4.43	11.81	6.03	5.42	10.64
MnO	0.16	0.02	0.02	0.10	0.25	0.16	0.19	0.11	0.09	0.17
MgO	3.50	0.01	0.01	1.31	0.24	0.01	5.38	0.92	0.01	5.80
CaO	3.86	6.88	9.08	3.12	9.66	17.78	8.43	3.61	2.89	4.78
Na_2O	0.68	0.41	0.83	1.30	0.62	0.51	1.14	1.32	0.02	0.40
K_2O	0.28	0.64	0.34	0.53	0.28	0.14	0.17	0.55	0.16	0.22
P_2O_5	0.13	0.18	0.13	0.11	0.17	0.11	0.04	0.23	0.04	0.10
S	1.05	0.51	0.49	0.01	0.94	0.04	0.05	0.51	0.04	0.01
LOI	11.03	15.27	20.01	10.66	22.51	26.44	3.64	11.55	21.08	7.75
Total	98.98	100.10	100.89	99.63	99.53	99.25	99.76	98.77	99.84	101.13
Trace elements (ppm)										
Cl	241	200	123	528	145	67	213	360	18.1	206
V	240	177	239	140	325	275	267	148	291.8	266
Cr	n.d.	n.d.	n.d.	n.d.	n.d.	n.d.	n.d.	n.d.	n.d.	n.d.
Co	17	6	8	19	107	22	22	11	10.0	19
Ni	n.d.	n.d.	n.d.	n.d.	n.d.	n.d.	n.d.	n.d.	n.d.	n.d.
Cu	26	67	78	45	62	30	31	40	62.3	27
Zn	73	55	55	61	79	51	83	58	98.7	78
Ga	16	16	16	14	12	9	16	14	19.3	15
Ge	< 0.3	< 0.5	1	1	< 0.3	< 1	1	< 0.5	0.9	1
As	19	64	78	27	59	23	13	23	44.0	22
Se	9	4	3	5	12	1	26	4	3.9	7
Br	< 0.5	5	3	1	3	3	< 0.5	1	0.7	0.2
Rb	11	32	18	18	16	13	6	22	12.9	8
Sr	269	194	188	121	336	89	202	370	58.8	125
Y	14	17	17	23	14	17	12	24	9.6	13
Zr	25	102	103	53	49	35	16	59	79.0	23
Nb	< 1.0	3	3	1	1	1	0.4	1	1.3	< 0.1
Mo	< 1.0	< 1.0	< 1.0	< 1.0	< 1.0	n.d.	< 1.0	< 1.0	< 1.0	< 1.0
Cd	8	n.d.	3	5	< 1.7	n.d.	< 0.3	< 0.1	n.d.	< 2.0
Sn	< 3.0	2	1	< 3.0	1	< 1	0.2	0.2	0.4	< 3.0
Sb	< 3.0	< 3.0	< 3.0	< 3.0	< 3.0	< 3	< 3.0	< 3.0	< 3.0	< 3.0
Cs	< 4.0	< 4.0	< 4.0	< 4.0	< 4.0	< 3	< 4.0	< 4.0	< 4.0	< 4.0
Ba	141	235	257	121	130	90	89	186	193.8	147
La	12	< 2.0	11	< 2.0	11	2	< 2.0	17	13.3	< 2.0
Ce	< 2.0	32	< 2.0	14	27	18	< 2.0	24	25.6	< 2.0
Hf	2	n.d.	2	4	2	1	1	3	n.d.	2
Ta	< 1.0	5	2	2	< 1.0	< 1	< 1.0	1	< 1.0	3
W	< 1.0	0	1	< 0.7	< 1.0	0	< 1.0	1	< 1.0	< 1.0
Hg	2	1	0	< 1.0	0.4	< 1	1	2	1.7	1
Pb	2	15	18	5	4	4	1	7	6.0	2
Bi	n.d.	n.d.	n.d.	n.d.	n.d.	n.d.	n.d.	n.d.	n.d.	n.d.
Th	< 1.0	4.3	4.8	< 0.2	0.6	1.0	< 1.0	0.7	1.4	< 1.0
U	0.8	1.8	0.9	1.5	2.8	2.1	6.6	2.7	0.3	1.2

Table A2.3. Continued.

Sample	MM82	MM83	MM84	MM85	MM86	MM87	MM88	MM89	MM90	MM91
Facies	Fh	Tm	Fh	Tm	Fh	Fh	Fh	Tm	Fh	Tm
Major elements (Wt %)										
SiO_2	43.01	54.58	57.41	54.93	50.12	33.97	39.88	49.79	57.75	53.26
TiO_2	0.46	0.69	0.53	0.83	0.96	0.34	0.33	0.68	0.50	0.79
Al_2O_3	13.00	16.42	17.49	16.88	20.98	12.74	11.16	18.75	16.62	19.93
Fe_2O_3	4.57	10.54	5.67	6.44	6.90	4.00	5.39	10.72	7.50	10.04
MnO	0.03	0.16	0.07	0.17	0.18	0.03	0.10	0.73	0.24	0.18
MgO	0.18	4.98	0.58	0.81	0.47	0.61	0.78	3.94	0.88	4.21
CaO	14.12	3.50	3.27	4.80	3.73	16.54	16.33	9.28	3.88	7.69
Na_2O	0.24	0.10	0.72	0.75	0.24	0.35	0.02	1.17	1.15	1.38
K_2O	0.21	0.24	0.50	0.38	0.33	0.33	0.13	0.16	0.52	0.23
P_2O_5	0.08	0.09	0.16	0.15	0.28	0.17	0.08	0.06	0.22	0.10
S	0.08	0.05	0.27	0.01	0.61	0.91	0.03	0.01	0.01	0.01
LOI	24.05	10.19	13.08	12.87	18.09	26.58	26.11	4.11	12.48	4.20
Total	100.02	101.52	99.73	99.01	102.88	96.57	100.34	99.40	101.74	102.02
Trace elements (ppm)										
Cl	61	199	419	274	131	32	80	228	n.d.	279
V	199	260	126	190	195	172	202	267	78	255
Cr	n.d.	n.d.	n.d.	n.d.	n.d.	n.d.	n.d.	n.d.	n.d.	n.d.
Co	6	16	12	15	18	< 3.0	9	33	7	18
Ni	n.d.	n.d.	n.d.	n.d.	n.d.	n.d.	n.d.	n.d.	n.d.	n.d.
Cu	34	27	50	54	43	33	43	32	37	22
Zn	48	93	52	65	68	50	63	110	75	86
Ga	11	14	13	16	18	10	9	14	11	15
Ge	< 0.5	< 0.5	1.2	< 1	<1	< 0.5	<1	<1	< 1	< 0.5
As	21	28	36	23	35	20	22	21	12	13
Se	1	3	7	6	7	11	2	18	17	11
Br	6	0	2	1	2	8	12	<1	1	1
Rb	13	10	18	17	13	8	11	7	16	9
Sr	114	88	121	209	188	405	45	176	124	164
Y	8	13	21	13	33	11	10	28	32	15
Zr	49	26	56	63	64	49	48	18	55	25
Nb	1	< 0.2	1	3	2	1	2	<1	0.4	< 0.2
Mo	< 1.0	< 1.0	<1	< 1	<1	< 1.0	<1	<1	n.d.	< 1.0
Cd	16	n.d.	<2	n.d.	6	< 2.0	<2	<2	n.d.	6
Sn	0	< 3.0	2	1.1	< 3.0	< 3.0	0.1	< 3.0	< 1	3
Sb	< 3.0	< 3.0	< 3.0	< 3	< 3.0	< 3.0	< 3.0	< 3.0	4	< 3.0
Cs	< 4.0	< 4.0	< 4.0	n.d.	< 4.0	< 4.0	< 4.0	< 4.0	< 3	< 4.0
Ba	106	166	156	227	294	168	106	230	442	145
La	< 2.0	< 2.0	<2	< 2	19	25	<2	<2	17	< 2.0
Ce	< 2.0	< 2.0	27	< 2	<2	50	<2	8	< 2	< 2.0
Hf	2	n.d.	3	4	3	3	2	2	4	3
Ta	< 1.4	5	< 1.0	6	2	< 1.0	< 1.0	3	< 1	< 1.0
W	< 1.0	< 1.0	2	< 1	1	1	< 1.0	< 1.0	< 1	< 1.0
Hg	< 0.5	3	< 1.0	2	1	< 1.0	< 1.0	1	7	2
Pb	6	2	5	9	19	7	3	< 1.0	7	2
Bi	n.d.	n.d.	n.d.	n.d.	n.d.	n.d.	n.d.	n.d.	n.d.	n.d.
Th	1.2	< 1.0	< 1.0	2.3	1.4	2.8	1.8	< 0.4	1.4	< 1.0
U	1.0	< 1.0	0.6	1.4	3.9	1.6	< 1.0	< 1.0	< 0.5	0.8

Table A2.3. Continued.

Sample	MM92	MM93	MM94	MM95	MM96	MM97	MM98	MM99	MM100	MM101	MM102
Facies	Tm	Fh	Tm	Tm	Tm	Tm	Fh	Fh	Fh	Fh	Fh
Major elements (Wt %)											
SiO_2	52.13	40.76	60.70	61.03	50.71	61.12	49.71	44.71	49.82	48.47	49.94
TiO_2	0.79	0.46	0.59	0.59	0.78	0.58	0.38	0.58	0.71	0.58	0.62
Al_2O_3	18.23	12.22	15.70	15.65	18.12	15.47	13.00	15.74	16.54	16.25	15.56
Fe_2O_3	10.20	6.19	6.78	6.78	11.60	6.71	8.53	6.16	5.90	6.73	6.51
MnO	0.19	0.13	0.11	0.12	0.19	0.10	0.07	0.05	0.06	0.06	0.41
MgO	3.54	0.92	1.14	1.21	4.02	0.76	0.01	0.55	0.15	0.01	0.01
CaO	7.87	12.66	4.18	4.33	6.02	2.97	6.95	11.25	7.03	8.73	7.19
Na_2O	1.12	0.18	1.94	2.03	1.20	1.82	0.02	0.02	1.56	0.98	1.98
K_2O	0.23	0.18	0.62	0.63	0.30	0.61	0.17	0.16	0.45	0.19	0.22
P_2O_5	0.06	0.16	0.12	0.12	0.06	0.11	0.20	0.14	0.13	0.11	1.35
S	0.01	0.20	0.01	0.01	0.12	0.01	0.01	0.03	0.23	0.01	0.02
LOI	5.59	25.15	8.43	7.67	7.12	9.54	21.71	22.29	14.68	18.44	17.25
Total	99.96	99.21	100.32	100.17	100.23	99.80	100.76	101.67	97.27	100.55	101.06
Trace elements (ppm)											
Cl	444	121	701	670	399	771	47	117	161	92	69
V	246	276	107	110	271	108	391	260	230	214	176
Cr	n.d.	n.d.	n.d.	n.d.	n.d.	n.d.	n.d.	n.d.	n.d.	n.d.	n.d.
Co	24	19	18	11	23	10	8	7	8	8	47
Ni	n.d.	n.d.	n.d.	n.d.	n.d.	n.d.	n.d.	n.d.	n.d.	n.d.	n.d.
Cu	25	58	50	47	37	43	57	42	45	42	58
Zn	88	71	66	65	81	54	73	59	69	85	105
Ga	14	16	14	13	16	12	9	11	15	16	15
Ge	<1	3	2.1	1	1.3	2	< 1	< 0.5	< 1	< 0.5	< 0.5
As	14	12	27	27	23	44	192	81	29	32	14
Se	9	0.4	11	14	13	3	7	5	4	1	1
Br	2	2	2	2	2	3	4	8	2	1	2
Rb	9	29	21	21	9	20	15	11	25	17	16
Sr	158	185	124	129	155	104	64	109	272	199	190
Y	15	19	28	28	15	26	11	10	17	12	102
Zr	27	69	61	61	27	65	49	45	54	54	55
Nb	<1	2	0.4	0.3	<1	1	1	3	2	2	2
Mo	<1	<1	<1	< 1.0	<1	< 1.0	n.d.	< 1.0	n.d.	< 1.0	< 1.0
Cd	<2	7	<2	< 2.0	<2	4	n.d.	n.d.	n.d.	< 0.1	n.d.
Sn	< 3.0	2	2	< 3.0	< 3.0	1	< 1	3	< 1	6	0.2
Sb	< 3.0	< 3.0	< 3.0	< 3.0	< 3.0	< 3.0	< 3	< 3.0	2	< 3.0	< 3.0
Cs	< 4.0	< 4.0	< 4.0	< 4.0	< 4.0	< 4.0	< 3	< 4.0	< 3	< 4.0	< 4.0
Ba	163	137	249	244	245	186	95	108	208	160	309
La	6	<2	16	12	1	24	8	11	4	< 2.0	17
Ce	11	<2	<2	< 2.0	7	30	< 2	< 2.0	< 2	< 2.0	24
Hf	2	2	3	3	0.3	3	3	n.d.	3	2	n.d.
Ta	4	4	3	2	2	3	6	5	6	< 1.0	< 1.0
W	< 1.0	1	1	1	< 1.0	1	< 1	< 1.0	< 1	< 1.0	3
Hg	1	< 1.0	< 1.0	1	1	< 1.0	1	0.4	1	1	< 0.5
Pb	3	9	8	7	2	6	4	5	7	6	8
Bi	n.d.	n.d.	n.d.	n.d.	n.d.	n.d.	n.d.	n.d.	n.d.	n.d.	n.d.
Th	< 1.0	2.7	< 1.0	< 1.0	< 1.0	< 1.0	1.3	2.0	1.9	1.7	2.2
U	< 0.5	0.4	1.0	0.6	< 1.0	0.8	< 1.0	< 1.0	0.6	0.4	6.6

Table A2.3. Continued.

Sample	MM103	MM104	MM105	MM106	MM107	MM108	MM109	MM110	MM111	MM112
Facies	Tm	Fh	Tm	Fh	Fh	Tm	Fh	Fh	Fh	Fh
Major elements (Wt %)										
SiO_2	55.91	49.83	49.18	40.91	37.90	60.23	47.41	53.28	37.12	46.41
TiO_2	0.74	0.70	0.70	0.31	0.45	0.58	0.80	0.68	0.37	0.45
Al_2O_3	15.18	15.65	16.69	12.21	12.98	15.02	20.14	22.36	11.19	14.76
Fe_2O_3	10.70	8.72	8.37	3.06	5.74	6.70	5.81	4.08	5.00	14.23
MnO	0.19	0.23	0.23	0.02	0.02	0.11	0.01	0.02	0.01	0.04
MgO	2.96	0.68	1.58	0.12	0.01	1.31	0.01	0.01	0.15	1.01
CaO	6.43	6.56	6.46	16.89	17.17	4.45	5.10	2.97	15.66	2.49
Na_2O	1.40	2.50	1.96	0.13	1.36	1.68	0.16	0.26	1.33	0.89
K_2O	0.39	0.53	0.55	0.17	0.29	0.74	0.21	0.27	0.72	1.07
P_2O_5	0.06	0.15	1.81	0.08	0.20	0.15	0.04	0.05	0.07	0.18
S	0.01	0.25	0.96	0.07	0.27	0.51	0.03	0.03	3.21	4.68
LOI	4.87	13.94	10.68	25.51	22.45	8.10	19.52	17.96	24.83	19.92
Total	98.84	99.74	99.18	99.48	98.83	99.59	99.26	101.96	99.66	106.12
Trace elements (ppm)										
Cl	455	120	204	543	143	503	64	80	65	95
V	237	206	324	130	302	162	330	170	144	453
Cr	n.d.	n.d.	n.d.	n.d.	n.d.	n.d.	n.d.	n.d.	n.d.	n.d.
Co	21	37	43	< 4.8	9	12	11	13	7	< 4.7
Ni	n.d.	n.d.	n.d.	n.d.	n.d.	n.d.	n.d.	n.d.	n.d.	n.d.
Cu	25	59	91	20	61	41	63	53	36	78
Zn	103	116	79	44	52	57	72	47	34	111
Ga	13	14	15	8	11	13	20	21	10	9
Ge	< 0.5	< 0.5	< 0.2	< 0.5	< 0.5	1	2	2	< 0.5	< 0.5
As	21	40	50	9	58	34	78	39	20	118
Se	1	1	5	1	3	2	17	2	1	2
Br	0.3	0.2	1	4	3	2	1	1	8	2
Rb	14	20	19	15	16	22	13	16	16	24
Sr	144	182	368	154	194	139	59	104	207	218
Y	26	20	15	7	12	30	20	14	6	10
Zr	43	50	46	29	35	64	142	80	35	41
Nb	< 0.2	1	2	1	2	0.4	3	2	2	1
Mo	< 1.0	< 1.0	< 1.0	< 1.0	< 1.0	< 1.0	< 1.0	< 2.3	< 1.0	< 1.0
Cd	n.d.	n.d.	< 2.0	< 0.1	< 2.0	< 0.1	< 0.1	< 1.0	< 1.1	n.d.
Sn	< 3.0	0	< 3.0	3	< 3.0	2	< 3.0	1	< 3.0	< 3.0
Sb	< 3.0	< 3.0	< 3.0	< 3.0	< 3.0	< 3.0	< 3.0	< 3.0	< 3.0	< 3.0
Cs	< 4.0	< 4.0	< 4.0	< 4.0	< 4.0	< 4.0	< 4.0	< 4.0	< 4.0	< 4.0
Ba	103	362	321	142	179	129	144	279	170	242
La	< 2.0	< 2.0	4	9	< 2.0	< 2.0	2	< 2.0	7	5
Ce	17	35	< 2.0	< 2.0	< 2.0	18	19	< 2.0	< 2.0	< 2.0
Hf	n.d.	n.d.	1	2	1	4	4	2	< 1.0	n.d.
Ta	2	< 1.0	6	< 1.0	< 1.0	3	< 1.0	< 1.0	< 1.0	9
W	< 1.0	< 1.0	< 1.0	< 0.6	1	2	1	1	< 0.7	< 1.0
Hg	2	2	1	< 0.4	< 1.0	1	< 1.0	1	0.4	< 0.6
Pb	3	5	6	3	4	6	12	10	4	< 0.4
Bi	n.d.	n.d.	n.d.	n.d.	n.d.	n.d.	n.d.	n.d.	n.d.	n.d.
Th	< 1.0	0.7	1.7	1.1	1.6	< 1.0	3.7	1.8	0.7	< 1.0
U	< 1.0	< 1.0	< 1.0	1.3	1.1	< 1.0	1.6	1.0	0.6	< 1.0

Table A2.3. Continued.

Sample	MM113	MM114	MM115	MM116	MM117	MM118	MM119	MM120	MM121	MM122
Facies	Fh	Fh	Fh	Fh	Fh	Tm	Fh	Fh	Tm	Lm
Major elements (Wt %)										
SiO_2	50.54	48.46	40.32	49.22	29.11	52.27	55.56	43.26	53.06	11.25
TiO_2	0.48	0.56	0.55	0.59	0.31	0.69	0.47	0.46	0.71	0.14
Al_2O_3	16.06	14.75	12.31	14.19	8.53	19.22	17.15	13.08	22.68	3.45
Fe_2O_3	5.05	6.21	5.61	7.06	4.15	9.97	8.34	6.17	6.29	1.77
MnO	0.04	0.77	0.09	0.15	0.13	0.17	0.09	0.09	0.12	0.13
MgO	0.61	0.92	0.99	0.86	1.00	4.50	1.37	1.15	1.27	0.58
CaO	4.30	8.77	14.94	8.85	24.98	9.40	6.34	12.28	10.36	43.39
Na_2O	0.02	0.21	0.92	1.08	0.94	0.88	2.34	0.47	2.36	1.19
K_2O	0.24	0.33	0.21	0.27	0.15	0.26	0.37	0.37	0.52	0.07
P_2O_5	0.03	0.15	0.14	0.13	0.35	0.10	0.08	0.15	0.15	0.22
S	0.00	0.05	0.01	0.01	0.04	0.01	0.02	0.02	0.01	0.02
LOI	22.19	19.78	23.29	17.16	29.63	2.80	7.63	22.65	4.41	38.08
Total	99.55	100.95	99.37	99.57	99.32	100.26	99.76	100.16	101.94	100.29
Trace elements (ppm)										
Cl	73	102	70	100	41	173	344	218	349	37
V	316	248	261	223	255	279	119	291	180	82
Cr	n.d.	n.d.	n.d.	n.d.	n.d.	n.d.	n.d.	n.d.	n.d.	n.d.
Co	10	76	22	22	14	27	12	19	15	< 3.0
Ni	n.d.	n.d.	n.d.	n.d.	n.d.	n.d.	n.d.	n.d.	n.d.	n.d.
Cu	56	68	72	62	42	28	46	55	56	25
Zn	78	106	77	85	52	80	81	79	69	34
Ga	13	14	11	14	8	15	12	12	18	4
Ge	< 0.5	< 1	< 0.4	< 0.5	< 0.5	< 0.3	< 0.5	< 0.5	< 0.5	< 0.5
As	46	23	20	19	11	16	41	21	6	3
Se	1	1	1	0.3	1	1	1	1	0.4	1
Br	4	2	5	3	9	0.2	1	8	1	4
Rb	25	23	18	19	13	8	13	17	18	4
Sr	58	130	173	181	76	190	154	223	487	52
Y	11	41	16	15	21	12	15	17	13	11
Zr	101	57	60	58	44	23	41	54	47	14
Nb	1	2	3	2	2	< 0.1	0.4	2	3	2
Mo	< 1.0	n.d.	< 1.0	< 1.0	< 1.0	< 1.0	< 1.0	< 1.0	< 1.0	< 1.0
Cd	< 2.0	n.d.	4	< 2.0	< 0.2	n.d.	< 0.2	< 0.2	< 0.2	n.d.
Sn	2	< 1	< 3.0	0.3	2	< 3.0	< 3.0	1	< 3.0	2
Sb	< 3.0	< 3	< 3.0	< 3.0	< 3.0	< 3.0	< 3.0	< 3.0	< 3.0	< 3.0
Cs	< 4.0	< 3	< 4.0	< 4.0	< 4.0	< 4.0	< 4.0	< 4.0	< 4.0	< 4.0
Ba	137	517	198	202	131	104	183	293	243	79
La	< 2.0	15	5	< 2.0	< 2.0	3	< 2.0	5	< 2.0	< 2.0
Ce	28	34	< 2.0	< 2.0	< 2.0	< 2.0	25	45	44	< 2.0
Hf	3	3	4	1	3	n.d.	2	3	3	n.d.
Ta	2	< 1	< 1.0	< 1.3	< 1.0	< 1.0	< 1.0	2	< 1.6	< 1.0
W	< 1.0	1	1	< 1.0	1	0.3	< 1.0	< 1.0	< 1.0	2
Hg	1	1	< 1.0	1	< 1.0	2	1	0.3	1	< 1.0
Pb	6	7	12	20	9	2	8	10	9	2
Bi	n.d.	n.d.	n.d.	n.d.	n.d.	n.d.	n.d.	n.d.	n.d.	n.d.
Th	< 0.4	1.8	1.7	1.5	1.8	< 1.0	< 0.5	4.2	2.4	1.6
U	< 1.0	1.5	1.1	< 0.5	4.0	< 0.6	1.8	0.4	< 0.6	2.3

Table A2.3. Continued.

Sample	MM123	MM124	MM125	MM126	MM127	MM128	MM129	MM130	MM131	MM132
Facies	Tm	Tm	Lm	Fh	Fh	Lm	Tm	Tm	Tm	Tm
Major elements (Wt %)										
SiO_2	52.86	54.39	26.08	58.46	48.74	9.10	54.02	51.12	54.96	50.43
TiO_2	0.83	0.85	0.37	0.65	0.76	0.13	0.68	0.67	0.59	0.86
Al_2O_3	19.83	19.29	8.72	18.86	19.05	2.82	21.32	18.74	17.63	20.88
Fe_2O_3	7.96	6.88	3.65	5.29	7.17	1.62	6.67	10.55	7.66	3.52
MnO	0.11	0.10	0.12	0.05	0.04	0.17	0.10	0.19	0.11	0.02
MgO	1.89	1.77	0.61	0.51	0.51	0.78	1.79	3.88	1.45	0.01
CaO	9.54	7.92	29.95	2.77	3.71	45.59	9.28	9.43	6.33	2.22
Na_2O	2.98	3.43	1.38	0.66	0.90	1.28	2.53	1.20	1.76	0.58
K_2O	0.54	0.71	0.18	0.82	0.24	0.08	0.54	0.19	0.31	0.30
P_2O_5	0.12	0.13	0.22	0.05	0.04	0.76	0.21	0.06	0.10	0.13
S	0.01	0.02	0.03	0.01	0.02	0.05	0.01	0.01	0.01	0.84
LOI	3.52	4.57	28.27	12.36	18.74	39.13	3.18	2.45	7.83	17.74
Total	100.18	100.08	99.58	100.48	99.92	101.50	100.31	98.49	98.74	97.54
Trace elements (ppm)										
Cl	420	413	133	142	66	240	346	198	151	154
V	235	206	145	257	336	106	194	371	202	145
Cr	n.d.	n.d.	n.d.	n.d.	n.d.	n.d.	n.d.	n.d.	n.d.	n.d.
Co	19	13	36	16	12	< 3.0	15	23	19	< 3.0
Ni	n.d.	n.d.	n.d.	n.d.	n.d.	n.d.	n.d.	n.d.	n.d.	n.d.
Cu	57	73	67	86	79	21	57	73	91	81
Zn	79	82	50	88	72	30	71	97	128	52
Ga	18	17	10	17	19	3	18	13	14	19
Ge	< 0.5	< 0.2	< 0.5	< 1	< 0.5	< 0.5	< 0.5	< 0.5	< 0.5	< 0.5
As	16	21	15	23	26	3	9	8	17	29
Se	1	1	1	0.3	1	0.4	0.4	2	1	2
Br	1	1	5	2	3	2	1	< 0.1	1	2
Rb	18	24	11	22	15	5	22	8	12	21
Sr	460	419	158	335	166	51	497	205	172	241
Y	16	16	22	24	7	13	16	15	21	12
Zr	49	57	32	69	95	18	53	20	46	89
Nb	3	3	2	4	3	2	4	< 0.1	1	4
Mo	< 1.0	< 1.0	< 1.0	< 1	< 1.0	< 1.0	< 1.0	< 1.0	< 1.0	< 3.6
Cd	< 2.0	11	< 2.0	n.d.	< 0.1	n.d.	< 2.0	n.d.	n.d.	n.d.
Sn	< 3.0	< 3.0	< 3.0	2	1	4	< 3.0	1	< 3.0	4
Sb	< 3.0	< 3.0	< 3.0	< 3	< 3.0	< 3.0	< 3.0	< 3.0	< 3.0	< 3.0
Cs	< 4.0	< 4.0	< 4.0	n.d.	< 4.0	< 4.0	< 4.0	< 4.0	< 4.0	< 4.0
Ba	234	320	195	289	287	105	254	79	140	440
La	< 2.0	10	14	8	< 2.0	4	< 2.0	13	15	< 2.0
Ce	< 2.0	< 2.0	17	33	24	9	51	12	19	24
Hf	3	4	< 1.0	4	3	n.d.	2	n.d.	n.d.	n.d.
Ta	2	2	< 1.0	4	< 1.2	< 1.0	3	5	< 1.0	5
W	< 1.0	< 0.7	2	< 1	< 0.6	1	< 1.0	< 1.0	< 1.0	1
Hg	2	1	< 1.0	1	2	< 1.0	1	2	1	1
Pb	8	9	4	9	16	2	8	3	6	18
Bi	n.d.	n.d.	n.d.	n.d.	n.d.	n.d.	n.d.	n.d.	n.d.	n.d.
Th	2.7	2.7	2.0	3.0	3.1	2.0	3.2	< 1.0	< 0.1	3.5
U	0.3	0.5	2.2	3.5	< 0.5	2.4	< 1.0	< 1.0	0.5	1.5

Table A2.4. Major-and trace-element composition of samples from Wolo Sege.

Sample	WS01	WS02	WS03	WS04	WS05	WS06	WS07	WS08	WS09	WS10	WS11A
Facies	Pa	Pa	Pa	Pa	Pv	Pv	Tms	Tmp	Tma	Tmp	LTmp
Major elements (Wt %)											
SiO_2	61.09	74.15	52.65	53.84	54.10	58.14	67.56	66.50	67.53	69.16	70.38
TiO_2	0.70	0.39	0.78	0.95	0.93	1.21	0.32	0.41	0.37	0.28	0.26
Al_2O_3	14.24	8.19	16.10	17.57	15.48	14.11	14.91	15.52	15.19	14.41	14.23
Fe_2O_3	6.84	3.80	7.55	8.81	7.27	6.83	2.97	3.74	3.43	2.49	2.29
MnO	0.06	0.01	0.04	0.04	0.04	0.10	0.08	0.09	0.08	0.20	0.08
MgO	1.31	0.01	0.74	0.97	0.87	0.08	0.27	0.35	0.29	0.07	0.10
CaO	1.68	1.06	1.87	2.79	1.74	2.06	2.23	2.90	2.66	2.49	2.46
Na_2O	0.02	0.02	0.02	0.17	0.02	0.34	0.94	1.34	1.13	1.19	1.48
K_2O	0.09	0.07	0.08	0.16	0.13	0.18	2.30	2.04	2.28	2.46	2.48
P_2O_5	0.02	0.08	0.01	0.04	0.04	0.02	0.09	0.09	0.10	0.11	0.08
S	0.004	0.01	0.0004	0.01	0.01	0.01	0.01	0.01	0.005	0.01	0.01
LOI	16.71	12.52	18.17	15.12	19.06	15.98	8.94	8.13	8.16	8.30	7.76
Total	102.77	100.30	98.03	100.47	99.69	99.06	100.62	101.12	101.23	101.17	101.61
Trace elements (ppm)											
Cl	42	8	8	34	35	57	830	843	840	998	1019
V	292	160	282	273	179	183	52	67	60	49	27
Cr	n.d.	n.d.	n.d.	n.d.	n.d.	n.d.	n.d.	n.d.	n.d.	n.d.	n.d.
Co	14	8	12	30	13	26	< 4	6	< 4	< 4	< 3.0
Ni	n.d.	n.d.	n.d.	n.d.	n.d.	n.d.	n.d.	n.d.	n.d.	n.d.	n.d.
Cu	48	28	50	55	49	45	12	12	14	8	5
Zn	68	39	79	78	68	58	48	52	58	49	42
Ga	12	7	15	16	15	16	12	13	14	13	12
Ge	1	< 1	2	< 1	3	1	< 1	< 1	2	1	3
As	10	5	10	11	13	11	12	14	15	6	6
Se	0.3	0.2	< 1	0.2	0.4	0.4	0.3	1	1	0.4	1
Br	< 1	1	< 1	< 1	1	1	2	2	2	2	3
Rb	9	5	7	13	10	11	72	65	76	79	78
Sr	114	65	122	185	130	147	205	237	238	223	217
Y	16	9	26	23	22	21	17	18	16	16	14
Zr	54	33	64	67	98	109	113	104	107	105	102
Nb	1	1	1	2	2	3	2	3	2	3	3
Mo	< 1	< 1	< 1	< 1	< 1.0	< 1.0	< 1	< 1	< 1	< 1	< 0.7
Cd	n.d.	n.d.	n.d.	n.d.	< 2.0	< 2.0	n.d.	n.d.	n.d.	n.d.	< 2.0
Sn	< 3	< 3	< 3	0.2	1	< 3.0	3	0.1	1	5	1
Sb	2	< 3	< 3	< 3	< 3.0	< 3.0	< 3	< 3	< 3	< 3	< 3.0
Cs	n.d.	n.d.	n.d.	n.d.	< 4.0	< 4.0	n.d.	n.d.	n.d.	n.d.	< 4.0
Ba	210	50	153	135	154	201	415	409	409	577	422
La	11	5	22	7	2	3	7	12	8	< 2	16
Ce	30	9	< 2	34	21	55	20	23	< 2	33	< 2.0
Hf	3	2	4	4	5	3	4	4	4	4	4
Ta	3	5	7	5	1	< 1.0	2	2	< 1	< 1	< 1.0
W	2	1	1	< 1	2	4	0.4	< 1	< 1	1	1
Hg	2	2	1	2	< 1.0	1	2	2	< 1	1	< 1.0
Pb	7	3	6	10	8	13	12	12	18	15	11
Bi	n.d.	n.d.	n.d.	n.d.	n.d.	n.d.	n.d.	n.d.	n.d.	n.d.	n.d.
Th	1.1	0.8	1.1	2.3	3.2	3.9	7.7	6.7	7.1	7.4	7.7
U	< 1.0	< 0.4	< 1.0	< 0.5	< 1.0	0.7	1.9	1.5	1.9	2.0	2.3

Table A2.4. Continued.

Sample	WS11B	WS12	WS13	WS14	WS15	WS16	WS17	WS18	WS19	WS20	WS21	WS22
Facies	LTmp	Trma	Trma	Trm	Trmp	Trmp	Pa	Ts	LTmp	Trmp	Trmp	Pa
Major elements (Wt %)												
SiO_2	67.66	65.21	67.49	69.53	68.38	68.25	59.32	70.98	71.11	69.86	70.29	54.71
TiO_2	0.31	0.34	0.33	0.28	0.29	0.30	0.65	0.23	0.23	0.23	0.24	0.74
Al_2O_3	14.65	15.40	15.56	13.61	14.54	15.20	19.10	14.07	13.90	14.65	15.42	18.51
Fe_2O_3	2.77	3.15	3.03	2.56	2.53	2.82	5.31	1.62	1.73	1.76	2.06	8.00
MnO	0.08	0.08	0.10	0.06	0.09	0.08	0.05	0.07	0.07	0.07	0.07	0.07
MgO	0.15	0.50	0.68	0.40	0.17	0.17	0.42	0.01	0.01	0.01	0.13	0.17
CaO	2.42	2.12	2.28	2.01	2.12	2.06	2.82	1.87	1.94	2.33	1.91	3.60
Na_2O	1.39	0.93	0.57	0.83	1.17	0.53	0.35	0.63	1.25	1.66	0.97	1.06
K_2O	2.31	2.13	2.40	2.21	2.27	2.16	0.85	2.75	2.70	2.31	2.48	0.71
P_2O_5	0.07	0.08	0.10	0.11	0.08	0.09	0.07	0.10	0.09	0.09	0.09	0.03
S	0.01	0.04	0.14	0.05	0.01	0.02	0.03	0.01	0.01	0.01	0.01	0.00
LOI	8.43	10.16	9.36	7.98	8.58	9.56	12.62	8.02	7.18	6.55	8.30	13.12
Total	100.24	100.14	102.04	99.63	100.24	101.25	101.59	100.35	100.23	99.53	101.96	100.72
Trace elements (ppm)												
Cl	993	654	953	702	795	695	133	868	890	812	808	211
V	35.7	86	33	43	43	46	96	17	16	14	23	199
Cr	n.d.	n.d.	n.d.	n.d.	n.d.	n.d.	n.d.	n.d.	n.d.	n.d.	n.d.	n.d.
Co	6.8	8	< 4	8	< 4	< 4	13	< 4	< 4	6	< 4	19
Ni	n.d.	n.d.	n.d.	n.d.	n.d.	n.d.	n.d.	n.d.	n.d.	n.d.	n.d.	n.d.
Cu	9.8	17	9	13	11	18	45	14	11	11	11	63
Zn	56	53	46	53	50	52	83	53	43	40	43	88
Ga	13.2	13	12	13	12	13	17	12	12	13	12	17
Ge	< 0.3	1	1	< 1	< 1	< 1	5	1	1	4	2	4
As	4.8	27	5	9	7	6	21	3	3	6	7	22
Se	0.3	0.4	0.3	1	0.3	0.3	0.4	0.3	0.4	1	0.4	0.2
Br	3.1	2	2	1	2	2	2	2	2	2	2	0.4
Rb	78.3	72	76	80	81	80	45	87	84	80	85	40
Sr	213.7	211	193	198	200	190	204	174	189	200	171	182
Y	19.9	17	15	15	15	18	20	16	15	14	14	22
Zr	108.8	122	104	104	109	110	117	124	117	113	123	80
Nb	2.5	3	3	3	3	3	3	3	3	2	3	3
Mo	< 1.1	< 1.0	< 1	< 1	< 1	< 1	< 1	< 1	< 1	< 1	< 1	< 1.0
Cd	n.d.	12	n.d.	n.d.	n.d.	n.d.	n.d.	n.d.	n.d.	n.d.	n.d.	< 2.0
Sn	3.6	3	7	4	2	5	0.4	3	4	4	7	< 3.0
Sb	< 3.0	< 3.0	< 3	< 3	< 3	3	2	< 3	< 3	< 3	< 3	< 3.0
Cs	< 4.0	< 4.0	n.d.	n.d.	n.d.	n.d.	n.d.	n.d.	n.d.	n.d.	n.d.	< 4.0
Ba	429.1	472	425	479	449	410	284	460	456	403	455	304
La	9.2	35	22	11	36	22	24	16	< 2	14	10	14
Ce	32.1	< 2.0	31	27	64	30	< 2	30	42	28	28	25
Hf	n.d.	5	4	3	4	4	4	5	4	3	5	3
Ta	< 1.0	4	1	< 1	1	< 1	1	< 1	< 1	< 1	3	3
W	1.3	< 1.0	< 1	< 1	0.3	1	< 1	1	1	1	< 1	< 1.0
Hg	1.5	1	1	2	1	2	< 1	2	2	< 1	1	1
Pb	12.4	14	12	12	13	13	16	13	12	10	14	11
Bi	n.d.	n.d.	n.d.	n.d.	n.d.	n.d.	n.d.	n.d.	n.d.	n.d.	n.d.	n.d.
Th	7.2	8.0	7.2	7.2	7.2	7.3	6.4	7.2	6.9	6.6	7.8	6.6
U	1.5	1.4	1.9	2.0	2.6	1.5	0.6	2.3	1.7	2.1	2.2	1.2

Table A2.4. Continued.

Sample	WS23	WS24	WS25	WS26	WS27	WS28	WS29	WS30	WS31	WS32	WS33	WS34
Facies	Tm	Pa	Trm	Trmp	Pa	Pa	Trmp	Pa	Fmm	Fmm	Sm	Sm
Major elements (Wt %)												
SiO_2	68.99	53.53	66.67	61.10	65.83	53.21	53.00	52.39	58.10	52.96	50.72	51.36
TiO_2	0.24	0.62	0.37	0.56	0.36	0.65	0.69	0.63	0.64	0.75	0.85	0.88
Al_2O_3	15.01	18.58	13.69	16.21	13.92	16.53	17.82	18.32	15.32	17.09	18.13	17.05
Fe_2O_3	2.32	8.16	3.09	5.02	3.07	7.03	7.63	7.48	6.55	7.94	9.37	10.07
MnO	0.13	0.10	0.10	0.12	0.09	0.10	0.10	0.12	0.10	0.12	0.12	0.15
MgO	0.11	1.06	0.94	1.51	0.87	2.26	2.32	2.60	1.79	2.11	3.50	4.47
CaO	1.65	6.63	3.15	4.64	2.88	6.19	6.12	7.40	4.54	5.77	7.83	8.48
Na_2O	1.24	1.27	2.56	2.72	2.38	1.97	1.99	1.72	1.50	1.73	1.78	1.90
K_2O	4.57	0.69	2.17	1.37	2.01	0.70	0.47	0.37	0.50	0.43	0.31	0.37
P_2O_5	0.09	0.03	0.09	0.05	0.07	0.06	0.05	0.10	0.03	0.05	0.06	0.13
S	0.01	n.d.	0.02	0.03	0.02	0.04	0.04	0.14	0.04	0.05	0.02	0.03
LOI	7.06	9.54	6.46	6.20	7.48	7.37	8.46	8.39	10.38	10.42	6.95	4.84
Total	101.41	100.20	99.31	99.53	98.97	96.11	98.69	99.65	99.49	99.42	99.63	99.74
Trace elements (ppm)												
Cl	1678	215	1097	776	943	341	249	202	141	190	160	207
V	62	207	30	51	21	138	121	167	70	122	140	169
Cr	n.d.	57	< 1	< 1	< 1	5	7	5	5	16	7	2
Co	< 4.5	34	51	48	16	42	39	76	58	38	39	45
Ni	n.d.	16	0	1	1	13	12	12	7	16	24	24
Cu	16	64	12	17	2	51	55	72	59	69	78	71
Zn	45	73	51	61	53	72	70	80	70	73	79	81
Ga	13	18	14	16	8	17	18	17	17	18	18	16
Ge	2	2	< 1	< 1	< 1	< 1	< 1	< 1	2	< 1	1	< 1
As	4	12	< 1	< 1	< 1	3	9	19	6	16	13	11
Se	0.4	0.3	< 1	< 1	< 1	< 1	< 1	< 1	< 1	< 1	< 1	< 1
Br	5	1	< 1	< 1	< 1	< 1	< 1	< 1	< 1	< 1	< 1	< 1
Rb	185	35	66	53	64	32	22	23	32	24	16	18
Sr	128	219	251	315	231	265	259	288	223	260	279	283
Y	24	17	19	24	18	18	19	29	17	19	15	15
Zr	152	44	131	108	131	71	69	41	78	68	49	44
Nb	11	2	2	2	2	1	1	1	1	1	1	1
Mo	< 4.3	n.d.	< 1	< 1	< 1	< 1	< 1	< 1	< 1	< 1	< 1	< 1
Cd	< 0.1	n.d.	< 1	< 1	< 1	< 1	< 1	< 1	< 1	< 1	< 1	< 1
Sn	2	< 3	5	3	5	1	2	0.2	2	< 3	0.2	< 3
Sb	< 3.0	< 3	< 3	< 3	< 3	< 3	< 3	< 3	< 3	< 3	< 3	< 3
Cs	< 4.0	< 4	< 4	< 4	< 4	< 4	< 4	< 4	< 4	< 4	< 4	< 4
Ba	1088	391	385	319	413	230	234	187	223	202	178	131
La	52	13	30	25	16	10	14	1	< 2	10	10	< 2
Ce	75	37	43	< 2	< 2	< 2	32	18	32	< 2	23	< 2
Hf	5	n.d.	2	4	11	4	3	2	< 1	3	3	7
Ta	1	< 2	< 1	< 1	33	< 1	< 1	< 1	< 1	< 1	< 1	< 1
W	3	< 1	179	170	165	82	47	49	32	26	48	80
Hg	1	< 1	< 1	< 1	0.3	0.4	1	1	< 1	3	< 1	0.4
Pb	26	6	11	10	11	7	7	5	8	8	6	5
Bi	n.d.	n.d.	1	1	< 1	1	< 1	1	1	< 1	< 1	< 1
Th	35.3	4.0	5.1	3.9	5.7	2.5	2.8	1.5	2.6	2.3	2.9	1.1
U	7.0	0.9	5.4	3.5	4.8	1.6	0.8	1.6	0.8	< 1.0	0.4	0.6

Table A2.4. Continued.

Sample	WS35	WS36	WS37	WS38	WS39	WS40	WS41	WS42	WS43	WS44	WS45	WS46
Facies	Pa	Pa	Pa	Pa	Sm	Pa	Pa	Pa	Pa	Sm	Pa	Pa
Major elements (Wt %)												
SiO_2	50.07	49.03	48.00	48.12	48.66	56.44	55.08	53.72	50.65	51.96	50.69	49.75
TiO_2	0.88	0.84	0.84	0.74	0.94	0.64	0.68	0.81	0.84	0.90	0.97	0.85
Al_2O_3	18.48	18.30	17.96	15.68	16.30	15.58	15.15	17.28	17.76	19.86	20.78	18.97
Fe_2O_3	9.63	9.21	9.00	7.69	9.44	6.18	6.50	7.88	8.25	8.84	9.35	8.79
MnO	0.11	0.14	0.16	0.08	0.17	0.10	0.05	0.09	0.11	0.10	0.12	0.27
MgO	1.96	1.09	1.52	2.23	2.18	1.28	1.36	1.40	1.08	1.75	1.24	1.12
CaO	6.05	4.21	3.79	2.55	5.30	3.09	3.62	5.41	5.15	6.63	5.60	4.58
Na_2O	1.43	1.02	0.76	0.39	1.57	1.29	1.26	1.65	1.77	1.97	1.82	1.43
K_2O	0.21	0.16	0.14	0.05	0.32	0.62	0.31	0.44	0.35	0.31	0.41	0.35
P_2O_5	0.07	0.05	0.03	0.01	0.28	0.15	0.02	0.05	0.06	0.05	0.06	0.04
S	0.03	0.02	0.03	0.04	0.29	0.10	0.07	0.05	0.05	0.03	0.05	0.05
LOI	10.89	15.75	17.32	19.53	12.24	13.99	14.20	10.63	12.13	8.81	12.23	13.56
Total	99.81	99.83	99.54	97.11	97.68	99.46	98.29	99.43	98.19	101.22	103.31	99.76
Trace elements (ppm)												
Cl	72	38	54	44	149	184	79	110	107	108	85	59
V	138	115	126	195	192	97	92	113	104	141	100	114
Cr	12	4	5	5	13	7	7	3	< 1	< 1	2	4
Co	43	45	48	74	45	49	34	66	58	27	36	52
Ni	21	17	17	12	11	10	10	10	11	17	15	13
Cu	82	81	92	85	55	54	59	79	73	61	77	73
Zn	82	89	84	69	66	64	67	81	82	71	89	88
Ga	19	19	19	17	17	16	17	19	19	18	19	20
Ge	2	3	3	2	< 1	< 1	< 1	< 1	2	< 1	1	3
As	28	28	28	14	28	9	7	13	17	13	21	15
Se	< 1	< 1	< 1	< 1	< 1	< 1	< 1	< 1	< 1	< 1	< 1	< 1
Br	< 1	< 1	< 1	< 1	< 1	< 1	< 1	< 1	< 1	< 1	< 1	< 1
Rb	16	17	15	7	22	37	26	41	28	21	28	29
Sr	249	200	139	54	208	142	176	256	246	273	195	200
Y	13	22	18	28	14	22	18	23	22	14	20	25
Zr	51	58	61	57	62	104	80	74	68	57	79	81
Nb	1	1	2	2	1	2	2	2	2	2	2	2
Mo	< 1	< 1	< 1	< 1	< 1	< 1	< 1	< 1	< 1	< 1	< 1	< 1
Cd	< 1	< 1	< 1	< 1	< 1	< 1	< 1	< 1	< 1	< 1	< 1	4
Sn	< 3	< 3	1	< 3	< 3	< 3	4	2	< 3	1	1	2
Sb	< 3	< 3	< 3	< 3	< 3	< 3	< 3	< 3	< 3	< 3	< 3	< 3
Cs	< 4	< 4	< 4	< 4	< 4	< 4	< 4	< 4	< 4	< 4	< 4	< 4
Ba	120	145	189	47	328	267	131	233	374	347	327	694
La	< 2	< 2	15	< 2	8	11	< 2	9	6	< 2	< 2	< 2
Ce	23	< 2	8	24	19	< 2	< 2	19	< 2	27	45	27
Hf	5	4	4	1	5	4	1	1	4	6	4	3
Ta	< 1	< 1	< 1	< 1	< 1	< 1	< 1	< 1	< 1	< 1	< 1	< 1
W	23	18	18	21	48	22	18	41	35	43	25	20
Hg	2	1	< 1	1	< 1	2	< 1	1	1	2	2	< 1
Pb	6	7	9	1	9	15	10	10	10	8	12	14
Bi	< 1	1	< 1	< 1.0	1	1	2	< 1	< 1	< 1	< 1	2
Th	2.2	1.9	2.4	1.8	2.2	4.4	3.1	2.7	2.6	2.5	3.6	3.7
U	0.6	< 1.0	< 1.0	< 1.0	0.5	0.7	< 0.6	0.8	0.8	1.8	0.4	0.3

Table A2.4. Continued.

Sample	WS47	WS48	WS49	WS50	WS51	WS52
Facies	Pa	Pa	Pa	Pa	Pa	Smm
Major elements (Wt %)						
SiO_2	50.49	48.59	51.12	52.37	52.28	58.99
TiO_2	0.77	0.74	0.66	0.74	0.79	0.62
Al_2O_3	16.40	15.73	15.96	16.97	17.98	16.07
Fe_2O_3	7.45	7.49	6.83	7.29	8.07	6.08
MnO	0.05	0.08	0.05	0.07	0.07	0.16
MgO	1.75	1.70	1.95	1.80	1.90	1.93
CaO	3.66	3.44	4.46	5.34	5.99	5.66
Na_2O	0.95	0.92	1.12	1.69	1.85	2.83
K_2O	0.30	0.20	0.26	0.38	0.40	0.68
P_2O_5	0.02	0.02	0.02	0.04	0.04	0.14
S	0.06	0.05	0.04	0.07	0.07	0.03
LOI	17.24	20.90	16.20	13.48	10.79	5.87
Total	99.14	99.85	98.66	100.23	100.21	99.05
Trace elements (ppm)						
Cl	54	34	45	117	107	813
V	212	301	181	157	139	47
Cr	16	15	4	< 1	9	< 1
Co	41	71	18	60	41	40
Ni	19	13	13	12	13	1
Cu	66	69	56	72	68	18
Zn	75	71	62	78	79	85
Ga	17	17	15	18	19	16
Ge	< 1	< 1	3	< 1	< 1	< 1
As	2	3	6	4	9	< 1
Se	< 1	< 1	< 1	0	< 1	< 1
Br	< 1	< 1	< 1	< 0.1	< 1	< 1
Rb	33	24	29	32	33	26
Sr	135	117	136	195	211	345
Y	16	18	13	21	22	28
Zr	75	70	64	73	69	83
Nb	2	1	1	< 1	1	1
Mo	< 1	< 1	< 1	< 1	< 1	< 1
Cd	< 1	23	< 1	< 1	< 1	< 1
Sn	< 3	1	< 3	1	< 3	2
Sb	< 3	< 3	< 3	< 3	< 3	< 3
Cs	< 4	< 4	< 4	< 4	< 4	< 4
Ba	101	122	94	187	187	198
La	16	< 2	23	14	13	11
Ce	49	22	21	< 2	21	18
Hf	3	3	5	3	3	2
Ta	< 1	< 1	< 1	< 1	< 1	< 1
W	22	21	13	20	22	101
Hg	< 1	1	< 1	2	2	< 1
Pb	10	11	7	10	9	10
Bi	< 1	< 1	< 1	1	< 1	1
Th	3.6	2.4	2.6	2.9	2.6	1.1
U	0.4	< 1.0	0.5	1.2	0.4	2.2

Table A2.5. Major-and trace-element compositions of samples from Wae Bha, Turekeo and Kopowatu.

Sample	WB-01	WB-02	WB-03	TRK-01	TRK-02	KPW-01
Facies	Tma	LTmp	Trma	Ts	LTmp	Tm
Locality	Wae Bha			Turekeo		Kopowatu
Major elements (Wt %)						
SiO_2	54.84	55.94	57.29	61.78	65.69	67.94
TiO_2	0.38	0.36	0.38	0.28	0.25	0.23
Al_2O_3	15.81	17.44	16.05	15.15	14.62	13.72
Fe_2O_3	3.45	3.46	4.28	2.22	1.99	1.82
MnO	0.05	0.13	0.09	0.33	0.08	0.13
MgO	3.58	3.06	2.81	1.57	1.11	0.33
CaO	3.94	2.67	2.47	1.95	2.41	1.17
Na_2O	0.80	0.75	0.98	1.28	2.26	2.13
K_2O	0.33	0.35	0.67	1.89	2.24	4.59
P_2O_5	0.03	0.03	0.04	0.02	0.03	0.02
SO_3	0.05	0.02	0.11	0.02	0.02	0.02
LOI	16.24	14.86	14.35	12.78	8.32	7.26
Total	99.50	99.06	99.51	99.27	99.02	99.34
Trace elements (ppm)						
Cl	37	37	119	437	751	1909
V	235	235	67	62	36	34
Cr	1	1	1	< 1	6	< 1
Co	5	5	7	21	33	21
Ni	8	8	3	7	4	4
Cu	16	16	20	15	8	11
Zn	66	66	63	38	17	20
Ga	16	16	16	15	14	12
Ge	2	2	1	1	< 1	2
As	4	4	19	2	2	3
Se	1	1	1	< 1	< 1	< 1
Br	1	1	1	1	2	6
Rb	12	12	36	63	72	196
Sr	187	187	195	175	201	150
Y	21	21	25	15	14	24
Zr	132	132	142	144	124	187
Nb	3	3	3	3	3	12
Mo	1	1	1	< 1	< 1	< 1
Cd	6	6	1	< 2	< 2	< 2
Sn	4	4	3	4	2	3
Sb	3	3	3	< 3	< 3	< 3
Cs	4	4	4	< 4	< 4	< 4
Ba	96	96	249	494	333	1426
La	15	15	11	< 2	28	61
Ce	26	26	41	58	44	138
Hf	6	6	5	3	3	5
Ta	< 1	< 1	< 1	1	2	6
W	< 1	3	1	57	147	156
Hg	1	< 1	1	1	2	< 1.0
Pb	18	18	16	14	11	28
Bi	1	1	1	< 1	< 1	< 1
Th	7.8	7.8	9.3	8.9	7.6	38.1
U	0.8	0.8	1.1	0.9	2.0	7.5

Table A2.6. Major-and trace-element composition of samples from Matago.

Sample	MTG-01	MTG-02	MTG-03	MTG-04	MTG-05	MTG-06	MTG-07	MTG-08	MTG-09
Facies	Tms	Tmp	Tma	Tmp	LTmp	LTmp	Pa	Ts	LTmp
Major elements (Wt %)									
SiO_2	55.84	65.88	61.87	63.06	68.34	66.66	57.25	63.56	67.97
TiO_2	0.37	0.40	0.36	0.36	0.27	0.26	0.68	0.24	0.24
Al_2O_3	16.04	14.16	14.65	14.64	13.35	13.30	16.88	14.01	13.83
Fe_2O_3	3.45	3.68	3.35	3.37	2.24	2.42	5.45	1.75	2.04
MnO	0.10	0.09	0.08	0.19	0.11	0.14	0.10	0.08	0.09
MgO	3.20	0.96	1.73	1.52	0.59	0.91	1.68	1.77	0.59
CaO	2.39	3.06	2.46	2.53	2.49	2.77	2.67	2.21	2.55
Na_2O	0.80	1.97	1.55	1.73	2.05	2.16	1.11	1.17	2.38
K_2O	0.68	2.26	1.74	2.05	2.59	2.55	0.48	2.13	2.59
P_2O_5	0.02	0.06	0.04	0.05	0.05	0.05	0.01	0.04	0.03
SO_3	0.04	0.10	0.08	0.04	0.08	0.19	0.07	0.02	0.11
LOI	16.35	7.62	11.48	10.73	7.1	8.65	13.22	12.43	10.04
Total	99.28	100.23	99.39	100.26	99.26	100.08	99.59	99.41	102.47
Trace elements (ppm)									
Cl	301	1145	1364	741	1331	3520	< 2	632	887
V	78	65	71	54	33	48	100	23	28
Cr	15	4	7	4	2	3	29	9	4
Co	17	49	23	28	30	72	20	10	30
Ni	21	4	9	8	2	3	14	3	2
Cu	24	13	13	15	4	9	48	10	6
Zn	32	26	38	51	26	< 1	88	51	22
Ga	16	13	14	13	12	12	17	14	12
Ge	2	2	1	1	2	< 1	2	1	< 1
As	14	6	6	5	3	2	5	2	4
Se	< 1	< 1	< 1	< 1	< 1	1	< 1	< 1	< 1
Br	1	3	3	2	3	7	< 1	1	2
Rb	31	72	61	74	81	78	34	73	77
Sr	167	240	214	207	215	232	204	165	214
Y	14	16	16	17	16	14	23	16	14
Zr	141	103	123	113	109	105	122	136	112
Nb	2	3	3	3	3	3	4	3	3
Mo	< 1	< 1	< 1	< 1	< 1	< 1	< 1	< 1	< 1
Cd	< 2	< 2	< 2	< 2	< 2	< 2	< 2	< 2	< 2
Sn	5	< 3	2	2	9	4	2	4	5
Sb	< 3	< 3	< 3	< 3	< 3	< 3	< 3	< 3	< 3
Cs	< 4	< 4	< 4	< 4	< 4	< 4	< 4	< 4	< 4
Ba	157	391	324	458	429	468	315	339	458
La	16	24	22	13	< 2	32	< 2	29	18
Ce	30	< 2	40	35	36	< 2	< 2	41	30
Hf	3	2	3	3	3	2	5	2	2
Ta	4	< 2	3	1	4	1	3	1	3
W	22	130	86	67	100	309	16	33	103
Hg	< 1.0	< 1.0	2	< 1.0	< 0.5	1	1	< 0.4	2
Pb	8	11	17	15	11	11	13	14	13
Bi	< 1	< 1	< 1	< 1	< 1	< 1	< 1	< 1	< 1
Th	8.8	6.8	8.1	7.3	7.8	8.4	7.1	8.6	6.6
U	< 1	2	1	1.4	2	2.8	< 1	1.1	1.7

Table A2.7. Major-and trace-element composition of samples from Tangi Talo.

Sample	TT01	TT02	TT03	TT04	TT06	TT07	TT08	TT09	TT10
Facies	Pa	Tm	Pa	Tm	Fmm	Fmm	Tm	Fmm	Tm
Major elements (Wt %)									
SiO_2	60.65	64.88	61.42	63.83	57.63	53.91	88.82	57.31	58.50
TiO_2	0.54	0.26	0.48	0.27	0.49	0.84	0.06	0.51	0.75
Al_2O_3	15.48	12.87	15.83	13.97	14.91	17.71	1.82	15.73	17.02
Fe_2O_3	4.70	2.66	4.23	3.32	4.32	7.70	1.06	4.92	7.86
MnO	0.07	0.05	0.08	0.09	0.05	0.08	0.01	0.13	0.16
MgO	1.11	2.39	1.28	2.88	1.83	1.49	0.39	1.43	2.37
CaO	3.15	2.43	3.64	2.21	2.06	3.13	0.42	2.40	6.65
Na_2O	1.93	0.87	2.09	0.74	0.88	1.57	0.19	1.06	3.27
K_2O	1.27	1.23	1.44	1.23	0.41	0.63	0.04	0.74	0.80
P_2O_5	0.04	0.03	0.04	0.04	0.08	0.06	0.01	0.25	0.15
S	0.08	0.02	0.03	0.02	0.11	0.25	0.02	0.09	0.02
LOI	9.53	12.05	9.63	10.80	16.76	12.1	6.74	14.41	3.03
Total	98.55	99.74	100.18	99.41	99.52	99.47	99.57	98.99	100.59
Trace elements (ppm)									
Cl	273	401	358	69	83	210	n.d.	187	457
V	57	80	30	202	245	122	n.d.	68	191
Cr	1	1	1	19	1	18	n.d.	5	2
Co	40	5	8	45	5	43	n.d.	17	39
Ni	3	2	4	14	14	16	n.d.	12	5
Cu	38	3	25	55	27	58	n.d.	36	10
Zn	83	59	76	72	100	77	n.d.	84	24
Ga	17	10	14	20	11	19	n.d.	16	15
Ge	1	4	1	2	1	1	n.d.	1	2
As	10	9	5	14	3	35	n.d.	18	< 1
Se	1	1	1	1	1	1	n.d.	1	< 1
Br	1	1	1	1	1	1	n.d.	1	1
Rb	63	49	58	21	40	34	n.d.	50	22
Sr	228	198	228	152	172	195	n.d.	172	354
Y	20	14	15	13	45	23	n.d.	33	18
Zr	113	121	109	147	134	126	n.d.	138	65
Nb	2	2	2	3	3	2	n.d.	3	2
Mo	1	1	1	1	1	1	n.d.	1	< 1
Cd	10	11	< 1	< 1	< 1	< 1	n.d.	4	< 2
Sn	3	6	2	3	5	1	n.d.	3	< 3
Sb	< 3	< 3	< 3	< 3	< 3	< 3	n.d.	< 3	< 3
Cs	< 4	< 4	< 4	< 4	< 4	< 4	n.d.	< 4	< 4
Ba	230	214	240	147	184	216	n.d.	190	190
La	9	18	20	19	30	< 2	n.d.	12	10
Ce	41	46	< 2	23	77	35	n.d.	< 2	27
Hf	2	9	5	5	12	3	n.d.	4	2
Ta	< 1	18	< 1	< 1	12	< 1	n.d.	< 1	< 2
W	50	19	38	10	8	32	n.d.	17	196
Hg	< 1	< 1	2	2	2	3	n.d.	3	< 1.0
Pb	15	15	17	21	17	17	n.d.	19	5
Bi	3	< 1	1	2	< 1	2	n.d.	1	< 1
Th	5.8	4.2	4.4	2.8	6	5.5	n.d.	6.4	2.1
U	2.8	1.9	2.8	1.1	1.3	0.7	n.d.	1.9	< 1

Table A2.7. Continued.

Sample	TT11	TT12	TT13	TT14	TT15	TT16	TT17	TT18	TT19	TT20
Facies	Pa	Pa	Pa	Pa	Fm	Pa	Pa	Pa	Tm	Pa
Major elements (Wt %)										
SiO_2	48.35	52.75	55.31	52.78	52.24	53.43	55.95	53.81	60.31	57.68
TiO_2	0.65	0.82	0.78	0.84	0.70	0.69	0.65	0.73	0.52	0.66
Al_2O_3	15.92	18.87	15.84	18.65	19.45	16.22	15.96	17.38	14.20	15.99
Fe_2O_3	6.07	7.84	7.25	7.79	7.33	6.57	6.65	6.08	4.77	6.37
MnO	0.09	0.15	0.18	0.25	0.16	0.45	0.03	0.05	0.04	0.04
MgO	1.44	1.83	0.05	1.78	2.52	0.72	1.62	1.74	1.58	1.39
CaO	9.45	2.35	3.12	2.76	5.93	2.75	3.15	2.79	2.65	3.71
Na_2O	2.82	0.02	0.84	< 0.020	0.88	0.27	0.02	0.02	0.02	0.14
K_2O	0.44	0.30	0.22	0.30	0.21	0.22	0.26	0.33	0.29	0.38
P_2O_5	4.16	0.07	0.07	0.12	0.35	0.07	0.24	0.09	0.11	0.13
S	0.10	0.09	0.05	0.14	0.04	0.07	0.06	0.08	0.05	0.06
LOI	13.02	17.70	14.79	17.52	13.07	17.22	17.41	19.09	16.63	14.96
Total	102.50	102.79	98.49	102.91	102.89	98.66	102.00	102.17	101.16	101.50
Trace elements (ppm)										
Cl	9	12	52	43	29	22	43	35	48	46
V	109	129	120	156	179	94	331	244	170	269
Cr	n.d.	n.d.	n.d.	n.d.	n.d.	n.d.	n.d.	n.d.	n.d.	n.d.
Co	13	20	18	16	15	28	8	8	5	11
Ni	n.d.	n.d.	n.d.	n.d.	n.d.	n.d.	n.d.	n.d.	n.d.	n.d.
Cu	66	70	60	79	64	83	67	68	49	50
Zn	72	76	88	87	79	75	71	75	75	74
Ga	16	16	14	15	15	16	13	15	12	14
Ge	1	1	1	1	< 1	2	1	3	1	< 1
As	26	27	21	29	18	16	11	12	8	8
Se	0.4	0.3	0.2	0.2	0.2	0.3	0.2	0.3	0.2	0.2
Br	< 1	< 1	< 1	< 1	< 1	< 1	0.4	< 1	< 1	< 1
Rb	25	22	15	22	10	17	20	29	22	33
Sr	164	164	191	177	258	178	188	190	172	204
Y	21	21	20	17	22	15	28	21	13	14
Zr	84	89	69	86	42	61	64	82	78	67
Nb	2	2	1	2	0.4	1	2	2	2	1
Mo	n.d.	n.d.	n.d.	n.d.	n.d.	n.d.	n.d.	n.d.	n.d.	n.d.
Cd	n.d.	n.d.	n.d.	n.d.	n.d.	n.d.	n.d.	n.d.	n.d.	n.d.
Sn	< 3	1	< 3	1	< 3	< 3	< 3	< 3	2	< 3
Sb	< 3	< 3	< 3	2	2	< 3	< 3	< 3	< 3	< 3
Cs	< 4	n.d.	< 4	n.d.	n.d.	< 4	< 4	< 4	n.d.	< 4
Ba	95	216	176	252	154	425	114	118	94	97
La	< 2	< 2	< 2	12	< 2	< 2	< 2	28	< 2	6
Ce	< 2	14	24	< 2	< 2	< 2	28	< 2	< 2	16
Hf	n.d.	5	n.d.	4	3	n.d.	n.d.	n.d.	4	n.d.
Ta	< 2	7	4	10	3	< 2	8	6	6	< 2
W	2	1	< 1	< 1	< 1	5	< 1	1	< 1	< 1
Hg	1	1	1	2	1	1	2	< 1	2	2
Pb	8	10	7	12	5	7	8	9	12	9
Bi	n.d.	n.d.	n.d.	n.d.	n.d.	n.d.	n.d.	n.d.	n.d.	n.d.
Th	3.1	3.4	2.1	2.9	1.5	1.9	2.6	3.6	4.3	2.6
U	0.8	0.9	0.9	0.7	1.1	0.4	1.0	1.1	1.0	0.5

Table A2.7. Continued.

Sample	TT21	TT22	TT23	TT24	TT25	TT26	TT27	TT28	TT29	TT30
Facies	Sl	Pa	Pa	Pa	Pv	Tmp	LTmp	Trma	Ts	LTmp
Major elements (Wt %)										
SiO_2	57.49	56.34	51.76	55.56	53.63	56.05	63.32	65.91	66.57	67.56
TiO_2	0.87	0.73	0.73	0.85	0.40	0.38	0.32	0.31	0.29	0.23
Al_2O_3	17.76	17.17	15.48	15.84	17.01	16.58	15.06	14.71	13.86	13.98
Fe_2O_3	7.68	6.92	6.93	6.54	3.91	3.42	2.91	2.89	2.39	1.76
MnO	0.08	0.16	0.04	0.05	0.40	0.16	0.09	0.08	0.07	0.07
MgO	2.42	1.07	2.12	1.95	3.46	2.77	1.04	0.86	0.89	1.00
CaO	5.76	3.07	1.83	1.99	2.68	2.61	2.74	2.38	2.51	2.35
Na_2O	0.51	0.02	0.02	0.02	0.02	0.02	0.49	0.67	1.97	2.37
K_2O	0.58	0.30	0.43	0.39	0.40	0.53	1.75	2.11	2.26	2.31
P_2O_5	0.11	0.08	0.09	0.08	0.08	0.11	0.14	0.14	0.04	0.03
S	0.11	0.17	0.16	0.11	0.00	0.02	0.01	0.02	0.03	0.02
LOI	8.76	16.80	20.27	18.11	20.78	19.41	11.17	10.34	8.34	8.44
Total	102.12	102.82	99.86	101.50	102.77	102.05	99.04	100.43	99.21	100.12
Trace elements (ppm)										
Cl	124	83	12	18	4	57	606	638	651	710
V	215	158	203	274	117	207	41	44	43	36
Cr	n.d.	n.d.	n.d.	n.d.	n.d.	n.d.	n.d.	n.d.	7	3
Co	17	28	23	15	44	28	< 5	< 5	26	20
Ni	n.d.	n.d.	n.d.	n.d.	n.d.	n.d.	n.d.	n.d.	4	2
Cu	50	70	57	49	15	17	11	11	11	6
Zn	76	68	65	70	65	69	55	50	28	21
Ga	16	15	14	15	16	18	15	12	13	12
Ge	< 1	2	< 1	< 1	1	1	1	1	1	< 1
As	27	37	15	11	2	2	4	6	3	2
Se	0.4	0.3	0.3	0.3	0.3	0.3	0.3	0.4	< 1	< 1
Br	0.4	1	1	< 1	< 1	< 1	1	1	1	1
Rb	31	21	29	22	16	20	65	71	80	75
Sr	300	235	223	203	196	189	212	212	209	202
Y	18	30	32	26	18	20	16	17	16	15
Zr	81	85	107	122	130	136	114	115	118	120
Nb	1	1	2	3	3	3	3	3	3	3
Mo	n.d.	n.d.	n.d.	n.d.	n.d.	n.d.	n.d.	n.d.	< 1	< 1
Cd	n.d.	n.d.	n.d.	n.d.	n.d.	n.d.	n.d.	n.d.	< 2	< 2
Sn	0	1	< 3	3	3	2	< 3	< 3	3	4
Sb	3	2	< 3	< 3	< 3	< 3	< 3	< 3	< 3	< 3
Cs	n.d.	n.d.	< 4	n.d.	n.d.	n.d.	< 4	< 4	< 4	< 4
Ba	168	352	140	172	457	283	327	403	378	370
La	< 2	7	16	25	19	9	17	21	10	25
Ce	18	29	< 2	54	46	37	36	34	< 2	< 2
Hf	3	5	n.d.	5	4	3	n.d.	n.d.	3	3
Ta	2	5	8	4	< 1	< 1	< 2	2	3	< 2
W	< 1	2	1	2	1	2	< 1	< 1	141	116
Hg	2	1	1	1	1	1	1	1	2	2
Pb	11	17	12	13	20	22	15	13	12	12
Bi	n.d.	n.d.	n.d.	n.d.	n.d.	n.d.	n.d.	n.d.	< 1	< 1
Th	3.6	2.5	5.0	5.0	8.1	9.1	8.2	7.9	6.8	7.4
U	1.4	< 0.5	0.9	0.4	< 0.5	0.6	1.9	1.7	1.5	1.7

Table A2.8. Major-and trace-element composition of samples from Pumaso.

Sample	PM-01	PM-02	PM-03	PM-04	PM-05	PM-06	PM-07	PM-08	PM-09	PM-10
Facies	Tm	Sl	Sl	Sl	Sl	Tms	Tmp	Tma	Tmp	LTmp
Major elements (Wt %)										
SiO_2	65.49	55.25	54.41	51.85	50.66	60.55	64.12	61.50	63.42	64.61
TiO_2	0.21	0.89	0.88	0.84	0.85	0.31	0.34	0.31	0.32	0.29
Al_2O_3	16.53	19.50	20.13	21.21	21.18	16.54	16.06	16.97	16.22	16.05
Fe_2O_3	1.73	8.45	8.36	9.36	10.42	3.14	3.33	3.03	3.15	3.01
MnO	0.06	0.12	0.13	0.10	0.08	0.19	0.14	0.11	0.16	0.09
MgO	1.83	1.90	1.97	2.03	2.57	2.11	1.18	2.35	1.65	1.17
CaO	1.84	5.01	5.01	4.39	4.83	2.22	2.48	2.25	2.32	2.28
Na_2O	1.76	2.23	2.27	1.41	1.41	1.21	1.86	1.13	1.54	1.95
K_2O	1.98	0.53	0.48	0.33	0.33	1.41	1.77	1.38	1.78	1.91
P_2O_5	0.02	0.08	0.08	0.02	0.05	0.02	0.06	0.02	0.05	0.05
SO_3	0.04	0.06	0.06	0.02	0.05	0.01	0.03	0.05	0.02	0.03
LOI	8.34	5.85	6.12	8.33	7.45	12.16	8.45	10.76	9.20	8.38
Total	99.83	99.85	99.89	99.88	99.87	99.86	99.81	99.85	99.82	99.82
Trace elements (ppm)										
Cl	n.d.	n.d.	n.d.	n.d.	n.d.	n.d.	n.d.	n.d.	n.d.	n.d.
V	n.d.	n.d.	n.d.	n.d.	n.d.	n.d.	n.d.	n.d.	n.d.	n.d.
Cr	n.d.	n.d.	n.d.	n.d.	n.d.	n.d.	n.d.	n.d.	n.d.	n.d.
Co	n.d.	n.d.	n.d.	n.d.	n.d.	n.d.	n.d.	n.d.	n.d.	n.d.
Ni	n.d.	n.d.	n.d.	n.d.	n.d.	n.d.	n.d.	n.d.	n.d.	n.d.
Cu	n.d.	n.d.	n.d.	n.d.	n.d.	n.d.	n.d.	n.d.	n.d.	n.d.
Zn	n.d.	n.d.	n.d.	n.d.	n.d.	n.d.	n.d.	n.d.	n.d.	n.d.
Ga	n.d.	n.d.	n.d.	n.d.	n.d.	n.d.	n.d.	n.d.	n.d.	n.d.
Ge	n.d.	n.d.	n.d.	n.d.	n.d.	n.d.	n.d.	n.d.	n.d.	n.d.
As	n.d.	n.d.	n.d.	n.d.	n.d.	n.d.	n.d.	n.d.	n.d.	n.d.
Se	n.d.	n.d.	n.d.	n.d.	n.d.	n.d.	n.d.	n.d.	n.d.	n.d.
Br	n.d.	n.d.	n.d.	n.d.	n.d.	n.d.	n.d.	n.d.	n.d.	n.d.
Rb	n.d.	n.d.	n.d.	n.d.	n.d.	n.d.	n.d.	n.d.	n.d.	n.d.
Sr	n.d.	n.d.	n.d.	n.d.	n.d.	n.d.	n.d.	n.d.	n.d.	n.d.
Y	n.d.	n.d.	n.d.	n.d.	n.d.	n.d.	n.d.	n.d.	n.d.	n.d.
Zr	n.d.	n.d.	n.d.	n.d.	n.d.	n.d.	n.d.	n.d.	n.d.	n.d.
Nb	n.d.	n.d.	n.d.	n.d.	n.d.	n.d.	n.d.	n.d.	n.d.	n.d.
Mo	n.d.	n.d.	n.d.	n.d.	n.d.	n.d.	n.d.	n.d.	n.d.	n.d.
Cd	n.d.	n.d.	n.d.	n.d.	n.d.	n.d.	n.d.	n.d.	n.d.	n.d.
Sn	n.d.	n.d.	n.d.	n.d.	n.d.	n.d.	n.d.	n.d.	n.d.	n.d.
Sb	n.d.	n.d.	n.d.	n.d.	n.d.	n.d.	n.d.	n.d.	n.d.	n.d.
Cs	n.d.	n.d.	n.d.	n.d.	n.d.	n.d.	n.d.	n.d.	n.d.	n.d.
Ba	n.d.	n.d.	n.d.	n.d.	n.d.	n.d.	n.d.	n.d.	n.d.	n.d.
La	n.d.	n.d.	n.d.	n.d.	n.d.	n.d.	n.d.	n.d.	n.d.	n.d.
Ce	n.d.	n.d.	n.d.	n.d.	n.d.	n.d.	n.d.	n.d.	n.d.	n.d.
Hf	n.d.	n.d.	n.d.	n.d.	n.d.	n.d.	n.d.	n.d.	n.d.	n.d.
Ta	n.d.	n.d.	n.d.	n.d.	n.d.	n.d.	n.d.	n.d.	n.d.	n.d.
W	n.d.	n.d.	n.d.	n.d.	n.d.	n.d.	n.d.	n.d.	n.d.	n.d.
Hg	n.d.	n.d.	n.d.	n.d.	n.d.	n.d.	n.d.	n.d.	n.d.	n.d.
Pb	n.d.	n.d.	n.d.	n.d.	n.d.	n.d.	n.d.	n.d.	n.d.	n.d.
Bi	n.d.	n.d.	n.d.	n.d.	n.d.	n.d.	n.d.	n.d.	n.d.	n.d.
Th	n.d.	n.d.	n.d.	n.d.	n.d.	n.d.	n.d.	n.d.	n.d.	n.d.
U	n.d.	n.d.	n.d.	n.d.	n.d.	n.d.	n.d.	n.d.	n.d.	n.d.

Table A2.8. Continued.

Sample	PM-11	PM-12	PM-13	PM-14	PM-15	PM-16	PM-17	PM-18	PM-19	PM-20
Facies	LTmp	LTmp	Trma	Pa	Ts	LTmp	Trmp	Tm	Tm	Tm
Major elements (Wt %)										
SiO_2	66.21	63.57	63.15	57.55	66.57	68.07	65.97	66.28	53.29	52.55
TiO_2	0.25	0.36	0.28	0.49	0.21	0.20	0.21	0.62	0.578	0.486
Al_2O_3	15.36	16.10	16.55	19.57	15.15	15.07	15.53	14.34	22.22	23.83
Fe_2O_3	2.26	3.61	2.92	3.63	1.65	1.69	1.63	4.12	7.99	7.25
MnO	0.08	0.11	0.08	0.05	0.07	0.07	0.07	0.17	0.236	0.198
MgO	1.08	1.55	2.48	2.29	1.03	0.74	1.76	1.32	3.03	2.76
CaO	2.33	3.27	2.06	2.55	2.04	2.00	2.20	3.88	7.57	8.13
Na_2O	2.19	2.03	1.18	0.99	2.02	2.52	1.97	2.46	2.48	2.58
K_2O	2.03	1.70	1.66	0.64	2.24	2.25	1.89	1.84	0.199	0.175
P_2O_5	0.06	0.08	0.02	0.01	0.02	0.04	0.04	0.16	0.138	0.0564
SO_3	0.02	0.02	0.07	0.04	0.01	0.01	0.02	0.02	0.0461	0.0229
LOI	7.92	7.37	9.40	12.10	8.82	7.10	8.54	5.26	2.09	1.85
Total	99.79	99.78	99.86	99.91	99.83	99.78	99.83	100.47	99.867	99.888
Trace elements (ppm)										
Cl	n.d.	n.d.	n.d.	n.d.	n.d.	n.d.	n.d.	n.d.	n.d.	n.d.
V	n.d.	n.d.	n.d.	n.d.	n.d.	n.d.	n.d.	n.d.	n.d.	n.d.
Cr	n.d.	n.d.	n.d.	n.d.	n.d.	n.d.	n.d.	n.d.	n.d.	n.d.
Co	n.d.	n.d.	n.d.	n.d.	n.d.	n.d.	n.d.	n.d.	n.d.	n.d.
Ni	n.d.	n.d.	n.d.	n.d.	n.d.	n.d.	n.d.	n.d.	n.d.	n.d.
Cu	n.d.	n.d.	n.d.	n.d.	n.d.	n.d.	n.d.	n.d.	n.d.	n.d.
Zn	n.d.	n.d.	n.d.	n.d.	n.d.	n.d.	n.d.	n.d.	n.d.	n.d.
Ga	n.d.	n.d.	n.d.	n.d.	n.d.	n.d.	n.d.	n.d.	n.d.	n.d.
Ge	n.d.	n.d.	n.d.	n.d.	n.d.	n.d.	n.d.	n.d.	n.d.	n.d.
As	n.d.	n.d.	n.d.	n.d.	n.d.	n.d.	n.d.	n.d.	n.d.	n.d.
Se	n.d.	n.d.	n.d.	n.d.	n.d.	n.d.	n.d.	n.d.	n.d.	n.d.
Br	n.d.	n.d.	n.d.	n.d.	n.d.	n.d.	n.d.	n.d.	n.d.	n.d.
Rb	n.d.	n.d.	n.d.	n.d.	n.d.	n.d.	n.d.	n.d.	n.d.	n.d.
Sr	n.d.	n.d.	n.d.	n.d.	n.d.	n.d.	n.d.	n.d.	n.d.	n.d.
Y	n.d.	n.d.	n.d.	n.d.	n.d.	n.d.	n.d.	n.d.	n.d.	n.d.
Zr	n.d.	n.d.	n.d.	n.d.	n.d.	n.d.	n.d.	n.d.	n.d.	n.d.
Nb	n.d.	n.d.	n.d.	n.d.	n.d.	n.d.	n.d.	n.d.	n.d.	n.d.
Mo	n.d.	n.d.	n.d.	n.d.	n.d.	n.d.	n.d.	n.d.	n.d.	n.d.
Cd	n.d.	n.d.	n.d.	n.d.	n.d.	n.d.	n.d.	n.d.	n.d.	n.d.
Sn	n.d.	n.d.	n.d.	n.d.	n.d.	n.d.	n.d.	n.d.	n.d.	n.d.
Sb	n.d.	n.d.	n.d.	n.d.	n.d.	n.d.	n.d.	n.d.	n.d.	n.d.
Cs	n.d.	n.d.	n.d.	n.d.	n.d.	n.d.	n.d.	n.d.	n.d.	n.d.
Ba	n.d.	n.d.	n.d.	n.d.	n.d.	n.d.	n.d.	n.d.	n.d.	n.d.
La	n.d.	n.d.	n.d.	n.d.	n.d.	n.d.	n.d.	n.d.	n.d.	n.d.
Ce	n.d.	n.d.	n.d.	n.d.	n.d.	n.d.	n.d.	n.d.	n.d.	n.d.
Hf	n.d.	n.d.	n.d.	n.d.	n.d.	n.d.	n.d.	n.d.	n.d.	n.d.
Ta	n.d.	n.d.	n.d.	n.d.	n.d.	n.d.	n.d.	n.d.	n.d.	n.d.
W	n.d.	n.d.	n.d.	n.d.	n.d.	n.d.	n.d.	n.d.	n.d.	n.d.
Hg	n.d.	n.d.	n.d.	n.d.	n.d.	n.d.	n.d.	n.d.	n.d.	n.d.
Pb	n.d.	n.d.	n.d.	n.d.	n.d.	n.d.	n.d.	n.d.	n.d.	n.d.
Bi	n.d.	n.d.	n.d.	n.d.	n.d.	n.d.	n.d.	n.d.	n.d.	n.d.
Th	n.d.	n.d.	n.d.	n.d.	n.d.	n.d.	n.d.	n.d.	n.d.	n.d.
U	n.d.	n.d.	n.d.	n.d.	n.d.	n.d.	n.d.	n.d.	n.d.	n.d.

Table A2.8. Continued.

Sample	PM-21	PM-22	PM-23	PM-24	PM-25	PM-26	PM-27	PM-28	PM-29	PM-30
Facies	Tm	Tm	Tm	Tm	Tm	Tm	Tm	Tm	Tm	Tm
Major elements (Wt %)										
SiO_2	50.55	52.60	50.54	48.34	49.77	50.04	48.41	53.52	49.17	43.94
TiO_2	0.32	0.51	0.65	0.60	0.67	0.63	0.64	0.63	0.59	0.60
Al_2O_3	15.29	24.20	19.28	23.21	23.02	23.16	23.18	21.25	23.54	16.93
Fe_2O_3	10.91	6.38	7.48	9.63	9.09	8.62	9.89	8.16	9.05	14.87
MnO	0.07	0.17	0.16	0.34	0.20	0.18	0.20	0.16	0.18	0.23
MgO	0.79	2.41	2.87	4.61	4.07	4.14	5.00	3.69	4.21	6.48
CaO	2.63	8.14	6.05	8.75	8.91	8.80	8.83	7.38	9.16	11.68
Na_2O	0.84	2.40	2.44	2.11	2.29	2.49	2.17	2.58	2.32	1.65
K_2O	0.14	0.20	0.30	0.12	0.17	0.18	0.13	0.28	0.16	0.24
P_2O_5	0.01	0.08	0.11	0.05	0.03	0.06	0.05	0.08	0.06	0.04
SO_3	0.02	0.27	0.94	0.09	0.13	0.18	0.15	0.17	0.18	0.12
LOI	17.63	2.52	9.05	1.99	1.49	1.33	1.19	1.95	1.21	3.14
Total	99.20	99.88	99.86	99.83	99.84	99.81	99.84	99.85	99.83	99.92
Trace elements (ppm)										
Cl	n.d.	n.d.	n.d.	n.d.	n.d.	n.d.	n.d.	n.d.	n.d.	n.d.
V	n.d.	n.d.	n.d.	n.d.	n.d.	n.d.	n.d.	n.d.	n.d.	n.d.
Cr	n.d.	n.d.	n.d.	n.d.	n.d.	n.d.	n.d.	n.d.	n.d.	n.d.
Co	n.d.	n.d.	n.d.	n.d.	n.d.	n.d.	n.d.	n.d.	n.d.	n.d.
Ni	n.d.	n.d.	n.d.	n.d.	n.d.	n.d.	n.d.	n.d.	n.d.	n.d.
Cu	n.d.	n.d.	n.d.	n.d.	n.d.	n.d.	n.d.	n.d.	n.d.	n.d.
Zn	n.d.	n.d.	n.d.	n.d.	n.d.	n.d.	n.d.	n.d.	n.d.	n.d.
Ga	n.d.	n.d.	n.d.	n.d.	n.d.	n.d.	n.d.	n.d.	n.d.	n.d.
Ge	n.d.	n.d.	n.d.	n.d.	n.d.	n.d.	n.d.	n.d.	n.d.	n.d.
As	n.d.	n.d.	n.d.	n.d.	n.d.	n.d.	n.d.	n.d.	n.d.	n.d.
Se	n.d.	n.d.	n.d.	n.d.	n.d.	n.d.	n.d.	n.d.	n.d.	n.d.
Br	n.d.	n.d.	n.d.	n.d.	n.d.	n.d.	n.d.	n.d.	n.d.	n.d.
Rb	n.d.	n.d.	n.d.	n.d.	n.d.	n.d.	n.d.	n.d.	n.d.	n.d.
Sr	n.d.	n.d.	n.d.	n.d.	n.d.	n.d.	n.d.	n.d.	n.d.	n.d.
Y	n.d.	n.d.	n.d.	n.d.	n.d.	n.d.	n.d.	n.d.	n.d.	n.d.
Zr	n.d.	n.d.	n.d.	n.d.	n.d.	n.d.	n.d.	n.d.	n.d.	n.d.
Nb	n.d.	n.d.	n.d.	n.d.	n.d.	n.d.	n.d.	n.d.	n.d.	n.d.
Mo	n.d.	n.d.	n.d.	n.d.	n.d.	n.d.	n.d.	n.d.	n.d.	n.d.
Cd	n.d.	n.d.	n.d.	n.d.	n.d.	n.d.	n.d.	n.d.	n.d.	n.d.
Sn	n.d.	n.d.	n.d.	n.d.	n.d.	n.d.	n.d.	n.d.	n.d.	n.d.
Sb	n.d.	n.d.	n.d.	n.d.	n.d.	n.d.	n.d.	n.d.	n.d.	n.d.
Cs	n.d.	n.d.	n.d.	n.d.	n.d.	n.d.	n.d.	n.d.	n.d.	n.d.
Ba	n.d.	n.d.	n.d.	n.d.	n.d.	n.d.	n.d.	n.d.	n.d.	n.d.
La	n.d.	n.d.	n.d.	n.d.	n.d.	n.d.	n.d.	n.d.	n.d.	n.d.
Ce	n.d.	n.d.	n.d.	n.d.	n.d.	n.d.	n.d.	n.d.	n.d.	n.d.
Hf	n.d.	n.d.	n.d.	n.d.	n.d.	n.d.	n.d.	n.d.	n.d.	n.d.
Ta	n.d.	n.d.	n.d.	n.d.	n.d.	n.d.	n.d.	n.d.	n.d.	n.d.
W	n.d.	n.d.	n.d.	n.d.	n.d.	n.d.	n.d.	n.d.	n.d.	n.d.
Hg	n.d.	n.d.	n.d.	n.d.	n.d.	n.d.	n.d.	n.d.	n.d.	n.d.
Pb	n.d.	n.d.	n.d.	n.d.	n.d.	n.d.	n.d.	n.d.	n.d.	n.d.
Bi	n.d.	n.d.	n.d.	n.d.	n.d.	n.d.	n.d.	n.d.	n.d.	n.d.
Th	n.d.	n.d.	n.d.	n.d.	n.d.	n.d.	n.d.	n.d.	n.d.	n.d.
U	n.d.	n.d.	n.d.	n.d.	n.d.	n.d.	n.d.	n.d.	n.d.	n.d.

Table A2.8. Continued.

Sample Facies	PM-31 Tm	PM-32 Tm	PM-33 Tm	PM-34 Tm	PM-35 Tm	PM-36 Tm	PM-37 Tm	PM-38 Tm	PM-39 Tm	PM-40 Tm	PM-41 Tm
Major elements (Wt %)											
SiO_2	50.80	59.63	40.35	33.92	62.14	51.21	45.40	31.85	41.90	60.15	54.26
TiO_2	0.57	0.57	0.42	0.51	0.51	0.62	0.84	0.52	0.68	0.53	0.63
Al_2O_3	22.70	17.54	18.61	14.46	17.26	22.81	16.47	15.92	15.95	17.37	20.26
Fe_2O_3	9.32	7.01	6.30	6.92	4.89	8.40	11.75	5.51	8.80	6.09	8.38
MnO	0.15	0.11	0.13	0.12	0.11	0.17	0.16	0.08	0.18	0.16	0.18
MgO	2.92	1.48	2.01	1.78	1.44	3.26	4.23	1.12	2.85	1.63	2.56
CaO	6.46	4.28	21.15	24.80	4.66	8.18	11.58	26.71	18.01	5.20	7.11
Na_2O	1.86	2.37	1.70	1.76	2.71	2.37	2.58	1.57	1.87	2.76	2.67
K_2O	0.25	0.49	0.16	0.22	0.61	0.23	0.51	0.31	0.20	0.60	0.41
P_2O_5	0.10	0.14	0.05	0.07	0.06	0.05	0.10	0.08	0.03	0.09	0.07
SO_3	0.08	0.03	0.10	1.12	0.11	0.16	0.02	0.19	0.03	0.53	0.53
LOI	4.65	6.16	8.89	14.19	5.34	2.39	4.72	16.02	9.36	4.72	2.79
Total	99.85	99.81	99.88	99.88	99.83	99.85	98.36	99.86	99.85	99.83	99.85
Trace elements (ppm)											
Cl	n.d.	n.d.	n.d.	n.d.	n.d.	n.d.	n.d.	n.d.	n.d.	n.d.	n.d.
V	n.d.	n.d.	n.d.	n.d.	n.d.	n.d.	n.d.	n.d.	n.d.	n.d.	n.d.
Cr	n.d.	n.d.	n.d.	n.d.	n.d.	n.d.	n.d.	n.d.	n.d.	n.d.	n.d.
Co	n.d.	n.d.	n.d.	n.d.	n.d.	n.d.	n.d.	n.d.	n.d.	n.d.	n.d.
Ni	n.d.	n.d.	n.d.	n.d.	n.d.	n.d.	n.d.	n.d.	n.d.	n.d.	n.d.
Cu	n.d.	n.d.	n.d.	n.d.	n.d.	n.d.	n.d.	n.d.	n.d.	n.d.	n.d.
Zn	n.d.	n.d.	n.d.	n.d.	n.d.	n.d.	n.d.	n.d.	n.d.	n.d.	n.d.
Ga	n.d.	n.d.	n.d.	n.d.	n.d.	n.d.	n.d.	n.d.	n.d.	n.d.	n.d.
Ge	n.d.	n.d.	n.d.	n.d.	n.d.	n.d.	n.d.	n.d.	n.d.	n.d.	n.d.
As	n.d.	n.d.	n.d.	n.d.	n.d.	n.d.	n.d.	n.d.	n.d.	n.d.	n.d.
Se	n.d.	n.d.	n.d.	n.d.	n.d.	n.d.	n.d.	n.d.	n.d.	n.d.	n.d.
Br	n.d.	n.d.	n.d.	n.d.	n.d.	n.d.	n.d.	n.d.	n.d.	n.d.	n.d.
Rb	n.d.	n.d.	n.d.	n.d.	n.d.	n.d.	n.d.	n.d.	n.d.	n.d.	n.d.
Sr	n.d.	n.d.	n.d.	n.d.	n.d.	n.d.	n.d.	n.d.	n.d.	n.d.	n.d.
Y	n.d.	n.d.	n.d.	n.d.	n.d.	n.d.	n.d.	n.d.	n.d.	n.d.	n.d.
Zr	n.d.	n.d.	n.d.	n.d.	n.d.	n.d.	n.d.	n.d.	n.d.	n.d.	n.d.
Nb	n.d.	n.d.	n.d.	n.d.	n.d.	n.d.	n.d.	n.d.	n.d.	n.d.	n.d.
Mo	n.d.	n.d.	n.d.	n.d.	n.d.	n.d.	n.d.	n.d.	n.d.	n.d.	n.d.
Cd	n.d.	n.d.	n.d.	n.d.	n.d.	n.d.	n.d.	n.d.	n.d.	n.d.	n.d.
Sn	n.d.	n.d.	n.d.	n.d.	n.d.	n.d.	n.d.	n.d.	n.d.	n.d.	n.d.
Sb	n.d.	n.d.	n.d.	n.d.	n.d.	n.d.	n.d.	n.d.	n.d.	n.d.	n.d.
Cs	n.d.	n.d.	n.d.	n.d.	n.d.	n.d.	n.d.	n.d.	n.d.	n.d.	n.d.
Ba	n.d.	n.d.	n.d.	n.d.	n.d.	n.d.	n.d.	n.d.	n.d.	n.d.	n.d.
La	n.d.	n.d.	n.d.	n.d.	n.d.	n.d.	n.d.	n.d.	n.d.	n.d.	n.d.
Ce	n.d.	n.d.	n.d.	n.d.	n.d.	n.d.	n.d.	n.d.	n.d.	n.d.	n.d.
Hf	n.d.	n.d.	n.d.	n.d.	n.d.	n.d.	n.d.	n.d.	n.d.	n.d.	n.d.
Ta	n.d.	n.d.	n.d.	n.d.	n.d.	n.d.	n.d.	n.d.	n.d.	n.d.	n.d.
W	n.d.	n.d.	n.d.	n.d.	n.d.	n.d.	n.d.	n.d.	n.d.	n.d.	n.d.
Hg	n.d.	n.d.	n.d.	n.d.	n.d.	n.d.	n.d.	n.d.	n.d.	n.d.	n.d.
Pb	n.d.	n.d.	n.d.	n.d.	n.d.	n.d.	n.d.	n.d.	n.d.	n.d.	n.d.
Bi	n.d.	n.d.	n.d.	n.d.	n.d.	n.d.	n.d.	n.d.	n.d.	n.d.	n.d.
Th	n.d.	n.d.	n.d.	n.d.	n.d.	n.d.	n.d.	n.d.	n.d.	n.d.	n.d.
U	n.d.	n.d.	n.d.	n.d.	n.d.	n.d.	n.d.	n.d.	n.d.	n.d.	n.d.

Table A2.9. Major-and trace-element compositions of samples from Lowo Mali.

Sample	LM-01	LM-02	LM-03	LM-04	LM-05	LM-06	LM-07	LM-08	LM-09	LM-10
Facies	Pa	Tm	Ts	LTmp	Tms	Tmp	Tma	Tmp	LTmp	Pa
Major elements (Wt %)										
SiO_2	65.54	59.21	59.50	50.84	60.26	62.15	64.56	65.00	69.55	61.81
TiO_2	0.47	0.78	0.76	1.13	0.35	0.43	0.35	0.36	0.21	0.49
Al_2O_3	10.63	15.97	16.24	21.48	15.22	16.04	14.48	14.05	13.19	16.17
Fe_2O_3	5.21	5.82	5.72	8.41	3.30	4.26	3.39	3.36	1.64	4.58
MnO	0.11	0.14	0.14	0.05	0.08	0.08	0.08	0.09	0.08	0.17
MgO	1.52	1.57	1.51	0.99	1.67	1.02	1.15	0.98	0.63	1.08
CaO	1.82	4.89	4.67	2.42	2.25	2.53	2.44	2.57	2.13	2.72
Na_2O	0.68	3.07	3.04	1.24	1.23	1.79	1.55	1.98	2.34	1.75
K_2O	0.24	1.12	1.20	0.22	1.57	1.67	1.97	2.20	2.49	1.49
P_2O_5	0.04	0.17	0.16	0.02	0.01	0.03	0.04	0.03	0.03	0.03
SO_3	0.04	0.01	0.03	0.01	0.01	0.05	0.07	0.02	0.01	0.06
LOI	12.71	6.29	6.07	12.69	12.65	9.47	9.59	8.42	7.32	9.56
Total	99.00	99.04	99.04	99.51	98.61	99.51	99.66	99.07	99.62	99.91
Trace elements (ppm)										
Cl	33	662	698	< 2	483	674	650	712	948	306
V	66	91	81	159	54	81	61	59	18	84
Cr	15	5	10	23	5	5	6	3	2	14
Co	27	30	28	18	12	22	15	31	23	19
Ni	14	6	8	12	5	4	4	4	2	8
Cu	46	14	19	32	16	13	13	15	6	36
Zn	90	55	57	62	59	43	51	49	22	80
Ga	10	16	16	23	15	15	14	13	12	15
Ge	1	2	1	3	2	1	< 1	< 1	1	2
As	2	4	4	13	2	5	5	6	2	5
Se	< 1	< 1	< 1	< 1	< 1	< 1	< 1	< 1	< 1	< 1
Br	< 1	3	3	< 1	2	5	1	2	3	1
Rb	14	30	30	10	54	63	61	75	75	66
Sr	111	243	238	156	195	209	242	221	205	218
Y	23	38	39	34	12	16	14	16	13	22
Zr	47	140	151	164	130	115	118	108	110	123
Nb	1	3	3	4	3	3	3	3	3	3
Mo	< 1	< 1	< 1	< 1	< 1	< 1	< 1	< 1	< 1	< 1
Cd	< 2	< 2	< 2	< 2	< 2	< 2	< 2	< 2	< 2	< 2
Sn	2	< 3	< 3	< 3	3	5	3	< 3	3	2
Sb	< 3	< 3	< 3	< 3	< 3	< 3	< 3	< 3	< 3	< 3
Cs	< 4	< 4	< 4	< 4	< 4	< 4	< 4	< 4	< 4	< 4
Ba	215	246	288	136	343	355	410	397	424	349
La	< 2	< 2	< 2	36	13	16	27	26	< 2	15
Ce	15	31	13	5	< 2	30	< 2	31	29	25
Hf	2	4	5	6	3	3	3	4	2	4
Ta	3	1	2	2	1	< 2	2	2	3	2
W	15	104	113	20	23	63	49	96	123	30
Hg	2	< 1.0	< 1.0	< 1.0	0	1	1	< 1.0	< 1.0	< 1.0
Pb	4	9	10	8	13	14	18	16	11	16
Bi	< 1	< 1	< 1	< 1	< 1	< 1	< 1	< 1	< 1	< 1
Th	0.4	3.4	3.9	4.1	8.9	7	7.4	6.8	8.5	8.1
U	< 1	< 1	1.1	< 1	1.1	1.7	1.2	1.8	2.2	< 1

Table A2.9. Continued.

Sample	LM-11	LM-12	LM-13	LM-14
Facies	Ts	LTmp	Tm	Tm
Major elements (Wt %)				
SiO_2	69.64	72.04	62.69	65.41
TiO_2	0.21	0.20	0.24	0.56
Al_2O_3	12.84	13.25	14.99	14.89
Fe_2O_3	1.63	1.41	1.80	4.42
MnO	0.07	0.07	0.12	0.10
MgO	0.37	0.36	1.66	1.56
CaO	2.06	2.03	1.50	4.02
Na_2O	2.03	3.07	1.46	2.61
K_2O	2.84	2.64	3.27	1.92
P_2O_5	0.03	0.02	0.01	0.13
SO_3	0.01	0.01	0.01	0.02
LOI	7.17	5.67	11.57	4.6
Total	98.90	100.77	99.32	100.25
Trace elements (ppm)				
Cl	945	855	1064	995
V	18	13	138	92
Cr	3	2	< 1	3
Co	35	27	27	45
Ni	2	4	9	4
Cu	8	6	17	14
Zn	26	18	47	22
Ga	12	12	15	16
Ge	1	1	3	1
As	3	2	3	1
Se	< 1	< 1	< 1	< 1
Br	2	2	4	2
Rb	85	77	195	50
Sr	190	186	166	348
Y	14	13	20	23
Zr	117	117	235	112
Nb	3	3	11	2
Mo	< 1	< 1	< 1	< 1
Cd	< 2	< 2	< 2	< 2
Sn	3	3	5	3
Sb	< 3	< 3	< 3	< 3
Cs	< 4	< 4	< 4	< 4
Ba	412	417	1142	309
La	29	22	66	< 2
Ce	30	< 2	94	35
Hf	2	2	5	3
Ta	2	< 2	5	< 2
W	81	117	45	215
Hg	1	1	< 1.0	< 1.0
Pb	11	11	28	9
Bi	< 1	< 1	< 1	< 1
Th	6.8	7.4	43.1	3.9
U	1.9	2.2	5.0	1.3

Table A2.10. Major-and trace-element composition of samples from Gero.

Sample	GR-01	GR-02	GR-03	GR-04	GL-01
Facies	Tm	Tm	Tm	Tm	Lv
Major elements (Wt %)					
SiO_2	60.55	50.07	46.70	50.67	61.97
TiO_2	0.60	0.67	0.49	0.53	1.05
Al_2O_3	16.38	17.98	16.07	19.69	15.32
Fe_2O_3	5.96	10.77	7.71	8.65	7.13
MnO	0.18	0.25	0.19	0.20	0.11
MgO	1.80	4.91	3.36	4.20	1.56
CaO	5.61	11.18	15.28	11.26	5.32
Na_2O	2.92	1.86	1.85	1.95	3.86
K_2O	0.67	0.14	0.18	0.14	1.16
P_2O_5	0.21	0.08	0.09	0.06	0.26
SO_3	0.01	0.02	0.03	0.02	0.01
LOI	5.19	2.97	7.76	2.15	1.80
Total	100.08	100.90	99.69	99.54	99.53
Trace elements (ppm)					
Cl	941	314	280	259	108
V	19	69	22	90	33
Cr	6	1	87	1	1
Co	39	41	48	50	16
Ni	1	1	1	1	2
Cu	19	5	12	9	40
Zn	89	63	58	52	84
Ga	17	12	13	14	17
Ge	1	1	1	1	1
As	2	1	11	1	4
Se	1	1	1	1	1
Br	1	1	1	1	1
Rb	20	6	7	6	32
Sr	390	241	207	238	237
Y	30	11	11	11	44
Zr	92	14	18	15	154
Nb	2	< 1	1	< 1	3
Mo	1	1	1	1	1
Cd	1	< 1	1	< 1	1
Sn	1	< 3	3	< 3	1
Sb	3	< 3	3	< 3	3
Cs	4	< 4	4	< 4	4
Ba	203	75	85	73	276
La	11	< 2	2	< 2	11
Ce	49	< 2	2	< 2	50
Hf	1	2	1	1	7
Ta	1	10	1	8	1
W	3	187	6	216	3
Hg	2	< 1	1	< 1	1
Pb	11	1	3	2	9
Bi	1	< 1	1	< 1	1
Th	1	< 1.0	1	< 1.0	4.4
U	0.7	< 1.0	0.6	< 0.6	4.3

APPENDIX 3. GEOCHEMICAL COMPOSITION OF VOLCANIC GLASS BY ELECTRON PROBE MICROANALYSIS (EPMA)

Table A3.1. Major-element compositions of glass shards of the Tangi Talo Tephra (TTL).

Tangi Talo T1 (TTL-T1)

Glass Number	SiO_2	TiO_2	Al_2O_3	FeO	MnO	MgO	CaO	Na_2O	K_2O	Cl	Total
12-10-18-3	74.13	0.16	12.62	1.07	0.11	0.23	1.34	3.09	2.06	0.19	94.99
12-10-18-5	75.71	0.24	11.93	1.17	0.04	0.24	1.19	2.00	3.17	0.13	95.82
12-10-18-8	72.01	0.15	12.15	1.01	0.09	0.20	1.31	2.35	2.56	0.18	92.01
12-10-18-9	72.72	0.14	12.21	0.96	0.11	0.24	1.29	2.78	2.04	0.18	92.67
12-10-18-14	74.46	0.17	12.19	0.98	0.10	0.20	1.05	2.67	2.46	0.18	94.47
12-10-18-15	75.24	0.16	12.32	1.14	0.06	0.21	1.05	3.18	2.42	0.17	95.95
12-10-18-16	74.87	0.12	12.15	1.01	0.11	0.19	1.04	3.04	2.16	0.15	94.85
Average	74.16	0.16	12.22	1.05	0.09	0.21	1.18	2.73	2.41	0.17	94.39
Standard Deviation	1.34	0.04	0.21	0.08	0.03	0.02	0.13	0.43	0.39	0.02	1.51

Tangi Talo T2 (TTL-T2)

Glass Number	SiO_2	TiO_2	Al_2O_3	FeO	MnO	MgO	CaO	Na_2O	K_2O	Cl	Total
12-10-17-1	74.98	0.14	12.09	1.01	0.13	0.19	1.20	2.36	2.93	0.16	95.21
12-10-17-2	74.34	0.13	12.24	0.99	0.08	0.21	1.21	3.32	2.06	0.17	94.75
12-10-17-3	75.02	0.14	12.32	0.99	0.06	0.20	1.20	3.09	2.03	0.16	95.21
12-10-17-4	74.03	0.22	11.71	2.09	0.22	1.20	1.08	4.27	2.61	0.16	97.58
Average	74.59	0.16	12.09	1.27	0.12	0.45	1.17	3.26	2.41	0.16	95.69
Standard Deviation	0.49	0.04	0.27	0.55	0.07	0.50	0.06	0.79	0.44	0.01	1.28

Tangi Talo T4 (TTL-T4)

Glass Number	SiO_2	TiO_2	Al_2O_3	FeO	MnO	MgO	CaO	Na_2O	K_2O	Cl	Total
12-10-15-18	73.92	0.18	12.89	1.22	0.13	0.27	1.49	3.35	1.62	0.21	95.28
12-10-15-15	71.78	0.30	9.16	5.02	0.04	0.75	0.68	0.23	0.25	0.01	88.21
12-10-15-7	74.82	0.23	8.15	4.06	0.01	0.70	0.59	0.13	0.24	0.02	88.95
12-10-15-2	71.01	0.37	9.74	5.14	0.02	0.59	0.72	0.25	0.20	0.01	88.05
Average	72.88	0.27	9.99	3.86	0.05	0.58	0.87	0.99	0.58	0.06	90.12
Standard Deviation	1.78	0.08	2.05	1.82	0.06	0.21	0.42	1.57	0.70	0.10	3.46

Tangi Talo T5 (TTL-T5)

Glass Number	SiO_2	TiO_2	Al_2O_3	FeO	MnO	MgO	CaO	Na_2O	K_2O	Cl	Total
12-22-30_1	75.06	0.23	11.62	1.40	0.09	0.29	1.48	3.04	2.87	n.d.	96.08
12-22-30_2	75.32	0.21	11.46	1.34	0.06	0.24	1.53	2.35	3.22	n.d.	95.73
12-22-30_4	74.79	0.20	11.74	1.26	0.05	0.25	1.58	3.16	2.68	n.d.	95.71
12-22-30_5	74.89	0.23	11.71	1.50	0.03	0.25	1.63	3.21	2.40	n.d.	95.85
12-22-30_6	76.81	0.25	12.14	1.40	0.03	0.27	1.69	3.87	2.41	n.d.	98.86
12-22-30_7	74.64	0.23	11.39	1.98	0.06	0.34	1.59	2.55	2.88	n.d.	95.67
12-22-30_8	74.97	0.22	11.35	1.35	0.08	0.24	1.50	3.11	2.65	n.d.	95.47
12-22-30_9	76.04	0.22	11.85	1.38	0.06	0.24	1.62	3.66	2.34	n.d.	97.41
12-22-30_11	76.42	0.22	12.03	1.40	0.04	0.26	1.65	3.49	2.37	n.d.	97.89
12-22-30_12	76.30	0.23	11.90	1.45	0.07	0.30	1.65	3.20	2.60	n.d.	97.70
12-22-30_13	72.47	0.18	11.03	1.39	0.10	0.29	1.53	2.72	2.93	n.d.	92.63
12-22-30_14	75.87	0.24	11.86	1.40	0.01	0.26	1.58	3.37	2.41	n.d.	97.01
12-22-30_16	72.90	0.25	11.26	1.38	0.06	0.26	1.58	2.78	2.70	n.d.	93.17
12-22-30_19	74.22	0.22	11.39	1.49	0.03	0.26	1.64	3.09	2.40	n.d.	94.74
Average	75.05	0.22	11.62	1.44	0.05	0.27	1.59	3.11	2.63		95.99
Standard Deviation	1.26	0.02	0.32	0.17	0.03	0.03	0.06	0.42	0.27		1.74

Table A3.3. Major-element compositions of glass shards of the Wolo Wawo Tephra (WLW).

Locality	Glass Number	SiO_2	TiO_2	Al_2O_3	FeO	MnO	MgO	CaO	Na_2O	K_2O	Cl	Total
Tangi Talo	12-10-14-1	75.35	0.17	12.51	1.04	0.09	0.26	1.18	2.93	2.30	0.18	95.99
	12-10-14-3	76.96	0.15	12.47	0.86	0.06	0.25	1.18	2.67	2.82	0.17	97.58
	12-10-14-4	74.81	0.14	12.29	1.13	0.11	0.21	1.21	3.19	2.00	0.18	95.26
	12-10-14-5	73.51	0.17	11.80	1.00	0.08	0.25	1.19	3.02	1.90	0.16	93.06
	12-10-14-6	72.35	0.16	11.69	0.99	0.06	0.22	1.17	2.78	1.97	0.18	91.57
	12-10-14-7	73.90	0.15	11.85	1.01	0.07	0.25	1.19	2.00	3.34	0.20	93.95
	12-10-14-8	75.52	0.16	12.32	1.10	0.09	0.25	1.17	2.92	1.97	0.19	95.68
	12-10-14-10	71.95	0.15	11.21	1.06	0.06	0.20	1.19	2.07	2.89	0.17	90.94
	12-10-14-11	74.35	0.14	11.87	0.95	0.05	0.21	1.15	1.99	2.87	0.18	93.76
	12-10-14-12	75.59	0.15	12.28	1.02	0.10	0.25	1.16	2.67	2.53	0.17	95.91
	12-10-14-14	75.13	0.17	12.23	1.04	0.09	0.23	1.17	1.48	3.40	0.17	95.10
	Average	74.49	0.15	12.05	1.02	0.08	0.23	1.18	2.52	2.54	0.18	94.44
	Standard Deviation	1.48	0.01	0.40	0.07	0.02	0.02	0.02	0.55	0.56	0.01	2.00
Pumaso	12-21-21_1	76.17	0.18	12.49	0.96	0.01	0.23	1.22	3.73	2.26	n.d.	97.28
	12-21-21_2	75.29	0.16	12.68	0.94	0.08	0.24	1.20	3.72	2.38	n.d.	96.70
	12-21-21_3	75.26	0.14	12.35	1.01	0.09	0.25	1.16	3.89	2.34	n.d.	96.49
	12-21-21_4	74.74	0.15	12.25	0.99	0.07	0.22	1.22	3.67	2.41	n.d.	95.71
	12-21-21_5	73.97	0.14	12.13	0.95	0.07	0.21	1.16	3.16	2.64	n.d.	94.41
	12-21-21_6	75.82	0.13	12.33	1.00	0.09	0.22	1.21	3.77	2.20	n.d.	96.78
	12-21-21_7	75.74	0.15	12.32	0.94	0.04	0.24	1.21	3.90	2.32	n.d.	96.84
	12-21-21_8	75.73	0.16	12.36	0.98	0.06	0.25	1.16	3.64	2.46	n.d.	96.80
	12-21-21_9	76.43	0.13	12.26	0.86	0.07	0.21	1.16	3.51	2.51	n.d.	97.14
	12-21-21_10	75.32	0.15	12.08	0.99	0.06	0.23	1.19	3.58	2.21	n.d.	95.82
	12-21-21_11	75.51	0.15	12.12	0.91	0.07	0.25	1.16	3.76	2.51	n.d.	96.45
	12-21-21_12	74.03	0.14	11.95	1.01	0.10	0.23	1.21	2.43	3.11	n.d.	94.19
	12-21-21_13	75.63	0.14	12.24	1.11	0.05	0.26	1.20	3.68	2.44	n.d.	96.76
	12-21-21_14	75.56	0.13	12.45	1.12	0.08	0.23	1.18	3.69	2.36	n.d.	96.80
	12-21-21_15	76.03	0.15	12.27	1.07	0.06	0.24	1.20	3.73	2.29	n.d.	97.04
	12-21-21_16	75.53	0.14	12.27	1.02	0.07	0.22	1.16	3.84	2.40	n.d.	96.65
	12-21-21_17	75.99	0.17	12.30	1.06	0.08	0.23	1.18	3.71	2.50	n.d.	97.22
	12-21-21_18	74.52	0.15	12.56	1.04	0.08	0.22	1.22	3.96	2.40	n.d.	96.16
	Average	75.40	0.15	12.30	1.00	0.07	0.23	1.19	3.63	2.43		96.40
	Standard Deviation	0.69	0.01	0.18	0.07	0.02	0.01	0.02	0.35	0.20		0.88

Table A3.4. Major-element compositions of glass shards of the Wolo Sege Ignimbrite (WSI).

Locality	Sub-unit	Facies	Glass Number	SiO_2	TiO_2	Al_2O_3	FeO	MnO	MgO	CaO	Na_2O	K_2O	Cl	Total
Wolo Sege	B	Tmp	12-11-20-3	78.62	0.19	13.02	1.33	0.06	0.25	1.88	1.79	2.65	0.19	9.31
			12-11-20-4	77.89	0.22	13.73	1.28	0.06	0.33	1.90	1.88	2.54	0.18	8.94
			12-11-20-5	77.38	0.17	14.19	1.32	0.07	0.34	1.75	2.22	2.41	0.14	-0.06
			12-11-20-6	78.78	0.21	13.31	1.11	0.11	0.28	1.79	1.77	2.48	0.16	7.22
			12-11-20-7	77.81	0.17	13.35	1.24	0.06	0.31	1.89	2.70	2.25	0.21	6.82
			12-11-21-2	77.41	0.17	13.79	1.35	0.08	0.35	1.90	2.56	2.19	0.21	5.38
			12-11-21-5	78.02	0.18	14.11	1.10	0.05	0.35	1.71	1.82	2.45	0.22	2.38
			12-11-21-6	76.75	0.20	13.63	1.27	0.11	0.30	1.90	3.61	2.04	0.19	6.02
			12-11-21-7	76.42	0.17	14.19	1.25	0.07	0.27	2.21	3.30	1.93	0.19	5.43
			12-11-21-8	77.13	0.17	13.70	1.24	0.10	0.34	1.86	3.03	2.24	0.19	6.23
			12-11-21-9	78.04	0.19	13.89	1.21	0.08	0.31	1.89	1.60	2.62	0.17	8.06
			12-11-21-10	77.03	0.20	13.75	1.10	0.09	0.31	1.95	3.09	2.30	0.18	5.94
			12-11-21-11	77.13	0.19	14.13	1.42	0.06	0.35	2.08	2.44	2.07	0.13	6.20
			12-11-21-12	76.92	0.17	13.65	1.35	0.11	0.29	1.85	3.33	2.14	0.20	4.42
			12-11-21-13	77.71	0.18	13.78	1.54	0.12	0.36	2.03	1.82	2.27	0.18	4.95
			Average	77.54	0.18	13.75	1.27	0.08	0.32	1.91	2.46	2.31	0.18	5.82
			Standard Deviation	0.67	0.02	0.34	0.12	0.02	0.03	0.13	0.68	0.22	0.02	2.39
	C	Tma	12-11-19-2	77.40	0.15	13.62	1.16	0.08	0.33	1.84	3.18	2.05	0.19	4.35
			12-11-19-3	78.11	0.17	13.61	1.26	0.09	0.32	1.91	1.86	2.49	0.17	4.22
			12-11-19-4	77.98	0.16	13.32	1.28	0.04	0.30	2.03	2.18	2.51	0.20	14.02
			12-11-19-5	78.13	0.16	13.84	1.22	0.05	0.31	1.87	1.60	2.66	0.17	5.92
			12-11-19-6	77.56	0.19	13.70	1.16	0.08	0.29	1.88	2.81	2.12	0.21	7.21
			12-11-19-7	76.88	0.19	13.89	1.36	0.11	0.30	1.88	3.05	2.14	0.21	6.97
			12-11-19-8	76.91	0.18	13.83	1.26	0.08	0.36	1.81	3.27	2.12	0.20	4.62
			12-11-19-11	77.37	0.20	13.69	1.31	0.04	0.34	1.91	2.86	2.09	0.19	5.68
			12-11-19-12	77.60	0.18	13.67	1.32	0.10	0.32	1.81	2.37	2.43	0.20	6.43
			12-11-19-13	77.18	0.18	13.76	1.30	0.08	0.35	1.83	2.95	2.20	0.16	3.67
			12-11-19-14	77.25	0.17	13.71	1.25	0.12	0.32	1.85	2.91	2.24	0.19	4.07
			12-11-19-15	77.13	0.18	13.73	1.30	0.09	0.34	1.90	3.03	2.12	0.19	4.91
			12-11-19-16	76.74	0.21	14.06	1.36	0.07	0.34	2.12	2.74	2.13	0.23	5.52
			12-11-19-17	78.40	0.19	12.38	1.05	0.06	0.28	2.24	3.03	2.15	0.21	11.12
			12-11-19-18	77.07	0.18	13.79	1.23	0.10	0.32	1.85	3.05	2.24	0.16	4.70
			12-11-19-19	77.24	0.15	13.92	1.19	0.09	0.32	1.80	2.85	2.27	0.16	4.75
			12-11-19-20	79.07	0.15	12.11	0.87	0.01	0.24	1.81	3.73	1.81	0.20	12.47
			Average	77.53	0.18	13.57	1.23	0.08	0.32	1.90	2.79	2.22	0.19	6.51
			Standard Deviation	0.74	0.02	0.70	0.15	0.03	0.04	0.16	0.36	0.17	0.02	3.17
	D	Tmp	12-12-30-1	77.49	0.16	13.50	1.23	0.09	0.31	1.89	2.98	2.17	0.19	5.73
			12-12-30-2	77.18	0.17	13.58	1.23	0.07	0.30	1.83	3.45	2.01	0.19	4.19
			12-12-30-3	77.14	0.16	13.59	1.32	0.10	0.27	1.81	3.26	2.16	0.19	4.46
			12-12-30-5	76.86	0.16	13.74	1.22	0.10	0.31	1.82	3.37	2.23	0.19	3.75
			12-12-30-7	77.50	0.16	13.62	1.27	0.09	0.32	1.86	2.82	2.15	0.20	6.87
			12-12-30-8	77.80	0.17	13.62	1.22	0.06	0.31	1.96	2.64	2.10	0.12	5.29
			Average	77.33	0.16	13.61	1.25	0.09	0.30	1.86	3.09	2.13	0.18	5.05
			Standard Deviation	0.33	0.00	0.08	0.04	0.02	0.02	0.06	0.32	0.07	0.03	1.15
	F	LTmp	12-12-29-1	77.46	0.18	13.63	1.27	0.10	0.30	1.84	2.91	2.12	0.20	4.68
			12-12-29-2	77.12	0.19	13.67	1.19	0.05	0.35	1.86	3.26	2.09	0.20	5.64
			12-12-29-3	76.83	0.19	13.79	1.15	0.11	0.33	1.88	3.44	2.09	0.20	5.32
			12-12-29-4	76.91	0.17	13.74	1.18	0.09	0.32	1.86	3.51	2.01	0.19	5.73
			12-12-29-5	77.37	0.17	13.67	1.22	0.11	0.33	1.86	2.79	2.30	0.20	5.91
			12-12-29-6	77.13	0.16	13.77	1.36	0.09	0.33	1.83	3.08	2.05	0.21	4.77
			12-12-29-7	77.82	0.16	13.38	1.34	0.14	0.31	1.91	2.26	2.50	0.20	9.23
			12-12-29-8	78.00	0.15	13.55	1.34	0.06	0.32	1.80	2.71	1.86	0.21	8.43
			12-12-29-9	76.96	0.16	13.69	1.24	0.07	0.32	1.88	3.42	2.05	0.21	5.18
			12-12-29-10	77.36	0.17	13.73	1.18	0.08	0.31	1.89	3.08	2.02	0.19	7.56
			12-12-29-11	77.19	0.20	13.64	1.17	0.11	0.33	1.89	3.17	2.10	0.20	5.71
			12-12-29-12	77.29	0.15	13.68	1.20	0.08	0.31	1.84	3.14	2.10	0.22	4.51
			12-12-29-13	76.98	0.19	13.73	1.43	0.08	0.32	1.86	3.03	2.20	0.19	4.89
			12-12-29-14	77.03	0.18	13.67	1.31	0.10	0.30	1.85	3.16	2.18	0.21	6.39
			12-12-29-15	77.05	0.19	13.79	1.11	0.10	0.32	1.83	3.30	2.12	0.20	3.96
			Average	77.23	0.17	13.68	1.25	0.09	0.32	1.86	3.08	2.12	0.20	5.86
			Standard Deviation	0.33	0.02	0.10	0.09	0.02	0.01	0.03	0.32	0.14	0.01	1.49

Table A3.4. Continued.

Locality	Sub-unit	Facies	Glass Number	SiO_2	TiO_2	Al_2O_3	FeO	MnO	MgO	CaO	Na_2O	K_2O	Cl	Total
	G	Trma	12-12-28-1	77.31	0.18	13.74	1.24	0.06	0.33	1.86	2.94	2.14	0.19	6.29
			12-12-28-2	77.42	0.16	13.61	1.33	0.07	0.32	1.87	3.04	1.97	0.21	6.20
			12-12-28-4	77.20	0.19	13.50	1.31	0.08	0.32	1.92	2.98	2.27	0.22	9.38
			12-12-28-5	77.30	0.19	13.76	1.32	0.09	0.31	1.79	2.98	2.08	0.19	3.85
			12-12-28-6	76.92	0.18	13.77	1.35	0.05	0.33	1.90	3.18	2.12	0.20	6.08
			12-12-28-7	76.85	0.20	13.72	1.26	0.09	0.33	1.83	3.37	2.15	0.20	3.51
			12-12-28-8	77.26	0.17	13.72	1.39	0.04	0.33	1.81	2.89	2.21	0.18	4.79
			12-12-28-9	77.19	0.21	13.64	1.28	0.11	0.34	1.81	3.18	2.06	0.17	4.67
			12-12-28-10	77.59	0.16	13.63	1.15	0.05	0.36	1.88	3.03	1.96	0.18	6.97
			12-12-28-11	77.23	0.19	13.88	1.27	0.05	0.30	1.85	2.97	2.04	0.20	5.02
			12-12-28-12	77.79	0.19	13.56	1.17	0.06	0.32	1.91	2.67	2.13	0.21	7.09
			12-12-28-13	77.23	0.16	13.67	1.28	0.07	0.34	1.86	3.19	2.02	0.19	5.65
			12-12-28-14	77.28	0.16	13.74	1.23	0.10	0.28	1.90	3.12	2.00	0.20	6.64
			12-12-28-15	77.35	0.17	13.80	1.33	0.04	0.29	1.82	3.05	1.98	0.17	4.79
			12-12-28-16	77.51	0.17	13.84	1.25	0.09	0.33	1.78	2.86	1.97	0.21	6.11
			12-12-28-17	77.28	0.18	13.63	1.39	0.08	0.31	1.84	3.05	2.04	0.20	4.83
			Average	77.30	0.18	13.70	1.28	0.07	0.32	1.85	3.03	2.07	0.20	5.74
			Standard Deviation	0.23	0.02	0.10	0.07	0.02	0.02	0.04	0.16	0.09	0.01	1.44
	H	Trma	12-12-27-1	77.04	0.15	13.50	1.22	0.12	0.32	1.86	3.55	2.02	0.22	4.34
			12-12-27-2	76.86	0.16	13.61	1.30	0.06	0.29	1.87	3.48	2.17	0.20	5.12
			12-12-27-3	77.26	0.17	13.71	1.25	0.09	0.34	1.86	3.14	1.98	0.21	5.77
			12-12-27-4	77.27	0.20	13.69	1.37	0.08	0.31	1.83	3.05	2.00	0.19	4.73
			12-12-27-5	76.81	0.19	13.83	1.40	0.06	0.31	1.82	3.13	2.25	0.20	4.62
			12-12-27-6	77.28	0.16	13.65	1.24	0.11	0.33	1.87	2.89	2.29	0.18	4.93
			12-12-27-7	77.12	0.20	13.51	1.28	0.07	0.34	1.83	3.42	2.00	0.21	4.21
			12-12-27-8	77.23	0.15	13.68	1.25	0.04	0.33	1.81	3.30	1.98	0.21	3.67
			12-12-27-9	76.78	0.17	13.83	1.39	0.06	0.30	1.79	3.39	2.08	0.19	4.09
			12-12-27-10	77.72	0.21	13.65	1.29	0.03	0.33	1.88	2.75	1.96	0.19	7.03
			12-12-27-11	76.75	0.16	13.85	1.18	0.10	0.29	1.89	3.44	2.15	0.20	5.20
			12-12-27-12	77.34	0.15	13.99	1.31	0.05	0.31	1.76	2.62	2.28	0.18	1.87
			12-12-27-13	77.66	0.18	13.64	1.27	0.08	0.33	1.81	2.81	2.01	0.21	6.78
			12-12-27-14	77.27	0.17	13.59	1.19	0.08	0.29	1.88	3.13	2.21	0.21	4.12
			Average	77.17	0.17	13.70	1.28	0.07	0.31	1.84	3.15	2.10	0.20	4.75
			Standard Deviation	0.30	0.02	0.14	0.07	0.03	0.02	0.04	0.30	0.12	0.01	1.29

Locality	Sub-unit	Facies	Glass Number	SiO_2	TiO_2	Al_2O_3	FeO	MnO	MgO	CaO	Na_2O	K_2O	Cl	Total
Tangi Talo	F	LTmp	12-10-13-1	73.25	0.15	13.09	1.21	0.06	0.32	1.75	3.49	2.02	0.20	95.53
			12-10-13-2	73.90	0.16	13.21	1.24	0.12	0.30	1.76	3.34	2.00	0.21	96.24
			12-10-13-3	73.70	0.17	13.11	1.16	0.08	0.30	1.79	3.49	2.01	0.21	96.02
			12-10-13-4	74.09	0.18	13.05	1.15	0.10	0.35	1.78	3.36	2.10	0.21	96.36
			12-10-13-5	73.82	0.15	13.08	1.21	0.10	0.33	1.74	3.29	2.22	0.20	96.13
			12-10-13-6	74.41	0.16	13.09	1.23	0.10	0.29	1.83	3.57	2.04	0.21	96.93
			12-10-13-7	73.60	0.17	13.15	1.25	0.10	0.32	1.76	3.57	2.01	0.21	96.15
			12-10-13-8	75.12	0.18	13.57	1.30	0.08	0.31	1.83	3.56	2.09	0.18	98.21
			12-10-13-9	72.87	0.17	12.89	1.26	0.11	0.29	1.77	3.17	1.96	0.22	94.71
			12-10-13-10	73.98	0.18	13.19	1.26	0.09	0.34	1.74	3.47	2.15	0.19	96.57
			12-10-13-11	73.05	0.17	12.98	1.21	0.08	0.30	1.80	3.38	1.91	0.20	95.09
			12-10-13-12	73.78	0.16	13.13	1.03	0.12	0.33	1.77	3.40	2.08	0.21	95.99
			12-10-13-13	72.53	0.15	12.86	1.21	0.12	0.28	1.76	3.64	2.03	0.19	94.78
			12-10-13-14	74.13	0.16	13.14	1.22	0.07	0.34	1.81	3.57	2.02	0.21	96.66
			12-10-13-16	73.28	0.17	13.12	1.23	0.10	0.32	1.77	3.56	1.98	0.19	95.72
			12-10-13-17	74.94	0.16	13.39	1.23	0.07	0.29	1.82	3.46	1.95	0.18	97.50
			12-10-13-18	74.25	0.15	13.28	1.20	0.05	0.31	1.81	3.44	2.10	0.19	96.76
			12-10-13-19	73.94	0.17	13.15	1.12	0.09	0.33	1.81	3.46	1.95	0.22	96.24
			12-10-13-20	73.60	0.17	13.18	1.31	0.06	0.29	1.74	3.34	1.99	0.17	95.85
			Average	73.80	0.16	13.14	1.21	0.09	0.31	1.78	3.45	2.03	0.20	96.18
			Standard Deviation	0.65	0.01	0.16	0.06	0.02	0.02	0.03	0.12	0.08	0.01	0.86
	G	Trma	12-11-24-1	73.59	0.19	12.98	1.28	0.10	0.31	1.74	3.09	1.95	0.21	95.45
			12-11-24-2	73.57	0.17	13.16	1.20	0.09	0.30	1.70	2.65	2.18	0.19	95.21
			12-11-24-3	72.08	0.17	12.85	1.14	0.09	0.31	1.72	2.98	1.86	0.19	93.39
			12-11-24-4	71.56	0.17	12.85	1.09	0.13	0.33	1.72	2.09	2.38	0.19	92.50
			12-11-24-5	71.66	0.17	12.83	1.22	0.08	0.30	1.71	2.72	1.93	0.19	92.82
			12-11-24-6	73.26	0.16	13.09	1.17	0.09	0.29	1.75	2.89	1.86	0.20	94.76
			12-11-24-7	72.45	0.16	13.02	1.12	0.04	0.33	1.76	2.96	1.81	0.19	93.85
			12-11-24-8	74.84	0.17	13.32	1.26	0.11	0.33	1.76	3.27	2.01	0.19	97.25
			12-11-24-9	73.46	0.18	12.98	1.20	0.08	0.32	1.71	2.95	1.97	0.17	95.02
			12-11-24-10	72.33	0.18	12.71	1.15	0.09	0.30	1.72	2.17	2.18	0.17	93.00
			12-11-24-11	71.85	0.14	12.71	1.26	0.07	0.31	1.73	2.85	1.90	0.18	93.01
			12-11-24-13	75.30	0.30	12.14	1.11	0.08	0.36	2.03	3.05	2.93	0.19	97.48
			12-11-24-14	74.63	0.14	13.25	1.10	0.09	0.32	1.76	2.61	2.11	0.19	96.20
			12-11-24-16	73.63	0.18	13.06	1.29	0.06	0.29	1.75	2.77	2.13	0.20	95.35
			12-11-24-17	73.93	0.17	13.23	1.16	0.08	0.31	1.78	3.27	2.04	0.21	96.17
			12-11-24-18	73.06	0.18	12.93	1.19	0.07	0.30	1.76	2.69	1.86	0.19	94.21
			12-11-24-19	73.29	0.19	13.02	1.14	0.11	0.33	1.69	2.63	2.06	0.18	94.64
			12-11-24-20	72.39	0.18	12.89	1.32	0.09	0.29	1.71	2.35	1.77	0.19	93.19
			Average	73.17	0.18	12.95	1.19	0.08	0.31	1.75	2.79	2.05	0.19	94.65
			Standard Deviation	1.06	0.03	0.26	0.07	0.02	0.02	0.07	0.32	0.26	0.01	1.47

Table A3.5. Major-element compositions of glass shards of the Turekeo Ignimbrite (TRI).

Locality	Facies	Glass Number	SiO_2	TiO_2	Al_2O_3	FeO	MnO	MgO	CaO	Na_2O	K_2O	Cl	Total
Turekeo	Ts	12-22-25_1	73.17	0.15	12.44	1.09	0.10	0.28	1.56	3.19	2.41	n.d.	94.38
		12-22-25_2	73.40	0.18	12.54	1.15	0.07	0.30	1.64	3.33	2.24	n.d.	94.84
		12-22-25_3	73.50	0.19	12.73	1.16	0.09	0.34	1.59	2.42	2.67	n.d.	94.69
		12-22-25_4	73.06	0.19	12.80	1.27	0.07	0.33	1.68	3.00	2.39	n.d.	94.77
		12-22-25_5	74.48	0.15	12.51	1.12	0.08	0.28	1.54	2.23	2.88	n.d.	95.25
		12-22-25_6	73.30	0.18	12.74	1.21	0.08	0.37	1.77	2.73	2.35	n.d.	94.73
		12-22-25_7	72.58	0.19	12.56	1.35	0.08	0.33	1.74	2.97	2.32	n.d.	94.12
		12-22-25_8	73.21	0.21	12.90	1.38	0.03	0.34	1.74	3.23	2.16	n.d.	95.20
		12-22-25_9	73.85	0.16	12.73	1.27	0.08	0.32	1.64	2.74	2.65	n.d.	95.43
		12-22-25_10	72.45	0.16	12.71	1.21	0.08	0.31	1.73	3.29	2.19	n.d.	94.13
		12-22-25_11	72.00	0.16	12.54	1.19	0.07	0.29	1.70	2.49	2.49	n.d.	92.93
		12-22-25_12	72.88	0.19	12.66	1.16	0.07	0.31	1.65	2.21	2.49	n.d.	93.61
		12-22-25_13	73.36	0.17	12.98	1.18	0.06	0.32	1.73	3.31	2.17	n.d.	95.27
		12-22-25_14	72.42	0.16	12.56	1.18	0.10	0.34	1.72	2.48	2.53	n.d.	93.48
		12-22-25_15	72.41	0.16	12.44	1.11	0.05	0.31	1.62	3.08	2.35	n.d.	93.54
		12-22-25_16	73.20	0.17	12.79	1.22	0.04	0.29	1.65	3.27	2.37	n.d.	95.00
		12-22-25_17	76.11	0.28	11.93	1.52	0.09	0.28	1.54	3.19	3.62	n.d.	98.55
		12-22-25_18	73.54	0.18	12.80	1.19	0.04	0.30	1.72	3.23	2.26	n.d.	95.26
		12-22-25_19	74.03	0.18	12.73	1.14	0.04	0.32	1.61	3.02	2.82	n.d.	95.90
		12-22-25_20	73.26	0.17	12.82	1.21	0.08	0.29	1.67	3.08	2.29	n.d.	94.87
		Average	73.31	0.18	12.65	1.21	0.07	0.31	1.66	2.92	2.48		94.80
		Standard Deviation	0.89	0.03	0.22	0.10	0.02	0.02	0.07	0.37	0.34		1.17
Turekeo	LTmp	12-22-26_1	74.09	0.19	12.60	1.14	0.07	0.33	1.68	3.11	2.43	n.d.	95.64
		12-22-26_2	73.99	0.18	13.13	1.14	0.08	0.34	1.72	3.56	2.26	n.d.	96.42
		12-22-26_3	73.67	0.19	12.66	1.27	0.07	0.35	1.70	3.22	2.16	n.d.	95.30
		12-22-26_4	74.58	0.16	12.96	1.17	0.13	0.31	1.65	3.67	2.20	n.d.	96.83
		12-22-26_5	74.06	0.17	12.91	1.21	0.10	0.34	1.65	3.40	2.23	n.d.	96.07
		12-22-26_6	74.49	0.20	12.92	1.12	0.08	0.31	1.66	3.57	2.26	n.d.	96.60
		12-22-26_7	73.54	0.16	12.94	1.19	0.07	0.29	1.68	3.09	2.49	n.d.	95.45
		12-22-26_8	74.20	0.19	13.12	1.18	0.06	0.32	1.69	3.71	2.19	n.d.	96.66
		12-22-26_9	74.70	0.19	12.88	1.06	0.04	0.33	1.70	3.81	2.27	n.d.	96.97
		12-22-26_10	73.58	0.21	12.59	1.22	0.09	0.32	1.63	3.37	2.23	n.d.	95.24
		12-22-26_11	72.21	0.19	12.82	1.32	0.09	0.31	1.79	3.20	2.25	n.d.	94.18
		12-22-26_12	74.37	0.18	12.71	1.10	0.07	0.33	1.67	3.66	2.21	n.d.	96.30
		12-22-26_13	75.08	0.18	12.86	1.01	0.10	0.29	1.55	2.87	2.68	n.d.	96.63
		12-22-26_14	73.37	0.16	12.72	1.16	0.06	0.32	1.69	3.55	2.17	n.d.	95.20
		12-22-26_15	74.68	0.18	12.98	1.19	0.08	0.32	1.68	3.60	2.21	n.d.	96.92
		12-22-26_16	73.65	0.22	13.10	1.28	0.08	0.39	1.76	3.58	2.22	n.d.	96.28
		12-22-26_17	74.30	0.19	13.02	1.18	0.10	0.32	1.71	3.49	2.33	n.d.	96.62
		12-22-26_18	73.58	0.17	12.83	1.18	0.07	0.34	1.70	3.63	2.15	n.d.	95.64
		Average	74.01	0.18	12.88	1.17	0.08	0.33	1.68	3.45	2.27		96.05
		Standard Deviation	0.66	0.02	0.17	0.07	0.02	0.02	0.05	0.25	0.13		0.77
Tangi Talo	Ts	12-22-27_1	73.14	0.17	12.74	1.28	0.07	0.33	1.64	3.45	2.19	n.d.	95.02
		12-22-27_3	73.65	0.17	12.75	1.13	0.06	0.32	1.67	3.14	2.11	n.d.	95.00
		12-22-27_4	73.46	0.20	12.69	1.36	0.07	0.33	1.70	3.16	2.29	n.d.	95.26
		12-22-27_5	73.60	0.17	12.75	1.14	0.08	0.30	1.75	3.38	2.27	n.d.	95.42
		12-22-27_6	74.39	0.17	12.78	1.19	0.05	0.26	1.63	3.47	2.40	n.d.	96.34
		12-22-27_7	74.49	0.16	13.01	1.22	0.09	0.33	1.64	3.55	2.36	n.d.	96.86
		12-22-27_8	74.33	0.17	12.82	1.23	0.08	0.29	1.64	3.48	2.26	n.d.	96.30
		12-22-27_9	73.75	0.18	12.67	1.11	0.11	0.31	1.66	3.26	2.35	n.d.	95.40
		12-22-27_10	73.07	0.18	12.85	1.08	0.10	0.33	1.66	3.08	2.19	n.d.	94.52
		12-22-27_11	74.23	0.19	12.95	1.19	0.04	0.34	1.72	3.50	2.15	n.d.	96.29
		12-22-27_12	73.55	0.16	12.71	1.11	0.08	0.32	1.72	3.28	2.36	n.d.	95.29
		12-22-27_13	72.98	0.18	12.80	1.17	0.05	0.33	1.75	3.35	2.28	n.d.	94.90
		12-22-27_14	73.82	0.14	12.68	1.15	0.10	0.33	1.70	3.35	2.25	n.d.	95.53
		12-22-27_15	74.62	0.15	12.96	1.18	0.04	0.34	1.71	3.49	2.34	n.d.	96.81
		12-22-27_16	73.60	0.17	12.81	1.21	0.06	0.32	1.69	3.42	2.28	n.d.	95.55
		12-22-27_17	73.23	0.15	12.84	1.22	0.07	0.29	1.68	3.23	2.14	n.d.	94.85
		12-22-27_18	73.13	0.16	12.62	1.04	0.09	0.30	1.61	3.04	2.34	n.d.	94.33
		Average	73.71	0.17	12.79	1.18	0.07	0.32	1.68	3.33	2.27		95.51
		Standard Deviation	0.53	0.02	0.11	0.08	0.02	0.02	0.04	0.16	0.09		0.76

Table A3.5. Continued.

Locality	Facies	Glass Number	SiO_2	TiO_2	Al_2O_3	FeO	MnO	MgO	CaO	Na_2O	K_2O	Cl	Total
Tangi Talo	LTmp	12-22-28_1	73.70	0.20	12.94	1.13	0.13	0.35	1.75	3.60	2.18	n.d.	95.98
		12-22-28_2	74.30	0.17	12.73	1.06	0.05	0.31	1.62	3.45	2.14	n.d.	95.83
		12-22-28_3	73.58	0.18	12.79	1.12	0.10	0.32	1.72	3.61	2.19	n.d.	95.61
		12-22-28_4	75.15	0.16	12.68	1.17	0.08	0.32	1.58	3.60	2.27	n.d.	97.01
		12-22-28_5	74.45	0.14	12.60	1.04	0.07	0.28	1.64	3.54	2.32	n.d.	96.08
		12-22-28_6	75.13	0.16	12.92	1.12	0.06	0.34	1.70	3.81	2.29	n.d.	97.53
		12-22-28_7	74.21	0.20	13.04	1.10	0.06	0.33	1.77	3.62	2.29	n.d.	96.62
		12-22-28_8	73.97	0.15	12.68	1.15	0.04	0.31	1.64	3.32	2.31	n.d.	95.58
		12-22-28_9	74.37	0.15	13.03	1.10	0.05	0.37	1.70	3.63	2.22	n.d.	96.61
		12-22-28_12	73.85	0.18	12.87	1.22	0.09	0.33	1.67	3.57	2.23	n.d.	96.01
		12-22-28_14	72.38	0.19	12.84	1.23	0.10	0.34	1.80	3.21	2.21	n.d.	94.31
		12-22-28_15	74.86	0.14	12.73	1.07	0.09	0.27	1.54	3.65	2.33	n.d.	96.68
		12-22-28_16	73.99	0.15	13.05	1.25	0.06	0.37	1.78	3.22	2.37	n.d.	96.24
		12-22-28_17	74.13	0.19	12.85	1.13	0.06	0.33	1.62	3.34	2.26	n.d.	95.91
		12-22-28_18	74.45	0.18	12.84	1.18	0.05	0.33	1.67	3.52	2.21	n.d.	96.42
		Average	74.17	0.17	12.84	1.14	0.07	0.33	1.68	3.51	2.25		96.16
		Standard Deviation	0.68	0.02	0.14	0.06	0.02	0.03	0.08	0.17	0.06		0.74
Tangi Talo	Tma	12-22-29_1	74.78	0.19	13.01	1.17	0.04	0.32	1.65	3.44	2.26	n.d.	96.86
		12-22-29_2	73.28	0.16	12.81	1.08	0.09	0.34	1.62	2.87	2.62	n.d.	94.86
		12-22-29_3	73.07	0.17	12.48	1.10	0.05	0.28	1.61	3.09	2.50	n.d.	94.34
		12-22-29_4	73.97	0.17	12.97	1.17	0.08	0.35	1.70	3.39	2.26	n.d.	96.05
		12-22-29_5	73.10	0.19	12.93	1.12	0.13	0.32	1.75	3.01	2.40	n.d.	94.94
		12-22-29_6	72.18	0.18	12.65	1.15	0.09	0.31	1.67	2.90	2.32	n.d.	93.44
		12-22-29_7	72.75	0.18	12.73	1.18	0.07	0.33	1.73	1.98	3.02	n.d.	93.98
		12-22-29_8	73.94	0.16	12.51	1.13	0.05	0.31	1.59	3.31	2.36	n.d.	95.36
		12-22-29_9	73.74	0.18	12.80	1.14	0.05	0.32	1.62	3.44	2.17	n.d.	95.47
		12-22-29_10	73.39	0.17	12.96	1.18	0.08	0.34	1.73	3.20	2.17	n.d.	95.22
		12-22-29_11	74.10	0.19	12.60	1.16	0.02	0.28	1.54	3.31	2.32	n.d.	95.51
		12-22-29_12	73.92	0.21	12.92	1.17	0.10	0.36	1.68	3.26	2.38	n.d.	95.99
		12-22-29_13	73.04	0.17	12.57	0.96	0.06	0.26	1.60	3.31	2.25	n.d.	94.20
		12-22-29_14	74.40	0.14	12.47	1.05	0.05	0.26	1.48	3.10	2.60	n.d.	95.55
		12-22-29_15	74.74	0.14	12.81	0.98	0.09	0.30	1.48	3.56	2.20	n.d.	96.29
		12-22-29_16	75.04	0.16	13.11	1.04	0.07	0.33	1.62	3.59	2.26	n.d.	97.21
		12-22-29_17	73.55	0.20	12.73	1.18	0.07	0.30	1.70	2.92	2.43	n.d.	95.09
		12-22-29_18	73.76	0.16	12.67	1.19	0.05	0.33	1.63	2.77	2.74	n.d.	95.30
		Average	73.71	0.17	12.76	1.12	0.07	0.31	1.63	3.14	2.40		95.32
		Standard Deviation	0.75	0.02	0.19	0.07	0.03	0.03	0.08	0.38	0.22		0.97
Pumaso	Ts	12-21-19_1	73.48	0.18	12.84	1.21	0.07	0.33	1.76	3.29	2.27	n.d.	95.43
		12-21-19_2	73.58	0.18	12.97	1.14	0.06	0.33	1.69	3.24	2.33	n.d.	95.49
		12-21-19_3	72.65	0.18	12.74	1.10	0.08	0.30	1.61	3.10	2.29	n.d.	94.05
		12-21-19_4	69.20	0.17	12.29	1.22	0.07	0.46	1.61	1.81	2.72	n.d.	89.55
		12-21-19_5	73.62	0.19	12.91	1.15	0.08	0.31	1.68	3.51	2.27	n.d.	95.71
		12-21-19_6	73.45	0.16	12.84	1.21	0.07	0.35	1.71	3.27	2.26	n.d.	95.32
		12-21-19_7	69.71	0.19	12.14	1.25	0.09	0.39	1.79	2.07	2.54	n.d.	90.18
		12-21-19_8	74.32	0.16	13.05	1.17	0.10	0.31	1.67	3.46	2.29	n.d.	96.53
		12-21-19_9	73.94	0.16	12.76	1.22	0.06	0.32	1.66	3.05	2.29	n.d.	95.45
		12-21-19_10	73.00	0.18	12.60	1.17	0.08	0.32	1.69	3.29	2.17	n.d.	94.49
		12-21-19_11	73.33	0.18	12.94	1.15	0.05	0.31	1.66	3.25	2.20	n.d.	95.07
		12-21-19_12	72.24	0.17	12.59	1.17	0.06	0.32	1.67	3.33	2.21	n.d.	93.74
		12-21-19_13	73.57	0.17	12.77	1.13	0.07	0.32	1.70	3.40	2.21	n.d.	95.33
		12-21-19_14	74.22	0.20	12.83	1.24	0.08	0.33	1.70	3.51	2.44	n.d.	96.54
		12-21-19_15	74.20	0.16	12.90	1.23	0.13	0.31	1.70	3.58	2.22	n.d.	96.43
		12-21-19_16	74.10	0.19	12.90	1.22	0.06	0.32	1.63	3.38	2.15	n.d.	95.94
		12-21-19_17	74.97	0.17	12.78	1.19	0.09	0.32	1.58	3.20	2.45	n.d.	96.74
		12-21-19_18	73.21	0.18	12.74	1.25	0.06	0.35	1.72	2.61	2.36	n.d.	94.46
		Average	73.15	0.18	12.75	1.19	0.08	0.33	1.68	3.13	2.31		94.80
		Standard Deviation	1.49	0.01	0.23	0.04	0.02	0.04	0.05	0.49	0.14		1.99

Table A3.6. Major-element compositions of glass shards of the Kopowatu Tephra (KPW).

Locality	Glass Number	SiO_2	TiO_2	Al_2O_3	FeO	MnO	MgO	CaO	Na_2O	K_2O	Cl	Total
Kopowatu	12-21-24_1	73.51	0.12	12.89	0.95	0.16	0.10	0.62	3.59	4.75	n.d.	96.69
	12-21-24_2	74.01	0.16	13.02	1.07	0.11	0.09	0.62	3.74	4.90	n.d.	97.71
	12-21-24_3	71.55	0.14	13.48	1.15	0.15	0.11	0.82	2.42	4.86	n.d.	94.68
	12-21-24_4	73.05	0.14	12.88	1.01	0.12	0.10	0.65	3.54	4.84	n.d.	96.32
	12-21-24_5	73.61	0.15	13.07	0.87	0.15	0.08	0.60	3.60	5.13	n.d.	97.24
	12-21-24_6	73.88	0.13	12.88	0.93	0.14	0.28	0.63	3.75	4.98	n.d.	97.59
	12-21-24_7	72.90	0.13	12.99	0.99	0.13	0.08	0.62	3.11	5.37	n.d.	96.31
	12-21-24_8	72.83	0.17	12.77	0.89	0.10	0.09	0.60	3.20	5.15	n.d.	95.79
	12-21-24_9	73.56	0.16	12.96	0.92	0.15	0.08	0.60	3.38	5.28	n.d.	97.09
	12-21-24_10	73.93	0.13	12.95	0.84	0.10	0.08	0.64	3.52	5.25	n.d.	97.45
	12-21-24_11	73.63	0.14	12.97	1.10	0.12	0.09	0.63	3.47	4.71	n.d.	96.87
	12-21-24_12	73.97	0.14	12.87	1.03	0.14	0.10	0.58	3.65	5.14	n.d.	97.62
	12-21-24_13	73.61	0.14	13.00	0.98	0.15	0.06	0.63	3.84	4.90	n.d.	97.31
	12-21-24_14	72.68	0.12	13.71	1.03	0.11	0.12	0.79	3.99	4.94	n.d.	97.48
	12-21-24_15	71.04	0.14	13.89	1.06	0.12	0.14	0.91	3.61	4.78	n.d.	95.69
	12-21-24_16	73.68	0.13	12.83	0.96	0.12	0.08	0.63	3.62	4.66	n.d.	96.72
	12-21-24_17	72.72	0.15	13.59	1.06	0.12	0.12	0.81	3.61	4.89	n.d.	97.07
	12-21-24_18	74.11	0.13	13.27	1.06	0.13	0.12	0.65	3.75	4.89	n.d.	98.11
	Average	73.24	0.14	13.11	0.99	0.13	0.11	0.67	3.52	4.97		96.87
	Standard Deviation	0.85	0.01	0.33	0.08	0.02	0.05	0.10	0.35	0.21		0.86
Lowo Mali	12-21-22_1	74.04	0.15	13.13	0.97	0.13	0.09	0.62	3.77	4.77	n.d.	97.68
	12-21-22_2	73.83	0.14	13.06	0.93	0.16	0.11	0.62	3.91	4.72	n.d.	97.47
	12-21-22_3	72.03	0.15	14.12	1.16	0.12	0.14	0.95	3.90	4.69	n.d.	97.25
	12-21-22_4	72.66	0.13	13.82	1.09	0.12	0.11	0.85	4.08	4.78	n.d.	97.64
	12-21-22_5	73.65	0.16	12.94	0.89	0.12	0.11	0.64	3.36	4.99	n.d.	96.85
	12-21-22_6	71.41	0.16	14.04	1.03	0.16	0.11	0.94	3.86	4.77	n.d.	96.48
	12-21-22_7	73.52	0.14	12.82	0.88	0.14	0.09	0.61	3.05	5.88	n.d.	97.13
	12-21-22_8	74.11	0.14	13.10	0.90	0.14	0.10	0.64	3.58	5.11	n.d.	97.83
	12-21-22_9	71.95	0.17	14.22	1.31	0.18	0.11	0.97	3.33	5.27	n.d.	97.52
	12-21-22_10	71.34	0.17	14.10	1.17	0.17	0.13	0.93	3.82	4.62	n.d.	96.44
	12-21-22_11	73.54	0.13	12.99	0.95	0.15	0.12	0.64	3.70	4.60	n.d.	96.82
	12-21-22_12	72.50	0.14	13.61	1.15	0.12	0.14	0.81	3.39	4.90	n.d.	96.75
	12-21-22_13	71.47	0.15	13.49	1.08	0.12	0.12	0.80	3.56	5.26	n.d.	96.05
	12-21-22_14	73.86	0.16	12.95	0.98	0.12	0.09	0.63	3.71	4.72	n.d.	97.23
	12-21-22_15	73.48	0.15	13.04	0.92	0.12	0.08	0.63	3.22	5.70	n.d.	97.35
	12-21-22_16	70.84	0.14	13.72	1.21	0.12	0.14	0.94	2.83	5.69	n.d.	95.61
	12-21-22_17	73.99	0.14	12.94	0.90	0.17	0.10	0.61	3.73	5.28	n.d.	97.85
	12-21-22_18	73.19	0.15	13.47	1.04	0.12	0.10	0.80	3.88	4.66	n.d.	97.42
	Average	72.86	0.15	13.42	1.03	0.14	0.11	0.76	3.59	5.02		97.08
	Standard Deviation	1.09	0.01	0.48	0.13	0.02	0.02	0.14	0.33	0.41		0.62

Table A3.7. Major-element compositions of glass shards of the Pumaso Tephra (PMS).

Locality	Glass Number	SiO_2	TiO_2	Al_2O_3	FeO	MnO	MgO	CaO	Na_2O	K_2O	Cl	Total
Pumaso	12-21-20_1	72.05	0.22	12.97	1.37	0.09	0.36	1.80	3.13	2.05	n.d.	94.04
	12-21-20_2	73.68	0.19	13.25	1.33	0.05	0.39	1.69	3.38	2.00	n.d.	95.96
	12-21-20_3	73.22	0.20	13.35	1.41	0.05	0.36	1.81	3.05	2.11	n.d.	95.56
	12-21-20_4	72.67	0.20	12.77	1.27	0.07	0.35	1.72	3.17	2.09	n.d.	94.33
	12-21-20_5	73.85	0.19	13.35	1.40	0.08	0.41	1.77	3.56	2.07	n.d.	96.69
	12-21-20_6	70.11	0.21	12.25	1.25	0.10	0.37	1.74	2.06	2.43	n.d.	90.52
	12-21-20_7	70.66	0.20	12.60	1.39	0.10	0.33	1.77	2.36	2.38	n.d.	91.78
	12-21-20_8	73.29	0.22	12.98	1.37	0.10	0.38	1.79	3.09	2.14	n.d.	95.37
	12-21-20_9	72.18	0.22	12.85	1.30	0.08	0.41	1.72	2.46	2.39	n.d.	93.61
	12-21-20_10	71.33	0.20	12.57	1.19	0.09	0.34	1.71	2.87	2.08	n.d.	92.38
	12-21-20_11	73.34	0.20	13.09	1.41	0.07	0.36	1.75	2.36	2.33	n.d.	94.91
	12-21-20_12	73.84	0.23	13.27	1.26	0.08	0.40	1.76	3.68	2.00	n.d.	96.52
	12-21-20_13	70.04	0.21	12.49	1.32	0.12	0.35	1.76	1.64	3.10	n.d.	91.04
	12-21-20_14	71.43	0.22	12.64	1.32	0.09	0.33	1.76	2.83	2.07	n.d.	92.68
	12-21-20_15	72.95	0.23	12.71	1.22	0.08	0.32	1.66	2.28	2.82	n.d.	94.26
	12-21-20_17	72.02	0.22	12.78	1.27	0.09	0.35	1.70	2.95	2.01	n.d.	93.39
	12-21-20_18	71.59	0.21	12.30	1.23	0.10	0.36	1.62	1.58	3.12	n.d.	92.11
	Average	72.25	0.21	12.84	1.31	0.09	0.36	1.74	2.73	2.31		93.83
	Standard Deviation	1.25	0.01	0.35	0.07	0.02	0.03	0.05	0.62	0.37		1.88
Lowo Mali	12-21-23_1	73.41	0.18	13.02	1.25	0.08	0.37	1.69	3.78	2.01	n.d.	95.78
	12-21-23_2	72.75	0.21	13.07	1.37	0.07	0.39	1.71	3.21	2.02	n.d.	94.80
	12-21-23_3	71.90	0.22	12.75	1.28	0.12	0.38	1.70	3.46	1.92	n.d.	93.73
	12-21-23_4	72.84	0.16	13.09	1.29	0.11	0.37	1.79	4.02	1.88	n.d.	95.57
	12-21-23_5	72.94	0.19	12.80	1.35	0.09	0.36	1.73	2.65	2.27	n.d.	94.38
	12-21-23_6	71.73	0.21	12.84	1.29	0.10	0.33	1.72	2.98	2.03	n.d.	93.22
	12-21-23_7	72.19	0.19	12.82	1.25	0.06	0.32	1.67	3.23	1.93	n.d.	93.66
	12-21-23_8	73.36	0.21	13.07	1.26	0.10	0.37	1.82	3.63	2.01	n.d.	95.84
	12-21-23_9	74.23	0.23	13.38	1.29	0.11	0.40	1.75	3.40	2.11	n.d.	96.89
	12-21-23_10	73.13	0.21	13.03	1.24	0.12	0.37	1.79	3.78	2.00	n.d.	95.67
	12-21-23_11	72.06	0.21	12.87	1.27	0.10	0.44	1.71	3.17	2.18	n.d.	94.00
	12-21-23_12	73.60	0.20	12.67	1.24	0.08	0.35	1.63	3.46	2.05	n.d.	95.29
	12-21-23_13	73.33	0.20	13.12	1.37	0.09	0.35	1.76	3.67	2.03	n.d.	95.93
	12-21-23_14	71.78	0.21	12.77	1.30	0.11	0.37	1.72	2.95	2.22	n.d.	93.44
	12-21-23_15	72.11	0.22	12.04	1.33	0.09	0.36	1.56	1.89	2.87	n.d.	92.47
	12-21-23_16	74.41	0.21	13.35	1.32	0.11	0.36	1.66	3.93	2.11	n.d.	97.46
	12-21-23_18	71.56	0.23	12.84	1.39	0.10	0.37	1.67	2.93	2.42	n.d.	93.49
	Average	72.79	0.20	12.91	1.30	0.10	0.37	1.71	3.30	2.12		94.80
	Standard Deviation	0.88	0.02	0.30	0.05	0.02	0.03	0.06	0.53	0.24		1.39

Table A3.8. Major-element compositions of glass shards of the Wulubara, Nata Randang and Kolopanu Tephras.

Wulabara Tephra (WLB-T4)

Glass Number	SiO_2	TiO_2	Al_2O_3	FeO	MnO	MgO	CaO	Na_2O	K_2O	Cl	Total
12-19-7_1	73.38	0.31	12.28	1.67	0.05	0.37	1.85	3.70	1.72	n.d.	95.32
12-19-7_2	73.82	0.32	12.20	1.78	0.07	0.34	1.89	3.88	1.68	n.d.	95.98
12-19-7_3	73.37	0.29	12.34	1.77	0.05	0.37	1.90	3.45	1.61	n.d.	95.16
12-19-7_4	73.66	0.33	12.28	1.64	0.03	0.41	1.90	3.71	1.69	n.d.	95.65
12-19-7_5	69.75	0.35	11.24	1.65	0.03	0.36	1.82	2.79	1.90	n.d.	89.89
12-19-7_6	74.49	0.32	12.33	1.67	0.06	0.38	1.83	3.70	1.65	n.d.	96.43
12-19-7_7	73.36	0.34	12.22	1.51	0.09	0.36	1.88	3.86	1.71	n.d.	95.33
12-19-7_8	73.51	0.35	12.28	1.64	0.08	0.39	1.86	3.45	1.71	n.d.	95.26
12-19-7_9	73.64	0.31	12.22	1.61	0.09	0.36	1.88	3.72	1.75	n.d.	95.58
12-19-7_10	73.92	0.32	12.41	1.65	0.05	0.36	1.92	3.90	1.69	n.d.	96.22
12-19-7_11	73.73	0.31	12.23	1.56	0.11	0.34	1.81	3.67	1.71	n.d.	95.48
12-19-7_12	72.21	0.33	12.06	1.78	0.05	0.38	1.82	3.06	1.66	n.d.	93.33
12-19-7_13	74.18	0.32	12.23	1.75	0.05	0.38	1.94	3.96	1.69	n.d.	96.50
12-19-7_14	73.63	0.28	12.19	1.70	0.07	0.34	1.90	3.83	1.76	n.d.	95.70
12-19-7_15	73.50	0.31	12.38	1.69	0.06	0.36	1.82	3.68	1.64	n.d.	95.44
12-19-7_16	73.37	0.32	12.21	1.65	0.07	0.37	1.85	3.78	1.68	n.d.	95.30
12-19-7_17	74.02	0.33	12.42	1.62	0.08	0.40	1.89	3.85	1.65	n.d.	96.26
12-19-7_18	73.81	0.34	12.40	1.63	0.09	0.34	1.81	3.90	1.70	n.d.	96.02
Average	73.41	0.32	12.22	1.66	0.06	0.37	1.86	3.66	1.70		95.27
Standard Deviation	1.03	0.02	0.26	0.07	0.02	0.02	0.04	0.31	0.06		1.52

Nata Randang Tephra

Glass Number	SiO_2	TiO_2	Al_2O_3	FeO	MnO	MgO	CaO	Na_2O	K_2O	Cl	Total
12-19-8_1	72.78	0.29	11.93	2.38	0.13	0.25	1.73	3.67	1.23	n.d.	94.39
12-19-8_2	73.83	0.29	12.23	2.64	0.12	0.31	1.82	4.21	1.34	n.d.	96.78
12-19-8_3	73.60	0.29	12.00	2.57	0.11	0.23	1.84	3.48	1.31	n.d.	95.44
12-19-8_4	73.06	0.30	12.06	2.39	0.15	0.27	1.79	3.60	1.32	n.d.	94.93
12-19-8_5	73.13	0.25	12.11	2.51	0.11	0.23	1.74	3.55	1.32	n.d.	94.95
12-19-8_6	73.94	0.25	12.23	2.48	0.20	0.26	1.84	3.99	1.30	n.d.	96.48
12-19-8_7	73.62	0.25	12.11	2.55	0.10	0.26	1.79	4.01	1.30	n.d.	95.99
12-19-8_8	72.87	0.31	11.90	2.50	0.10	0.24	1.72	3.55	1.26	n.d.	94.44
12-19-8_9	73.95	0.29	12.27	2.54	0.14	0.28	1.85	4.12	1.32	n.d.	96.76
12-19-8_10	71.74	0.25	11.89	2.42	0.15	0.26	1.76	3.22	1.23	n.d.	92.91
12-19-8_11	76.46	0.13	11.68	2.11	0.07	0.09	1.42	4.36	1.45	n.d.	97.78
12-19-8_12	73.75	0.31	12.19	2.65	0.13	0.31	1.91	4.07	1.32	n.d.	96.64
12-19-8_13	73.20	0.29	11.96	2.62	0.14	0.26	1.75	3.64	1.24	n.d.	95.10
12-19-8_14	72.71	0.26	11.81	2.44	0.15	0.27	1.73	3.20	1.28	n.d.	93.85
12-19-8_15	74.58	0.27	12.18	2.42	0.12	0.28	1.79	3.97	1.31	n.d.	96.91
12-19-8_16	72.38	0.25	11.89	2.45	0.17	0.26	1.73	3.32	1.23	n.d.	93.67
12-19-8_17	73.30	0.27	11.96	2.41	0.13	0.26	1.81	3.60	1.42	n.d.	95.15
12-19-8_18	73.35	0.29	12.13	2.54	0.11	0.25	1.77	3.92	1.29	n.d.	95.66
Average	73.46	0.27	12.03	2.48	0.13	0.25	1.77	3.75	1.30		95.44
Standard Deviation	1.00	0.04	0.16	0.13	0.03	0.05	0.10	0.34	0.06		1.30

Kolopanu Tephra

Glass Number	SiO_2	TiO_2	Al_2O_3	FeO	MnO	MgO	CaO	Na_2O	K_2O	Cl	Total
12-19-9_2	71.28	0.37	13.11	2.13	0.08	0.44	2.14	2.15	1.95	n.d.	93.65
12-19-9_3	71.03	0.40	13.03	2.03	0.11	0.49	2.07	3.21	1.85	n.d.	94.22
12-19-9_4	71.68	0.43	13.31	2.14	0.09	0.52	2.23	3.65	1.90	n.d.	95.95
12-19-9_5	71.59	0.36	13.16	2.05	0.08	0.44	2.02	3.77	1.87	n.d.	95.34
12-19-9_6	72.05	0.36	13.18	2.09	0.08	0.47	2.00	4.12	1.89	n.d.	96.24
12-19-9_7	71.51	0.41	12.99	2.16	0.06	0.48	2.26	3.04	1.91	n.d.	94.82
12-19-9_8	72.63	0.38	13.06	2.11	0.08	0.44	2.04	4.05	1.95	n.d.	96.74
12-19-9_9	70.87	0.41	12.92	2.12	0.06	0.47	2.18	2.66	1.95	n.d.	93.63
12-19-9_10	71.71	0.39	13.13	2.25	0.08	0.49	2.06	3.68	1.88	n.d.	95.65
12-19-9_11	71.67	0.38	12.74	2.14	0.07	0.45	2.09	2.17	1.98	n.d.	93.69
12-19-9_12	71.53	0.38	13.20	2.30	0.07	0.47	2.24	3.04	1.84	n.d.	95.08
12-19-9_13	72.06	0.40	13.14	2.08	0.08	0.46	1.97	2.26	2.01	n.d.	94.45
12-19-9_14	70.26	0.40	13.19	2.19	0.06	0.50	2.23	2.47	1.75	n.d.	93.06
12-19-9_15	72.12	0.38	13.09	2.09	0.06	0.45	2.02	3.83	1.86	n.d.	95.89
Average	71.57	0.39	13.09	2.14	0.08	0.47	2.11	3.15	1.90		94.89
Standard Deviation	0.59	0.02	0.14	0.07	0.01	0.03	0.10	0.71	0.07		1.14

APPENDIX 4. MINERALOGICAL COMPOSITION BY X-RAY DIFFRACTION ANALYSIS (XRD)

Table. A4.1. X-ray diffraction (XRD) analysis of samples from the Welas Caldera Complex and Kobatuwa).

List of Minerals	WLB-01 Tm	NTR-01 Tm	KBT04/1 Scl
Calcite			
Dolomite			
Albite	6.2	25.9	7.2
Anorthite	10.5	21.9	13.4
Labradorite			
Quartz	2.0	0.8	1.2
Cristobalite			
Tridymite	2.0	2.1	
Microcline			
Biotite		1.5	0.6
Hornblende	4.2		1.6
Augite			5.6
Hematite			
Gibbsite			
Diopside			
Cummingtonite	4.5	3.2	
Jadeite	2.2		
Enstatite			
Muscovite	3.0	14.2	
Apatite			
Sanidine	1.9		
Maghemite			2.3
Kaolin	19.4	13.4	19.3
Chabazite	2.3		1.7
Heulandite			
Stilbite	5.4		12.1
Faujasite	4.0	2.9	4.8
Natrolite	4.3	4.7	3.0
Clinoptilolite	10.4	6.9	5.2
Riebeckite	2.3	2.3	3.3
Illite			
Montmorillonite			18.8
Illite - Smectite			
Smectite-chlorite	15.5		
X^2 [Chi sq.]	3.52	4.28	2.88

Note: Mineral abundances are in weight percent (wt %).

Table. A4.2. X-ray diffraction (XRD) analysis of samples from Mata Menge.

List of Minerals	MM02 Pa	MM03 Tm	MM05 Pa	MM08 Pa	MM11 LTmp	MM13 Pa	MM19 Fmm	MM23 Pa	MM24 Ss	MM25 Pa
Calcite										5.7
Dolomite										
Albite	0.7					1.7	0.7			0.5
Anorthite		1.9		1.0	0.7		2.8	0.7	14.7	
Labradorite							5.7	3.9	15.7	2.4
Quartz		1.1	1.2	3.2	2.1			0.8	0.8	
Cristobalite	0.6					2	0.8			0.5
Tridymite		2.5			2.6					
Microcline						1.5				
Biotite	1.4	3.1	1.3	1.3	1.6	1.2	1.1	1.3		1.1
Hornblende	2.6	7.3	4		5.4	3.6	2.9	3.4		3
Augite										
Hematite				1.1						
Gibbsite									1.5	
Diopside										
Cummingtonite		6.8			4.9					
Jadeite		3.0			2.1					
Enstatite		2.8			2.9					
Muscovite		8.1			3.0					
Apatite										
Sanidine					3.2					
Maghemite	1.4								0.7	
Riebeckite	3.2	2.9	3.3	4.0		2.7	2.9	3.1	3.3	3
Kaolin	23.6	28.7	26.4	19.2	31.3	24.1	19.4	17.6	14.6	19.3
Chabazite	3	1.9	2.3	2.4	1.7	1.9	2.3	2.8	1.6	2.6
Heulandite	5.6		6.5	6.8		6.5	5.4	6.1		5.1
Stilbite	6.6	8.5	5.2	6.9	6.8	5.4	5.4	3.9	2.9	6.2
Faujasite	3.3	4.3	3.3	2.9	4.6	3.8	4	3.1	3.4	3.2
Natrolite	2.6		2.8	2.6	4.0	2.5	2.6	2.6	2.1	2.4
Clinoptilolite	2.1		1.1		9.9	3.7	1	0.7	8	2.9
Illite										
Montmorillonite										
Illite - Smectite	31.8		32	37.3		27	32.1	39.1	20.8	29.6
Smectite-chlorite	11.5	17.0	10.5	11.2	13.2	12.3	10.8	11.1	10.1	12.3
X^2 [Chi sq.]	2.89	3.53	2.83	2.98	3.55	3.07	2.75	2.74	2.85	2.95

Note: Mineral abundances are in weight percent (wt %).

Table. A4.2. Continued.

List of Minerals	MM26 Pa	MM27 Smm	MM28 Scl	MM29 Scl	MM30 Sm	MM31 Sl	MM33 Fh	MM35 Fh	MM36 Pa	MM37 Pa
Calcite										
Dolomite										
Albite		11	18.9	7.5	1.6	10.4		5.8	4.7	9.1
Anorthite	8.6	29.4	34	25.2	14.7	18	3.6	9.2	4.7	6.4
Labradorite	23.9				15.7	2.6	11			9.9
Quartz		0.8	0.9	0.8	0.8	3	1	1.2	0.7	0.9
Cristobalite	0.7									
Tridymite							1.2	1.1		
Microcline						2.4				
Biotite				0.4			1.5		0.9	
Hornblende		1.9			8.5		3.5		1.8	1.8
Augite		6.7	5.6	10.6	3					
Hematite					0.6					
Gibbsite										
Diopside										
Cummingtonite										
Jadeite										
Enstatite										
Muscovite										
Apatite										
Sanidine										
Maghemite	1.4	1.5	0.5	1				1.2	1	
Riebeckite	4	3	2.6	3.2	2	3.1	2.6	3.2	2.9	2.8
Kaolin	16.5	16.5	14.2	14.5	13.7	14.8	17.1	16.6	16.6	18.7
Chabazite		1.3		1.8	3.2	2.8	1.3	1.8	2.5	2.8
Heulandite				5.3	1	5.3	4.4	3.9	3.6	2.8
Stilbite	1.3	4.9	3.1	6	2.6	5.3	5.2	6.4	4.9	7.6
Faujasite	3.2	4		5.3	3.1	3.7	3.7	4.1	3.8	3.1
Natrolite	2.4	3.3	2.3	3	3.4	5.1	2.5	2.5	2.9	2.3
Clinoptilolite	5	5.6	4.5	7.6	4.4	5	1.7	1.9	3.2	2.4
Illite										
Montmorillonite		10.1		13.1						
Illite - Smectite	23.5				11.7	12.3	29.2	31	35.9	19.4
Smectite-chlorite	9.4		8.4		9.8	11.2	10.7	10	9.6	10
X^2 [Chi sq.]	2.99	2.85	3.35	2.92	2.93	3.10	2.75	2.85	2.79	3.00

Note: Mineral abundances are in weight percent (wt %).

Table. A4.2. Continued.

List of Minerals	MM38 Pa	MM39 Smm	MM40 Pa	MM41 Pa	MM42 Tm	MM43 Pa	MM44 Pa	MM45 Pa	MM46 Pa	MM47 Pa
Calcite							9.6	5.9	9.9	31.7
Dolomite										
Albite	3.6	5.3	4.4	2.6	10.8	6.3	5		2.4	1.5
Anorthite	6	14	9.2	9	11.6	14.4	13.6	12.2	5.2	
Labradorite	3	5.5		6		9.2	10.9	9.8	4.5	
Quartz	0.8	1.1	0.7	0.9	1.1	1.1	1.5	1	1.1	0.9
Cristobalite										
Tridymite										
Microcline										
Biotite	1.2	0.8		0.6	3.2	0.6			0.7	
Hornblende	2.6	2.9		3.1	3.6	2.4	1.1	4.7	2.7	4.2
Augite		4.4								
Hematite										
Gibbsite										
Diopside					3.6					
Cummingtonite					6.6					
Jadeite					2.2					
Enstatite					4.4					
Muscovite					6.2					
Apatite					1.0					
Sanidine					3.5					
Maghemite			1.1	1.3				1		
Riebeckite	2.9	2.3	3.6	2.9		2.8	2.1	2.2	3.0	2.4
Kaolin	17.9	13.6	16.1	17.3	0	16	14.7	16.3	15.5	12.9
Chabazite	2.6	15.4	2	2.4		2.7	1.9	1.9	3.1	1.9
Heulandite	3.9		3.3	3.4		2.9	3.3	2.9	3.0	
Stilbite	4.8	3.4	5.2	4.9		3.4	3.2	3.4	2.9	3.4
Faujasite	3.1	2.6	4.2	3.5		3.7	3.4	2.6	2.8	2.7
Natrolite	2.6	2.7	3.1	2.5		3.0	2.7	2.5	2.6	2.3
Clinoptilolite	2.5	5.3	3.4	3.2		3.8	1.8	4.1	3.0	4.7
Illite										
Montmorillonite										
Illite - Smectite	32.4	12.8	32.7	26.6		18.7	16.4	19.6	27.8	22.1
Smectite-chlorite	10.3	7.9	11	9.9		9.0	8.8	9.9	9.7	9.3
X^2 [Chi sq.]	2.70	3.18	2.77	2.78	3.07	2.75	2.82	2.8	2.77	2.67

Note: Mineral abundances are in weight percent (wt %).

Table. A4.2. Continued.

List of Minerals	MM48 Pv	MM49 Sh	MM50 Fh	MM51 Fh	MM52 Fh	MM53 Fh	MM54 Tm	MM55 Fh	MM57 Fh	MM58 Fh
Calcite	8.0		14.6	17.2	3.3	1.1		2.2	4.4	11.2
Dolomite										
Albite		0.7	2.6	2.3	1.9	4.1	15.7	4.0		3.5
Anorthite	1.2	1.0	3.3	4.8	3.7	5.9	16.9	6.5	17.0	7.1
Labradorite	0.6	7.5							8.9	
Quartz	1.1	0.9	0.7	0.7	0.7	0.5	0.9	0.6	1.5	0.8
Cristobalite										
Tridymite			0.9	0.8	1.1	0.7	1.1	1.2		1.2
Microcline		2.6								
Biotite	1.3						2.0			
Hornblende	3.1						2.7			
Augite										
Hematite										
Gibbsite										
Diopside							3.2			
Cummingtonite							5.0			
Jadeite							1.7			
Enstatite							3.3			
Muscovite							7.0			
Apatite							1.1			
Sanidine							2.5			
Maghemite		0.9				1.9				
Riebeckite	3.4	3.7	3.4	3.2	4.1	4.4	3.3	3.6	3.3	3.4
Kaolin	16.8	22.1	19.1	18.2	21.4	21.5	20.7	19	16.3	18.5
Chabazite	2.6	2.5	1.7	1.4	1.9	1.7	2.2	2.2	0.0	1.7
Heulandite	6.8	6.2	4.7	6.6	4.4	4.7		4.6	0.0	6.8
Stilbite	1.4	9.3	5.0	3.9	5.0	4.1	6.7	7.0	3.0	4.3
Faujasite	2.9	3.7	3.2	3.0	3.5	3.8	4.2	3.8	2.5	3.3
Natrolite	2.7	3.2	3.0	2.7	3.1	2.8		2.9	1.7	2.5
Clinoptilolite	0.5	0.1	1.8	0.0	1.8	1.9		1.2	7.3	0.3
Illite										
Montmorillonite										
Illite - Smectite	36.3	25.3	26.4	25.4	33.2	30.5		30.6	24.8	23.7
Smectite-chlorite	11.3	10.1	9.8	9.8	10.8	10.4		10.7	9.4	11.5
X^2 [Chi sq.]	2.8	2.94	2.67	2.79	2.76	2.79	3.08	2.75	3.24	2.65

Note: Mineral abundances are in weight percent (wt %).

Table. A4.2. Continued.

List of Minerals	MM59 Tm	MM60 Fh	MM62 Fh	MM64 Tm	MM65 Fh	MM66 Fh	MM68 Fh	MM70 Fh	MM71 Fh	MM73 Fh
Calcite		1.9	10.8		9.7	4.9	2.5	0.0	0.0	4.5
Dolomite					2.0					
Albite	21.9	1.7	0.5	3.1	5.9	2.0	2.9	8.5	4.2	4.1
Anorthite	40.6		0.6	20.6	10.4	3.9	5.6	11.1	11.1	4.0
Labradorite		1.1				4.4				
Quartz	0.5	1.0	0.7	1.5	1.0	1.0	1.8	1.0	1.1	1.1
Cristobalite						1.7				
Tridymite	2.1	1.3	1.0	2.4	1.3	4.8	1.9		1.8	2.1
Microcline										
Biotite	1.0			2.4						
Hornblende				2.7						
Augite										
Hematite										
Gibbsite										
Diopside	2.0									
Cummingtonite	1.2			4.9						
Jadeite				1.1						
Enstatite	5.3			5.5						
Muscovite	4.1			4.2						
Apatite										
Sanidine	2.0									
Maghemite										
Riebeckite	2.8	3.2	3.6	4.2	3.2	3.3	4.1	3.1	3.4	2.9
Kaolin	14.3	23.8	21	28.7	18.3	19.4	19.4	16.1	18.3	20.4
Chabazite		2.4	2.1		3.0	0.6	2.8	3.3	2.0	1.5
Heulandite		5.5	5.3		2.5	0.0	6.0	5.8	3.5	4.6
Stilbite		5.8	4.2	2.8	5.6	9.5	5.3	6.1	4.5	10.0
Faujasite	2.1	4.3	3.3	5.0	3.8	3.6	4.6	4.2	4.6	4.3
Natrolite		2.8	3.0		3.6	0.0	3.1	3.0	2.8	2.4
Clinoptilolite		4.1	2.0		4.1	5.5	3.7	2.3	6.4	2.1
Illite										9.4
Montmorillonite										15.2
Illite - Smectite		27.3	31.3		15.9	19.6	22.0	23.1	24.6	
Smectite-chlorite		13.7	10.5	10.9	9.6	15.8	14.2	12.1	11.4	11.4
X^2 [Chi sq.]	3.83	3.17	2.79	3.39	2.84	3.00	2.88	2.98	3.06	2.95

Note: Mineral abundances are in weight percent (wt %).

Table. A4.2. Continued.

List of Minerals	MM74 Fh	MM75 Fh	MM76 Fh	MM77 Fh	MM78 Tm	MM79 Fh	MM80 Fh	MM81 Tm	MM82 Fh	MM84 Fh
Calcite	8.6	0.8	9.9	18.2		0.9	1.5		14.9	1.3
Dolomite										
Albite	2.0	3.3	1.2	1.3	25.6	4.2		7.9	1.3	2.7
Anorthite	3.4	5.6		2.7	27.8	7.2	1.8	9.2	1.6	3.4
Labradorite			1.1							
Quartz	1.1	0.9	0.8	0.7	0.6	0.9	0.8	0.8	0.8	1.1
Cristobalite										
Tridymite	1.3	1.0	0.9	0.8	1.5	1.1	1.7	1.4	1.5	1.6
Microcline								2.1		
Biotite		1.5	1.3		3.6					
Hornblende		2.9	3.9					4.9		
Augite										
Hematite										
Gibbsite										
Diopside					1.9			4.6		
Cummingtonite					2.9			7.1		
Jadeite								2.4		
Enstatite					4.2			4.6		
Muscovite					7.4			2.0		
Apatite										
Sanidine					2.7					
Maghemite						0.7				
Riebeckite	3.3	3.5	3.4	3.6	2.6	3.5	3.9	3.3	3.2	4.0
Kaolin	24	19.4	21.3	19.9	16.6	19.2	23.6	25.4	19.1	22.1
Chabazite	2.0	2.7	2.1	1.9		2.3	1.7	2.9	1.9	2.9
Heulandite	5.4	5.2	6.0	4.5		5.2	5.3		5.1	5.2
Stilbite	8.1	3.7	5.3	5.7		4.9	7.0	4.3	6.4	6.4
Faujasite	3.9	4.5	3.7	3.5	2.5	4.8	3.2	3.9	2.9	4.3
Natrolite	2.9	3.0	3.0	2.5		2.8	2.8		2.5	3.2
Clinoptilolite	2.4	5.1	1.6	2.5		3.8	0.8		1.4	4.6
Illite										
Montmorillonite										
Illite - Smectite	18.8	23.1	24.6	21.9		25.2	35.2		27.1	24.2
Smectite-chlorite	12.7	12.3	10.0	10.5		13.1	10.6	13.2	10.4	13.2
X^2 [Chi sq.]	2.86	2.96	2.79	2.95	3.27	2.92	2.87	3.01	2.71	2.99

Note: Mineral abundances are in weight percent (wt %).

Table. A4.2. Continued.

List of Minerals	MM86 Fh	MM87 Fh	MM88 Fh	MM89 Tm	MM90 Fh	MM91 Tm	MM92 Tm	MM93 Fh	MM94 Tm	MM95 Tm
Calcite	2.5	19.2	17.3		0.6					
Dolomite										
Albite	2.9	1.3	0.8	14.3	4.4	5.2	4.1	4.0	8.8	2.7
Anorthite	4.2	2.0	1.4	41.8	7.1	33.3	8.1	9.6	24.1	4.0
Labradorite										
Quartz	0.7	0.7	0.8	1.1	1.3	0.7	0.8	0.6	0.7	1.5
Cristobalite										
Tridymite	1.1	0.6	0.7	1.6	1.8	1.7	2.0	2.1	1.1	3.0
Microcline				1.0			3.2	5.4		
Biotite						1.3	2.5	4.4	1.0	3.5
Hornblende						3.0	4.2	4.2	1.5	5.0
Augite										
Hematite										
Gibbsite										
Diopside				1.2		2.4			1.3	
Cummingtonite						3.6	4.4	5.7	3.2	6.1
Jadeite						1.8	2.1	1.7		2.4
Enstatite				4.4		5.9	1.2	4.0	5.4	3.2
Muscovite				3.9		1.8	4.3	4.3	6.1	4.9
Apatite										
Sanidine						3.6	1.7	1.7		3.2
Maghemite	1.1				0.9					
Riebeckite	4.2	3.5	3.3	3.5	3.9	2.6	2.6	2.3	3.1	2.6
Kaolin	24.2	20.4	18.8	14.2	17.9	15.4	20.8	22.0	22.1	24.9
Chabazite	1.6	2.2	2.1		2.6		1.7	1.6	2.0	1.9
Heulandite	5.6	4.7	4.8		4.5					
Stilbite	4.1	3.5	3.6		5.6	2.6	5.9	5.9	3.1	9.6
Faujasite	4.4	3.5	3.3	2.1	4.3	3.2	3.8	3.8	3.5	4.5
Natrolite	2.9	3.1	2.6		2.9		4.2			
Clinoptilolite	2.6	2.4	2.7		4.0		8.1			
Illite										
Montmorillonite										
Illite - Smectite	27.1	22.0	27.5		25.3					
Smectite-chlorite	10.7	10.8	10.6	10.8	12.8	12.0	14.1	16.6	13.0	16.8
X^2 [Chi sq.]	2.91	2.74	2.75	3.35	2.86	3.03	3.05	3.30	3.0	3.30

Note: Mineral abundances are in weight percent (wt %).

Table. A4.2. Continued.

List of Minerals	MM98 Fh	MM99 Fh	MM100 Fh	MM101 Fh	MM102 Fh	MM103 Tm	MM105 Tm	MM106 Fh	MM108 Tm	MM110 Fh
Calcite	5.5	10.6	4.5	5.9	3.0			18.0		0.9
Dolomite										
Albite	1.2	2.3	5.5	4.9	4.5	6.9	8.6	1.7		1.6
Anorthite	2.2	3.2	11.9	8.6	7.8	25.5	11.8	1.9	15.5	4.0
Labradorite										
Quartz	0.9	0.7	0.8	0.7	1.0	0.9	0.9	0.9	1.5	1.0
Cristobalite										
Tridymite	1.3	1.0	0.8	0.7	0.8	1.4	1.2		2.0	2.1
Microcline										
Biotite						2.4	0.8		1.4	
Hornblende						0.8	2.7		2.2	
Augite										
Hematite										
Gibbsite										
Diopside										
Cummingtonite						3.5	4.2		4.5	
Jadeite						1.6	2.1		1.9	
Enstatite						5.6			1.2	
Muscovite						2.3	5.4		3.6	
Apatite										
Sanidine						1.1	2.1		2.4	
Maghemite				1.8						
Riebeckite	3.6	3.9	3.8	3.4	3.0	2.5	3.1	3.1	2.5	3.6
Kaolin	20.5	23	18.1	17.9	17.7	17.5	21	19.6	22.2	23.2
Chabazite	2.2	1.9	1.8	2.0	2.9		1.7	2.6	1.6	1.7
Heulandite	4.9	5.1	6.2	4.4	3.3			4.5		5.2
Stilbite	6.5	3.5	3.7	4.8	4.5		6.7	4.1	8.0	7.4
Faujasite	3.5	3.9	4.3	4.3	3.8	3.9	4.7	3.9	4.2	3.9
Natrolite	3.0	2.5	2.3	2.6	2.6	2.1	3.8	2.5	3.3	2.8
Clinoptilolite	2.7	3.2	2.3	2.0	3.5	8.9	6.9	3.1	8.3	2.0
Illite										
Montmorillonite										
Illite - Smectite	29.1	24.4	21.9	25.3	25.9			23.2		29.3
Smectite-chlorite	12.8	10.9	12.1	10.4	10.1	13.2	12.4	10.9	13.7	11.3
X^2 [Chi sq.]	2.76	2.78	2.81	2.79	2.78	3.29	2.91	2.86	3.07	2.95

Note: Mineral abundances are in weight percent (wt %).

Table. A4.2. Continued.

List of Minerals	MM111 Fh	MM112 Fh	MM114 Fh	MM117 Fh	MM118 Tm	MM120 Fh	MM122 Lm	MM123 Tm	MM124 Tm	MM125 Lm
Calcite	21.7	1.9	7.1	28.4		11.3	61.7			37.5
Dolomite										
Albite	1.5	1.5	2.7	1.1	11.6	3.0	1.5	21.2	18.6	4.2
Anorthite	2.9	3.3	5.6	6.7	35.8	6.5	3.3	23.2	18.8	10.5
Labradorite										
Quartz	0.9	1.0	1.1	1.1	0.8	0.6		0.8	0.8	
Cristobalite										
Tridymite	0.5	0.6	1.0	0.5	1.5	0.7				
Microcline			3.1							
Biotite								1.5	1.5	
Hornblende								1.1	0.8	
Augite										
Hematite										
Gibbsite										
Diopside										
Cummingtonite					2.0			3.0	3.3	
Jadeite					1.8			0.8	2.1	
Enstatite					1.4			3.7	3.8	
Muscovite					6.9			5.3	4.6	
Apatite										
Sanidine									3.2	
Maghemite										
Riebeckite	3.3	3.7	4.1	3.0	3.4	3.6		2.1	2.3	
Kaolin	17.3	21.8	18.8	14.8	11.7	16.6	17.2	11.8	13.6	14.3
Chabazite	2.7	3.2	2.2	1.5		1.8	2.1	3.2	1.9	1.8
Heulandite	4.1	6.5	4.9	2.9		3.3				
Stilbite	2.6	4.5	5.5	3.0	2.5	3.7	1.8	1.2	3.9	3.2
Faujasite	3.6	3.8	4.1	3.3	3.9	3.4		2.7	3.3	
Natrolite	3.0	3.2	2.6	2.4	3.6	2.5		3.9	2.4	
Clinoptilolite	3.4	1.4	2.3	3.7	4.5	3.2		6.2	5.6	
Illite										
Montmorillonite										
Illite - Smectite	20.5	26.5	23.7	18.0		28.6				17.2
Smectite-chlorite	11.8	13.6	11.4	9.7	8.7	11.0	12.4	8.5	9.5	11.2
X^2 [Chi sq.]	2.87	2.88	2.78	2.71	3.02	2.65	2.70	2.81	2.76	2.72

Note: Mineral abundances are in weight percent (wt %).

Table. A4.2. Continued.

List of Minerals	MM128 Lm	MM130 Tm	MM131 Tm	MM132 Tm
Calcite	63.4			
Dolomite				
Albite	1.7	16.1	13.9	6.0
Anorthite	2.3	65	13.5	3.8
Labradorite				
Quartz		0.7	1.7	1.5
Cristobalite				
Tridymite		1.5	3.0	2.2
Microcline				
Biotite		3.2	0.9	0.7
Hornblende			3.5	4.3
Augite				
Hematite				
Gibbsite				
Diopside				
Cummingtonite		0.9	3.6	4.9
Jadeite			1.9	2.3
Enstatite		12.4	2.0	1.2
Muscovite			4.1	4.1
Apatite				
Sanidine			1.6	3.1
Maghemite				
Riebeckite			2.4	3.1
Kaolin	16.8	0	17.3	26.8
Chabazite	2.5			1.1
Heulandite				
Stilbite	2.1		9.5	8.1
Faujasite			3.3	4.0
Natrolite			3.5	3.6
Clinoptilolite			4.4	6.7
Illite				
Montmorillonite				
Illite - Smectite				
Smectite-chlorite	11.2		9.9	12.3
X^2 [Chi sq.]	2.66	5.05	2.7	3.09

Note: Mineral abundances are in weight percent (wt %).

Table. A4.3. X-ray diffraction (XRD) analysis of samples from Wolo Sege.

List of Minerals	WS18 Ts	WS19 LTmp	WS22 Pa	WS23 Tm	WS24 Pa	WS28 Pa	WS30 Pa
Calcite							
Dolomite							
Albite		4.9	9.9	1.1	4	1.6	1.8
Anorthite	4.1	9.4	6.7	4.5	13.8	16.5	6
Labradorite					7.9	12.4	10.1
Quartz	1.8	1.7	1.5	1.5	0.9	1.1	3.1
Cristobalite							
Tridymite	2.1	2.1	1.9	1.6			
Microcline							
Biotite	3.4	3.6	1.7	3.3	0.9	1.0	0.8
Hornblende	4.2	2.2	3.8	4.5		2.2	1.1
Augite							
Hematite							
Gibbsite							
Diopside							
Cummingtonite	4.8	4.3	4.8	4.8			
Jadeite	2.6	1.6	1.8	2.1			
Enstatite			0.8	1.2			
Muscovite	4.5	5.6	6.7	3.7			
Apatite				0.6			
Sanidine	4.5	3.0	3.2	4.9			
Maghemite					1.3		
Kaolin	20.4	19.3	24.7	20.0	17.6	14.8	17.6
Chabazite	2.6	1.9	1.9	2.9	2.6	3.1	2
Heulandite					3.7	2.1	4.7
Stilbite	7.5	4.4	3.4	6.8	1.9	3.9	4.4
Faujasite	4.4	4.0	3.1	4.7	4.1	3.8	3.2
Natrolite	4.1	4.0	4.1	3.5	3	3.0	2.9
Clinoptilolite	10.5	10.7	6.4	10.1	3.3	3.9	2.4
Riebeckite	2.1	2.1	2.8	2.2	3.5	3.4	3
Illite							
Montmorillonite							
Illite - Smectite					18.7	15.1	26.8
Smectite-chlorite	16.4	15.2	10.8	16.0	9.7	12.1	10.2
X^2 [Chi sq.]	3.50	3.61	2.95	3.35	2.81	2.73	2.86

Note: Mineral abundances are in weight percent (wt %).

Table. A4.3. Continued.

List of Minerals	WS36 Pa	WS37 Pa	WS38 Pa	WS41 Pa	WS44 Sm	WS45 Pa	WS46 Pa
Calcite							
Dolomite							
Albite	2.2	0.5			10.8		1.6
Anorthite	5.4	3.8		5.2	22.2	7.1	5.0
Labradorite	5.6	7.6	1.4	9.4		17.0	10.5
Quartz	0.7	0.7	1.9	0.8	0.7	0.6	1.2
Cristobalite							
Tridymite							
Microcline							
Biotite	1.1	1.4	1.4	0.7	0.3		0.8
Hornblende	2.8	2.7	3.0	4.1	2.0	2.5	3.4
Augite					2.8		
Hematite							
Gibbsite							
Diopside							
Cummingtonite							
Jadeite							
Enstatite							
Muscovite							
Apatite							
Sanidine							
Maghemite				0.8	2.1	1.3	2.2
Kaolin	18.7	17.5	13.7	15.6	17.8	17.8	18.0
Chabazite	2.7	4.1	2.7	1.8		1.3	2.4
Heulandite	5.7	4.4	6.6	4.2	0.9	5.9	3.7
Stilbite	4.7	3.2	2.5	3.3	4.6	3.9	5.1
Faujasite	3.8	3.2	2.7	3.3	4.9	3.7	3.5
Natrolite	2.8	3.3	2.9	3.1	2.8	2.0	3.0
Clinoptilolite	1.5	2.1		2.5	7.0	0.7	2.4
Riebeckite	3.5	3.1	3.1	2.7	3.2	2.9	2.9
Illite							
Montmorillonite					17.9		
Illite - Smectite	27.9	32.1	47.0	32.1		23.3	24.4
Smectite-chlorite	10.9	10.3	11.0	10.1		9.9	9.9
X^2 [Chi sq.]	2.72	2.76	2.74	2.74	2.92	2.83	2.70

Note: Mineral abundances are in weight percent (wt %).

Table. A4.4. X-ray diffraction (XRD) analysis of samples from Tangi Talo.

List of Minerals	TT01 Pa	TT02 Tm	TT03 Pa	TT05 Fm	TT06 Fmm	TT08 Fmm	TT10 Pa	TT11 Pa	TT12 Pa	TT14 Fm
Calcite										
Dolomite										
Albite				2.5	4.1	3.1	1.6	1.9	4.4	1.7
Anorthite	9.9	6.5	12.2	2.5	9.4	2.5	3.0	5.4	3.2	7.0
Labradorite							5.5		6.2	17.2
Quartz	5.9	0.8	2.2	2.1	1.8	2	0.8	0.6	1.6	1.0
Cristobalite										
Tridymite										
Microcline										
Biotite	1.3	2.2	1.5	0.9	0.7	0.9	1.0		0.5	
Hornblende		2.6		0.9		3.8	2.6		2.4	2.5
Augite										
Hematite	1.2		1.6	1.3	1.7	1.1				
Gibbsite										
Diopside		1.2								
Cummingtonite		6.8								
Jadeite										
Enstatite		3.4								
Muscovite										
Apatite										
Sanidine										
Maghemite							1.5		1.6	2.6
Kaolin	15.2	4.5	14.5	17.0	21.4	18.8	17.9	19.4	18.2	14.0
Chabazite	2.6		2.4	2.5	1.7	2.5	1.7	2.3	2.3	2.0
Heulandite	6.6		6.4	4.9	5.4	5.2	5.8		5.2	2.8
Stilbite	6.8	8.2	7.3	5.7	8.7	5.6	7.2	14.1	8.8	5.5
Faujasite	4.0	5.1	4.0	3.2	3.6	3.7	2.3	2.8	3.1	2.6
Natrolite	2.3		2.6	2.4	2.1	2.6	2.3	2.9	2.1	2.7
Clinoptilolite				1.9		2.1		5.1		1.1
Riebeckite	3.2	1.6	2.7	2.6	2.9	2.7	2.9	2.6	2.4	2.4
Illite										
Montmorillonite										
Illite - Smectite	28.6	57.3	29.3	37.7	24.9	31.9	33.3	30.8	28.1	24.6
Smectite-chlorite	12.4		13.3	11.8	11.7	11.5	10.4	12.2	9.9	10.1
X^2 [Chi sq.]	3.09	3.81	3.06	2.86	2.85	2.81	2.74	3.11	2.73	2.73

Note: Mineral abundances are in weight percent (wt %).

Table. A4.4. Continued.

List of Minerals	TT17 Pa	TT18 Tm	TT20 Sl	TT22 Pa	TT26 LTmp	TT28 Ts	TT29 LTmp
Calcite							
Dolomite							
Albite	4.0	6.3	5.8		6.1	3.6	2.1
Anorthite	3.7	3.6	12.5	4.2	3.1	4.5	4.0
Labradorite							
Quartz	0.8	1.6	7.5	1.4	2.8	3.0	1.6
Cristobalite							
Tridymite		2.5			1.5	2.0	1.9
Microcline							
Biotite	1.3	1.5			2.4	2.8	3.8
Hornblende		2.2		2.7	2.7	5.1	3.9
Augite				2.5			
Hematite							
Gibbsite							
Diopside							
Cummingtonite		5.9			6.0	4.8	4.9
Jadeite		1.9			1.9	2.6	2.3
Enstatite		3.0			2.8		1.7
Muscovite						4.4	5.2
Apatite					1.4		
Sanidine		1.1			3.3	4.0	4.2
Maghemite	1.5		2.6				
Kaolin	16.9	0.0	16.5	15.2	0.0	19.8	19.6
Chabazite	2.5	2.1	2.8	3.0	2.4	2.3	2.5
Heulandite	4.3		3.5	2.9			
Stilbite	6.7	7.7	8.0	9.4	8.0	6.9	6.1
Faujasite	3.2		3.7	2.3	4.7	4.0	4.2
Natrolite	2.3		2.3	3.5		4.0	3.6
Clinoptilolite	1.1		2.8	3.9		8.4	10.6
Riebeckite	3.3	2.0	3.0	2.5	1.9	2.5	2.0
Illite							
Montmorillonite							
Illite - Smectite	36.3	54.2	18.3	36.1	49.0		
Smectite-chlorite	12.2		10.9	10.3		15.3	15.6
X^2 [Chi sq.]	2.80	3.55	2.91	3.08	3.65	3.41	3.59

Note: Mineral abundances are in weight percent (wt %).

Table. A4.5. X-ray diffraction (XRD) analysis of samples from the Lowo Mali, Matago, Kopowatu and Gero.

List of Minerals	LM-01 Pa	LM-02 Tm	LM-03 Ts	LM-04 LTmp	LM-09 LTmp	LM-10 Pa	LM-11 Ts	LM-13 Tm	LM-14 Tm
	Lowo Mali								
Calcite									
Dolomite									
Albite		13.2	12.9				5.1		9.1
Anorthite	3.7	8.6	14.8	6.4	3.2	16.0	8.0	2.7	9.8
Labradorite									
Quartz	0.9	1.5	0.9	1.9	1.8	3.8	1.9	1.2	2.6
Cristobalite									
Tridymite		1.3	2.4		2.1		2.1	1.8	1.5
Microcline									
Biotite		2.6	2.3	1.2	3.4		3.4	3.2	
Hornblende		3.0			5.9		2.7	5.1	10.4
Augite									
Hematite	1.4			1.2					
Gibbsite									
Diopside									
Cummingtonite		4.9	4.5		4.8		4.4	5.4	3
Jadeite		1.6			2.6		1.9	2.9	1.4
Enstatite		3.6	3.9					1.4	
Muscovite		5.0	5.4				3.8	7.3	
Apatite									
Sanidine			1.9	5.6			3.4	4.1	3.3
Maghemite									
Kaolin	12.2	17.2	16.8	22.4	20.5	12.9	19.1	21.6	16.2
Chabazite	3.5	2.4		2.0	2.8	1.9	2.0	2.9	1.7
Heulandite	7.1			5.5		6.3			
Stilbite	7.9	3.1	4.9	7.6	8.1	6.5	5.1	6.3	3.1
Faujasite	3.3	3.9	4.0	3.8	4.6	3.9	4.2	3.8	3.8
Natrolite	2.9	3.1	3.1	2.1	4.3	3.5	3.9	3.9	3.8
Clinoptilolite		8.8	7.7	3.3	10.7	3.3	11.1	8.3	8.2
Riebeckite	2.6	2.2	2.3	3.3	2.2	3.3	2.3	2.3	7.9
Illite									
Montmorillonite									
Illite - Smectite	38.3			30.1		28.2			
Smectite-chlorite	13.4	12.7	12.1	10.2	17.6	11.1	15.6	15.9	14.3
X^2 [Chi sq.]	3.17	3.13	3.22	3.08	3.67	3.10	3.70	3.52	3.50

Note: Mineral abundances are in weight percent (wt %).

Table. A4.5. Continued.

List of Minerals	MTG-07 Pa Matago	KPW-01 Tm Kopowatu	GL-01 Lv Gero
Calcite			
Dolomite			
Albite			20.3
Anorthite	10.9	4.9	33.4
Labradorite			
Quartz	2.0	1.6	
Cristobalite			
Tridymite		1.7	
Microcline			
Biotite		3.3	
Hornblende		5.3	5.6
Augite			
Hematite	1.1		
Gibbsite			
Diopside			7.8
Cummingtonite		4.8	8.3
Jadeite		2.7	5.3
Enstatite			5.4
Muscovite		3.5	
Apatite			
Sanidine		5.2	
Maghemite			
Kaolin	13.2	20.3	
Chabazite	1.7	2.7	
Heulandite	6.2		
Stilbite	6.6	6.6	
Faujasite	4.8	4.3	
Natrolite	2.5	4.1	
Clinoptilolite		10.6	
Riebeckite	2.5	2.1	
Illite			
Montmorillonite			
Illite - Smectite	35.8		
Smectite-chlorite	10.3	16.4	
X^2 [Chi sq.]	3.10	3.54	3.71

Note: Mineral abundances are in weight percent (wt %).